Universidade de Aveiro
2021

RICARDO NAZARÉ SERRAZINA

SINTERIZAÇÃO FLASH DE ÓXIDOS DE PEROVESQUITES SEM CHUMBO PARA O PROCESSAMENTO SUSTENTÁVEL DE MATERIAIS PARA APLICAÇÕES EM ENERGIA

FLASH SINTERING OF LEAD FREE PEROVSKITE OXIDES TOWARDS SUSTAINABLE PROCESSING OF MATERIALS FOR ENERGY AND RELATED APPLICATIONS

Universidade de Aveiro
2021

RICARDO NAZARÉ
SERRAZINA

FLASH SINTERING OF LEAD FREE PEROVSKITE OXIDES
TOWARDS SUSTAINABLE PROCESSING OF MATERIALS
FOR ENERGY AND RELATED APPLICATIONS

Universidade de Aveiro
2021

RICARDO NAZARÉ SERRAZINA

SINTERIZAÇÃO FLASH DE ÓXIDOS DE PEROVESQUITES SEM CHUMBO PARA O PROCESSAMENTO SUSTENTÁVEL DE MATERIAIS PARA APLICAÇÕES EM ENERGIA

FLASH SINTERING OF LEAD FREE PEROVSKITE OXIDES TOWARDS SUSTAINABLE PROCESSING OF MATERIALS FOR ENERGY AND RELATED APPLICATIONS

Universidade de Aveiro
2021

RICARDO NAZARÉ SERRAZINA

SINTERIZAÇÃO FLASH DE ÓXIDOS DE PEROVESQUITES SEM CHUMBO PARA O PROCESSAMENTO SUSTENTÁVEL DE MATERIAIS PARA APLICAÇÕES EM ENERGIA

FLASH SINTERING OF LEAD FREE PEROVSKITE OXIDES TOWARDS SUSTAINABLE PROCESSING OF MATERIALS FOR ENERGY AND RELATED APPLICATIONS

Tese apresentada à Universidade de Aveiro para cumprimento dos requisitos necessários à obtenção do grau de Doutor em Materiais e Processamento Avançados realizada sob a orientação científica da Doutora Paula Maria Lousada Silveirinha Vilarinho, Professora Associada do Departamento de Engenharia de Materiais e Cerâmica da Universidade de Aveiro, e sob a coorientação do Doutor Luis Miguel Nunes Pereira, Professor Associado do Departamento de Ciência dos Materiais da Universidade NOVA de Lisboa e da Doutora Ana Maria Rocha de Oliveira e Senos, Professora Associada do Departamento de Engenharia de Materiais e Cerâmica da Universidade de Aveiro

Apoio financeiro da FCT e do FSE no âmbito do III Quadro Comunitário de Apoio

I dedicate this work to my family and, specially, to Daniela, for always believing in its realization and in my capabilities. Thanks for all the love, companionship, and patience.

Dedico este trabalho à minha família e, em especial, à Daniela, que sempre acreditou na sua concretização e na minha capacidade. Obrigado pelo amor, companheirismo e paciência.

o júri

presidente	Prof. Doutor Nuno Miguel Gonçalves Borges de Carvalho Full professor from University of Aveiro, Portugal
vogais	Prof. Doutor Michael John Reece Full professor from Queen Mary University of London, UK
	Prof. Doutor Jian Luo Full professor from University of California, San Diego, USA
	Prof. Doutor Manuel Fernando Gonçalves Vieira Associated professor from University of Porto, Portugal
	Prof. Doutor Florinda Mendes da Costa Associated professor from University of Aveiro, Portugal
	Prof. Doutor Paula Maria Lousada Silveirinha Vilarinho Associated professor from University of Aveiro, Portugal (supervisor)

agradecimentos

To my family, in special to my mother that always supported me and my decisions, and to my life partner Daniela for all the love and support.

To the supervision team for providing me with the right tools, collaborations, and environment for the healthy development of this work. All the scientific and non-scientific arguments will follow me through the years. A greet to Dr. Alexander Tkach for the help on ferroelectric analysis.

To all DEMaC/CICECO technical and administrative staff, with a special note for Ana Ribeiro, Célia Miranda, Tiago Silva, Marta Ferro, Artur Sarabando, Rosário Soares, Octávio Contente, Jacinto Alves, Luísa Costa and Alexandra Vale for the collaboration and assistance when needed.

To José Diogo Oliveira and Miguel Machado, from Vhelsi; to Eng. Francisco Simões, António José and technical and administrative staff from Termolab, for accepting the challenge of building our custom equipment; without it, this work would not be possible.

To Dr. Alexandre Bastos and prof. Mário Ferreira for being available and allowing the use of computing facilities at their laboratories.

To professor Ian M. Reaney, Dr. Julian Dean and the University of Sheffield for welcoming me at Sir Robert Hadfield Building and allowing me to develop skills and expertise in a completely new field for me and our research group.
To JECS trust for funding this stay in Sheffield (Contract No. 2018193)

To prof. Joaquim Agostinho, Dr. Rui Vilarinho Silva, Mariana Gomes, and University of Porto for providing the conditions for the Raman characterization of our materials

To Dr. Sabyasachi Saha, Dr. Leonard Francis and Prof. Paulo Ferreira from INL for the collaboration on TEM observation and analysis.

To my laboratory colleagues and friends, in special Pedro Duarte, Rui Pinho, André Santos, Camila Ribeiro, Anna Wlódarkiewicz and Joana Sousa. To my home and work friends that, by one way or another, participated on my daily fights, in special João Carvalheiras, Inês Oliveira, Ricardo Silva, Violeta Girão and Monica Faria. A special thanks to Dr. José Carlos Almeida for scientific and personal advice. My gratitude to the master students, Nuno Ferreira, Luis Figueiredo, Isabel Gomes and Madalena Roque, that accepted the challenge of working in this new field; by one way or the other, they have helped me reaching this stage.

To FCT for the financial support (SFRH/PD/BD/128411/2017 and POCI-01-0247-FEDER-029078) and CICECO - University of Aveiro (UIDB/50011/2020 & UIDP/50011/2020) for hosting this work.

palavras-chave

Sinterização por FLASH, sinterização, cerâmicos, piezoelétricos, KNN, sinterização a baixa temperatura, técnicas alternativas de sinterização, microestrutura, MEF, propriedades elétricas.

resumo

Piezoelétricos como o $K_{0.5}Na_{0.5}NbO_3$ (KNN) têm uma importância emergente devido à sua natureza livre de chumbo e variada aplicabilidade em componentes como sensores, atuadores, dispositivos de recolha de energia, biossensores, etc. No entanto, o KNN monofásico continua a ser difícil de produzir devido à elevada temperatura e tempo associados ao processo de sinterização convencional.

Este doutoramento propõe a utilização de um método alternativo de densificação, a sinterização FLASH, que acima de uma condição limite promove a densificação repentina de cerâmicos por uma combinação de ambiente do forno (atmosfera e/ou temperatura) com a aplicação de campo elétrico diretamente no material. Existem vários mecanismos reportados para explicar a sinterização FLASH. O aquecimento por efeito de Joule é um dos mais reportados e aceites, mas também têm sido sugeridos mecanismos envolvendo a criação e movimento de defeitos por efeito do campo elétrico. Uma compreensão clara do fenómeno continua por ser apresentada, mas muito provavelmente a sinterização por FLASH resulta duma combinação destes dois efeitos, sendo que a energia e condutividade das superfícies das partículas desempenham um papel fundamental.

Este trabalho pretende explorar a sinterização por FLASH de cerâmicos, mas também estudar os seus fenómenos fundamentais, mais especificamente, na sinterização FLASH de KNN. O objetivo último deste trabalho é o desenvolvimento de processos de sinterização de cerâmicos que operem à temperatura ambiente, contribuindo para a economia energética e sustentabilidade da indústria cerâmica.

A utilização de ferramentas de Modelação por Elementos Finitos (MEF, ou FEM) permitiu estudar o efeito da orientação das partículas na geração de calor por efeito de Joule durante o FLASH, enquanto a modelação da distribuição temperatura local e respetivos gradientes térmicos foram usados para explicar tensões induzidas em cerâmicos densos. A produção de pós de KNN com diferentes tamanhos e pureza permitiu estabelecer a sua relação com a temperatura de FLASH (T_F). Em consequência, o estabelecimento de um ciclo térmico apropriado, antes da aplicação do campo elétrico, permitiu obter cerâmicos de KNN com densidade relativa de 95%. A ligação entre os parâmetros de FLASH, como densidade de corrente e tempo, foi determinada, e a relação com a densidade final e tamanho de grão dos cerâmicos foi estudada. Estudos em TEM e FEM permitiram propor um mecanismo para a sinterização por FLASH de KNN, em que o fluxo de corrente pelas superfícies das partículas promove uma fusão parcial nos seus contactos e o rearranjo para a remoção de poros e densificação do compacto.

De forma a permitir um decréscimo acentuado na T_F do KNN, a sinterização FLASH assistida por atmosfera foi apresentada, e a temperatura foi diminuída para $T_F \approx 265$ ºC. No entanto, a densificação final foi limitada aos 79%.

As propriedades ferroelétricas e dielétricas do KNN sinterizado por FLASH foram estudadas e comparadas com as de cerâmicos sinterizados convencionalmente. Um desempenho semelhante entre ambos foi obtido após um tratamento térmico para cura de elétrodos. No entanto, uma análise detalhada mostrou que as propriedades são afetadas pelo processo de FLASH em cerâmicos tratados ou não termicamente.

Este trabalho apresenta uma contribuição clara no desenvolvimento da sinterização FLASH de cerâmicos, especificamente, no piezoelétrico KNN.

keywords

FLASH sintering, sintering, ceramics, piezoelectrics, KNN, low temperature sintering, alternative sintering techniques, microstructure, FEM, electrical properties.

abstract

Piezoelectrics as $K_{0.5}Na_{0.5}NbO_3$ (KNN) have currently an emerging importance due to their lead-free nature and high transition temperature, which permits a wide range of high-tech applications as sensors, actuators, energy harvesters, biosensors, etc. However, monophasic dense KNN products are yet difficult to obtain, due to the high temperature and long time of conventional sintering processes.

This PhD proposes a new method to densify materials abruptly above a threshold condition using FLASH sintering, where the densification occurs by a combination of furnace environment (temperature and/or atmosphere) and electrical field directly applied to the specimen. There are several proposed mechanisms for FLASH. Joule heating is the most reported one, but also defect-related theories have been proposed. The phenomena are not yet completely understood, but most probably, FLASH sintering is a combination of both effects, with particle surfaces energy and conductivity performing a significant role.

The present work aims to exploit FLASH for sintering of KNN ceramics but also to depict the fundamental phenomena behind FLASH sintering, and specifically, FLASH sintering of KNN. The ultimate goal is to develop sintering of ceramics towards room temperature, contributing to the energy economy low thermal budget of ceramic industry.

The use of Finite Element Modelling (FEM) tools allowed to study the particle orientation effect on the Joule heating during FLASH, while the simulated temperature gradients were used to explain the presence of FLASH sintering-induced stresses in dense ceramics. The production of different size and purity KNN powders permitted to establish the link between FLASH temperature (T_F) and particle size/purity. Following, the establishment of an engineered thermal cycle before the application of the electric field for the FLASH was responsible for increasing the final densification of KNN ceramics to 95%. The link between FLASH parameters, as current density and holding time, was determined and the relationship with final density and grain size of ceramics studied. TEM and FEM studies allowed to propose a FLASH sintering mechanism for KNN, in which the current flow through particles' surfaces promotes the partial melting of contacts and the particle sliding towards pore removal and compact densification.

To allow a significant decrease on the T_F of KNN, atmosphere-assisted FLASH sintering (AAFS) was presented, and the temperatures were decreased to $T_F \approx$ 265 ºC, however, the final densification was limited to 79%.

The ferroelectric and dielectric performance of FLASH sintered KNN was studied and compared with that of conventionally sintered ceramics. Similar performance was attained after a heat treatment for electrode cure; however, a detailed analysis revealed FLASH sintering-fingerprints in both as-sintered and heat-treated ceramics.

This work presents a clear contribution for the development of FLASH sintering in ceramics, namely in piezoelectric KNN.

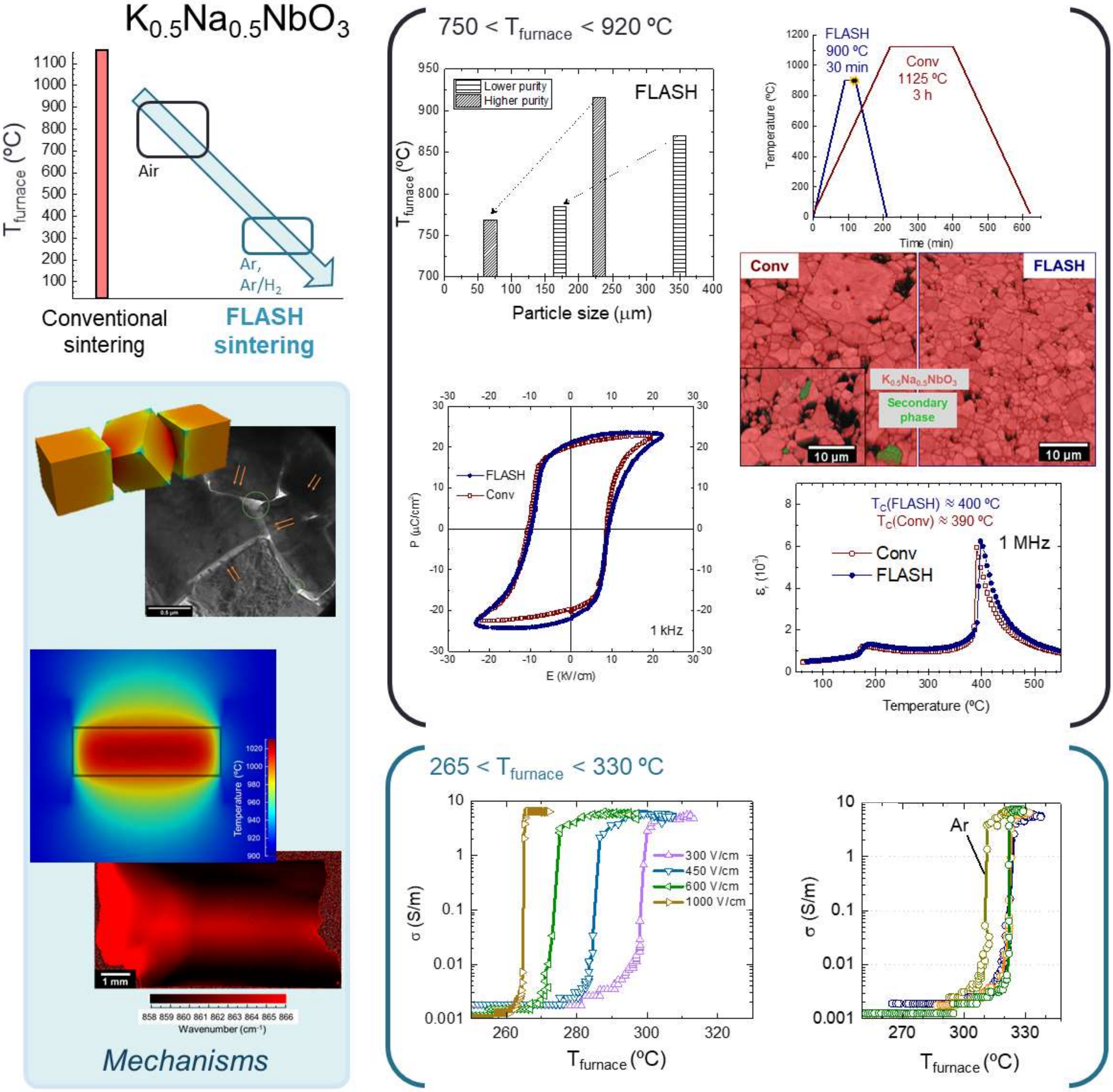
K0.5Na0.5NbO3
Tfurnace (ºC)
Air
Ar,
Ar/H2
Conventional sintering
FLASH sintering
Mechanisms
750 < Tfurnace < 920 ºC
Lower purity
Higher purity
FLASH
Particle size (μm)
Temperature (ºC)
Time (min)
FLASH 900 ºC 30 min
Conv 1125 ºC 3 h
Conv
FLASH
K0.5Na0.5NbO3
Secondary phase
10 μm
10 μm
P (μC/cm²)
E (kV/cm)
1 kHz
TC(FLASH) ≈ 400 ºC
TC(Conv) ≈ 390 ºC
1 MHz
εr (10³)
Temperature (ºC)
Temperature (ºC)
Wavenumber (cm⁻¹)
1 mm
0.5 μm
265 < Tfurnace < 330 ºC
σ (S/m)
300 V/cm
450 V/cm
600 V/cm
1000 V/cm
Tfurnace (ºC)
Ar
σ (S/m)
Tfurnace (ºC)

General Index

Figure Index

Table Index

Nomenclature

The following list gives the abbreviations and symbols used to describe variables, techniques, or quantities throughout this work. When no other indication is given through the text, the units used to describe each variable are shown between brackets.

A	
A	Material parameter (sintering theory)
A_a	Area of an adsorbed gas molecule
A_S	Section area (mm^2)
A_e	Electrode area (mm^2)
A_C	Curie constant
AAFS	Atmosphere-assisted FLASH sintering
AC	Alternated field/current
α	Relative displacement (%)
α_d	Thermal diffusivity (m^2/s)
B	
BET	Brunauer, Emmett, Teller method
BBR	Black Body Radiation
C	
C.H.R.	Constant Heating Rate
C	Capacitance
CSP	Cold Sintering Process
D	
D_{BET}	Equivalent particle size calculated from SSA-BET
D50	Average particle size
DC	Direct field/current
d_{ij}	Piezoelectric coefficient
d_{33}	Longitudinal piezoelectric coefficient
d	Interplanar spacing (Å)
d_s	Distance between electrodes (mm)
E	
E	Electric field (V/cm)
E_c	Coercive field (kV/cm)
E_Y	Young Modulus (GPa)
E_a	Activation energy for densification (kJ/mol)
$E_a(\sigma)$	Activation energy for conduction (eV)
EBSD	Electron Backscattered Diffraction
ε_r	Relative permittivity or dielectric constant
ε^*	Complex dielectric constant
ε_0	Dielectric constant of vacuum (8.85 x 10^{-12} F/m)
F	
f_{as}	Anisotropy factor
$f(\rho)$	Function of the density (sintering technology)

FEM	Finite Element Modelling
G	
G	Grain size
$G_{eq.}$	Equivalent grain size
$(\overline{G_{eq.}})$	Average equivalent grain size
GSD	Grain Size Distribution
GB	Grain boundary
g_{ij}	Strain coefficients
γ_L	Liquid surface tension
γ_{sv}	Solid-vapor surface tension
γ_{ss}	Solid-solid surface tension
H	
HP	Hot pressing
HIP	Hot Isostatic Pressing
I	
I	Current (mA)
I_C	Charging current
I_R	Loss current
I.C.	Isothermal Conditions
ICPS	Inductively Coupled Plasma (mass) Spectroscopy
IS	Impedance spectroscopy
J	
J	Current density (mA/mm^2)
K	
KNN	Potassium Sodium Niobate, $K_{0.5}Na_{0.5}NbO_3$
k_{ij}	Electromechanical coupling coefficients
k	Linear regression slope
K_B	Boltzmann Constant (eV/K)
L	
λ	Wavelength
L_m	Length at a certain point (Dilatometry) (mm)
L_0	Initial length (mm)
M	
m	Mass (g)
m_{humid}	Humidified mass (Archimedes method) (g)
m_{imm}	Immersed mass (Archimedes method) (g)
M*	Complex electric modulus
MIP	Mercury Intrusion Porosity
N	
n	Integer number
N_A	Avogadro Number (mol^{-1})
n_c	Characteristic constant for the densification mechanism
O	
P	

PSD	Particle Size Distribution
P	Polarization (μC/cm^2)
P_S	Saturation polarization (μC/cm^2)
P_r	Remnant polarization (μC/cm^2)
PZT	Lead Zirconate Titanate
Q	
Q_m	Mechanical quality factor
θ	Incident angle (º)
θ_c	Contact angle (º)
R	
ρ	Relative density (%)
ρ_c	Calculated density (% or g/cm^3)
$\rho_{measured}$	Measured density (geometric or Archimedes) (g/cm^3)
ρ_t	Theoretical density (g/cm^3)
$\rho_{geom.}$	Measured geometric density (g/cm^3)
$\rho_{Archim.}$	Measured Archimedes density (g/cm^3)
ρ_{green}	Relative green geometrical density (%)
ρ_{sint}	Relative sintered geometrical density (%)
$\rho_{rel.}$	Relative sintered Archimedes density (%)
P_W	Power dissipation (mW/mm^3)
P_P	Pressure
P_0	Saturation vapor pressure
r_p	Pore size
R	Resistance (Ω)
R_G	Gas Constant (J/(K mol))
RFS	reactive FLASH sintering
S	
SSA	Specific Surface Area
SEM	Scanning Electron Microscopy
EDS	Energy dispersive X-Ray Spectroscopy
S	Average thickness
SF	Particle Shape Factor
σ	Electrical conductivity
S_j	Piezoelectric strain
STP	Standard temperature and pressure
SPS	Spark Plasma Sintering
T	
TEM	Transmission Electron Microscopy
T	Absolute temperature (K)
Tcalc	Estimated specimen temperature (K)
T_F	FLASH temperature (ºC)
T_{O-T}	Orthorhombic to tetragonal transition temperature (ºC)
T_C	Tetragonal to cubic transition temperature (ºC)
T_0	Curie temperature (ºC)
t	Time (s)

th	Thickness (mm)
T_i	Applied stress
$\tan\delta$	Loss tangent or dissipation factor
τ	Time constant
U	
υ	Poison ratio
U	Voltage (V)
V	
V_G	Volume of adsorbed gas
V_m	Volume of an absorbed gas monolayer
V_0	Volume of one mole of gas at STP
Vol	Volume (cm^3)
W	
ω	Angular frequency (rad/s)
ω_a	Wave number
X	
XRD	X-ray Diffraction
w	Width (mm)
Y	
ψ	Impedance phase
Z	
Z	Impedance
Z*	Complex impedance

Introduction

Framework

Alternative sintering techniques promise to revolutionize the ceramic industry by significantly decreasing sintering temperature and time. Among them, and one of the most promising, is FLASH sintering, in which an electric field is directly applied to a ceramic compact, imposing a current flow. Such technique allows the total densification of ceramics in less than 1 min, at temperatures significantly lower than those of conventional processes. However, FLASH sintering and its mechanisms are not fully understood from the scientific point of view, as this technology is yet far from being transferrable to the industry.

The body of knowledge of such technique is increasing, and one of the most challenging and interesting application of FLASH is the production of materials that are difficult, or even impossible, to produce by conventional means. For instance, complex oxides that have volatile species on their composition are prone to be problematic, as volatile elements tend to vaporize at the conventional sintering temperatures (typically over 1000 ºC). The consequences are loss of stoichiometry, compromising the material application. KNN, or potassium sodium niobate, is among such complex oxides. The undoped 50% solid solution ($K_{0.5}Na_{0.5}NbO_3$), KNN, is one of the most promising lead-free materials for piezoelectric applications, capable of substituting the market leader of piezoelectrics, i.e. $Pb(Zr_{1-x}Ti_x)O_3$ (PZT). However, its poor densification is a scientific and industrial issue.

In this scope, the presented work aims to study and produce KNN ceramics by FLASH sintering (at lower temperatures and shorter times than conventional sintering) avoiding K and Na vaporization and the consequent secondary phase formation, while contributing for the development of low energy-budget sintering techniques for ceramics. The mechanisms behind such promising technology will be explored for the specific case of KNN.

General and specific goals of the thesis

This PhD thesis has three main lines of investigation: (i) the scientific depict of the mechanisms for FLASH sintering of KNN; (ii) the development of alternative sintering techniques, as FLASH, to densify lead-free ceramics, as KNN; ultimately, to sinter ceramics at room temperature; and (iii) the contribution for the comprehension of FLASH as a sintering process.

Specifically, six global goals are listed for this work:

1. **To develop the infrastructures for the processing of KNN by FLASH sintering**
    - Proof-of-concept of KNN FLASH sintering.
    - Dilatometer development.
2. **To experimentally explore FLASH sintering of KNN**
    - To establish electric field and current conditions for FLASH of bulk KNN.
    - To explore the possibility of FLASH sintering of KNN films in flexible substrates.
3. **To investigate the influence of powder characteristics and sintering environment on FLASH**
    - To explore the influence of particle size/shape on FLASH process.
    - To study the influence of sintering environment factors as atmosphere or external pressure.
4. **To establish relations between the process and final KNN properties**
    - To evaluate the impact of the FLASH process on the dielectric and piezoelectric properties of KNN.
    - To study the KNN defect chemistry and its influence on the process and final properties.
5. **To model the FLASH process**
    - To use computing modelling to simulate the process.
    - To evaluate the separate contribution of different phenomena for the densification by FLASH.
6. **To contribute for sustainable studies within ceramic industry**
    - To understand the sustainable gains with KNN densification by FLASH and its relationship with resources saving and decarbonization of industry.

To fulfil these objectives, the work is presented in 8 major chapters. A comprehensive and critic state of the art revision is given in chapter 1. Following, chapter 2 gives experimental details on the development of simulation tools, sintering equipment and characterization techniques. Chapters 3 to 7 correspond to the results presentation and discussion. Here, each chapter is intended to discuss one thematic, and the topics are organized in articles or papers layout. Some of the presented studies were already peer-reviewed and published, some are submitted, and various will be submitted soon. These indications are given in each section. Results chapters comprise, namely, the simulation (3), the influence of powders and processing parameters on FLASH sintering (4), the mechanisms operating on FLASH sintering of KNN (5), the process of decreasing the FLASH sintering temperature (6) and finally, the dielectric and piezoelectric properties of sintered ceramics (7). A final remarks and conclusion chapter (8) is presented, giving a view on the prospects of the technology and a critical view on the general topic, highlighting the major accomplishments of this work.

Chapter

1. State of the art

Contents

Preamble

This chapter will give a general overview on the state of the art and theoretical concepts of relevance for the thesis subject. The FLASH sintering technology is relatively recent; therefore, a full, comprehensive, and critical review of this topic is presented here. Additionally, during the results presentation (chapters 3 to 7) each sub-chapter (i.e., each article) will be provided with an introduction and motivation for that specific study.

The state of the art review is divided in 4 major sub-chapters. The first, describes shortly the conventional sintering concepts and provides the motivation for the development of alternative sintering techniques as FLASH. Consequently, FLASH sintering is presented in detail, with the major features, parameters, and mechanisms being reviewed in the sub-chapter 1.2. Additionally, modelling and simulation breakthroughs are presented, together with a statistical analysis on the published scientific works on the topic.

The last two sub-chapters are dedicated to piezoelectric materials. The first, section 1.3, is devoted to the general piezo and ferroelectric properties of ceramics, and those specific of KNN. Section 1.4 is focused on the sintering of potassium sodium niobate, $K_{0.5}Na_{0.5}NbO_3$ (KNN); after knowing the characteristics of conventional and FLASH sintering, the reader will find the motivation for the work clearly: there is a need to decrease the sintering temperature and time of lead-free alkali-based piezoceramics as KNN. In that sub-chapter, the few works on FLASH sintering of KNN that were published out of this thesis framework, i.e., not published within this work' group, are critically reviewed. A summary table is attached to the chapter and shows experimental details and accomplishments of published works in the field between 2017 and 2020.

1.1. Conventional and alternative sintering processes

Sintering is the process for consolidation of powder compacts into coherent polycrystalline solids, through particle bonding, with the development of grain boundaries. This process is developed by use of heat and/or pressure and occurs below fusing temperature. The overall goal is to sinter with controlled microstructure, porosity and grain size [1], [2].

In this work, we designate the sintering processes without the application of external pressure, magnetic or electric fields, as *conventional sintering*. Here, surface curvatures are the only driving force for densification; thermal energy is the source of energy to promote movement of species (diffusion). A schematic representation of conventional sintering process is shown in Figure 1-1, with the starting powder particles (grey) in a compact (a) evolving to coherent grains in a body (b) with reduction/elimination of air content (represented in amber).

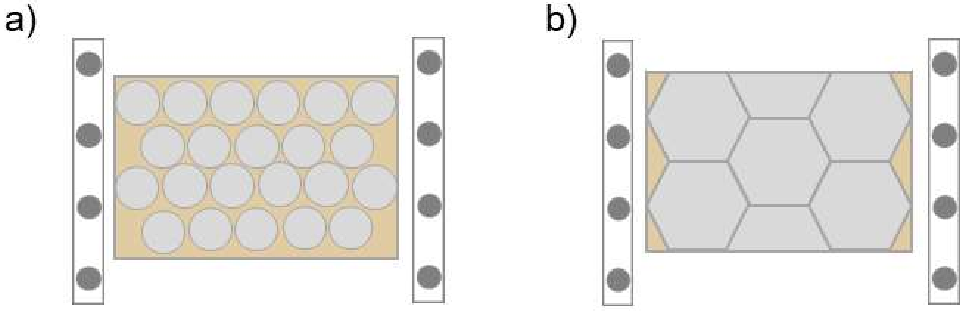

Figure 1-1 - Schematic representation of conventional sintering. Vertical side bars represent the furnace heating elements; a) represents the green body, with particles contacting with each other (grey), and b) a coherent dense body after sintering.

Conventional sintering can be divided into three classes: (i) solid-state, (ii) liquid-phase assisted sintering, respectively, SSS and LPS and, and (iii) vitrification or “viscous” sintering. For SSS and LPS, in parallel with densification, growth (coarsening) of grains (particles), also occurs. This is not the case of amorphous materials, where densification occurs through viscous flow of material (vitrification class) without any boundary between the particles [2]. Both densification and coarsening are thermodynamically favoured, decreasing the total energy of the system. They are based on matter transport from a source (high chemical potential) to a sink (lower potential). The matter sink is the formed neck region or pore and can be identified in Figure 1-2. During sintering, particle free surfaces will evolve to grain boundaries [3]–[5].

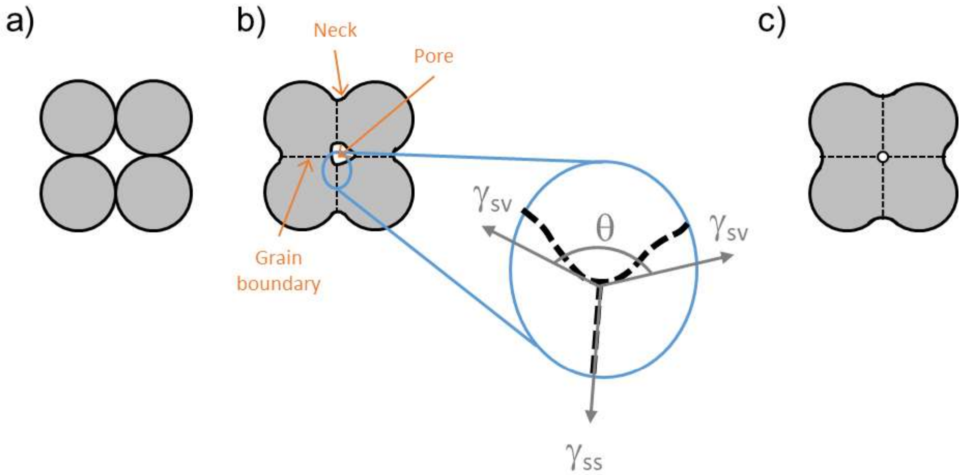

Figure 1-2 – Sintering evolution process; a) green state; b) beginning of sintering, with particle coalescence and pore formation; c) pores change size and shape. The grey arrows represent the different surface energies on a particle-pore interface: γ_{sv} (solid-vapor) and γ_{ss} (solid-solid). Adapted and re-designed from [6]

As contacting surfaces, pores and particles have surface energies, the pore wall is designated as solid-vapor surface tension (γ_{sv}) and the grain boundary as solid-solid surface tension (γ_{ss}). To promote densification, γ_{ss} must be smaller than the sum of the γ_{sv} projections – equation 1-1 and Figure 1-2. Densification process will contribute to density increase while coarsening decreases the curvature of the neck and hinders (or retards) the densification [3].

$$\gamma_{ss} < 2\gamma_{sv} \cos\left(\frac{\theta}{2}\right) \tag{1-1}$$

Based on the connectivity of particles and pores, sintering is divided into three stages: initial, intermediate and final, as described by theoretical models [7]. The initial stage is associated with bonding of particles and neck formation and growth; the densification is very limited. During the intermediate stage, both solid and porous phases are connected, and significant densification occurs. In the final stage, the solid phase is connected, while pores are isolated; here, for crystalline materials, significant grain growth occurs and the microstructure is controlled by the interaction pores/grain boundaries [2].

Both SSS and LPS occur with atomic transport from a source towards a sink, via detachment, movement, and attachment of atoms. Attachment and detachment of atoms are interface reactions, while atomic movement is associated with diffusion. The process for grain growth is similar: movement of atoms from the surface of a small grain towards the surface of a large grain. It occurs across the grain boundary (GB) for SSS, and across the liquid phase for LPS [2]. Consequently, the kinetics of bonding, densification and coarsening must be controlled by the slower process, either diffusion or interface reaction. Conventionally, it is assumed that diffusion governs densification and grain growth [2], [7]. For detailed descriptions of SSS, LPS and vitrification works from R. K. Bordia *et al.* [2], M. N. Rahaman *et al.* [4], and others [7]–[9] are suggested.

Some ceramics are difficult or even impossible to densify by conventional methods, due to their high processing temperature and time. Also, abnormal grain growth (AGG), structure instability or shrinkage anisotropy, which difficult densification, are commonly observed in ceramic conventional sintering. As a way of decreasing sintering temperature, time, and to produce materials difficult or almost impossible to densify by conventional processes, since the 20th century, alternative sintering techniques have been developed. The most relevant groups of alternative sintering techniques are laser, pressure, field and current assisted. Figure 1-3 schematically represents the most studied alternative sintering techniques, that will be briefly described in this section.

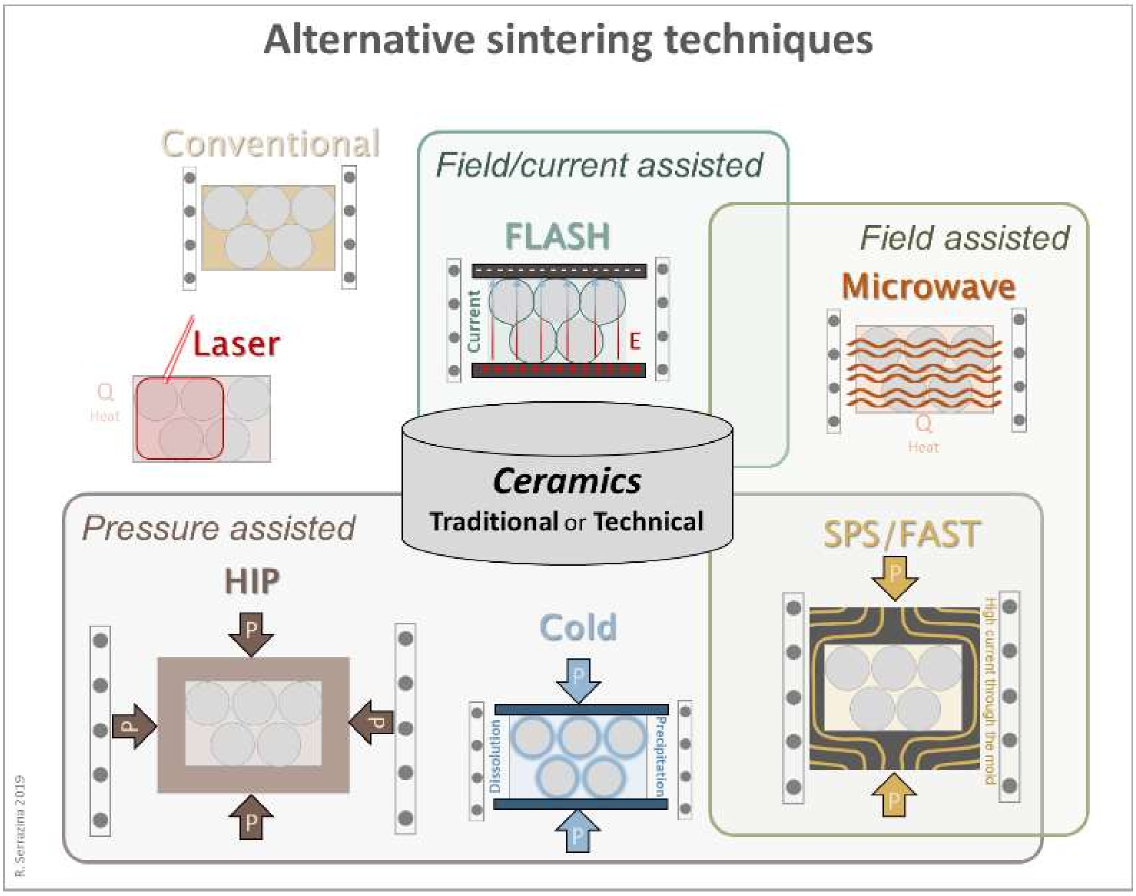

Figure 1-3 – Alternative sintering techniques schematic representation, namely SPS/FAST and Microwave, Cold, Hot Isostatic Pressing, Laser and FLASH sintering. Conventional sintering is also represented for comparison. Particle size is exaggerated for understanding.

Pressure-assisted was one of the first alternative sintering methods to be developed being Hot Pressing (HP) and Hot Isostatic Pressing (HIP) the most relevant. Here, the application of an external pressure to a powder compact results in a direct increase in the driving force for densification. Hence, the sintering temperature and time can be reduced, and grain growth diminished [7], [10], [11]. On HP, a uniaxial pressure is applied, while in HIP gases (for ceramics, typically argon) or oils are used to perform an isostatic pressurization. A long list of materials has been produced by HP or HIP and these processes are also commonly used in industrial applications [7], [10], [11]

Spark Plasma Sintering (SPS) was developed after HIP and makes use of pressure and very fast heating rates to densify ceramics. It was reported as a pressure-electric field assisted technique and designated as SPS, FAST (Field Assisted Sintering Technique) or PECS (Pulsed Electric Current Sintering). For the sake of understanding, we will consider the commercial designation of SPS. Here, the ceramic powder is placed in a graphite die and pressed by external punches, while the die is heated by a high electric current flow. The heating rate is of the 100 ºC/min order and most of the DC pulsed current flows through the die and not through the sample. In SPS the densification is very fast, (few minutes) while the grain growth is very limited. Such features are related with the very high heating rates and external pressure employed to the ceramic. Despite the significant initial investment needed, SPS has been successfully applied to several systems, including Al_2O_3, ZrO_2, Si_3N_4, MgB_2 and KNN [7], [10], [12], [13]. SPS still faces issues related with specimen reduced state after sintering (due to the use of graphite dies), equipment cost, and thermal gradients developed during sintering. In addition, the automatization of such process for an industrial application is limited.

Still among pressure-assisted sintering techniques, a very interesting and new technique was recently reported by C. Randall and co-workers, designated as Cold Sintering Process, *CSP*. Despite that the original technique was firstly described for metals (with plastic flow) in 1979 [14], recently, cold sintering was successfully developed for ceramics [3], [15], [16]. In this method, the inter-diffusion between particles is enhanced by adding a transient solvent to the powders during pressure-assisted sintering. This contributes to keep both the temperature and pressure low during the consolidation process (120 °C to 200 °C and 350 MPa, respectively). The technique seems simple for non-complex shaped ceramics, but technological questions arise. For instance, the dissolution/precipitation process of some ceramics is complex, hence, secondary phases may form, and properties be impaired, as for instance, mechanical properties.

Moving towards field-assisted sintering techniques, microwave sintering (MWS) is one example of electromagnetic energy coupling with temperature for alternative sintering. MWS was firstly reported for ferrites in 1981 [17] and it uses the ceramics high dielectric loss at grain boundaries to couple in extra energy, promoting sintering at lower temperature than conventional processes [3]. MWS advantages are the simplicity of equipment and the absence of any contact, pressure, or moulds. On the other hand, microwaves are dangerous to living beings; exposure to powerful microwaves induces an uncontrolled increase in body temperature and, ultimately, dead. Some studies also relate MW with cancer development [17]. Consequently, strong and expensive furnace isolation is needed.

Laser sintering is another alternative sintering technique that makes use of a laser to selectively sinter ceramics or metals. For instance, SLS, selective laser sintering, is a well-known additive manufacturing technique [18]. SLS is very powerful for the construction of small complex shapes, impossible to produce by other means [19]. However, dense ceramics are difficult to obtain due to thermal gradients and cracking [20].

FLASH sintering was firstly introduced in 1957 as a route to densify graphite powders [21]. More recently, R. Raj and co-workers presented FLASH as a way to densify yttria-stabilized zirconia, YSZ, in less than 60 s. A temperature decrease of ~600 ºC, when compared with conventional cycle, was achieved [22].

FLASH sintering combines, together with thermal energy, the application of moderated electric fields (hundreds of V per cm), *E*, and relatively low currents (< 100 mA/mm^2), *J*, directly to the material. At a specific onset combination of electric field and furnace environment (temperature and/or atmosphere), the material starts to conduct and dissipates power, densifying in a matter of seconds. Early reports defined FLASH as a densification process occurring within less than one minute [10], [22], [23].

At first, FLASH was categorized as a Field-Assisted Sintering Technique (FAST) [10]. However, the process consists in the direct application of the electric field and current (typically DC, but also AC or pulsed) to the ceramics, without the use of external dies or moulds. Therefore, FLASH belongs to the Electric Current-Assisted Sintering (ECAS) processes [23], in which the direct current flow through the ceramic is responsible for its densification. The lower operating temperature and the absence of external pressure are the main advantages of FLASH when compared with SPS. Additionally, FLASH does not require the use of specific atmospheres or dies/moulds. Thus, FLASH can be cost-effective and energy-efficient [24], despite that the knowledge on its densification mechanisms is still limited. For these reasons, FLASH sintering is the alternative technique under study in this work. The following sub-sections will describe its features, parameters and mechanisms.

1.2. FLASH as an alternative sintering technique

1.2.1. Features and signatures

On the onset of furnace environment (temperature and/or atmosphere) and electric field, when FLASH occurs, the material undergoes significant changes in its properties, that are observable by two events. These events are called FLASH signatures and are revealed as (i) a sudden non-linear increase in the material's conductivity, followed by an increase in the power dissipation, and (ii) its fast shrinkage (densification). The furnace temperature at which these phenomena occur is called FLASH temperature (T_F) and is identified by such non-linearity [10]. These signatures are shown, respectively, in Figure 1-4 a) and b). The Arrhenius dependence of the power dissipation behaviour with temperature is shown in Figure 1-4 a). The strain behaviour, or the absolute shrinkage, as a function of the temperature, of materials sintered conventionally (blue), by low electric fields (green) or by FLASH (red) are shown in Figure 1-4 b). The abrupt shrinkage of materials by FLASH occurs at furnace temperatures significantly lower than those of conventional sintering. Frequently, as the magnitude of the applied field increases, T_F is decreased [10], [23].

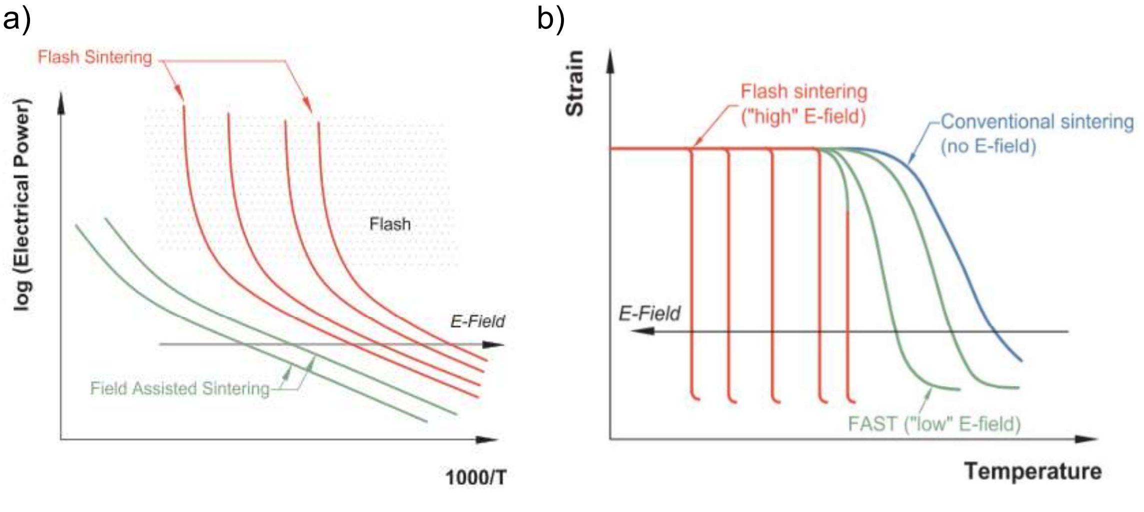

Figure 1-4 - a) Evolution of the electrical power dissipation with 1000/T under different electric fields. b) Sintering strain, or shrinkage representation, over temperature for specimens subjected to the same electric fields. Adapted from [23].

Figure 1-5 illustrates the Arrhenius representation of power density over inverse of absolute furnace temperature (1000/T) for FLASH experiments of a wide variety of ceramics, subjected to the same FLASH conditions. At the time of such publication [25], early 2017, $CoMnO_4$ had the lowest reported T_F. A year later, 2018, ZnO was FLASH sintered at room temperature, under specific atmosphere conditions [26]. Dielectrics as $BaTiO_3$ or TiO_2

presented T_F between 650 and 900 ºC, depending on the applied electric field. Highly dielectric materials, as MgO-doped Al_2O_3 presented T_F higher than 1200 ºC.

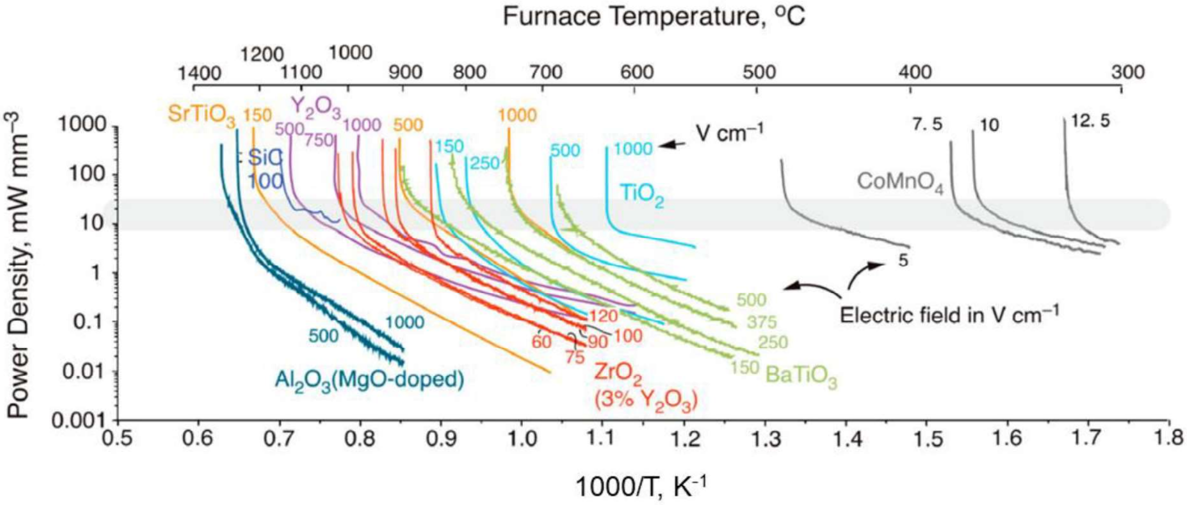

Figure 1-5 - Power dissipation (volumetric) Arrhenius representation for FLASH sintered ceramics, with different nominal *E*, but constant *J* (80 mA/mm^2), heating rate (10 ºC/min), and sample size/format (dog-bone: cross section 3 x 1,6 mm^2; gauge section 20 mm). Adapted from [25].

This non-linear increase in power dissipation, upon FLASH, seems to happen between a range of 7 to 50 mW/mm^3, regardless of the sintered material and the applied electric field [25]. One of the explanations for this interesting observation was given by R. Chaim [27]. The author argues that FLASH phenomena is initiated from the need of this ~7 - 50 mW/mm^3 electric energy density, that is used to locally melt the particle contacts and to form a liquid-film. This liquid film, despite being transient, is needed to percolate the flow of current, and that is the reason why power density has the non-linear behaviour with the measured temperature. After the liquid is formed, particles may rearrange, promoting the very fast densification observed during FLASH [27]. Regarding the short interval of power dissipation values being independent of the material (Figure 1-5), R. Chaim claims that such narrow interval is in accordance with the formation of the liquid film (in the particle contacts), independently of the material, since all melted oxides exhibit relatively high electronic conductivity, when compared with the solid material. This is still an open subject, but the formation of transient liquid films during FLASH process seems to explain many of the observed phenomena.

The non-Arrhenius dependence of power dissipation with furnace temperature is directly related with the conductive behaviour of materials. Figure 1-6 depicts the representation of FLASH sintered TiO_2 at different electric field, E*,* values. The conductivity of conventionally sintered TiO_2 is shown in black for comparison. The data demonstrates that the material conductivity rises abruptly at the onset of FLASH, revealing two behaviour regimes: (i) before the FLASH, with ionic conductivity similar to dense specimens; (ii) after the FLASH, with significantly higher conductivity [28].

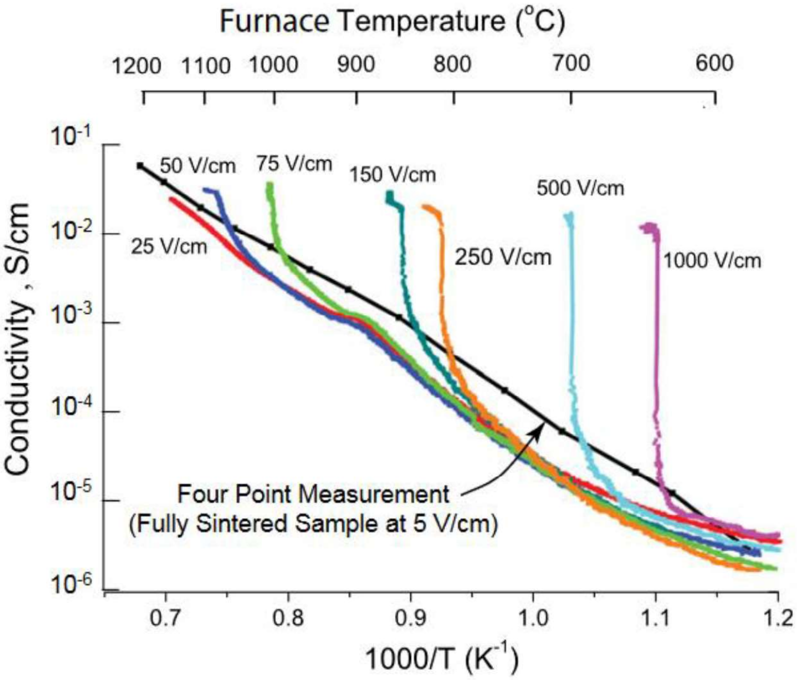

Figure 1-6 – Change in conductivity of Titania (TiO_2) as FLASH sintering occurs. The abrupt increase in conductivity is a signature of FLASH. Black line gives a baseline of the conductivity measured in conventionally densified specimens [28]

There are different ways of performing FLASH, in what concerns furnace heating and electric power configurations. On furnace heating, there are, typically, two main procedures: (i) constant heating rate (C.H.R.) and (ii) isothermal condition (I.C.) furnace temperature, represented in Figure 1-7 a) and b), respectively. C.H.R. experiments are relevant to study both T_F and the conductivity behaviour of materials [24], [29]. On the other hand, isothermal steps, before application of any electric field (E), can be used to understand the phenomena of defect nucleation [30] and as an experimental route to obtain highly dense, uniform ceramics [31].

In C.H.R. experiments, three FLASH stages are typically identified: stage I, incubation, in which E is applied, with no significant J deployment; stage II, FLASH event, when J increases non-linearly with the temperature and a power spike is registered, with sintering occurring at very fast rate; stage III, steady state, where J is limited and roughly constant, with the material undergoing the remaining sintering towards full density. During stage III, a key parameter for the maximum temperature reached by the system (sample + furnace) is the current density. Increasing J will promote a larger power through the system and higher sample temperatures [23]. It is important to note that, regardless of the type of FLASH process, the current must be limited. Otherwise, the material will melt in an non-controlled process [32]. The three stages are represented in Figure 1-7 a), with parallel representations of electric field, current density and furnace temperature.

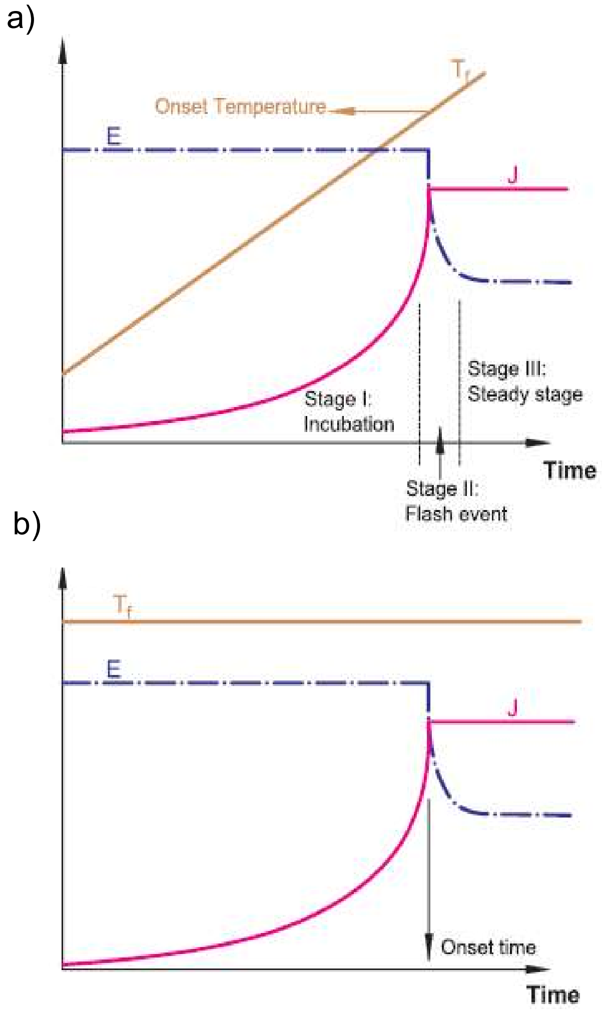

Figure 1-7 – Electric field, E, current density, J, and furnace temperature T_f evolution during FLASH process at a) constant heating rate (C.H.R.) and b) isothermal (I.C.) furnace temperature. Adapted from [23].

More recently, variations of FLASH sintering C.H.R. and I.C. were proposed in what concerns electric power management. Examples are shown in Figure 1-8 a) and b). In the first case (a), an isothermal furnace temperature is kept and the field applied with a steady rate, reaching the onset field for FLASH [23]. In (b), a current rate is imposed, and the field is monitored. This allowed fine-grained microstructure across the section of the specimen due to the highly transient conditions of voltage-to-current switching [33], [34].

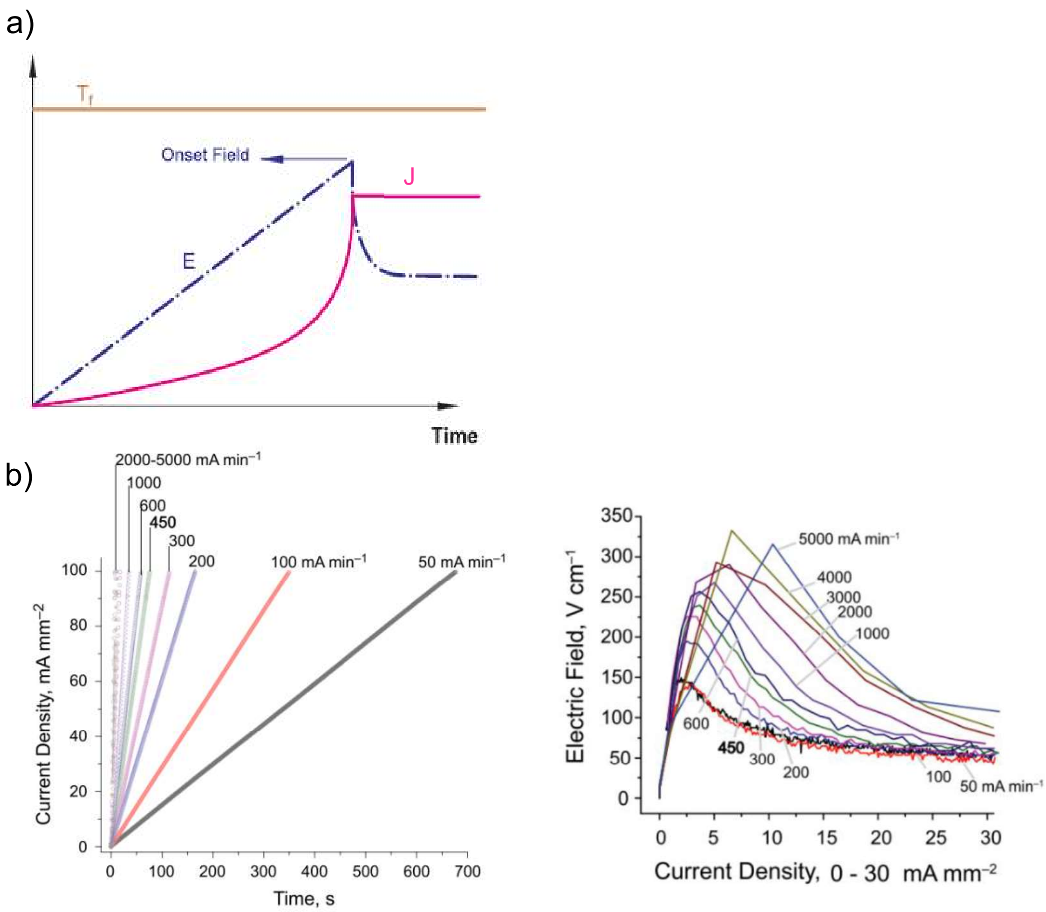

Figure 1-8 – a) Electric field rate (EFR) with isothermal temperature technique [23]. b) current rate (CR) experiments and respective electric field dependence with the applied current [33].

Still regarding recent advances on FLASH, Reactive FLASH sintering (RFS) was presented for the production of polycrystalline single-phase $MgAl_2O_4$ ceramics from MgO and α-Al_2O_3 precursors [35]. Contrarily to the trend of previous powder calcination for single phase FLASH sintering of complex oxides, B. Yoon and co-workers mixed the precursors and FLASH sintered them to a single-phase complex oxide, that was completely transformed after just 3 seconds during stage II. This work deployed several research works [36]–[40], including on the study of diffusion mechanisms that allow such a fast atomic recombination, that will be discussed later on.

1.2.2. Parameters

The list of parameters that influence FLASH is extensive. A schematic representation of the most relevant is illustrated in Figure 1-9. In addition, some are a consequence of others, more relevant. For instance, the powder particle size will influence the green density of the specimen and its porosity channels that, when using atmospheres, may play a significant role on FLASH. Some other parameters were already discussed, as electric field, current and material conductivity. However, other relevant parameters still need some discussion and will now be presented.

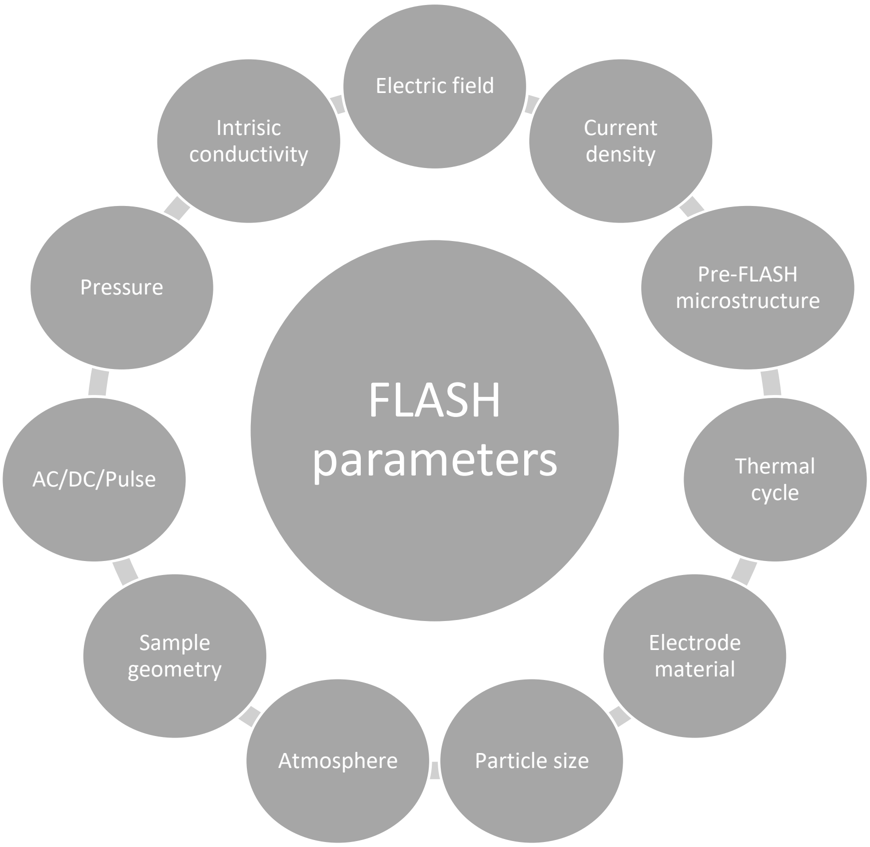

Figure 1-9 – Schematic representation of parameters that influence FLASH sintering process. Adapted from [23]

Sample geometry is an important aspect that may influence results interpretation. There are two main types of sample's geometry: dog-bone and regular shape (comprising rectangular or circular section area). The typical dog-bone shape specimen, as represented in Figure 1-10 a), has the advantage of easy contact with the electrodes, because they are wrapped around the holes on the edges of the bone. However, even though field and temperature distributions in the gauge section are homogeneous, electrode areas are extremely heterogeneous in terms of densification and grain growth [10], [41]. The remaining b) and c) types of pellets are typically used for experimentation by ceramic industry researchers. In this case, the electrodes are conductive sheets or plates that contact directly to the specimen. Contact issues may arise, but conductive paints may be used directly into the specimens to avoid such problems.

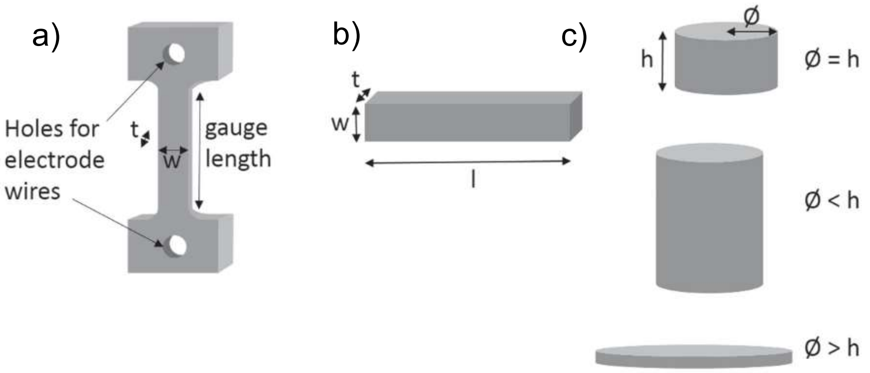

Figure 1-10 – Sample geometries used in FLASH experiments: a) dog-bone, b parallelepipedal bar, c) cylindrical bars, or pellets with different aspect ratios [10].

To control and register FLASH parameters, simple techniques are used; dilatometry is used to register pellets shrinkage and, typically, contact dilatometers are suitable for b) and c) types of compacts, while non-contact ones for a)-type. Thermal cameras, or optical emission spectroscopy, can be used to estimate the sample temperature, however its accuracy is still a challenge. The electric power apparatus may or may not be integrated in the temperature and shrinkage control/registration system [25]. To evaluate the specimen electrical behaviour during FLASH experiments, or even after sintering, impedance spectroscopy (IS) may be used [34], [42].

Another relevant parameter, that dramatically influences T_F, is the atmosphere. Oxides are prompt to have lattice defects, as interstitials or vacancies. Hence, when the oxygen equilibrium (partial pressure) is changed by oxidizing or reducing atmospheres, the insulating oxides can become more conductive at lower temperatures [43]. Furthermore, for water sensitive materials, humidity can also contribute for the FLASH process. Zinc oxide, ZnO, was successfully densified to 98% of theoretical density (ρ_t) at room temperature, using a reducing-water saturated atmosphere, by J. Luo and co-workers [26].

This variety of parameters have a significant influence on the development of the FLASH sintering process and must play a significant role in changing or activating different FLASH mechanisms.

1.2.3. Mechanisms

The mechanisms contributing to the fast densification in FLASH are not yet completely understood. Nevertheless, it is well accepted that the electric field applied directly to the green compacts can promote the formation of intrinsic and extrinsic electronic and/or ionic defects, as for instance Frenkel or anti-Frenkel defects, equations 1-2 and 1-3, respectively, shown in Kröger-Vink notation, where M is 2+ metal and V is a vacancy.

$$\mathrm{M_M^x} + \mathrm{V_i^x} \leftrightarrow \mathrm{M_i^{\circ\circ}} + \mathrm{V_M^{\prime\prime}} \tag{1-2}$$

$$\mathrm{O_O^x} + \mathrm{V_i^x} \leftrightarrow \mathrm{O_i^{\prime\prime}} + \mathrm{V_O^{\circ\circ}} \tag{1-3}$$

Under the influence of the field, defects and free electrons will move, generating an electrical current flow and consequent heating by Joule effect. Thermal runaway, that occurs when the rate of generated heat (Joule heating) is higher than the dissipated one, contributes to the very fast densification; such fast heating and densification, typically, reduces the effects of grain growth [3], [44]. However, the question on how the compact starts to develop a long-range conduction is a matter of debate. The topic is here deconstructed.

In a general way, three mechanisms are proposed to explain FLASH: (i) Joule heating, (ii) field induced defects and (iii) changes of interfacial energy. These should not be described as individuals, because they all influence the process and may take place at the same time. Generally, sintering is highly dependent on the diffusion rate at grain boundaries. The presence of an electric field and movable defects enhance this diffusion. Additionally, the movement of electronic/ionic defects induce a current flow through the sample, which increases its temperature by Joule heating. The question now is to understand where that conduction originates from and how it is spread through the specimen; it is argued that it occurs through the particle contacts. Due to the dangling bonds at the surface of particles, the number of energy states for electrons is higher, and, consequently, the electrical resistance should be lower than that of the particles themselves. Since the particles are interconnected in the green body, there is a network of particle' surfaces, which provides a low-resistance path for conductive species and defects [3], [45]–[47].

One could argue that it would be easy to FLASH sinter ceramics at room temperature. However, that is not the case, as ceramics (dielectric materials) present very high resistivity at room temperature. In fact, one of two strategies must be employed to allow conduction (FLASH) in ceramics: (i) to increase the temperature, and the atomic vibrations will allow the activation of conduction mechanisms (recall Figure 1-6); (ii) to engineer the materials' defect chemistry, by changing the partial pressure of oxygen, or doping, for instance.

In the search for FLASH sintering mechanisms, K. Naik and co-workers found that isothermally FLASH sintered Al_2O_3-3YSZ composites exhibit an incubation time for the onset of the process. Weaker applied fields and lower temperatures lengthen the incubation period; this effect is highly non-linear, i.e., the increase in incubation time does not have a linear dependence with decrease of temperature and electric field. Such behaviour can be compared to nucleation and growth phenomena in chemically driven experiments involving solid state phase transformations. Hence, it was argued that nucleation of defects, as a consequence of the applied electric field, is the precursor to the onset of a FLASH [48]. Moreover, D. Liu and co-workers, while studying the effect of holding time during stage III of FLASH sintering of 3YSZ, found that both the bulk and intrinsic grain-boundary conductivity increased with an increase in the holding time, indicating that the FLASH process was responsible for the creation of additional oxygen vacancies ($V_O^{\circ\circ}$), in both grains and grain boundaries, that accumulated with such increase in time [49]. Recently, recurring to molecular dynamics, M. Jongmanns and co-workers showed that a minimum temperature is needed for Frenkel defects to be formed and FLASH sintering to occur. Such temperature was proved to be the Debye temperature, and the work suggests a link between the defect formation and the role of phonons [50].

Related with Joule heating and heating rate during FLASH, two separated studies, in YSZ and ZnO, [51], [52] suggest that the ultrahigh heating rate generated during FLASH is a critical factor that leads to fast densification by (i) keeping a high densification driving force by preventing the initial coarsening, as already explained, and (ii) providing non-equilibrium defects that would enhance matter flow. Those defects can be, for instance, grain boundary structures (or complexions [53], [54]) with enhanced mass transport rates [24], or Frenkel pairs nucleation [46], [55], [56]. All the described factors increase the diffusion rate at grain boundaries (i.e. particle surfaces) and, consequently, enhance the densification rate [3].

Knowing the effects of defect generation and movement by the presence of the electric field, the reader is reported to the conductivity and power dissipation behaviour of materials during stage I of FLASH (Figures 1-5 and 1-6, respectively). A still debatable but possible way to explain those non-linear behaviours takes Frenkel defects as crucial. On one side, calculations have shown that the field needed to generate Frenkel pairs in HfO_2 (an example) is of the order of 10^{11} V/cm [57], while that employed during FLASH processes is typically lower than 1000 V/cm. On the other side, prof. R. Raj's group argues that both the observations of a narrow band of power density for the occurrence of FLASH, as well as the very fast atomic recombination observed on reactive FLASH sintering, must be related with lattice vibrations and, ultimately, with Frenkel's formation [50]. In addition, R.

Chaim argues that all the observations (narrow power band [27], reactive FLASH [38], fast densification [58], relationship with Debye temperature [59], etc.) are explained by the formation of localized liquid phases at particle contacts that spread at a very fast rate and allow particle to slide, promoting extremely fast densification. R. Chaim and Y. Wang and respective co-workers presented several studies in this topic [60]–[63]. A final note on another work by R. Chaim: by assuming that, during FLASH, liquid films form on nanoparticle contacts, the velocity of ion movement through that liquid phase was estimated to be ~$3x10^{-7}$ m/s. On the other hand, the capillary forces induced upon such liquid were calculated to promote a melt spreading velocity of ~1 m/s. This means that, if the liquid films are formed, its spreading with consequent particle sliding and rearrange should be the ruling phenomena contributing to FLASH sintering [60].

In summary, defects (electronic, ionic or others) are crucial to promote FLASH. They may be formed as a consequence of lattice vibrations, by a Frenkel process, influenced by the oxygen equilibria or by the defect chemistry of the materials itself; what looks most certain is that, after such nucleation, the vibration and movement of electric field activated species must induce the formation of low melting point phases that promote particle sliding and very accelerated atomic diffusion and/or recombination through particles’ surface.

1.2.4. Modelling and simulation

As briefly demonstrated before, modelling and simulation have been recently used to describe and elucidate the FLASH sintering process. Two types of models have been presented, namely, (i) mathematical and (ii) computational.

The mathematical models (i) were the first to be presented. For example, the thermal runaway model for describing the onset condition for a proposed uncontrolled heating process, triggering FLASH sintering, was independently developed by Todd *et al.* [64] and Zhang *et al.* [45] in 2015. Following, the Black Body Radiation (BBR) model has been largely used to estimate specimen temperature. While BBR model faces strong discussion nowadays, a more precise model for specimen temperature description during FLASH is still to be presented.

On the other hand, computation models (ii) have been used to describe either specific FLASH stages or the evolution of the overall process. Firstly, the scientific community was interested in understanding the electric field, current density and temperature distribution through a dog-bone shape specimen. W. Qin and co-workers [65] showed that the macroscopic electric field distribution in a YSZ dog-bone shape is uniform within the gauge section but heterogeneous at the electrode contacting areas. Similar conclusions were attained by Grasso *et al.* [41], however, for temperature distribution. Nonetheless, contradictive results to those of Grasso's work were presented by M. Yoshida and co-workers, which found that dog-bone-like specimens present a non-homogeneous macroscopic distribution of the current density, power dissipation and temperature during stage III of FLASH [66]. Similar conclusions (thermal gradients) were attained by Eqbal and co-workers [67]. Even when FLASH sintering under AC conditions, which is proposed to diminish the temperature gradients during FLASH, Finite Element Modelling (FEM) reveals that thermal gradients between the core and the surface of ceramics occur [68].

More recently, simulations at the atomistic level have been presented. The possible generation of Frenkel defects is, as said, a critical question, however, contradictory results were found in this matter by Schie *et al.* [57] and R. Raj *et al.* [50], [69]. While R.Raj argues that Frenkel defects are the major factor contributing to the occurrence and development of FLASH sintering, Schie *et al.* have shown that, at least for the case of HfO_2, the rate of Frenkel defects recombination is so high that their formation and movement cannot explain the occurrence of the FLASH process.

A recent work by Vikrant *et al*. [70] presented, for the first time, a nano-scaled model that describes the incubation phenomena of FLASH sintering in YSZ – Figure 1-11. The model proposes that the stage I is divided in three consequent phases; first, a small subset of particle-particle contacts and surfaces of the green body define percolative paths for the charge to flow along and across the interfaces; then, the charge transport is suppressed across particle contact misorientations and deflects to surface and small angle particle contact misorientations, resulting in Joule heating; finally, the concentration of defects increases at the particle contacts, surfaces and triple junctions, enabling charge to flow through multiple paths and FLASH sintering to occur. This model seems to be the most complete on the description of the process and gives an un-precedent contribution for its understanding.

As briefly described, the contradictions on results obtained from both mathematical and computational modelling are frequent. Nevertheless, the relevance of simulation and modelling tools is highlighted and will be later discussed in chapter 3.

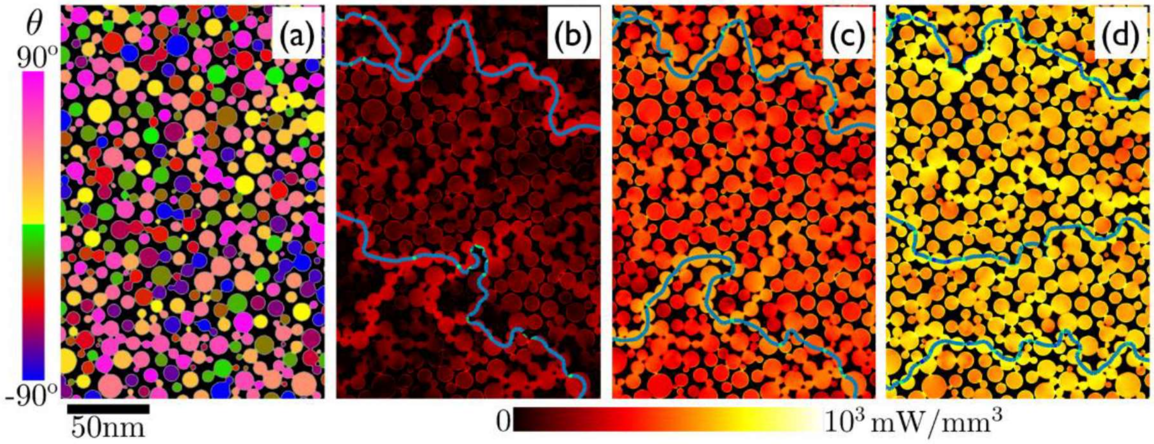

Figure 1-11 – Simulated Joule heating distribution of a ceramic green body during stage I of FLASH sintering, with a) starting YSZ particles and respective misorientation angle; b) spatial distribution of the generated Joule heating, with charge flowing through the particle contacts and surfaces (streamlines); c) Joule heating is increasing with consequent sample temperature increase and the charge flow is suppressed across the particles that develop wider depletion zones, while locally finding surficial and small angle grain boundaries that favor charge transport; d) the concentration of oxygen vacancies greatly increases at the grain contact cores, which promotes charge to flow in a larger number of percolating paths and FLASH onset to occur [70].

1.2.5. FLASH sintered materials

Table A-1 (in attachment) is a summary, organised by group of materials, of experimental conditions and properties of FLASH sintered materials, focused on the last four years of publications (2021 excluded). A similar table for years 2010 to 2016 may be found elsewhere [25]. Some data was replicated from that table, and new data added specifically for years 2017 to 2020.

Figure 1-12 are the pie charts for the number of publications related with FLASH by type of materials; a) presents the data from 2010 to 2016 (M. Reece's work [25]) and b) the data for years 2017 to 2020 (from WebOfScience search, with "flash sintering" keywords). A clear evolution in terms of target groups for FLASH research is observed: a decrease of the focus on zirconia-based materials (from 49% in the 2010 – 2016 period, to 25% in 2017 – 2020) and a clear increase in R&D in ceramics with application in electronics (electroceramics): from 9% in 2010 – 2016 to 29% in 2017 – 2020. This is due to the evolution of the knowledge in FLASH and the opportunity of its use to densify materials that are typically difficult or expensive to produce.

The net number of publications in FLASH has been increasing since the first *modern* report on FLASH of YSZ [22]. (Figure 1-13). The increase in FLASH sintering number of publications reflects the growing interest in the technique. There are however still opportunities for research and publishing, with possible contribution to the body of knowledge on FLASH.

Figure 1-14 illustrates the time-table evolution of the most relevant events regarding research in FLASH sintering. Behind this breakthrough events, FLASH has been used for other applications than rather sintering or densification at low temperatures. Recent reports describe the use of FLASH to join different materials, with reversible effects [71], [72] and solve composite preparation issues [73].

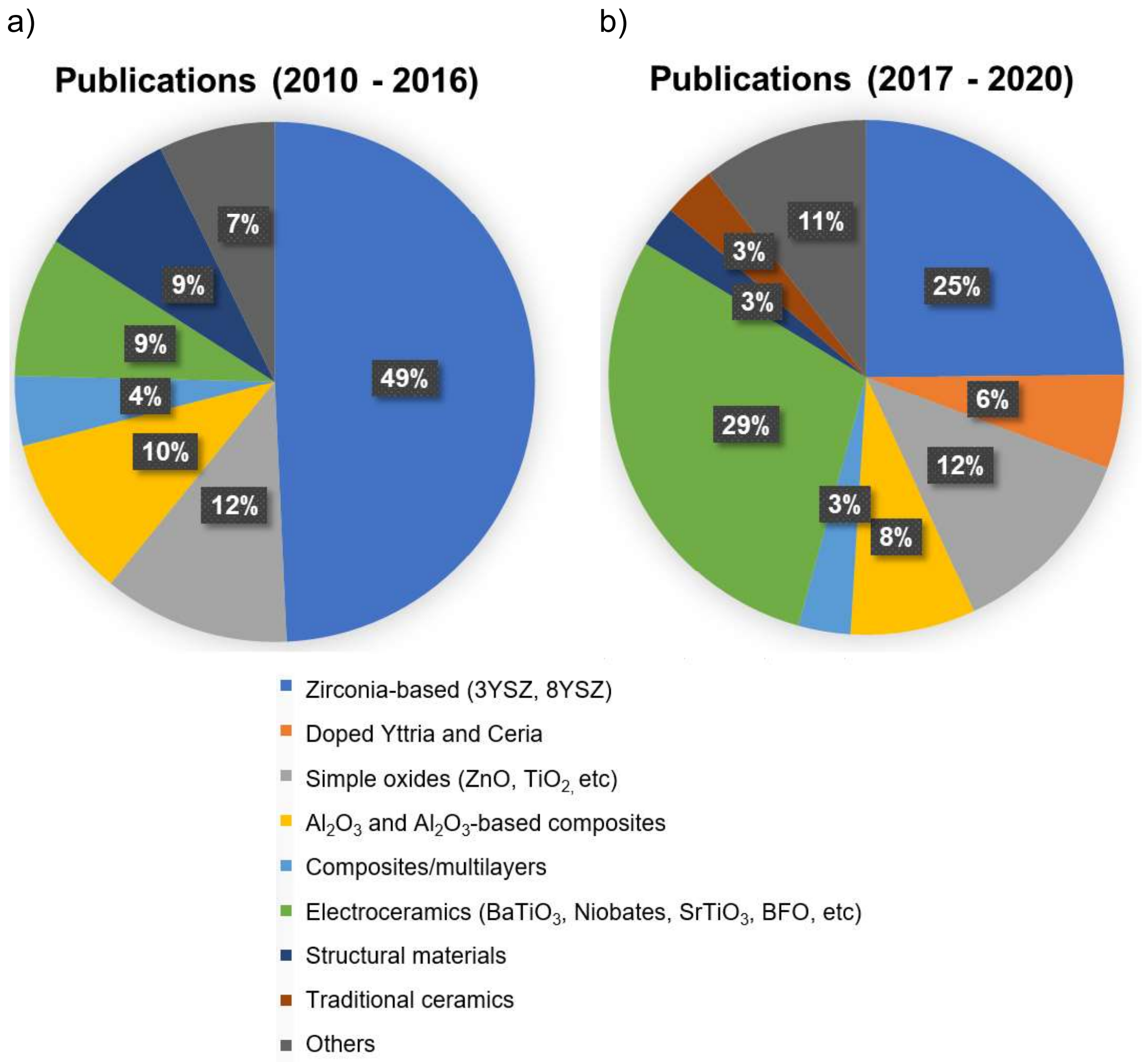

Figure 1-12 – Pie charts of publications on FLASH sintering by type of materials from a) 2010 to 2016 (data from [25]) and b) from 2017 to 2020.

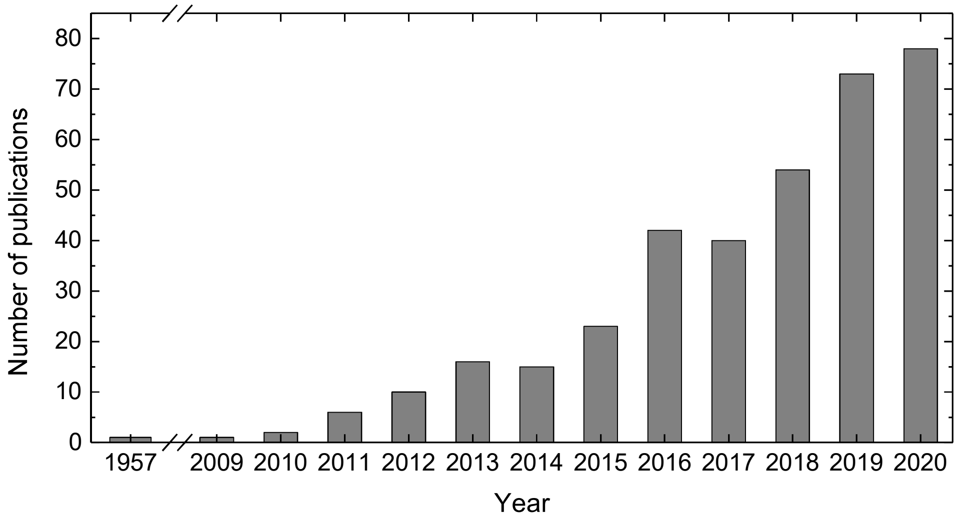

Figure 1-13 – Net number of publications related with FLASH sintering by year. Source: *WebOfScience, search key words “flash sintering”, December 2020.*

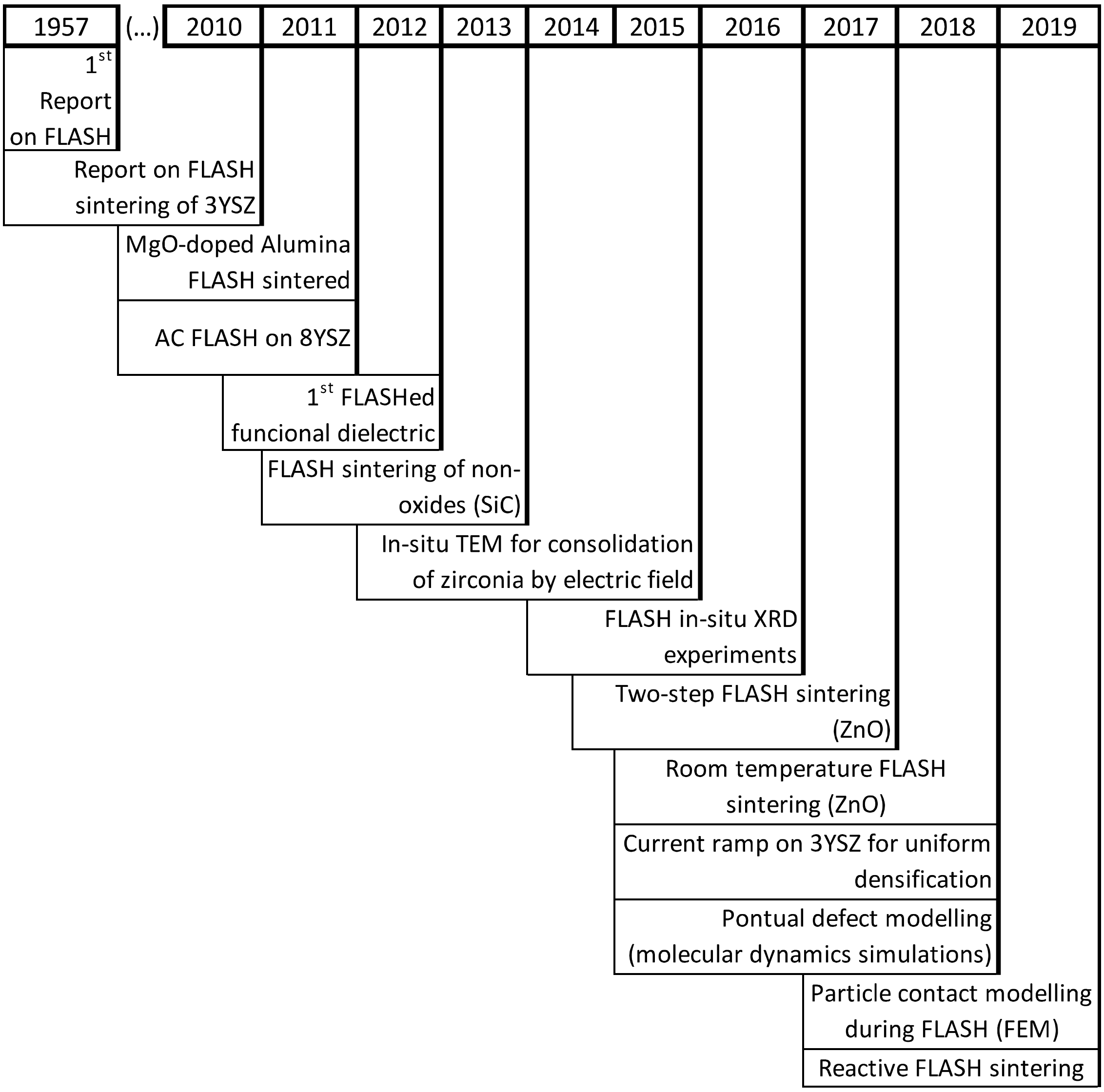

Figure 1-14 – Time-table of the most relevant and breakthrough events related with FLASH sintering.

1.3. Piezoelectrics and potassium sodium niobate (KNN)

The previous Figure 1-12 reveals the growing interest in FLASH sintering of electroceramics. Potassium sodium niobate, KNN ($K_{0.5}Na_{0.5}NbO_3$) is one of the most promising lead-free piezoelectrics with high transition temperature, capable of reaching piezoelectric response coefficients close to that of the market-leader materials based on lead (PZT-based family). Therefore, the present work addresses the development and study of FLASH sintering of KNN.

Ceramic piezoelectrics, or piezoceramics, command a huge market (only piezo-actuators are responsible for more than 20 billion $ per year) and act as enabling technologies for other areas, such as microelectronics, medical diagnostics, sensors and actuators [74]. Ferro and piezoelectric behaviour will be very summarily introduced. For extended information in this topic works as [75]–[79] are suggested.

In a perfect dielectric, when an electric field E is applied, there is no long-range current, however, there is a short-range dislocation of the positive and negative charge centre – appearance of electric dipole moments. [80]–[82]. If at zero field conditions a mechanical stress provokes the development of electric charges (polarization, P) these materials are called piezoelectric. Piezoelectricity is the ability of certain crystalline materials (non-centrosymmetric structures) to develop an electrical charge proportional to a mechanical stress or vice versa (Figure 1-15). Mathematically, these effects can be described as presented in equations 1-4 and 1-5, where d_{ij} is the piezoelectric coefficient, E_i the applied electric field, S_j the strain, P_j the polarization and T_i the applied stress [82], [83]:

$$P_j = d_{ij} \times T_i \tag{1-4}$$

$$S_j = d_{ij} \times E_i \tag{1-5}$$

The most reported d_{ij} coefficient is d_{33}, which represents the measurement of the material response in the same axis as the applied tension or electric field. Other coefficients for piezoelectric properties evaluation are: piezoelectric voltage or strain coefficients (g_{ij}), electromechanical coupling coefficients (k_{ij}), and mechanical quality factor (Q_m) [84].

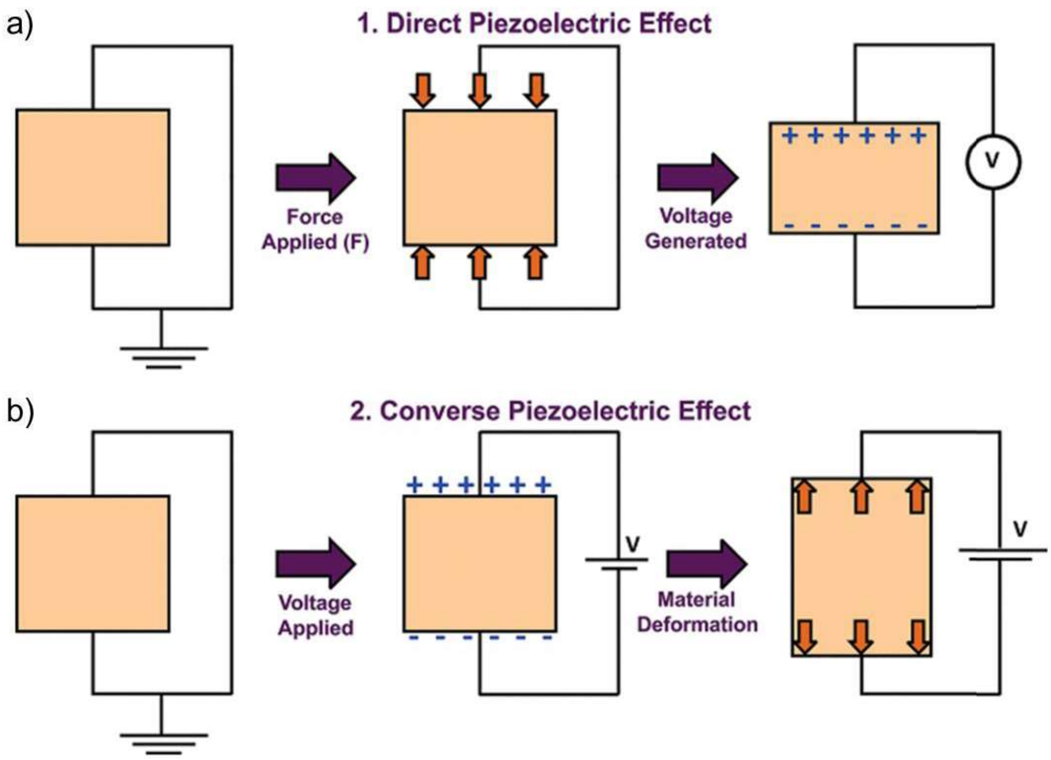

Figure 1-15 – Schematic representation of the piezoelectric effect: a) direct – voltage from mechanical input – and b) indirect/converse – deformation from voltage input. Adapted from [78]

If a material presents a spontaneous polarization and if its direction can be switched by an applied electric field, it is called a ferroelectric [82]. In ferroelectrics the relationship between the applied field and the polarization is described by a P-E hysteresis loop, Figure 1-16. The application of an increasing low electric field to a non-polarized ferroelectric provokes a linear and reversible increase of the polarization [82], [85].

Ferroelectrics undergo phase transitions, that are dependent on the temperature. Above a certain temperature, called Curie temperature (T_C), ferroelectrics adopt a non-polar centrosymmetric structure, and the material does not exhibit spontaneous polarization, i.e. it is in the paraelectric state. This structural phase transition is reversible, and near T_C, due to a distortion in the crystalline lattice as the phase structure changes, the thermodynamic properties (dielectric, elastic, optical, and thermal constants) show an anomalous behaviour; the permittivity (ε_r) reaches a maximum at T_C [82], [85].

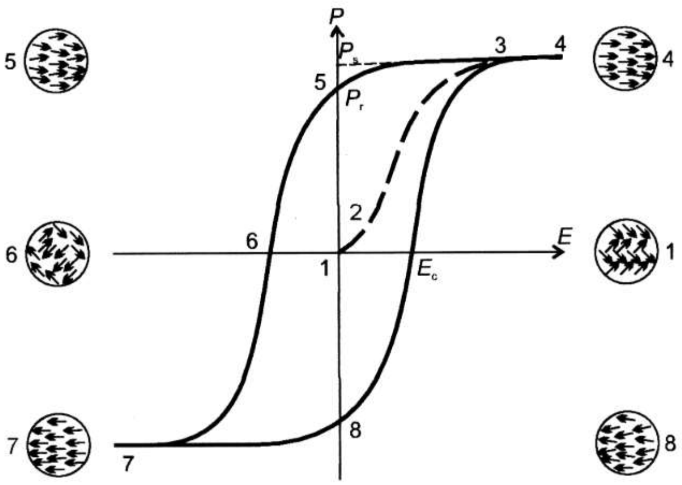

Figure 1-16 – Typical hysteresis loop (polarization over electric field) of a ferroelectric material. Numbers indicate the typical *route* to read the figure, with increasing, decreasing and opposite field conditions. P_S: saturation polarization; further increase in field does not cause higher polarization. P_r: remnant polarization; when external field is removed, the polarization does not fall to zero, keeping a remnant value. E_c: coercive field; to cancel P_r, a field in the opposite direction and magnitude should be applied [82].

Perovskite-type structured materials are the most relevant family for piezo and ferroelectric applications. The ideal structure of a perovskite is cubic (space group Pm3m-O_h); the unit cell of perovskites is ABO_3, where A is the largest cation (12-fold coordinated with the O^{2-}) and B is the smallest cation (6-fold coordinated) (Figure 1-17). Some of the most important compositions of the perovskite family are $BaTiO_3$ (BT), $PbTiO_3$ (PT) (doped with T, La, Zn, Nb, Mg…) and $K_xNa_{1-x}NbO_3$ solid solution [81], [86]. For piezoelectric applications, barium titanate was the first developed material, however, rapidly replaced by lead zirconate titanate, $PbZr_{1-x}Ti_xO_3$ (PZT) family [87], due to its relatively low piezoelectric coefficient ($d_{33} \cong 190$ pC/N for BT) [88], compared to that of PZT-based materials ($220 < d_{33} < \sim 1000$ pC/N) [77]. However, lead toxicity induced a set of legislation (as Directive 2002/95/EC and 2011/65/EU [89]) demanding the elimination of lead-based materials. Some exceptions created for electronics, mainly due to the lack of suitable substitutes for PZT [84], [90].

KNN is considered as a leading lead-free candidate for the replacement of PZT, because of its high T_C and good piezoelectric properties. $K_{0.5}Na_{0.5}NbO_3$ is a specific composition of a complete solid solution between the antiferroelectric $NaNbO_3$ and the ferroelectric $KNbO_3$. This composition is attracting attention due to its high piezoelectric response, that is attributed to the polymorphic phase boundary (PPB) between the two orthorhombic phases present on either side (K-rich and Na-rich) of the phase diagram, presented in Figure 1-18 [84], [85].

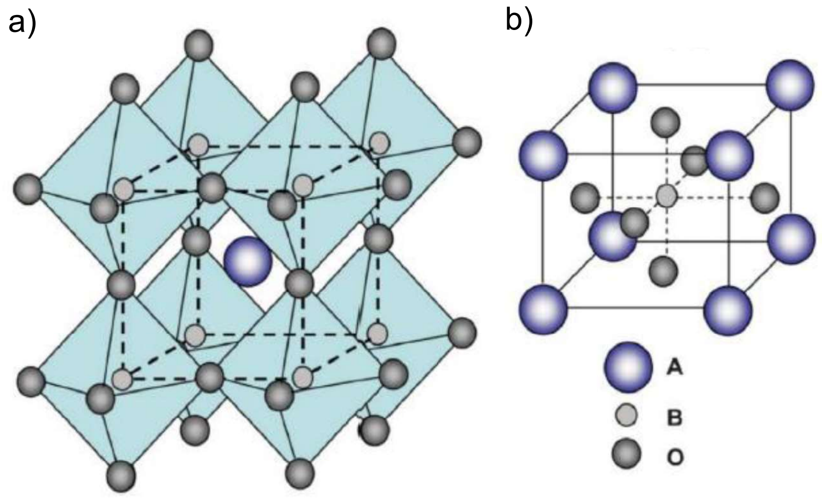

Figure 1-17 – Perovskite structure ABO_3: a) Corner-sharing (BO_6) octahedral with A ions located in 12-coordinated interstices. b) B-site cation at the centre of the cell [91].

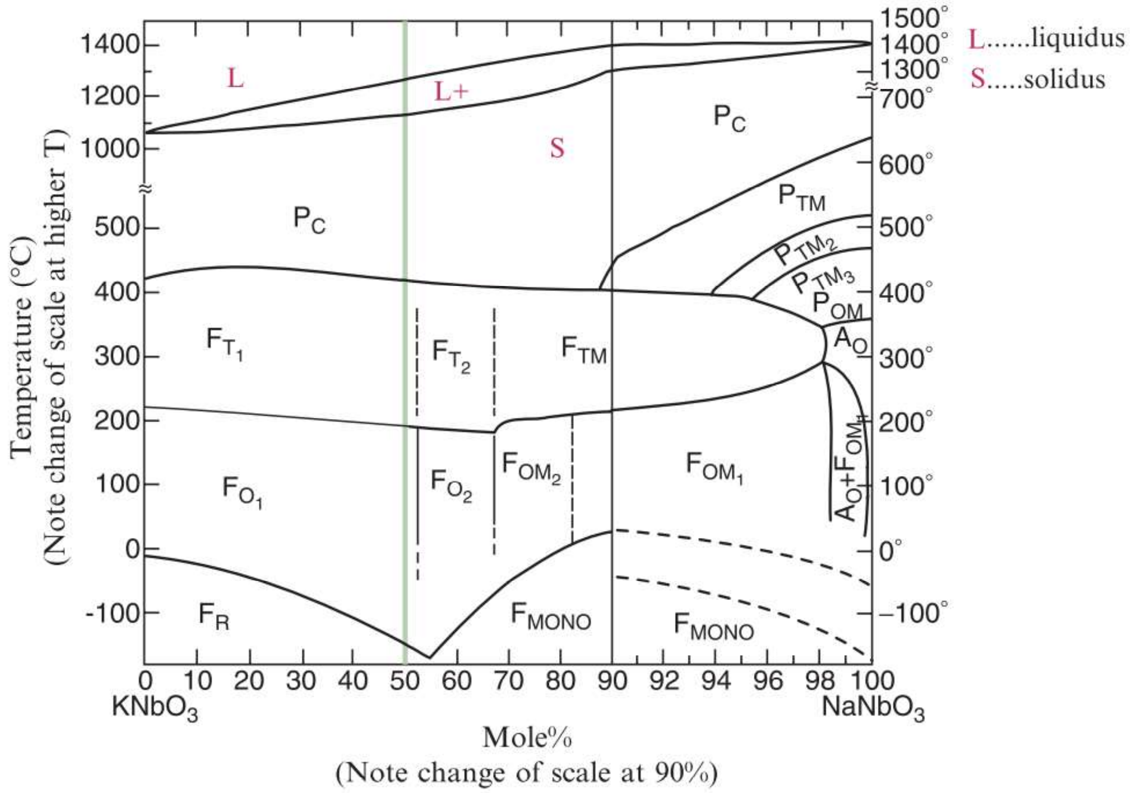

Figure 1-18 - $KNbO_3$–$NaNbO_3$ binary phase diagram [75]. Original figure from Jaffe, 1971 [88] [1]

---

[1] FR: ferroelectric rhombohedral with high potassium; F_{MONO}: ferroelectric monoclinic; F_{O1}: ferroelectric orthorhombic; F_{O2}: ferroelectric orthorhombic; F_{OM1}: ferroelectric orthorhombic field enforced in pure $NaNbO_3$; F_{OM2}: ferroelectric orthorhombic; F_{T1}: ferroelectric tetragonal with high potassium; F_{T2}: ferroelectric tetragonal; F_{TM}: ferroelectric tetragonal obtained with additives; A_O: antiferroelectric orthorhombic; P_C: paraelectric cubic; P_{OM}: paraelectric orthorhombic; P_{TM}: paraelectric tetragonal; P_{TM2}: paraelectric pseudo-tetragonal; P_{TM3}: paraelectric pseudo- tetragonal

As in many other perovskites the composition affects markedly the electrical response of the material. Similar behaviour applies for KNN as illustrated in Table 1-1 for the piezoelectric coefficients of different compositions of KNN-based ceramics. A tendency for the d_{33} decrease with increase in K content is observable, however one should take note that the heavily doped compositions might not be comparable among each other.

Table 1-1 - Effect of K/Na ratio on piezoelectric properties of KNN-based ceramics

Composition	**d_{33} (pC/N)**	**Reference**
$(K_xNa_{0.96-x}Li_{0.04})(Nb,Ta,Sb)O_3$, x = 0.38	306	[92]
$0.95(K_xNa_{1-x})NbO_3-0.05LiSbO_3$, x = 0.40	280	[93]
$(K_xNa_{1-x})_{0.95}Li_{0.05}(Nb,Ta)O_3$, x = 0.42	242	[94]
$(K_xNa_{1-x})_{0.94}Li_{0.06}NbO_3$, x = 0.50	220	[95]
$(Na_xK_y)(Nb,Sb)-LiTaO_3$, x = 0.52, y = 0.455	183	[96]
$(K_xNa_{0.96-x}Li_{0.04})(Nb,Ta)O_3$, x = 0.44	291	[97]

The Curie temperature of $K_{0.5}Na_{0.5}NbO_3$ is at about 420 ºC. Upon cooling, the tetragonal phase transforms to orthorhombic at about 200 ºC (Figure 1-19). A third phase transition occurs at T = -160 ºC: orthorhombic to rhombohedral [98], [99]. The typical d_{33} value for this undoped piezoceramic is not higher than 160 pC/N [100]–[103]. However, such value can be increased with specific processing. One example is the work of Saito and co-workers [104], that reported textured KNN piezoceramics to have PZT-like values of piezoelectric coefficients (d_{33} = 416 pC/N). Table 1-2 presents a set of several dielectric properties for different bulk piezoelectrics, lead-free and lead-based. Undoped KNN does not have the highest piezoelectric coefficients and neither the lowest losses, but it is the only material with T_C over 400 ºC. This uniqueness turns KNN in a market competitor and in particular for high temperature applications, for which PZT is inadequate. In addition, KNN piezoelectric coefficients can be tuned via texturing [81] [273] or by doping with Li, Cu, Ti, Bi, Sb among others [77], [105].

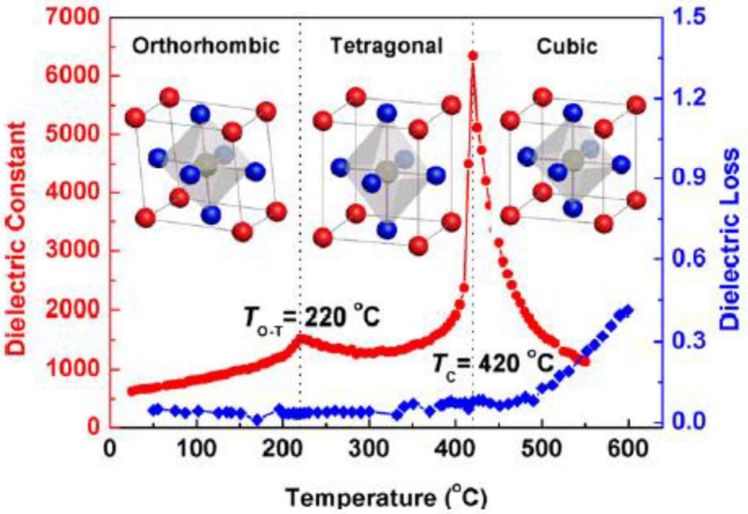

Figure 1-19 – Dielectric permittivity and losses of KNN ceramics, with increasing temperature. The polymorphs are schematically represented. Red, green and blue spheres represent A-site (K and Na), B-site (Nb) and oxygen atoms, respectively [106].

Table 1-2 – Electrical properties of some selected lead-free piezoelectrics and undoped PZT, at room temperature. Adapted from [81] and [107].

Material	**T_C**	ε_r @1 kHz	**d_{33}** (pC/N)	**K_{33}**	**Q_m**	**tanδ**	**Ref**
KNN ($K_{0.5}Na_{0.5}NbO_3$)	420	400	80-160	0.40		0.02-0.05	[100]–[103]
NBT ($Na_{0.5}Ba_{0.5}TiO_3$)	335	500	74	0.42	225		[107]
BT ($BaTiO_3$)	120	1500	190	0.49	100	0.01	[77], [88]
PZT ($PbZr_{0.52}Ti_{0.48}O_3$)	360	800	220	0.67	~800		[88]
PZT $Pb_{0.98}Ba_{0.01}(Zr_{1-x}Ti_x)_{0.98}Nb_{0.02}O_3$			221- 465	0.7-1			[108]

1.4. Sintering of KNN: conventional *vs.* FLASH

Despite the promising lead-free piezoelectric applications, KNN is a ceramic material that is not trivial to produce by conventional processing [109]. Solid state reaction route is the most common and convenient way to synthesize KNN powders. Carbonates (sodium and potassium) and niobium oxide are used as precursors. The melting points of these starting materials are 851, 891 and 1520 ºC, respectively. The range of KNN calcination temperatures is typically 800 - 900 ºC, which is very close to the melting point of the two alkali precursors. During calcination, the carbonates decompose and $K_xNa_{1-x}NbO_3$ desired phase is stabilized [110], [111]. Alternatively, chemical methods as sol-gel are commonly used to produce small amounts of powders or thin films by spin coating methods [112].

The sintering temperature for the composition under study in this work, x = 0.5, $K_{0.5}Na_{0.5}NbO_3$, is reported to be around 1100 ºC. Therefore, K and Na can vaporize during both calcination and sintering but especially during the last one. In consequence, non-monophasic, non-dense bodies, as well as possible abnormal grain growth, were previously reported [110], [111]. An example of the obtained microstructure and respective densification for KNN sintered at 1075, 1100 and 1125 ºC can be seen in Figure 1-20. Densification above 91% of theoretical density (ρ_t = 4.5 g/cm^3), for T = 1100 ºC, is difficult to obtain. When the temperature is increased, the grain grows and evidences of liquid phase start to be revealed [111].

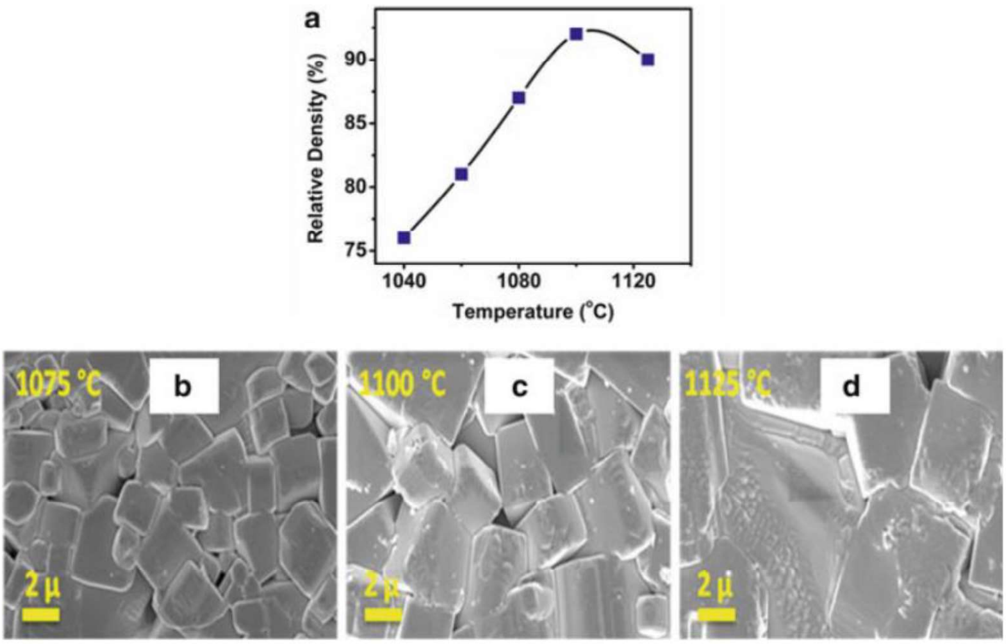

Figure 1-20 – a) variation of relative density of KNN with temperature of sintering. Microstructure of specimens sintered at b) 1075, c) 1100 and d) 1125 ºC [111].

Both grain growth and alkali volatilization originate perovskite phase instability and may result in secondary phase formation, as for instance, the K-rich tetragonal structured tungsten bronze [111], [113]. These factors hinder piezoelectric and ferroelectric properties of KNN. For instance, KNN sintered at 1125 and 1075 ºC exhibit piezoelectric coefficient values of 48 and 104 pC/N, respectively [111].

Over the last years, some solutions have been proposed to overcome non-monophasic and/or non-dense KNN ceramics. Without changing composition (i.e., doping), and using conventional processes, the sintering variables, as sintering temperature, or even time, as well as the creation of a saturated atmosphere of alkali during sintering have been extensively investigated. More recently, alternative sintering techniques have been used to densify materials of interest, either to improve properties or to overcome conventional sintering issues. In the specific case of KNN, full densification was obtained only by techniques as hot-pressing (HP) [114], SPS [12], [115], [116], spark plasma texturing (SPT) [13] and microwave sintering (MW) [117]. Generally, such techniques require high cost and complex structures for mass production. Due to the experimental and industrial issues related with KNN conventional sintering, the use of techniques as FLASH sintering may be a way to produce monophasic, highly dense, high performance piezoceramics.

In fact, KNN was FLASH sintered by Corapcioglu and co-workers [99] and this is one of the two publications on the topic, besides our own work. Corapcioglu *et al.* work was focused on the FLASH experiment, study of FLASH parameters and microstructure development. For that, dog-bone shaped compacts were used, avoiding electrode heterogeneities issues, and C.H.R. FLASH experiments were conducted; a local density of 94% was achieved in 30 s under 250V/cm electric-field at 990°C. It was established that such electric field promotes the highest ceramic shrinkage, while $E > 500$ V/cm promotes current localization and hotspots, with non-uniform densification. Additionally, when $J \geq 40$ mA/mm^2, melting was observed, especially in the electrode areas. For $J < 7$ mA/mm^2, densification did not occur. Despite that no dielectric nor piezoelectric properties of FLASH sintered KNN were reported, microstructural analysis revealed chemical heterogeneities for K and Na distributions [99]. Following that, a core-shell densification mechanism was proposed by the same authors, with EDX mapping of FLASH sintered ceramics showing K-rich areas in the shell and Na-rich areas in the core of the KNN grains, not observed in conventionally sintered ceramics (Figure 1-21 a) and b) respectively).

To summarize on the sintering challenges and development on sintering of KNN, Table 1-3 shows a group of properties of KNN ceramics sintered by different methods. HP, SPS and SPT seem to be the most suitable techniques to densify KNN ceramics to very high degree of density, with controlled grain growth and relevant piezo and ferroelectric properties. However, no reports for dielectric, piezo and ferroelectric properties of FLASH sintered KNN were published yet.

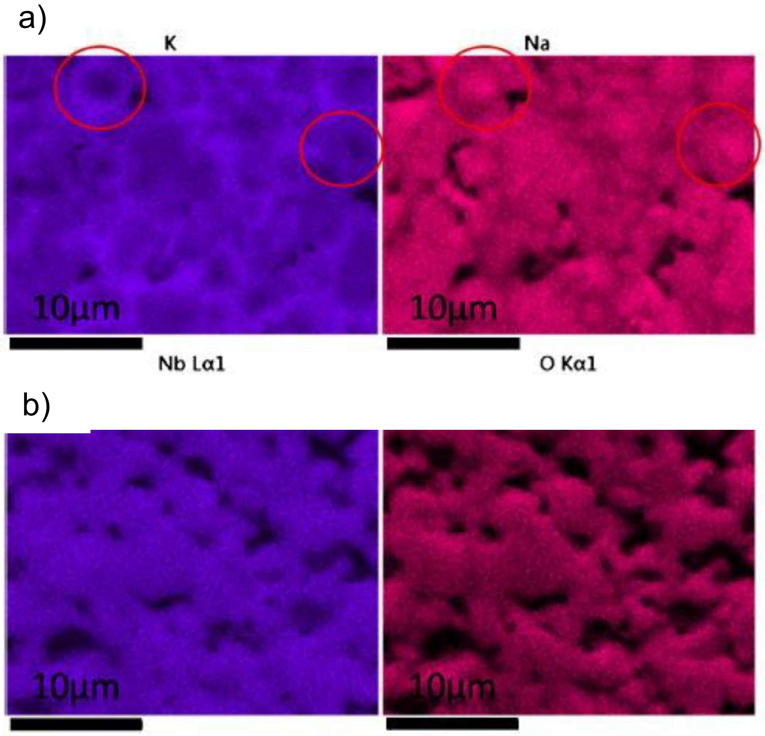

Figure 1-21 – SEM EDX mapping for a) FLASH sintered 250 V/cm, 20mA/mm^2, 30 s, 990 ºC and b) conventionally sintered 1000 ºC, 4 h specimens. Adapted from [99]

Table 1-3 The dielectric, piezoelectric and ferroelectric properties of SPS and SPT KNN ceramics developed in University of Aveiro [13]. Comparison with equivalent reported physical properties of KNN single crystals (SC) and KNN ceramics prepared by conventional sintering (Conv), SPS and Hot Pressing (HP).

	$\rho_{rel.}$ (%)	$\overline{G_{eq.}}$ (µm)	ε_r	ε_r at T_C	T_{O-T} (°C)	T_C (°C)	d_{33} (pC/N)	g_{33} (mV.m/N)	P_r (µC/cm^2)	E_c (kV/cm)	Ref.
KNN-SC			300		215	429	160	60.3	19.4	10.6	[118]
KNN-Conv	95.3		472		190	400	110	26.3	20	20	[119]
KNN-SPS	96	3.0	617	4413	218	357	50	9.2	44.7	22.8	[13]
KNN-HP	98.9		420				160	43			[103]
KNN-SPS	99		606				148	27.6	13	6.49	[120]
KNN-SPT	99.8	1.4	576	4672	184	370	125	24.5	43.3	15.0	[13]

More recently (2020), $K_{0.5}Na_{0.5}NbO_3$ ceramics were produced by reactive FLASH sintering (RFS) [121]. In this case, $KNbO_3$ and $NaNbO_3$ are produced individually by molten salt method. Then, an unreacted 1:1 mol mixture of K and Na niobates was pressed into dog-bone shaped compacts and C.H.R. FLASH sintered at different electric fields. Both electric field and current density limits were increased in comparison with the previous work by Corapcioglu *et al.* [99]. Therefore, a significantly lower FLASH temperature was observed - 444 to 583 ºC -, for electric fields ranging from 700 to 400 V/cm, together with high relative density (98 – 99%), with a current limit of ~42 mA/mm^2. The FLASH occurred during 30 s. X-Ray diffraction (XRD) suggests that $K_{0.5}Na_{0.5}NbO_3$ single phase was stabilized during the FLASH sintering process, with the characteristic cuboid particle shape being revealed by Scanning Electron Microscopy (SEM). Piezoelectric coefficients (d_{33}) between 126 and 135 pC/N were obtained. A clear explanation of the process was not yet presented, however, high local temperature (achieved by Joule effect) together with accelerated rates of defect and atomic diffusion at the particle contacts are the proposed mechanism [121].

Further on this work, the designation of FLASH sintering (FS) is not referred to Reactive FLASH Sintering (RFS) but to the densification process of previously calcined and stabilized ceramic powders. Despite being a promising technique, RFS is not the focus of this work. To properly understand and engineer RFS, FLASH sintering mechanisms and features must be clearly described and understood, so that the sustainable production of lead-free piezoeceramics can reach the production plants.

Summary

The need for alternative sintering techniques for ceramics is unquestionable. Either to produce complex piezoceramics or traditional materials, the decrease of sintering temperature and time are crucial, not only from the energy and environmental point of view, but also from the technological challenge.

FLASH sintering is a suitable technique to achieve such sustainability and technological goals. The alkali-based lead-free piezoelectrics as KNN, difficult to produce by conventional processes, make the use of FLASH particularly relevant. Despite that two studies were already published, one just before the starting of this work, and the second one during the work plan execution, the mechanisms behind FLASH of KNN are still unclear. Additionally, the piezoelectric and ferroelectric properties of FLASH sintered KNN are yet to be presented. A relationship between the low thermal budget processing and the consequences in terms the of properties of the final ceramics is not established. Furthermore, the development of dedicated simulation tools is still needed to explain the FLASH sintering process.

It is precisely within this framework that this work finds its pertinence and scientific relevance. Additionally, the comprehension on FLASH mechanisms will allow a faster engineering on the technological challenges, either from the materials side (particle size and morphology, additives, doping, etc) as from the equipment development side (electrodes, apparatus, thermal cycle, power input). This understanding and engineering will allow a quicker technology transfer to the industry.

Therefore, this work aims to depict the mechanisms for FLASH sintering of KNN, to develop alternative sintering techniques, as FLASH, to densify lead-free ceramics, as KNN, studying its parameters and ceramics properties and, ultimately, to sinter ceramics at room temperature.

Attachments

Table A-1 – Experimental details and final properties of FLASH sintered materials. Complete description for publications after December 2016. Details until such date on [25]

Material composition	Specimen shape size* (mm)	FLASH conditions			Type of signal	T_F (ºC)	Final densification (%)	Properties Characterization Conclusions	Year	Ref
		E (V/cm)	J (mA/mm^2)	time (s)						
Zirconia-based										
ZrO_2	Parallelepipedal 15x5x5	175	12		DC	1335	98	Conventional specimen breaks during cooling and FLASH don't. Grains with 001 orientation with electric field	2017	[122]
3YSZ	Dog-bone 21x3x1.58	20 – 120	210 – 1054	"few"	DC	900 - 1300	"full" density		2010	[22]
3YSZ	Parallelepipedal 10x5x1.5	80 – 1200	70	10	DC	800 – 1200	99		2015	[64]
3YSZ	Dog-bone 21x3x1.58	100	50 – 100	2 – 60	DC AC	900 (isothermal)		Grain size = 1 – 100 μm	2016	[65]
3YSZ	Dog-bone 3.5x1.3x0.65	100 (step)	32, 67, 105	720	DC	1000 (isothermal)	70 – 80	Grain size = 200 – 350 nm	2015	[123]
3YSZ	Dog-bone Lx2.4x1	120	100, 200, 300, 375, 500	0 - 3000	DC	900 (isothermal)	Grain growth evaluation	Grain size = 0.23 – 3.25 μm	2019	[61]
3YSZ	Dog-bone 15x3.5x1.5		Ramped 50 to 5000	7 - 700	DC	900 (isothermal)			2018	[33]
3YSZ	Parallelepipedal 18.7x3.52x1.44	95	150	0	DC	900 (isothermal)	90.6	Injected $V_O^{\cdot\cdot}$ at the incubation stage with direct influence on the densification Ea.	2018	[63]
3YSZ	Cylindrical 5x2	1.5, 15, 150			DC	Max 1300		Microcomprension testing. Revealed plasticity of 3YSZ above 600 ºC	2018	[124]
3YSZ	Dog-bone 20x3.4x1.34	80, 120, 140				Max 1400		Onset T_F increased with PO_2	2018	[43]
3YSZ	Cylindrical 2x5	150			DC	1170 (Air) 1125(Argon)	~100	SEM + TEM	2019	[125]
3YSZ	Parallelepipedal 15x5.8x2.3	100	27 – 118		DC	900 (isothermal) + C.H.R.		Macroscopic modelling of current, power and temperature during stage III	2018	[66]
3YSZ	Cylindrical 5x5	140	25 – 300		AC (0.5 – 1kHz)	1100 (isothermal)	55 – 90	1 kHz AC shrinkage and IS analysis is comparable with DC FLASH	2018	[126]
3YSZ	Dog-bone 20x3.4x1.36	100	20	10 - 600	DC	1100 (isothermal)	89 – 97	Decrease in resistivity with time. Linear increase of density with FLASH t.	2017	[49]
3YSZ	Dog-bone 20x3.5x0.5	100	100	0 or 10	AC	900	97 – 99 (TEM)	Macroscopic FEM modelling of specimen temperature	2017	[68]
3YSZ	Parallelepipedal 5x1.65x0.74	185	80	60	DC	800 (isothermal)		In-situ lattice expansion	2017	[127]
3YSZ	Dog-bone ?x4x2	62.5 – 112.5	100		DC	750 - 950 (isothermal) + C.H.R	94	Similar mechanical behaviour with conventional	2017	[128]

3YSZ	Cylindrical (2-10)x6	90	100		AC (1 kHz)	850 - 1250	88 - 98	The larger the samples, the lower T_F and density, with more heterogeneous microstructure.	2020	[129]
3YSZ	Cylindrical 4.5x6	75	100 Current rate: 10 start – 10 to 100 final	10 10	AC (1 kHz)	1000	94 - 96		2020	[130]
3YSZ	Cylindrical 0.32x7	2000		0 - 30				Contactless FLASH sintering with cold plasma	2020	[131]
3YSZ	Parallelepipedal 26x6x2	150	~42	0 - 120	DC	1280	82 – 100		2020	[132]
3YSZ	Dog-bone	100 – 150	40 – 60		DC	700	60 – 75		2020	[133]
3YSZ	Cylindrical 5x6	120	Current rate 100 – 200	142 – 300	AC 1 kHz	995	85 – 94		2020	[134]
3YSZ								FEM simulation of FLASH onset	2020	[70]
3YSZ	Parallelepipedal 15x3.5x3.5	100	82	300 - 10800	AC 100 Hz	C.H.R. 770 I.C. 1000 – 1200		Blue light emission of FS ceramics, even after thermal annealing at 1400 ºC	2020	[135]
3YSZ								Novel model of particle coalescence under thermal gradients	2020	[136]
3YSZ Films	Dog-bone 15x3.6x0.12-0.5	120	100, 200, 300 (1st for thick)	60	DC	740 – 1000	74 – 96	T_F decrease with thickness increase. If power is normalized for section area, transition occurs at 8-10 W/mm^2	2019	[137]
3YSZ (FSPS)**	Disk 20	10	0.15-0.3 kA/mm^2	30, 60, 90	DC		80 - 86	Polarity dependent grain size	2019	[138]
8YSZ	Cylindrical 3x(5 or 7)	50	10		AC (1kHz)	900	94	Grain size = 200 nm	2011	[139]
8YSZ	Cylindrical 2x8	40 – 500	30	3 – 60	AC (1kHz)	800 - 975	90 – 97	Grain size = 100 nm	2013	[31]
8YSZ	Dog-bone 21x3.2x2	30 – 150			DC	750 – 1150 ºC	84 – 96	Grain size = 470 – 590 nm	2011	[140]
8YSZ	Dog-bone Lx1.9x3	100	45 - 150	20	DC	800 (isothermal)	50 - 95		2019	[141]
8YSZ	Dog-bone 20x3x2	150	5 - 25	900	DC	850 (isothermal)		Role of current: current application activates alternative densification mechanisms when it exceeds a certain threshold value	2018	[142]
8YSZ	Dog-bone 15x3x(1.5-1.6)	100	60 – 100	60	DC	850 (isothermal)		IS. Ionic conductivity and grain size increases with J increase, associated with defect structure.	2019	[143]
8YSZ	Cylindrical 6.1x3	260	34 – 119	30, 600, 1200	DC	900 Isothermal	60 – 82		2019	[144]
8YSZ	Parallelepipedal 25x5x1.5	100 – 300	67	600	DC	690 - 790	~96		2017	[145]
8YSZ γ–ray before sintering	Cylindrical 5x5	150	50	120	AC (1 kHz)	860 – 900		γ -ray exposure increases densification obtained by FLASH.	2019	[146]

8YSZ (dense)	Dog-bone 15.25x2.49x1.32	260	15		DC	420 hot plate (isothermal)	Already dense	Surface temperature inhomogeneity at stage III	2018	[147]
8YSZ Polycrystals Single crystals	Dog-bone 6.5x1.7x1.6 10x2x1	 50	 82.5		DC; AC(0.1-10 Hz)	700 (isothermal)	Already dense	Electrochemical blackening of both poly and single crystals. Temperature distributions with thermal camera	2018	[148]
8YSZ single crystal	Parallelepipedal 4x2x0.7	50 – 490	25		DC	325 – 750	Already dense	Activation energy calculation for conduction	2017	[149]
(2-10mol%)Y_2O_3-ZrO_2	Parallelepipedal 15x3.5x3.5	100	~82	300	AC 100 Hz	1200		Blue light emission (at RT) of FLASH sintered YSZ ceramic	2020	[150]
Doped Yttria and Ceria										
Si^{4+}-doped Y_2O_3	Dog-bone	500	16	60	AC (0.5 Hz)	~1400	99	Photoluminescence under a UV light due to excess point defects induced by the flash-sintering and Si^{4+}-doping	2019	[151]
$Ce_{0.9}Gd_{0.1}O_{1.95}$	Dog-bone	70 – 170	36 – 220	30 – 300	DC	440 – 650	60 – 90		2017	[152]
$Ce_{0.9}Gd_{0.1}O_{1.95}$	Dog-bone 15x3.3x1.95		Current rate = 50 – 1000 mA/min; max 200 mA/mm^2		DC	680	96		2020	[153]
$Ce_{0.9}Gd_{0.1}O_{1.95}$	Dog-bone 15x3.3x1.95	70 - 400	100		DC	50 - 400		Air and Ar/5%H_2 atmospheres	2020	[154]
$Gd_2Zr_2O_7$	Dog-bone 20x3x1.6	100	83.3	0 – 300	DC	1050			2020	[155]
$Ce_{0.9}Gd_{0.1}O_{2-x}$ FLASH SPS**	Cylindrical ?x8	~4 – 130	400		DC	500 – 700	67 - > 99		2020	[156]
$Ce_{1-x}Gd_xO_{2-x/2}$, x = 0 - 0.20; $Ce_{0.9}Sm_{0.1}O_{1.95}$	Cylindrical 4x9	5 – 250	13.5	120	DC	600 – 900	69 – 99	Similar conductivity of FLASH and conventional specimens (when dense)	2017	[157]
CeO_2 + $MnCo_2O_4$	Dog-bone 20x3x1.65	12.5 – 150	830 - 1500	60	DC	175 - 1240			2018	[158]
$Ce_{0.8}Gd_{0.2}O_{1.9}Ce_{0.9}Gd_{0.1}$ $Ce_{0.8}Sm_{0.2}O_{1.9}$	Bar 25x6.5x1.6	55	87		DC	554 – 667	94 - 100	Grain size = 250 – 330 nm	2015	[159]
$(La_{0.6}Sr_{0.4})(Co_{0.2}Fe_{0.8})O_3$-$Gd_{0.1}Ce_{0.9}O_2$ composite	Dog-bone 20x3.5x1	5 – 150	560 – 1500	60	DC	210 – 990	99	Grain size = 1 – 2.5 μm	2015	[160]
$(Sc_2O_3)_{10}(CeO_2)(ZrO_2)$	Cylindrical 4-14x2-5	100 – 150	14 – 64	120 – 300	AC (1kHz)	1050 (isothermal)	> 95	The higher the porosity, the higher the final densification of the flash-sintered samples, showing that pores play a role as a preferential path in the flash sintering mechanism.	2018	[161]
Sm_2O_3-doped CeO_2 + graphite	Parallelepipedal 5x3x1	30	5 to 20, stepped by 2.5	~100 s per step	DC	25		Grain size = 540 nm	2019	[162]

Simple oxides										
ThO_2	Cylindrical 3.75x6	1600 - 533		10	DC	700 – 1050	82 - 96		2017	[163]
Y_2O_3	Dog-bone 20x3.5x1	75 – 1000	5 – 60		DC	985 - 1387	93 - 99	Grain size = 970 nm at 100 V/cm	2014	[164]
Doped- Y_2O_3	Dog-bone 20x3.3x1.1	0 - 1000	60	60	DC	~800 – 1400	60 - 99		2020	[165]
CeO_2	Cylindrical 6x3.7-4.0	200	100	1000	DC AC	900 (isothermal)		In-situ XRD (lattice expansion in stage III); TEM (amorphous GBs);	2018	[166]
TiO_2	Dog-bone 19.8x3.4x1.1	50 - 1000	18		DC	640 - 1150	90 - 98		2014	[28]
TiO_2	Parallelepipedal 3.72x1.33x0.55	100	25	On-off 100 s	DC		Conventionally dense	In-situ XRD for lattice expansion		[167]
TiO_2	Cylindrical 1x6.4	500	20	30	DC	900 - 1078	86 - 97	Grain size = 0.21 – 1.22 μm	2016	[168]
TiO_2	Cylindrical tx6	50	50	60	DC	775		Raman characterization: cathode, anode, middle and conv	2018	[169]
TiO_2	Parallelepipedal 6x1.6x0.8	100	62 – 124	100 On-off cycles	DC	920 (isothermal)		On-off in-situ synchrotron	2018	[170]
SnO_2 MnO_2-doped SnO_2	Cylindrical 5x(5-7)	80 – 100	50 – 250		AC (1 kHz)	900 - 1300	94	Grain size = 722 – 757 nm	2014	[171]
ZnO	Cylindrical 5.04x5	40 – 160	140		AC (50 Hz)	700 (isothermal)	94 - 95	Grain size = 970 nm	2014	[44]
ZnO	Cylindrical 1x6.4	300 – 1000	30 – 125	30	DC	120 ºC in $Ar+H_2$	97	Grain size = ~1 μm	2015	[172]
ZnO	Cylindrical 3x6.4	300	20, 30, 39	< 30	DC	600	64 – 95	For ZnO the rapid heating is the key factor for densification by FLASH. RTA experiments as comparison	2017	[52]
ZnO	Cylindrical 1x6.4	100 – 200	75	30	DC	RT in $(Ar+H_2)+H_2O$	98	Grain size = 1.8 μm	2018	[26]
ZnO	Cylindrical 6x5	60	50 5 ramp 50 (CRF)	60 10	DC	700 (isothermal)	98 90	Fast current ramp, G = 1.28 μm Slow current ramp, G = 0.22 μm	2018	[34]
ZnO	Cylindrical 3x6	60	50 – 300	60	DC	800 (isothermal)	86 – 95	In-situ XRD and cell expansion with current increase	2018	[173]
ZnO	Cylindrical 3x6	60 120	100 Ramp	60 Total 92	DC	700 (isothermal)	94 – 95	More intragranular pores on J ramp specimens	2019	[174]
ZnO	Cylindrical 3x6	60	100	60	DC	700 (isothermal)		In-situ high-T mechanical behaviour	2020	[175]
ZnO	Dog-bone 14x3.3x1.7	1765	50	480	AC			New electrode design	2020	[176]
ZnO	Dog-bone 14.5x3.3x1.7	3530	~18	40	AC	RT	99		2020	[177]
ZnO + Water	Dog-bone	1500 - 3750				RT			2020	[178]
ZnO	Cylindrical	33 – 66	750 – 1500	10 – 50	DC	RT	81 – 98	New method that combines Cold and FLASH sintering	2020	[179]

FLASH-Cold Sintering	~3x5									
AZO FSPS**					DC and AC			FSPS with Boron nitride as matrix material	2020	[180]
ZnO Two-step FS	Cylindrical 2.8x6.4	150	95 95+63	2 – 30 6+(150 – 300)	DC	500 (isothermal)	One step= 98 Two step= 97	Argon Flow = 33 mL/min Grain size (one step) = 1750 nm Grain size (two step) = 370 nm	2017	[181]
Bi_2O_3-doped ZnO	Cylindrical 6.4x1	300	30 – 125	30	DC	870	88 – 91	Grain size = ~13 μm	2015	[45]
$CuO \rightarrow Cu_2O$ $Mn_2O_3 \rightarrow Mn_3O_4$ Reactive FLASH	Dog-bone 20x3.3x(1.7-2.0)	62.5 – 125	90 – 1130	40 – 120	DC			Study on the reactivity of CuO and Mn_2O_3 to change the oxidation state.	2020	[182]
Alumina and Alumina-based composites										
Al_2O_3	Dog-bone 20x3.3x1.6	500 – 1500	2 – 7		DC	900 - 1400	95		2016	[183]
Al_2O_3	Dog-bone ?x3x2.5	750 – 1000	2, 4, 6		DC	1200 (isothermal)	94	Optical emission study during stage III of FLASH	2018	[184]
$(90)Al_2O_3+(8)SiO_2+(2)MgO$ (wt.%)										
Al_2O_3	Dog-bone ?x3x3	500 – 1500	0.6 – 2	120	DC	900 – 1250	75 – 96	Density decrease with E	2017	[185]
$(90)Al_2O_3+(8)SiO_2+(2)MgO$ (wt.%)						800 – 1200	Porosity < 4%	Mg segregation on the cathode		
Al_2O_3	Dog-bone	1000	2 – 6	180	DC	1200		Abnormal grain growth	2018	[186]
α-Al_2O_3	Dog-bone Parallelepipedal 4x1.6x1	250 – 450	25 – 75		DC			Voltage-current and current rate FLASH experiments In-situ and ex-situ XRD experiments. Stabilization of spinel after FLASH	2019	[187]
$MgAl_2O_4$	Dog-bone 20x3.5x1.4	300 – 1000	13	60	DC	1410	97.9	E < 750 have no influence Grain size = 0.199 – 5.23 μm	2017	[188]
α–Al_2O_3+$MgAl_2O_4$+ 8YSZ	Dog-bone 20x3.5x1.3	50 – 500	25	30	DC	1150 – 1350	90 – 96	Grain size = 470 – 1500 nm Lattice parameters analysis	2017	[189]
MgO-doped Al_2O_3	Dog-bone 21x3.3x1.8	1000	60 mA		DC	800 - 1400	99	Grain size = 1.9 μm	2011	[190]
3YSZ- Al_2O_3 composite	Dog-bone 21x3.3x1.8	50 – 150	84		DC	1060 - 1400	97 - 99	Grain size (3YSZ) = 652 nm Grain size (Al_2O_3) = 772 nm	2014	[191]
Al_2O_3 -3YSZ	Dog-bone	0 – 150	70	“mere”	DC	740 – 1300	82 – 96		2020	[192]
$MgNa_2Al_{10}O_{17}$	Cylinder 4x8	100 – 120	8 - 100		AC (1kHz)	550	88		2015	[42]
MgO+α-Al_2O_3 – reaction into $MgAl_2O_4$	Dog-bone 15x3.5x1.3		Current rate 0 – 100	60 s for rate	DC	960 (isothermal)		Reaction in 45 s. full density in 60 s.	2019	[39]
MgO+α-Al_2O_3 – reaction into $MgAl_2O_4$ (with 8YSZ)	Dog-bone 15x3.5x1.5	300 – 1000	60		DC	~620 – ~950	93 – 97	8YSZ addition accelerates FLASH and spinel stabilization	2019	[35]
$MgAl_2O_4$-8YSZ Reactive FLASH	Dog-bone 15x3.5x1.5	500	60	60	DC	710 - 1014	95	Role of dispersion of powders in RFS	2020	[193]
Al_2O_3 – YAG Reactive FLASH	Dog-bone 9.8x2.85x1.16	500 - 900	20	30	DC	1200 - 1350	97		2019	[194]
Al_2O_3–$Y_3Al_5O_{12}$ (YAG) Reactive FLASH	Parallelepipedal	900	60	150	DC	1350	99		2020	[195]

Composites/multilayers										
3YSZ – Al_2O_3 composite	Dog-bone 21x3.3x1.8	50 – 100	85	60	DC	1000 – 1300 (isothermal)	95 – 99	Grain size (YSZ) = 610 – 680 nm Grain size (Al_2O_3) = 670- 730 nm	2014	[48]
3YSZ – SiC composite	Dog-bone 20x3.34x1.26	70 – 140	80	60	DC	1000 (isothermal)	97	Grain size = 230 nm	2016	[73]
75-3YSZ + 25-Al_2O_3 (vol%)	Cylindrical 4x6	200 – 300	71 – 106	60	AC 1 kHz	963 – 1061	82 - 95		2020	[196]
15mol% CaO-3YSZ	Dog-bone	100	100			727 - 847	53 – 59	Impedance spectroscopy	2020	[197]
rGO-3YSZ	Dog-bone 21x3x2	60	160	20	DC	RT	>99	rGO was “trapped” inside 3YSZ	2020	[198]
NiO-ZrO_2-Cubic ZrO_2 Multilayer	Dog-bone 21x3.2x2.7	150	120		DC	390 – 960	99		2013	[56]
Y_2O_3, $MgAl_2O$, Yb:$(LaO)_2O_3$	Cylindrical 2.5x(10-15)	100 – 300		30 – 300			98 – 99	Adsorbed microwave heating power = 20– 400 W/cm^3 100 – 200 ºC/min heating	2018	[199]
ZrNbHfTa foil + grafite Interfacial reaction	270 μm thick foil	SPS aparattus						High heating rates of FLASH-SPS allow metal foil to melt before deformation.	2020	[200]
NLC+GDC	Cylindrical ?x5	200	5		AC (1kHz)	420			2020	[201]
			100	120	DC	420				
8YSZ + Graphene	Cylindrical 4x6	75 – 500	35 – 175	60	DC	650 – 1250	71 – 90		2020	[202]
8YSZ + LiF and KCl	Cylindrical 3x5	200	25-100	1200 - 7200	AC	650		LiF and KCl are used as liquid phase additives.	2020	[203]
Electroceramics										
$BaTiO_3$	Dog-bone 20x3.5x1.6-2.0	150 – 500	1000		DC	612 - 900	92 - 97	Grain size = 300 – 400 nm ε_r (35 ºC) = 2.1 – 3.5 (x10^3) tanδ = 2.6 – 3.9 (x10^{-2}) T_C = 127 – 129 ºC	2014	[204]
$BaTiO_3$	Parallelepipedal (30x10x2)	25 - 350	monitored	60	DC	1020	90-95		2014	[205]
$BaTiO_3$	Dog-bone 7.5x3x?	150	20		DC	900	80	Kinetics of sintering	2020	[206]
$BaTiO_3$	Parallelepipedal 15x5x5	285			AC 250 Hz	1000	95.5		2020	[207]
$BiFeO_3$ and Ti-doped $BiFeO_3$	Cylindrical 8x10	30 – 50 DC 40 AC	33 DC 9 AC	10 – 15 min	DC AC (0.05, 0.5, 1 kHz)	600 - 650 (isothermal) @0.15 MPa	90 (BFO)	Grain size BFO = 20 μm (DC) non-monophasic Grain size BFO = 3 – 5 μm (AC) Grain size BFTO = 0.2 – 0.4 μm (AC)	2019	[208]
$BiFeO_3$	Dog-bone	15 - 150	20	15	DC	400 – 600	“high density”	Low dielectric constant	2017	[209]
$BiFeO_3$	Cylindrical 5x5	50	25		DC	500	90	In situ XRD	2019	[210]
$BiFeO_3$	Cylindrical 5x¼ ´´	100	25	75	DC	350	90	In-situ by energy dispersive X-ray diffraction (ED-XRD)	2019	[211]

	Dob-bone 1 mm thickness									
$Bi_{0.93}La_{0.07}FeO_3$	Dog-bone 21x4x1	50 - 200	20 – 60	60	DC	465 – 575		Small window of E and J combination for sintering wi/out secondary phases	2020	[212]
$Bi_{2/3}Cu_3Ti_4O_{12}$	Dog-bone	5 – 15	53	60	DC	855 – 912	92 - 97		2020	[213]
$(Bi_{0.2}Na_{0.2}K_{0.2}Ba_{0.2}Ca_{0.2})TiO_3$	Paralelepipedal 15x3.5x1.4	200	20	~300	DC	840			2020	[214]
$Bi_2O_3 + Fe_2O_3 \rightarrow BiFeO_3$ Reactive FLASH	Dog-bone	25 – 100	20 – 50	60	DC	575 - 625		Grain size = 83 nm	2018	[215]
R(La, Sm, Y)-doped BFO $Bi_{0.98}R_{0.02}FeO_3$	Dog-bone 21x(As)4.74	50	40	5	DC	650	"nearly full"	Grain size = 22 – 28 nm	2019	[216]
$CaCu_3Ti_4O_{12}$	Dog-bone	0 – 60	75		DC	750 – 1000	90 - 95	εr = 1820 - 4900 tanδ = 0.05 – 0.13	2017	[217]
$Na_{0.5}Bi_{0.5}TiO_3$	Dog-bone	100 – 180	30	30		1000 – 785	Not value	Dense ceramics. Smaller Grain size for FLASH than conventional	2019	[218]
$MgTiO_3$	Dog-bone 20x3x0.9	500 – 800	37	30	DC	1125 – 1250	85 – 98	Grain size = 68 – 1242 nm	2018	[219]
Nb-doped $BaTiO_3$	Dog-bone 20x3.1x1.4	120 - 160	20 50 80	30 60 300	DC	1055	95 (max J and t)		2019	[220]
Nb_2O_5 doped $BaTiO_3$	Dog-bone 20x3.1x1.4	100 – 160	80	30	DC	1030 - 1123	94 – 95	Dielectric breakdown	2020	[221]
$KNbO_3$	Cylindrical 3x10	600	14		DC	750	95	Grain size = 1 – 3 μm	2014	[222]
$NaNbO_3$	Parallelepipedal 20x3x0.9	400 – 700	37	3	DC	860 - 1010	"Dense"	Grain size decrease with E	2019	[223]
$K_{0.5}Na_{0.5}NbO_3$	Dog-bone 20x3.5x1.2	100 – 500	7 – 40	10 - 60	DC	900 - 1090	95	Core-shell structures of K-Na as explanatory of sintering mechanisms	2016	[99]
$K_{0.5}Na_{0.5}NbO_3$	Parallelepipedal 15x5x2	300	60	60	DC	290	Non-uniform	Argon + Water atmosphere. Local melting as possible sintering mechanism	2019	[224]
$K_{0.5}Na_{0.5}NbO_3$	Parallelepipedal 15x5x2	300	20	60	DC	~900	>90	FEM simulation of particle contact influence on Joule heating distribution	2020	[225]
$K_{0.5}Na_{0.5}NbO_3$	Parallelepipedal 15x5x2	300	20	60	DC	C.H.R + I.C. ~900	89 – 95	The role of particle contact on FLASH sintering	2020	[226]
$K_{0.5}Na_{0.5}NbO_3$ Reactive FLASH	Dog-bone 20x3x0.8	400-700	~42	30	DC	444 - 583	98 - 99		2020	[121]
$SrTiO_3$	Dog-bone 21x3.3x1.8	150 – 1000	60 mA		DC	390 - 960	95	Grain size = 1 μm	2012	[227]
$SrTiO_3$	Cylindrical 6x8	500	2 – 10	600 – 1200	DC	1120-1150 (isothermal)	85 – 90		2017	[228]
$SrTiO_3$	Cylindrical 10x10	140	3.2	Until material stops conducting	DC	697 – 1014	77 – 96	Model material for defect redistribution	2019	[229]

$SrTi_{1-x}Fe_xO_{3-\delta}$	Parallelepipedal 10x3x3	50 – 1000	11	~20	DC	580 - 1400	> 90	Theoretical calculation of heat dissipation by radiation, convection and conduction	2017	[230]
$Sr(Ti_{0.2}Y_{0.2}Zr_{0.2}Sn_{0.2}Hf_{0.2})\_O_{3-x}$	Dog-bone 20x3.1x1.8	350	40	60	DC	1000	70		2020	[231]
SiO_2-coated $BaTiO_3$	Dog-bone 10x3.34x1.16	500	2.5 step until 15.5	10 per step. 40 s final	DC	650 – 925 (increase with SiO_2 %)		T_C = 120 Good agreement of ε_r and tanδ with conventional	2019	[232]
K, Li, Mn-doped NBT	Cylindrical 6.35	100	10, 15, 20	300, 600, 1200, 1800	DC AC (1 kHz)	880	5.58 – 5.72 (g/cm^3)	For J = 15 and t = 600 ε_r (1 kHz) = 334; tanδ (1 kHz) = 1.44; d_{33} = 92; T_C = 210 ºC; 7% more polarization for FLASH samples	2019	[233]
$Li_{6.25}La_3Zr_2Al_{0.25}O_{12}$ (Al-doped LLZO)	Dog-bone 15x3.5x1	40	190	15	DC	850	96		2019	[234]
$LiNi_{1/3}Co_{1/3}Mn_{1/3}O_2$	Dog-bone 20x3x2.1	20	64 – 256	0 - 600	DC	320		Increase in J, increase resistivity (IS measurements)	2018	[235]
$Li_{5.95}La_3Zr_2Al_{0.35}O_{12}$ Reactive FLASH	Dog-bone	30 – 50	160 – 200		DC		86		2019	[40]
$Li_{0.5}La_{0.5}TiO_3$ Reactive FLASH	Dog-bone 15x3.5x1.3	80 – 120	60	45	DC	800 - 960	96 - 98	Impedance spectroscopy reveals that: σ(bulk) = 0.5 mS/cm (field independent) σ(Grain boundary) - dependent on E	2020	[236]
$La_{0.8}Sr_{0.2}Ga_{0.8}Mg_{0.2}O_{3-\delta}$ (LSGM electrolyte)	Parallelepipedal 25x5x1.5	100	Rate 40 - 73	600 - 1800	DC	690	64 – 97		2020	[237]
$Na_3Zr_2(SiO_4)_2(PO_4)$	Dog-bone	45	60	30	AC 800 Hz	700	91		2020	[238]
Mn_2O_3 into Mn_3O_4	Dog-bone 20x3x1.5	12.5	0.095	hours	DC	285	Already dense	Transformation during stage III via a moving reaction front	2019	[36]
$MnCo_2O_4$	Dog-bone 20x1.65x3	15 – 17.5	$1.4x10^{-3}$ – $1.6x10^{-3}$		DC	120 – 150		Grain size = 8 μm	2014	[239]
$MnCo_2O_4$	Dog-bone 20x3x1.65	10 – 17.5	$1.4x10^{-3}$ – $1.6x10^{-3}$	60	DC	120 - 145		EDX; Raman Role of electric field	2018	[240]
Mg-doped $Ca_3(PO_4)_2$	Cylindrical 4.5x6	0 - 2000	2	< 60	DC	700 - 1000		Beta-phase stabilization	2019	[241]
PbO-(0.52)ZrO_2-(0.48)TiO_2	Dog-bone 20x3x0.9	300 – 600	37 10 – 50	30	DC	538 – 860	84 - 94	d_{33} = 217 - 228	2018	[242]
PbO-ZrO_2-TiO_2 Reactive FLASH	Dog-bone 20x3x0.9	300 – 600	37.5	30		520 – 560	97 – 99	Grain size increase with E d_{33} = 228 - 236	2019	[243]
PbO-ZrO_2-TiO_2	Dog-bone 20x3x0.9	80 – 140	40 – 150	30	AC (60 Hz)	710 - 830	98 – 99	Lower J, lower grain size	2019	[244]
ZnO–Bi_2O_3-M (M = Cr_2O_3, MnO_2 or Co_2O_3)	Cylindrical 3x7	300	Current rate: 40 to 66 (13 each 10 s)	10	DC	< 750	95 - 9	Application: varistors	2020	[245]
ZnO-Bi_2O_3-MnO_2	Cylindrical 3x7	200 – 400	Current rate Max = ~66	10	DC	C.H.R. 700 – 768; I.C. 750	89 - 98	Application: varistors	2020	[246]
SiO_2-doped ZnO–Bi_2O_3–MnO_2	Cylindrical 3x7	300	140 - 214	10	DC		94 – 98	Application: varistors	2020	[247]

Structural materials										
B_6O	Parallelepipedal 13x13x4.6	96	50	1800	DC	1000			2018	[248]
$TaSi_2/MoSi_2$ coatings on SiOC/CBCF	Multilayer							High emissivity of FLASH sintered samples	2018	[249]
SiC	Cylindrical (2.5 – 3)x10	1200 – 1440	190		DC	1170 – 1670	56 - 88	Grain size = 1 – 2 μm	2013	[250]
SiC	Cylindrical 5x5	Increased in-situ	660	50	DC	900			2017	[251]
SiC (FSPS)**	Cylindrical 3x20 and 10x60	10 – 33	0.7 – 6.4	15	Pulsed DC	2300 @ 15 MPa	96	Grain size = 10 – 20 μm	2016	[252]
Traditional ceramics										
Whiteware	Parallelepipedal 10x5.6x0.4	2100 - 2500		Continu-ous	DC	900 (isothermal)	“safe” and “fail experiments		2018	[253]
Porcelain	Dog-bone 20x3x1.4-1.8	350 - 500 1750	4 – 20	30	DC	900 – 1050 1000 (isoth.)	98		2018	[254]
Porous glass $95SiO_2+2.3Na_2O+1.6Al_2O_3$ (wt.%)	Cylindrical 4x6	1000 - 3000	2	30	DC	600 – 750	75 – 95	Almost linear dependence of conductivity with T_{sample} (calculated)	2017	[255]
Soda-lime glass	Parallelepipedal 20x(16 A_S)	Increased to current limit	0.3 - 4		DC	400	--	Test of different electrodes on the heterogeneous heating during FLASH.	2020	[256]
Others										
$BaZr_{0.1}Ce_{0.7}Y_{0.2}O_{3-\delta}$	Parallelepipedal 20x5.3x2.2	100 - 500	25 - 125	40 - 360	DC	678 - 967			2020	[257]
$Ca_3(PO_4)_2$	Cylindrical 2-5x8	1000 – 1500	2	300 - 6000	DC		79 – 93		2018	[258]
Sb_2Te_3	Cylindrical 3x10	5	15 k	0.01 - 600	AC (100 Hz)	< 800	82 – 97	FEM analysis of temperature distribution in SPS-like apparatus. Similar thermoelectric behaviour with conventional.	2018	[259]
Hydroxyapatite	Parallelepipedal 20x5.4x1	600 – 1250	0.5 - 9		DC	950 – 1150	< 95	Air and vacuum	2020	[260]
Carbon Fibber		--	Current rate: 50 $A/mm^2\ min^{-1}$			650 – 1800 (No external heating)		The greater the current, the more crystalline fibbers get.	2020	[261]
(Mg, Co, Cu, Ni, Zn)O	Dog-bone 20x3.4x2.9	100	61 – 91	180	DC	350	92 – 95		2020	[262]
$Mg_{0.2}Ni_{0.2}Co_{0.2}Cu_{0.2}Zn_{0.2}O$	Dog-bone	15 – 60	30 – 150	60	DC	~500 - 1000	70 – 80		2020	[263]
$TiNiCu_{0.05}Sn$ Hybrid-FSPS	Cylindrical ?x15						90 – 93	Thermoelectric material	2020	[264]
Graphene								Production of graphene from coal, biochar, rubber, etc.	2020	[265]
$(Nb_{1/3}Ta_{1/3}Ti_{1/3})N_{1-\delta}$	Cylindrical 2.5x3.1	32	~30k – 40k	120	DC		RT		2020	[266]
$UO_{2.00}$, $UO_{2.08}$, and $UO_{2.16}$	Cylindrical 5.25x4.75	57 - 125	50	12	DC	26 - 600	Pre-sintered to 95%	Excess oxygen lowering the field required to FLASH	2017	[267]

UO_2 and $UO_{2.16}$	Cylindrical 6x4.49	188	442 – 632	120 – 180	DC	600	81 – 91		2018	[268]
ZrB_2 (FSPS)**	Cylindrical 20x8	25 kW	1.5 kA		DC	1452 - 2198 @16 MPa	76 - 95	Grain size = 2.6 – 11.8 μm	2014	[269]
HfB_2 (FSPS)**	Cylindrical 5x20	10, 20 kW		20, 35		600 (isothermal)	95	SEM, TEM	2018	[270]
TiB_2-*h*BN (FSPS)**	Cylindrical Hx35	17 – 40 Kw		60	Pulsed		97	Die-less FSPS; texturing effect typical of hot forging	2017	[271]
Nd-Fe-B (FSPS)**	Cylindrical 20x12	12 kW			DC	1080 @15 MPa	~100		2016	[272]

* Dog bone

LxWxT (WxT gauge section)

Parallelepipedal

LxWxT

Cylindrical

HxD,

With L = length; W = width; T = thickness; H = height; D = diameter

**FSPS is a technique based on SPS that used isolating dies (alumina, for instance) to allow current flow through the specimen

References

[1] R. F. Walker. “Mechanism of Material Transport During Sintering”. J. Am. Ceram. Soc., vol. 38, no. 6, pp. 187–197, 1955.

[2] R. K. Bordia, S.-J. L. Kang, and E. A. Olevsky. “Current understanding and future research directions at the onset of the next century of sintering science and technology”. J. Am. Ceram. Soc., vol. 100, no. 6, pp. 2314–2352, 2017.

[3] D. Sohrabi Baba Heidary, M. Lanagan, and C. A. Randall. “Contrasting energy efficiency in various ceramic sintering processes”. J. Eur. Ceram. Soc., vol. 10, no. October, pp. 1018–1029, 2017.

[4] M. N. Rahaman. Sintering of Ceramics. Boca Raton: CRC Press, 2007.

[5] M. N. Rahaman. Ceramic processing and sintering. Second. New York: Marcel Dekker, Inc., 2003.

[6] D. G. R. William D. Callister. “Fundamentals of Materials Science and Engineering: An Integrated Approach”. p. 910, 2009.

[7] S.-J. L. Kang. Sintering: Densification, Grain growth, and Microstructure. 2005.

[8] S. Lee and S.-J. L. Kang. “Evaluation of densification mechanisms of liquid-phase sintering”. Zeitschrift fur Met., vol. 92, no. 7, pp. 669–674, 2001.

[9] I. M. Liftshitz and V. V. Slyozov. “The kinetics of precipitation from supersaturated solid solutions”. J. Phys. Chem. Solids, vol. 19, no. 1, pp. 35–50, 1961.

[10] C. E. J. Dancer. “Flash sintering of ceramic materials”. Mater. Res. Express, vol. 3, no. 10, pp. 102001–102025, 2016.

[11] Nick Gilbert. “Hot Isostatic Pressing (HIP) – The Fundamentals, Industrial Applications and Benefits”. 2012. [Online]. Available: https://www.azom.com/article.aspx?ArticleID=6039. [Accessed: 18-Oct-2019].

[12] K. Wang, B.-P. Zhang, J.-F. Li, and L.-M. Zhang. “Lead-free $Na_{0.5}K_{0.5}NbO_3$ piezoelectric ceramics fabricated by spark plasma sintering: Annealing effect on electrical properties”. J. Electroceramics, vol. 21, no. 1–4, pp. 251–254, 2008.

[13] R. Pinho *et al.*. “Spark plasma texturing: A strategy to enhance the electro-mechanical properties of lead-free potassium sodium niobate ceramics”. Appl. Mater. Today, vol. 19, p. 100566, 2020.

[14] E. Y. Gutmanas, A. Rabinkin, and M. Roitberg. “Cold sintering under high pressure”. Scr. Met., vol. 13, pp. 11–15, 1979.

[15] J. Guo *et al.*. “Cold Sintering: A Paradigm Shift for Processing and Integration of Ceramics”. Angew. Chemie - Int. Ed., vol. 55, no. 38, pp. 11457–11461, 2016.

[16] H. Guo, A. Baker, J. Guo, and C. A. Randall. “Cold Sintering Process: A Novel Technique for Low-Temperature Ceramic Processing of Ferroelectrics”. J. Am. Ceram. Soc., vol. 99, no. 11, pp. 3489–3507, 2016.

[17] M. Krage. “Microwave sintering of ferrites”. Am. Ceram. Soc. Bull., vol. 60, no. 11, pp. 1232–1234, 1981.

[18] M. Mapley, J. P. Pauls, G. Tansley, A. Busch, and S. D. Gregory. “Selective laser sintering of bonded magnets from flake and spherical powders”. Scr. Mater., vol. 172, pp. 154–158, 2019.

[19] C. Shuai *et al.*. “Construction of an electric microenvironment in piezoelectric scaffolds fabricated by selective laser sintering”. Ceram. Int., vol. 45, no. 16, pp. 20234–20242, 2019.

[20] I. Shishkovsky, I. Yadroitsev, P. Bertrand, and I. Smurov. “Alumina-zirconium ceramics synthesis by selective laser sintering/melting”. Appl. Surf. Sci., vol. 254, no. 4, pp. 966–970, 2007.

[21] F. A. Lewis, J. Orr, and A. R. Ubbelohde. “Contact Effects resulting from Compression and Flash Sintering in Graphite Powders”. Proc. Phys. Soc. Sect. B, vol. 70, no. 10, pp. 928–936, Oct. 1957.

[22] M. Cologna, B. Rashkova, and R. Raj. “Flash Sintering of Nanograin Zirconia in <5 s at 850°C”. J. Am. Ceram. Soc., vol. 93, no. 11, pp. 3556–3559, Nov. 2010.

[23] M. Biesuz and V. M. Sglavo. “Flash sintering of ceramics”. J. Eur. Ceram. Soc., vol. 39, no. 2–3, pp. 115–143, 2019.

[24] J. Luo. “The scientific questions and technological opportunities of flash sintering: From a case study of ZnO to other ceramics”. Scr. Mater., vol. 146, pp. 260–266, 2018.

[25] M. Yu, S. Grasso, R. Mckinnon, T. Saunders, and M. J. M. Reece. “Review of flash sintering: materials, mechanisms and modelling”. Adv. Appl. Ceram., vol. 116, no. 1, pp. 24–60, 2017.

[26] J. Nie, Y. Zhang, J. M. Chan, R. Huang, and J. Luo. “Water-assisted flash sintering: Flashing ZnO at room temperature to achieve ~ 98% density in seconds”. Scr. Mater., vol. 142, pp. 79–82, 2018.

[27] R. Chaim. “Effect of the liquid fragility on flash sintering behavior of oxide nanoparticles”. Scr. Mater., vol. 178, pp. 261–263, 2020.

[28] S. K. Jha and R. Raj. “The effect of electric field on sintering and electrical conductivity of Titania”. J. Am. Ceram. Soc., vol. 97, no. 2, pp. 527–534, 2014.

[29] Y. Dong and I. W. Chen. “Onset Criterion for Flash Sintering”. J. Am. Ceram. Soc., vol. 98, no. 12, pp. 3624–3627, 2015.

[30] J. S. C. Francis and R. Raj. “Influence of the field and the current limit on flash sintering at isothermal furnace temperatures”. J. Am. Ceram. Soc., vol. 96, no. 9, pp. 2754–2758, 2013.

[31] M. C. Steil, D. Marinha, Y. Aman, J. R. C. Gomes, and M. Kleitz. “From conventional ac flash-sintering of YSZ to hyper-flash and double flash”. J. Eur. Ceram. Soc., vol. 33, no. 11, pp. 2093–2101, 2013.

[32] S. K. Jha, K. Terauds, J. Lebrun, and R. Raj. “Beyond flash sintering in 3 mol % yttria stabilized zirconia”. J. Ceram. Soc. Japan, vol. 124, no. 4, pp. 283–288, 2016.

[33] M. K. Punith Kumar, D. Yadav, J. M. Lebrun, and R. Raj. “Flash sintering with current rate: A different approach”. J. Am. Ceram. Soc., vol. 102, no. 2, pp. 823–835, 2018.

[34] H. Charalambous, S. K. Jha, K. H. Christian, R. T. Lay, and T. Tsakalakos. “Flash Sintering using Controlled Current Ramp”. J. Eur. Ceram. Soc., vol. 38, no. 10, pp. 3689–3693, Aug. 2018.

[35] B. Yoon, D. Yadav, S. Ghose, and R. Raj. “Reactive flash sintering: MgO and α-Al_2O_3 transform and sinter into single-phase polycrystals of $MgAl_2O_4$”. J. Am. Ceram. Soc., vol. 102, pp. 2294–2303, 2019.

[36] S. E. Murray, T. J. Jensen, S. S. Sulekar, Y. Y. Lin, N. H. Perry, and D. P. Shoemaker, “Propagation of the contact-driven reduction of Mn_2O_3 during reactive flash sintering”. J. Am. Ceram. Soc., vol. 102, pp. 7210–7216, 2019.

[37] R. Chaim and Y. Amouyal. “Liquid-Film Assisted Mechanism of Reactive Flash Sintering in Oxide Systems”. Materials, vol. 12, p. 1494, 2019.

[38] R. Chaim. “Reactive flash sintering (RFS) in oxide systems: kinetics and thermodynamics”. J. Mater. Sci., vol. 56, pp. 278–289, 2021.

[39] B. Yoon, D. Yadav, S. Ghose, P. Sarin, and R. Raj. “On the synchronicity of flash sintering and phase transformation”. J. Am. Ceram. Soc., vol. 102, pp. 3110–3116, 2019.

[40] V. Avila and R. Raj. “Reactive flash sintering of powders of four constituents into a single phase of a complex oxide in a few seconds below 700°C”. J. Am. Ceram. Soc., vol. 102, pp. 6443–6448, 2019.

[41] S. Grasso *et al.*. “Modeling of the temperature distribution of flash sintered zirconia”. J. Ceram. Soc. Japan, vol. 119, no. 1386, pp. 144–146, 2011.

[42] L. B. Caliman, E. Bichaud, P. Soudant, D. Gouveia, and M. C. Steil. “A simple flash sintering setup under applied mechanical stress and controlled atmosphere”. MethodsX, vol. 2, pp. 392–398, 2015.

[43] D. Liu, Y. Cao, J. Liu, Y. Gao, and Y. Wang. “Effect of oxygen partial pressure on temperature for onset of flash sintering 3YSZ”. J. Eur. Ceram. Soc., vol. 38, no. 2, pp. 817–820, 2018.

[44] C. Schmerbauch, J. Gonzalez-Julian, R. Röder, C. Ronning, and O. Guillon. “Flash sintering of nanocrystalline zinc oxide and its influence on microstructure and defect formation”. J. Am. Ceram. Soc., vol. 97, no. 6, pp. 1728–1735, 2014.

[45] Y. Zhang, J. Il Jung, and J. Luo. “Thermal runaway, flash sintering and asymmetrical microstructural development of ZnO and ZnO-Bi_2O_3 under direct currents”. Acta Mater., vol. 94, pp. 87–100, 2015.

[46] R. Raj, M. Cologna, and J. S. C. Francis. “Influence of externally imposed and internally generated electrical fields on grain growth, diffusional creep, sintering and related phenomena in ceramics”. J. Am. Ceram. Soc., vol. 94, no. 7, pp. 1941–1965, 2011.

[47] M. Z. ev Becker, N. Shomrat, and Y. Tsur. “Recent Advances in Mechanism Research and Methods for Electric-Field-Assisted Sintering of Ceramics”. Adv. Mater., vol. 30, no. 41, p. 1706369, 2018.

[48] K. S. Naik, V. M. Sglavo, and R. Raj. “Flash sintering as a nucleation phenomenon and a model thereof”. J. Eur. Ceram. Soc., vol. 34, no. 15, pp. 4063–4067, 2014.

[49] D. Liu, Y. Gao, J. Liu, Y. Wang, and L. An. “Effect of holding time on the microstructure and properties of flash-sintered Y_2O_3-doped ZrO_2,” Ceram. Int., vol. 42, no. 15, pp. 17442–17446, 2016.

[50] M. Jongmanns, R. Raj, and D. E. Wolf. “Generation of Frenkel defects above the Debye temperature by proliferation of phonons near the Brillouin zone edge”. New J. Phys., vol. 20, p. 093013, 2018.

[51] W. Ji, B. Parker, S. Falco, J. Y. Zhang, Z. Y. Fu, and R. I. Todd. “Ultra-fast firing: Effect of heating rate on sintering of 3YSZ, with and without an electric field”. J. Eur. Ceram. Soc., vol. 37, no. 6, pp. 2547–2551, 2017.

[52] Y. Zhang, J. Nie, J. M. Chan, and J. Luo. “Probing the densification mechanisms during flash sintering of ZnO”. Acta Mater., vol. 125, pp. 465–475, 2017.

[53] W. D. Kaplan, D. Chatain, P. Wynblatt, and W. C. Carter. “A review of wetting versus adsorption, complexions, and related phenomena: The rosetta stone of wetting”. J. Mater. Sci., vol. 48, no. 17, pp. 5681–5717, 2013.

[54] P. R. Cantwell, M. Tang, S. J. Dillon, J. Luo, G. S. Rohrer, and M. P. Harmer. “Grain boundary complexions”. Acta Mater., vol. 62, no. 1, pp. 1–48, 2014.

[55] M. Jiang *et al.*. “Seed-Free Solid-State Growth of Large Lead-Free Piezoelectric Single Crystals: $(Na_{1/2}K_{1/2})NbO_3$”. J. Am. Ceram. Soc., vol. 98, no. 10, pp. 2988–2996, 2015.

[56] J. S. C. Francis, M. Cologna, D. Montinaro, and R. Raj. “Flash sintering of anode-electrolyte multilayers for SOFC applications”. J. Am. Ceram. Soc., vol. 96, no. 5, pp. 1352–1354, 2013.

[57] M. Schie, S. Menzel, J. Robertson, R. Waser, and R. A. De Souza. “Field-enhanced route to generating anti-Frenkel pairs in HfO_2”. Phys. Rev. Mater., vol. 2, no. 3, p. 35002, 2018.

[58] R. Chaim. “Liquid film capillary mechanism for densification of ceramic powders during flash sintering”. Materials, vol. 9, no. 4, p. 280, 2016.

[59] R. Chaim. “Relations between flash onset-, Debye-, and glass transition temperature in flash sintering of oxide nanoparticles”. Scr. Mater., vol. 169, pp. 6–8, 2019.

[60] R. Chaim. “On the kinetics of liquid-assisted densification during flash sintering of ceramic nanoparticles”. Scr. Mater., vol. 158, pp. 88–90, 2019.

[61] K. Ren, J. Xia, and Y. Wang. “Grain growth kinetics of 3 mol. % yttria-stabilized zirconia during flash sintering”. J. Eur. Ceram. Soc., vol. 39, no. 4, pp. 1366–1373, 2019.

[62] R. Chaim, G. Chevallier, A. Weibel, and C. Estournès. “Grain growth during spark plasma and flash sintering of ceramic nanoparticles: A review”. J. Mater. Sci., vol. 53, pp. 3084–3105, 2018.

[63] K. Ren, Q. Wang, Y. Lian, and Y. Wang. “Densification kinetics of flash sintered 3mol% Y_2O_3 stabilized zirconia”. J. Alloys Compd., vol. 747, pp. 1073–1077, 2018.

[64] R. I. Todd, E. Zapata-Solvas, R. S. Bonilla, T. Sneddon, and P. R. Wilshaw. “Electrical characteristics of flash sintering: Thermal runaway of Joule heating”. J. Eur. Ceram. Soc., vol. 35, no. 6, pp. 1865–1877, 2015.

[65] W. Qin, H. Majidi, J. Yun, and K. van Benthem. “Electrode Effects on Microstructure Formation During FLASH Sintering of Yttrium-Stabilized Zirconia”. J. Am. Ceram. Soc., vol. 99, no. 7, pp. 2253–2259, 2016.

[66] M. Yoshida, S. Falco, and R. I. Todd. “Measurement and modelling of electrical resistivity by four-terminal method during flash sintering of 3YSZ”. J. Ceram. Soc. Japan, vol. 126, no. 7, pp. 579–590, 2018.

[67] A. Eqbal, K. S. Arya, and T. Chakrabarti. “In-depth study of the evolving thermal runaway and thermal gradient in the dog bone sample during flash sintering using finite element analysis”. Ceram. Int., vol. 46, pp. 10370–10378, 2020.

[68] W. Qin, J. Yun, A. M. Thron, and K. van Benthem. “Temperature gradient and microstructure evolution in AC flash sintering of 3 mol% yttria-stabilized zirconia”. Mater. Manuf. Process., vol. 32, no. 5, pp. 549–556, 2017.

[69] R. Raj, A. Kulkarni, J.-M. Lebrun, and S. Jha. “Flash sintering: A new frontier in defect physics and materials science”. MRS Bull., vol. 46, no. 1, pp. 36–43, 2021.

[70] K. S. N. Vikrant, H. Wang, A. Jana, H. Wang, and R. E. García. “Flash sintering incubation kinetics”. Comput. Mater., vol. 6, p. 98, 2020.

[71] J. Xia, K. Ren, Y. Wang, and L. An. “Reversible flash-bonding of zirconia and nickel alloys”. Scr. Mater., vol. 153, pp. 31–34, 2018.

[72] J. Xia, K. Ren, and Y. Wang. “One-second flash joining of zirconia ceramic by an electric field at low temperatures”. Scr. Mater., vol. 165, pp. 34–38, 2019.

[73] D. Liu *et al.*. “SiC whisker reinforced ZrO_2 composites prepared by flash-sintering”. J. Eur. Ceram. Soc., vol. 36, no. 8, pp. 2051–2055, 2016.

[74] W. Jo *et al.*. “Giant electric-field-induced strains in lead-free ceramics for actuator applications - Status and perspective”. J. Electroceramics, vol. 29, no. 1, pp. 71–93, 2012.

[75] A. Safari and E. K. Akdogan. Piezoelectric and Acoustic Materials for Transducer Applications. 2008.

[76] I. Coondoo, N. Panwar, and A. Kholkin. “Lead-free piezoelectrics: Current status and perspectives”. J. Adv. Dielectr., vol. 03, no. 02, p. 1330002, 2013.

[77] T. R. Shrout and S. J. Zhang. “Lead-free piezoelectric ceramics: Alternatives for PZT?”. J. Electroceramics, vol. 19, no. 1, pp. 111–124, 2007.

[78] A. M. Manjón-Sanz and M. R. Dolgos. “Applications of Piezoelectrics: Old and New”. Chem. Mater., vol. 30, no. 24, pp. 8718–8726, 2018.

[79] D. Damjanovic. “Piezoelectric Properties of Perovskite Ferroelectrics: Unsolved Problems and Future Research”. Ann. Chim. Sci. des Matériaux, vol. 26, pp. 99–106, 2001.

[80] A. J. Moulson and J. M. Herbert. Electroceramics: Materials, Properties, Applications, 2nd ed. Chichester: Wiley, 2003.

[81] M. A. Rafiq. “Electromechanical properties of engineered lead free potassium sodium niobate based materials”. University of Aveiro, 2013.

[82] P. M. Vilarinho, Y. Rosenwaks, and A. Kingon. “Functional materials: properties, processing and applications” in Scanning Probe Microscopy: Characterization, Nanofabrication and Device Application of Functional Materials: proceedings of NATO advanded study II:

mathematics, physics and chemistry., vol. 186, Dordrecht: Klumer Academic Publ., 2005, pp. 3–33.

[83] A. L. Kholkin, N. A. Pertsev, and A. V. Goltsev. “Piezoelectricity and crystal symmetry”. Piezoelectric Acoust. Mater. Transducer Appl., pp. 17–38, 2008.

[84] J. Rödel, K. G. Webber, R. Dittmer, W. Jo, M. Kimura, and D. Damjanovic. “Transferring lead-free piezoelectric ceramics into application”. J. Eur. Ceram. Soc., vol. 35, no. 6, pp. 1659–1681, 2015.

[85] P. Kumari, R. Rai, S. Sharma, M. Shandilya, and A. Tiwari. “State-of-the-art of lead free ferroelectrics: A critical review”. Adv. Mater. Lett., vol. 6, no. 6, pp. 453–484, 2015.

[86] M. Pena and J. L. G. Fierro. “Chemical structures and performances of perovskite oxides”. Chem. Rev., vol. 101, pp. 1981–2017, 2001.

[87] P. Boch and J.-C. Niepce. Ceramic Materials: Processes, Properties and Applications, 1st ed. London: ISTE, 2001.

[88] B. Jaffe, W. R. Cook Jr., and H. Jaffe. Piezoelectric Ceramics, vol. 3. Academic press. London and New York, 1971.

[89] E. Commission. “Directive 2002/95/EC of the European Parliament and of the Council of 27 January 2003”. Off. J. Eur. Union, vol. 4, no. 11, pp. 19–23, 2003.

[90] European Commission. “Directive 2011/65/EU of the European Parliament and of the Council of 8 June 2011 - ROHS”. Off. J. Eur. Union, vol. 54, no. 1 July, pp. 88–110, 2011.

[91] J. Sunarso, S. S. Hashim, N. Zhu, and W. Zhou. “Perovskite oxides applications in high temperature oxygen separation, solid oxide fuel cell and membrane reactor: A review”. Prog. Energy Combust. Sci., vol. 61, pp. 57–77, 2017.

[92] J. Wu, D. Xiao, Y. Wang, J. Zhu, L. Wu, and Y. Jiang. “Effects of K/Na ratio on the phase structure and electrical properties of $(K_xNa_{0.96-x}Li_{0.04})(Nb,Ta,Sb)O_3$ lead-free ceramics”. Appl. Phys. Lett., vol. 91, no. 25, p. 14103, 2007.

[93] J. Wu, D. Xiao, Y. Wang, J. Zhu, and P. Yu. “Effects of K content on the dielectric, piezoelectric, and ferroelectric properties of $0.95(K_xNa_{1-x})NbO_3$ - $0.05LiSbO_3$ lead-free ceramics”. J. Appl. Phys., vol. 103, p. 024102, 2008.

[94] W. Jiagang, X. Dingquan, W. Yuanyu, W. Lang, J. Yihang, and Z. Jianguo. “K/Na ratio dependence of the electrical properties of $[(K_xNa_{1-x})_{0.95}Li_{0.05}](Nb_{0.95}Ta_{0.05})O_3$ lead-free ceramics”. J. Am. Ceram. Soc., vol. 91, no. 7, pp. 2385–2387, 2008.

[95] J. Hao, W. Bai, B. Shen, and J. Zhai, “Improved piezoelectric properties of $(K_xNa_{1-x})_{0.94}Li_{0.06}NbO_3$ lead-free ceramics fabricated by combining two-step sintering”. J. Alloys Compd., vol. 534, pp. 13–19, 2012.

[96] Y. Kang, Y. Zhao, R. Huang, Y. Zhao, and H. Zhou. “Effect of changing Na/K ratio on structure and electrical properties of (Na_xK_y) $(Nb_{0.885}Sb_{0.08})$-$0.035LiTaO_3$ lead-free piezoelectric ceramics”. J. Am. Ceram. Soc., vol. 94, no. 6, pp. 1683–1686, 2011.

[97] Y. Chang, Z. Yang, D. Ma, Z. Liu, and Z. Wang. “Phase coexistence and high electrical properties in $(K_xNa_{0.96-x}Li_{0.04})(Nb_{0.85}Ta_{0.15})O_3$ piezoelectric ceramics”. J. Appl. Phys., vol. 105, p. 054101, 2009.

[98] A. Boutarfaia, C. Boudaren, A. Mousser, and S. E. Bouaoud. “Study of phase transition line of PZT ceramics by X-ray diffraction”. Ceram. Int., vol. 21, no. 6, pp. 391–394, 1995.

[99] G. Corapcioglu, M. A. Gulgun, K. Kisslinger, S. Sturm, S. K. Jha, and R. Raj. “Microstructure and microchemistry of flash sintered $K_{0.5}Na_{0.5}NbO_3$”. J. Ceram. Soc. Japan, vol. 124, no. 4, pp. 321–328, 2016.

[100] M. Kosec and D. Kolar. “On activated sintering and electrical properties of $NaKNbO_3$”. Mater. Res. Bulletim, vol. 10, pp. 335–340, 1975.

[101] E. Ringgaard, T. Wurlitzer, and W. W. Wolny. “Lead-free piezoceramics based on alkali niobates”. Ferroelectrics, vol. 319, no. April, pp. 97–107, 2005.

[102] B. P. Zhang, J. F. Li, K. Wang, and H. Zhang. “Compositional dependence of piezoelectric properties in $Na_xK_{1-x}NbO_3$ lead-free ceramics prepared by spark plasma sintering”. J. Am. Ceram. Soc., vol. 89, no. 5, pp. 1605–1609, 2006.

[103] R. E. Jaeger and L. Egerton. “Hot Pressing of Potassium-Sodium Niobates”. J. Am. Ceram. Soc., vol. 45, no. 5, pp. 209–213, 1962.

[104] Y. Saito *et al.*. “Lead-free piezoceramics”. Nature, vol. 432, no. November, pp. 84–87, 2004.

[105] X. X. Wang *et al.*. “Giant piezoelectricity in potassium-sodium niobate lead-free ceramics”. J. Am. Ceram. Soc., vol. 136, p. 2905−2910, 2014.

[106] J.-F. Li, K. Wang, F.-Y. Zhu, L.-Q. Cheng, and F.-Z. Yao. “(K, Na) NbO_3-based lead-free piezoceramics: Fundamental aspects, processing technologies, and remaining challenges”. J. Am. Ceram. Soc., vol. 96, no. 12, pp. 3677–3696, 2013.

[107] K. Sakata, T. Takenaka, and Y. Naitou. “Phase relations, dielectric and piezoelectric properties of ceramics in the system $(Bi_{0.5}Na_{0.5})TiO_3$-$PbTiO_3$”. Ferroelectrics, vol. 131, no. 1, pp. 219–226, 1992.

[108] Y. H. Seo, J. Koruza, A. Benčan, B. Malič, J. Rödel, and K. G. Webber. “Simultaneous enhancement of fracture toughness and unipolar strain in Pb(Zr, Ti)O_3-ZrO_2 composites through composition adjustment”. J. Am. Ceram. Soc., vol. 97, no. 5, pp. 1582–1588, 2014.

[109] K. Wang, B. Malič, and J. Wu. “Shifting the phase boundary: Potassium sodium niobate derivates”. MRS Bull., vol. 43, no. 8, pp. 607–611, 2018.

[110] B. Malič *et al.*. “Sintering of lead-free piezoelectric sodium potassium niobate ceramics”. Materials, vol. 8, no. 12, pp. 8116–8146, 2015.

[111] S. Priya and S. Nahm. “Development of KNN-Based Piezoelectric Materials”. in Lead-Free Piezoelectrics, 1st ed., S. Priya and S. Nahm, Eds. Springer, 2012.

[112] A. Tkach, A. Santos, S. Zlotnik, R. Serrazina, and O. Okhay. “Strain-Mediated Substrate Effect on the Dielectric and Ferroelectric Response of Potassium Sodium Niobate Thin Films”. Coatings, vol. 8, p. 449, 2018.

[113] Y. Wang, D. Damjanovic, N. Klein, and N. Setter. “High-temperature instability of Li- and Ta-modified (K,Na)NbO_3 piezoceramics”. J. Am. Ceram. Soc., vol. 91, no. 6, pp. 1962–1970, 2008.

[114] R. E. Jaeger and L. Egerton. “Hot Pressing of Potassium-Sodium Niobates”. J. Am. Ceram. Soc., vol. 45, no. 5, pp. 209–213, 1962.

[115] M. Bah, F. Giovannelli, F. Schoenstein, G. Feuillard, E. Le Clezio, and I. Monot-Laffez. “High electromechanical performance with spark plasma sintering of undoped $K_{0.5}Na_{0.5}NbO_3$ ceramics”. Ceram. Int., vol. 40, no. 5, pp. 7473–7480, 2014.

[116] R. Wang, R. Xie, T. Sekiya, and Y. Shimojo. “Fabrication and characterization of potassium-sodium niobate piezoelectric ceramics by spark-plasma-sintering method”. Mater. Res. Bull., vol. 39, no. 11, pp. 1709–1715, 2004.

[117] M. R. Bafandeh, R. Gharahkhani, and J.-S. Lee. “Comparison of sintering behavior and piezoelectric properties of (K,Na)NbO_3-based ceramics sintered in conventional and microwave furnace”. Mater. Chem. Phys., vol. 143, pp. 1289–1295, 2014.

[118] M. A. Rafiq, M. E. V. Costa, and P. M. Vilarinho. “Establishing the Domain Structure of $(K_{0.5}Na_{0.5})NbO_3$ (KNN) Single Crystals by Piezoforce-Response Microscopy”. Sci. Adv. Mater., vol. 6, no. 3, pp. 426–433, 2014.

[119] H. Birol, D. Damjanovic, and N. Setter. “Preparation and characterization of $(K_{0.5}Na_{0.5})NbO_3$ ceramics”. J. Eur. Ceram. Soc., vol. 26, no. 6, pp. 861–866, 2006.

[120] J. F. Li, K. Wang, B. P. Zhang, and L. M. Zhang. “Ferroelectric and piezoelectric properties of fine-grained $Na_{0.5}K_{0.5}NbO_3$ lead-free piezoelectric ceramics prepared by spark plasma sintering”. J. Am. Ceram. Soc., vol. 89, no. 2, pp. 706–709, 2006.

[121] Y. Wu, X. Su, G. An, and W. Hong. “Dense $Na_{0.5}K_{0.5}NbO_3$ ceramics produced by reactive flash sintering of $NaNbO_3$ - $KNbO_3$ mixed powders”. Scr. Mater., vol. 174, pp. 49–52, 2020.

[122] N. Morisaki, H. Yoshida, T. Tokunaga, K. Sasaki, and T. Yamamoto. “Consolidation of undoped, monoclinic zirconia polycrystals by flash sintering”. J. Am. Ceram. Soc., vol. 100, no. 9, pp. 3851–3857, 2017.

[123] J. M. Lebrun, T. G. Morrissey, J. S. C. Francis, K. C. Seymour, W. M. Kriven, and R. Raj. “Emergence and Extinction of a New Phase during On-Off Experiments Related to Flash Sintering of 3YSZ”. J. Am. Ceram. Soc., vol. 98, no. 5, pp. 1493–1497, 2015.

[124] J. Cho *et al.*. “High temperature deformability of ductile flash-sintered ceramics via in-situ compression”. Nat. Commun., vol. 9, no. 1, pp. 1–9, 2018.

[125] H. Wang *et al.*. “Key microstructural characteristics in flash sintered 3YSZ critical for enhanced sintering process”. Ceram. Int., vol. 45, no. 1, pp. 1251–1257, 2019.

[126] S. G. M. Carvalho, E. N. S. Muccillo, and R. Muccillo. “AC Electric Field Assisted Pressureless Sintering Zirconia: 3 mol% Yttria Solid Electrolyte”. Phys. Status Solidi Appl. Mater. Sci., vol. 215, p. 1700647, 2018.

[127] J. M. Lebrun *et al.*. “In-situ measurements of lattice expansion related to defect generation during flash sintering”. J. Am. Ceram. Soc., vol. 100, no. 11, pp. 4965–4970, 2017.

[128] J. G. Pereira da Silva *et al.*. “Mechanical strength and defect distributions in flash sintered 3YSZ”. J. Eur. Ceram. Soc., vol. 37, no. 8, pp. 2901–2905, 2017.

[129] J. V. Campos *et al.*. “Flash sintering scaling-up challenges: Influence of the sample size on the microstructure and onset temperature of the flash event”. Scr. Mater., vol. 186, pp. 1–5, Sep. 2020.

[130] K. H. Christian, H. Charalambous, S. K. Jha, and T. Tsakalakos. “Current-ramp assisted sintering of 3YSZ: Electrochemical and microstructural comparison to flash and thermal sintering”. J. Eur. Ceram. Soc., vol. 40, pp. 436–443, 2020.

[131] J. Dong *et al.*. “Contactless flash sintering based on cold plasma”. Scr. Mater., vol. 175, pp. 20–23, 2020.

[132] W. Ji, J. Zhang, W. Wang, Z. Fu, and R. I. Todd. “The microstructural origin of rapid densification in 3YSZ during ultra-fast firing with or without an electric field”. J. Eur. Ceram. Soc., vol. 40, pp. 5829–5836, 2020.

[133] D. Liu *et al.*. “Effect of the current density on the densification of 3 mol% yttria-stabilized zirconia in flash sintering”. J. Alloys Compd., vol. 825, p. 154061, 2020.

[134] I. R. Lavagnini, J. V. Campos, J. A. Ferreira, and E. M. J. Eliria. “Microstructural evolution of 3YSZ flash-sintered with current ramp control”. J. Am. Ceram. Soc., vol. 103, pp. 3493–3499, 2020.

[135] Y. Yamashita, T. Kurachi, T. Tokunaga, H. Yoshida, and T. Yamamoto. “Blue photo luminescence from 3 mol%Y_2O_3-doped ZrO_2 polycrystals sintered by flash sintering under an alternating current electric field”. J. Eur. Ceram. Soc., vol. 40, pp. 2072–2076, 2020.

[136] Y. Yang, T. D. Oyedeji, P. Kühn, and B. X. Xu. “Investigation on temperature-gradient-driven effects in unconventional sintering via non-isothermal phase-field simulation”. Scr. Mater., vol. 186, pp. 152–157, 2020.

[137] V. Avila and R. Raj. “Flash sintering of ceramic films: The influence of surface to volume ratio”. J. Am. Ceram. Soc., vol. 102, no. 6, pp. 3063–3069, 2019.

[138] M. Biesuz *et al.*. “Flash spark plasma sintering of 3YSZ”. J. Eur. Ceram. Soc., vol. 39, no. 5, pp. 1932–1937, 2019.

[139] R. Muccillo, M. Kleitz, and E. N. S. Muccillo. “Flash grain welding in yttria stabilized zirconia”. J. Eur. Ceram. Soc., vol. 31, no. 8, pp. 1517–1521, 2011.

[140] M. Cologna, A. L. G. Prette, and R. Raj. “Flash-sintering of cubic yttria-stabilized zirconia at 750°C for possible use in SOFC manufacturing”. J. Am. Ceram. Soc., vol. 94, no. 2, pp. 316–319, 2011.

[141] M. Biesuz *et al.*. “Thermally-insulated flash sintering”. Scr. Mater., vol. 162, pp. 99–102, 2019.

[142] M. Biesuz, D. Rizzi, and V. M. Sglavo. “Electric current effect during the early stages of field-assisted sintering”. J. Am. Ceram. Soc., vol. 102, no. 2, pp. 813–822, 2019.

[143] X. Vendrell, D. Yadav, R. Raj, and A. R. West. “Influence of flash sintering on the ionic conductivity of 8 mol% yttria stabilized zirconia”. J. Eur. Ceram. Soc., vol. 39, no. 4, pp. 1352–1358, 2019.

[144] C. A. Grimley, A. L. G. Prette, and E. C. Dickey. “Effect of boundary conditions on reduction during early stage flash sintering of YSZ”. Acta Mater., vol. 174, pp. 271–278, 2019.

[145] J. Zhang *et al.*. “Densification of 8 mol% yttria-stabilized zirconia at low temperature by flash sintering technique for solid oxide fuel cells”. Ceram. Int., vol. 43, no. 16, pp. 14037–14043, 2017.

[146] R. Muccillo and E. N. S. Muccillo. “Improved densification and ionic conductivity in flash-sintered gamma-ray irradiated yttria-stabilized zirconia”. Scr. Mater., vol. 170, pp. 120–123, 2019.

[147] G. Liu, D. Liu, J. Liu, Y. Gao, and Y. Wang. “Asymmetric temperature distribution during steady stage of flash sintering dense zirconia”. J. Eur. Ceram. Soc., vol. 38, no. 7, pp. 2893–2896, 2018.

[148] M. Biesuz *et al.*. “Investigation of electrochemical, optical and thermal effects during flash sintering of 8YSZ”. Materials, vol. 11, p. 1214, 2018.

[149] D. Yadav and R. Raj. “The onset of the flash transition in single crystals of cubic zirconia as a function of electric field and temperature”. Scr. Mater., vol. 134, pp. 123–127, 2017.

[150] Y. Yamashita, A. Itoh, T. Tokunaga, H. Yoshida, and T. Yamamoto. “Blue photoluminescence at room temperature from Y_2O_3-doped ZrO_2 polycrystals sintered by flash sintering”. Appl. Phys. Express, vol. 13, pp. 35506-1-35506–5, 2020.

[151] K. Nambu, H. Hayasaka, T. Yamamoto, and H. Yoshida. “Photoluminescence properties of undoped and Si^{4+} -doped polycrystalline Y_2O_3 phosphors prepared by flash-sintering”. Appl. Phys. Express, vol. 12, no. 7, p. 075504, 2019.

[152] J. U. Valdebenito, A. Akbari-Fakhrabadi, and M. R. Viswanathan. “Effect of flash sintering on microstructure of $Ce_{0.9}Gd_{0.1}O_{1.95}$ electrolyte fabricated by tape-casting”. Mater. Lett., vol. 209, pp. 291–294, 2017.

[153] T. P. Mishra, R. R. I. Neto, R. Raj, O. Guillon, and M. Bram. “Current-rate flash sintering of gadolinium doped ceria: Microstructure and Defect generation”. Acta Mater., vol. 189, pp. 145–153, 2020.

[154] T. P. Mishra *et al.*. “Electronic conductivity in gadolinium doped ceria under direct current as a trigger for flash sintering”. Scr. Mater., vol. 179, pp. 55–60, 2020.

[155] C. Xu, L. Wang, B. Bai, L. Peng, and S. Cai. “Rapid synthesis of $Gd_2Zr_2O_7$ ceramics by flash sintering and its aqueous durability”. J. Eur. Ceram. Soc., vol. 40, pp. 1620–1625, 2020.

[156] V. Tyrpekl, M. Cologna, M. Holzhäuser, and P. Svora. “Power-controlled flash spark plasma sintering of gadolinia-doped ceria”. J. Am. Ceram. Soc., vol. 104, pp. 793–802, 2021.

[157] L. Spiridigliozzi, M. Biesuz, G. Dell’Agli, E. Di Bartolomeo, F. Zurlo, and V. M. Sglavo. “Microstructural and electrical investigation of flash-sintered Gd/Sm-doped ceria”. J. Mater. Sci., vol. 52, no. 12, pp. 7479–7488, 2017.

[158] A. Gaur and V. M. Sglavo. “Tuning the flash sintering characteristics of ceria with $MnCo_2O_4$”. Mater. Sci. Eng. B Solid-State Mater. Adv. Technol., vol. 228, no. November 2017, pp. 160–166, 2018.

[159] T. Jiang *et al.*. “Understanding the flash sintering of rare-earth-doped ceria for solid oxide fuel cell”. J. Am. Ceram. Soc., vol. 98, no. 6, pp. 1717–1723, 2015.

[160] A. Gaur and V. M. Sglavo. “Flash sintering of (La, Sr)(Co, Fe)O_3-Gd-Doped CeO_2 composite”. J. Am. Ceram. Soc., vol. 98, no. 6, pp. 1747–1752, 2015.

[161] E. N. S. Muccillo, S. G. M. Carvalho, and R. Muccillo. “Electric field-assisted pressureless sintering of zirconia–scandia–ceria solid electrolytes”. J. Mater. Sci., vol. 53, no. 3, pp. 1658–1671, 2018.

[162] L. Guan, J. Li, X. Song, J. Bao, and T. Jiang. “Graphite assisted flash sintering of Sm_2O_3 doped CeO_2 ceramics at the onset temperature of 25 °C”. Scr. Mater., vol. 159, pp. 72–75, 2019.

[163] W. Straka, S. Amoah, and J. Schwartz. “Densification of thoria through flash sintering”. MRS Commun., vol. 7, no. 3, pp. 677–682, 2017.

[164] H. Yoshida, Y. Sakka, T. Yamamoto, J. M. Lebrun, and R. Raj. “Densification behaviour and microstructural development in undoped yttria prepared by flash-sintering”. J. Eur. Ceram. Soc., vol. 34, no. 4, pp. 991–1000, 2014.

[165] H. Yoshida, H. Hayasaka, K. Soga, K. Morita, B. Kim, and T. Yamamoto. “Doping effect on the flash sintering of Y_2O_3: Promotion of densification and optical translucency”. J. Eur. Ceram. Soc., vol. 40, pp. 6053–6060, 2020.

[166] S. K. Jha *et al.*. “In-situ observation of oxygen mobility and abnormal lattice expansion in ceria during flash sintering”. Ceram. Int., vol. 44, no. 13, pp. 15362–15369, 2018.

[167] S. K. Jha, J. M. Lebrun, K. C. Seymour, W. M. Kriven, and R. Raj. “Electric field induced texture in titania during experiments related to flash sintering”. J. Eur. Ceram. Soc., vol. 36, no. 1, pp. 257–261, 2016.

[168] Y. Zhang, J. Nie, and J. Luo. “Effects of phase and doping on flash sintering of TiO_2”. J. Ceram. Soc. Japan, vol. 124, no. 4, pp. 296–300, 2016.

[169] H. Charalambous, S. K. Jha, H. Wang, X. L. Phuah, H. Wang, and T. Tsakalakos. “Inhomogeneous reduction and its relation to grain growth of titania during flash sintering”. Scr. Mater., vol. 155, pp. 37–40, Oct. 2018.

[170] B. Yoon *et al.*. “Measurement of O and Ti atom displacements in TiO_2 during flash sintering experiments”. J. Am. Ceram. Soc., vol. 101, no. 5, pp. 1811–1817, 2018.

[171] R. Muccillo and E. N. S. Muccillo. “Electric field-assisted flash sintering of tin dioxide”. J. Eur. Ceram. Soc., vol. 34, no. 4, pp. 915–923, 2014.

[172] Y. Zhang and J. Luo. “Promoting the flash sintering of ZnO in reduced atmospheres to achieve nearly full densities at furnace temperatures of <120 °C”. Scr. Mater., vol. 106, pp. 26–29, 2015.

[173] H. Charalambous, S. K. Jha, R. T. Lay, A. Cabales, J. Okasinski, and T. Tsakalakos. “Investigation of temperature approximation methods during flash sintering of ZnO”. Ceram. Int., vol. 44, no. 6, pp. 6162–6169, Apr. 2018.

[174] X. L. Phuah *et al.*. “Comparison of the grain growth behavior and defect structures of flash sintered ZnO with and without controlled current ramp”. Scr. Mater., vol. 162, pp. 251–255, 2019.

[175] J. Cho *et al.*. “Temperature effect on mechanical response of flash-sintered ZnO by in-situ compression tests”. Acta Mater., vol. 200, pp. 699–709, 2020.

[176] X. Li, R. Huang, X. Wang, G. Liu, Z. Jia, and L. Wang. “A simple optimized design of an electrode to conduct flash sintering at room temperature and low onset electric field”. Scr. Mater., vol. 186, pp. 158–162, 2020.

[177] J. Liu, X. Li, X. Wang, R. Huang, and Z. Jia. “Alternating current field flash sintering 99% relative density ZnO ceramics at room temperature”. Scr. Mater., vol. 176, pp. 28–31, 2020.

[178] J. Liu *et al.*. “Mechanism of flash sintering with high electric field: In the view of electric discharge and breakdown”. Scr. Mater., vol. 187, pp. 93–96, 2020.

[179] M. Kermani *et al.*. “Flash cold sintering: Combining water and electricity”. J. Eur. Ceram. Soc., vol. 40, no. 15, pp. 6266–6271, 2020.

[180] C. Gorynski, U. Anselmi-Tamburini, and M. Winterer. “Controlling current flow in sintering: A facile method coupling flash with spark plasma sintering”. Rev. Sci. Instrum., vol. 91, pp. 15112-1-15112–2, Jan. 2020.

[181] J. Nie, Y. Zhang, J. M. Chan, S. Jiang, R. Huang, and J. Luo. “Two-step flash sintering of ZnO: Fast densification with suppressed grain growth”. Scr. Mater., vol. 141, pp. 6–9, 2017.

[182] S. E. Murray, Y. Y. Lin, S. S. Sulekar, M. S. Gebre, N. H. Perry, and D. P. Shoemaker. “Predicting transformations during reactive flash sintering in CuO and Mn_2O_3”. J. Am. Ceram. Soc., vol. 104, pp. 76–85, 2021.

[183] M. Biesuz and V. M. Sglavo. “Flash sintering of alumina: Effect of different operating conditions on densification”. J. Eur. Ceram. Soc., vol. 36, no. 10, pp. 2535–2542, 2016.

[184] M. Biesuz, P. Luchi, A. Quaranta, A. Martucci, and V. M. Sglavo. “Photoemission during flash sintering: An interpretation based on thermal radiation”. J. Eur. Ceram. Soc., vol. 37, no. 9, pp. 3125–3130, 2017.

[185] M. Biesuz and V. M. Sglavo. “Liquid phase flash sintering in magnesia silicate glass-containing alumina”. J. Eur. Ceram. Soc., vol. 37, no. 2, pp. 705–713, 2017.

[186] M. Biesuz and V. M. Sglavo. “Current-induced abnormal and oriented grain growth in corundum upon flash sintering”. Scr. Mater., vol. 150, pp. 82–86, 2018.

[187] D. Kok *et al.*. “α-Alumina and spinel react into single-phase high-alumina spinel in <3 seconds during flash sintering”. J. Am. Ceram. Soc., vol. 102, no. 2, pp. 644–653, 2019.

[188] H. Yoshida, P. Biswas, R. Johnson, and M. K. Mohan. “Flash-sintering of magnesium aluminate spinel ($MgAl_2O_4$) ceramics”. J. Am. Ceram. Soc., vol. 100, no. 2, pp. 554–562, 2017.

[189] D. Kok, S. K. Jha, R. Raj, and M. L. Mecartney. “Flash sintering of a three-phase alumina, spinel, and yttria-stabilized zirconia composite”. J. Am. Ceram. Soc., vol. 100, no. 7, pp. 3262–3268, 2017.

[190] M. Cologna, J. S. C. Francis, and R. Raj. “Field assisted and flash sintering of alumina and its relationship to conductivity and MgO-doping”. J. Am. Ceram. Soc., vol. 31, no. 15, pp. 2827–2837, Dec. 2011.

[191] K. S. Naik, V. M. Sglavo, and R. Raj. “Field assisted sintering of ceramic constituted by alumina and yttria stabilized zirconia”. J. Eur. Ceram. Soc., vol. 34, no. 10, pp. 2435–2442, 2014.

[192] J. C. M’Peko. “Flash sintering in well-dispersed insulator-ionic conductor composites: The case of diphasic alumina-zirconia (Al_2O_3-3YSZ) system”. Scr. Mater., vol. 175, pp. 38–42, 2020.

[193] B. Yoon, V. Avila, R. Kathiria, and L. M. Jesus. “Effects of powder dispersion on reactive flash sintering of 8 mol % yttria-stabilized zirconia and $MgAl_2O_4$ composites”. Scr. Mater., vol. 189, pp. 117–121, 2020.

[194] H. Zhang, Y. Wang, J. Liu, X. Xu, L. Chen, and D. Liu. “Reaction assisted flash sintering of Al_2O_3-YAG ceramic composites with eutectic composition” Ceram. Int., vol. 45, no. 10, pp. 13551–13555, 2019.

[195] J. Liu, X. Xu, D. Liu, L. Chen, K. Zhao, and L. An. “Ultrafast formation of Al_2O_3–$Y_3Al_5O_{12}$ eutectic ceramic by flash sintering”. J. Am. Ceram. Soc., vol. 103, pp. 4051–4056, 2020.

[196] C. L. Ojaimi, J. A. Ferreira, A. L. Chinelatto, A. S. A. Chinelatto, and E. M. de J. A. Pallone. “Microstructural analysis of ZrO_2/Al_2O_3 composite: Flash and conventional sintering”. Ceram. Int., vol. 46, pp. 2473–2480, 2020.

[197] J. Ramírez-gonzález and A. R. West. “Flash phenomena in lime-stabilised zirconia oxide ion conductor”. Energy Reports, vol. 6, pp. 142–147, 2020.

[198] W. Xiao, N. Ni, X. Fan, X. Zhao, Y. Liu, and P. Xiao. “Ambient flash sintering of reduced graphene oxide/zirconia composites: Role of reduced graphene oxide”. J. Mater. Sci. Technol., vol. 60, pp. 70–76, 2020.

[199] Y. V. Bykov *et al.*. “Flash Sintering of Oxide Ceramics under Microwave Heating”. Tech. Phys., vol. 63, no. 3, pp. 391–397, 2018.

[200] M. Biesuz *et al.*. “Interfacial reaction between ZrNbHfTa foil and graphite: Formation of high-entropy carbide and the effect of heating rate on its microstructure”. J. Eur. Ceram. Soc., vol. 40, pp. 2699–2708, 2020.

[201] S. G. M. Carvalho, E. N. S. Muccillo, F. M. B. Marques, and R. Muccillo. “Electric field-assisted sintering (gadolinia-doped ceria/alkali salts) composite membranes”. Materialia, vol. 11, p. 100679, 2020.

[202] G. Fele, M. Biesuz, P. Bettotti, R. Moreno, and V. M. Sglavo. “Flash sintering of yttria-stabilized zirconia/graphene nano-platelets composite”. Ceram. Int., vol. 46, pp. 23266–23270, 2020.

[203] J. C. C. A. Diaz and R. Muccillo. “Liquid-phase flash sintering 8YSZ with alkali halide sintering aids”. J. Eur. Ceram. Soc., vol. 40, pp. 4299–4303, 2020.

[204] J. C. M’Peko, J. S. C. Francis, and R. Raj. “Field-assisted sintering of undoped $BaTiO_3$: Microstructure evolution and dielectric permittivity”. J. Eur. Ceram. Soc., vol. 34, no. 15, pp. 3655–3660, 2014.

[205] A. Uehashi, K. Sasaki, T. Tokunaga, H. Yoshida, and T. Yamamoto. “Formation of secondary phase at grain boundary of flash-sintered $BaTiO_3$”. Microscopy, vol. 63, no. suppl 1, pp. i18–i19, 2014.

[206] K. Ren, S. Huang, Y. Cao, G. Shao, and Y. Wang. “The densification behavior of flash sintered $BaTiO_3$”. Scr. Mater., vol. 186, pp. 362–365, 2020.

[207] R. Umemura, T. Tokunaga, and T. Yamamoto. “Flash sintering for $BaTiO_3$ with square alternating current field including zero- field duration”. J. Ceram. Soc. Japan, vol. 128, pp. 1018–1023, 2020.

[208] M. S. Bernardo, T. Jardiel, A. C. Caballero, M. Bram, J. Gonzalez-Julian, and M. Peiteado. “Electric current activated sintering (ECAS) of undoped and titanium-doped $BiFeO_3$ bulk ceramics with homogeneous microstructure”. J. Eur. Ceram. Soc., vol. 39, no. 6, pp. 2042–2049, 2019.

[209] L. A. Perez-Maqueda, E. Gil-Gonzalez, A. Perejon, J. M. Lebrun, P. E. Sanchez-Jimenez, and R. Raj. “Flash sintering of highly insulating nanostructured phase-pure $BiFeO_3$”. J. Am. Ceram. Soc., vol. 100, no. 8, pp. 3365–3369, 2017.

[210] M. A. B. Wassel *et al.*. “Anisotropic lattice expansion determined during flash sintering of $BiFeO_3$ by in-situ energy-dispersive X-ray diffraction”. Scr. Mater., vol. 162, pp. 286–291, 2019.

[211] L. A. Perez-Maqueda *et al.*. “Insight into the $BiFeO_3$ flash sintering process by in-situ energy dispersive X-ray diffraction (ED-XRD)”. Ceram. Int., vol. 45, no. 2, pp. 2828–2834, 2019.

[212] E. Gil-gonzález, A. Perejón, P. E. Sánchez-jiménez, D. Román-gonzález, and L. A. Pérez-maqueda. “Control of experimental conditions in reaction flash-sintering of complex stoichiometry ceramics”. Ceram. Int., vol. 46, pp. 29413–29420, 2020.

[213] L. M. Jesus, R. S. Silva, R. Raj, and J. C. M’Peko. “Electric field-assisted flash sintering of $Bi_{2/3}Cu_3Ti_4O_{12}$ starting from a multi-phase precursor powder”. J. Eur. Ceram. Soc., vol. 40, pp. 4004–4009, 2020.

[214] J. Liu, K. Ren, C. Ma, H. Du, and Y. Wang. “Dielectric and energy storage properties of flash-sintered high-entropy $(Bi_{0.2}Na_{0.2}K_{0.2}Ba_{0.2}Ca_{0.2})TiO_3$ ceramic”. Ceram. Int., vol. 46, pp. 20576–20581, 2020.

[215] E. Gil-González, A. Perejón, P. E. Sánchez-Jiménez, M. J. Sayagués, R. Raj, and L. A. Pérez-Maqueda. “Phase-pure $BiFeO_3$ produced by reaction flash-sintering of Bi_2O_3 and Fe_2O_3”. J. Mater. Chem. A, vol. 6, no. 13, pp. 5356–5366, 2018.

[216] E. Gil-González, A. Perejón, P. E. Sánchez-Jiménez, R. Raj, and L. A. Pérez-Maqueda. "Processing and properties of $Bi_{0.98}R_{0.02}FeO_3$ (R = La, Sm, Y) ceramics flash sintered at ~650°C in less than 5s". J. Am. Ceram. Soc., vol. 103, no. 1, pp. 136–144, 2019.

[217] L. M. Jesus, R. S. Silva, R. Raj, and J. C. M'Peko. "Electric field-assisted flash sintering of $CaCu_3Ti_4O_{12}$: Microstructure characteristics and dielectric properties". J. Alloys Compd., vol. 682, pp. 753–758, 2016.

[218] R. Shi *et al.*. "Particle transport mode during flash sintering of sodium bismuth titanate ceramic". Ceram. Int., vol. 45, no. 10, pp. 13269–13274, 2019.

[219] X. Su, G. Bai, J. Zhang, J. Zhou, and Y. Jia. "Preparation and flash sintering of $MgTiO_3$ nanopowders obtained by the polyacrylamide gel method." Appl. Surf. Sci., vol. 442, no. 3, pp. 12–19, 2018.

[220] R. Shi *et al.*. "Flash sintering of barium titanate". Ceram. Int., vol. 45, no. 6, pp. 7085–7089, Apr. 2019.

[221] R. Shi *et al.*. "Correlation between flash sintering and dielectric breakdown behavior in donor-doped barium titanate ceramics". Ceram. Int., vol. 46, no. 8, pp. 12846–12851, 2020.

[222] N. Shomrat, S. Baltianski, C. A. Randall, and Y. Tsur. "Flash sintering of potassium-niobate". J. Eur. Ceram. Soc., vol. 35, no. 7, pp. 2209–2213, 2014.

[223] X. Su *et al.*. "Flash sintering of sodium niobate ceramics". Mater. Lett., vol. 235, pp. 15–18, 2019.

[224] R. Serrazina, J. S. Dean, I. M. Reaney, L. Pereira, P. M. Vilarinho, and A. M. O. R. Senos. "Mechanism of densification in low-temperature FLASH sintered lead free Potassium Sodium Niobate (KNN) piezoelectrics". J. Mater. Chem. C, vol. 7, pp. 14334–14341, 2019.

[225] R. Serrazina, P. M. Vilarinho, A. M. O. R. Senos, L. Pereira, I. M. Reaney, and J. S. Dean. "Modelling the particle contact influence on the Joule heating and temperature distribution during FLASH sintering". J. Eur. Ceram. Soc., vol. 40, pp. 1205–1211, 2020.

[226] R. Serrazina, A. M. O. R. Senos, L. Pereira, J. S. Dean, I. M. Reaney, and P. M. Vilarinho. "The Role of Particle Contact in Densification of FLASH Sintered Potassium Sodium Niobate". Eur. J. Inorg. Chem., vol. 2020, no. 39, pp. 3720–3728, 2020.

[227] A. Karakuscu *et al.*. "Defect structure of flash-sintered strontium titanate". J. Am. Ceram. Soc., vol. 95, no. 8, pp. 2531–2536, 2012.

[228] F. Lemke, W. Rheinheimer, and M. J. Hoffmann. "A comparison of power controlled flash sintering and conventional sintering of strontium titanate". Scr. Mater., vol. 130, pp. 187–190, 2017.

[229] W. Rheinheimer, X. L. Phuah, H. H. Wang, F. Lemke, M. J. Hoffmann, and H. H. Wang. "The role of point defects and defect gradients in flash sintering of perovskite oxides". Acta Mater., vol. 165, pp. 398–408, 2019.

[230] N. Shomrat, S. Baltianski, E. Dor, and Y. Tsur. "The influence of doping on flash sintering conditions in $SrTi_{1-x}Fe_xO_{3-y}$". J. Eur. Ceram. Soc., vol. 37, no. 1, pp. 179–188, 2017.

[231] K. Wang *et al.*. "Fabrication of high-entropy perovskite oxide by reactive flash sintering". Ceram. Int., vol. 46, pp. 18358–18361, 2020.

[232] B. Ma *et al.*. "Microstructure and dielectric property of flash sintered SiO_2-coated $BaTiO_3$ ceramics" Scr. Mater., vol. 170, pp. 1–5, 2019.

[233] E. Taghaddos, H. Charalambous, T. Tsakalakos, and A. Safari. "Electromechanical properties of flash sintered BNT-based piezoelectric ceramic". J. Eur. Ceram. Soc., vol. 39, no. 9, pp. 2882–2888, 2019.

[234] T. Clemenceau *et al.*. "Flash sintering of Li-ion conducting ceramic in a few seconds at 850 °C". Scr. Mater., vol. 172, pp. 1–5, 2019.

[235] P. Shi, G. Qu, S. Cai, Y. Kang, T. Fa, and C. Xu. "An ultrafast synthesis method of $LiNi_{1/3}Co_{1/3}Mn_{1/3}O_2$ cathodes by flash/field-assisted sintering". J. Am. Ceram. Soc., vol. 101, no. 9, pp. 4076–4083, 2018.

[236] V. Avila *et al.*. "Reactive flash sintering of the complex oxide $Li_{0.5}La_{0.5}TiO_3$ starting from an amorphous precursor powder". Scr. Mater., vol. 176, pp. 78–82, 2020.

[237] J. Zhang, Y. Zhao, J. Qiao, W. Sun, K. Sun, and Z. Wang. "An easily controllable flash sintering process for densification of electrolyte for application in solid oxide fuel cells". Int. J. Hydrogen Energy, vol. 45, pp. 17824–17832, 2020.

[238] K. Ren, Y. Cao, Y. Chen, G. Shao, J. Dai, and Y. Wang. "Flash sintering of $Na_3Zr_2(SiO_4)_2(PO_4)$ solid-state electrolyte at furnace temperature of 700 °C". Scr. Mater., vol. 187, pp. 384–389, 2020.

[239] A. Gaur and V. M. Sglavo. "Flash-sintering of $MnCo_2O_4$ and its relation to phase stability". J. Eur. Ceram. Soc., vol. 34, no. 10, pp. 2391–2400, 2014.

[240] A. Gaur, M. A. Mohiddon, and V. M. Sglavo, "Phenomenological understanding of flash sintering in $MnCo_2O_4$". J. Eur. Ceram. Soc., vol. 38, no. 13, pp. 4543–4552, 2018.

[241] M. Frasnelli, A. Pedranz, M. Biesuz, S. Dirè, and V. M. Sglavo. "Flash sintering of Mg-doped tricalcium phosphate (TCP) nanopowders". J. Eur. Ceram. Soc., vol. 39, no. 13, pp. 3883–3892, 2019.

[242] X. Su *et al.*. "Flash sintering of lead zirconate titanate (PZT) ceramics: Influence of electrical field and current limit on densification and grain growth". J. Eur. Ceram. Soc., vol. 38, no. 10, pp. 3489–3497, 2018.

[243] Y. Jia *et al.*. "Fabrication of lead zirconate titanate ceramics by reaction flash sintering of $PbO-ZrO_2-TiO_2$ mixed oxides". J. Eur. Ceram. Soc., vol. 39, no. 13, pp. 3915–3919, 2019.

[244] X. Su *et al.*. "Flash sintering of lead zirconate titanate ceramics under an alternating current electrical field". Ceram. Int., vol. 45, pp. 5168–5173, 2019.

[245] B. Cui *et al.*. "Flash sintering preparation and electrical properties of $ZnO–Bi_2O_3$-M (M = Cr_2O_3, MnO_2 or Co_2O_3) varistor ceramics". Ceram. Int., vol. 46, pp. 14913–14918, 2020.

[246] Y. Mei *et al.*. "Processing and characterizations of flash sintered $ZnO-Bi_2O_3-MnO_2$ varistor ceramics under different electric fields". J. Eur. Ceram. Soc., vol. 40, pp. 1330–1337, 2020.

[247] P. Peng *et al.*. "Fabrication and electrical characteristics of flash-sintered SiO_2-doped $ZnO–Bi_2O_3–MnO_2$ varistors". J. Adv. Ceram., vol. 9, pp. 683–692, 2020.

[248] J. H. Yu, B. A. McWilliams, and T. C. Parker. "Densification behavior of flash sintered boron suboxide". J. Am. Ceram. Soc., vol. 101, no. 11, pp. 4976–4982, 2018.

[249] B. Du, S. Zhou, X. Zhang, C. Hong, and Q. Qu. "Preparation of a high spectral emissivity $TaSi_2$ -based hybrid coating on SiOC-modified carbon-bonded carbon fiber composite by a flash sintering method". Surf. Coatings Technol., vol. 350, no. July, pp. 146–153, 2018.

[250] E. Zapata-Solvas, S. Bonilla, P. R. Wilshaw, and R. I. Todd. "Preliminary investigation of flash sintering of SiC". J. Eur. Ceram. Soc., vol. 33, no. 13–14, pp. 2811–2816, 2013.

[251] V. M. Candelario, R. Moreno, R. I. Todd, and A. L. Ortiz. "Liquid-phase assisted flash sintering of SiC from powder mixtures prepared by aqueous colloidal processing". J. Eur. Ceram. Soc., vol. 37, no. 2, pp. 485–498, 2017.

[252] S. Grasso, T. Saunders, H. Porwal, B. Milsom, A. Tudball, and M. Reece. "Flash Spark Plasma Sintering (FSPS) of alfa and beta SiC". J. Am. Ceram. Soc., vol. 99, no. 5, pp. 1534–1543, 2016.

[253] E. Sortino, J.-M. Lebrun, A. Sansone, and R. Raj. "Continuous flash sintering". J. Am. Ceram. Soc., vol. 101, pp. 1432–1440, 2018.

[254] M. Biesuz, W. D. Abate, and V. M. Sglavo. "Porcelain stoneware consolidation by flash sintering". J. Am. Ceram. Soc., vol. 101, no. 1, pp. 71–81, 2018.

[255] M. O. Prado, M. Biesuz, M. Frasnelli, F. E. Benedetto, and V. M. Sglavo. "Viscous flow flash sintering of porous silica glass". J. Non. Cryst. Solids, vol. 476, no. September, pp. 60–66, 2017.

[256] M. Biesuz, M. Cipriani, V. M. Sglavo, and G. D. Sorarù. "Electrode-dependent Joule heating in soda lime silicate glass during flash processes". Scr. Mater., vol. 182, pp. 94–98, 2020.

[257] M. Soleimany and M. H. Paydar. “Investigation on flash sintering of $BaZr_{0.1}Ce_{0.7}Y_{0.2}O_{3-\delta}$ compound; using nickel wire as electrode material”. Ceram. Int., vol. 46, pp. 2128–2138, 2020.

[258] M. Frasnelli and V. M. Sglavo. “Flash sintering of tricalcium phosphate (TCP) bioceramics”. J. Eur. Ceram. Soc., vol. 38, no. 1, pp. 279–285, 2018.

[259] M. Mikami, Y. Kinemuchi, K. Kubo, N. Uchiyama, H. Miyazaki, and Y. Nishino. “Flash-sintering of antimony telluride and its thermoelectric properties”. J. Appl. Phys., vol. 124, no. 10, 2018.

[260] C. Hwang and J. Yun. “Flash sintering of hydroxyapatite ceramics”. J. Asian Ceram. Soc., vol. XX, pp. 1–8, 2020.

[261] R. R. Ingraci Neto and R. Raj. “The flash effect in electronic conductors: The case of amorphous carbon fibers”. Scr. Mater., vol. 179, pp. 20–24, 2020.

[262] A. Kumar, G. Sharma, A. Aftab, and M. I. Ahmad. “Flash assisted synthesis and densification of five component high entropy oxide (Mg, Co, Cu, Ni, Zn)O at 350 °C in 3 min”. J. Eur. Ceram. Soc., vol. 40, pp. 3358–3362, 2020.

[263] B. Yoon, V. Avila, R. Raj, and L. M. Jesus. “Reactive flash sintering of the entropy-stabilized oxide $Mg_{0.2}Ni_{0.2}Co_{0.2}Cu_{0.2}Zn_{0.2}O$”. Scr. Mater., vol. 181, pp. 48–52, 2020.

[264] F. Gucci *et al.*. “Hybrid Flash-SPS of $TiNiCu_{0.05}Sn$ with reduced thermal conductivity”. J. Alloys Compd., vol. 837, pp. 1–6, 2020.

[265] D. X. Luong *et al.*. “Gram-scale bottom-up flash graphene synthesis”. Nature, vol. 577, no. 7792, pp. 647–651, 2020.

[266] S. Mondal, A. Durygin, V. Drozd, J. Belisario, and Z. Cheng. “Multicomponent bulk metal nitride $(Nb_{1/3}Ta_{1/3}Ti_{1/3})N_{1-\delta}$ synthesis via reaction flash sintering and characterizations”. J. Am. Ceram. Soc., vol. 103, pp. 4876–4893, 2020.

[267] A. M. Raftery *et al.*. “Onset conditions for flash sintering of UO_2” J. Nucl. Mater., vol. 493, pp. 264–270, 2017.

[268] J. A. Valdez, D. D. Byler, E. Kardoulaki, J. S. C. Francis, and K. J. McClellan. “Flash sintering of stoichiometric and hyper-stoichiometric urania”. J. Nucl. Mater., vol. 505, pp. 85–93, 2018.

[269] S. Grasso *et al.*. “Flash Spark Plasma Sintering (FSPS) of Pure ZrB_2”. J. Am. Ceram. Soc., vol. 97, no. 8, pp. 2405–2408, 2014.

[270] J. Zou, S. Grasso, L. F. Liu, H. Bin Ma, M. Reece, and J. Binner. “Flash spark plasma sintering of HfB_2 ceramics without pre-sintering”. Scr. Mater., vol. 156, pp. 115–119, 2018.

[271] R. McKinnon, S. Grasso, A. Tudball, and M. J. Reece. “Flash spark plasma sintering of cold-Pressed TiB_2 -hBN”. J. Eur. Ceram. Soc., vol. 37, no. 8, pp. 2787–2794, 2017.

[272] E. Castle, R. Sheridan, S. Grasso, A. Walton, and M. Reece. “Rapid sintering of anisotropic, nanograined Nd-Fe-B by flash-spark plasma sintering”. J. Magn. Magn. Mater., vol. 417, pp. 279–283, 2016.

[273] M. Rafiq, M. Costa, P. Vilarinho. “Pairing High Piezoelectric Coefficients, d_{33}, with High Curie Temperature (T_C) in Lead-Free $(K,Na)NbO_3$”. ACS Appl. Mater. Interfaces, vol. 8, pp. 33755-33764, 2016

Chapter

2. Experimental procedure

Contents

Preamble

The following chapter is designated Experimental procedure and contemplates the detailed description of software (2.1) and hardware (2.2) development for the realization of this work. Following, the details on KNN powder preparation and sintering processes are described (2.3). The characterization of powders and sintered ceramics is given in the last section of the chapter (2.4).

The understanding of FLASH sintering process and mechanism benefits of the development of computational tools, that allow to rapidly change different parameters and test different conditions. Thus, computing simulation have grown attention through the scientific community. Here, a *COMSOL Multiphysics* model (section 2.1) was built step by step, for the description of current density distribution as a dependence of particle orientation and contact shape (micrometre-scale) and, later, the temperature gradient arising from Joule heating in a millimetric block of material.

To perform the experimental FLASH sintering studies, in parallel with simulation, hardware equipment was needed. Therefore, a dedicated adapted dilatometer and respective data acquisition software were developed. Detailed description is given in section 2.2.

The material under study is the lead-free piezoelectric $K_{0.5}Na_{0.5}NbO_3$, KNN, which was produced through the calcination of precursors (solid state reaction method). Different KNN particle-sized and purity powders were synthesised and studied. Afterwards, FLASH and conventional sintering processes were studied, and the description of both powder production and sintering is given in section 2.3.

Finally, the produced materials were characterized, so that links among particle features, sintering process-parameters and final properties, were established. A comprehensive description on the techniques and procedures used for the characterization is given in section 2.4. Additionally, more specific or detailed information will sequentially be provided throughout the results presentation in each specific article. The bibliography used for the characterization techniques description is presented by the end of chapter 2.

2.1. Development of computing simulation tools

The relevance of modelling and simulation of the FLASH sintering process towards its understanding was recognized since the early stages of this work. Within a collaboration with University of Sheffield (Dr. Julian S. Dean and Prof. Ian M. Reaney), Finite Element Modelling (FEM) tools were used to simulate the FLASH process. In a first stage of development, simulation was performed at a distance, with the facilities of Sheffield. Later, a funded *JECS trust* scholarship allowed a 2 months stay in the University of Sheffield for the development of new and improved models, that will be described below.

2.1.1. Preliminary – *ANSYS* platform

Finite element modelling (FEM) preliminarily developed in this work used the *ANSYS® Academic Research Mechanical, Release 18.1 package*. Simulations were performed using electrical analysis to study current density, electric field and associated Joule heating effects arising from the microstructure. The microstructure preliminary studied comprised different arranges of cuboids with 0.5 μm side, that are representative of KNN primary particles. Figure 2-1 schematically represents such particles with four different possible orientation as respect to one-another, namely: face-face, both in (100) direction; edge-face, (100) with (110) direction, vertex-face, direction (111) with (100); and vertex with vertex, both in (111) direction.

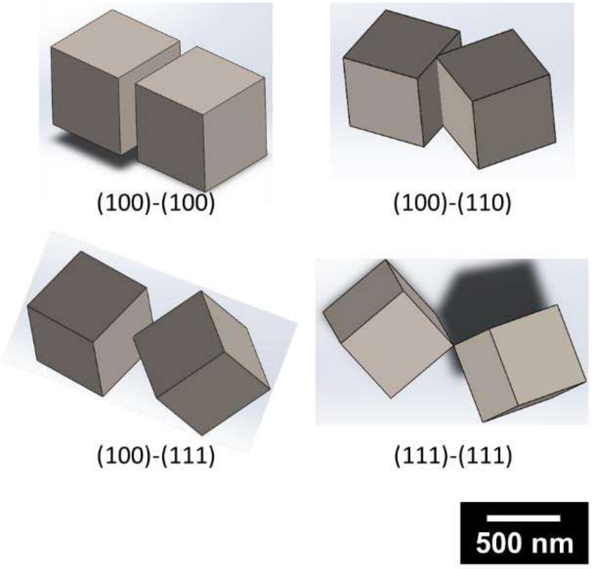

Figure 2-1 – Particle arrange for simulation of current density and Joule heating under ANSYS platform.

To reach convergence in the models a mesh size of 25 nm was used, generating over 1 million tetrahedral elements. This model was performed in a stationary system where the temperature is kept constant and the electrical properties of the material do not change with the application of the field. In fact, a constant electrical conductivity of ~10^{-3} S/m. In this preliminary study, the goal was to understand the role of contact geometry rather than attempting on a full FEM analysis of field distributions in FLASH sintering. To perform FEM simulations, a potential difference was applied over the cubes. To calibrate the voltage and provide a value to allow comparison, the (100)-(100) face-face configuration was selected, and the voltage gradually raised from 0 to the respective potential that gave rise to the experimentally tested maximum current density. To ensure similarity between the models, the same voltage was then used to highlight current density changes on the remaining particle orientation-dependent models. The associated Joule heating was simultaneously calculated from the simulated power dissipation. It should be noted that the approach of keeping this voltage constant may lead to unreasonable current densities and heating effects, as the material may melt before the resultant current could be reached. The absolute values are thus not as important as the comparison between them, and this was the main goal of this preliminary study. In fact, this model was essential to describe the proposed mechanism of KNN FLASH sintering; details on building the model and the correspondent results will be presented in section 5.1.

2.1.2. Temperature distribution models – *COMSOL Multiphysics*

The development of *ANSYS*-based FEM models was essential to understand the limitations of such platform and to perform more complex simulations. A major limitation of *ANSYS* is the impossibility for the coupling of Joule heating with the consequent local temperature. While the simulation of the current distribution and Joule heating as a dependence of particle size and orientation was possible, the consequent estimation of the local temperature, and possible thermal gradients, were not possible to simulate.

Using *COMSOL Multiphysics*, a similar approach was considered, with an applied voltage and the calculation of the current density, Joule heating, and now, the local temperature. Two different models were developed: (i) one based on particle orientation, similarly to the previously described one and (ii) macroscopic model for the estimation of local temperature in a millimetre sized *block* of material. These will be presented in detail in sections 3.1 and 3.2, respectively. Both models are based on same logic: the application of a 300 V/cm electric field to the opposite faces of the model under study and the simulation of the generated current. To achieve this, the referred opposite faces are assigned with a

Terminal and *Ground* functions, respectively. However, different strategies were then used in each model. For the particles (i), the *Terminal* function was associated with *global equation* function for the description of the three stages of FLASH. This last function (*global equation*) is responsible for the establishment of a current limit in the system, therefore, describing all the FLASH sintering process, from steady state (I), FLASH (II) and current limit (III). Additionally, a *Thermal insulation* boundary condition was considered to the particle faces, with no further radiation nor convection heat transfer occurring to the environment. Because this was a time dependent model, the electrical conductivity of the simulated particles was assigned with that measured during FLASH sintering experiments. Details are given in section 3.1.

Two major differences (or updates) were considered for the macroscopic model (ii), namely in what concerns the thermal dissipation limitation and the conductivity (σ) of the KNN material. Here, an *Air* box was modelled to involve the KNN material and electrodes. Thereby, thermal dissipation through convection and radiation was considered. Additionally, the electrical conductivity vs. temperature dependence was re-considered. The strategy used in the particles model (i) consisted in assigning the electrical conductivity of KNN compacts measured *in-situ* during the FLASH sintering process. However, this measurement is known to have a significant delay in the measured (furnace) temperature. Therefore, in the macroscopic model (ii), previously dense KNN ceramics were heated to ca. 1000 ºC and their electrical conductivity was measured at 1 V/cm (instead of the 300 V/cm during FLASH), avoiding the Joule heating effects, providing a much more precise dependence of σ with T. This dependence was then assigned to the modelled KNN material. Section 3.2 presents the details on this model and its relevance for the interpretation and understanding of identified local stresses in FLASH sintered ceramics.

2.2. Development of the FLASH sintering setup: furnace and software

A parallelepipedal sample and electrode-contact experimental apparatus was selected to perform FLASH sintering (remember Figure 1-10). The reasons to choose this apparatus over the dog-bone shaped specimen were: (i) easy acquisition of in-situ FLASH data using a dilatometric apparatus (ii) easiness on industrial transfer. However, the production of homogeneous specimens is more challenging, because the electrodes are part of the actual produced ceramic, contrarily to what happens in the dog-bone specimen, in which electrodes are not considered.

The schematic representation of the developed sample holder FLASH setup is presented in Figure 2-2. The specimen is placed in between two platinum electrodes that are connected to platinum wires and those to the power source (*DC, EPS HV 5006-400*, when no other indication is given). One of the electrodes is fixed by an alumina fixed part and the second one is free to move and follow the shrinkage or expansion of the compact, trough the movement of an external alumina stub.

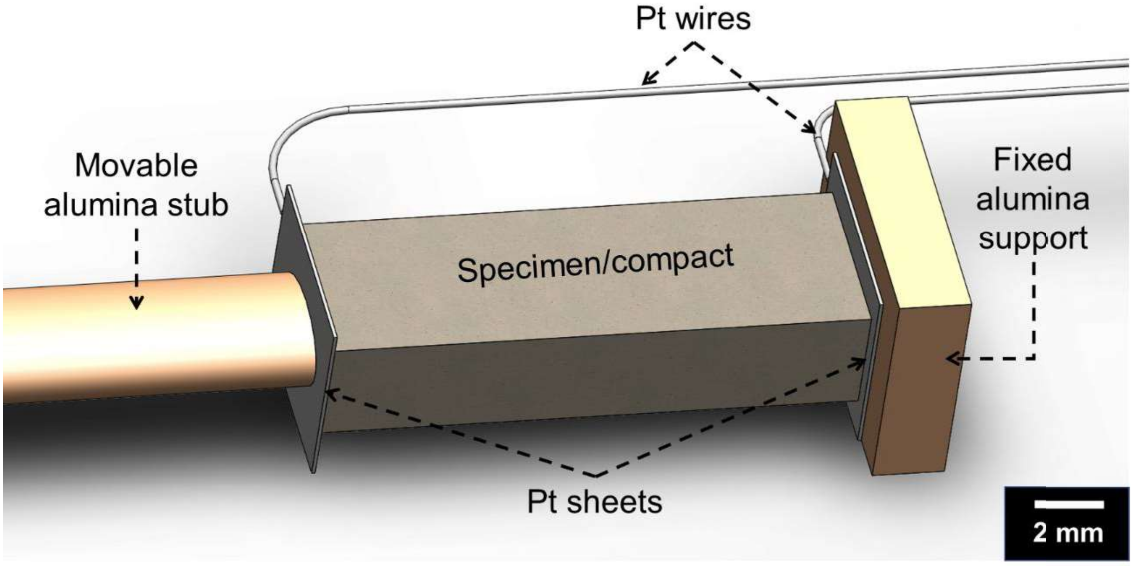

Figure 2-2 – Schematic representation of the FLASH sintering setup used in this work.

Following the design and validation of the FLASH sintering setup in preliminary testes, using used alumina tubes and parts, a dedicated furnace that would allow the *in-situ* study of FLASH parameters was developed. A horizontal dilatometer-type furnace was designed and built. Figure 2-3 shows the technical drawings of the developed dilatometer. This was the result of a collaboration between University of Aveiro and two companies: Termolab, that built all the structure and furnace, and Vhelsi, which was responsible for the data acquisition and control software development. However, all the conception, design and supervision tasks regarding the dilatometer development were from R. Serrazina and the supervision team of this work.

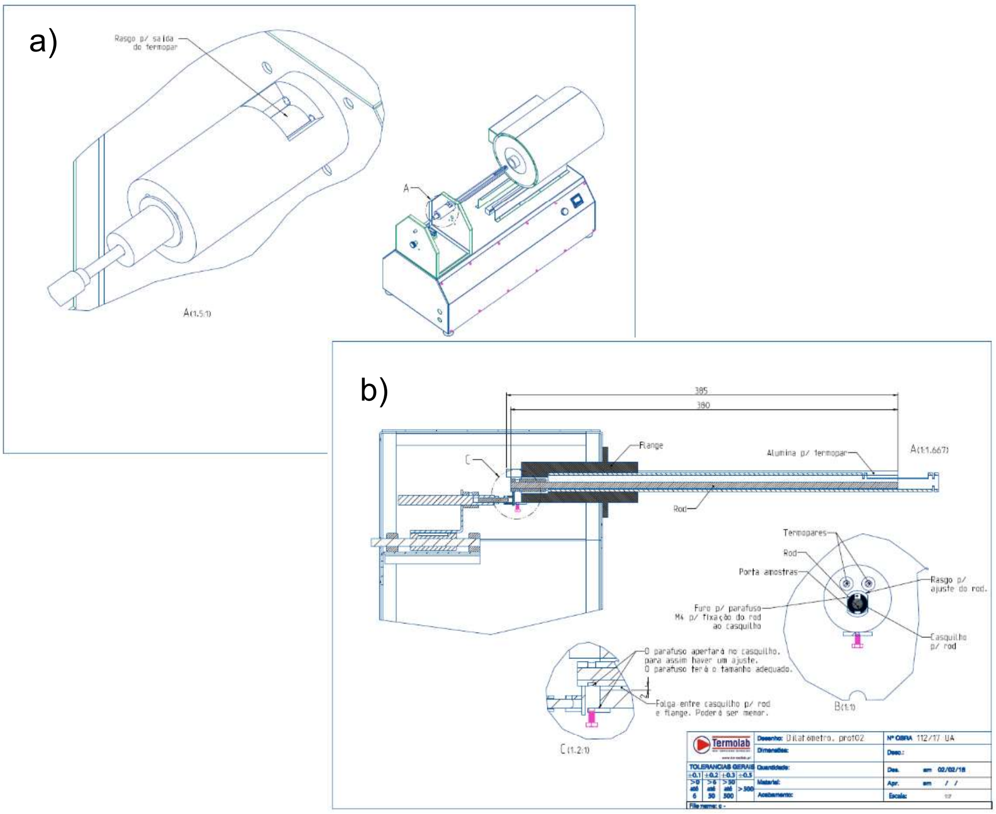

Figure 2-3 – Technical drawing of a) dilatometer and b) sample holder and LVDT sensor with respective platform details [1].

The dilatometer is composed of six main parts (identified in Figure 2-4): (i) furnace, that rolls in a train line; (ii) furnace power supply system; (iii) furnace control system; (iv) displacement and temperature recording; (v) sample holder and (vi) control and data acquisition software. Figure 2-5 shows the sample holder in detail. Being a contact dilatometer, the working principle of this furnace is based on the measurement of specimen length variation. For that, an alumina rod or stub is externally pushed by a spring, that guarantees the contact between the alumina pushing rod and the specimen being analysed (sintered, in this case). In our setup, the LVDT sensor (*RDP D5/400AG*) contains a spring (1.4 N, corresponding to ca. 0.15 MPa in our compacts) that is responsible for the referred function. The LVDT sensor consists in an inner metallic rod that slides on an outside coil;

the change in the inner rod position (specimen shrinkage/expansion) results in an alteration on the resistance between the external coil and the rod. This signal is sent then to its specific amplifier (*RDP DR7AC*) that converts the measured resistance into a scaled -3.5 to 3.5 V, corresponding to the maximum and minimum shrinkage (-12 mm - +12 mm). This signal, together with the voltage measured at the "sample thermocouple" (equivalent to the latter referred *furnace temperature*) are connected to a *E-DAM 8017* board for analogic to digital (USB connection) data conversion. The data is then received and interpreted by the software, together with the *Eurotherm 3216* furnace controller, and compiled in a graphic representation, exportable as a .csv file.

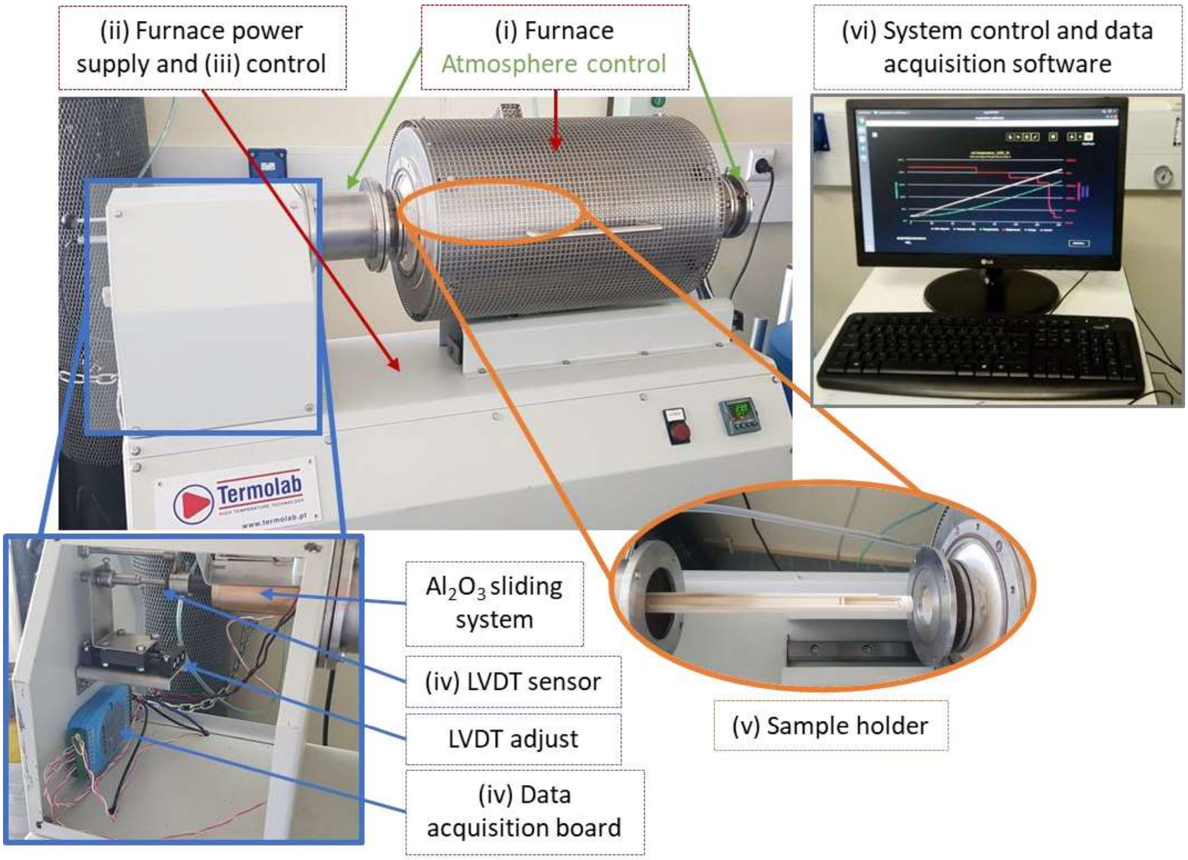

Figure 2-4 – FLASH dilatometer developed in the scope of the present work. Schematic representation of each main part with respective caption.

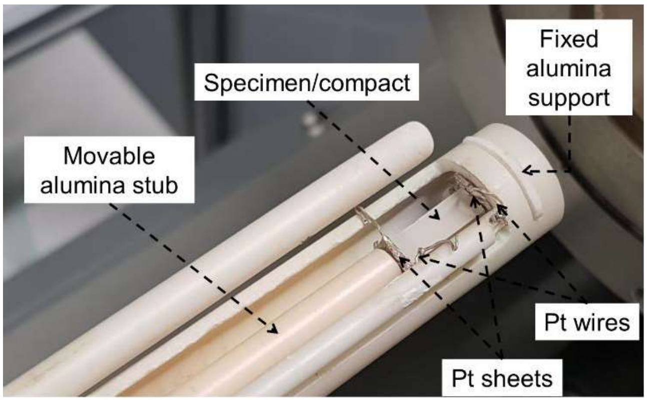

Figure 2-5 – Details of sample holder with respective identification of each part.

To guarantee that the shrinkage and/or expansion of the ceramic compacts was properly determined, the said measured length size variation was calibrated for the sample holder thermal expansion, at different heating rates, namely 2, 5, 10 and 15 ºC/min. For that, a sintered alumina ceramic, with known length and thermal expansion (dependent on the heating rate) was used. The experimentally measured dilatometric curve of the sintered alumina was then analysed, and the known expansion of the sample subtracted from the data. The resultant temperature dependent length curve was accessed to the sample holder contributions. These were fitted with mathematical functions (typically linear or quadratic), as a dependence of heating and cooling regimes. The mathematical data treatment was compiled in different software files, as respect to the heating and cooling rates, for post-treatment of the dilatometric curves.

A major advantage of this equipment is that the external power source to apply the electric field and current needed to perform FLASH is completely independent of the furnace. One can use the more suitable power source for a specific experiment. The software is developed specifically for the *EPS HV 5006-400* and *Keysight N5752A*, however, if the power source has a computer communication software, it can be easily connected to the system.

Additionally, to have control on the sintering atmosphere during FLASH sintering, a gas system control was added to the furnace. As schematically depicted n Figure 2-6, the system allows the use of dry or wet atmospheres, depending if the gas flows through a water flask or not. This method was designated by Atmosphere-Assisted FLASH sintering (AAFS) and is presented in detail in Chapter 6.

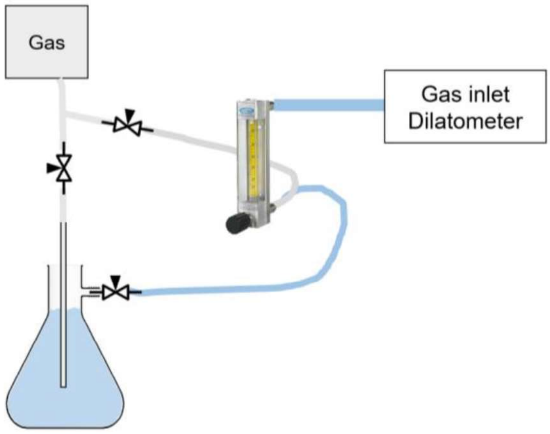

Figure 2-6 – Schematic representation of the gas circuit for atmosphere-assisted FLASH.

2.3. Preparation of KNN powders and ceramics

2.3.1. KNN powders production

$K_{0.5}Na_{0.5}NbO_3$, KNN, powders were prepared by conventional solid-state route. The process is schematically represented in Figure 2-7. Potassium and sodium carbonates (K_2CO_3 and Na_2CO_3, respectively) and niobium oxide (Nb_2O_5) were dried (200 ºC, 24h) and stoichiometrically weighted. A ball milling process was then used to mix the precursors, with YSZ balls and commercial 99% ethanol media for 6h at 200 RPM in teflon jars. Mixed carbonates and oxide were then calcined in dense alumina crucibles at 900 ºC for 3h, with heating and cooling rates of 10 ºC/min. The particle size of single-phase $K_{0.5}Na_{0.5}NbO_3$ powders was controlled by a final milling step. Additionally, to synthesise KNN powders with different degrees of purity, initial precursors with different purity level were used. Details in both purity and final particle size will be given in section 4.1.

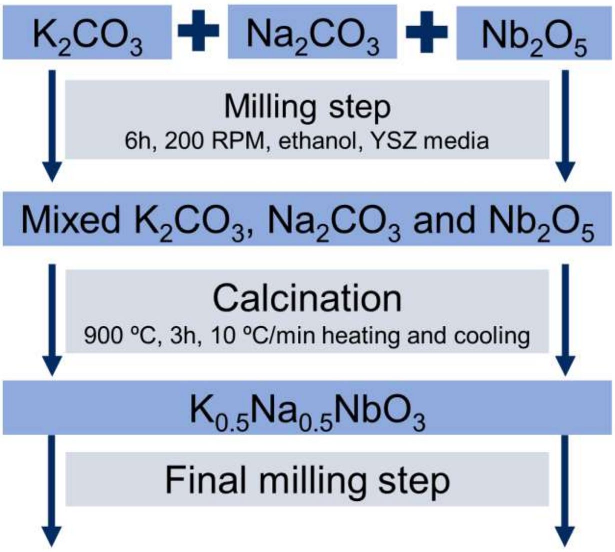

Figure 2-7 – Powder production experimental procedure scheme

After the synthesis and final milling steps, powders were uniaxially (130 MPa) and isostatically pressed (approximately 200 to 250 MPa for 15 min) in ca. 15 x 5 x 2 mm^3 parallelepipedal shaped compacts, with approximately 60 to 65% of green density.

2.3.2. FLASH and conventional sintering

FLASH sintering procedures and studies were performed in the Dilatometer setup described in section 2.2. When no other indication is given, the KNN compacts were FLASH sintered with the use of flat platinum sheet electrodes directly contacting with the compact (Figure 2-2). In specific cases, silver electrodes were painted on the compacts.

While all the FLASH experiments were developed under DC electric field and currents, different approaches were used in what concerns the thermal cycle, namely, Constant Heating Rate (C.H.R.) and Isothermal Conditions (I.C.).

Preliminary results determined that a suitable electric field for C.H.R. experiments was 300 V/cm. Lower electric fields than this one result in a slow FLASH transition and incomplete sintering, while higher electric fields are prone to induce current localization (hotspots) and consequent non-uniform densification. Therefore, in C.H.R., compacts were heated to ca. 500 ºC and the electric field applied at such temperature and subsequently under constant heating until FLASH temperature, T_F, was reached. At that point, the power supply (*EPS HV 5006-400*) was automatically switched from voltage to current control when a 20 mA/mm^2 limit was achieved. For I.C., before the application of the electric field, compacts were heated to a furnace temperature of 900 ºC, and a 30 min dwell was employed. The 300 V/cm electric field was applied after the isothermal step and following an incubation time, the pellets FLASH sintered with similar current limiting conditions of C.H.R. All FLASH sintering experiments were performed at 10 ºC/min heating and cooling rates. In the absence of a different indication, FLASH sintering was performed with a holding time (in current limiting conditions) of 60 s.

For the atmosphere assisted FLASH sintering experiments, specifics are given in sections 5.1 and chapter 6.

For conventional sintering (CS), different thermal profiles were tested for the densification of the produced KNN compacts, namely in what concerns maximum temperature, time, and heating rate, with the goal of obtaining dense ceramics without traceable secondary phases (traced by X-Ray Diffraction analysis). Slower heating rates are known to avoid the formation of secondary cases, and this was verified when comparing 5 and 10 ºC/min heating and cooling. Therefore, 5 ºC/min was selected as the suitable rate for CS. Temperatures over 1130 ºC resulted in significant loss of K and Na, while temperatures below 1050 ºC did not allowed densification greater than 87% to be reached. 1125 ºC was selected as the suitable conventional sintering temperature. The dwell time was also optimized to 3 h.

2.4. Characterization techniques and procedure

In the following sub-sections, a description of the techniques used to characterize either powders, compacts or sintered ceramics is given. The details on procedures for sample preparation and analysis are described.

2.4.1. Structural, chemical, and morphologic analysis

X-Ray Diffraction - XRD

The crystalline structure and symmetry of powders and sintered bodies were studied by X-Ray diffraction (XRD). The wavelength of X-Rays is comparable with the size of atoms, thus making XRD a suitable technique for the characterization of atomic arrangements in materials, i.e., their crystalline structure.

X-Rays are produced from the interaction of high energy electrons with a target, typically, metals as copper. A monochromatic X-ray beam, with a known wavelength λ, that focuses on a crystalline material at a certain angle θ, results in a diffracted beam, when the distance travelled by the X-rays reflected from successive planes differs by a complete number, n, of wavelengths. With changing θ, the Braggs's law [2] (eq. 2-1) is satisfied at different d-spacings in polycrystalline materials [3].

$$2\ d \sin(\theta) = n\ \lambda \tag{2-1}$$

In this work, a *PANalytical XPERT-PRO* equipment, with a copper X-ray source ($K\alpha_1 = 1.54060$ Å)) in a Bragg-Brentano apparatus was used. The scan range was from $2\theta \approx 10°$ to 80°, with a step size of 0.0263° and a scanning step time of $\approx$ 96.4 s. Both powders and ceramics were grinded with a mortar and pestle before XRD analysis. For phase identification, the JCPDS data base was used and the following files considered for comparison (and Rietveld analysis when referred): PDF file 01-085-7128 for $K_{0.5}Na_{0.5}NbO_3$, orthorhombic symmetry perovskite structured phase (space group Amm2 (38)) and a PDF file 04-007-9405 for $K_{0.8}Nb_5O_{15}$ (Nb-rich) secondary phase with tetragonal structure (space group: 100).

XRD was additionally used for the determination of residual stresses on as-sintered (not grinded) polished ceramics. Polishing was performed with SiC papers from P800 to P4000 (approximately ~5 μm grain size). An incident angle tilt and equation 2-2 were used for the determination, where k is the gradient of the d-spacing (of 311 planes, in this case) vs. $\sin^2\Psi$ curve and E_Y and υ are the Young Modulus (~100 GPa) and Poison ratio (0.25) of the material, respectively. For details on the method, consult [4], [5].

$$\sigma_\phi = \left(\frac{E_Y}{1+\nu}\right)k \tag{2-2}$$

Raman Spectroscopy

Raman spectroscopy is based on inelastic scattering of a monochromatic laser source light, in which the frequency of photons changes upon interaction with a material. The frequency of the reemitted photons (after being absorbed) is shifted up or down in comparison with original monochromatic frequency, which is called the Raman effect. This shift provides information about vibrational, rotational and other low frequency transitions in molecules. In other words, every substance has an individual spectrum and therefore the method can be used to identify a chemical compound and its structural elements [6]. In practice, a sample is illuminated with a laser beam in the ultraviolet (UV), visible (Vis) or near infrared (NIR) range. Scattered light is collected with a lens and is sent through an interference filter or spectrophotometer to obtain a Raman spectrum.

In this work, polished (~5 μm grain size SiC papers) sintered ceramics were analysed by unpolarized micro-Raman single spot and imaging (details and schematics given in section 3.2) using a state-of-the-art Renishaw InViaTM Qontor® Confocal spectrometer. The 633 nm line of a He-Ne laser (power at 50%) was chosen for excitation of KNN ceramics and depending on the experiment (size of analysed area), 50x or 100x lens were used for focusing the laser beam, with an exposure time of 0.1 s for each acquisition. In imaging setup, the pixel size varied from 1 to 30 μm^2, depending on the map area. The scattered light was analysed using an 1800 lines/mm diffraction grating, providing a spectral resolution better than 1.5 cm^{-1} and a lateral resolution of 10 nm. The frequency, linewidth, and intensity of the Raman bands were determined through the best fit of a Lorentzian function. Between measurements, the spectrometer was calibrated for the 521 cm^{-1} Silicon band. These studies were possible due to a collaboration with the University of Porto (prof. Joaquim Agostinho, Dr. Rui Vilarinho Silva and Mariana Gomes).

Inductively Coupled Plasma (mass) Spectroscopy – ICPS

In most of Inductively Coupled Plasma Spectroscopy analyses, a liquid sample is needed for analysis, which means that solid materials need to be dissolved. The liquid is then converted into an aerosol using a nebulizer and is sprayed into the centre of a plasma. In this stage, the particles within the aerosol are dried, atomized, ionized, excited and relaxed in a very short distance and time. An ICP-Mass Spectrometer directs the generated ions into a quadrupole mass spectrometer, that filters the ions based on their mass to charge ratio. Within the calibration range of the method, the signal intensity for a given ion is proportional to its concentration in the solution [7].

In this work, the content in K, Na and Nb, as well as trace contaminations (Al and Zr), was determined by Inductively Coupled Plasma (ICP) mass spectrometry of powders, using HNO_3 and HF as digestion agents, in a microwave heater. A 100 ml solution volume was analysed in a *Thermo X Series* equipment.

Scanning Electron Microscopy – SEM

In Scanning Electron Microscopy (SEM), the surface of a specimen is scanned with an electron beam, and the reflected (or backscattered) electrons are collected and treated by analogic or digital means. The surface to be analysed must be electrically conductive, which means that insulators need to be covered with a carbon or metallic layer. The interactions of electrons with materials can be divided into elastic and inelastic. Elastic scattering results from the deflection of the incident electron by the sample atomic nucleus or by outer shell electrons of similar energy. Incident electrons that are elastically scattered through an angle of more than 90° are called backscattered electrons (BSE) [8], [9]. Inelastic scattering occurs through a variety of interactions between the incident electrons and the atoms of the sample, and results in the primary electron beam transferring substantial energy to the material. Thus, the excitation of the specimen electrons leads to the generation of secondary electrons (SE), which can be used to image or analyse the sample [8], [9].

Accessory equipment in SEM allows qualitative and semi quantitative analysis of the elemental composition of very localized surface areas. Energy Dispersive X-ray Spectroscopy (SEM-EDS) is an example. In this case, the electron beam is directed to one area or point of the sample and the interaction of the beam within the sample produces characteristics X-Rays [9]. Additionally, Electron Backscattered Diffraction (EBSD) detectors allow to assess chemical, structural, and texturing information through the simultaneous analysis of grain topography, crystalline structure, and specific orientation as respect to the neighbouring grains.

In this work, SEM was performed in field-emission scanning electron microscope (*Hitachi SU-70*), used for morphological and chemical analysis of powders and sintered products. All specimens were covered with a Carbon layer using a *Emitech K950X* evaporator before analysis. Chemical information of powders and ceramics was acquired with SEM analysis by energy-dispersive X-ray spectroscopy (EDS) using a *Bruker QUANTAX 400* detector. When no other indication is given, the beam acceleration voltage was set for 15 kV.

The particle size and morphology of powders were accessed through observation of both dispersed powders and green compacts. For the first, powders were sonicated in ethanol. A glass substrate was used to dry a droplet of the dispersed powders. In the case of compacts, after the pressing steps, the specimens were broken, and the fracture area observed. For particle size distribution estimation, *ImageJ* software (https://imagej.net/) was used. More than 500 particles were considered.

As-sintered ceramic's topography was analysed after polishing with SiC papers, from P800 to P4000. KNN is a relatively soft ceramic, thus diamond polishing was not required, as P4000 SiC paper (~5 μm grain size) was sufficient to avoid scratching. For grain size analysis, polished ceramics were chemically etched with HF for 5 min. A sonicated water and ethanol washing procedure was employed afterwards. Grain Size Distribution (GSD) was determined from etched micrographs.

Electron Backscattered Scanning Electron Diffraction – EBSD

The microstructure and microchemistry of the sintered ceramics was further analysed by Electron Backscattered Diffraction Analysis (EBSD), using a *Bruker e-Flash Quantax CrystAlign.* Prior to the EBSD analysis, ceramics were polished using SiC papers, diamond paste and colloidal silica. To precisely determine the GSD, the phase map' EBSD data was used, and the equivalent grain diameter calculated from the grain area, using *ImageJ* software. The calculation of grain size and texturing was not directly performed using EBSD data due to filtering limitations associated with the available software package.

Transmission Electron Microscopy – TEM

Transmission Electron Microscope (TEM) is also a technique that takes advantages of the interaction of electrons with matter. In this case, the range of acceleration voltages is typically between 100 to 400 kV, while the specimens need to be thin enough to allow transmission of electrons. Through the selection of different types of electrons, bright (atomic mass-related interaction) and dark field images are possible to obtain. The transmitted and forward scattered electrons form a magnified image with very high resolution, allowing the analysis of features at the atomic scale. While the image of thin samples is given through electronic contrast, the diffraction mode allows to access the reciprocal space of the material under study, therefore assessing its crystalline structure [10].

In the present work, when no other indication is given, a *JEOL HD-2200FS* transmission electron microscope was used, together with an *Oxford INCA Energy TEM 250* EDS detector. Sintered ceramics were analysed by TEM and their thinning process is described in each specific section of the Results chapters.

Mercury Intrusion Porosity - MIP

Mercury, Hg, has a non-wetting behaviour in most substances. It will not enter sample's pores if a pressure is not applied. An external pressure forces Hg to enter the pores of a specimen under analysis, where the pore size (r_p) is inversely proportional to the pressure (P), and the proportionality constant depends on Hg's surface tension (γ_L) and respective contact angle (θ_c) – equation 2-3 [11].

$$P_P = \frac{2\,\gamma_L \cos\theta_c}{r_p} \tag{2-3}$$

The measurement of pore size distribution, total open pore volume and apparent density of compacts through the described procedure is called Mercury Intrusion Porosity (MIP) and allow to scan a wide pore size range (from few nanometres to ~400 μm). Though, some limitations are known, as for instance the assumption that all pores are accessible through larger pores or from the surfaces, which make big pores with small entrances be identified as having the size of the entrance. Additionally, closed pores are not accessible to mercury [11]. In this work, a MIP equipment (*Micromeritics, Autopore IV 9500*) was used to determine the porosity of green (un-sintered) compacts.

2.4.2. Particle size determination

Particle Size Distribution – PSD

Particle Size Distribution (PSD) was assessed by laser diffraction through a *Coulter LS-200* equipment in water medium (ranging from 0.04 to 2000 μm). In this technique, the dispersed powder specimen passes through the measurement area where a laser beam illuminates the particles. Several detectors accurately measure the intensity of the scattered light by the particles. The scattered light signal is converted to particle size by the algorithm of the adequate refraction model [12]. This technique was employed in the current work for the determination of PSD in calcined and milled KNN powders. Those were dispersed in water and sonicated for 5 min before the measurement.

Specific Surface Area

The adsorption measurements based on the Brunauer Emmet Teller (BET) isotherm are used to determine the Specific Surface Area (SSA) of dense and porous materials. N_2 is the most used gas in BET analysis. To determine the SSA of a specimen, a known mass of the sample in placed in contact with a known volume of gas. The sample will adsorb the gas, creating a decrease in pressure, from which the amount of adsorbed gas can be calculated. As so, a plot of the amount of gas adsorbed *versus* the relative pressure of gas (P_P/P_0, being P_0 the saturation vapor pressure of the adsorption used gas) is represented and is called adsorption isotherm [13].

To calculate de SSA, the BET equation is applied to the lower values of P/P_0 isotherm (between 0.05 and 0.3) according to eq. 2-4, where V_G is the volume of adsorbed gas, C_{BET} is a constant and V_m is the volume of an absorbed monolayer and is calculated from the slope and the intercept of the isotherm line. This variable is then applied in eq. 2-5 in which SSA stands for the surface area, N_A for Avogadro Number, A_a for the area of an adsorbed gas molecule and V_0 for the volume of one mole of gas at STP – standard temperature and pressure [13]

$$\frac{P_P}{V_G(P_0-P_P)} = \frac{1}{V_m C_{BET}} + \frac{C_{BET}-1}{V_m C_{BET}} \frac{P_P}{P_0} \tag{2-4}$$

$$SSA = \frac{N_A\, A_a\, V_m}{V_0} \tag{2-5}$$

The specific surface area (SSA) of the powders and pre-sintered compacts was determined by N_2 adsorption in a *Micromeritics Gemini 2.0* equipment, using the Brunauer, Emmett, Teller (BET) adsorption isotherm. The equivalent particle size (D_{BET}) was calculated according to equation 2-6, where SF is the shape factor (SF = 7.4 for cubes) and ρ_t is the theoretical density of the material (4.5 g/cm^3 for KNN). An overnight drying step at 120 °C was performed before analysis.

$$D_{BET} = \frac{SF}{SSA \times \rho_t} \tag{2-6}$$

2.4.3. Density determination

The density of the compacts was assessed by a geometric method, while that of sintered bodies was estimated either by Archimedes or geometric method. With one or the other, the relative density (ρ), or densification, was calculated following the equation 2-7, where $\rho_{measured}$ is the measured density (geometric or Archimedes) and ρ_t is the theoretical density (4.5 g/cm^3 for KNN).

$$\rho = \frac{\rho_{measured}}{\rho_t} \times 100 \tag{2-7}$$

Geometrical

The density of compacts and sintered ceramics was geometrically determined, following equation 2-8. The mass (m) was measured using a 4-digits analytic scale and the volume (Vol) calculated from length x width x thickness dimensions, acquired with a calliper rule. In the case of irregular specimens (as for instance, FLASH sintered ceramics), several size measurements were taken, and the average considered.

$$\rho_{geom.} = \frac{m}{Vol} \tag{2-8}$$

Archimedes

Sintered ceramics were dried at 110 °C, for 2 h. Archimedes density ($\rho_{Archim.}$) was measured in water medium. The ceramic dry mass (m) was recorded. Following, the specimens were boiled in water for 30 min and placed in cold water for 4 h. After that, the excess of water was removed with a humidified paper and the mass was again measured (m_{humid}). Subsequently, an Archimedes setup was used to measure the immerse mass of ceramics (m_{imm}). The final Archimedes density was calculated following the equation 2-9 – water density was approximated to 1.00 g/cm^3.

$$\rho_{Archim.} = \frac{m}{m_{humid} - m_{imm}} \tag{2-9}$$

2.4.4. Dilatometry and *in-situ* electrical measurements

Dilatometric studies were used to characterize the sintering behaviour of both FLASH and conventionally sintered ceramics. As described in section 2.2 of this work, the length displacement of compacts during sintering was recorded using a horizontal adapted dilatometer. In FLASH sintering experiments, the platinum electrodes were placed in the opposite faces of the parallelepipedal pellets (Figure 2-2), and an electric field applied through them; for the comparative study of conventional process, the Pt electrodes were removed and the compacts sintered without the electric field. In both cases, the length displacement, or variation, was measured, and the specimen's relative displacement, α, calculated following the equation 2-10, where L_m and L_0 are the measured and initial length.

$$\alpha = \frac{\Delta L}{L_o}(\%) = \frac{\Delta L}{L_o} \times 100 = \frac{L_m - L_o}{L_o} \times 100 \qquad (2\text{-}10)$$

In particular cases, the density of ceramics during dilatometric analysis, ρ_c, was calculated after the relative displacement, considering an isotropic shrinkage, following equation 2-11.

$$\rho_c = \frac{\rho_{green}}{(1+\alpha)^3} \qquad (2\text{-}11)$$

To calculate the activation energy for densification of both conventional and FLASH processes, an isotropic shrinkage behaviour was considered (valid for $0 < -\alpha < 2\%$). The classical description of sintering kinetics [14] states that the instantaneous densification rate, $d\rho/dt$, is expressed by an Arrhenius dependence (eq. 2-12), in which E_a is the activation energy for the densification process, R_G is the gas constant, T is the absolute temperature, G is the grain size, n_c is the Herring exponent, A is the material parameter (independent of G, ρ or T) and $f(\rho)$ is a function of the density [14], [15].

$$\frac{d\rho}{dt} = A.\exp\left(\frac{-E_a}{R_G T}\right).\frac{f(\rho)}{T.G^{n_c}} \qquad (2\text{-}12)$$

Valid only for FLASH sintering experiments, the *in-situ* current density (J) and electric field (E) were calculated from the direct measurement of the output signals on the power source, and following equations 2-13 and 2-14, respectively, where I is the measured current, A_S the initial section area of the compact and U the voltage (or potential). The respective volume normalized power dissipation (P_W) was calculated in accordance with equation 2-15. Additionally, the conductivity of compacts (σ) was calculated following eq. 2-16.

$$J = \frac{I}{A_S} \qquad (2\text{-}13)$$

$$E = \frac{U}{L_0} \qquad (2\text{-}14)$$

$$P_W = E\,J \qquad (2\text{-}15)$$

$$\sigma = \frac{J}{E} \qquad (2\text{-}16)$$

2.4.5. Electrical and piezoelectric performance

DC conductivity

The DC conductivity (σ) of sintered KNN ceramics was compared with that of KNN single crystals (SCs). The $K_{0.5}Na_{0.5}NbO_3$ SCs were produced by high temperature self-flux method, using calcined KNN powders – the experimental details may be found in [16] and detail information is provided in section 4.1.

To perform the DC conductivity measurements of KNN bodies (ceramics and SCs), platinum electrodes were painted (*SPI-CHEM 04990-AB*) in ca. 1 mm thick ceramics and SC faces. After a drying step at 50 ºC, the Pt electrodes were cured at 900 ºC for 1 h. The electrical conductivity was measured as a function of temperature, using a *Keithley 2410* electrometer, and heating these specimens at a constant heating rate of 10 ºC/min from 500 ºC to ca. 1000 ºC, with an applied electric field of 1 V/cm. The activation energy for conduction ($E_a(\sigma)$) of KNN bodies, was determined based on an Arrhenius dependence, equation 2-17, where σ_o is the pre-exponential term, T the temperature and K_B the Boltzmann constant.

$$\ln(\sigma) = \ln(\sigma_0) - \frac{E_a(\sigma)}{K_B}\frac{1}{T} \tag{2-17}$$

Dielectric characterization

The electrical behaviour of dielectric materials is typically assessed in a parallel plate capacitor configuration, in which the material is placed in between two conductive plates (electrodes). The capacitance, C, is then measured, being a parameter that reflects the ability of a material to store electrical charge. C is related to the material dielectric constant or relative permittivity (ε_r). If an AC sinusoidal voltage source U is applied through a capacitor, the resulting current, I, is the sum of the charging current I_C and the loss current I_R (that is related to the dielectric constant), in accordance with eq. 2-18, where i is the imaginary operator, $\omega = 2 \pi f$ the angular frequency, ε_0 the dielectric constant of vacuum (8.85×10^{-12} F/m), A_e the electrode area, d_s the distance between electrodes (typically the thickness of the sample) and ε^* the complex dielectric constant. The complex dielectric constant[2] (ε^*) consists of a real part ε' (storage) and an imaginary part ε'' (loss) [17], [18].

---

[2] $\varepsilon^* = \varepsilon_0\varepsilon_r$

$$I = I_C + I_R = \frac{i\omega\varepsilon^* U \varepsilon_0 A_e}{d_s} = \frac{i\omega(\varepsilon' - i\varepsilon'') U \varepsilon_0 A_e}{d_s} \tag{2-18}$$

The real part of the relative permittivity (ε_r') is a measure of how much energy from an external electric field is stored in a material, while the imaginary part (ε_r'') is called the loss factor and measured how dissipative a material is. ε_r'' is greater than zero and is usually much smaller than (ε_r'). The vector diagram of complex permittivity is drawn in Figure 2-8 and shows that the real and imaginary components are 90° out of phase. The vector sum forms an angle δ with the real axis (ε_r'). The loss tangent (tanδ) is defined as the ratio of the imaginary part of the dielectric constant to the real part [18].

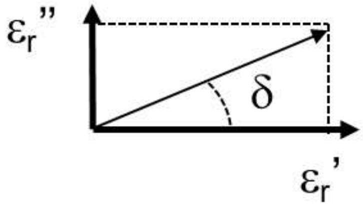

Figure 2-8 – Loss or dissipation factor (tanδ) vector diagram. Adapted from [18]

To access the dielectric and ferroelectric behaviour of KNN ceramics, 1 mm thick samples, with ca. 5 x 3 mm^2 section area were prepared from sintered bodies, using a diamond cutting wire and SiC papers for thickness reduction. After a fine polishing (SiC P2500), platinum electrodes were brush painted (*SPI-CHEM 04990-AB*) at the opposite faces of the ceramics to guarantee an appropriate electric contact. A drying step at 50 ºC was employed, followed by a cure and sintering electrode process, following the manufacturer indications (maximum temperature of 900 ºC, for 1 h) as done before. To study the influence of the post-sintering (for electrode cure) heat treatment of FLASH ceramics on their dielectric behaviour, an intermediate heat treatment was considered, with maximum temperature of 350 ºC. For room temperature measurements, gold (Au) electrodes were deposited by DC magnetron sputtering of an Au target (99.95%) in Argon atmosphere.

The real part of the relative dielectric permittivity (ε_r) and dissipation factor (tanδ) were accessed in the parallel-plate-capacitor configuration, using an impedance bridge (HP 4284A), with a 1 V oscillation potential and over a 41-points frequency variation (from 100 Hz to 1 MHz). A temperature dependence was obtained on heating and cooling in a tubular furnace with alumina sample holder, using a 2 ºC/min rate, and a dwell time of 2 min before each measurement.

Impedance spectroscopy - IS

Impedance spectroscopy (IS) studies were performed using the previously acquired temperature-dependent data for dielectric measurements, choosing the data for cooling. The referred dielectric parameters were calculated from the measurement of dual impedance parameter Z - ψ. Impedance (Z) extends the concept of resistance to AC circuits and possesses both magnitude and phase contributions. IS usually involves the application of an alternating voltage signal to a sample and the measurement of the phase shifted current response. Complex impedance (Z*) is defined as in equation 2-19, where Z_0 is the measured impedance, ψ the phase angle and Z' and Z'' are the real and imaginary components, respectively [19].

$$Z^*(\omega) = Z_0\big(\cos(\psi) + i\sin(\psi)\big) = Z'(\omega) + iZ''(\omega) \tag{2-19}$$

The real part of the impedance is related to a pure resistance behaviour, while that of imaginary part (eq. 2-20) is typically associated with capacitance, C, in accordance with eq. 2-21 [20].

$$Z'' = \frac{1}{i\omega C} \tag{2-20}$$

$$C = \varepsilon_r \varepsilon_0 \frac{A_e}{d_s} \tag{2-21}$$

A polycrystalline material will present a microstructure dependent impedance response. A simple brick-layer model might be used, under certain assumptions, to simulate the differentiated contribution of grain bulk and grain boundaries (GBs) [20], [21]. For each contribution, the product of R and C gives the time constant, τ, (eq. 2-22) and, at the frequency of maximum loss (ω_{max}), eq. 2-23 is valid. Different contributions (bulk and GB) will show dissimilar τ [20].

$$\tau = RC \tag{2-22}$$

$$\omega_{max} RC = 1 \tag{2-23}$$

IS data is typically shown in a Nyquist (or Cole-Cole) plot, in which imaginary impedance Z'' (capacitive) is represented over real impedance Z' (resistive) these being normalized to the specimen dimensions or not. Each RC element (grains, GBs, electrode, others), will give rise to a semicircle in such representation. Alternative formalism of data presentation may be used to assess additional information. An example is the calculation of complex electric modulus, M*, as follows in eq. 2-24, with C_0 being defined in 2-25 [20].

$$M^* = i\omega C_0 Z^* \tag{2-24}$$

$$C_0 = \frac{\varepsilon_0 A_e}{d_s} \tag{2-25}$$

Polarization – P-E loops

The polarization behaviour of ferroelectrics was previously described in section 1.3. To determine the polarization of sintered ceramics as a function of AC electric field at room temperature, a ferroelectric analyser (*aixACCT, TF Analyzer 2000*) was used. Previously to the analysis, Pt electrodes were painted, and heat treated (900 ºC, 1 h) as previously described for dielectric measurements.

Piezoelectric coefficient – d_{33}

Similarly, piezoelectric effect was also described in section 1.3. The longitudinal piezoelectric coefficient (d_{33}) of ceramics was measured in specimens with Pt electrodes (900 ºC, 1h heat tretatment), after a Corona poling step at 70 ºC for 15 min under 10 kV potential, followed by an additional 15 min step, at 65 ºC, under 12.5 kV. A Berlincourt-type piezoelectric meter (*Sinocera YE 2730A*) with force frequency of 110 Hz and amplitude of 0.25 N was used. Several measurements were done on the same ceramics, and different ceramics were used to determine an average d_{33} value and the respective standard deviation.

References

[1] Termolab - High Temperature Technology, “Dilatometer prototipe,” 2018.

[2] W. L. Bragg. “The diffraction of short electromagnetic Waves by a Crystal”. Scientia, vol. 23, p. 153, 1929.

[3] M. De Graef, M. E. McHenry, and V. Keppens. “Structure of materials: An introduction to crystallography, diffraction, and symmetry”. The Journal of the Acoustical Society of America, vol. 124, no. 3. p. 1385, 2008.

[4] M. E. Fitzpatrick, A. T. Fry, P. Holdway, F. A. Kandil, J. Shackleton, and L. Suominen. “Determination of Residual Stresses by X-ray Diffraction - Issue 2” in Measurement Good Practice Guide, no. 52, Crown, Ed. United Kingdom: NPL, 2005.

[5] B. D. Cullity. Elements of X-ray diffraction, Second. 1978.

[6] J. R. Ferraro, K. Nakamoto, and C. W. Brown. Introductory Raman spectroscopy. Academic Press, 2003.

[7] G. Nageswaran, Y. S. Choudhary, and S. Jagannathan. “Inductively Coupled Plasma Mass Spectrometry” in Spectroscopic Methods for Nanomaterials Characterization, Elsevier, 2017, pp. 163–194.

[8] W. D. Callister Jr. and D. G. Rethwisch. Materials Science and Engineering: an Introduction. Eighth edition, Wiley, 2009.

[9] M. F. Chisholm. Scanning Microscopy for Nanotechnology. 2006.

[10] D. B. Williams and C. B. Carter. Transmission Electron Microscopy: A Textbook for Materials Science. Springer Science Business Media, 2009.

[11] H. Giesche. “Mercury Porosimetry: A General (Practical) Overview”. Part. Syst. Charact., vol. 23, no. 1, pp. 9–19, Jun. 2006.

[12] Henk G. Merkus. Particle Size Measurements, vol. 17. Dordrecht: Springer Netherlands, 2009.

[13] R. M. A. Roque-Malherbe. “Adsortion and Diffusion in Nanoporous Materials”. CRC Press New York, pp. 79–105, 2007.

[14] J. Wang and R. Raj. “Estimate of the Activation Energies for Boundary Diffusion from Rate-Controlled Sintering of Pure Alumina, and Alumina Doped with Zirconia or Titania”. J. Am. Ceram. Soc., vol. 73, no. 5, pp. 1172–1175, 1990.

[15] K. Ren, Q. Wang, Y. Lian, and Y. Wang. “Densification kinetics of flash sintered 3mol% Y_2O_3 stabilized zirconia”. J. Alloys Compd., vol. 747, pp. 1073–1077, 2018.

[16] M. A. Rafiq, M. E. Costa, A. Tkach, and P. M. Vilarinho. “Impedance analysis and conduction mechanisms of lead free potassium sodium niobate (KNN) single crystals and polycrystals: A comparison study”. Cryst. Growth Des., vol. 15, no. 3, pp. 1289–1294, 2015.

[17] R. Waser. Ceramic Materials for Electronics; Processing, Properties, and Applications. Second edition John Wiley & Sons, Ltd, 1992.

[18] “Agilent Basics of Measuring the Dielectric Properties of Materials.”

[19] E. Barsoukov and J. Macdonald, Impedance spectroscopy: theory, experiment, and applications. Second edition, Wiley. 2005

[20] A. West, J. Irvine, and D. Sinclair. “Electroceramics: Characterization by Impedance Spectroscopy”. Adv. Mater., vol. 2, no. 3, pp. 132–138, 1990.

[21] J. Fleig and J. Maier. “The impedance of ceramics with highly resistive grain boundaries: Validity and limits of the brick layer model”. J. Eur. Ceram. Soc., vol. 19, pp. 693–696, 1999.

Chapter

3. Simulation as a tool for the comprehension of FLASH sintering

Contents

Preamble

Chapter 3 begins the presentation of results obtained in the present work. As referred before in section 1.2.4, simulation tools have acquired interest in the field of sintering, either at the atomic level (molecular dynamics) or at the macroscopic level (using Finite Element Modelling (FEM)-based tools for temperature distribution). The theoretical and time dependent description of an out of equilibrium, extremely fast process as FLASH sintering, is of major interest for the understanding of the mechanisms.

Our models are based on experimental observations and experimentally measured materials' properties. Whereas all the details on the materials and process features are given in each article of this chapter, the reader will find the link between those and FLASH sintering studies in the following chapters.

This chapter is divided in two contributions, each with its introduction/motivation, experimental section, results, conclusions, and references. In specific, the modelling and simulation of the particle contact influence on the distribution of current density and Joule heating (3.1) and the relationship between the macroscopic simulated thermal gradients and the local stresses identified in FLASH sintered ceramics (3.2) are presented.

There are punctual simulation contributions in other parts of this thesis that are not presented in this chapter. This occurs because they were used to demonstrate or explain specific experimental observations, therefore, they are shown and discussed in each correspondent article of chapters 4 to 7.

The development of these simulations would not be possible without the collaboration between University of Aveiro and University of Sheffield, personified by Dr. Julian S. Dean and Prof. Ian M. Reaney.

3.1. Article: Modelling the particle contact influence on the Joule heating and temperature distribution during FLASH sintering

Published: https://doi.org/10.1016/j.jeurceramsoc.2019.12.015

Abstract

FLASH sintering is a field-assisted technique that allows the densification of ceramics in a few seconds at temperatures significantly lower than those of conventional cycles. There is still discussion among the scientific community about the mechanism behind this sintering process, that has been typically attributed to Joule heating, defect creation and movement or liquid phase assisted sintering. Computational modelling can be a powerful tool in helping to explain and predict this process. Using potassium sodium niobate (KNN) as a case study, a lead-free piezoelectric, this work explores Finite Element Modelling to evaluate the dependence of Joule heating generation and temperature distribution as a function of the cubic particle orientation.

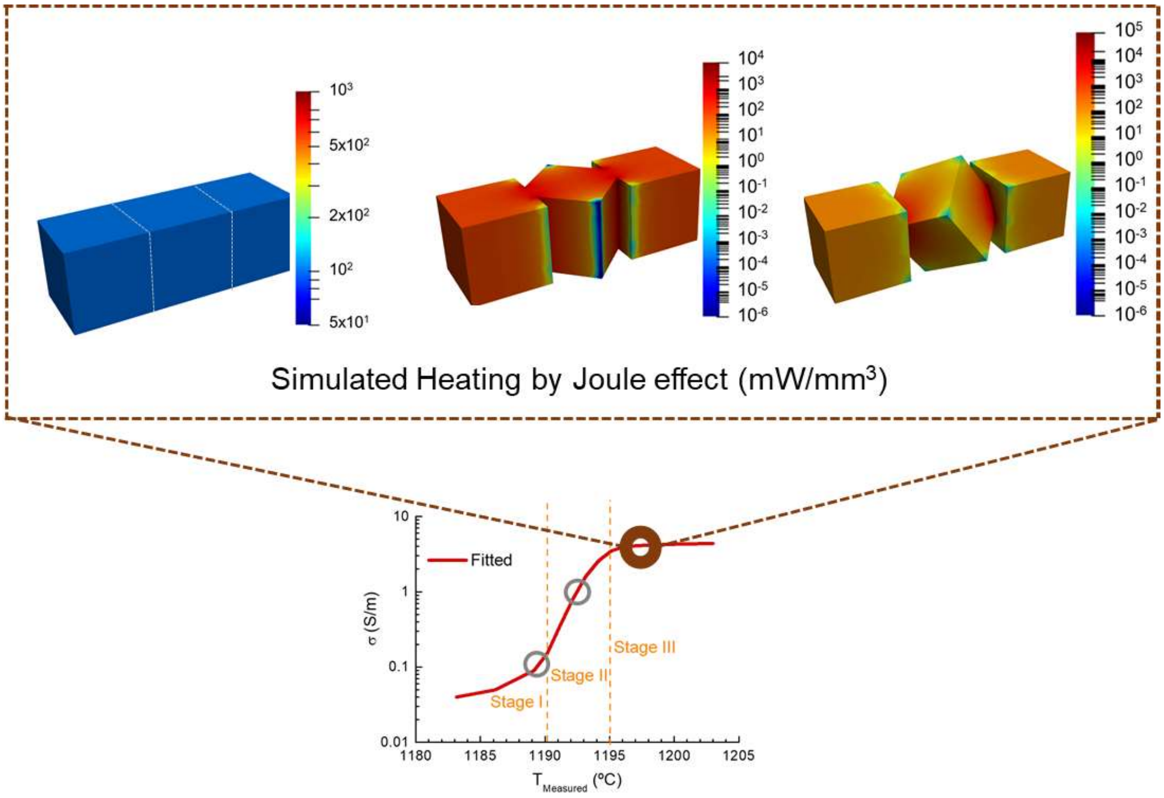

Key words

Finite element modelling; FLASH sintering; Joule heating; Microstructure property relationships

3.1.1. Introduction

Sintering is a well-established technique to consolidate powders using high temperatures. Among all know techniques, FLASH sintering provides rapid densification of particulate materials through the combination of external and Joule heating, the latter generated by relatively low current densities, J, as result of an applied electric field (E) directly within the specimen. This process does not require pressure, specific atmospheres or specialised dies. Thus, FLASH sintering has the potential to be a cost-effective, energy-efficient technique for densifying ceramics [1]. FLASH sintering was first reported for graphite powders by Lewis *et al.* [2] and more recently exploited by M. Cologna and co-workers to sinter oxides, such as yttria-stabilized zirconia, YSZ. Densification in less than 60s was reported with a temperature reduction of ~ 600 ºC, compared with conventional sintering [3]. The FLASH technique has been used to densify a wide variety of materials with YSZ one of the most studied systems. Simple oxides and carbides, such as alumina, zirconia, titania or silicon carbide have also been studied with further published work on ternary compounds such as strontium titanate or niobate systems [4]–[8].

When FLASH occurs, the material undergoes changes observable through two events; the so-called FLASH signatures that consist of a sudden shrinkage and a non-linear increase in conductivity. This is followed by an increase in the power dissipated by the system under current limit [9]. Without this current limit, the specimen would drawn too much current and melt instead of densifying. This allows an abrupt shrinkage at furnace temperatures significantly lower than those of conventional sintering. Typically, the sintering temperature is decreased as the magnitude of the applied field increases [10].

During a constant heating rate FLASH experiment, three distinct stages can be identified: stage I, incubation, in which an electric field is applied, with no significant current draw; stage II, FLASH event, when the current drawn increases non-linearly with the furnace temperature and a spike in dissipated power is registered; stage III, steady state, where current is limited and held constant while the material undergoes the remaining shrinkage towards full densification [10], [11]. Such an out-of-equilibrium phenomenon is complex, but two main theories have been proposed [4], [9], [10]. Thermal runaway through Joule heating is one of the widest accepted theories. In this proposed mechanism, the rate of generated Joule heat is higher than heat dissipation, inducing a very fast increase in temperature during stages II and III of FLASH and therefore responsible for the abrupt densification [12]–[15]. Liquid phase formation and viscous flow has also been associated to Joule heating effects. The formation of a liquid phase upon grain boundaries and small particle melting suggests the existence of thermal gradients between particle surfaces and cores [16]–[19].

Despite good agreement with the onset criterion for FLASH, thermal runaway does not explain the increase in specimen conductivity nor the light emission from the materials upon FLASH [10]. Defect generation and movement induced by the relatively high electric fields have been shown to have a high influence in FLASH sintering, namely in semi-conductors and ionic conductors [20]–[23]. However, work by Biesuz and Sglavo [10] and Cologna *et al.* [24] concluded that the neck growth rate of 3YSZ is unaffected when the samples are subject to electric fields similar to those used in FLASH, i.e., the electric field by itself has no influence on particle welding and surface diffusion. In accordance with Biesuz, FLASH should be considered as a current- rather than field- (voltage) assisted sintering process [10].

Several mathematical models have been shown to explain a specific stage or phenomena of FLASH. For example, the thermal runaway model for describing the onset condition for the uncontrolled heating process, triggering FLASH sintering, was independently developed by Todd *et al.* [14] and Zhang *et al.* [15] in 2015. Furthermore, the black body radiation (BBR) model has been largely used to estimate specimen temperature. Grasso *et al.* [25] have shown through the use of computational modelling, that the macroscopic temperature distribution in a YSZ dog-bone shape is uniform within the gauge section but heterogeneous in the electrode contacting areas. In contrast with Grasso's work, M. Yoshida and co-workers found that dog-bone-like specimens present a non-homogeneous macroscopic distribution of current density, power dissipation and temperature during stage III of FLASH [26].

Our previous work using Finite Element Modelling (FEM) to map out the Joule heating distribution in cubic particles upon FLASH has shown that the heat generation magnitude is dependent on the contact area and geometry. As the contact area becomes smaller, the Joule heating is higher and more localized. Such observations suggested that a temperature non-uniformity between particle surface (contacts) and core is created [27].

Potassium sodium niobate, ($K_{0.5}Na_{0.5}NbO_3$, KNN) is a lead-free piezoelectric potentially suggested as a replacement for the market-leader, lead zirconate titanate in piezoelectric applications [28], [29]. KNN possesses a cuboid particle shape, that influences its densification; important in FLASH since surface phenomena are critical [30]. KNN was previously FLASH sintered at 900 ºC to 94 % of its theoretical density and it was shown that the densification mechanism was related to the formation of core-shell structures with non-homogeneous distribution of alkali Na and K [7].

However, no studies on the local Joule heating effect, nor thermal gradient were presented. Until now, the local temperature distribution as a function of Joule heating during FLASH sintering has not been studied. Furthermore, the modelling of FLASH process through the three stages has not been presented. In this work, we used *COMSOL Multiphysics* [31] to set up a time dependent modelling procedure to simulate the evolution of the FLASH process in a given microstructure.

3.1.2. Experimental

Powder production and processing

KNN powders were produced by a conventional solid-state route as previously reported [32]. Ultra-high purity alkali carbonates and niobium oxide (99.99 %) were used, and the precursors ball milled in ethanol. Calcination was performed at 900 ºC for 3 h. KNN was ball milled 24 h after calcination, and uniaxially and isostatically pressed (130 and 250 MPa, respectively) into ca. 15 x 5 x 2 mm pellets.

Pellets were FLASH sintered, and the DC electrical conductivity measured throughout the process to provide experimental inputs for the finite element model. The conductivity of green pellets (relative density, ρ_{green} = 65±3 %) was measured using an alumina sample holder and platinum contact sheet electrodes, at a constant heating rate of 10 K/min, with an electric field of 300 V/cm and current limited to 20 mA/mm^2. Densities > 90% were obtained after FLASH sintering for 60 s. Specimen displacement, current and voltage were recorded during FLASH experiments, and the respective relative length variation, conductivity and power dissipation were calculated and are shown, as a function of the measured furnace temperature, in Figure 3.1-1 a). The temperature was measured with a thermocouple, placed within a distance of 5 to 7 mm from the specimen. Figure 3.1-1 b) shows a magnification of a), overlaid with the fitted conductivity. The three distinct FLASH stages are identified, consistent with previous work [10].

Figure 3.1-2 shows the microstructure of a green KNN specimen heated at 900 ºC (1173.15 K) for 30 min, with no electric field applied. The cuboid particle shape, characteristic of KNN, induces anisotropy in the contact between particles. This provides a qualitative structure of packed cuboid grains that will be replicated in the FEM model. To simplify the model, the cuboid particles were considered to contact through flat surfaces, edges or vertexes. Also, as shown in Figure 3.1-2, the particle size of pre-FLASH ceramic is typically < 3 μm; most particles are micron-sized, with a few small particles, 0.2 to 0.5 μm.

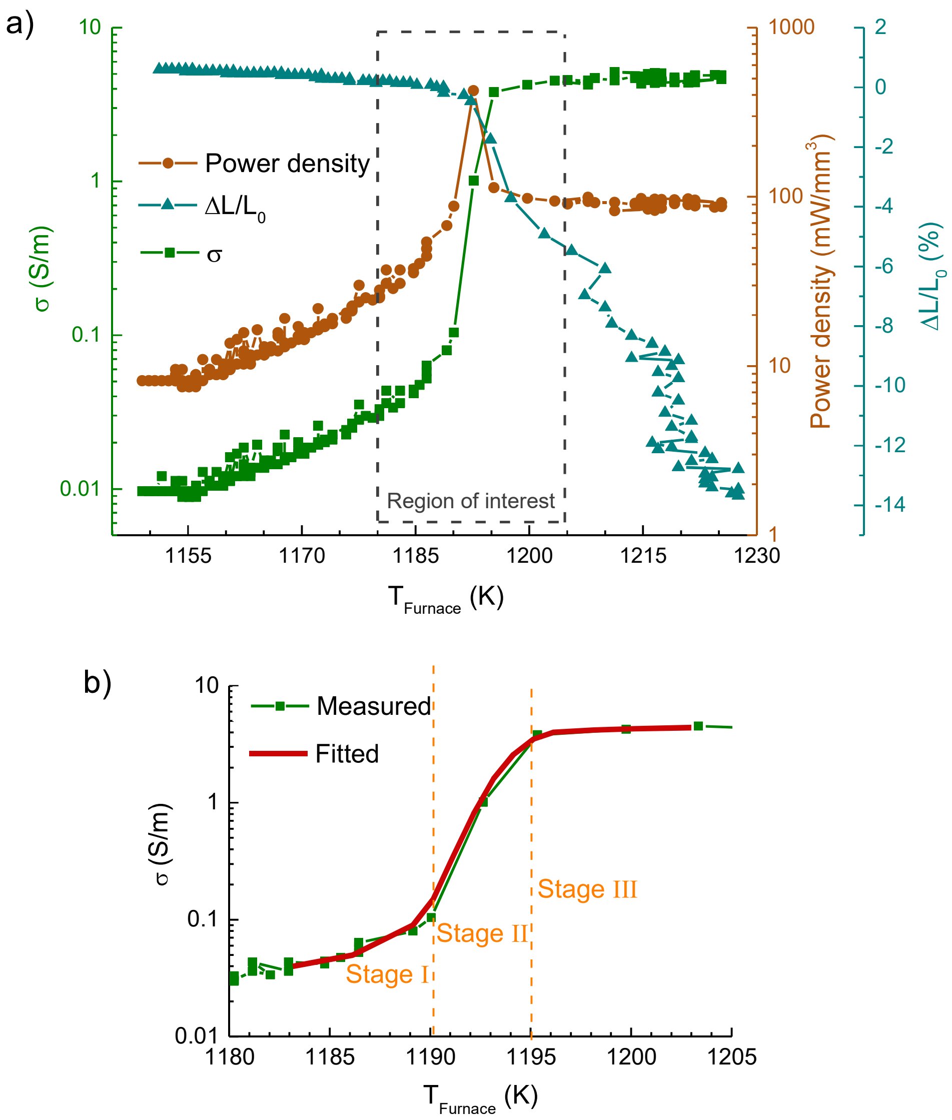

Figure 3.1-1 - a) Measured relative displacement (light blue, ▲), conductivity (green, ■) and power dissipation (brown, ●) dependence with measured temperature ($T_{Furnace}$), for KNN under 300 V/cm and 20 mA/mm^2 current limit; the experimental time interval between each acquired point is 1 s. b) magnification of a), with measured (green) and fitted (red) conductivity dependence with measured temperature ($T_{Furnace}$); the three stages of FLASH are identified and separated by orange dashed lines.

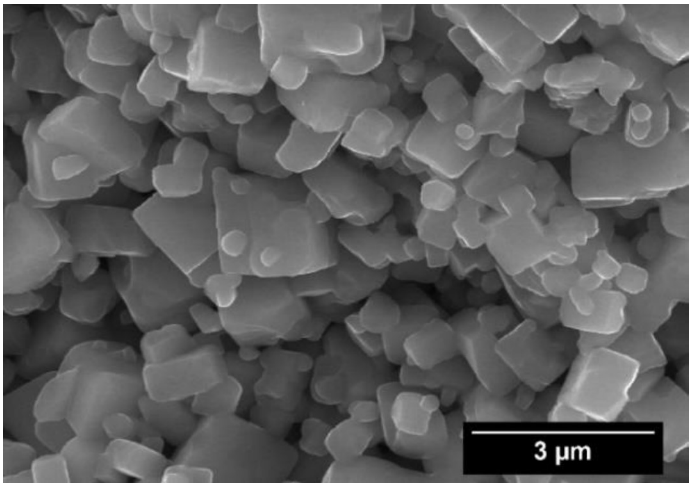

Figure 3.1-2 – SEM micrograph of green KNN body, heated at 1173 K for 30 min, showing the pre-FLASH microstructure that is implemented in the model.

Modelling

The local Joule heating and temperature distribution within the particle as a function of time were simulated in *COMSOL Multiphysics* models [31]. This included a thermal dependence change in the conductivity of KNN during the FLASH sintering process.

To mimic the experimental process and observe the effect of the microstructure, a range of different particle orientation were generated. A potential difference of 9×10^{-5} V (in the case of face contacts) was applied across the longitudinal surfaces of the system (Figure 3.1-3 shows the schematic representation of DC voltage application). This voltage was calculated for each particle arrangement by scaling the 300 V/cm applied field.

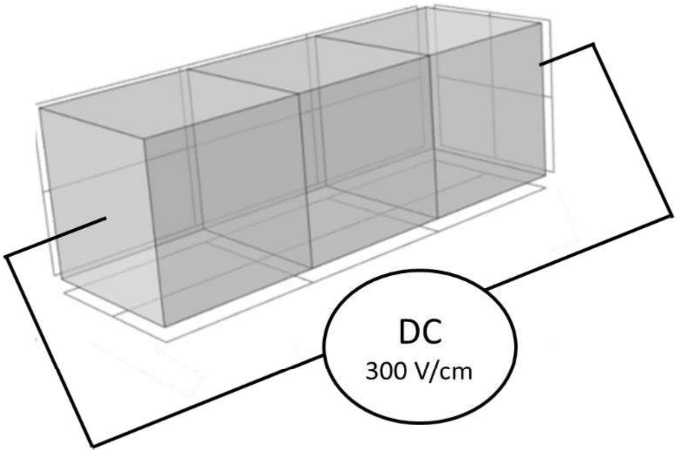

Figure 3.1-3 – Representation of DC voltage application onto particle arrangements. Example for face contacting cuboids.

During stage I and stage II, where no current limit is imposed, the current density in the sample constantly increases as result of the increase in the electrical conductivity with temperature. In stage III the voltage rises until the current density reaches the nominal 20 mA/mm^2. At this point, the model becomes current controlled. Such control allows the model to accurately represent the three stages of FLASH as a function of the experimentally measured temperature.

To describe the electric field and current control during the 3 stages of FLASH sintering by FEM, the electric potential was applied to the different arrangement of particles through the use of a *terminal* function. The end faces (Figure 3.1-3) were assigned to be either *terminal* or *ground*, while all the other surfaces were assigned with *electric insulation*. The *terminal* was associated with g*lobal equation* functions, responsible during stage I and II in limiting and recording the current. This allows the model to maintain a 300 V/cm electric field. During stage III, the *terminal is set to* control the current to the pre-set value of 20 mA/mm^2, limiting the applied potential. After stage II, a relevant shrinkage starts to occur on the specimen (Figure 3.1-1). To reflect this observation, COMSOL models were assigned a linear shrinkage of 4%. For simplification, the shrinkage was considered to occur only at the middle particle. For edge and vertex contact cases, a respective increase of contact area was considered.

A *Thermal insulation* boundary condition was considered to all the faces, with no further radiation nor convection heat transfer concern. Such approximation should not compromise the validity of the simulations, as this meso-scale model is intended to simulate only the Joule heating and local temperature distribution in μm-sized particles. For the description of the complete FLASH curve (Figure 3.1-1), the fitted conductivity curve was integrated into small temperature steps, typically of 1 K. The starting temperature was 913 ºC (1186.15 K) and the particles assigned to the KNN properties (σ = 0.05 S/m, Figure 3.1-1) for that specific condition. The model was run and halted when the next integrated temperature was reached (in this case, when T = 1187.15 K). The Joule heating and temperature distributions were recorded, and the particles electrical conductivity updated for the next temperature to be considered. This was then repeated to describe all experimental points in the conductivity curve. Two outputs are used to study the FLASH process: (i) the total power dissipation density, considered as Joule heating, and temperature distribution at the end of each integration step; (ii) the modelled time interval between each integration step. For each integration step, the reference temperature in the model was updated. A representation of the integration steps for stage II is shown in Figure 3.1-4.

Due to the speed of the process, and to simplify the model, we assume that there is no heat dissipation from the particles to the surrounding environment. It is thus expected that the modelled integration time, i.e., the small integration steps, will be less than that measured experimentally, which is ca. 3 s between beginning and end of stage II, and ca. 10 - 15 s for the all interest region, from 1180 to 1205 K (Figure 3.1-1). Grain boundaries were not considered in this simple model. The properties of such structures, namely, their conductivity and size, are yet being studied and core-shell structures might describe more precisely the system. Furthermore, thermal conductivity and specific heat capacity of bulk KNN were considered constant and set as 2.6 W/(m.K) and 800 J/(kg.K), respectively.

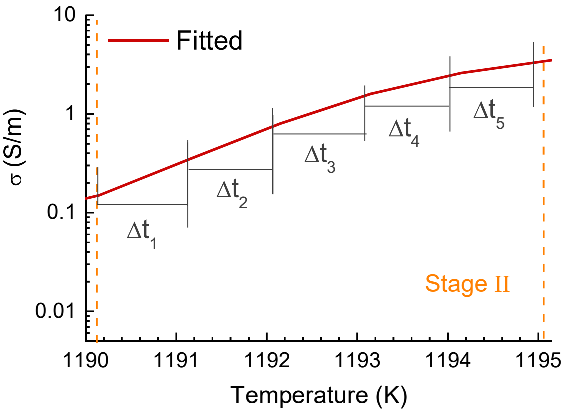

Figure 3.1-4 – Integration steps demonstration for stage II of FLASH. This is a magnification for the fitted conductivity curve of Figure 3.1-1b) during stage II.

3.1.3. Results and discussion

Three cubic particles, of 1 μm length, were described in the model and placed in a series arrangement. The three possible orientations, resulting in face/face, face/edge and face/vertex type contacts are shown in Figure 3.1-5.

Electric field, current density, and Joule heating (or total power dissipation density) were simulated using the process described above. The results for face/face contacts are shown in supplementary information (SI) Figure SI-3.1-1 a), b) and c), respectively. The three stages of FLASH, the latter part of stage I, stage II and stage III are shown in vertical order. The respective conductivity vs. temperature dependence and the points being simulated are highlight in supplementary information (SI) Figure SI-3.1-1 d). Results show good agreement with experimental conditions (electric field of 300 V/cm and current limit of 20 mA/mm^2). During stage II, the current density is slightly increased over the limit placed on the value. This agrees well with experimentally data obtained (Figure 3.1-1 (a)) and published [9], [10], that shows a power spike upon FLASH onset during stage II. Such particle configuration should not generate disorder or anisotropy in the electric field generation and current flow, due to the lack of geometry disorder (as sharp contact or edges, for instance); thus, it is suitable for validating this approach.

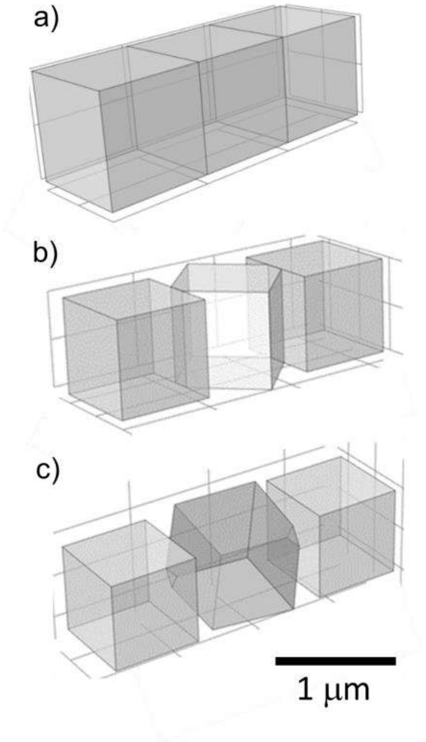

Figure 3.1-5 – Representation of “in-series” cubes contacting with a) faces, b) face/edge and c) face/vertex, respectively from left to right.

As shown in the supplementary information (SI) Figure SI-3.1-1, for models where the three particles are in face/face contact, a uniform distribution of Joule heating is generated. With no discontinuities in either shape or properties, or grain boundaries present, the system behaves as one single block. The maximum dissipated power can be seen to be generated during stage II, in accordance with the maximum current density.

Joule heating distributions for face/edge and face/vertex particle configuration for the three stages of FLASH are shown in Figure 3.1-6 (a) and (b), respectively and behave differently. Figure 3.1-6 (c) highlights the corresponding FLASH stages, with the conductivity fitted curve overlaid with grey circles. For the edge contact (Figure 3.1-6 (a)), non-uniform Joule heating distributions were generated, directly related to the contact area. In the sharp contact edge, Joule heating is, typically, three orders of magnitude higher than in the “far-from-contact” areas. Further increase was determined as the contact area decreases, as is the case of the face/vertex configuration (Figure 3.1-6 (b)). Furthermore, cross-sectional plane views are represented for late stage I for both edge and vertex geometry and show that Joule heating distribution on the surface of the particles is similar to that of grain cores, revealing again the Joule heating concentration on the particle-particle contact areas.

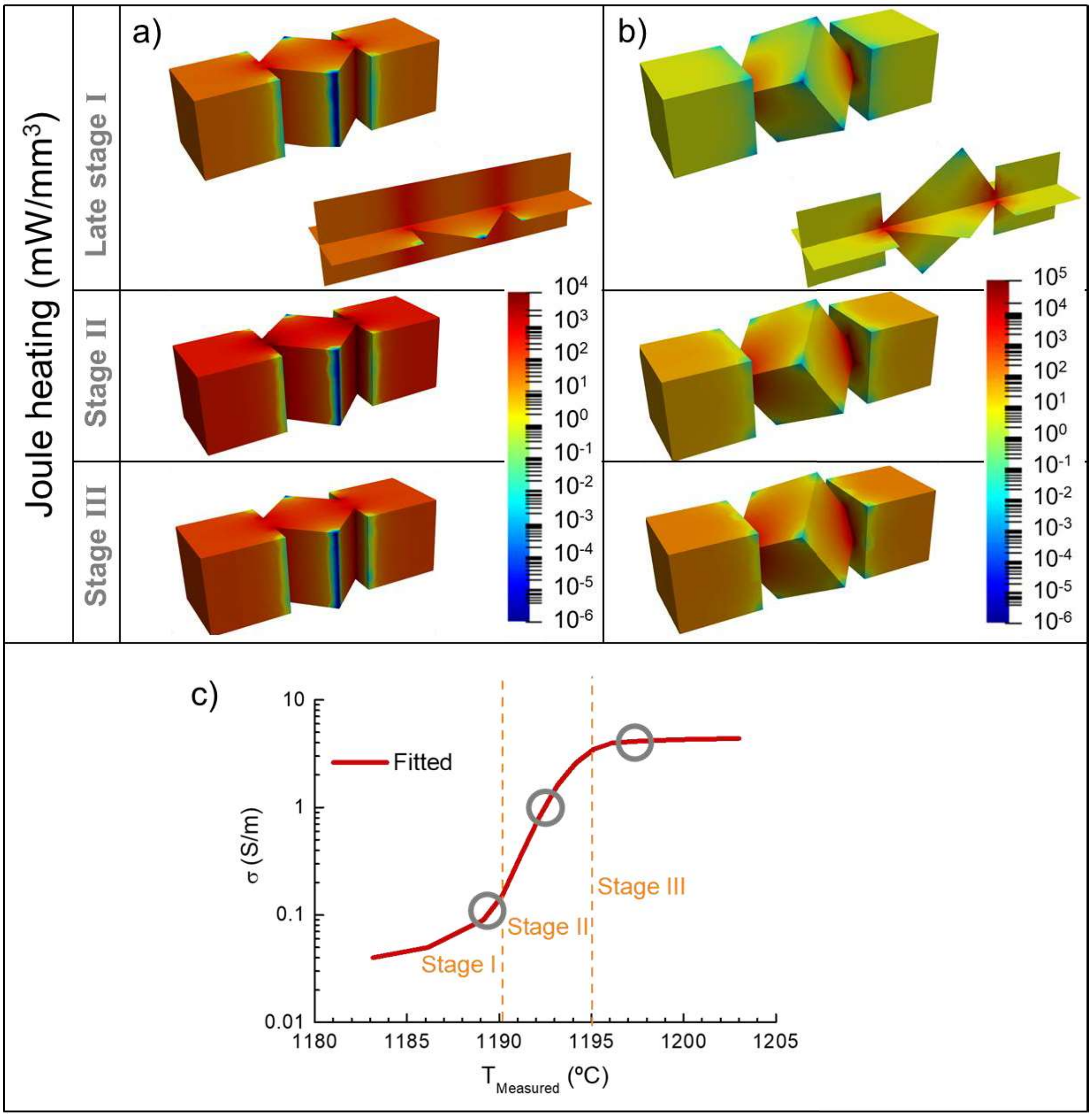

Figure 3.1-6 – Joule heating distribution (in mW/mm^3) for sharp contact arrange of particles: a) face/edge and b) face/vertex. Three snapshots of the FLASH process are shown, corresponding to late stage I, stage II and stage III. A section view for late stage I case is also shown, for clarification. c) represents the corresponding stages with the conductivity fitted curve overlaid with grey circles.

Overall electric power simulations of stage III, shown in Figure SI-3.1-2, for both geometries do not show any gradients. The total power is found to be between 0.9 and $2x10^{-18}$ W and not concentrated on the particle contacts, because this is a volume independent variable. These simulated power values may seem low, however for a net power of $1x10^{-18}$ on a volume of 1 μm^3 would result in a power density of 1 W/m^3 (or $1x10^{-6}$ mW/mm^3), which relates well with the low Joule heating dissipation areas on the previously discussed Figure 3.1-6 a) and b). The overall particle surfaces (except the contacting ones) of face and vertex contacts presented, respectively, a light red and light orange colour in Joule heating representations. These colours represent a power dissipation (or Joule heating) of ca. 100 mW/mm^3 which relates very well with experimental observations (Figure 3.1-1 a)).

The proposed model suggests that the maximum Joule heating increases two orders of magnitude from face/face contact compared to face/vertex. As the contact area is decreased and made sharper, the Joule heating intensity increases due to the increased local current density. Interestingly, the higher values of Joule heating are typically observed for stage II of FLASH, specifically in face/face case, in which no contact shape influence is expected. Such observation explains the experimentally measured fast increase in temperature during stage II of FLASH sintering.

The temperature distribution for cubes with face/edge (a) and face/vertex (b) contacts for late stage I in the simulated FLASH process can be seen in Figure SI-3.1-3 and do not show any thermal gradients, with similar results for stage II and III.

Following the work presented by W. Ji and co-workers [33], thermal diffusivity of KNN, α_d, was calculated under the conditions of our model: $\alpha_d = 7.2x10^{-7}$ m^2/s. The respective time for thermal equilibrium is defined as D^2/α_d, where D is the distance. For D = 1 μm (micron-sized particles), equilibrium time is equal to $1.4x10^{-6}$ s. Such micro-scale time for temperature equilibrium did not allow to observe any thermal gradient on the integration approximation of our simulations. On the other hand, when simulation integration time is changed to 0.5 μs (graphical results not shown), thermal gradients were only observable on the 5th decimal place of temperature scale.

This suggests that when 1 µm side cubes (1 x 1 x 1 μm^3) KNN particles are considered in the defined conditions, there are no significant thermal gradients between grains, since they are suppressed by the heat dissipation from surface to core. The lack of radiation and thermal dissipation from the particles towards the environment may contribute to the unexpected homogeneous temperature distribution, because diffusive effects would decrease particle surface temperature and increase the temperature difference between the heat source (particle contacts) and surfaces. On the other hand, the exclusion of grain boundaries from the model or defect formation and movement contributions may also explain the absence of observable temperature gradients between particle contact zones and the core.

Despite the lack of thermal gradients observation on the simulated scenarios, liquid phase formation on grain boundaries of FLASH sintering ceramics has been observed [18], [27], [34], [35]. A plausible explanation for such observations is that the fast heating upon grain boundaries allows the formation of low melting point phases that contribute for grain boundary amorphization and particle sliding, as previously proposed [27].

Despite the recognize limitation of the model, the suggested absence of temperature gradients might also be directly related with the speed of heat dissipation from contacts to particle cores. The simulated time of each integration step was determined by the model. In each condition, the theoretical/simulated time between integration step *n* and *n+1* was determined. The simulations were run for each particle contact scenario and results of cumulative time evolution are represented in Figure 3.1-7. Each point of the curve represents an integration step. Note that the total FLASH time between the beginning of stage I and beginning of stage III (region of interest in Figure 3.1-1 (a)) was measured experimentally to be 10 to 15 s.

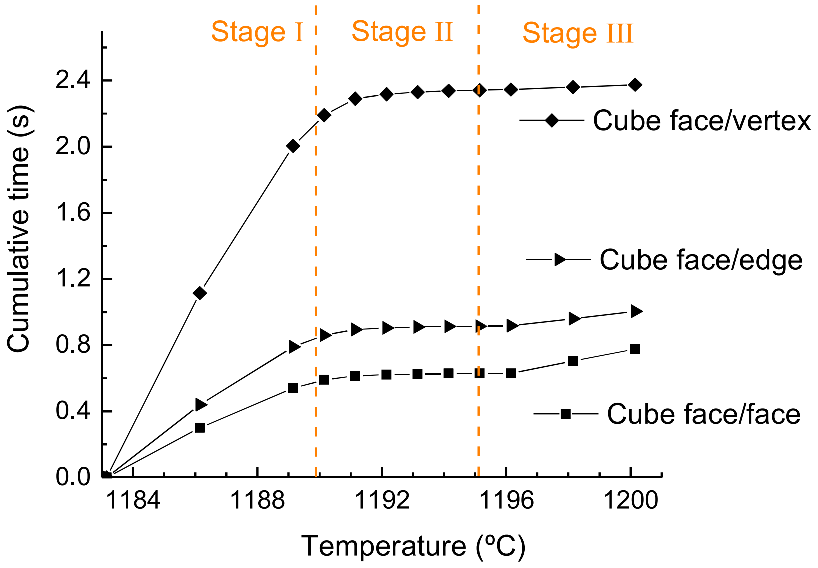

Figure 3.1-7 – Cumulative time needed to reach the correspondent temperature for cubes with face contacts (squares) face/edge (triangles) and face/vertex (diamond).

From Figure 3.1-7 we conclude that:

(i) Regardless of the particle contact area and type, the time extracted from the model is lower than that observed experimentally during FLASH process, potentially because heat dissipation by the specimen is not considered in the model. However, the simulated times are comparable.

(ii) For stage I, the sharper the contact area, the slower the heating process by Joule heating. Despite the higher recorded local current density for sharper contacts (Figure 3.1-6), the Joule heating requires more time to dissipate through the particles (not to the environment). This observation can further explain non-uniformity in specimen densification by FLASH sintering [36].

(iii) During stage II, the time evolution behaviour is independent of the contact type. There is a significant increase in temperature, as the cumulative time dependence has an almost zero gradient. This is consistent with experimental observations during stage II of FLASH process.

(iv) For stage III, the vertex configuration maintains an almost zero gradient. As such, we find configurations with blunter contacts (e.g., edge or faces as opposed to vertexes) heat up more slowly due to current limiting conditions in this stage.

The proposed model and observations suggest that the process can be summarised as the following:

(i) At stage I there is a homogeneous heat generation which spreads from the contact region to the surrounding particles.

(ii) During stage II, the high thermal gradients and localized heat in the contact region explain the non-linear behaviour of specimen temperature, conductivity and significant thermal runaway that are typical of stage II.

(iii) Despite the significant non-uniform Joule heating generation, we find that, in the conditions of this model, micron-sized particles dissipate all the generated heat at a higher rate than that necessary to register relevant thermal gradients.

Although negligible thermal gradients are observed, we note that this model does not account for grain boundary behaviour nor defect movement nor even thermal dissipation through the environment. In these conditions, the proposed simulations allow the conclusion that thermal gradients from Joule heating generation should not be observed during FLASH sintering.

However, previously reported observations and theoretical descriptions of amorphized grain boundaries in FLASH sintered ceramics and liquid phase formation during FLASH [18], [27], [34], [35] suggest, at least, two possibilities: (i) significant thermal gradients are formed during FLASH sintering and/or (ii) compositional changes arising from current flow promote low melting point phase formation and their preferential melting without significant temperature gradients between particles and grain boundaries. The proposed model aimed to depict the first hypothesis; however, results show that, in the conditions of the simulations, micron-sized particles dissipate the possible heat gradients at a rate, too fast to identify in this model.

Further modelling work is now being developed to describe grain boundaries as shells covering the bulk core of ceramics, and their influence on temperature gradients. Moreover, low melting point phases are being considered at the grain boundaries.

3.1.4. Conclusions

In this work we show that the proposed Finite Element Model describe FLASH sintering experiments with particle orientation dependences. Despite the significant Joule heating and non-uniform distribution found for sharp edges contacts, no relevant thermal gradients between particle surfaces and cores are found. We conclude that if differences in grain boundary electrical conduction in respect to the bulk and heat dissipation to the surrounding environment are neglected, Joule heating alone does not contribute to temperature gradients in micron-sized particles, even when very sharp contacts are considered. However, one important output of this model is that grain boundaries are mandatory to account for liquid phase formation at particle contacts during FLASH sintering. Further works should include the grain boundary description using, as for instance, core-shell structures. Moreover, models are now being developed to account for heat dissipation and radiation through the environment. Nevertheless, it was shown that simple modelling techniques as FEM can be useful to understand and depict the FLASH phenomena, isolating contributions of different events in the process.

3.1.5. Supplementary Information

Figure SI-3.1-1 a) to c) shows the simulated FLASH process for face/face contacted models. The conductivity change as a function of temperature for each of the stages is shown in Figure SI-3.1-1 d) with the specific stages that have been simulated highlight on the curve. A uniform distribution of Joule heating is generated through the systems. With no discontinuities in either shape or properties, or grain boundaries present, the system behaves as one single block. The maximum dissipated power can be seen to be generated during stage II, in accordance with the maximum current density.

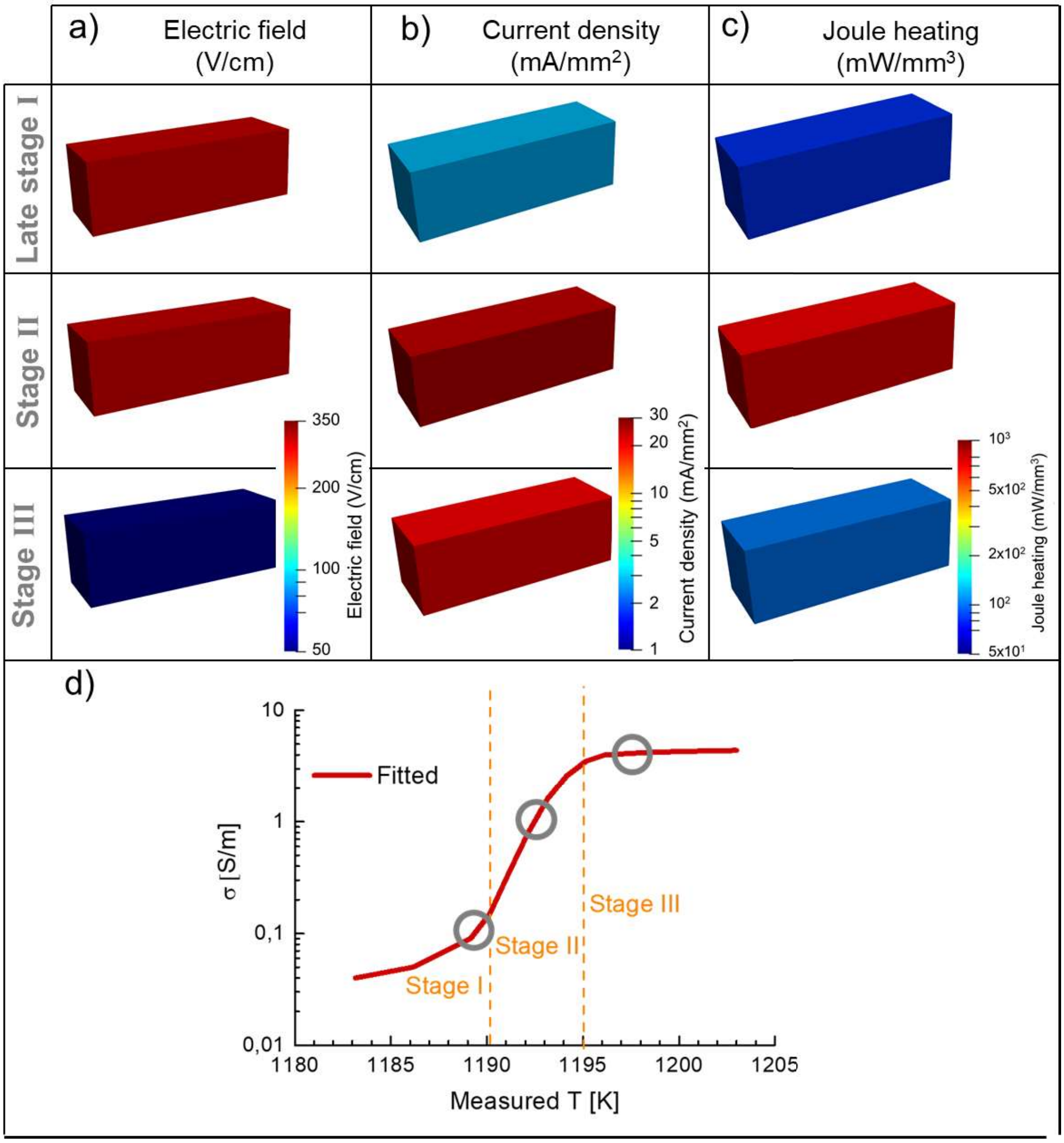

Figure SI-3.1-1 – a) Simulated electric field, b) current density and c) total power dissipation density (or Joule heating) for face/face contact particles. The respective conductivity over temperature curve is shown in d) to highlight the simulated steps over the curve.

The electric power simulations of stage III are shown in Figure SI-3.1-2, for both the face/edge and face/vertex models. While the total power is found to be between 0.9 and 2x10^{-18} W for the two geometries, no significant gradients are observed on the particle contacts

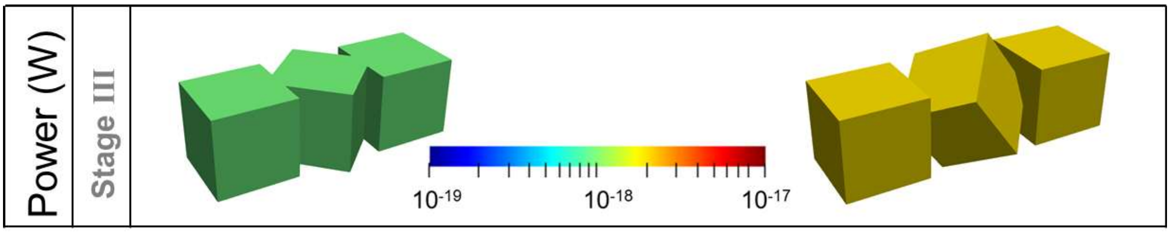

Figure SI-3.1-2 – a representation of total power for face/edge and face/vertex models. While the face/vertex shows higher power, no significant power gradients are observed.

Simulated temperature profiles are shown in Figure SI-3.1-3. It should be noted that the temperature scale is the same for both representation and that similar representations of temperature distributions were found for stage II and III which are not shown here.

The temperature distribution for face/face contacts can be seen to be homogeneous, as expected, consistent with the results from Figure SI-3.1-1. However, for sharp contacts, despite the tight scale used for temperature representation (a 0.80 K total variation) and contrary to expectation, the model does not show any thermal gradient for cubic particle contacts.

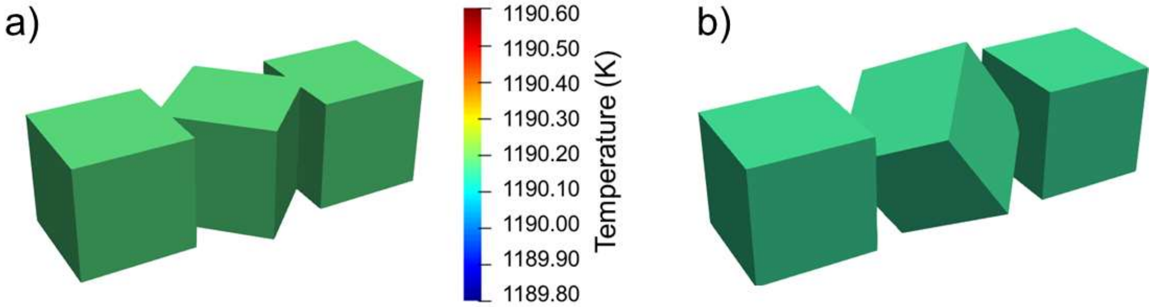

Figure SI-3.1-3 – Late stage I temperature representation (in K) for a) face/edge and b) face/vertex contacts. Temperature scale is the same for both.

3.1.6. References

[1] J. Luo. “The scientific questions and technological opportunities of flash sintering: From a case study of ZnO to other ceramics”. Scr. Mater., vol. 146, pp. 260–266, 2018.

[2] F. A. Lewis, J. Orr, and A. R. Ubbelohde. “Contact Effects resulting from Compression and Flash Sintering in Graphite Powders”. Proc. Phys. Soc. Sect. B, vol. 70, no. 10, pp. 928–936, 1957.

[3] M. Cologna, B. Rashkova, and R. Raj. “Flash Sintering of Nanograin Zirconia in <5 s at 850°C”. J. Am. Ceram. Soc., vol. 93, no. 11, pp. 3556–3559, 2010.

[4] M. Yu, S. Grasso, R. Mckinnon, T. Saunders, and M. J. M. Reece. “Review of flash sintering: materials, mechanisms and modelling”. Adv. Appl. Ceram., vol. 116, no. 1, pp. 1–37, 2017.

[5] L. A. Perez-Maqueda, E. Gil-Gonzalez, A. Perejon, J. M. Lebrun, P. E. Sanchez-Jimenez, and R. Raj. “Flash sintering of highly insulating nanostructured phase-pure $BiFeO_3$”. J. Am. Ceram. Soc., vol. 100, no. 8, pp. 3365–3369, 2017.

[6] N. Shomrat, S. Baltianski, C. A. Randall, and Y. Tsur. “Flash sintering of potassium-niobate”. J. Eur. Ceram. Soc., vol. 35, no. 7, pp. 2209–2213, 2014.

[7] G. Corapcioglu, M. A. Gulgun, K. Kisslinger, S. Sturm, S. K. Jha, and R. Raj. “Microstructure and microchemistry of flash sintered $K_{0.5}Na_{0.5}NbO_3$”. J. Ceram. Soc. Japan, vol. 124, no. 4, pp. 321–328, 2016.

[8] F. Lemke, W. Rheinheimer, and M. J. Hoffmann. “A comparison of power controlled flash sintering and conventional sintering of strontium titanate”. Scr. Mater., vol. 130, pp. 187–190, 2017.

[9] C. E. J. Dancer. “Flash sintering of ceramic materials”. Mater. Res. Express, vol. 3, no. 10, pp. 102001–102025, 2016.

[10] M. Biesuz and V. M. Sglavo. “Flash sintering of ceramics”. J. Eur. Ceram. Soc., vol. 39, no. 2–3, pp. 115–143, 2019.

[11] S. K. Jha, K. Terauds, J. Lebrun, and R. Raj. “Beyond flash sintering in 3 mol % yttria stabilized zirconia”. J. Ceram. Soc. Japan, vol. 124, no. 4, pp. 283–288, 2016.

[12] Y. Dong and I. W. Chen. “Onset Criterion for Flash Sintering”. J. Am. Ceram. Soc., vol. 98, no. 12, pp. 3624–3627, 2015.

[13] R. Raj. “Joule heating during flash-sintering”. J. Eur. Ceram. Soc., vol. 32, no. 10, pp. 2293–2301, 2012.

[14] R. I. Todd, E. Zapata-Solvas, R. S. Bonilla, T. Sneddon, and P. R. Wilshaw. “Electrical characteristics of flash sintering: Thermal runaway of Joule heating”. J. Eur. Ceram. Soc., vol. 35, no. 6, pp. 1865–1877, 2015.

[15] Y. Zhang, J. Il Jung, and J. Luo. “Thermal runaway, flash sintering and asymmetrical microstructural development of ZnO and $ZnO-Bi_2O_3$ under direct currents”. Acta Mater., vol. 94, pp. 87–100, 2015.

[16] R. Chaim and C. Estournès. “On thermal runaway and local endothermic/exothermic reactions during flash sintering of ceramic nanoparticles”. J. Mater. Sci., vol. 53, no. 9, pp. 6378–6389, 2018.

[17] R. Chaim and C. Estournès. “Effects of the fundamental oxide properties on the electric field-flash temperature during flash sintering”. Scr. Mater., vol. 163, pp. 130–132, 2019.

[18] R. Chaim. “On the kinetics of liquid-assisted densification during flash sintering of ceramic nanoparticles”. Scr. Mater., vol. 158, pp. 88–90, 2019.

[19] R. Chaim. “Liquid film capillary mechanism for densification of ceramic powders during flash sintering”. Materials, vol. 9, no. 4, pp. 19–21, 2016.

[20] A. R. Genreith-Schriever and R. A. De Souza. “Field-enhanced ion transport in solids: Reexamination with molecular dynamics simulations”. Phys. Rev. B, vol. 94, no. 22, p. 224304, 2016.

[21] S. K. R. S. Sankaranarayanan, E. Kaxiras, and S. Ramanathan. “Electric field tuning of oxygen stoichiometry at oxide surfaces: molecular dynamics simulations studies of zirconia”. Energy Environ. Sci., vol. 2, no. 11, p. 1196, 2009.

[22] M. Jongmanns, R. Raj, and D. E. Wolf. “Generation of Frenkel defects above the Debye temperature by proliferation of phonons near the Brillouin zone edge”. New J. Phys., vol. 20, no. 9, 2018.

[23] M. Schie, S. Menzel, J. Robertson, R. Waser, and R. A. De Souza. “Field-enhanced route to generating anti-Frenkel pairs in HfO_2”. Phys. Rev. Mater., vol. 2, no. 3, pp. 35002-1-35002–8, 2018.

[24] M. Cologna and R. Raj. “Surface diffusion-controlled neck growth kinetics in early stage sintering of zirconia, with and without applied DC electrical field”. J. Am. Ceram. Soc., vol. 94, no. 2, pp. 391–395, 2011.

[25] S. Grasso *et al.*. “Modeling of the temperature distribution of flash sintered zirconia”. J. Ceram. Soc. Japan, vol. 119, no. 1386, pp. 144–146, 2011.

[26] M. Yoshida, S. Falco, and R. I. Todd. “Measurement and modelling of electrical resistivity by four-terminal method during flash sintering of 3YSZ”. J. Ceram. Soc. Japan, vol. 126, no. 7, pp. 579–590, 2018.

[27] R. Serrazina, J. S. Dean, I. M. Reaney, L. Pereira, P. M. Vilarinho, and A. M. O. R. Senos. “Mechanism of densification in low-temperature FLASH sintered lead free Potassium Sodium Niobate (KNN) piezoelectrics”. J. Mater. Chem. C, vol. 7, pp. 14334–14341, 2019.

[28] C.-H. Hong *et al.*. “Lead-free piezoceramics and Where to move on?”. J Mater., vol. 2, pp. 1–24, 2016.

[29] X. Wang *et al.*. “Giant piezoelectricity in potassium-sodium niobate lead-free ceramics”. J. Am. Chem. Soc., vol. 136, no. 7, pp. 2905–2910, 2014.

[30] M. A. Rafiq, M. E. Costa, A. Tkach, and P. M. Vilarinho. “Impedance analysis and conduction mechanisms of lead free potassium sodium niobate (KNN) single crystals and polycrystals: A comparison study”. Cryst. Growth Des., vol. 15, no. 3, pp. 1289–1294, 2015.

[31] “COMSOL Multiphysics® Software - Understand, Predict, and Optimize.” [Online]. Available: https://www.comsol.com/comsol-multiphysics. [Accessed: 18-Jul-2019].

[32] M. A. Rafiq, A. Tkach, M. E. Costa, and P. M. Vilarinho. “Defects and charge transport in Mn-doped $K_{0.5}Na_{0.5}NbO_3$ ceramics”. Phys. Chem. Chem. Phys., vol. 17, no. 37, pp. 24403–24411, 2015.

[33] W. Ji, B. Parker, S. Falco, J. Y. Zhang, Z. Y. Fu, and R. I. Todd. “Ultra-fast firing: Effect of heating rate on sintering of 3YSZ, with and without an electric field”. J. Eur. Ceram. Soc., vol. 37, no. 6, pp. 2547–2551, 2017.

[34] J. Gonzalez-Julian and O. Guillon. “Effect of Electric Field/Current on Liquid Phase Sintering”. J. Am. Ceram. Soc., vol. 98, no. 7, pp. 2018–2027, 2015.

[35] R. Chaim and Y. Amouyal. “Liquid-Film Assisted Mechanism of Reactive Flash Sintering in Oxide Systems”. Materials, vol. 12, no. 1494, pp. 1–9, 2019.

[36] Y. Du, A. J. Stevenson, D. Vernat, M. Diaz, and D. Marinha. “Estimating Joule heating and ionic conductivity during flash sintering of 8YSZ”. J. Eur. Ceram. Soc., vol. 36, no. 3, pp. 749–759, 2016.

3.2. Article: Induced internal stresses and their relation to FLASH sintering of KNN ceramics

To be submitted

Abstract

Electric field and current applied to an unsintered ceramic body is known to promote low temperature and extremely fast densification, in a process referred to as FLASH sintering. Suitable experimental conditions result in dense ceramics but many issues relating to the effect of field and current on local chemistry, structure, and microstructure remain. FLASH sintering has been used to produce $K_{0.5}Na_{0.5}NbO_3$ (KNN), a lead-free compound suitable for piezoelectric applications. Here, we study the internal stress state arising from the FLASH process using X-ray diffraction and Raman spectroscopy. In addition, the internal stress state and its relation with local temperature is established by Finite Element Modelling (FEM). We conclude that, although the FLASH process may produce homogeneous ceramics with negligible concentration of secondary phase, macroscopic core-localized stresses remain which have significant consequences for its development as an alternative low thermal budget, sintering technology.

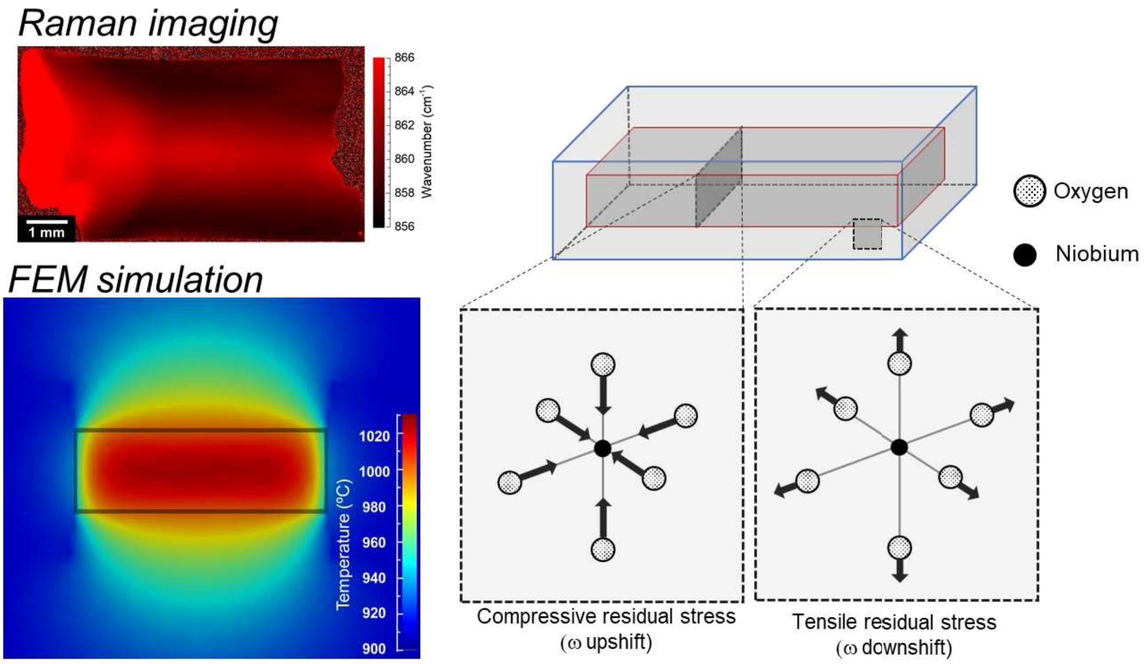

Key words:

FLASH sintering; Raman imaging; Finite Element Modelling; Stress state; Structure; Thermal gradient; Joule heating.

3.2.1. Introduction

FLASH is an electric field and current assisted densification technique for ceramics. This novel sintering process allows a considerable decrease in the processing time and temperature and thus it is considered a promising method to reduce the energy costs and environmental footprint associated with sintering [1], [2]. When an electric field is applied to a porous ceramic compact, no long-range current flow is observed. However, if the temperature is increased and/or enough defects are nucleated, a FLASH event occurs in which densification may take place in less than 60 s, depending on the field and current applied [3]. FLASH is one of a number of low energy sintering techniques such as Spark Plasma Sintering/Texturing (SPS/SPT) [4] and Cold Sintering Process (CSP) [5] which offer a path to reducing energy consumption within the ceramics industry.

In FLASH sintering, the ceramic is heated from the core to its surface by a Joule effect caused by an electric current imposed through surface mounted electrodes, typically metallic sheets. The appropriate operating conditions (e.g temperature, electric field, current density, time, atmosphere) have been reported to result in dense ceramics that are chemically and microstructurally uniform [6]–[8]. However, rapidity of the FLASH event can induce non-equilibrium microstructures [9]. Thermal gradients [10], [11] and accelerated mass transport [2], together with non-uniform electric current distribution (hotspots) [12] and electromigration [13] are known to trigger microstructural [14], [15] and chemical [16] heterogeneity.

Although X-Ray Diffraction (XRD) has been used to study mechanisms that promote non-equilibrium phenomena [17]–[19], the structural and microstructural changes during FLASH are still not well understood. Here, we study FLASH sintering on Potassium Sodium Niobate, $K_{0.5}Na_{0.5}NbO_3$ (KNN) a lead-free piezoelectric [20], [21]. Undoped KNN is difficult to sinter conventionally due to volatilisation of K and Na at high temperature [22] and alternative approaches such as SPS/SPT [23], CSP [24] and FLASH [16], [25] are often sought. Our previous work demonstrated a particle-contact (size and shape) dependent sintering process [6], [26], [27]. Such contacts partially melt which allows particle sliding and pore removal [28]. While microstructural differences between FLASH and conventionally sintered KNN ceramics are evident [16], [28], comparable electrical properties can be achieved by subsequent heat treatment [29].

Although analysis of the macroscopic stresses has been reported for SPS and SPT, [23], [30]), no such studies exist for FLASH sintering. In this work, not only is XRD used to gain information on the structure and, indirectly, the chemistry, Raman spectroscopy is used to assess the structure, microstructure and chemical composition of FLASH sintered KNN ceramics [31]. These techniques are combined with Finite Element Modelling (FEM) to establish a direct link between FLASH sintering and the resulting structure and microstructure, particularly focussing on the internal stress state.

3.2.2. Experimental

KNN powders were produced by a conventional solid-state route, and specimens obtained by uniaxial and isostatic pressing [6]. KNN ceramics were conventionally sintered 3 h at 1125 ºC, with heating and cooling rates of 5 ºC/min, in the absence of any electric field or current. Similarly, green compacts were FLASH sintered under Isothermal Conditions (I.C.) [6]. After an isothermal step of 30 min at 900 ºC, the electric field (300 V/cm) was applied, followed by an incubation time of ca. 60 s, and a current density rise to a limit of 20 mA/mm^2. Specimens were sintered 60 s.

Scanning electron microscopy, SEM (*Hitachi SU-70*) was used to study the microstructure of dense ceramics. SiC paper was used to grind and polish the sintered ceramics which were then etched 5 min, in 40 vol% HF, to reveal the grain structure. Polished ceramics were analysed by Electron Backscattered Diffraction Analysis (EBSD) and the average grain size ($\overline{G_{eq.}}$) determined from mapping more than 1000 grains [29]. For FLASH sintered ceramics, the regions immediately adjacent to the electrodes were not considered for microstructural studies (ca. 1-2 mm each side). Density of ceramics was determined using the Archimedes method (in water) on at least three specimens.

Polished sintered ceramics were analysed by X-Ray diffraction (XRD). A *PANalytical XPERT-PRO* diffractometer, using a Cu source (Kα_1 = 1.54060 Å), from 20 to 80º 2θ, with a step size of 0.026º and accumulation time of ca. 96 s was used. Lattice parameters were determined by Rietveld refinement of the experimental XRD data and were based on JCPDF 01-085-7128 file (KNN, A*mm2*). Residual stresses were estimated by XRD using different specimen tilt angles (Ψ), and by following eq. 2-2, where k is the curve gradient of the normalized d-spacing (311 planes) vs. sin$^2\Psi$, E_Y is the Young modulus (104 GPa) and υ is the Poison ratio (0.27). 2θ from 70 to 80º was analysed since this contained the (311) reflection. For further details on the method, we refer the reader to refs [23], [32], [33]

$$\sigma_{\phi} = \left(\frac{E_Y}{1+\nu}\right) k \tag{2-2}$$

Sintered and polished ceramics were further analysed by unpolarized micro-Raman single spot and imaging mode using a Renishaw InViaTM Qontor® Confocal spectrometer operated with a 633 nm He-Ne laser line (power at 5 mW). Each Raman spectrum was acquired with an exposure time of 0.1 s and to achieve good spatial resolution for Raman imaging, ca. 290 000 spectra were collected for the 500 x 500 μm^2 maps, and 1 500 000 spectra for the 9 x 5 mm^2 maps. The pixel size varied from 1 to 30 μm^2, depending on the map area with a lateral resolution of 100 nm. The scattered light was analysed using an 1800 lines/mm diffraction grating, providing a spectral resolution better than 1.5 cm^{-1}. The frequency, linewidth, and intensity of the Raman bands were determined through best fit to a Lorentzian function.

COMSOL Multiphysics simulations were carried out to access the current density and temperature distribution in a monolithic KNN block. The model was based on the approach described in ref. [26]. Prior to simulation, the DC electrical conductivity of conventionally dense KNN ceramics was determined using a *Keithley 2410* electrometer and the temperature dependence assigned to the material within the *COMSOL* software. An electric field of 300 V/cm was applied across the model and scaled to the model size. The current flow (as a function of conductivity) and temperature were simulated at 1 s interval. As the electric field is being controlled, we monitor that the current in the simulation does not rise above the experimental limit of 20 mA/mm^2.

3.2.3. Results and discussion

Representative SEM micrographs of conventionally (Conv) and FLASH sintered ceramics are shown in Figure 3.2-1 a) and b), respectively. Both ceramics exhibit a uniform density through the analysed region. A fine microstructure with uniform sized grains is depicted for FLASH ceramics, in Figure 3.2-1 b), while a coarser microstructure with abnormal grain growth is observed for conventionally sintered KNN (see Figure 3.2-1 a)). The average grain size is ~20% larger in conventionally than in FLASH sintered specimens (see average grain size, $\overline{G_{eq.}}$, in Table 3.2-1). Abnormal grain growth and secondary phases have been previously reported in conventionally sintered KNN [34], [35]. Chemical etching of conventionally sintered ceramics occurs differently from that of FLASH, with '*worm-like*' features within grains in Figure 3.2-1 a) but classically etched grains in FLASH ceramics (Figure 3.2-1 b)). FLASH sintered samples also showed evidence of grain pull out from the grinding, polishing and etching process which is attributed to the formation of mechanically and/or chemically unstable grain boundaries (GBs) [6].

The respective structure and chemical composition of the ceramics was evaluated by EBSD analysis. Figure 3.2-1 c) and d) show the phase mapping for conventional and FLASH sintered specimens, respectively. The maps were obtained by indexing two crystalline phases: i) a $K_{0.5}Na_{0.5}NbO_3$ orthorhombic A*mm*2 perovskite phase, displayed with red colour, and ii) a $K_{0.8}Nb_5O_{15}$ (Nb-rich) tetragonal tungsten bronze structured secondary phase (P*4bm*) [23] and represented with green in Figure 3.2-1 c). The conventional ceramics clearly exhibit grains indexed according to $K_{0.8}Nb_5O_{15}$, with far fewer in FLASH sintered samples. For both samples, well defined grain boundaries are observed. Based on the area fraction of grains assigned to the secondary phase, the estimated concentration of $K_{0.8}Nb_5O_{15}$ (C_{sp}) in conventional KNN is 0.4±0.1 vol% (Table 3.2-1). The relative density of FLASH and conventionally sintered ceramics were, within experimental error, similar, Table 3.2-1.

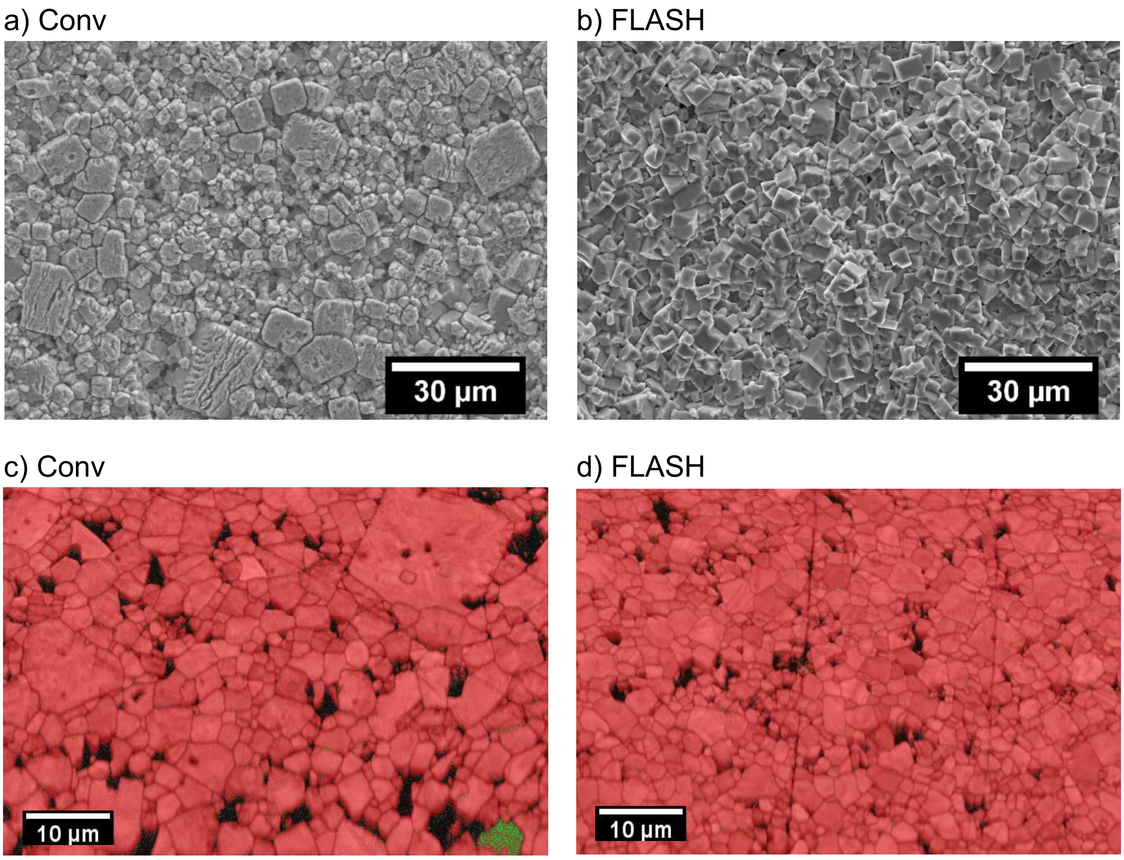
a) Conv
b) FLASH
c) Conv
d) FLASH

$K_{0.5}Na_{0.5}NbO_3$
(JCPDF 01-085-7128; orthorhombic; SG: 38)

$K_{0.8}Nb_5O_{15}$
(JCPDF 04-007-9405; tetragonal; SG: 100)

Figure 3.2-1 – SEM micrographs (a, b) and their respective EBSD phase maps (c, d) of conventionally (a, c) and FLASH (b, d) sintered KNN ceramics. FLASH KNN ceramics present a uniform grain size while conventionally sintered KNN exhibits some abnormal grain growth, together with more $K_{0.8}Nb_5O_{15}$ secondary phase.

Table 3.2-1 – Secondary phase concentration (C_{sp}), relative density (ρ_{rel}) and average equivalent grain size ($\overline{G_{eq.}}$) of conventionally and FLASH sintered KNN ceramics.

KNN	C_{sp} (vol.%)	$\rho_{rel.}$ (%)	$\overline{G_{eq.}}$ (μm)
Conv	0.4±0.1	96±2	1.77±0.05
FLASH	<0.05	93±3	1.49±0.02

Figure 3.2-2 a) shows representative XRD patterns of polished, as-sintered ceramics by FLASH and conventional sintering, respectively, recorded at room temperature from 20 - 80º 2θ. Qualitatively, the profile of the XRD patterns is similar to JCPDF file 01-085-7128, orthorhombic $K_{0.5}Na_{0.5}NbO_3$, previously indexed in EBSD data. The Rietveld refinement of the XRD data did not however, reveal the presence of secondary phases in conventional ceramics, suggesting the volume fraction is below the detection limit of the experimental equipment. The lattice parameters of FLASH and conventionally sintered ceramics are shown in Table 3.2-2. An isotropic volume decrease of the primitive cell is observed in FLASH (0.06±0.02% lattice parameter decrease), compared with conventionally sintered specimens.

Figure 3.2-2 b) shows the XRD estimated residual stress of the same polished as-sintered KNN ceramics. The plot gives the normalized (311) interplanar spacing as a function of $\sin^2\Psi$, where Ψ is the sample's tilt angle [32]. For this purpose, different XRD patterns were recorded from 70 to 80º, at different tilt angle, resulting in residual stresses calculated from the slope of the linear dependences shown in Figure 3.2-2 b) [36]. Because the data slopes of both FLASH and conventionally sintered ceramics are negative, residual compressive stresses are estimated at -170±35 and -57±9 MPa, respectively. The compressive stress level of FLASH is therefore, more than 3 times greater than conventional KNN, with a larger dispersion.

To establish the link between the sintering, local/internal stresses and structural/chemical changes in ceramics, spatially resolved data such as that generated from Raman imaging is needed. The representative unpolarized Raman spectra of FLASH and conventional KNN, recorded at room conditions in the 100 – 1000 cm^{-1} spectral range, is illustrated in Figure 3.2-3 a). The Raman profile agrees with previous reports for KNN [30], [37], with similar crystallographic structures in FLASH and conventional ceramics and corroborates XRD data. Factor group analysis of orthorhombic (A*mm2*) KNN yields the following 12 Raman-active optical modes at the Γ-point of the Brillouin zone:

$$\Gamma^{opt} = 4A_1 + 4B_1 + 3B_2 + A_2 \tag{3-1}$$

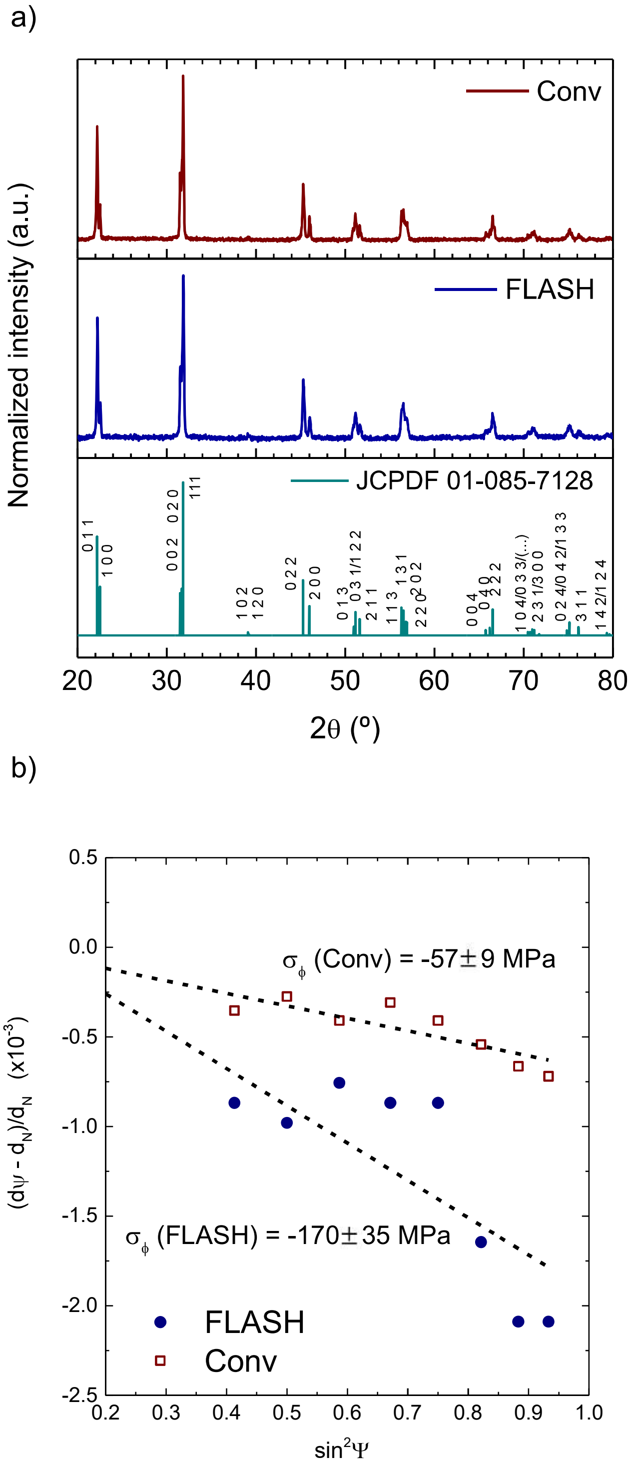

Figure 3.2-2 – a) X-ray diffraction patterns of $K_{0.5}Na_{0.5}NbO_3$ FLASH and conventional ceramics; for comparison, JCPDF 01-085-7128 file is presented (perovskite orthorhombic structure, space group A*mm2*, $K_{0.5}Na_{0.5}NbO_3$ composition). b) the d-spacing of (311) planes at different tilt angle Ψ normalized to "no tilt" d-spacing, versus the sinus square of Ψ ανγλε, and estimation of residual stresses on these ceramics.

Table 3.2-2 – Lattice parameters determined from the Rietveld analysis of the XRD patterns. The respective variation of parameters is represented by Δ = (FLASH-Conv)/Conv.

Specimen / Lattice parameter (Å)	Conv	FLASH	Δ (%)
a	3.944(6)	3.941(9)	-0.07
b	5.645(1)	5.642(8)	-0.06
c	5.675(4)	5.671(9)	-0.04

The Raman spectra are characterized by three main spectral regions, which are assigned to different vibrational modes. The bands observed between 100 and 180 cm^{-1} are translation modes of K+/Na+ cations [37], and 180 to 1000 cm^{-1} modes are assigned to bending and stretching vibrations of the NbO$_6$ octahedra [37]. According to Kakimoto *et al.* [37], the vibrational modes υ_1 to υ_3 are stretching vibrational modes, while υ_4 and υ_5 are assigned to the bending vibrations of the NbO$_6$ octahedra. The atomic displacements associated to each NbO$_6$ vibration are schematically represented in Figure 3.2-3 b).

Among the Raman-active modes, we will focus our attention on the symmetrical stretching mode υ_1 and the bending mode υ_5. υ_1 is characteristic of octahedral distortions, as its frequency depends on the mean Nb-O bond length, following Badger’s rule [38], [39]. υ_5 involves the octahedral tilt angle and is sensitive to the shear strain. Both modes therefore, give insight regarding the relation of residual stress to structural distortions. However, the accurate determination of the υ_5 mode frequency through spectral deconvolution of the spectral range where this band is observed is hindered by strong band overlap. To overcome this handicap, we have focused our attention on the band located at 860 cm^{-1}, which is assigned to the second-order mode υ_1+υ_5 and is compared with υ_1.

To gain insight into the relation of sintering with the structural distortions of the KNN ceramics, we performed a detailed Raman imaging study at room temperature on the polished surface of as-sintered ceramics. Figure 3.2-4 a) gives the optical microscope image of the FLASH sintered ceramic. The positive electrode area is visible on the left, adjacent to the area used for characterization (e.g., in microstructure analysis) and the negative electrode contact is revealed on the right. These areas are highlighted as 1 and 5 for positive and negative electrodes, respectively, 2, 3 and 4 for zones in a straight line between electrodes (specimen core) and 6 and 7 for the top and bottom surfaces. Figure 3.2-4 b) includes the representative unpolarized Raman spectra recorded at the locations identified by the numbered spots in Figure 3.2-4 a). The Raman spectral profile is not strongly dependent of the position on the FLASH ceramic (core, surface or electrodes) but does reveal sintering dependent structural distortions.

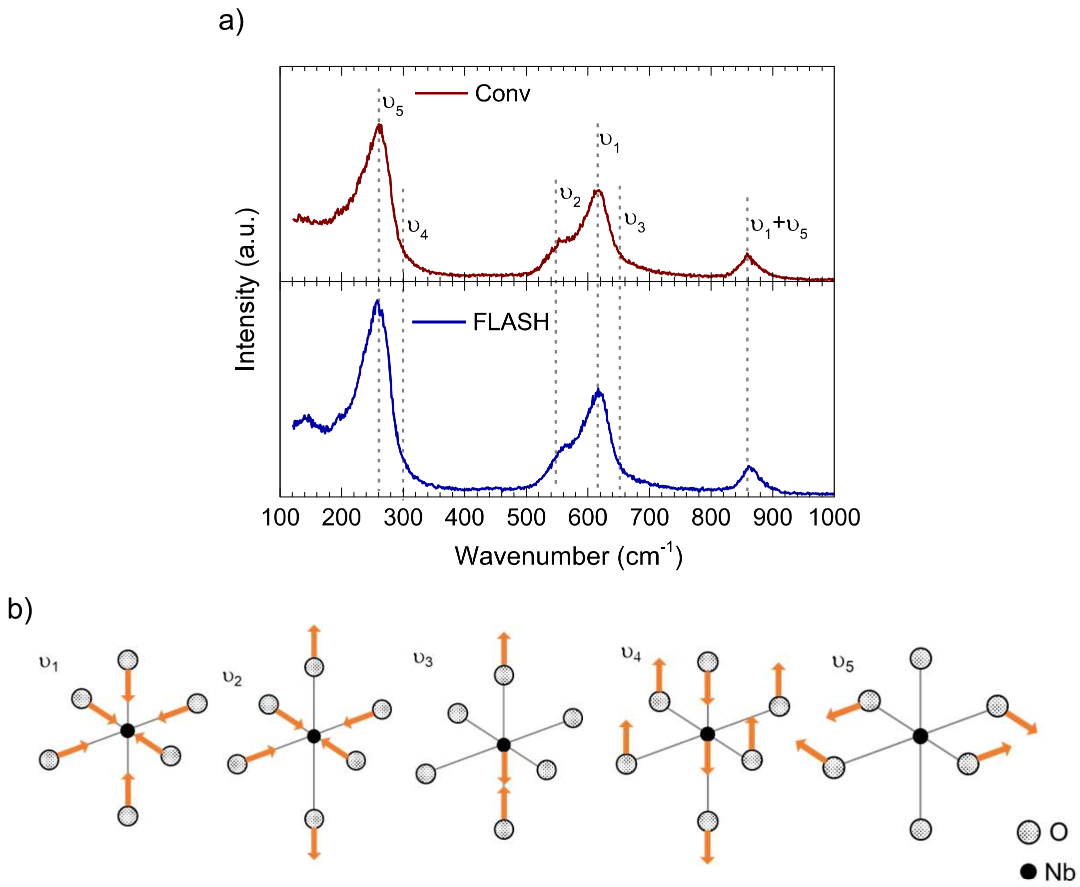

Figure 3.2-3 – a) Unpolarized Raman spectra of conventionally (Conv) and FLASH sintered ceramics with identified vibrational modes of NbO_6 octahedra (υ_1 to υ_5). b) Schematic representation of vibrational modes (adapted from [37]); υ_1 to υ_3 are stretching modes and υ_4 to υ_5 are bending modes.

The bands of interest for analysis are highlighted with colours in Figure 3.2-4 b) and are magnified in detail in c). For comparison, the wavenumber (ω_a) of each relaxed mode was considered at 615 and 859 cm^{-1}, as reported independently for single crystals [40], [41] and ceramics [30], [37], [42]. These are indicated in Figure 3.2-4 c) by the vertical dashed blue lines, and the ω_a shifts, relative to the assumed reference values, for υ_1 and $\upsilon_1+\upsilon_5$ bands, are revealed. The corresponding Raman images, weighted to the position of the Raman mode, are presented in Figure 3.2-4 d) and e) for υ_1 and $\upsilon_1+\upsilon_5$, respectively. The frequency of both υ_1 (d) and $\upsilon_1+\upsilon_5$ (e) modes is position dependent as revealed by a significant wavenumber shift ranging from 612 to 622 and 856 to 866 cm^{-1} (10 cm^{-1}), respectively. In both analyses, a significant upshift in the positive electrode (1) that corresponds to 6 to 7 cm^{-1} above the reference value is found, followed by an upshift at the ceramic core (numbers 2 to 5) of 5 to 6 cm^{-1}. Although a slight downshift is observed at the surfaces (6 and 7) of 1 to 2 cm^{-1}, the majority of the sample presents an $\upsilon_1+\upsilon_5$ upshift. Following Badger's rule (eq. 3-2) [38], [39] as the length of Nb-O bond ($d_{Nb\text{-}O}$) is decreased (indicating a volume reduction of the Nb-O octahedra), ω_a is augmented.

$$\omega_a \propto \frac{1}{d_{Nb-O}^{\frac{3}{2}}} \tag{3-2}$$

In accordance with equation 3-2 and Figure 3.2-4, the core areas of FLASH ceramics (corresponding to numbers 1 to 5 in Figure 3.2-4 b)) present a shorter Nb-O bond; the opposite occurs for the surfaces (numbers 6 and 7) of the FLASH ceramic but with a lower intensity. Nonetheless, an estimation of variation in $d_{Nb\text{-}O}$ with respect to the reported ω_a values (Figure 3.2-4) gives a maximum bond length variation of ~ - 1% at the core and + 0.5% at the surfaces. This observation agrees with the overall primitive cell compression and high residual compressive stresses found in X-ray scattering data of FLASH ceramics but suggests a non-uniform distribution of the stresses in the FLASH KNN, not identified by XRD.

To understand the non-uniform distribution of residual stresses on as-sintered FLASH ceramics, Finite Element Modelling (FEM) was used to simulate the temperature distribution in the KNN specimens during FLASH sintering. The results of simulated current density and respective temperature distribution profiles evolving as a function of time are represented in Figure 3.2-5. As seen, the current density increases with time which, due to the overall heating of the system (by Joule effect), is uniformly distributed throughout the KNN body. In contrast, the temperature distribution at each stage is inhomogeneous. The temperature increase by Joule effect occurs through the specimen core towards its surface. It should be noted that at the transition from t = 5 to t = 6 s, the simulation is no longer representative of the experimental setup, as the experimental current limit (20 mA/mm^2) is exceeded and therefore, t = 5 s was selected for comparison with the Raman imaging data in Figure 3.2-4 f).

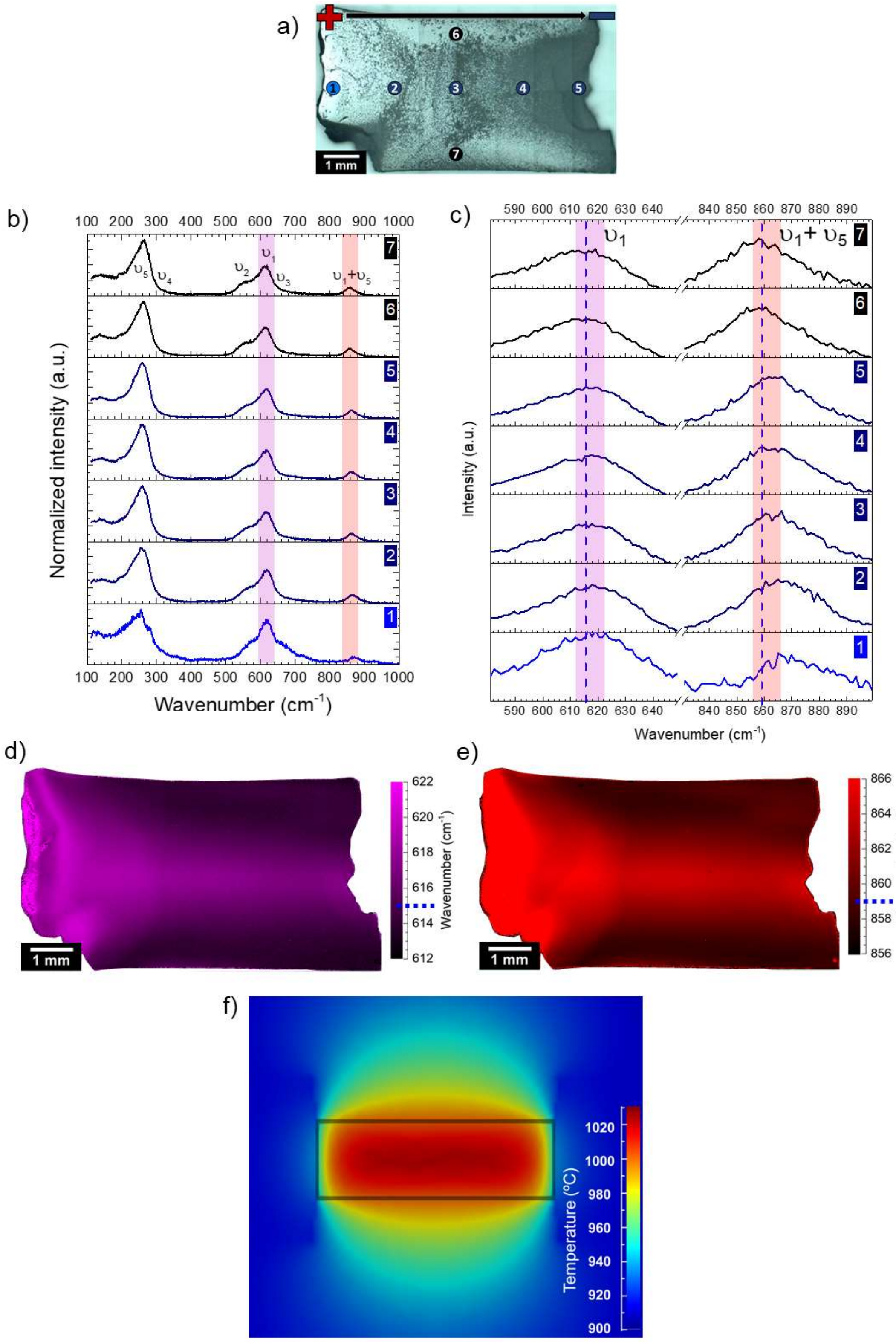

Figure 3.2-4 – a) optical microscope image of FLASH ceramic; b) Raman spectra of correspondent spots 1 to 7 identified in a); c) magnification of b) for the Raman modes of interest; Raman spectroscopy imaging for the peak position (wavenumber) fitted for d) υ_1 in purple and e) $\upsilon_1 + \upsilon_5$ in red; pixel size ≈ 30 μm^2. f) FEM simulation of temperature distribution during FLASH sintering; the surfaces of the simulated KNN block of material are represented by the grey rectangle.

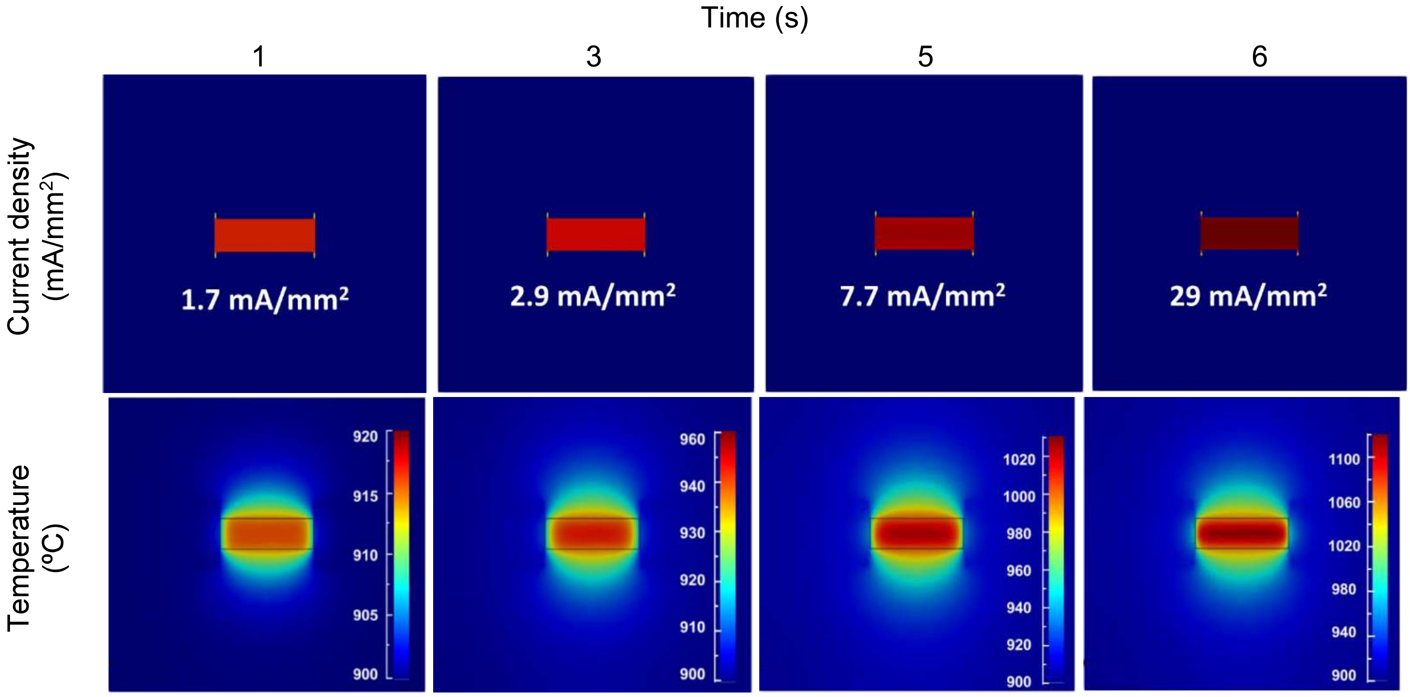

Figure 3.2-5 – Simulated current density (top) and temperature (bottom) distribution for simulation times of 1, 3, 5 and 6 seconds after the starting simulation condition: equilibrium temperature of 900 ºC. For clarity, the surface of KNN block is represented by a grey rectangle in the temperature representations. At t = 6 s, the experimentally imposed current density limit of 20 mA/mm^2 is exceeded and the simulation is no longer valid.

The simulated temperature distribution through the KNN modelled specimen (delineated by the grey rectangle in Figure 3.2-4 f)) during the FLASH reveals a spatial temperature dependence on the ceramic. At the core, ≈1030 ºC is achieved, while at the surface, the temperature drops to <1000 ºC. Due to thermal dissipation, the surroundings of the ceramic are at a temperature close to that of the furnace (900 ºC). The Raman imaging schemes (Figure 3.2-4 d), e)) and FEM simulation (Figure 3.2-4 f)) show agreement between the simulated temperature profile and the localized stresses of the KNN unit cell. A link between local temperature during FLASH and local structure in sintered ceramics is therefore evidenced, with the higher temperature at the core of the ceramics during FLASH sintering being related with a Nb-O bond decrease, equivalent to a unit cell compression. These local deformations result in a high overall residual compressive stress state in the as-sintered FLASH ceramics.

We propose the following hypothesis to explain the observed relationship between local temperature during FLASH sintering and the local stresses in as-sintered ceramics. During sintering, the inhomogeneous temperature distribution promotes a non-uniform expansion of the unit cell, that is larger at the core of the specimen in comparison with its surface (schematically represented in Figure 3.2-6 a). This induces a compressive stress at the core and a tensile one at the surfaces during FLASH. When the FLASH process is stopped, with the current being instantaneously decreased to zero, the heating by Joule effect, which was promoted by the ceramic core, is immediately reduced to zero. Therefore, the surface expanded unit cell is frozen (in the scheme, red "activated" arrows turn to black "frozen" ones), as the temperature is decreased which results in a downshift in ω_a of υ_1 mode – equation 3-2 and Figure 3.2-4. However, as the surface grains are cooling, the core grains are still at high temperature (the initial temperature was higher, and their correspondent cooling rate will be lower than that of surfaces), with the unit cell still expanded. As core grains are finally cool, residual mechanical stresses are imposed on the inner grains, as the outside atoms are already *frozen* and do not allow stress release (Figure 3.2-6 b)). Therefore, the core grains are left with compressive stress, that is revealed as an upshift in ω_a of υ_1 mode, discussed in Figure 3.2-4.

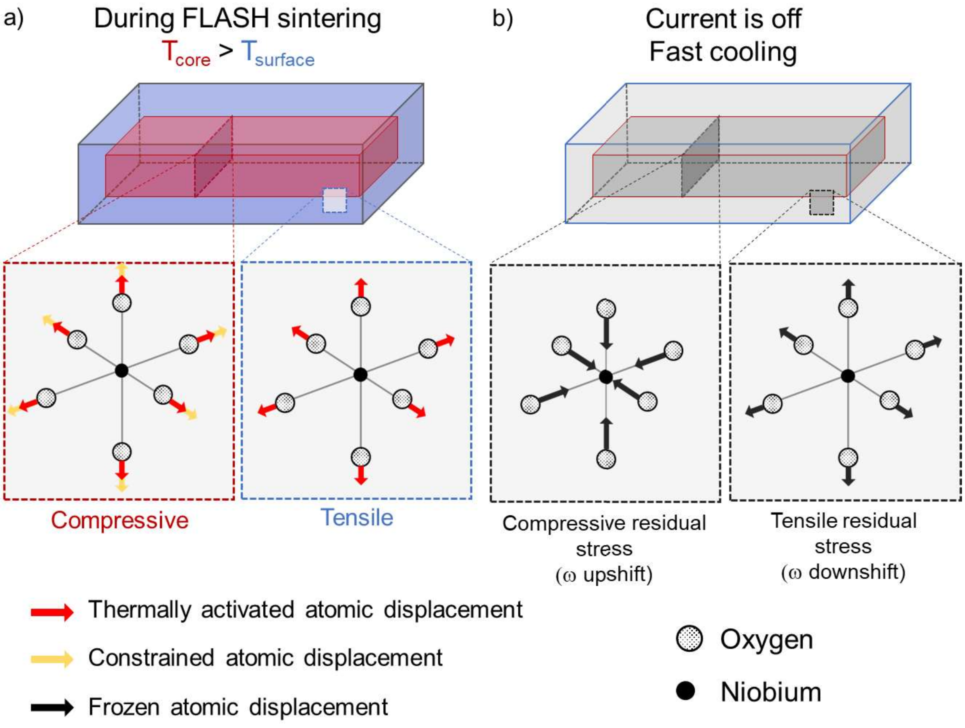

Figure 3.2-6 – Schematic representation of internal stresses due to FLASH sintering with a) differential Nb-O bond expansion as a function of the local temperature (higher, but constrained, in the core than in the surfaces); b) the frozen atomic arrange with residual compressive stresses at the core and tensile ones at the surfaces.

A second hypothesis to explain the residual stresses in FLASH sintered ceramics could be that it is related with differential densification; if the shrinkage at the core of ceramics is greater than that of the surfaces, the compressive stress at the core would be easily explained. However, the microstructural analysis, shown in this work and previous work [6], did not reveal significant density gradient between core and surface of ceramics, therefore, such hypothesis is deemed likely.

A first analysis of the proposed mechanism for stress development in FLASH sintered ceramics may be associated with thermal quenching of ceramics or glasses. In such process, during cooling, the surface of parts is initially under a tensile stress, while the cooling process is ongoing, however, they soon become compressive, as the core finally cools and stays in a tensile state [43], [44]. However, a careful analysis of the data and mechanism presented in this work suggest the opposite to the observed in quenching processes. FLASH sintered KNN ceramics present an overall compressive stress state, with strong core localized compressive stresses and moderated surface located tensile ones. This is because the heating by Joule effect during FLASH occurs through the ceramic core, promoting a thermal gradient, as shown by our FEM simulations (Figure 3.2-5). On contrary, in quenching processes, the heating of ceramics/glasses occurs from the surface towards the core. When cooling is started, the surface is at higher temperature than the core, which is the opposite to what happens in FLASH.

To validate the proposed mechanism of induced stresses during FLASH sintering, a conventionally sintered ceramic was studied. Figure 3.2-7 a) presents a representative Raman spectroscopy imaging based on the $\upsilon_1+\upsilon_5$ mode wavenumber. For comparison, the core area of the FLASH ceramic was analysed under the same experimental conditions as used for conventional ceramics and is revealed in b). Whereas FLASH ceramic (b) demonstrates a very uniform dependence of ω_a along all the analysed area, with a strong upshift from ω_a = 859 cm^{-1}, as shown in Figure 3.2-4 (corresponding to pin number 3 area), conventional ceramic (a) presents an overall lower ω_a, closer to the reported value [37]. However, conventional ceramic presents micron-sized non-uniformities, characterized by localized strong upshifts, highlighted with circles and the respective number 2. The uniform and representative zones in the ceramic are identified with the number 1. The Raman spectra of areas 1 and 2 are represented in Figure 3.2-7 c). While a typical KNN Raman spectrum is depicted for 1, indicating that such areas do not present any relevant structural or chemical dissimilarity, the same is not true for spectrum 2, where there is an anomaly in the background, with spurious bands being revealed (identified with *). These observations in conventionally sintered ceramics may be explained by the presence of the Nb-rich secondary phase, previously identified in EBSD (Figure 3.2-1), or the contribution of polishing residues trapped in pores.

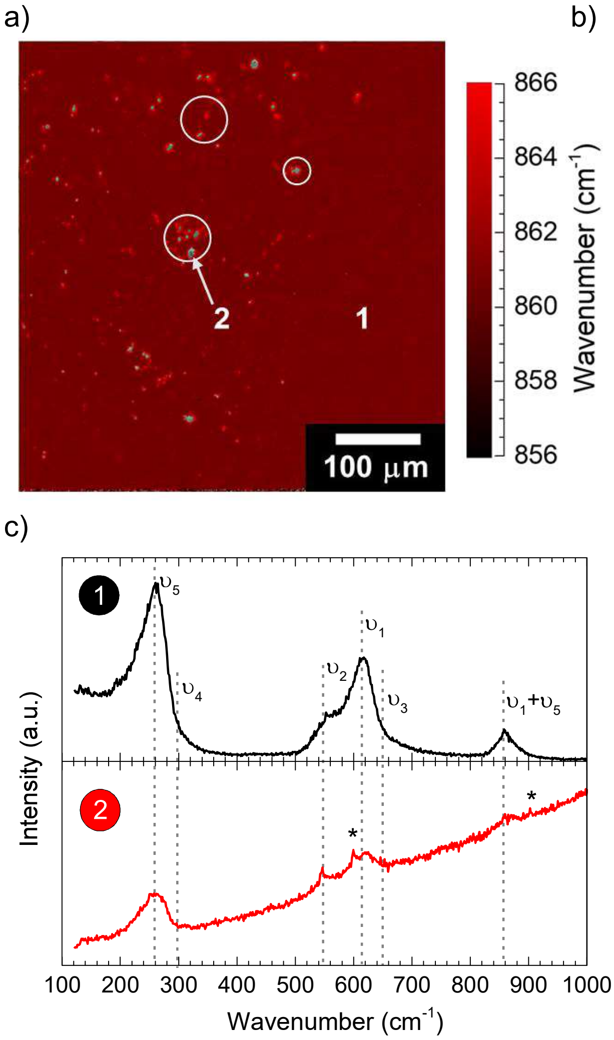

Figure 3.2-7 – Raman spectroscopy imaging on the mode at ca. 860 cm^{-1} of a) conventionally and b) FLASH sintered ceramics; pixel size = 1 μm^2. c) Respective Raman spectra for positions 1 and 2 in conventional ceramic's map, with identification of spurious peaks (*).

If the Raman modes with upshift in conventional ceramics are representative of secondary phases, such high concentration would result in secondary reflections in XRD patterns, since their volume fraction would be above the typical detection limit. Therefore, the presence of polishing impurities seems more plausible, which is consistent with the similar electrical properties of conventionally and FLASH sintered ceramics, obtained after post-sintering heat treatment [29]. The post processing heating step of FLASH sintered ceramics, e.g. associated with the application and cure of metallic electrodes [29] is associated with stress release and relaxation. Residual stress analysis by X-ray on a 900 ºC - 1 h heat treated FLASH ceramic did not revealed residual stresses. Thermal relaxation of FLASH ceramics is therefore, a topic requiring further exploration.

3.2.4. Conclusions

This study reveals that FLASH sintering induces stresses in the densified ceramics. By combining the overall structural and microstructural analysis provided by EBSD and XRD with Raman spectroscopy and FEM simulations of the FLASH sintering process, the relationship between densification and internal stresses in KNN ceramics was established. Conventional sintering gives macroscopic homogeneous ceramics but with a low volume fraction secondary phase. The FLASH process produces a microscopically homogeneous ceramic with even less secondary phases than conventional but macroscopic compressive stresses are present in the specimen core. The proposed mechanism for the development of stresses during FLASH sintering is consistent with the decrease in cell volume and higher residual compressive stresses compared to conventional samples observed by XRD.

3.2.5. Supplementary information

Figure SI-3.2-1 shows a schematic of the polishing process of as-sintered conventional and FLASH ceramics in a) and the respective surface of analysis in b). Approximately one third to one half of the ceramic thickness was removed (stripes in the figure) by polishing with SiC paper. The final polishing was performed with a P4000 paper, equivalent to a grain size of ≈ 5 μm. After polishing, specimens were washed in ethanol under sonication. The dried ceramics were then analysed by X-ray diffraction and Raman spectroscopy using single spot and imaging mode.

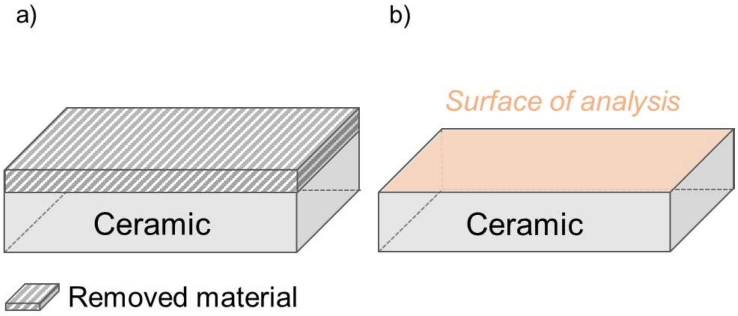

Figure SI-3.2-1 – Schematic representation of a) the polishing process with indication of removed material and b) the subsequent surface of analysis.

COMSOL Multiphysics was used to develop the Finite Element Model for the simulation of both current density distribution and respective temperature (due to heating by Joule effect). [26]. The DC electrical conductivity of conventional KNN ceramics was accessed using a *Keithley 2410* electrometer, with a 1 V/cm applied electric field. Platinum electrodes were painted and sintered on opposite faces of the ceramics prior to measurement. A constant heating rate of 10 ºC/min up to 1000 ºC was employed and the conductivity as a function of temperature is shown in Figure SI-3.2-2. The electrical conductivity of KNN was subsequently extrapolated for T > 1000 ºC based on an Arrhenius fit to the data. Measurements on several different conventionally sintered ceramics were performed, and the results were consistent and considered to be representative of KNN ceramics.

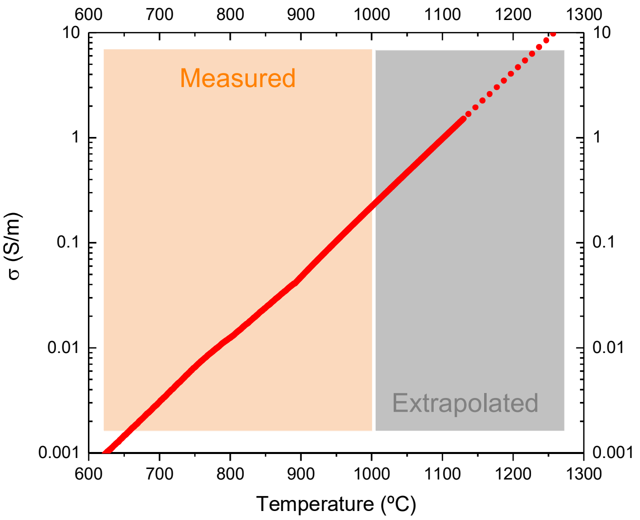

Figure SI-3.2-2 - Measured KNN conductivity σ (S/m) over measured temperature (with a 10 ºC/min heating rate) under an applied electric field of 1 V/cm.

To simulate the FLASH process, the sample holder and respective green KNN compact were described, as shown in Figure SI-3.2-3. For simulation, the green compact was approximated to a single 15 x 5 mm^2 monolithic block of material, identified as *KNN* in Figure SI-3.2-3. Thickness was not considered as only a 2D model was developed. The bi-dimensional approximation allows faster simulation times without compromising the results. KNN (with the respective electrical conductivity) was modelled to establish a perfect contact with two opposite platinum electrodes, that were also in contact with alumina parts, as in the experimental setup [28].

The FLASH process simulation was achieved using a *Terminal* function to one electrode, and a *Ground* function to the opposite electrode. A 300 V/cm electric field was scaled to the *terminal-ground* functions and the current was calculated and simulated as with respect to temperature and conductivity. To allow heat dissipation, the modelled setup was considered to be in air. Alumina electrical conductivity was taken as constant (10^{-12} S/m), while the thermal conductivity of KNN and alumina was considered temperature dependent and equal to 2.6 W/(m.K) and 27 W/(m.K), respectively. The time dependent model was run at a starting temperature of 900 ºC, representative of furnace equilibrium temperature before the application of the electric field. The results of current density and temperature profile were recorded at 1 s time intervals and are shown in Figure 3.2-5.

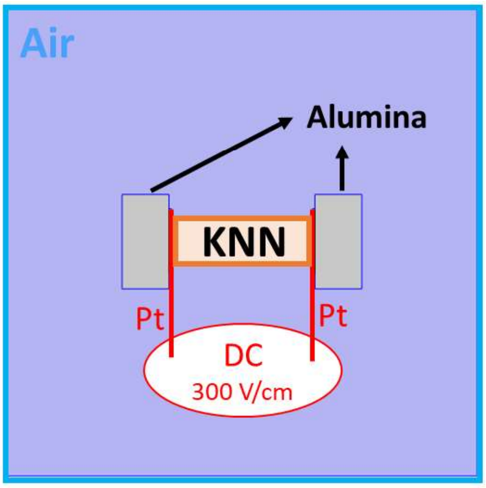

Figure SI-3.2-3 - Schematic representation of the model.

3.2.6. References

[1] C. E. J. Dancer. "Flash sintering of ceramic materials". Mater. Res. Express, vol. 3, no. 10, pp. 102001–102025, 2016.

[2] M. Biesuz, S. Grasso, and V. M. Sglavo. "What's new in ceramics sintering? A short report on the latest trends and future prospects". Curr. Opin. Solid State Mater. Sci., vol. 24, no. 5, p. 100868, 2020.

[3] M. Biesuz and V. M. Sglavo. "Flash sintering of ceramics". J. Eur. Ceram. Soc., vol. 39, no. 2–3, pp. 115–143, 2019.

[4] O. Guillon *et al.*. "Field-assisted sintering technology/spark plasma sintering: Mechanisms, materials, and technology developments". Adv. Eng. Mater., vol. 16, no. 7, pp. 830–849, 2014.

[5] J. Guo *et al.*. "Cold Sintering: Progress, Challenges, and Future Opportunities". Annu. Rev. Mater. Res., vol. 49, no. 1, pp. 275–295, 2019.

[6] R. Serrazina, A. M. O. R. Senos, L. Pereira, J. S. Dean, I. M. Reaney, and P. M. Vilarinho. "The Role of Particle Contact in Densification of FLASH Sintered Potassium Sodium Niobate". Eur. J. Inorg. Chem., vol. 2020, no. 39, pp. 3720–3728, 2020.

[7] D. Liu, Y. Gao, J. Liu, Y. Wang, and L. An. "Effect of holding time on the microstructure and properties of flash-sintered Y_2O_3-doped ZrO_2". Ceram. Int., vol. 42, no. 15, pp. 17442–17446, 2016.

[8] L. A. Perez-Maqueda, E. Gil-Gonzalez, A. Perejon, J. M. Lebrun, P. E. Sanchez-Jimenez, and R. Raj. "Flash sintering of highly insulating nanostructured phase-pure $BiFeO_3$". J. Am. Ceram. Soc., vol. 100, no. 8, pp. 3365–3369, 2017.

[9] J. V. Campos *et al.*. "Flash sintering scaling-up challenges: Influence of the sample size on the microstructure and onset temperature of the flash event". Scr. Mater., vol. 186, pp. 1–5, Sep. 2020.

[10] M. Biesuz *et al.*. "Investigation of electrochemical, optical and thermal effects during flash sintering of 8YSZ". Materials, vol. 11, p. 1214, 2018.

[11] J. G. Pereira Da Silva, J. M. Lebrun, H. A. Al-Qureshi, R. Janssen, and R. Raj. "Temperature Distributions during Flash Sintering of 8% Yttria-Stabilized Zirconia". J. Am. Ceram. Soc., vol. 98, no. 11, pp. 3525–3528, 2015.

[12] M. S. Bernardo, T. Jardiel, A. C. Caballero, M. Bram, J. Gonzalez-Julian, and M. Peiteado. "Electric current activated sintering (ECAS) of undoped and titanium-doped $BiFeO_3$ bulk ceramics with homogeneous microstructure". J. Eur. Ceram. Soc., vol. 39, no. 6, pp. 2042–2049, 2019.

[13] W. Rheinheimer, X. L. Phuah, H. H. Wang, F. Lemke, M. J. Hoffmann, and H. H. Wang. "The role of point defects and defect gradients in flash sintering of perovskite oxides". Acta Mater., vol. 165, pp. 398–408, 2019.

[14] W. Qin, H. Majidi, J. Yun, and K. van Benthem. "Electrode Effects on Microstructure Formation During FLASH Sintering of Yttrium-Stabilized Zirconia". J. Am. Ceram. Soc., vol. 99, no. 7, pp. 2253–2259, 2016.

[15] Y. Zhang, J. Il Jung, and J. Luo. "Thermal runaway, flash sintering and asymmetrical microstructural development of ZnO and ZnO-Bi_2O_3 under direct currents". Acta Mater., vol. 94, pp. 87–100, 2015.

[16] G. Corapcioglu, M. A. Gulgun, K. Kisslinger, S. Sturm, S. K. Jha, and R. Raj. “Microstructure and microchemistry of flash sintered $K_{0.5}Na_{0.5}NbO_3$”. J. Ceram. Soc. Japan, vol. 124, no. 4, pp. 321–328, 2016.

[17] S. K. Jha *et al.*. “The effects of external fields in ceramic sintering”. J. Am. Ceram. Soc., vol. 102, no. 1, pp. 5–31, 2019.

[18] H. Charalambous, S. K. Jha, R. T. Lay, A. Cabales, J. Okasinski, and T. Tsakalakos. “Investigation of temperature approximation methods during flash sintering of ZnO”. Ceram. Int., vol. 44, no. 6, pp. 6162–6169, Apr. 2018.

[19] J. M. Lebrun *et al.*. “In-situ measurements of lattice expansion related to defect generation during flash sintering”. J. Am. Ceram. Soc., vol. 100, no. 11, pp. 4965–4970, 2017.

[20] J. Rödel, K. G. Webber, R. Dittmer, W. Jo, M. Kimura, and D. Damjanovic. “Transferring lead-free piezoelectric ceramics into application”. J. Eur. Ceram. Soc., vol. 35, no. 6, pp. 1659–1681, 2015.

[21] H. Sun, J. Liu, X. Wang, Q. Zhang, X. Hao, and S. An. “$(K,Na)NbO_3$ ferroelectrics: a new class of solid-state photochromic materials with reversible luminescence switching behavior”. J. Mater. Chem. C, vol. 5, pp. 9080–9087, 2017.

[22] J. Pavlič, B. Malič, and T. Rojac. “Microstructural, structural, dielectric and piezoelectric properties of potassium sodium niobate thick films”. J. Eur. Ceram. Soc., vol. 34, no. 2, pp. 285–295, 2014.

[23] R. Pinho *et al.*. “Spark plasma texturing: A strategy to enhance the electro-mechanical properties of lead-free potassium sodium niobate ceramics”. Appl. Mater. Today, vol. 19, p. 100566, 2020.

[24] J. Ma *et al.*. “Composition, microstructure and electrical properties of $K_{0.5}Na_{0.5}NbO_3$ ceramics fabricated by cold sintering assisted sintering”. J. Eur. Ceram. Soc., vol. 39, no. 4, pp. 986–993, 2019.

[25] Y. Wu, X. Su, G. An, and W. Hong, “Dense $Na_{0.5}K_{0.5}NbO_3$ ceramics produced by reactive flash sintering of $NaNbO_3$ - $KNbO_3$ mixed powders”. Scr. Mater., vol. 174, pp. 49–52, 2020.

[26] R. Serrazina, P. M. Vilarinho, A. M. O. R. Senos, L. Pereira, I. M. Reaney, and J. S. Dean. “Modelling the particle contact influence on the Joule heating and temperature distribution during FLASH sintering”. J. Eur. Ceram. Soc., vol. 40, pp. 1205–1211, 2020.

[27] R. Serrazina, C. Ribeiro, M. E. Costa, L. Pereira, P. M. Vilarinho, and A. M. O. R. Senos. “Particle characteristics influence on FLASH sintering of Potassium Sodium Niobate: a relationship with conduction mechanisms”. Materials, vol. 14, p. 1321, 2021.

[28] R. Serrazina, J. S. Dean, I. M. Reaney, L. Pereira, P. M. Vilarinho, and A. M. O. R. Senos. “Mechanism of densification in low-temperature FLASH sintered lead free Potassium Sodium Niobate (KNN) piezoelectrics”. J. Mater. Chem. C, vol. 7, pp. 14334–14341, 2019.

[29] R. Serrazina, A. Tkach, L. Pereira, A. M. O. R. Senos, and P. M. Vilarinho. “FLASH sintered potassium sodium niobate: high performance piezoelectrics at low thermal budget processing”. *SUBMITTED*, 2021.

[30] M. M. Gomes *et al.*. "Revisiting the phase sequence and properties of $K_{0.5}Na_{0.5}NbO_3$ ceramics sintered by different processes". Ceram. Int., vol. 45, no. 6, pp. 8308-8314, 2021.

[31] N. Terakado, R. Sasaki, Y. Takahashi, T. Fujiwara, S. Orihara, and Y. Orihara. "A novel method for stress evaluation in chemically strengthened glass based on micro-Raman spectroscopy". Commun. Phys., vol. 3, no. 1, p. 37, Dec. 2020.

[32] M. E. Fitzpatrick, A. T. Fry, P. Holdway, F. A. Kandil, J. Shackleton, and L. Suominen. "Determination of Residual Stresses by X-ray Diffraction - Issue 2" in Measurement Good Practice Guide, no. 52, Crown, Ed. Teddington, Middlesex, United Kingdom: NPL - National Physical Laboratory, 2005.

[33] B. D. Cullity. Elements of X-ray diffraction. Second. 1978.

[34] B. Malič *et al.*. "Sintering of lead-free piezoelectric sodium potassium niobate ceramics". Materials, vol. 8, no. 12, pp. 8116–8146, 2015.

[35] S. Priya and S. Nahm. "Development of KNN-Based Piezoelectric Materials" in Lead-Free Piezoelectrics, 1st ed., S. Priya and S. Nahm, Eds. Springer, 2012.

[36] A. Tkach, A. Santos, S. Zlotnik, R. Serrazina, and O. Okhay. "Strain-Mediated Substrate Effect on the Dielectric and Ferroelectric Response of Potassium Sodium Niobate Thin Films". Coatings, vol. 8, p. 449, 2018.

[37] K. I. Kakimoto, K. Akao, Y. Guo, and H. Ohsato. "Raman scattering study of piezoelectric $(Na_{0.5}K_{0.5})NbO_3$-$LiNbO_3$ ceramics". Japanese J. Appl. Physics, Part 1 Regul. Pap. Short Notes Rev. Pap., vol. 44, no. 9 B, pp. 7064–7067, 2005.

[38] R. M. Badger. "A Relation Between Internuclear Distances and Bond Force Constants". J. Chem. Phys., vol. 2, no. 3, pp. 128–131, Mar. 1934.

[39] R. M. Badger. "The Relation Between the Internuclear Distances and Force Constants of Molecules and Its Application to Polyatomic Molecules". J. Chem. Phys., vol. 3, no. 11, pp. 710–714, Nov. 1935.

[40] S. Kojima, J. Zushi, Y. Noguchi, and M. Miyayama. "Successive phase transition of lead-free ferroelectric sodium potassium niobate crystals studied by Raman scattering". Ferroelectrics, vol. 532, no. 1, pp. 183–189, 2018.

[41] X. Zhao, J. J. Wang, and L. Q. Chen. "A thermodynamic study of phase transitions and electrocaloric properties of $K_{0.5}Na_{0.5}NbO_3$ single crystals". Appl. Phys. Lett., vol. 116, no. 9, pp. 0–5, 2020.

[42] E. Buixaderas *et al.*. "Lattice dynamics and phase transitions in $KNbO_3$ and $K_{0.5}Na_{0.5}NbO_3$ ceramics". IEEE Trans. Ultrason. Ferroelectr. Freq. Control, vol. 56, no. 9, pp. 1843–1849, 2009.

[43] C. C. Aydiner and E. Üstündag. "Residual stresses in a bulk metallic glass cylinder induced by thermal tempering". Mech. Mater., vol. 37, pp. 201–212, 2005.

[44] J. H. Nielsen, J. F. Olesen, and H. Stang. "Characterization of the Residual Stress State in Commercially Fully Toughened Glass". J. Mater. Civ. Eng., vol. 22, no. 2, pp. 179–185, 2010.

Summary

In this chapter, fully dedicated to the modelling and simulation tools, the time dependent *COMSOL* model was presented and validated in 3.1, however, without a satisfactory coupling with temperature distribution at the micron-scale. Even though the model presents some limitations, section 3.1 allows to conclude:

- There is a dependence of current density and consequent power dissipation (heat dissipation by Joule effect) on the relative orientation of cuboid particles between each other.
- As sharper the particle contacts, the greater the current localization and consequent localized heating by Joule effect.
- Despite the significant Joule heating and non-uniform distribution found for sharp edges contacts, no relevant thermal gradients between particle surfaces and cores were found, which is related with the lack of grain boundary description, as well as thermal dissipation limitations, in the model.
- Joule heating alone does not account for significant temperature gradients in micron-sized particles, even when very sharp contacts are considered.
- Description of particle contact boundaries (grain boundaries) and heat dissipation is mandatory for a more accurate simulation of the process.

In section 3.2, the model was scaled to millimetre-scale. While the particle-to-particle contact features were lost, as a *block* of material was modelled, the coupling between Joule heating, local temperature and thermal dissipation was achieved. A core-surface thermal gradient was identified and a direct relationship between local temperature and local structural stresses (measured by Raman spectroscopy) was established. This section allows to conclude:

- The relationship between FLASH sintering process and consequent local stresses in ceramics was established, due to the combination of FEM techniques and materials characterization (namely, EBSD, XRD and Raman spectroscopy).
- While the FLASH process is efficient in producing secondary phase-free ceramics, keeping a low thermal budget, macroscopic core-localized stresses are present in as-sintered ceramics.

The relevance of simulation tools is undoubtedly shown. Therefore, some simulations will be punctually utilized to explain or demonstrate some experimental features. In accordance with section 3.1, the particle size and shape (and consequent dissimilar particle contacts) should influence the FLASH process; even the thermal treatment of un-sintered compacts should impact the final microstructure. The FLASH sintering mechanisms and the properties of sintered ceramics, proven to be dependent on the FLASH process (section 3.2) will be analysed in the following chapters.

Chapter

4. Effect of powder characteristics and processing parameters on FLASH sintering process

Contents

Preamble

The effect of powder characteristics (as particle size and phase purity) and processing parameters (as thermal cycle, current density and time) will be presented and discussed in this chapter. Like in the previous chapter, each section comprises a specific article, designated as a *contribution*. These include the introduction/motivation, experimental, results and discussion, and conclusions. References of every contribution are presented at the end of each sub-chapter or section.

The chapter is divided in three contributions. Section 4.1 gives a detailed description and characterization of the four different KNN powders produced in this work. The effect of particle size and purity on the FLASH temperature (T_F) and respective conduction process is assessed through dilatometric studies in Constant Heating Rate (C.H.R.) FLASH experiments. Conduction mechanisms are studied through the activation energy determination and comparison with single crystals. In section 4.2, the role of the particle contacts is further studied, however, in this case, with focus on the microstructural consequences of having particles with sharper or smoother (and larger) contacts at the beginning of the FLASH event. To achieve this, C.H.R. FLASH was compared with Isothermal Conditions (I.C.) FLASH. The thermal cycle was used as a vehicle to change the particle-to-particle interaction, therefore, producing differentiated ceramics.

Sections 4.1 and 4.2 are focused on the development of FLASH sintering process during stage I and II of FLASH. On the other hand, section 4.3 is focused on studying the processing parameters during stage III, namely, the current density and holding time, and their influence on the density and grain growth of sintered ceramics.

4.1. Article: Particle characteristics influence on FLASH sintering of Potassium Sodium Niobate: a relationship with conduction mechanisms

Published: https://doi.org/10.3390/ma14051321

Abstract

The considerable decrease in temperature and time makes FLASH sintering a more sustainable alternative for materials processing. FLASH becomes also relevant if volatile elements are part of the material to be processed, as in alkali-based piezoelectrics like the promising lead-free $K_{0.5}Na_{0.5}NbO_3$ (KNN). Due to the volatile nature of K and Na, KNN is difficult to process by conventional sintering. Although some studies have been undertaken, much remains to be understood to properly engineer the FLASH sintering process of KNN. In this work the effect of FLASH temperature, T_F, is studied as a function of the particle size and impurity content of KNN powders. Differences are demonstrated: while the particle size and impurity degree markedly influence T_F, they do not significantly affect the densification and grain growth processes. The conductivity of KNN FLASH sintered ceramics and KNN single crystals (SCs) is compared to elucidate the role of particles' surface conduction. When particles' surfaces are not present as in the case of SCs, the FLASH process requires higher temperatures and conductivity values. These results have implications in understanding FLASH sintering towards a more sustainable processing of lead free piezoelectrics.

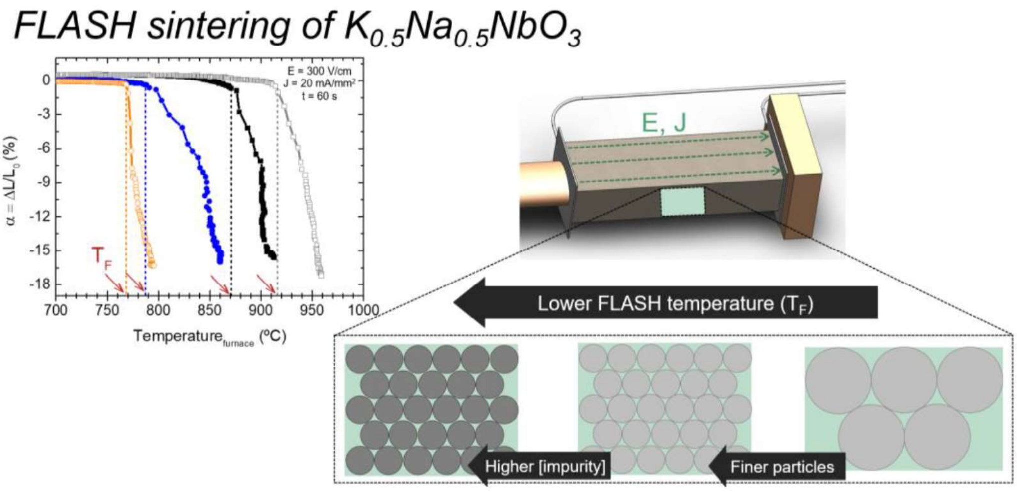

Key words

FLASH Sintering, $K_{0.5}Na_{0.5}NbO_3$, KNN, FLASH temperature, particle size, impurities, conduction mechanisms, ceramics, single crystals

4.1.1. Introduction

FLASH sintering is a powerful technique to sinter ceramics at low temperature in a very short period of time [1]. This occurs by the application of an electric field to a green compact. An increase in the specimen temperature promotes a raise in the conductivity, allowing sintering in seconds. The same is valid for a change in the operating atmosphere [1], [2]. The process is divided into three stages [3]: stage I, the incubation, when the material is externally heated and the electric field promotes the creation and movement of electronic and/or ionic defects; stage II, when the FLASH event takes place at the FLASH temperature, T_F, and heat generated by Joule effect densifies the material at a very high rate; stage III, or steady state, where the current is limited to avoid complete melting.

Recent reports revealed that, rather than applying an electric field to increase the current through the sample, a controlled current rate process produces denser and more uniform ceramics [4], [5]. However, this approach makes difficult to fully understand the role of the conductivity during stage I of FLASH sintering. In the present work, potassium sodium niobate, KNN, a lead-free piezoelectric with technological relevance [6], was used to study the effect of green compact conductivity. Some studies show that the thermal cycle prior to the application of the electric field has a significant influence on the FLASH sintering process of KNN [7]. Additionally, the decrease in T_F was reported to occur with the increase in the applied electric field [8]. However, the impact of the initial powder purity and particle size in T_F and final densification of ceramics was not yet reported.

The strategies to decrease T_F have been associated with the increase in the overall conductivity of the green pellets as for the case of YSZ, ZnO or Al_2O_3 where both the decrease of particle size and the increase of impurity content decrease T_F [9]–[11]. However, the role of particles' surface and their respective contact in semi-conductors (as ZnO) or ionic conductors (as YSZ) is not clear, as FLASH studies in single crystals of these materials reveal ambiguous results [12], [13]. Besides, the conduction mechanisms and the influence of particle characteristics on FLASH sintering of KNN are not known. If KNN is to replace lead-based piezoceramics, its low temperature processing is mandatory, not only for sustainability reasons but also because it is a technological challenge to sinter such alkali-based materials at high temperature [14], [15]. In this work, the KNN FLASH process is studied using KNN powders with different purities and particle size distributions to establish the relation between T_F variation and the particle size and impurity content.

4.1.2. Experimental

$K_{0.5}Na_{0.5}NbO_3$, KNN, powders were prepared by conventional solid-state route (Table 4.1-1). To achieve differences in powder purity, precursors with different purity were used. The final milling process was modified to promote changes on the particle size and morphology. In all cases, the precursors were dried before being mixed (in the stoichiometric amounts) in teflon jars with yttria stabilized zirconia (YSZ) balls (ball:powder ratio of 7:1) and ethanol at 200 RPM, for 6 h. After mixing, the calcination was performed in alumina crucibles at 900 ºC for 3 h, with 10 ºC/min heating and cooling rates.

Table 4.1-1 shows the precursors used to produce two types of calcined KNN powders having different purity which are here labelled as 99% KNN and 99.9% KNN, referring to the minimum precursor purity, respectively. After precursors mixing and calcination, KNN powders of the two batches (99% and 99.9%) were submitted to ball milling (BM) in ethanol, using teflon jars and YSZ media (ball:powder ratio of 7:1), at 200 RPM, for 24 h. The so ball milled powders were designated (Table 4.1-1) as 99% BM and 99.9% BM powders, respectively. To achieve a decreased particle size, a batch of 99% KNN was submitted to attrition milling (AM) at high speed – in this case teflon jars and YSZ balls (ball:powder ratio of 20:1), in ethanol, were used at 700 RPM for 14 h – and the resulting powders designated as 99% AM. A combination of both ball and attrition milling was also selected to decrease the particle size of 99.9% KNN. These powders were firstly ball milled for 12 h, and then attrition milled for 8 h, and designated as 99.9% BM+AM (Table 4.1-1).

Table 4.1-1 – Precursors and experimental details on powder preparation

	Precursors			**Final milling step**			
KNN	K	Na	Nb	Process	Medium	Speed (RPM)	Time (h)
99% BM	K_2CO_3 Merck 99.0%	Na_2CO_3 Chempur 99.5%	Nb_2O_5 Alfa Aesar 99.9%	Ball milling	Ethanol + YSZ balls	200	24
99% AM				Attrition milling		700	14
99.9% BM	K_2CO_3 Sigma-Aldrich 99.99%	Na_2CO_3 Sigma-Aldrich 99.999%		Ball milling		200	24
99.9% BM+AM				Ball + attrition milling		200+ 700	12+8

The produced powders were analysed by scanning electron microscopy (SEM – *Hitachi SU-70, 15 keV*), after being dispersed in ethanol with sonication. The particle size distribution (PSD) was accessed by particle laser diffraction *(Coulter LS-200)* in water and used to estimate the average particle size, D50. The specific surface area (SSA) of the powders was determined by N_2 adsorption in a *Micromeritics Gemini 2.0* equipment, using the Brunauer, Emmett, Teller (BET) adsorption isotherm. The equivalent particle size (D_{BET}) was calculated following equation 2-5 (section 2.4.2).

To access the crystalline structure of the produced powders, X-Ray diffraction (XRD - *PANalytical XPERT-PRO*, with a copper X-ray source ($K\alpha_1$ = 1.54060 Å)) was used. The chemical composition was determined by Inductively Coupled Plasma (ICP) mass spectrometry, by digesting the powders in a mixture of HNO_3 and HF, using microwaves. A 100 ml solution volume was used to determine the content in K, Na, Nb, Al and Zr.

Green compacts (ca. 15 x 5 x 2 mm^3) were shaped by uniaxial (130 MPa, *Carver, model-C*) and an additional isostatic pressing step (200 MPa, *Autoclave Engineers*). For isostatic pressing, compacts were vacuum packed in rubber sleeves. After pressing, samples were characterized by SEM and the particle equivalent spherical diameter ($D_{eq.}$) determined from particle cross section area measurements – at least 500 particles were considered for the determination. The green density was geometrically determined.

FLASH sintering studies were performed in air using the produced KNN powders. An adapted dilatometer was used as previously reported [7], at a constant heating rate (C.H.R.) of 10 ºC/min, an applied electric field of 300 V/cm and a current limit of 20 mA/mm^2. The furnace temperature and the respective sample size variation were recorded using an *in-house* developed software. The *in-situ* conductivity of KNN compacts was determined considering their initial dimensions and by measuring simultaneously the applied electric field and current flow in the system.

Sintered ceramics were analysed by SEM, after being polished and etched (as reported in [7]). The crystal structure of FLASH sintered bodies was studied by powder XRD analysis. The final density of FLASH sintered ceramics was determined geometrically (from mean values of geometrically measured volumes, using at least three different ceramics). To determine the relative density, the above reported value of 4.5 g/cm^3 for the KNN theoretical density was considered.

High density ceramics and single crystals (SCs) were produced to study the electrical conductivity of KNN polycrystalline ceramics and compare it with that of SCs. Ceramics were obtained by FLASH sintering 99.9% BM powders in Isothermal Conditions (I.C.), as reported before [7], at an isothermal furnace temperature of 900 ºC, with 300 V/cm applied after a 30 min dwell, a current limit of 20 mA/mm^2 and a holding time of 60 s. $K_{0.5}Na_{0.5}NbO_3$ SCs were produced by high temperature self-flux method, using 99% calcined KNN powders. The experimental details may be found in [16]. To perform the DC conductivity measurements of KNN bodies (ceramics and SCs), platinum electrodes were painted in ca. 1 mm thick ceramics and SC faces. After a drying step at 50 ºC, the Pt electrodes were cured at 900 ºC for 1h. The electrical conductivity was measured as a function of temperature, using a *Keithley 2410* electrometer. The specimens were heated at a constant rate of 10 ºC/min, from 500 ºC to ca. 950 ºC, with an applied electric field of 1 V/cm. The activation energy for conduction ($E_a(\sigma)$) of KNN bodies, was determined based on an Arrhenius dependence, equation 2-17 (section 2.4.5).

4.1.3. Results and discussion

Powders characterization

Figure 4.1-1 shows the SEM analysis of loose powders (left) and respective green compacts (right). KNN particles are typically cuboid-shaped, which is clearly revealed for the produced powders, namely for the coarsest ones. The particle size distribution (PSD), estimated from particle area measurements, is overlapped with the micrographs in Figure 4.1-1. The data reveal that the two powders that were ball milled (99% and 99.9%) present similar PSD. However, when attrition milling is employed (99% AM), the particle size is decreased, mostly at the expenses of the size reduction of largest particles. This effect is much more pronounced when a combination of ball and attrition milling is used (99.9% BM+AM).

Table 4.1-2 summarizes the obtained specific surface area (SSA) for each powder, together with the average particle size (D_{BET}) determined from SSA, using eq. (2-5), considering a shape factor (SF) for cubes of 7.4. The mean particle size (D50) determined by PSD (D50 – laser) and SEM (D50 – SEM) are shown in Table 4.1-2, for comparison. The particle size D50 determined by the different techniques presents, as expected, different values, but reveals equivalent trends: the coarser powders are the ball milled ones, with 99.9% BM (210-300 nm) being slightly finer than 99% BM (225-350 nm). On the other hand, when attrition milling is used alone (99% AM), particle size is decreased (171 - 210 nm). If ball and attrition milling (99.9% BM+AM) are combined, the particle size is markedly decreased (68 - 150 nm). In this case, the D50 analysis from SEM (150 nm) is bigger than both D50-laser and D_{BET} (86 and 68 nm, respectively). The same tendency was also observed for 99% AM. Difficulties in distinguishing the finer particles in SEM micrographs may have contributed to such observation. It should be noted that the particle size measurements by laser diffraction also presented some difficulties, due to minor KNN solubility in aqueous suspensions, and the agglomeration effects in fine powders. For these reasons, D_{BET} measurements are here considered as the most representative for particle size determination.

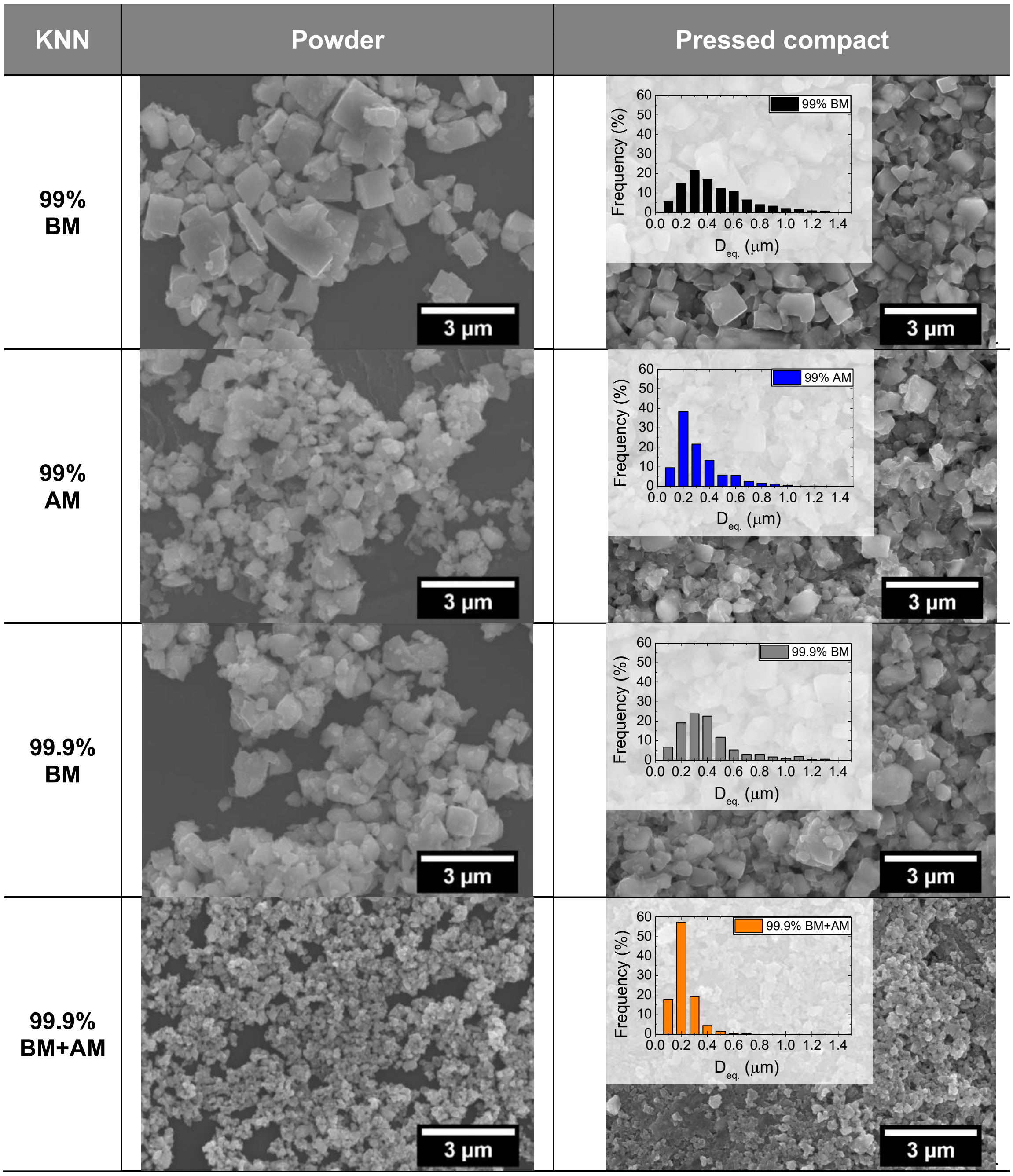

Figure 4.1-1 – SEM micrographs of different KNN powders and pressed compacts with the respective particle size distribution, highlighting the dissimilarities in particle size.

Table 4.1-2 – KNN powders physical characteristics. SSA and respective equivalent particle diameter (D_{BET}), mean particle size from laser diffraction (D50-laser) and SEM images (D50-SEM).

KNN	SSA (m^2/g)	D_{BET} (nm)	D50 - laser (nm)	D50 - SEM (nm)
99% BM	4.75	350	235	350
99% AM	9.61	171	204	210
99.9% BM	7.22	230	210	300
99.9% BM+AM	24.1	68	86	150

In summary, ball milled powders (BM) are the coarsest, while the use of attrition milling (AM) leads to the decrease of the particle size. The combined use of ball and attrition milling (BM+AM) produces the finest powder.

In terms of impurity content, previous work has shown that aluminium is a possible contaminant in our KNN produced powders [14]. Furthermore, zirconium was also considered a possible contaminant from the erosion of YSZ balls during milling. Thus, ICP analysis were performed on the produced KNN powders (Table 4.1-3). Both K/Na and (K+Na)/Nb ratios are, within the experimental error, in accordance with the $K_{0.5}Na_{0.5}NbO_3$ stoichiometry. Al content in 99% powders is ≈1 at%. On the other hand, the use of 99.9% pure precursors was effective to decrease Al contamination to residual values below 0.2 at%. Furthermore, the milling process did not promote relevant contamination from YSZ balls, and Zr content is ≈0.1 at% in all the prepared powders.

Table 4.1-3 – ICP mass spectroscopy analysis of KNN powders: the alkali ratios and the presence of impurities related with the precursor's purity grade.

Powder	K/Na	(K+Na)/Nb	Al (at%)	Zr (at%)
99% BM	1.0 ± 0.1	1.1 ± 0.1	1.1 ± 0.1	0.10 ± 0.01
99% AM				
99.9% BM			0.14 ± 0.01	
99.9% BM+AM				

X-Ray diffraction (XRD) analysis does not reveal neither secondary phases nor relevant structural changes for any of the produced KNN powders (Figure 4.1-2). In fact, all XRD patterns agree with JCPDF file #01-085-7128, a monophasic orthorhombic $K_{0.5}Na_{0.5}NbO_3$ phase. It is worth to notice that 99.9% BM+AM powder XRD pattern presents less sharp maxima, which is another indication of its finer particle size.

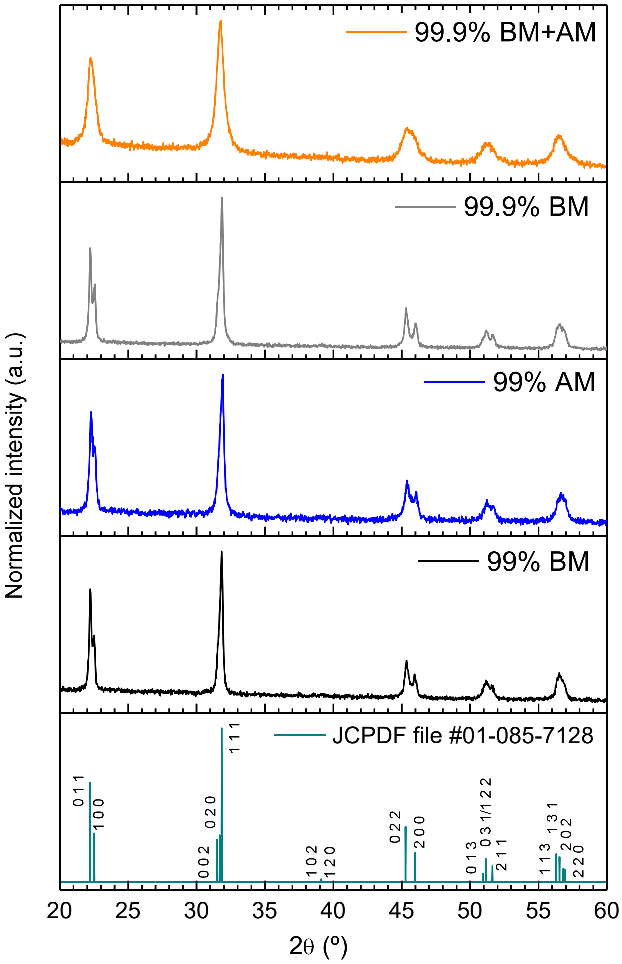

Figure 4.1-2 – XRD patterns of produced KNN powders. JCPDF file #01-085-7128 of orthorhombic $K_{0.5}Na_{0.5}NbO_3$ is included for comparison, and no secondary phases are identifiable.

FLASH sintering experiments

Dilatometric analysis was performed to study the FLASH sintering process of the produced KNN powders. Figure 4.1-3 presents the relative displacement (α) as a function of the furnace temperature during the sintering process. Data points were acquired with 1 s interval.

The very fast shrinkage, typical of FLASH, is observable. The furnace temperature at which FLASH occurs (T_F), is quite dependent on the powder chemical and morphological characteristics. From low to high T_F (dashed lines), the tendency is: 99.9% BM+AM (769 ºC)), followed by 99% AM (785 ºC), 99% BM (870 ºC), being the highest temperature for 99.9% BM (916 ºC) (Figure 4.1-3 a)). These data are summarized in Table 4.1-4. Two relevant powder features that influence T_F must be considered: (i) particle size and (ii) impurity content. Clearly shown in Figure 4.1-3 b), for the same impurity grade, the smaller the particles the lower T_F. In fact, the finest powder (99.9% BM+AM) can present even lower T_F than the other two impure powders with larger particle size, namely 99% AM. Moreover, T_F strongly decreases for similar particle sized powders (171 and 230 nm) with increasing Al-impurity content.

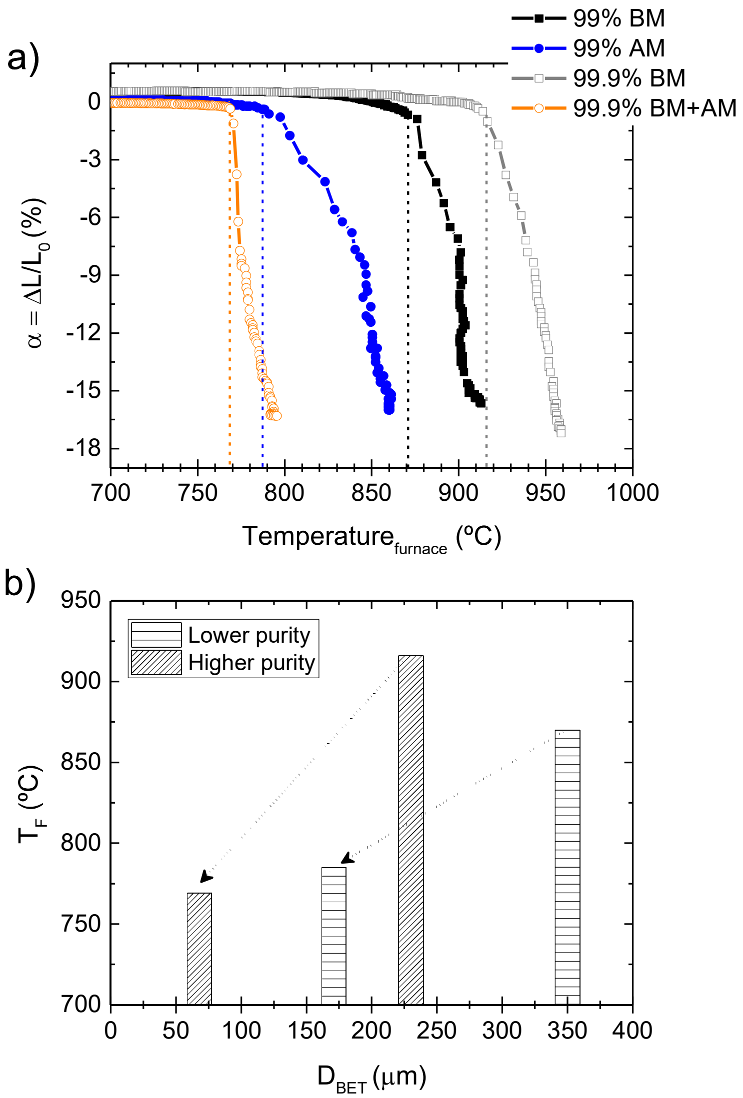

Figure 4.1-3 – a) relative displacement (α) as a function of furnace temperature during FLASH sintering of the produced powders (10 ºC/min heating, 300 V/cm, 20 mA/mm^2 current limit, 60 s holding time); b) schematic representation of T_F versus the particle size (D_{BET}) revealing the tendency of T_F to decrease with particle size diminution and impurity content increase.

Table 4.1-4 - FLASH temperature (T_F), relative densities – green (ρ_{green}) and after sintering (ρ_{sint}) – and mean grain size ($\overline{G_{eq.}}$).

	Compact		FLASH sintered ceramic	
KNN powder	ρ_{green} (%)	T_F (°C)	ρ_{sint} (%)	$\overline{G_{eq.}}$ (μm)
99% BM	63±2	870	89±2	2.4
99% AM	65±2	785	88±3	1.2
99.9% BM	65±1	916	89±1	2.2
99.9% BM+AM	63±2	769	89±1	0.5

In contrast, the final shrinkage registered during the FLASH process is not significantly affected by the powder's characteristics ($-\alpha = 16 - 17\%$). Figure 4.1-4 depicts the chemically etched micrographs of the ceramics, overlapped with the grain size distribution. Table 4.1-4 presents the green density, final density and the respective mean grain size ($\overline{G_{eq.}}$), estimated from the grain size distributions. In accordance with the final shrinkage (Figure 4.1-3 a)), and because the green density of compacts is equivalent (Table 4.1-4), there are no relevant dissimilarities in the final densification of FLASH sintered ceramics. However, grain growth occurred during FLASH sintering of KNN and the final grain size is directly dependent on the starting particle size (Table 4.1-4 and Figure 4.1-4 a to d). Nevertheless, Figure 4.1-4 e) reveals that the normalized grain size (by the respective average grain size of each distribution) is very similar, and such normalization results in a coincident distribution. Additionally, the coarser grains are not larger than ~2.7 x $\overline{G_{eq.}}$, which means that no abnormal grain growth occurred [17], regardless of the purity and PSD differences among the powders. The presence of impurities, usually segregated at grain boundaries, could result in dissimilar grain growth, if a classical grain boundary motion process was occurring [18]. This is not the case, and from the knowledge obtained so far, it is suggested that grain growth occurs by an Ostwald ripening mechanism. In this process, particles that are surrounded by a liquid [7], [14] can grow, in such a way that the finer ones dissolve and the solute precipitates on the coarser particles [19], [20].

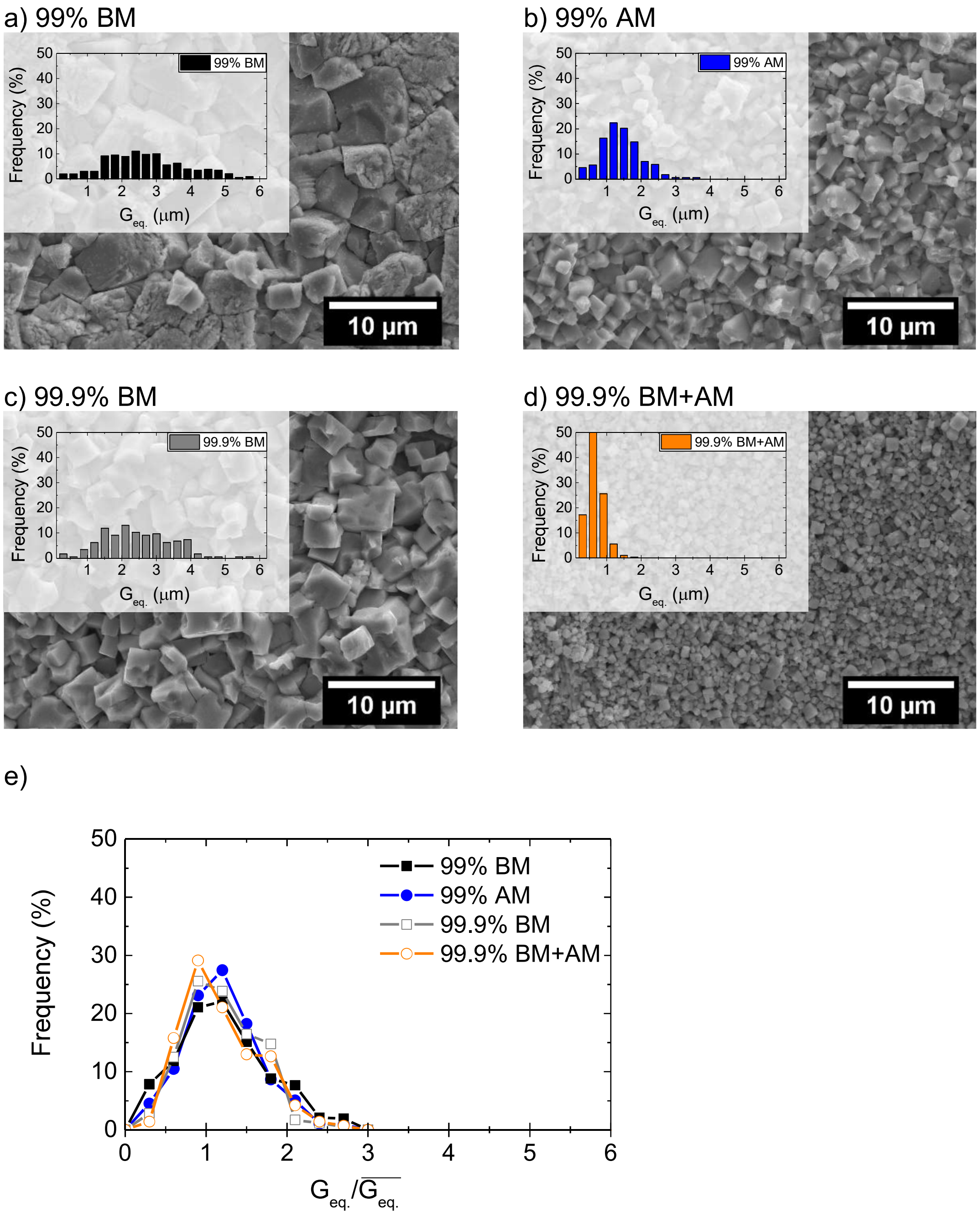

Figure 4.1-4 - SEM micrographs of FLASH sintered ceramics from a) 99% BM, b) 99% AM, c) 99.9%BM and d) 99.9% BM+AM powders, with overlapped respective measured equivalent grain size ($G_{eq.}$) distribution, and e) representation of normalized (with the respective $\overline{G_{eq.}}$) grain size.

The XRD patterns of grinded FLASH sintered ceramics are presented in Figure 4.1-5. As described above, the influence of the particle morphology and impurities on the crystal structure of KNN powders (Figure 4.1-2) seems to be residual. However, Figure 4.1-5 reveals that this is not exactly the case of sintered ceramics. The XRD data indicates that no secondary phases are identified, except for 99.9% BM+AM, which presents Nb-rich secondary phases ($K_{1.3}Nb_{5.8}O_{15}$ and K_3NbO_4, with space groups 127 and 114, respectively). These are the finest powders and because they are more reactive the localized Joule heating might be high enough not only to promote the dissolution of finer particles, but also to locally vaporize alkali elements. This may explain the presence of Nb-rich secondary phases, which is deleterious from the application point of view [21]. In addition, a previously described inversion on the intensity of the first and second XRD reflections occurs for 99.9% BM [7], that might be associated with some degree of preferential orientation of KNN grains, as reported to occur in KNN thin films [22].

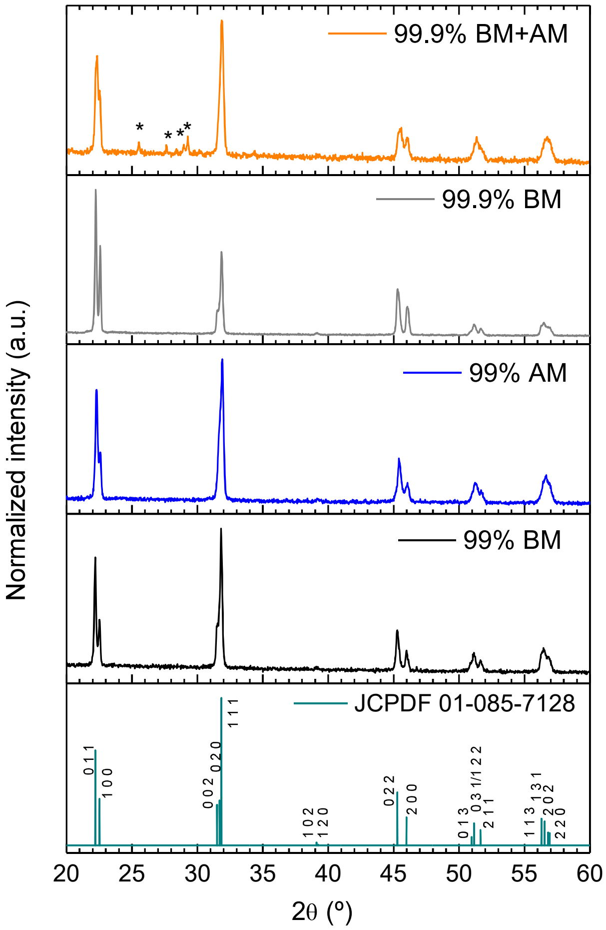

Figure 4.1-5 – XRD patterns of FLASH sintered ceramics. JCPDF file #01-085-7128 of orthorhombic $K_{0.5}Na_{0.5}NbO_3$ is shown for comparison. Nb-rich secondary phases are identified with * for 99.9% BM+AM ceramic.

Therefore, it can be postulated that, while the particle size and impurity degree of KNN powders significantly influence the T_F, the densification and grain growth processes are not appreciably affected, leading to final microstructures with the same densification and near equivalent grain growth (~7 times larger than the initial particle size). KNN phase remains stable in all the tested ceramics with exception of the ones derived from the finest precursor powder, where a secondary Nb-rich phase was detected.

Mechanism of conduction during FLASH sintering of KNN

To identify the reasons behind the significant dependence of T_F on the particle size and impurity content during the FLASH sintering of KNN, the electrical conductivity, σ, of green compacts was accessed (Figure 4.1-6 a)). These measurements were conducted under the same FLASH conditions previously used, i.e., 10 ºC/min heating rate, 300 V/cm electric field, 20 mA/mm^2 current limit and 60 s holding time. In total agreement with Figure 4.1-3 a), a typical *in-situ* FLASH sintering conductivity vs. temperature dependence is revealed for all the samples in Figure 4.1-6 a). A first regime, stage I, with a slower increase of σ with temperature than in the second regime, stage II, where a very fast increase of σ is observed, and a current limited one, stage III, where σ is nearly constant [3]. The transitions between these regimens are approximately identified with red horizontal dashed lines and respective designations in the figure. Despite the overall similar behaviour, the curves presented in Figure 4.1-6 a) reveal the already discussed differences in T_F (see arrows and respective temperatures).

Besides T_F, there are other powder-related features that change during the FLASH process. Figure 4.1-6 b), a magnification of a) for stage I, indicates that 99.9% KNN powders present a very similar stage I behaviour, irrespective of the particle size (BM or BM+AM). It is characterized by a slow and steady increase of σ with temperature. However, for σ > 0.02 S/m, the finest powders (99.9% BM+AM) reveal a faster conductivity increase with temperature. On the contrary, the lowest purity graded KNN powders (99%) present stronger disruptions, especially identifiable for 99% AM, where at least two σ regimes are revealed: i) a first one for σ < 0.015 S/m, and ii) a second one for 0.015 σ < 0.07 S/m (see blue arrow in Figure 4.1-6 b)). This non-uniform increase in σ corresponds to the rather unstable shrinkage behaviour visible in Figure 4.1-3 a).

During stage II (FLASH event) and III (steady stage) there are differences to highlight (Figure 4.1-6 a)). Although stage II seems very similar among the tested KNN powders, 99.9% BM+AM one presents a significantly faster process than the others. Regarding stage III, fine powders (both 99% and 99.9%) display more disperse values of maximum conductivity, while the behaviour of coarse ones is more constant.

As previously discussed, as the size decreases the number of particle-to-particle contacts per unit of volume (contacts density) increases. By considering that a regular body centred cubic (BCC) arrangement of spheres, with a packing factor of 68%, close to the determined ρ_{green} of KNN pellets, would be representative of particle packing in a green KNN body, an average coordination number of 8 can be assumed. In this case, for a particle size decrease from 300 to 100 nm, an increase of about ≈100 times in the density of particle contacts can be estimated. Thus, the overall conductivity of a green compact is expected to be significantly augmented as the number of contact points is increased, leading to the decrease of T_F [1], [23]. Besides, the contribution of surface conduction for the overall conduction is enhanced in relation to that of bulk.

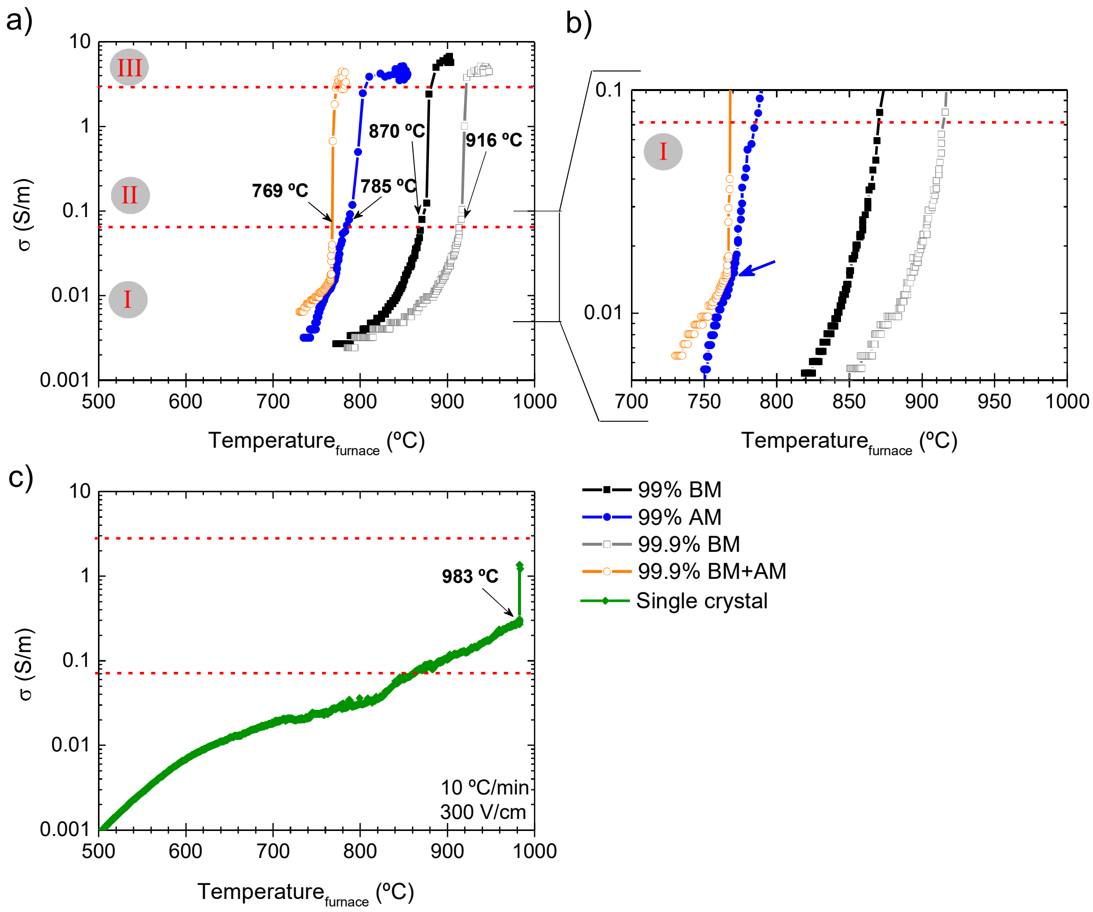

Figure 4.1-6 – DC conductivity dependence (300 V/cm) versus furnace temperature for the a) different four $K_{0.5}Na_{0.5}NbO_3$ powders and c) single crystal (SC). b) shows a detail on the representation of a). The effect of particle size/impurities is observed; additionally, the FLASH sintering of the SC is revealed.

Additionally, as the density of the particle contacts is increased, the number of local electrical discharges is augmented during stage III, raising the dispersion of measured σ values in that stage. In parallel, if the powder impurity degree is increased, the concentration of conductive defects, as interstitials, vacancies, electrons, and holes, is also enhanced, decreasing T_F. This effect was also described for impure and MgO-doped alumina [9], [10].

In face of the proposed explanation for the T_F dependence on the particle size, regarding the relation between particle-contact density and impurity presence contribution for the overall compact conductivity, the role of particle surfaces and contacts for that process must be clarified. In fact, the previously proposed FLASH sintering mechanism of KNN states that the current flows through particle surfaces, in a network of current pathways uniformly distributed in the compact [7], [14], [24]. To truly validate this mechanism, the conductivity of surface versus bulk KNN must be considered. KNN single crystals (SCs) were then used for this purpose.

Figure 4.1-6 c) presents the conductivity behaviour of KNN SCs under similar conditions to those used in FLASH sintering of compacts (Figure 4.1-3 a) and Figure 4.1-6 a)). As a first note, KNN SCs do FLASH (black arrow Figure 4.1-6 c)). However, the FLASH process occurs at higher temperature (T_F = 983 ºC) and conductivity values (σ = 0.3 S/m) than those observed for powder compacts. This observation agrees with the data reported for ZnO [13] and suggests that the presence of particle contacts allows T_F to be decreased as the density of contacts is augmented. Furthermore, SCs exhibit an "activated-state", i.e., a *jump* in conductivity for values higher than 1 S/m (stage III), although the maximum conductivity reached during this stage is lower than that of compacts (σ = 1.4 S/m).

Zhang and co-workers [13] proposed that, in the case of ZnO, enhanced electronic conduction trough the particles surfaces occurs in polycrystals, while it does not occur in SCs. This was the reason pointed for the decrease in T_F, when comparing poly- with single crystals. However, in the case of 8 mol% cubic YSZ, the opposite was reported: SCs presented lower T_F than the respective powder specimens [12]. It was suggested that the surface conductivity in YSZ is lower than the bulk one. However, a detailed explanation for the observation was not provided, as the authors were focused on studying the power dissipation effect, which is very similar in powders and SCs [12].

The reported measurements of *in-situ* conductivity of single and polycrystalline samples fall in debatable accuracy issues, for two main reasons: the dissimilar scale of single crystals (mm) and polycrystalline pellets (cm) and the densification degree of each: fully dense, for SCs, and 35 to 37% porosity in compacts. Issues with scaling of the applied potential for a constant electric field in different sized samples are known [25], as well as the detrimental effects of air (in porous compacts) for conductivity measurements.

Therefore, in this work, due to the interest in understanding the role of particle interfaces in T_F and respective FLASH sintering process, a modified method is proposed to study the conduction mechanisms of KNN powders and SCs. A low magnitude DC electric field (1 V/cm) was used in similar sized, previously densified polycrystalline ceramics and SCs, thus, reducing the influence of external factors such as the scaled electric potential and porosity. 99.9% BM powders were used to produce high-dense polycrystalline FLASH sintered KNN ceramics in Isothermal Conditions (I.C.), as previously reported [7].

The dependence of DC conductivity versus the furnace temperature for FLASH sintered ceramics and SCs is represented in Figure 4.1-7 a). FLASH does not occur under 1 V/cm, either in ceramics or in SCs. The electric field here is significantly lower than the one previously used (300 V/cm). The DC conduction processes in KNN ceramics and SCs is thermally activated, as σ increases with temperature. Furthermore, for temperatures between 500 and ≈710 ºC, SCs present higher conductivity than the equivalent ceramics, whereas the opposite happens for T > 710 ºC. From the best of our knowledge, the high temperature (T > 500 ºC) DC conductivity of KNN ceramics and SCs is here reported for the first time. AC measurements were previously described in our group by Rafiq's *et al.*, for KNN ceramics and SCs, however, for T < 500 ºC [16]. In the present work, the low limit of the DC representation (Figure 4.1-7 a)) is 500 ºC, because at lower temperature the samples are highly resistive thus leading to noisy, not representative, measurements. Even though, a similar trend between AC and DC conductivity measurements is revealed for the temperature range 500 to 710 ºC (Figure 4.1-7 a)); i.e., the conductivity of KNN ceramics is lower than that of SCs. To further understand the conduction process of KNN, the activation energy for conduction ($E_a(\sigma)$) must be estimated.

The Arrhenius representation of the DC conductivity (1 V/cm) for FLASH sintered ceramics and SC is shown in Figure 4.1-7 b) and c), respectively. $E_a(\sigma)$ is calculated for the two temperature regimes, identified in the figures by i and ii (not directly related with FLASH stages I, II or III). The linear regressions (and the respective $E_a(\sigma)$ estimations) are represented with dashed lines; $E_a(\sigma)$ values and respective temperature regimes are summarized in Table 4.1-5. Regimes i and ii occur at different temperatures for ceramics and SC and are differentiated by a low activation energy ($E_a(\sigma) < 1.2$ eV) for the first, and a high activation energy ($E_a(\sigma) > 1.2$ eV) for the second. The transition between each one occurs at T ≈ 710 ºC for ceramics, and at T ≈ 865 ºC for SCs.

Activation energies for conduction in ferroelectric perovskites reported between 0.4 and 1.2 eV are associated with charge transport by oxygen defects, namely, ionized oxygen vacancies [26], [27], which was previously confirmed in KNN ceramics and SCs [16]. On the other hand, $E_a(\sigma) > 1.2$ eV have been associated with ionic-based conduction mechanisms [16]. These activation energies are referred to AC studies. While DC conduction behaviour might be different from the AC one, previous work on vanadium-alumina ceramics revealed that similar values of $E_a(\sigma)$ may be estimated from both DC and AC conductivity measurements [28]. Therefore, it is here assumed that conducting species and respective mechanisms operating at high temperature DC conduction of KNN, namely conducting electrons from ionized oxygen vacancies, are comparable to those previously reported in AC experiments [16]. Additionally, the temperature regimes at which each mechanism is activated can be dependent on the signal. While the contribution of alkaline ions for the conduction (which was previously reported for SCs in AC studies [16]) is not ruled out in the present DC studies at the highest temperatures (where $Ea(\sigma) > 1.2$ eV), their representation might be conditioned by polarization effects at the electrodes [29].

Admitting that a direct link between reported AC-$E_a(\sigma)$ [16] and estimated DC-$E_a(\sigma)$ (this work) are comparable, the data of Figure 4.1-7 b and c) and Table 4.1-5 indicate that, in the case of SCs, while for T < 865 ºC, an oxygen vacancy-based charge transport phenomena occurs ($0.4 < E_a(\sigma) < 1.2$ eV is valid), for T > 865 ºC ionic conductivity might be a contributing mechanism [16]. For ceramics, a similar behaviour is identified, however, the considered ionic conductivity is revealed for T > 710 ºC, as $E_a(\sigma)$ slightly overcomes the 1.2 eV threshold. We assume that the expression of ionic conductivity in both cases can be delayed to higher temperatures, as a consequence of electrode polarization [29]. To undoubtedly establish the alkaline ionic contribution for conduction in KNN SCs and ceramics during DC excitation, further studies shall be conducted. Here, we assume that the condition of $E_a(\sigma) > 1.2$ eV is valid for such mechanism.

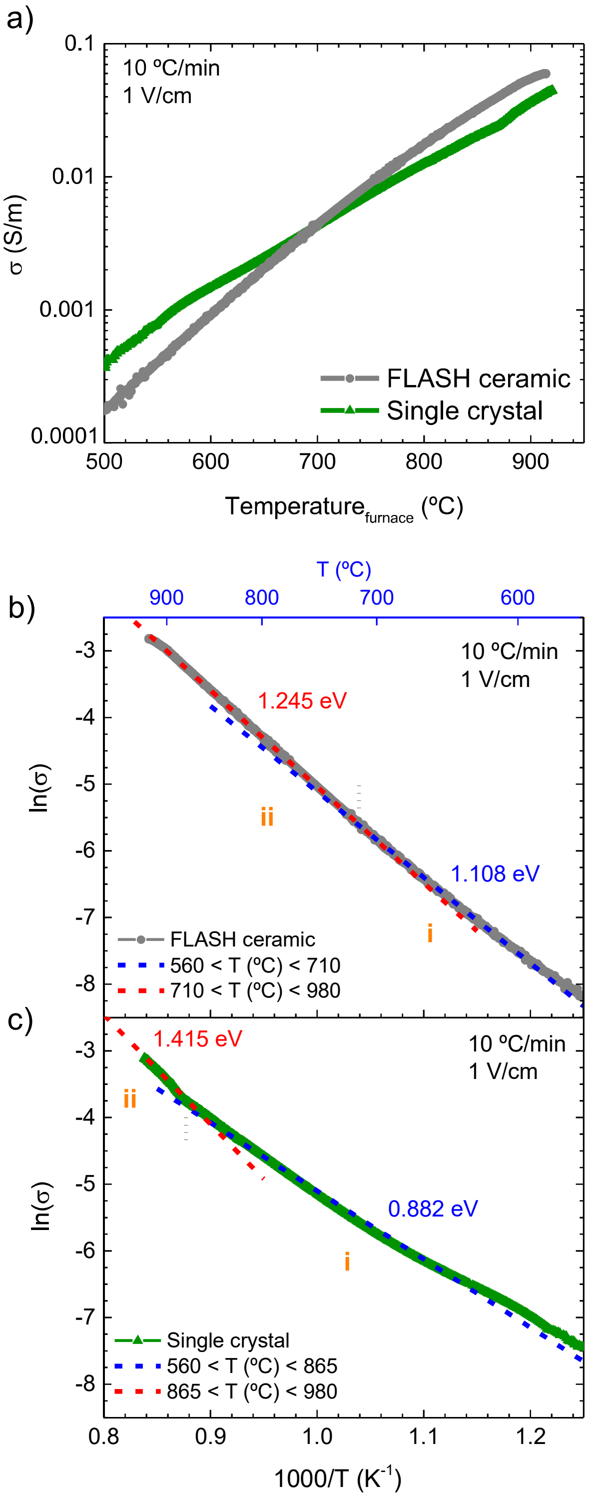

Figure 4.1-7 – a) DC conductivity vs. furnace temperature and respective Arrhenius plot of a) KNN FLASH sintered ceramics and b) single crystal, with applied 1 V/cm electric field. The mechanisms of conduction are depicted by the respective activation energies, calculated for specific temperature regimes (i, and ii).

Table 4.1-5 – Activation energies for the DC conductivity of KNN ceramics and single crystal (SC).

	$E_a(\sigma)$ (eV)	
Temperature range (ºC)	**Ceramic**	**SC**
560 - 710	1.108±0.002	0.882±0.002
710 - 865	1.245±0.001	
865 - 980		1.415±0.009

An additional fact is that ceramics are composed of grains surrounded by grain boundaries (GBs). Hence, the overall DC conductivity of ceramics is limited by that of GBs, as they form a network of pathways surrounding the grains. In AC measurements [16], [30], the conductivity of bulk (grains) and grain boundaries is frequently differentiated, as the conducting species (ions, defects, electrons, polarons, or others) are sensitive to the change in the frequency [27]. While GBs are associated with chemical and structural discontinuities or disorders [31], with higher concentration in electronic defects and impurities, their low-temperature conductivity is typically lower than that of grains [32]. This occurs because such defects and impurities are localized, creating Schottky barriers for the charge carrier transport. In fact, A. Tkach *et al.* have shown, through impedance spectroscopy, that in $SrTiO_3$ (at T < 600 ºC) the conductivity of GBs is, if not lower, similar to that of grains [30]. These facts may explain the lower DC conductivity of KNN ceramics at low temperature (T < 710 ºC) in comparison with that of SCs (Figure 4.1-7 a)). Furthermore, it may also explain the higher activation energy for conduction observed for ceramics, in comparison with SCs, during regime i (Table 4.1-5).

However, literature reports that the grain boundary space charge layer width can reach ≈100 nm [32] and, in semiconductors, for small grain sizes, the width of space charges can be high enough to allow GB conduction, as the grains became depleted [33]. Thus, the contribution of GBs for conduction may be increased by the raise in the volume ratio of GB/grain. Nonetheless, in the present study, GB conduction is only revealed at high temperature (T > 710 ºC), with the conductivity of ceramics overcoming that of SCs. At such point (T ≈ 710 ºC), the temperature is high enough to allow ionic mobility at the GBs of ceramics. Thus, the overall ceramic conductivity is increased, with a correspondent increase in the activation energy [16]. In SCs, the ionic conduction (from bulk KNN) is only revealed at higher temperature (T > 865 ºC).

The proposed mechanism for GB-based conduction in ceramics is in good agreement with the observations of T_F decrease with the respective particle size decrease, as the volume ratio of surface/bulk is increased. Furthermore, the fact that the FLASH sintering of KNN compacts occurred at lower temperature than that of SCs is also explained, in accordance with previous work in ZnO [13]. A direct link between FLASH process and ionic conduction in KNN was found.

In summary, it is suggested that, when the temperature is high enough, the ions (and other conducting species as vacancies) at the ceramics' GBs are thermally activated and the conduction is increased, overcoming the bulk conductivity of SCs. Being a surface phenomenon, as conductive the surface is (high content in impurities) or higher its volume ratio with respect to the bulk (small particle size), the lower the temperature needed to promote a long-range conduction process. When the electric field is high enough, that temperature is T_F. Additionally, our previously reported and proposed particle surface-based KNN FLASH sintering mechanism [7], [14] agrees with the findings presented now.

4.1.4. Conclusions

The dependence of FLASH temperature, T_F, on particle size and impurity content of KNN powders was studied. It is concluded that while the densification and grain growth processes of FLASH sintered KNN ceramics are not affected by the particle size and impurity content of precursor powders, T_F is. This is due to the raise in the density of particle contacts with the decrease on particle size. We propose that the DC electrical conduction of ceramics is dominated by the grain boundaries, which is directly linked with the development of the FLASH sintering as a particle surface conductivity process. Thus, as smaller the particle size, and greater the concentration of impurities, the lower the T_F. This work shows that, the density of particle contacts and surface-based conduction mechanisms dictate the FLASH temperature.

4.1.5. References

[1] M. Biesuz and V. M. Sglavo. “Flash sintering of ceramics”. J. Eur. Ceram. Soc., vol. 39, no. 2–3, pp. 115–143, 2019.

[2] M. Cologna, B. Rashkova, and R. Raj. “Flash Sintering of Nanograin Zirconia in <5 s at 850 °C”. J. Am. Ceram. Soc., vol. 93, no. 11, pp. 3556–3559, Nov. 2010.

[3] S. K. Jha, K. Terauds, J. Lebrun, and R. Raj. “Beyond flash sintering in 3 mol % yttria stabilized zirconia”. J. Ceram. Soc. Japan, vol. 124, no. 4, pp. 283–288, 2016.

[4] H. Charalambous, S. K. Jha, K. H. Christian, R. T. Lay, and T. Tsakalakos. “Flash Sintering using Controlled Current Ramp”. J. Eur. Ceram. Soc., vol. 38, no. 10, pp. 3689–3693, Aug. 2018.

[5] M. K. Punith Kumar, D. Yadav, J. M. Lebrun, and R. Raj. “Flash sintering with current rate: A different approach”. J. Am. Ceram. Soc., vol. 102, no. 2, pp. 1–13, 2018.

[6] C.-H. Hong *et al.*. “Lead-free piezoceramics and Where to move on?”. J Mater., vol. 2, pp. 1–24, 2016.

[7] R. Serrazina, A. M. O. R. Senos, L. Pereira, J. S. Dean, I. M. Reaney, and P. M. Vilarinho. “The Role of Particle Contact in Densification of FLASH Sintered Potassium Sodium Niobate”. Eur. J. Inorg. Chem., vol. 2020, no. 39, pp. 3720–3728, 2020.

[8] G. Corapcioglu, M. A. Gulgun, K. Kisslinger, S. Sturm, S. K. Jha, and R. Raj. “Microstructure and microchemistry of flash sintered $K_{0.5}Na_{0.5}NbO_3$”. J. Ceram. Soc. Japan, vol. 124, no. 4, pp. 321–328, 2016.

[9] M. Cologna, J. S. C. Francis, and R. Raj. “Field assisted and flash sintering of alumina and its relationship to conductivity and MgO-doping”. J. Am. Ceram. Soc., vol. 31, no. 15, pp. 2827–2837, Dec. 2011.

[10] M. Biesuz and V. M. Sglavo. “Flash sintering of alumina: Effect of different operating conditions on densification”. J. Eur. Ceram. Soc., vol. 36, no. 10, pp. 2535–2542, 2016.

[11] J. S. C. Francis, M. Cologna, and R. Raj. “Particle size effects in flash sintering”. J. Eur. Ceram. Soc., vol. 32, no. 12, pp. 3129–3136, 2012.

[12] D. Yadav and R. Raj. “The onset of the flash transition in single crystals of cubic zirconia as a function of electric field and temperature”. Scr. Mater., vol. 134, pp. 123–127, 2017.

[13] Y. Zhang, J. Il Jung, and J. Luo. “Thermal runaway, flash sintering and asymmetrical microstructural development of ZnO and ZnO-Bi_2O_3 under direct currents”. Acta Mater., vol. 94, pp. 87–100, 2015.

[14] R. Serrazina, J. S. Dean, I. M. Reaney, L. Pereira, P. M. Vilarinho, and A. M. O. R. Senos. “Mechanism of densification in low-temperature FLASH sintered lead free Potassium Sodium Niobate (KNN) piezoelectrics”. J. Mater. Chem. C, vol. 7, pp. 14334–14341, 2019.

[15] A. I. Orlova and M. I. Ojovan. “Ceramic mineral waste-forms for nuclear waste immobilization”. Materials, vol. 12, no. 16, 2019.

[16] M. A. Rafiq, M. E. Costa, A. Tkach, and P. M. Vilarinho. “Impedance analysis and conduction mechanisms of lead free potassium sodium niobate (KNN) single crystals and polycrystals: A comparison study”. Cryst. Growth Des., vol. 15, no. 3, pp. 1289–1294, 2015.

[17] M. Hillert. “On the theory of normal and abnormal grain growth”. Acta Metall., vol. 13, no. 3, pp. 227–238, 1965.

[18] J. P. Drolett and A. Galiboist. “The impurity-drag effect on grain growth”. Acta Metall., vol. 16, pp. 1387–1399, 1968.

[19] M. N. Rahaman. Ceramic processing and sintering, Second edition. New York: Marcel Dekker, Inc., 2003.

[20] R. M. German. Sintering Science: An Historical Perspective, First edition. California: German Materials Technology, 2016.

[21] S. Priya and S. Nahm. “Development of KNN-Based Piezoelectric Materials” in Lead-Free Piezoelectrics, First edition, S. Priya and S. Nahm, Eds. Springer, 2012.

[22] A. Tkach *et al.*. “Effect of solution conditions on the properties of sol–gel derived potassium sodium niobate thin films on platinized sapphire substrates”. Nanomaterials, vol. 9, no. 11, pp. 1–14, 2019.

[23] J. S. C. Francis and R. Raj. “Flash-Sinterforging of Nanograin Zirconia: Field Assisted”. J. Am. Ceram. Soc., vol. 95, pp. 138–146, 2012.

[24] R. Serrazina, P. M. Vilarinho, A. M. O. R. Senos, L. Pereira, I. M. Reaney, and J. S. Dean. “Modelling the particle contact influence on the Joule heating and temperature distribution during FLASH sintering”. J. Eur. Ceram. Soc., vol. 40, pp. 1205–1211, 2020.

[25] J. V. Campos *et al.*. “Flash sintering scaling-up challenges: Influence of the sample size on the microstructure and onset temperature of the flash event”. Scr. Mater., vol. 186, pp. 1–5, Sep. 2020.

[26] A. Peláiz-Barranco, J. D. S. Guerra, R. López-Noda, and E. B. Araújo. “Ionized oxygen vacancy-related electrical conductivity in $(Pb_{1-x}La_x)$ $(Zr_{0.90}Ti_{0.10})_{1-x/4}O_3$ ceramics”. J. Phys. D Appl. Phys. Phys., vol. 41, pp. 1–5, 2008.

[27] O. Raymond, R. Font, N. Suárez-Almodovar, J. Portelles, and J. M. Siqueiros. “Frequency-temperature response of $Pb(Fe_{1/2}Nb_{1/2})O_3$ ferroelectromagnetic ceramics obtained by different precursors. Part I: Structural and thermo-electrical characterization”. J. Appl. Phys., vol. 97, no. 084107, pp. 1–8, 2005.

[28] S. Seethalakshmi, B. Subramanian, A. Bendavid, and A. K. N. Kumar. “AC, DC conduction and dielectric behaviour of solid and liquid phase sintered Al_2O_3-15 mol% V_2O_5 pellets”. Ceram. Int., vol. 43, no. 3, pp. 3202–3211, 2017.

[29] P. Ben Ishai, M. S. Talary, A. Caduff, E. Levy, and Y. Feldman. “Electrode polarization in dielectric measurements: A review”. Meas. Sci. Technol., vol. 24, no. 10, pp. 1–21, 2013.

[30] A. Tkach, L. Amaral, P. M. Vilarinho, and A. M. R. Senos. “Oxygen vacancies as a link between the grain growth and grain boundary conductivity anomalies in titanium-rich strontium titanate”. J. Eur. Ceram. Soc., vol. 38, no. 6, pp. 2547–2552, 2018.

[31] D. R. Clarke. “Grain boundaries in polycrystalline ceramics”. Annu. Rev. Mater. Sci., vol. 17, pp. 57–75, 1987.

[32] R. Waser and R. Hagenbeck. “Grain boundaries in dielectric and mixed-conducting ceramics”. Acta Mater., vol. 48, no. 4, pp. 797–825, 2000.

[33] G. K. Deyu, J. Hunka, H. Roussel, J. Brötz, and A. Klein. “Electrical Properties of Low-Temperature Processed Sn-Doped In_2O_3 Thin Films: The Role of Microstructure and Oxygen Content and the Potential of Defect Modulation Doping”. Materials, vol. 12, no. 2232, pp. 1–16, 2019.

4.2. Article: The role of particle contact in densification of FLASH sintered Potassium Sodium Niobate

Published: https://doi.org/10.1002/ejic.202000458

Abstract

Potassium sodium niobate, $K_{0.5}Na_{0.5}NbO_3$ (KNN) is a lead-free piezoelectric with the potential to replace lead zirconate titanate (PZT) in electromechanical applications. Due to its cuboid particle morphology and volatile elements, monophasic and dense ceramics are difficult to obtain via conventional sintering. In this work, isothermal FLASH sintering produced uniformly densified KNN ceramics at 900 ºC, 200 ºC lower than conventional sintering. Specific surface area (SSA) analysis of *pre-FLASH* ceramics revealed that a 30 min isothermal hold at 900 ºC, before the application of electric field, increased the contact area between particles and was crucial to promote uniform densification. Finite element modelling (FEM) revealed why density is more uniform when using isothermal heating compared with a constant heating rate, commonly used in FLASH sintering. These results extend our understanding of FLASH sintering and illustrate its relevance for the development of lead-free piezoelectrics.

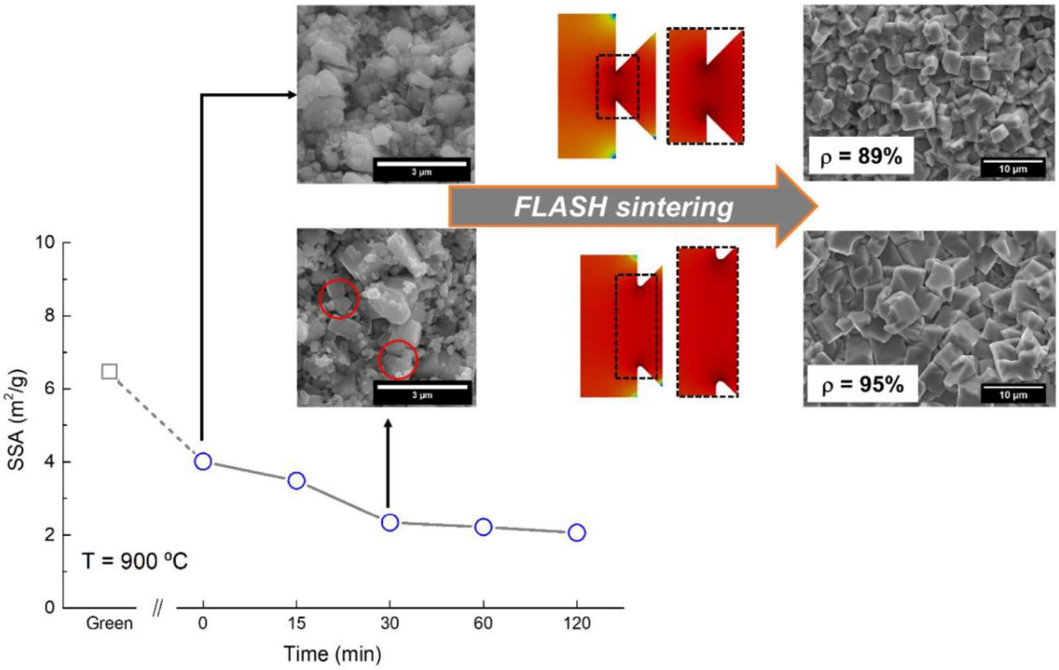

Key words

FLASH sintering, potassium sodium niobate, KNN, isothermal, Finite Element Modelling, lead-free piezoelectrics

4.2.1. Introduction

Potassium sodium niobate, $K_{0.5}Na_{0.5}NbO_3$ (KNN), is a promising lead free piezoelectric but it is difficult to densify by conventional sintering due to alkali volatilization (K and Na) at T > 1100 ºC [1], [2]. Further knowledge of the influence of ceramic processing on the fabrication of stoichiometric KNN is therefore, crucial if it is to replace $Pb(Zr_{1-x}Ti_x)O_3$ (PZT) [2]. KNN presents a relatively low piezoelectric coefficient when compared with PZT, however, a significantly higher transition temperature (ca. 420 ºC) [3]. Piezoelectric properties of KNN may be increased (up to 650 pC/N) if what was described as a New Phase Boundary (NPB) is constructed [4], or by doping [5], similarly to what was done for PZT.

However, the processing of KNN needs to be improved to realize homogenous ceramics with optimised, reliable and thermally stable electromechanical properties. Within this context, alternative sintering techniques have been developed, many of which exhibit lower thermal budgets than conventional methods. Among such methods, FLASH is capable of sintering a wide variety of ceramics at significantly lower temperature and time than conventional processes [6]–[8].

FLASH is a very fast, low-temperature, sintering technique, in which an electric field is directly applied to a green body. At a specific combination of electric field, temperature and/or atmosphere, densification occurs in a short period of time, typically a few seconds ($\leq$ 60 s) [7]. The mechanism of FLASH sintering depends on the material, but is typically associated with thermal runaway promoted by Joule heating [9], [10]. The electric field induces defect migration, most probably through grain boundaries, that often contain a transient liquid phase that also permits particles to slide, further aiding densification [11]. The speed of FLASH sintering is a crucial factor to promote densification. However, the net microstructure is far from equilibrium, with a high probability of inhomogeneous densification, grain growth and properties [12], [13]. Consequently, microstructural heterogeneities become problematic for larger and geometrically complex specimens [6], [14]. In a typical FLASH process, a constant electric field is applied directly to the ceramic, along with a constant heating rate step. When the material becomes sufficiently conductive, FLASH occurs, with a rapid increase of current density and shrinkage at which point current flow must be limited to avoid melting [7], [15].

When performed as described above, FLASH is designated as a Constant Heating Rate (C.H.R.) process, with three different stages: I) incubation, II) FLASH event and III) steady-state [16]. However, isothermal conditions (I.C.) may be used at the so-called FLASH temperature, for which the electric field is applied after a dwell time. After the application of the electric field, incubation allows the current to flow and FLASH to occur, followed by the same three stages mentioned above. The result is, typically, a higher degree of densification and a more uniform microstructure in comparison with C.H.R. FLASH [7], [17]. Recently, it has been reported that the degree of densification and uniformity can be further improved when current density is monitored and increased with a constant rate, either in C.H.R. or I.C. [18], [19].

Several research groups have already reported the densification of KNN [10], [20], [21]. Furthermore, a reactive-FLASH process has been used to produce monophasic KNN from a 50 mol.% mixture of $KNbO_3$ and $NaNbO_3$ [22]. Initial studies reported that dog-bone shaped KNN ceramics may be FLASH sintered in 30 s to 94% theoretical density at 990 ºC under 250 V/cm and 20 mA/mm^2. It was postulated that a core-shell of Na-K was formed to account for preferential heating at particle surfaces and Na volatilization [20].

Recently, we have suggested that current flow through grain boundaries is a possible mechanism for the FLASH densification of KNN, resulting in amorphization and particle sliding [10], [21]. Despite these advances, it remains unclear how to control the shrinkage. Moreover, if our theory is correct, then *pre-FLASH* microstructure, i.e., the green pellet particle-particle contacts and arrangement, must have an influence on the shrinkage uniformity and specimen final density.

In this work therefore, we have used different cycles (C.H.R. and I.C.) to produce KNN by FLASH to identify the influence of an isothermal step prior to the application of an electric field. Beyond the expected thermal uniformity, we propose that the isothermal step allows neck formation and particle contact uniformity, which triggers a more controlled and homogeneous current density distribution, ultimately leading to improved densification and microstructure. Finite Element Modelling (FEM) simulations provide key information on current flow through isothermally and non-isothermally heated KNN.

4.2.2. Experimental

Ultra-high purity alkali carbonates (K_2CO_3, Sigma-aldrich, 99.99% and Na_2CO_3, Sigma-aldrich, 99.999%) and niobium oxide (Nb_2O_5, Alfa Aesar, 99.9%) were weighed and mixed to produce $K_{0.5}Na_{0.5}NbO_3$ powders by a conventional solid-state route, producing what was previously designated as 99.9% BM powders. Green compacts (ca. 15 x 5 x 2 mm^3) were uniaxially (130 MPa) and isostatically (250 MPa) pressed, to 65 $\pm$ 2 % green density. After pressing, pellets were conventionally and FLASH sintered in a horizontal adapted dilatometer, using a contacting alumina rod to record shrinkage, with a sensor spring force of 1.4 N. All sintering steps (both FLASH and conventional) were performed in air, with constant heating and cooling rates of 10 ºC/min. Conventional sintering was performed at 1100 ºC for 1 h.

Constant heating rate (C.H.R.) FLASH experiments were performed at 300 V/cm DC electric field applied through two opposite platinum sheets. The power supply (*EPS HV 5006-400*) was automatically switched from voltage to current control when the limit of 20 mA/mm^2 was reached. The limited current was kept for 60 s and the furnace cooled after the FLASH. Isothermal condition (I.C.) FLASH was performed without any applied electric field until the furnace reached 900 ºC. At such temperature, a 30 min dwell was employed, and the 300 V/cm electric field was applied after the isothermal step. Following an incubation time, the pellets FLASH sintered with similar conditions of limiting current to C.H.R. FLASH. Table 4.2-1 shows the thermal cycle and FLASH conditions of the different sintering experiments in this work.

Table 4.2-1 – Sintering experimental conditions used in this work to sinter KNN ceramics by conventional and FLASH processes.

Specimen		**Heating/ cooling rate (ºC/min)**	**$T_{Furnace-max}$ (ºC)**	**Isothermal time (min) (at T_{max})**	**Electric field (V/cm)**	**Current density (mA/mm^2)**
Conventional		10 ºC/min	1100	60	0	0
FLASH	**C.H.R.**		900	0	300	20
	I.C.		900	30	300	20

During the sintering experiments, the specimen temperature was recorded with an S-type thermocouple located 5 to 7 mm from the ceramic body. Relative displacement, voltage and current were registered using home-made software, with data acquisition each 1 s. Electric field, current density and power dissipation were calculated from the initial dimensions of green compacts.

To determine the ideal time before FLASH in Isothermal Conditions (I.C. 30 min) and to understand its influence on the particle contacts, KNN green compacts were heated to 900 ºC for 15, 30, 60 and 120 min, without electric field. 900 ºC was chosen as the FLASH temperature (T_F) based on previous C.H.R. experiments. The Specific Surface Area, SSA, of each pre-sintered sample was measured by the Brunauer, Emmett, Teller method, BET (*Micromeritics Gemini 2.0*). A pre-measurement drying step of 12 h at 120 ºC was conducted in nitrogen. Relative densities were estimated considering the geometry of the pellet and the theoretical density of KNN (4.5 g/cm^3).

Scanning and transmission electron microscopy, SEM (*Hitachi SU-70*), TEM (*JEOL JEM 2200-FS)* and STEM (*Hitachi HD-2700*) were used to study the microstructure of dense ceramics. For SEM, polished samples were etched 5 min in 40 vol% HF to reveal the grain structure. The fracture surfaces of thermally treated samples were also inspected by SEM. For TEM, ceramics were polished with diamond paper in a tripod mounting and a Gatan Precision Ion Polishing System (*PIPS)* ion mill was used to obtain electron transparency. A *PANalytical XPERT-PRO* diffractometer, with a copper X-ray source ($K\alpha_1$ = 1.54060 Å), was used to obtain X-ray diffraction (XRD) patterns of KNN powders and crushed dense ceramics. A step size of 0.026º and accumulation time of 96.39 s was used to acquire XRD data.

COMSOL Multiphysics simulations were carried out to theoretically estimate the current flow and Joule heating as a function of particle contact. Models were based on representative microstructures and SSA results in *pre-FLASH* particle-particle contacts. Simulations were performed as previously reported [10].

4.2.3. Results and discussion

The densification of KNN ceramics was monitored by dilatometry. The length variation as a function of the temperature for conventional, C.H.R. FLASH and I.C. FLASH (30 min at 900ºC) KNN ceramics, is shown in Figure 4.2-1. Typical for a ceramic green body, there is an increase in linear shrinkage, corresponding to densification onset, after a minor expansion. Conventionally sintered KNN starts to shrink at ~1000 ºC and the process is completed after 1 h at 1100 ºC with a decrease in length of 13.5%, corresponding to a measured final density of 91%. When an electric field of 300 V/cm is applied along with C.H.R., KNN sinters at T_F (FLASH temperature) $\approx$ 900 ºC, in agreement with previous work [20]. Approximately 18% shrinkage was achieved after 60 s under current limited conditions and a final furnace temperature of 959 ºC. The total shrinkage of C.H.R. FLASH was higher than that of the conventionally sintered specimen, but its final density was lower (89%). In contrast, when the compacted green ceramic is maintained at 900 ºC for 30 min before the application of the electric field (I.C. FLASH), approximately 14% shrinkage is attained at 942 ºC after sintering. The shrinkage for I.C. FLASH therefore, is similar to that of the conventionally sintered body but the measured total densification is higher (95%) compared with 91% for conventional sintering.

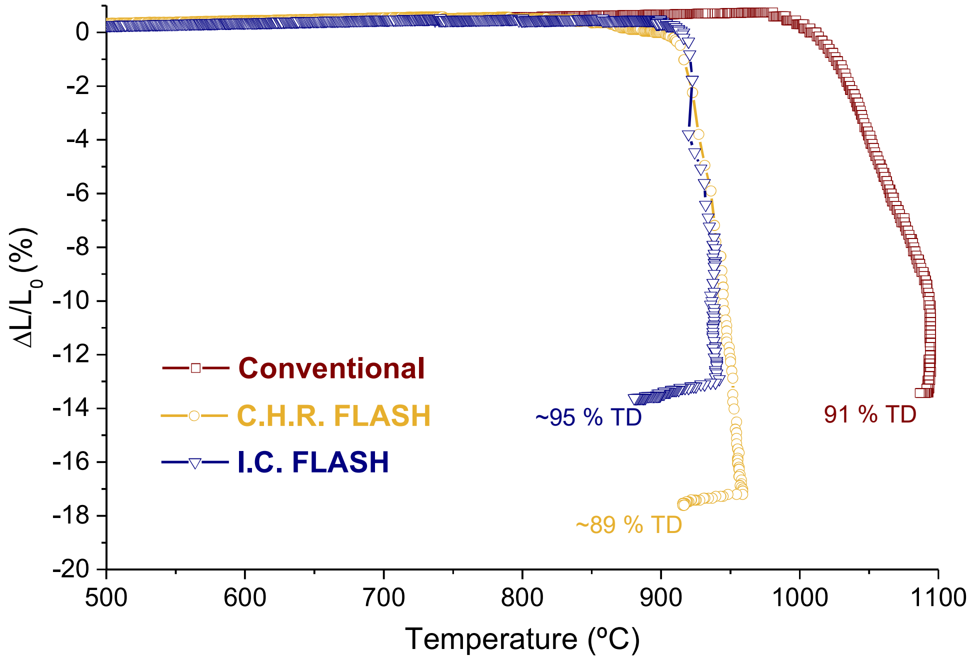

Figure 4.2-1 – Relative displacement in length as a function of measured temperature, from green state, for conventional (□), C.H.R. FLASH (○) and I.C. FLASH (30 min at 900ºC FLASH) (▽) specimens. Indications of the electric field (in V/cm), current density (in mA/mm^2) and final densification of ceramics are given.

To understand the discrepancies between the dilatometer length shrinkage and density, Table 4.2-2 presents the post-sintering shrinkage geometries for all ceramic bodies. At least 3 measurements were taken for each dimension, and an average was considered for calculation. Whereas the shrinkage in radial plan (width x thickness) is near isotropic, it is larger along the length, resulting in discrepancies between the linear shrinkage and measured density. Defining anisotropic shrinkage, f_{as}, as the ratio between the average radial shrinkage, $((\Delta w/w_0)+(\Delta th/th_0))/2$, and the length shrinkage ($\Delta L/L_0$), $f_{as} = 1$ is isotropic and anisotropy increases with a decreasing f_{as}. Conventionally sintered ceramics exhibited an anisotropic shrinkage factor $f_{as} = 0.6$, while that of C.H.R and I.C. FLASH is 0.2 and 0.4, respectively (Table 4.2-2). The observed shrinkage anisotropy in contact dilatometry is attributed to the pressure of the displacement sensor, that is more evident when viscous flow sintering occurs [23]. For direct comparison between samples, green compacts of the same dimension and a constant value of initial sensor pressure of 0.15 MPa were utilised. As a result, the net increase in the anisotropy of shrinkage for FLASH sintered ceramics, e.g. C.H.R. sample ($f_{as} = 0.2$), is directly related to non-uniform densification under an applied electric field, probably associated with viscous flow sintering. Isothermal treatment therefore, prior to the application of the electrical field, created conditions for lower anisotropic shrinkage for FLASH (I.C.) compared with C.H.R. FLASH.

Table 4.2-2 – Post-sintering dimension variation measurements of ceramic bodies in length ($\Delta L/L_0$), width ($\Delta w/w_0$) and thickness ($\Delta th/th_0$), average shrinkage in the three directions ($\Delta S/S_0$) and anisotropic shrinkage (f_{as}) for: conventional, C.H.R. FLASH and I.C. FLASH (30 min at 900ºC).

Ceramic		$\frac{\Delta L}{L_0}$ (%)	$\frac{\Delta w}{w_0}$ (%)	$\frac{\Delta th}{th_0}$ (%)	$\frac{\Delta S}{S_0}$ (%)	f_{as} $\left[\frac{\left(\frac{\Delta w}{w_0}\right)+\left(\frac{\Delta th}{th_0}\right)}{2}\right] / \frac{\Delta L}{L_0}$
Conventional		15.5	8.0	9.5	11.0	0.6
FLASH	**C.H.R.**	22.7	5.1	4.8	10.9	0.2
	I.C. (30 min at 900ºC)	20.6	8.1	7.5	12.1	0.4

To further investigate densification, plots of the furnace temperature are presented in Figure 4.2-2, overlapped with shrinkage behaviour (top graphs), for C.H.R. FLASH (a) and I.C. (30 min at 900 ºC) FLASH (b). Figure 4.2-2 also shows the electric field, current density and power density for C.H.R. (a) and I.C. (b) FLASH. Note that the same x-axis scale (process time) was used for each top and down plot, and t = 0 is FLASH onset in each case. The time scales have different magnitudes for a) and b), because of the different experimental setup (C.H.R. and I.C., respectively). The time t = 0 represents the transition between stage I and stage II of FLASH, with the electric field dropping from 300 V/cm and limited to ~50 V/cm, and the current density rising towards its limit (20 mA/mm^2). At this point, power density spikes and the specimen starts to shrink abruptly.

In both cases (C.H.R. (a) and I.C. (b)), stage I of FLASH starts at t ≈ -60 s. This incubation time is observed for C.H.R. (Figure 4.2-2 a)) by a non-linear increase of the power density (and of the current density) with temperature. For I.C. (Figure 4.2-2 b)), stage I starts immediately after the isothermal step when the electric field is applied. Current and power start to increase, and after incubation (60 s), FLASH occurs. Accordingly, for C.H.R. (Figure 4.2-2 a)), temperature increases as stage II is approached in the final seconds of stage I, while in the case of I.C. (Figure 4.2-2 b)), the temperature increase is distributed throughout stage I.

For both ceramics, after stage III (current limited period of 60 s) is completed, the power source is turned off, and shrinkage stops. At this point, the measured final temperatures are ~959 ºC and 942 ºC for C.H.R. (Figure 4.2-2 a)) and I.C. (Figure 4.2-2 b)), respectively.

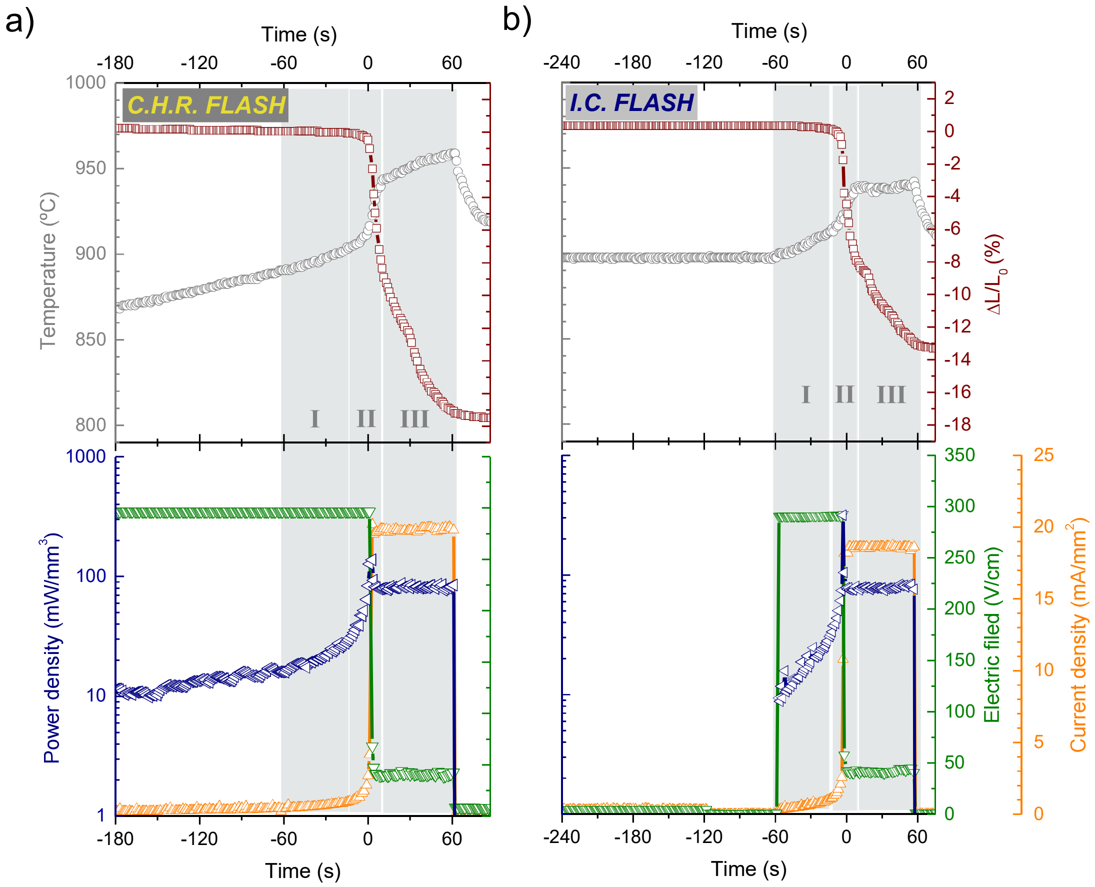

Figure 4.2-2 - Simultaneous representation of in-situ measurements (top graphs) of dilatometric behaviour (□), furnace measured temperature (○) and calculated (down graphs) applied electric field (▽), output current density (△) and power density/dissipation (◁) for a) C.H.R and b) I.C. FLASH specimens. Each dependence has a correspondent y-axis colour for correct reading. x-axis (time scale) is common for top and bottom graphs, and t = 0 s represents the FLASH event.

From Figure 4.2-2, and independent of the thermal cycle used to FLASH sinter KNN, the ceramic body undergoes three typical FLASH stages. The incubation time for both processes (stage I) is similar, implying that the conduction activation mechanism is the same. The increase in temperature is a consequence of thermal runaway with the ceramics dissipating heat to their surroundings. The shrinkage behaviour and temperature increase are markedly different for C.H.R. and I.C. FLASH and are influenced by the compact thermal history. When the electric field is applied along with heating (C.H.R.), the increase in temperature was more abrupt and reached a maximum higher than for I.C. FLASH. In other words, C.H.R. FLASH sintering is faster but less controlled than I.C..

To further analyse the densification of the KNN ceramics (C.H.R. FLASH, I.C. FLASH and conventional), the dependence of the shrinkage derivative with respect to time was calculated and plotted in red in Figure 4.2-3. The maximum shrinkage rate of the FLASH processes (C.H.R. (a) and I.C. (b)) is ~10^{-3} s^{-1}. For both FLASH bodies, the maximum shrinkage rate occurred at t ≈ 0 s, with a pronounced, sharp peak. This peak represents the FLASH onset, with C.H.R. and I.C. FLASH, achieving a shrinkage rate of ~8×10^{-3} s^{-1} and ~5×10^{-3} s^{-1}, respectively. Nevertheless, a second densification maximum is observed at t ≈ 30 s for both, although more evident for C.H.R. In contrast, conventionally sintered KNN exhibits a broader peak, with the maximum shrinkage rate occurring at 1050 ºC. In this case, the maximum shrinkage rate was ca. 1.3×10^{-4} s^{-1}, which is more than one order of magnitude lower than that of the FLASH process.

The shrinkage rate behaviour for conventional and FLASH suggests that densification in the latter, occurring through viscous flow [21], is significantly faster than that of conventional, but the two FLASH processes are also dissimilar. C.H.R. FLASH (Figure 4.2-3 a)) revealed a higher shrinkage rate than that of I.C. FLASH (Figure 4.2-3 b)). This, together with the higher and more abrupt increase in the measured temperature, revealed that stage II is significantly faster in C.H.R than in I.C. FLASH. The secondary shrinkage rate peak at t ≈ 30 s, more evident in C.H.R., occurs during stage III and may be due to further uncontrolled viscous deformation, that could increase the anisotropic shrinkage. However, a clear understanding of the sintering mechanism associated with the observed secondary shrinkage peak remains to be elucidated.

SEM micrographs (Figure 4.2-4) confirm that dense KNN ceramics were obtained after sintering for all the three processes, in agreement with calculated densities, and that the cuboid particle shape was maintained. However, a detailed analysis exposes differences in the microstructures, associated with each sintering process. A more defined grain morphology is observed for FLASH ceramics, suggesting preferential chemical attack at grain boundaries of those samples (Figures 4.2-4 a) and b)). In conventionally sintered KNN, chemical etching is less preferential in grain boundaries, also showing a worm-like morphology inside the grains. These observations show that the grain boundaries of FLASH and conventionally sintered KNN should be different. On the other hand, more uniform grain size was observed for FLASH sintered ceramics (Figure 4.2-4 a) and b)), especially for I.C. FLASH. This observation is related with the role of the isothermal step, that promoted a more controlled and uniform densification during FLASH.

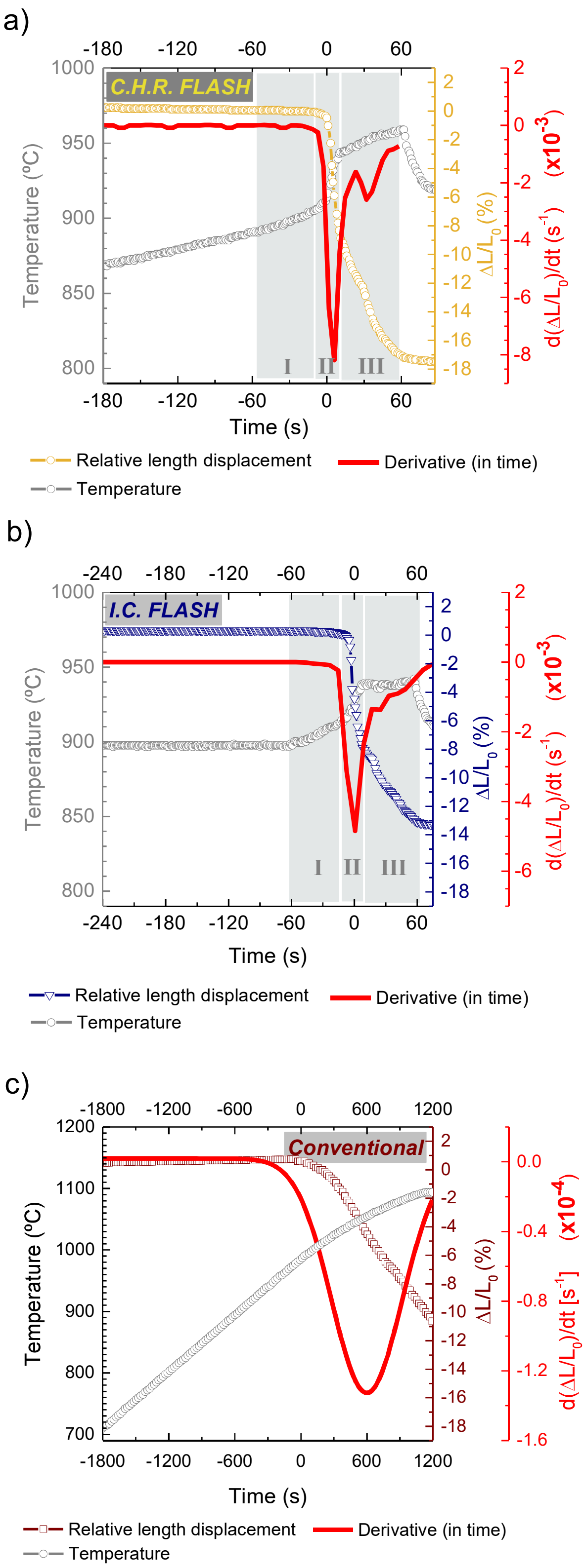

Figure 4.2-3 – Relative length variation (shrinkage) derivative as a function of the time (red line), overlapped with relative length variation for each studied KNN pellet, a) C.H.R. FLASH (○), b) I.C. (30 min at 900 ºC) FLASH (▽), and c) conventional (□). For x-axis, t = 0 s represents the onset of FLASH for FLASH ceramics and the beginning of shrinkage for conventional.

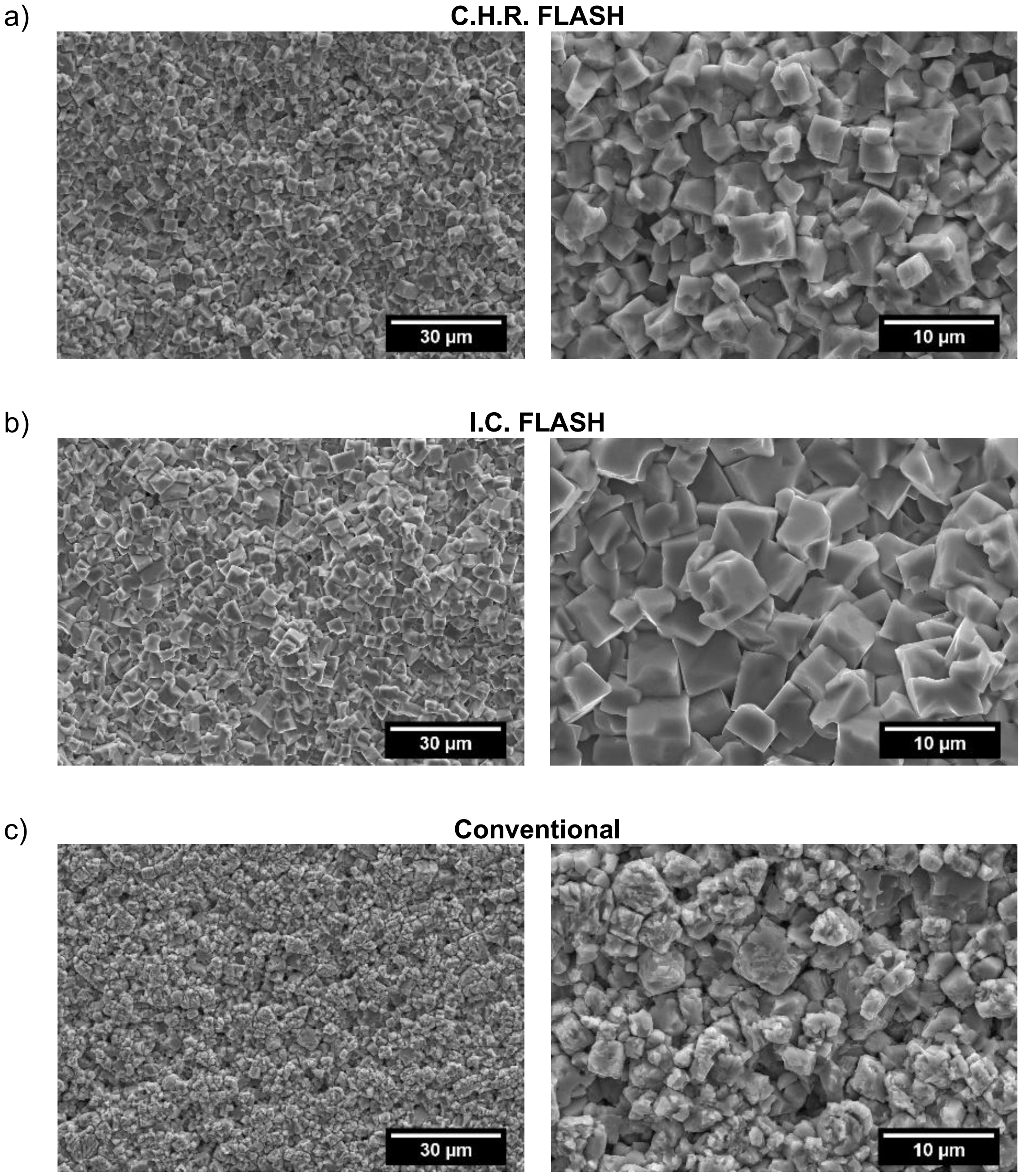

Figure 4.2-4 – Scanning electron microscopy (SEM) micrographs of a) C.H.R. FLASH, b) I.C. FLASH and c) conventionally sintered KNN ceramics, acquired with a 15 keV accelerating voltage at different magnifications, 1000 and 3000 times, left and right, respectively.

To analyse further the microstructures, Transmission Electron Microscopy, TEM, was carried out for I.C. FLASH and conventional ceramics, and representative images are shown in Figure 4.2-5 a) and b), respectively. Since I.C. FLASH produced uniform density, these ceramics ion thinned more evenly and were further characterized and compared with conventionally sintered KNN.

While conventional ceramic TEM micrographs (Figure 4.2-5 b)) show well defined cuboid grains, with no evidence of particle smoothing or contact melting, FLASH sintered TEM micrographs (Figure 4.2-5 a)) revealed that I.C. FLASH promotes rounding of KNN cuboid particles (red arrows) and filling of pores and grain boundaries with a glassy phase (green circles). These observations agree with the mechanisms for FLASH sintering KNN presented in Ref [21] and also with the viscous flow FLASH sintering mechanism already refereed.

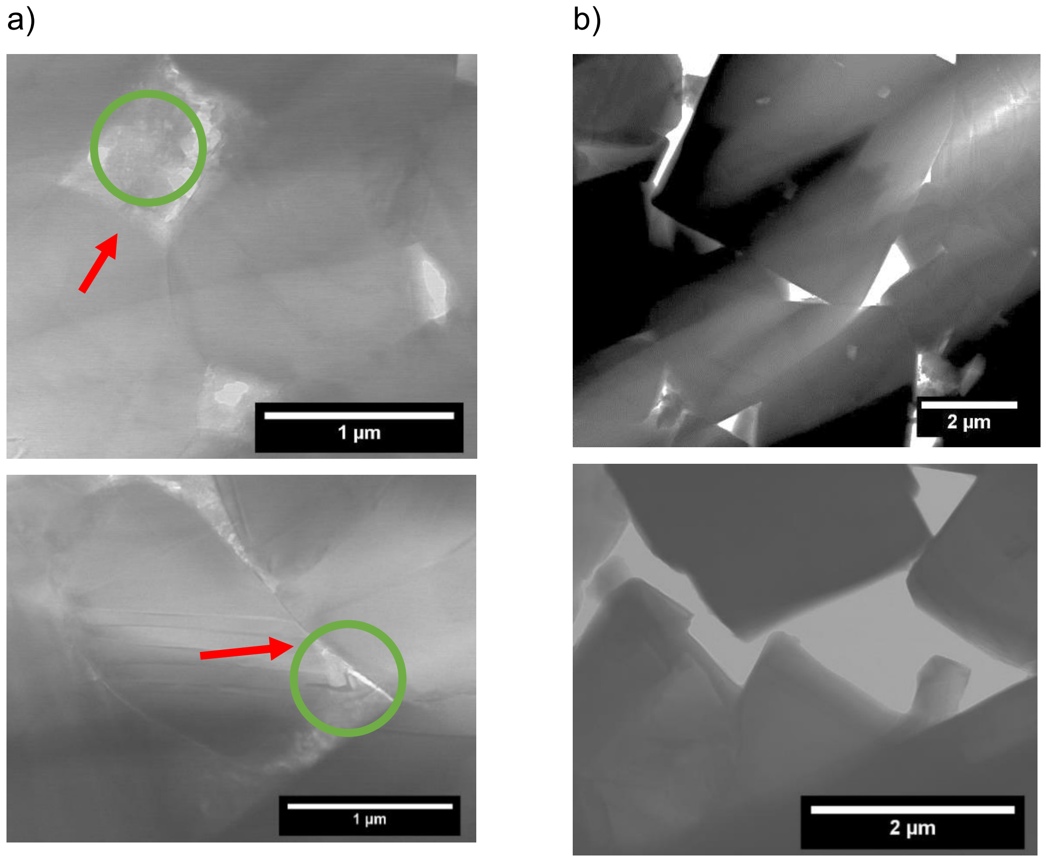

Figure 4.2-5 – Transmission electron microscopy micrographs of I.C. FLASH (a) and conventional (b) ceramics.

Despite these microstructural variations, XRD analysis did not reveal any secondary phase or peak broadening. Both FLASH and conventional ceramics are indexed according to a single perovskite structure, corresponding to the $K_{0.5}Na_{0.5}NbO_3$ (JCPDF file 01-085-7128), as shown in Figure 4.2-6. Conventional and I.C. FLASH ceramics are similar to KNN powders but the C.H.R. FLASH XRD pattern has less defined maxima and an inversion of the relative intensities of the first and second reflections (2θ ~22.5° and ~32°). This inversion indicates preferential grain orientation in (011) and (100), as observed in KNN thin films [24] and is possibly related to the high degree of shrinkage anisotropy in C.H.R. FLASH.

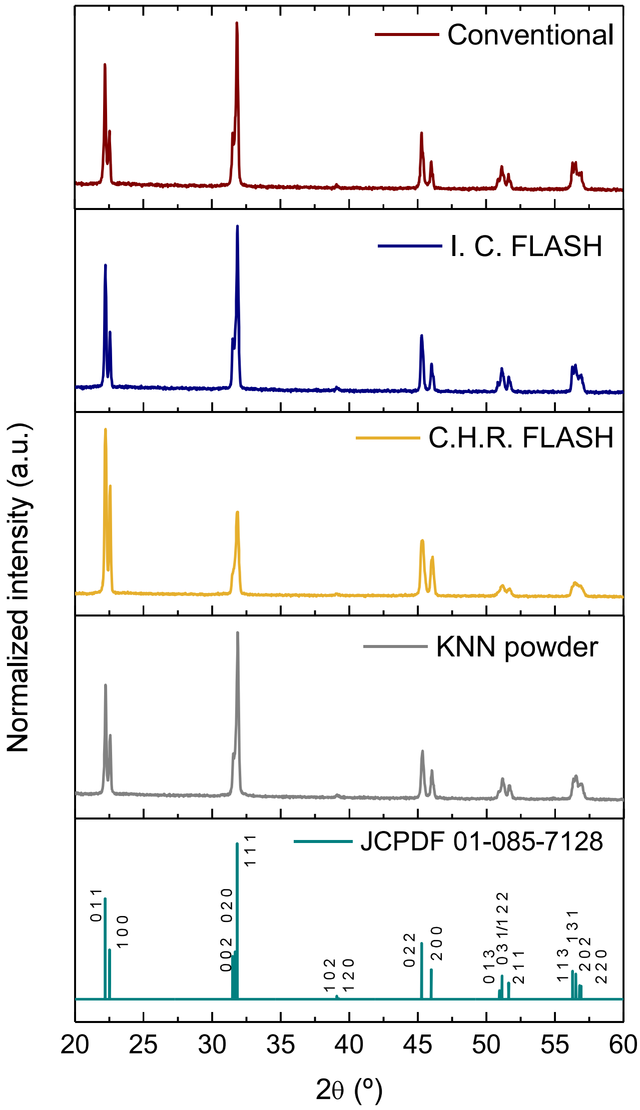

Figure 4.2-6 – Normalized X-ray diffraction patterns of KNN powders and sintered ceramics. JCPDF file 01-085-7128 corresponding to the orthorhombic $K_{0.5}Na_{0.5}NbO_3$ pattern is shown for comparison.

Our results provide evidence of densification as well as microstructural and structural differences between C.H.R. and I.C. FLASH, suggesting that the isothermal step has a significant influence. To further investigate the isothermal effect, Specific Surface Area (SSA) analysis by BET and SEM were conducted, as shown in Figure 4.2-7. Green KNN pellets were heated up to 900 ºC and isothermal steps (without the application of the electric field) were performed for: 0, 15, 30, 60 and 120 min. After each dwell, in which no significant shrinkage was recorded, pellets were cooled and the SSA of each pellet measured. In parallel, cross section SEM micrographs were collected. Green and isothermal sintered bodies are depicted in Figure 4.2-7. The SSA is continuously reduced under the isothermal steps. A decrease from ca. 6.5 m^2/g for the green pellets to ca. 2.3 m^2/g, after 30 min at 900 ºC, corresponding to ~ -64%, was determined and the micrographs clearly show that the isothermal step allowed particles to form necks and continuous contacts (red circles in Figure 4.2-7), not present in the green pellets. Longer isothermal periods (60 and 120 min) bring a more modest decrease of SSA and no relevant alterations of the microstructure are visible between 30 and 120 min.

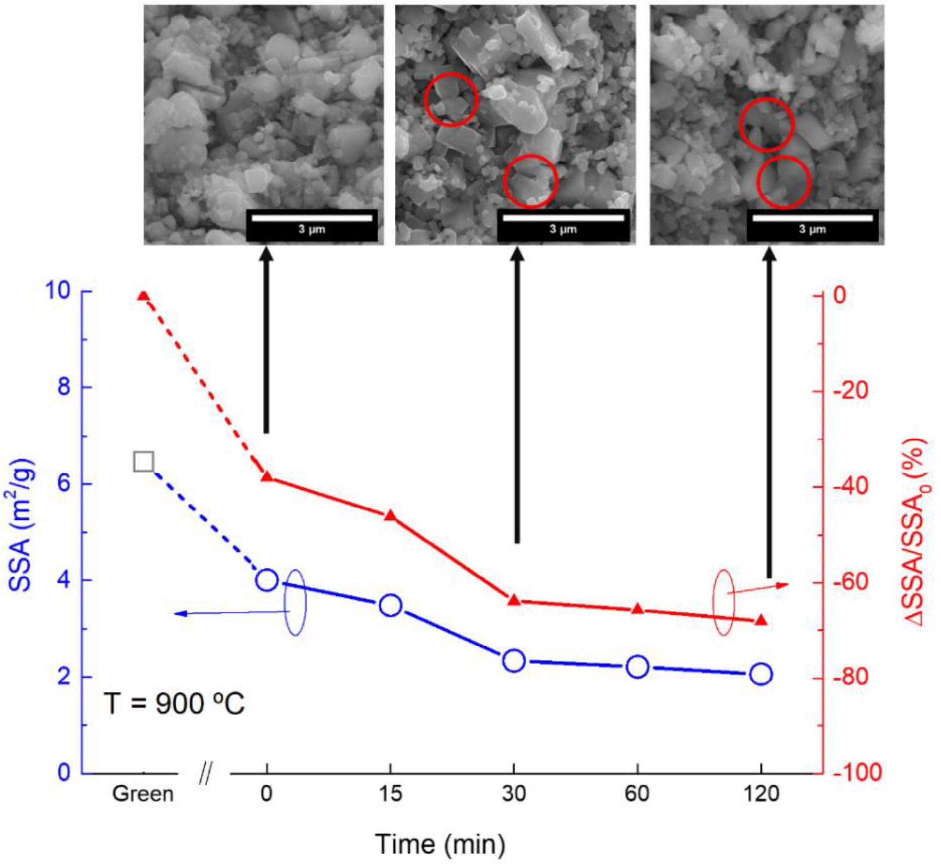

Figure 4.2-7 – Specific surface area (SSA) as a function of the tested compact (in blue). Isothermal compacts are identified with blue circles and the green pellet with a grey square. In red, calculated SSA relative variation: (SSA-SSA$_{Green}$)/SSA$_{Green}$. SEM micrographs of 0, 30 and 120 min isothermal are presented as inset on the graph, respectively from left to right.

Besides neck growth, particle surface smoothing, not detectable in SEM, is also expected to contribute to the SSA reduction. This SSA reduction, occurring without measurable shrinkage, takes place via non-densifying mass transport, as surface diffusion, typical of the initial stage of sintering in fine powders [25].

We have, thus far, gathered experimental evidence that a 30 min isothermal step promotes uniform particle contact, allowing neck formation and development of a dense, homogeneous microstructure compared with conventional and C.H.R FLASH KNN. We propose that neck formation permits a more uniform and continuous path for current flow during FLASH, compared with a green body. However, to support this mechanism, the theoretical distribution of the current and respective Joule heating as a function of the particle-particle contact is required. *COMSOL Multiphysics* software was therefore used to model current flow [10].

Two cuboid particles with 1 μm side size were considered to contact in an edge-face [10] configuration. For simplification, only simulations of stage II of FLASH were performed and a conductivity of 1 S/m (measured during FLASH experiments [10]) assigned to each particle. An electric field of 300 V/cm was scaled and applied to the different arrangements of particles. The modelled particles were designed to contact their neighbouring particle by only one face. Considering that each particle has a free-face surface area of 1 μm^2, an increase in contact area of 20, 40 and 60% represents a respective contact area of 0.2, 0.4 and 0.6 μm^2. These percentages of contact area relate to the observed values for SSA (Figure 4.2-7) but particle rounding also contributes to SSA and is not accounted for in our current study.

As the contact area increased, the model accounts for neck formation with a neck radius of 0.01 and 0.02 μm introduced for 40 and 60%, respectively. The model specification design is shown in Figure 4.2-8, prior to any current and Joule heating simulation.

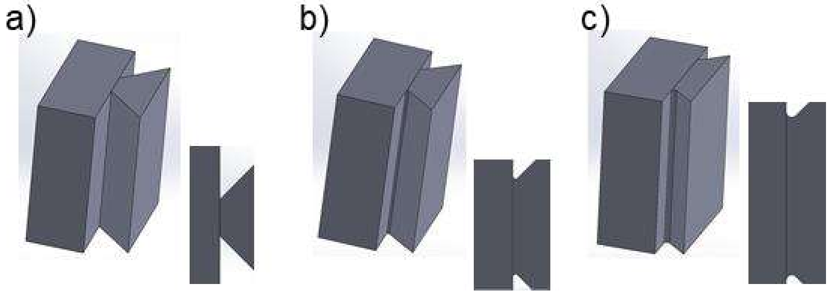

Figure 4.2-8 – Model design of particle-particle contact for a 20% (a), 40% (b) and 60% (c) increase in the area contact of a 1 μm^2 cubic face, with representative neck radius increase.

The simulation results for the current density and volumetric electromagnetic losses due to Joule heating, for the three studied particle arrangements, are plotted in Figure 4.2-9. A 3D view of the simulated results is presented for each case. Some details of planar views (cut through the middle plane) are also shown, specifically the magnification of the Joule heating distribution for 20 and 60% near the particle contacts (dashed lines). For 20% contact area, a particle-particle, corner-localized current density and Joule heating of approximately 10^2 mA/mm^2 and 10^4 mW/mm^3, respectively, occur. In comparison, with 40% contact area, the maximum current density and Joule heating decrease to, ~ 5×10^1 mA/mm^2 and 5×10^3 mW/mm^3, respectively. For 60%, a less localized current density and Joule heating distribution are observed, with maximum values of 10^1 mA/mm^2 and 10^3 mW/mm^3, respectively. These simulations (Figure 4.2-9) reveal that both the maximum values and the localization of current flow (with consequent heating) decrease as the particle area contact and neck radius increase.

Comparing the observations from the simulation of current flow and Joule heating with the properties of I.C. FLASH KNN ceramic suggest that the uniform and higher density are a consequence of the increase in particle-particle contact area, with neck formation promoted by the isothermal step at 900 ºC. For C.H.R. FLASH, the sharp contacts promote current localization and the consequent heat generation induces ‘hotspots’ and non-uniform densification.

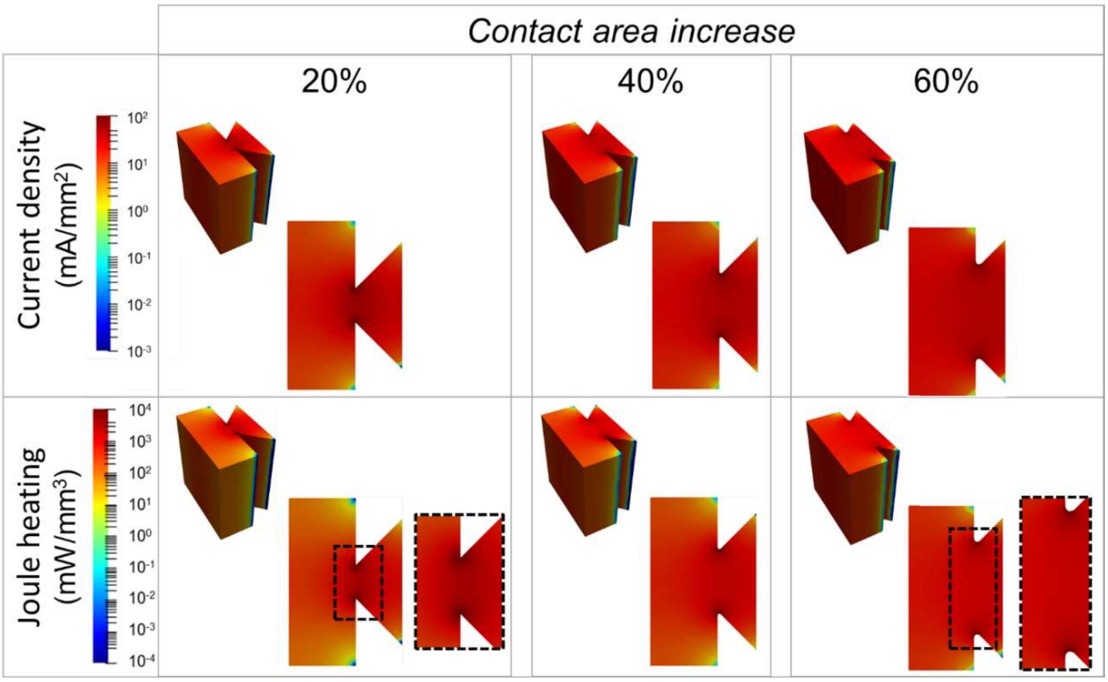

Figure 4.2-9 – Representation of the simulations of the current density (top) and Joule heating (down) for the modelled contacting particles with 0.2, 0.4 and 0.6 μm^2 contact area, when subjected to a 300 V/cm and electrical conductivity of 1 S/m.

4.2.4. Conclusions

In conclusion, we have FLASH sintered dense and uniform KNN ceramics in air, at 900 ºC, after a 30 min dwell time, which represents a processing time reduction of 25%, and a maximum temperature decrease of ~20% compared to the conventional processing. Using a combination of isothermal FLASH sintering, and Finite Element Modelling (FEM), we have unveiled the role of particle contact in the densification of FLASH sintered KNN ceramics. The isothermal step allows neck formation, increasing particle contact area and triggering a more uniform and controlled current flow through the body during FLASH. In addition, the anisotropic shrinkage is significantly decreased for I.C. FLASH. The present study reveals that the densification of KNN by FLASH is determined by factors such as electric field, temperature and the *pre-FLASH* microstructure. These observations provide insight into unexplored aspects of FLASH sintered KNN ceramics and highlight its complexity. Such studies are crucial for developing precise control of FLASH sintered materials and can potentially lead to accelerated development of lead free piezoelectrics.

4.2.5. References

[1] M. E. Villafuerte-Castrejón *et al.*. “Towards Lead-Free Piezoceramics: Facing a Synthesis Challenge”. Materials, vol. 9, no. 1, p. 21, 2016.

[2] C.-H. Hong *et al.*. “Lead-free piezoceramics and Where to move on?”. J Mater., vol. 2, pp. 1–24, 2016.

[3] S. Zhang, R. Xia, and T. R. Shrout. “Lead-free piezoelectric ceramics vs. PZT?”. J. Electroceramics, vol. 19, no. 4, pp. 251–257, 2007.

[4] X. Lv, J. Zhu, D. Xiao, X. X. Zhang, and J. Wu. “Emerging new phase boundary in potassium sodium-niobate based ceramics”. Chem. Soc. Rev., vol. 49, no. 3, pp. 671–707, 2020.

[5] J. Wu, D. Xiao, and J. Zhu. “Potassium−Sodium Niobate Lead-Free Piezoelectric Materials: Past, Present, and Future of Phase Boundaries”. Chem. Rev., vol. 115, pp. 2559–2595, 2015.

[6] C. E. J. Dancer. “Flash sintering of ceramic materials”. Mater. Res. Express, vol. 3, no. 10, pp. 102001–102025, 2016.

[7] M. Biesuz and V. M. Sglavo. “Flash sintering of ceramics”. J. Eur. Ceram. Soc., vol. 39, no. 2–3, pp. 115–143, 2019.

[8] M. Yu, S. Grasso, R. Mckinnon, T. Saunders, and M. J. M. Reece. “Review of flash sintering: materials, mechanisms and modelling”. Adv. Appl. Ceram., vol. 116, no. 1, pp. 1–37, 2017.

[9] R. Raj. “Joule heating during flash-sintering”. J. Eur. Ceram. Soc., vol. 32, no. 10, pp. 2293–2301, 2012.

[10] R. Serrazina, P. M. Vilarinho, A. M. O. R. Senos, L. Pereira, I. M. Reaney, and J. S. Dean. “Modelling the particle contact influence on the Joule heating and temperature distribution during FLASH sintering”. J. Eur. Ceram. Soc., vol. 40, pp. 1205–1211, 2020.

[11] R. Chaim. “On the kinetics of liquid-assisted densification during flash sintering of ceramic nanoparticles”. Scr. Mater., vol. 158, pp. 88–90, 2019.

[12] W. Qin, H. Majidi, J. Yun, and K. van Benthem. “Electrode Effects on Microstructure Formation During FLASH Sintering of Yttrium-Stabilized Zirconia”. J. Am. Ceram. Soc., vol. 99, no. 7, pp. 2253–2259, 2016.

[13] Y. Zhang and J. Luo. “Promoting the flash sintering of ZnO in reduced atmospheres to achieve nearly full densities at furnace temperatures of <120 °C”. Scr. Mater., vol. 106, pp. 26–29, 2015.

[14] S. Grasso *et al*.. “Modeling of the temperature distribution of flash sintered zirconia”. J. Ceram. Soc. Japan, vol. 119, no. 1386, pp. 144–146, 2011.

[15] M. Cologna, B. Rashkova, and R. Raj. “Flash Sintering of Nanograin Zirconia in <5 s at 850°C”. J. Am. Ceram. Soc., vol. 93, no. 11, pp. 3556–3559, Nov. 2010.

[16] S. K. Jha, K. Terauds, J. Lebrun, and R. Raj. “Beyond flash sintering in 3 mol % yttria stabilized zirconia”. J. Ceram. Soc. Japan, vol. 124, no. 4, pp. 283–288, 2016.

[17] Y. Du, A. J. Stevenson, D. Vernat, M. Diaz, and D. Marinha. “Estimating Joule heating and ionic conductivity during flash sintering of 8YSZ”. J. Eur. Ceram. Soc., vol. 36, no. 3, pp. 749–759, 2016.

[18] M. K. Punith Kumar, D. Yadav, J. M. Lebrun, and R. Raj. “Flash sintering with current rate: A different approach”. J. Am. Ceram. Soc., vol. 102, no. 2, pp. 1–13, 2018.

[19] H. Charalambous, S. K. Jha, K. H. Christian, R. T. Lay, and T. Tsakalakos. “Flash Sintering using Controlled Current Ramp”. J. Eur. Ceram. Soc., vol. 38, no. 10, pp. 3689–3693, Aug. 2018.

[20] G. Corapcioglu, M. A. Gulgun, K. Kisslinger, S. Sturm, S. K. Jha, and R. Raj. “Microstructure and microchemistry of flash sintered $K_{0.5}Na_{0.5}NbO_3$”. J. Ceram. Soc. Japan, vol. 124, no. 4, pp. 321–328, 2016.

[21] R. Serrazina, J. S. Dean, I. M. Reaney, L. Pereira, P. M. Vilarinho, and A. M. O. R. Senos. “Mechanism of densification in low-temperature FLASH sintered lead free Potassium Sodium Niobate (KNN) piezoelectrics”. J. Mater. Chem. C, vol. 7, pp. 14334–14341, 2019.

[22] Y. Wu, X. Su, G. An, and W. Hong. “Dense $Na_{0.5}K_{0.5}NbO_3$ ceramics produced by reactive flash sintering of $NaNbO_3$ - $KNbO_3$ mixed powders”. Scr. Mater., vol. 174, pp. 49–52, 2020.

[23] A. R. Boccaccini. “Shrinkage anisotropy of glass powder compacts sintered in dilatometers”. J. Mater. Res., vol. 13, no. 6, pp. 1693–1697, 1998.

[24] A. Tkach *et al*.. “Effect of solution conditions on the properties of sol–gel derived potassium sodium niobate thin films on platinized sapphire substrates”. Nanomaterials, vol. 9, no. 11, 2019.

[25] S.-J. L. Kang. Sintering Densification, Grain growth, and Microstructure. Elsevier. 2005.

4.3. Article: On the influence of current density and time during stage III FLASH sintering of potassium sodium niobate

To be submitted

Abstract

To produce microstructurally engineered lead-free ceramics, alternative sintering techniques may be a solution. Electric field-current assisted FLASH sintering has raised interest, especially to produce lead-free piezoelectrics as potassium sodium niobate, KNN. The parameters associated with the FLASH sintering of KNN are studied in this work. The influence of current limit and holding time on the final density and grain size of KNN ceramics is established. Suitable conditions to attain high dense specimens with controlled grain growth are accomplished. This work contributes for the knowledge of FLASH sintering process, specifically in systems in which liquid-assisted sintering takes place, as KNN, and to the production of low temperature, microstructure controlled, ceramics.

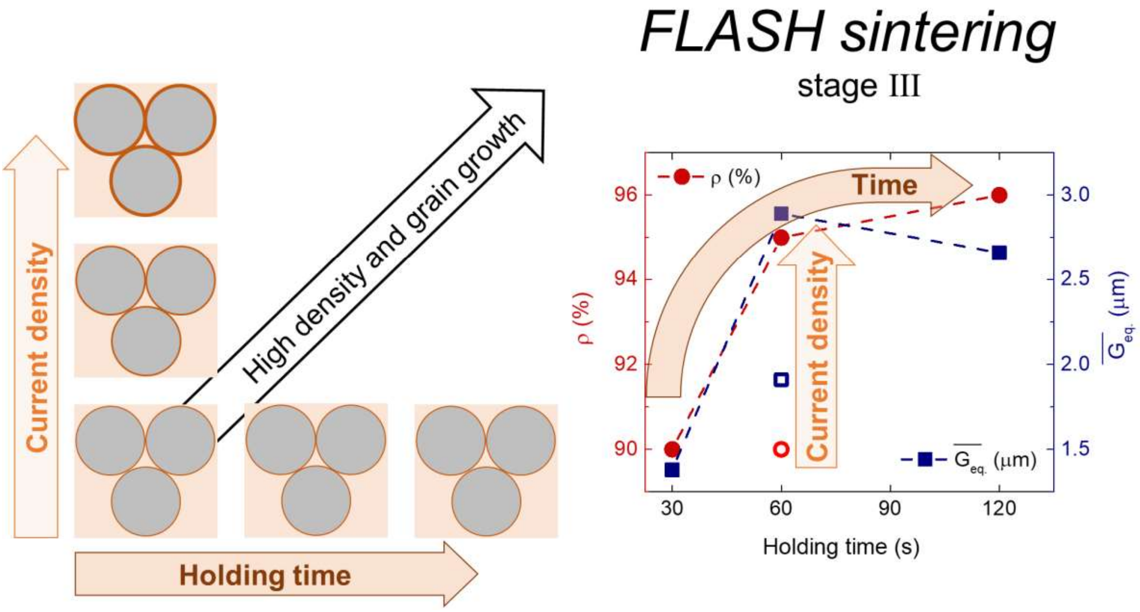

Key words

FLASH sintering; Current density; Holding time; Microstructure; KNN; Ceramics

4.3.1. Introduction

Among the substitutes for lead-based piezoelectric ceramics (PZT-family), high transition temperature (T_C) compositions on the potassium sodium niobate system, KNN, are promising [1], [2]. While the sustainability of KNN fabrication is still debatable, due to environmental impacts of niobium production [3], its technological interest is recognized [4], [5]. Nonetheless, if KNN is to replace lead-based piezoelectrics or to find new technological applications, its processing must be re-invented. Undoped 50 at% KNN, $K_{0.5}Na_{0.5}NbO_3$ is difficult to sinter, due to its alkali-based composition. The high temperatures (T > 1100 ºC) and long-time of sintering process induce the vaporization of K and Na, allowing secondary phases to be formed and properties to be negatively affected [6] – [8]. Therefore, it may be suitable to decrease the sintering time and temperature of KNN, reducing the associated drawbacks in terms of final microstructure and related properties. FLASH sintering consists in applying an electric field to a non-dense (green) ceramic compact, and after an incubation time (stage I), the specimen suffers a fast and non-linear increase on its conductivity (FLASH onset, stage II), and current starts to flow. In this current controlled process, the sintering occurs, typically in less than 60 s. The steady state, in which the current is limited and the holding time controlled, is designated as stage III [8], [9]. Observations that current density increase influences the sintering behaviour and the final densification of ceramics have been reported for systems as alumina [8], PZT [10] and 3-YSZ [11]. Such phenomena was related with the total amount of charge carriers passing through the particle surfaces [11]. Additionally, R. Chaim [12], [13] argues that a liquid transient film formed on the particle contacts is responsible, at least partially, for the very rapid sintering process observed in FLASH. The extent of this liquid film shall be dependent on the current density and consequent Joule heating. Furthermore, the particle sliding can be accelerated by the induced electrostatic forces at particle surfaces [14]. The effects of holding time are not so well studied, however, it was reported that a prolonged stage III is responsible by a raise in the grain size of YSZ [15].

KNN was previously reported to FLASH sinter at T < 900 ºC [16]. Afterwards, the proposed mechanism for FLASH sintering of KNN states that the densification occurs through particle sliding in a liquid-phase assisted sintering process, promoted by the localized heating of particle contacts induced by the current flow [17]. The influence of intrinsic KNN features, as the cuboid particle orientation [18], particle size and purity [19] and particle contact area (neck formation) [20] were reported to affect the process. However, the influence of material extrinsic parameters, related with the FLASH processing, are yet to be fully understood.

The actual proof of liquid-based FLASH sintering mechanism in KNN was given before [17], therefore, the increase in current density should have a relevant impact on the final densification of KNN ceramics, not yet investigated. In this work, the parameters of stage III FLASH sintering of KNN are studied. The influence of current limit and holding time on the final density and grain size of KNN ceramics is established.

4.3.2. Experimental

99.9% pure $K_{0.5}Na_{0.5}NbO_3$, KNN, powders were produced by solid-state reaction from alkali carbonates (K_2CO_3, Sigma-aldrich, 99.99% and Na_2CO_3, Sigma-aldrich, 99.999%) and niobium oxide (Nb_2O_5, Alfa Aesar, 99.9%). After calcination, the powders were ball milled at 200 RPM, for 24 h, with YSZ balls, in ethanol media, using teflon jars (previously designated as 99.9% BM). Pellets (ca. 15 x 5 x 2 mm^3) were then uniaxially and isostatically pressed. Details on the powder synthesis, pressing and characterization can be found in [19] and [20]. It is relevant to notice that powder's characterization by X-ray diffraction (XRD) did not reveal any secondary phases. Scanning electron microscopy (SEM) revealed the typical cuboid particle shape of KNN, and the mean particle size (D50), determined by several techniques, was agreed between 210 and 300 nm [19], [20].

To study the influence of current density and holding time during stage III of FLASH sintering, green KNN compacts were heated to a furnace temperature of 900 ºC at a constant heating rate of 10 ºC/min. An isothermal step of 30 min, before the application of the electric field, was performed, in accordance with the strategy previously reported [20]. While a constant electric field was applied (300 V/cm, *EPS HV 5006–400*), the current limit and holding time was changed in different experiments. The current limit was altered from 10, 20 and 40 mA/mm^2, while the FLASH holding time was set to 30, 60 and 120 s. Ceramics were designated after these experimental conditions (for instance, 20-60s means a current limit of 20 mA/mm^2 and a time of 60 s).

During the FLASH sintering, the relative length variation (α, indicating shrinkage when negative) was registered with a contact dilatometer and an in-house developed software [18], [20]. To study the sintering process of these compacts, the shrinkage rate ($-\frac{d\alpha}{dt}$) was calculated. The anisotropy shrinkage factor, f_{as}, defined before [20] as the ratio between the average of thickness and width shrinkages over the length shrinkage was calculated.

The final density of FLASH sintered ceramics was determined geometrically (ρ_{sint}) by considering average values of each dimension and at least two samples. To access the ceramics microstructure, SiC grinding papers (P4000 ≈ 5 μm grain size) were used for polishing before SEM (*Hitachi SU-70*) observation. In parallel, polished ceramics were etched in HF (50 vol%) during 5 minutes for grain revealing. Sonication and ethanol were used for cleaning etched ceramics. SEM was employed for microstructural analysis, with equivalent grain size ($G_{eq.}$) being determined using several SEM micrographs, with more than 500 grains, through ImageJ software. To access the crystalline structure of FLASH sintered specimens, XRD was performed on previously grinded ceramics.

4.3.3. Results and discussion

At isothermal conditions, the application of the electric field to a green compact promotes the nucleation regime (stage I), followed by the FLASH event (stage II), through the steady state with current limitation (stage III). To investigate the effect of the current density and holding time in FLASH sintering of KNN, these parameters were varied. Complementary to the experimental details and green density, Table 4.3-1 shows the final relative density of each sintered ceramic, together with its respective average grain size and shrinkage anisotropy factor. In accordance with Table 4.3-1, while the initial green density of pellets is indistinguishable, the final FLASH sintered ceramics density is very dependent on the parameters during stage III. It is observed that 20-60s presents the highest densification without bending (95%). A decrease in the current density (10-60s) or in time (20-30s) results in a reduction of the final densification (95 to 90%, for both cases). In comparison with 20-60s, the use of higher current densities (40-60s), results, not only in bending during sintering (*), but also on current localization and consequent non-uniform density (#), identically to what was previously reported for KNN [16]. Due to the current localization, the final density of this ceramic (40-60s) was very limited. On the other hand, if the current is kept at moderate limits and the time is increased (20-120s), a higher densification is attained (96%), however, bending is also observed in this case.

Figure 4.3-1 depicts a typical FLASH process, with the maximum of sintering rate occurring upon FLASH transition (stage II), and a moderately fast shrinkage process after that, in accordance with previous reports [20]. While the shrinkage rate maximum is kept almost constant for 10 to 20 mA/mm^2, a) and b), respectively, it is incremented when going from 20 ($-\frac{d\alpha}{dt} \approx 6\text{x}10^{-3}$ s^{-1}) to 40 mA/mm^2 ($-\frac{d\alpha}{dt} \approx 8\text{x}10^{-3}$ s^{-1}) – see Figure 4.3-1 b) to c). In the case of 40 mA/mm^2, not only the first shrinkage rate maximum is higher, as a secondary peak at t ≈ 30 s can be here clearly depicted. The correspondent shrinkage rate at such point is $-\frac{d\alpha}{dt} \approx 4\text{x}10^{-3}$ s^{-1} and it must be related with the bending process. The anisotropy shrinkage factor, f_{as}, presented in Table 4.3-1, reveals that a withdrawal from the isotropic condition (f_{as} = 1) is found for the increasing current. In fact, f_{as} (40-60s) $\approx$ 0, which means that the width and thickness shrinkage of this ceramic is irrelevant when compared with that of length. The two very fast sintering rate maxima are, therefore, associated with strong bending effects, that increase the shrinkage along the sample length without a correspondent enhancement of the densification.

Table 4.3-1 – Average relative green density, ρ_{green}, thermal cycle details, FLASH sintering operational parameters during stage III (current density, J, and holding time, t), anisotropy factor, f_{as}, final relative density (ρ_{sint}) and average grain size of sintered ceramics.

Specimen	ρ_{green} (%)	Thermal cycle	J (mA/mm^2)	t (s)	f_{as}	ρ_{sint} (%)	$\overline{G_{eq.}}$ (μm)
10-60s	65 ± 1	10 ºC/min up to 900 ºC; isothermal for 30 min.	10	60	0.6	90	1.91
20-60s			20	60	0.4	95	2.89
40-60s			40	60	0.0	84*#	--
20-30s			20	30	0.6	90	1.38
20-120s			20	120	0.2	96*	2.66

*high degree of bending #non-uniform densification

The effects of keeping the current density at a constant moderated value (20 mA/mm^2), with changing time, are revealed in Figure 4.3-2. The data shows that the shrinkage rate maximum during stage II is not significantly changed with the increase in holding time, because the current limit is kept constant. However, the final shrinkage, and respective density, are affected by the duration of stage III. For t = 30 s (Figure 4.3-2 a)), a smoother shrinkage curve was obtained during stage III, with a final $\alpha \approx$-11%. When the time is increased for 60 s, Figure 4.3-2 b), the shrinkage during stage III is disrupted at t $\approx$ 30 s, with two secondary small maxima being revealed. The total shrinkage ($\alpha \approx$-13%) is attained, similarly, when the current is interrupted. For t $\approx$ 120 s, comparable processes are identified, with further secondary maxima occurring over time, typically at each 30 s. In this case, the final shrinkage is $\approx$ 18%. When the current density is kept constant, the final shrinkage is dependent on the holding time, with a direct relationship with the final density (Table 4.3-1). However, for 20-120s ceramic, bending was observed. For these reasons, the f_{as} is decreased with the raise in holding time (Table 4.3-1); the longer the holding time, the more anisotropic the shrinkage is. In the case of these experiments, the shrinkage anisotropy was compensated by the increase in final density, however, at the expenses of (not severe) bending for 120 s.

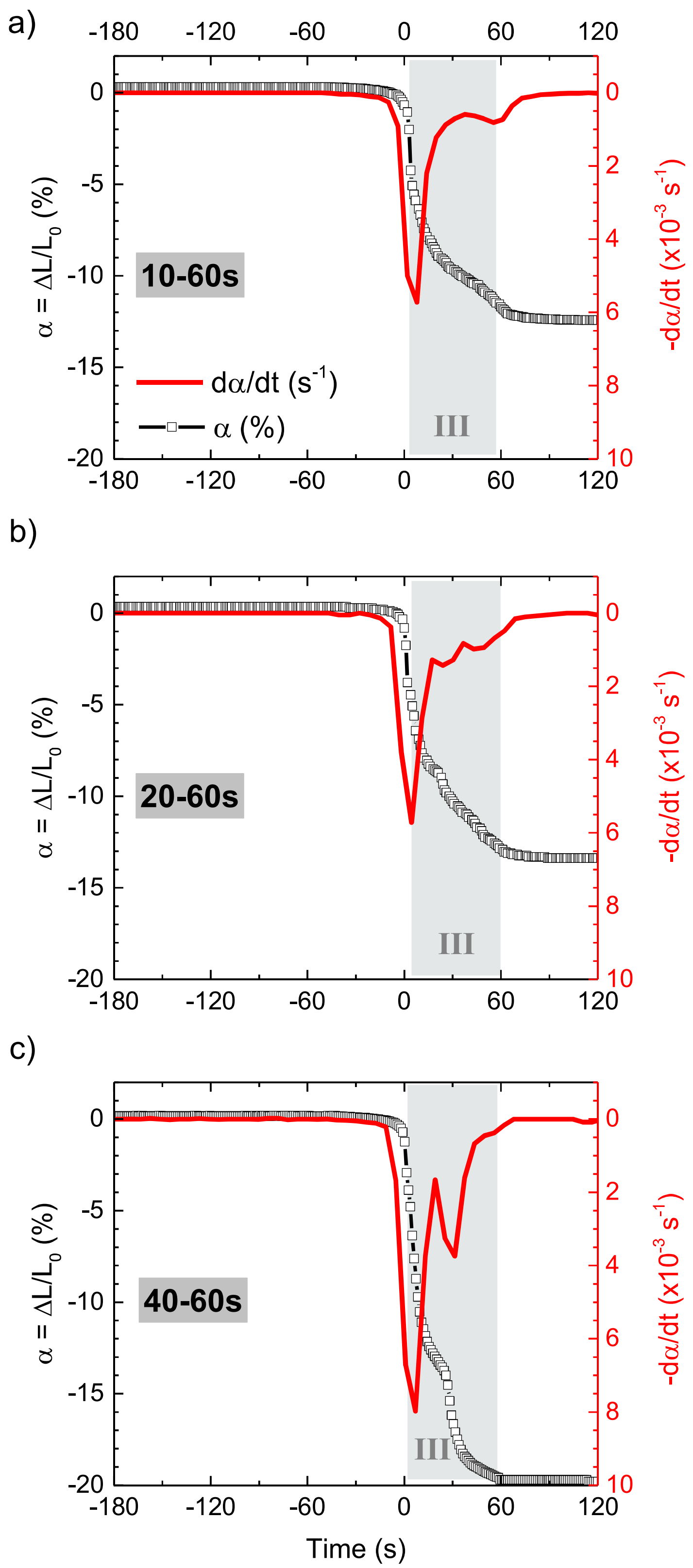

Figure 4.3-1 – Relative displacement (α) and respective derivative in respect with time (- $\frac{d\alpha}{dt}$) as a function of experiment time for constant 60s in stage III and variable current density, a) 10, b) 20 and c) 40 mA/mm^2.

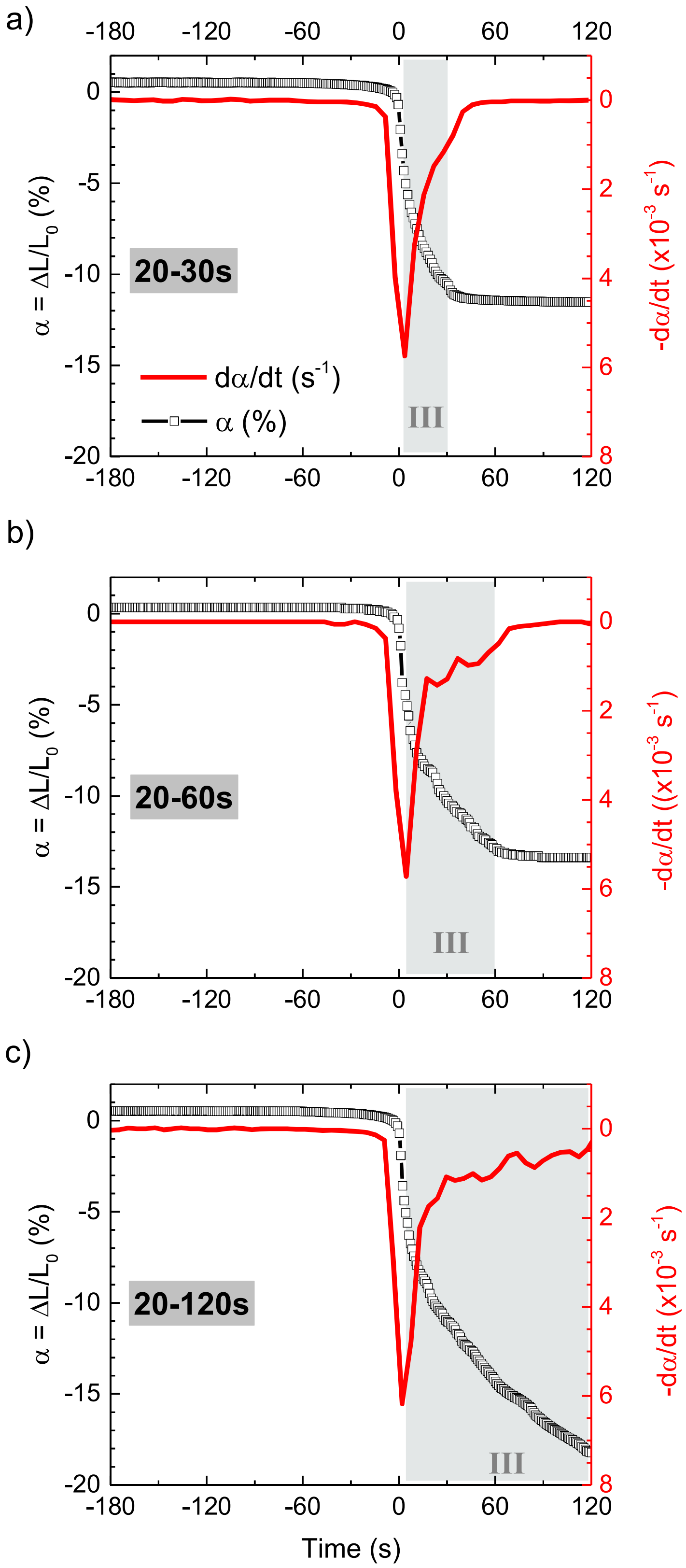

Figure 4.3-2 – Relative displacement (α) and respective derivative in respect with time (-$\frac{d\alpha}{dt}$) as a function of experiment time for constant current density (20mA/mm^2) during stage III, and variable time, a) 30, b) 60 and c) 120s.

To correlate the influence of both time and current limit on stage III of KNN FLASH sintering, Figure 4.3-3 shows the relative displacement (a) and respective shrinkage rate (b) as a dependence of the holding time on stage III ($t = 0$ s for FLASH onset), for ceramics sintered with increasing current density (1) or holding time (2). Dashed lines indicate the end of FLASH process (electric power is turned off) for each specific ceramic. The data shows, in accordance with Figure 4.3-1 and Figure 4.3-2, that the increase in current density (1) contributes to an increase in the initial shrinkage rate and, therefore, in the final total shrinkage. On the other hand, when current density is kept constant and the holding time is increased (2), the shrinkage velocity is not significantly changed, however, the final shrinkage is as larger as longer the time. Additionally, the densification process (shrinkage) is stopped almost instantly after the interruption of FLASH process for all the ceramics.

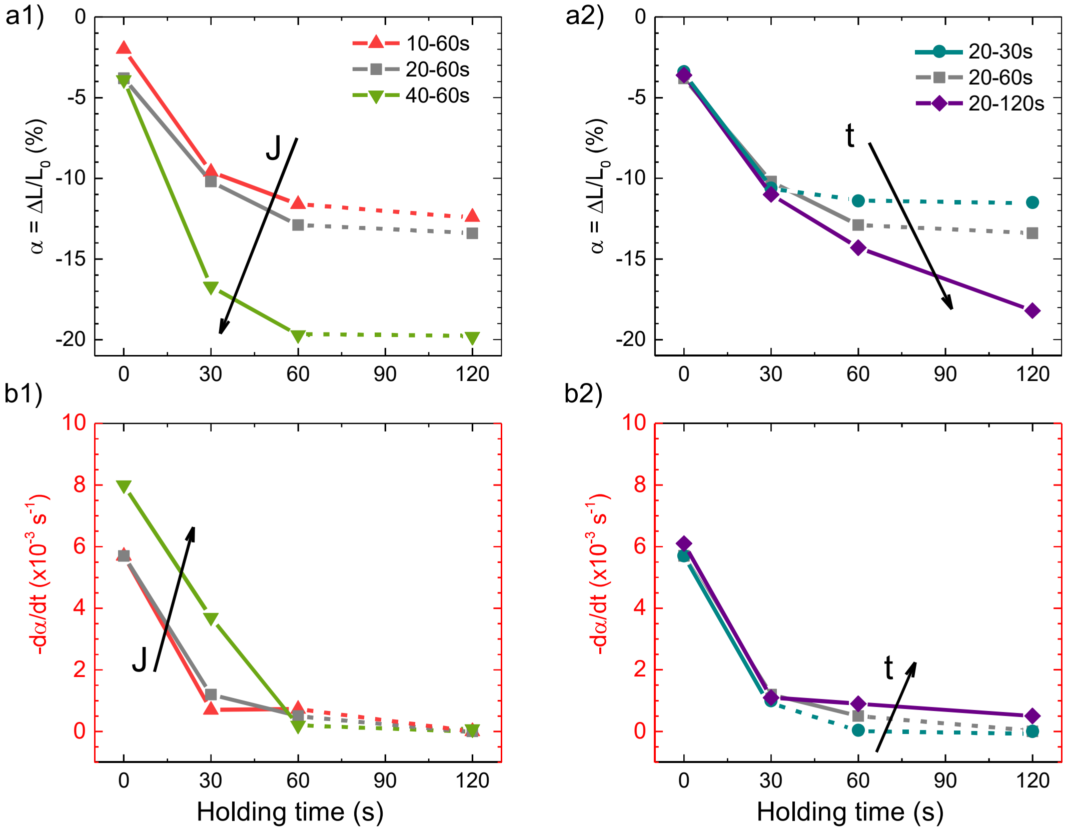

Figure 4.3-3 – a) relative displacement (α) and b) respective shrinkage rate ($-\frac{d\alpha}{dt}$) as a function of the holding time in stage III for 1) constant time and 2) constant current density.

The increase of current density to 40 mA/mm^2 (with holding time of 60 s) and the increase of holding time to 120 s (with current 20 mA/mm^2) produced ceramics with approximately the same final shrinkage, and both with observable bending, however, very dissimilar densities (84 and 96%, respectively) and shrinkage anisotropy factors - Table 4.3-1. The larger sintering maxima that occur at $t \approx 0$ and 30 s for 40-60s sample are indicative of localized densification, confirmed in the sintered ceramic. For this reason, while it is plausible to consider 20-120s ceramic for subsequent microstructural analysis, it is not for 40-60s, as this last one does not present identical density through its length, width, or thickness.

The structure and microstructure of FLASH sintered ceramics were characterized and Figure 4.3-4 shows the X-ray diffraction (XRD) patterns of some FLASH sintered ceramics, in comparison with the orthorhombic $K_{0.5}Na_{0.5}NbO_3$ phase JCPDF 01-085-7128 (space group 38 with Amm2 symmetry). The most extreme sintering conditions were selected for analysis; however, they are representative of all the sintered ceramics. A full agreement between the XRD patterns of ceramics and KNN single phase is identified, revealing that the different tested conditions for FLASH sintering processing did not affected the structure of KNN ceramics.

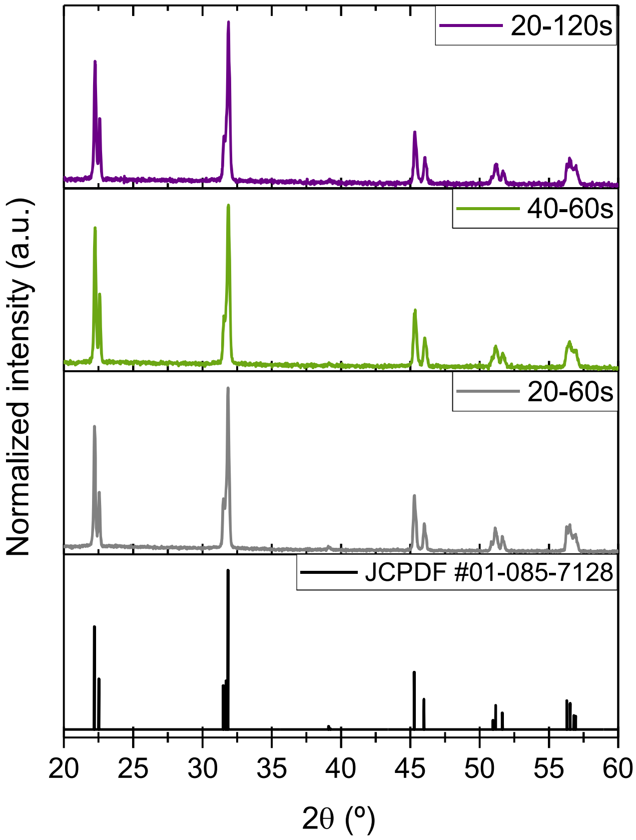

Figure 4.3-4 – XRD patterns of some FLASH sintered ceramics. JCPDF #01-085-7128 orthorhombic $K_{0.5}Na_{0.5}NbO_3$ is shown as a reference.

The microstructural consequences of different stage III parameters are revealed in the SEM micrographs (Figure 4.3-5) of the previously discussed ceramics. The 40-60s ceramic is not presented due to its said non-uniform densification. Figure 4.3-5 a) shows the polished surfaces of ceramics. A rather uniform densification in 20-60s is revealed, while the remaining ceramics present divergent areas. There is a link between the measured final density and the micrographs of Figure 4.3-5 a), with 20-60s and 20-120s ceramics presenting high density regions, while 10-60s and 20-30s less dense areas. The etched micrographs and the respective measured grain size distribution (GSD) and average grain size ($\overline{\mathrm{G_{eq.}}}$) are shown in Figure 4.3-5 b). While the micrographs reveal the typical cuboid grain shape of KNN, the data reveal that the FLASH process promoted, not only densification, but also grain growth (Table 4.3-1). Important to note that uniform grain size as found through all the analysed area, which corresponds to the great majority of the sintered ceramics, excluding the electrode contact areas (few mm each side). As said before, the mean particle size of KNN powders was determined between 210 to 300 nm [19]. A general observation of Figure 4.3-5 b) reveals a grain growth of ≈10 times, in comparison with the starting particle size. No significant abnormal grain growth was registered in Figure 4.3-5 b1-3), however, that was not the case for 20-120s ceramic (Figure 4.3-5 b4) [21]. It should be noted that the etching process promotes, together with the dissolution of the grain boundary glassy phases [20], smaller particles to be totally detached and removed during the cleaning process (sonication). This effect promotes an excess estimation of $G_{eq.}$.

Figure 4.3-5 b) reveals that stage III parameters create a dependence on the grain size distributions. To link these dependences, Figure 4.3-6 shows the final relative density and average grain size (with respective standard deviation) of the studied ceramics. The data show a direct relation between the final density and the ceramic grain size. When the current density is kept constant and the holding time is increased, the density and grain size are increased for 30 to 60 s; however, while the density is slightly increased for 120s, the grain size is kept roughly constant. Nonetheless, as referred before, abnormal grain growth was observed for the 20-120s ceramic. Because the content in abnormally grown grains is low, there is not a significant effect in the respective average grain size nor in its standard deviation. Additionally, when the current density is decreased from 20 to 10 mA/mm^2 (open symbols in Figure 4.3-6), not only the final density is decreased, as said, as the grain size follows the same trend.

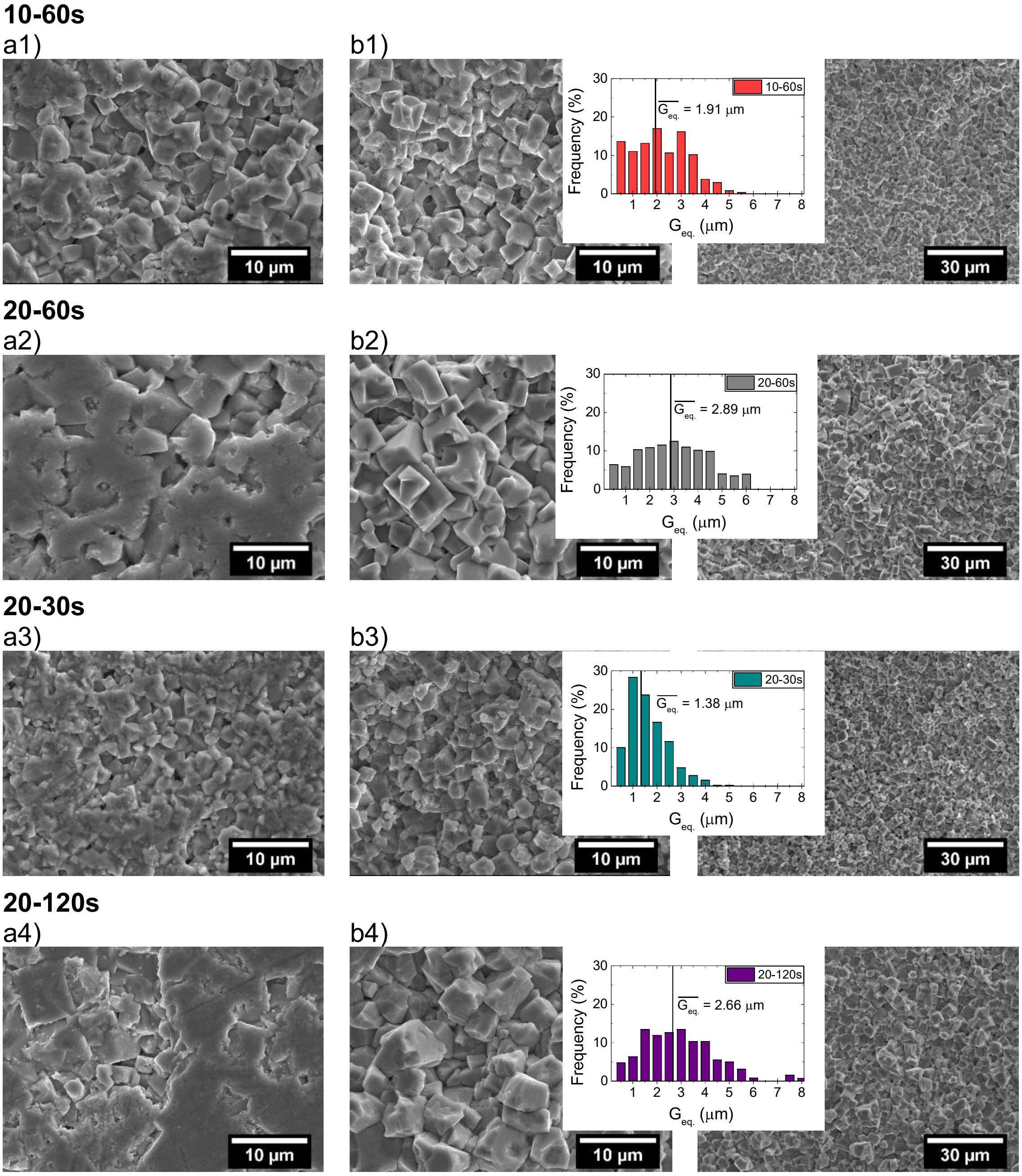

Figure 4.3-5 – SEM micrographs for FLASH sintered ceramics with varied time and current limit of a) polished and b) etched (HF 50 vol%) ceramics, with the respective grain size distribution and average grain size ($\overline{\mathrm{G}_{\mathrm{eq.}}}$).

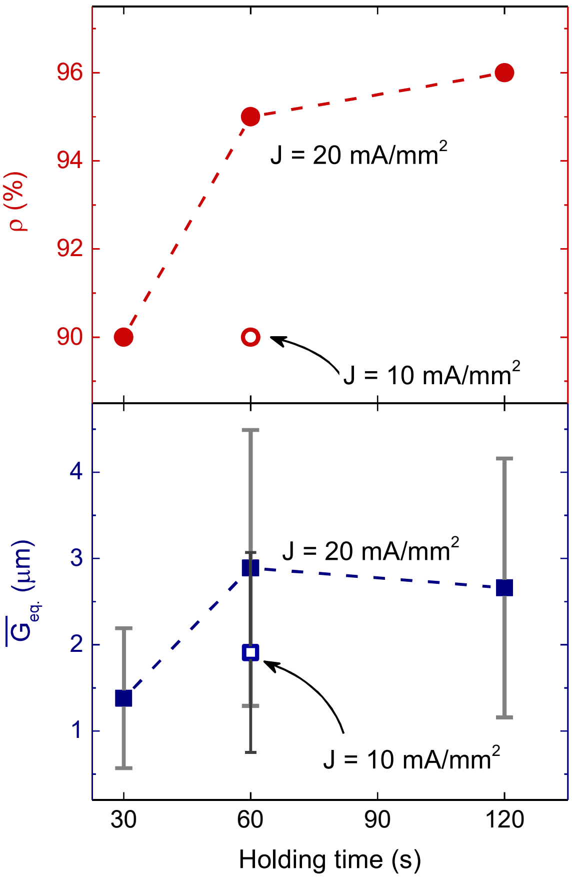

Figure 4.3-6 – Relative density, ρ (●) and $\overline{G_{eq.}}$ (■) with respective standard deviation of FLASH sintered ceramics at 20 mA/mm^2 current limit with increasing holding time (closed symbols). The 10-60s ceramic data is shown for comparison (open symbols).

The observed tendency of increase in densification and grain size with the increase in current density is in accordance with previous work [8], [10], [11]. This phenomenon is due to the escalation in charge flow through particle surfaces, that promote the dissolution of smaller, more reactive particles, along with particle sliding, facilitated by the formed liquid [20]. However, when the current is too high (example of 40-60s), non-uniform densification occurs as result of current localization and channelling [16].

The dependence of $G_{eq.}$ and ρ with holding time during stage III is slightly more complex. For an increase from 30 to 60 s, a direct relationship is found, with both density and grain size increasing. When 120 s are employed, the densification is somewhat increased, however, at the expenses of the beginning of abnormal grain growth phenomenon, together with ceramic bending. Similar observations where reported for YSZ [15]. In accordance with previous work [19], the process proposed for grain growth is Ostwald ripening: particles that are surrounded by a liquid [17], [20] grow with smaller particles dissolving and the solute precipitating on the larger particles [20], [22], [23].

Therefore, it is expected that the longer the time, the greater the number of fine particles that will be dissolved into the liquid, and the larger the grains will be.

During the FLASH sintering of KNN, the increase in final density is associated with an increase in the grain size. From the tested experimental conditions, the superior compromise between high density and uniform grain distribution was found for 20-60s ceramic. If a fine grain size microstructure is mandatory, 20-30s condition may be useful, with a compromise on the final densification. If a longer time is used (120 s), bending may occur, in parallel with increased grain growth and development of abnormally grown grains.

4.3.4. Conclusions

In summary, it is concluded that the parameters of stage III during FLASH, current and time, have a very significant influence on the final densification and grain size of $K_{0.5}Na_{0.5}NbO_3$ ceramics. On one hand, the increase of current density induces the increase of final densification and grain size. On the other hand, a limit condition was established for current density equal or greater than 40 mA/mm^2, due to current channelling, non-uniform heating and consequent non-uniform densification and grain size. In parallel, severe bending occurs for such high current. Furthermore, the increase on holding time also induces the increase in density and grain size. This is more evident for 30 to 60 s increase, while a further increase for 120 s does not promote a rise of densification, allowing bending to occur as well. The increase in densification and grain size associated with current is related with the intensification in charge movement, Joule heating generation and particle sliding velocity. On the other hand, the increase of time enables the prolongment of the matter transport processes both for densification and grain growth, with the growth of abnormal grains being observed for $t > 60$ s. This work contributes to the knowledge on FLASH sintering of KNN and to the establishment of the conditions for its proper microstructural engineering.

4.3.5. References

[1] J. Rödel, K. G. Webber, R. Dittmer, W. Jo, M. Kimura, and D. Damjanovic. "Transferring lead-free piezoelectric ceramics into application". J. Eur. Ceram. Soc., vol. 35, no. 6, pp. 1659–1681, 2015.

[2] C.-H. Hong *et al.*. "Lead-free piezoceramics and Where to move on?". J Mater., vol. 2, pp. 1–24, 2016.

[3] T. Ibn-Mohammed *et al.*. "Are lead-free piezoelectrics more environmentally friendly?". MRS Commun., vol. 7, no. 1, pp. 1–7, 2017.

[4] H. Sun, J. Liu, X. Wang, Q. Zhang, X. Hao, and S. An. "$(K,Na)NbO_3$ ferroelectrics: a new class of solid-state photochromic materials with reversible luminescence switching behavior". J. Mater. Chem. C, vol. 5, pp. 9080–9087, 2017.

[5] J. Wu, D. Xiao, and J. Zhu. "Potassium−Sodium Niobate Lead-Free Piezoelectric Materials: Past, Present, and Future of Phase Boundaries". Chem. Rev., vol. 115, pp. 2559–2595, 2015.

[6] J. Pavlič, B. Malič, and T. Rojac. "Microstructural, structural, dielectric and piezoelectric properties of potassium sodium niobate thick films". J. Eur. Ceram. Soc., vol. 34, no. 2, pp. 285–295, 2014.

[7] M. Cologna, B. Rashkova, and R. Raj. "Flash Sintering of Nanograin Zirconia in <5 s at 850°C". J. Am. Ceram. Soc., vol. 93, no. 11, pp. 3556–3559, Nov. 2010.

[8] M. Biesuz and V. M. Sglavo. "Flash sintering of ceramics". J. Eur. Ceram. Soc., vol. 39, no. 2–3, pp. 115–143, 2019.

[9] S. K. Jha, K. Terauds, J. Lebrun, and R. Raj. "Beyond flash sintering in 3 mol % yttria stabilized zirconia". J. Ceram. Soc. Japan, vol. 124, no. 4, pp. 283–288, 2016.

[10] X. Su *et al.*. "Flash sintering of lead zirconate titanate (PZT) ceramics: Influence of electrical field and current limit on densification and grain growth". J. Eur. Ceram. Soc., vol. 38, no. 10, pp. 3489–3497, 2018.

[11] D. Liu *et al.*. "Effect of the current density on the densification of 3 mol% yttria-stabilized zirconia in flash sintering". J. Alloys Compd., vol. 825, 2020.

[12] R. Chaim. "Liquid film capillary mechanism for densification of ceramic powders during flash sintering". Materials, vol. 9, no. 4, pp. 19–21, 2016.

[13] R. Chaim and C. Estournès. "On thermal runaway and local endothermic/exothermic reactions during flash sintering of ceramic nanoparticles". J. Mater. Sci., vol. 53, no. 9, pp. 6378–6389, 2018.

[14] R. Chaim, G. Chevallier, A. Weibel, and C. Estournès. "Grain growth during spark plasma and flash sintering of ceramic nanoparticles: A review". J. Mater. Sci., vol. 53, no. 5, pp. 1–19, 2018.

[15] K. Ren, J. Xia, and Y. Wang. "Grain growth kinetics of 3 mol. % yttria-stabilized zirconia during flash sintering". J. Eur. Ceram. Soc., vol. 39, no. 4, pp. 1366–1373, 2019.

[16] G. Corapcioglu, M. A. Gulgun, K. Kisslinger, S. Sturm, S. K. Jha, and R. Raj. "Microstructure and microchemistry of flash sintered $K_{0.5}Na_{0.5}NbO_3$". J. Ceram. Soc. Japan, vol. 124, no. 4, pp. 321–328, 2016.

[17] R. Serrazina, J. S. Dean, I. M. Reaney, L. Pereira, P. M. Vilarinho, and A. M. O. R. Senos. “Mechanism of densification in low-temperature FLASH sintered lead free Potassium Sodium Niobate (KNN) piezoelectrics”. J. Mater. Chem. C, vol. 7, pp. 14334–14341, 2019.

[18] R. Serrazina, P. M. Vilarinho, A. M. O. R. Senos, L. Pereira, I. M. Reaney, and J. S. Dean. “Modelling the particle contact influence on the Joule heating and temperature distribution during FLASH sintering”. J. Eur. Ceram. Soc., vol. 40, pp. 1205–1211, 2020.

[19] R. Serrazina, C. Ribeiro, M. E. Costa, L. Pereira, P. M. Vilarinho, and A. M. O. R. Senos. “Particle characteristics influence on FLASH sintering of Potassium Sodium Niobate: a relationship with conduction mechanisms”. Materials, vol. 14, p. 1321, 2021.

[20] R. Serrazina, A. M. O. R. Senos, L. Pereira, J. S. Dean, I. M. Reaney, and P. M. Vilarinho. “The Role of Particle Contact in Densification of FLASH Sintered Potassium Sodium Niobate”. Eur. J. Inorg. Chem., vol. 2020, no. 39, pp. 3720–3728, 2020.

[21] M. Hillert. “On the theory of normal and abnormal grain growth”. Acta Metall., vol. 13, no. 3, pp. 227–238, 1965.

[22] M. N. Rahaman. Ceramic processing and sintering, Second edition. New York: Marcel Dekker, Inc., 2003.

[23] R. M. German. Sintering Science: An Historical Perspective, First edition. California: German Materials Technology, 2016.

Summary

Chapter 4 was dedicated to the establishment of powder features and process parameters on both the FLASH temperature (T_F) and final density of FLASH sintered KNN ceramics. Regarding the particle size and purity, section 4.1 allowed to conclude that:

- The studied differences in particle features do not affect the final density of ceramics. However, T_F is strongly dependent on those.
- A smaller particle size induces a raise in the density of particle contacts, which promotes a decrease in T_F, as the conduction process was found to be very dependent on the grain contacts (grain boundaries).
- Therefore, the presence of impurities has a similar effect (decrease of T_F), however, not because of contact density, but due to an increase in the surface conductivity.
- In summary, the density of particle contacts and surface-based conduction mechanisms dictate the FLASH temperature.

Additionally, the role of the particle contact was studied in section 4.2, in this case, by isothermally treating KNN compacts at the FLASH temperature, without the application of an electric field. By the time that the field was applied, necks and particle contact enlargement had already occurred, and I.C. FLASH allowed higher and more uniform density to be obtained, in comparison with C.H.R. In specific, it was concluded that:

- The neck formation and particle contact area increase were responsible for a more uniform current distribution and consequent generation of heat by Joule effect, which was demonstrated by FEM simulations.
- An I.C. FLASH process is triggered with more uniform current distribution, which allows a more isotropic shrinkage of KNN compacts.
- Rather than the FLASH parameters (time, current and electric field), the thermal cycle is revealed to have a relevant influence on the alternative sintering of KNN by FLASH.

Section 4.3 was responsible for the presentation of the impact of FLASH parameters during stage III (current density and holding time) for the final density and microstructure of KNN ceramics. By changing the current between 10 and 40 mA/mm^2, and the holding time amongst 30 and 120 s, it was possible to conclude that:

- The increase of current density induces the increase of final densification and grain size; a limit condition was found for $J \geq 40$ mA/mm^2, in which current localization and channelling occurred.

- The density raise with current is related to intensification in charge movement, Joule heating generation and particle sliding velocity.
- The increase in holding time from 30 to 60 s induces a clear increase in density and grain size as well; however, a further increase to 120 s does not promote further densification, allowing bending to occur.
- In this case, the increase in density and grain size is related with an extended process in time, that promotes, abnormal grain growth for t > 60 s.

The importance of powder, thermal cycle, and operating parameters during FLASH sintering of KNN is undoubtedly shown. Simulation tools have been used to explain the effect of neck formation between particles. Following, the FLASH sintering operating mechanisms for KNN will be studied in detail in the next chapter (chapter 5).

Chapter

5. FLASH sintering operating mechanisms: a case study for KNN

Contents

Preamble

After establishing the role of particle size, impurity content and contact morphology to the development of FLASH process, as well as studying the effect of FLASH parameters (namely current density and holding time), the mechanisms associated with the FLASH sintering of KNN will be now investigated.

Chapter 5 is divided in two contributions. Section 5.1 gives a comprehensive and pioneer exploration of the FLASH sintering mechanisms of KNN. In fact, this was the first published work within this doctoral program. By using a low temperature Atmosphere-Assisted FLASH sintering (AAFS) process (that will be presented in detail in chapter 6), and a high current density, exaggerated current flow was promoted which was useful to evidence microstructural details related with the FLASH sintering mechanisms of KNN. Besides, preliminary FEM simulations allowed to relate the observations with a dependence of cuboid particle relative orientation.

Following, section 5.2 gives an estimation on the apparent activation energy for the FLASH sintering process of KNN powders, in comparison with conventional sintering process. In this case, a *controlled* FLASH process was employed, meaning that current channelling was avoided. The classical sintering kinetic analysis was then used to compare the KNN alternative and conventional sintering processes.

5.1. Article: Mechanism of densification in low-temperature FLASH sintered lead free potassium sodium niobate (KNN) piezoelectrics

Published: https://doi.org/10.1039/C9TC03117K

Abstract

Lead-free potassium sodium niobate ($K_{0.5}Na_{0.5}NbO_3$, KNN) piezoelectric ceramics have been densified at temperatures lower than 300 °C using atmosphere-water assisted FLASH sintering. Transmission electron microscopy (TEM) studies revealed amorphous phase at grain boundaries that resulted from surface melting of the cuboid particles in the presence of segregated impurities. We propose that preferential surface melting of the primary particles is induced in conductive channels of open pores in which water is adsorbed. This creates a network of pathways for the electric current. The resulting liquid phase induces fast densification through sliding of grain boundaries and viscous flow of the liquid driven by minimisation of surface energy. Finite Element Modelling (FEM) revealed that current density and Joule heating were also influenced by the geometry of contact between the cuboid KNN particles with vertex to vertex inducing the maximum current density and consequently creating the greatest volume of amorphous phase in adjacent pores. The lowest current density was predicted for face to face contacts, resulting in only a thin amorphous layer between grains.

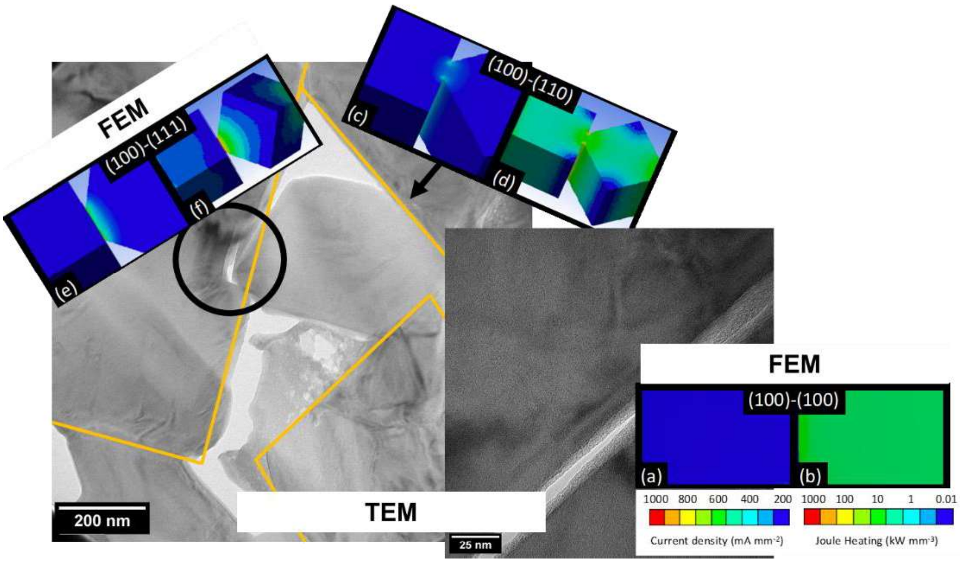

Key words

Cleaner synthesis technology, sustainable sintering, lead-free piezoceramics, FLASH, low temperature sintering, potassium sodium niobate, $K_{0.5}Na_{0.5}NbO_3$ (KNN), Finite Element Modelling (FEM), transmission electron microscopy (TEM).

5.1.1. Introduction

Reduction in CO_2 emissions during the fabrication and densification of ceramics is particularly important as this industry consumes a disproportionate amount of energy in comparison to the size of the sector [1]. Ferroelectrics are an important class of ceramics that find applications in sensors and actuators, critical for the development of Industry 4.0 and Internet of Things [2]. However, such materials are sintered commercially at > 1000 ºC for several hours.

As an alternative to such high energy consumption processes, FLASH sintering was proposed [3]. FLASH is a field-assisted, very fast, low-temperature, sintering technique, in which the specimen is placed between electrodes with densification occurring in a few seconds ($\leq$ 60 s) during a limited current controlled stage [4], [5]. With the use of specific atmospheres and water, as well as electric field/current conditions, FLASH sintering temperature and time can be significantly decreased from around 1000 ºC for several hours towards room temperature for a few seconds [6]. Reducing densification time and temperature can also minimise the loss of volatile components, potentially maintaining stoichiometry and improving the performance of compounds such as $(K_{1-x}Na_x)NbO_3$ (KNN). [7]

KNN is a potential PbO free substitute for $Pb_{1-x}Zr_xTiO_3$ (PZT), currently the market leader for piezoelectric actuators, sensors, and transducers [8]. Undoped monophasic $K_{0.5}Na_{0.5}NbO_3$ has a high Curie temperature ($T_C \approx 420$ °C) and a piezoelectric coefficient d_{33} between 80 to 160 pC/N [9]. However, undoped KNN is conventionally sintered at 1100 ºC for more than 1 h [10] which induces volatilization of K and Na, triggering the formation of secondary phases that affect properties. Sintering lead-free KNN at lower times and/or temperatures would alleviate these issues as well as making its production more energy efficient, contributing to sustainability. FLASH sintered KNN has previously been reported to achieve 94% density at 990 ºC, 250 V/cm and 20 mA/mm^2 for 30 s [11]. However, the road map towards a sustainable ceramics manufacturing demands drastic decreases in temperature and time and it is debateable whether a reduction of ~100 ºC is enough to warrant the cost of retooling production to utilise FLASH sintering.

In a general way, three mechanisms are proposed to explain FLASH: (i) Joule heating, (ii) field induced defects and (iii) changes of interfacial energy. These should not be described as individuals, because they all influence the process. Generally, sintering is highly dependent on the diffusion rate at grain boundaries. The electric field enhances this diffusion. During FLASH a current would pass through the sample, which increases its temperature by Joule heating. At low temperature, the amount of heat is negligible, since the current is low. However, the resistance of ceramics decreases with increasing temperature.

Furthermore, two separated studies [12], [13] suggest that the ultrahigh heating rate generated during FLASH is a critical factor that lead to fast densification by (i) preventing the initial coarsening, keeping a high densification driving force, as already explained, and (ii) providing non-equilibrium defects that would enhance matter flow. Those defects can be, for instance, grain boundary structures (or complexions [14], [15]) with enhanced mass transport rates [16], or Frenkel pairs nucleation [17]–[19]. All the described factors increase the diffusion rate at grain boundaries (i.e. particle surfaces) and, consequently, enhance the densification rate [20].

Recently, it was shown that, for YSZ, the FLASH sintering mechanism is controlled by the electric current limit; if a critical current threshold is exceeded ($J > 10$ mA/mm^2), alternative densification mechanisms are activated. On the other hand, for low current density (5 mA/mm^2) the densification mechanism is similar to an accelerated conventional sintering [21].

Regarding FLASH mechanisms, and as pointed out by Dancer [5], there are currently several contradictions in the community. FLASH sintering seems to be a material dependent process and general mechanism description is not easy to attain. Also, specific studies on the mechanism of FLASH sintering of complex oxides are mandatory to further understand the general phenomena but also the particularities of specific systems.

A limited number of efforts have been made to model FLASH phenomena. Furthermore, few works on modelling Joule heating have been published. The electric field distribution has been modelled for a dog-bone shape specimen [22]. Also, Naik and co-workers [23] proposed a model for the nucleation of defects under an electric field for isothermally FLASH sintered 3YSZ-Al_2O_3; the model shows that the Joule heating is a consequence of nucleation of defects and not the cause of it [23].

In this work, we conduct a systematic analysis of the GBs of low temperature (< 300 °C) water assisted FLASH sintered KNN ceramics; we support our observations with Finite Element Modelling (FEM) to estimate local Joule heating, considering the geometry of particle to particle contact. ZnO has already been FLASH sintered at room temperature [6] using similar conditions to those reported here, however, KNN is a complex, ternary oxide, with potential applications as a lead free piezoelectric and thus, this work has far reaching consequences for the potential commercial usage of water assisted FLASH sintering to reduce carbon emissions within the ceramic sector.

5.1.2. Experimental

$K_{0.5}Na_{0.5}NbO_3$ powders were prepared by a conventional solid-state route. High purity carbonates (K_2CO_3, Merck, 99.0% and Na_2CO_3, Chempur, 99.5%) and niobium oxide (Nb_2O_5, Alfa Aesar, 99.9%) were mixed in teflon jars, with YSZ and ethanol media, at 200 RPM for 6 h. A calcination step at 900 ºC, for 3 h, was performed. The final milling step was for 24 h, using the same initial milling conditions (this powder was previously designated as 99% BM – section 4.1). Particle size distribution was assessed by laser particle diffraction (*COULTER LS-200*), in which two maxima were identified: at ~200 nm and at 1.7 μm. More than 75% of the particle size distribution was below 445 nm. The largest registered particle size was 4 μm.

FLASH experiments were conducted with parallelepiped shape specimens on samples with 65 ± 3 % green density, which were shaped by uniaxial and isostatic pressing, at 130 MPa for 90 s and 350 MPa for 15 min, respectively. FLASH sintering was performed in an alumina tube furnace using a setup as represented in Figure 5.1-1 (as previously described in Figure 2-2). One fixed alumina part and platinum electrode were placed in one side of the setup. A movable alumina rod, which pushes the second Pt electrode, was placed in the opposite side. An external spring allows the system to maintain electrode contact during the specimen shrinkage. Two platinum wires were connected to the platinum electrodes and to the power source (DC, *EPS HV 5006-400*).

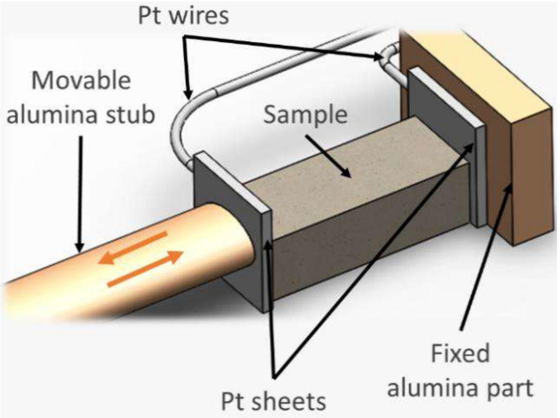

Figure 5.1-1 – Schematic of the FLASH sintering setup used in this work. The specimen is parallelepiped shaped and is placed in between two platinum electrodes. The electrodes are connected to platinum wires and those to the power source. One of the electrodes is fixed by an alumina part and the second one is free to move to follow the shrinkage of the specimen, trough the movement of an external alumina stub.

A mixture of gas and water was utilised following procedures described by ref. [6] by flowing argon through a flask of deionized water, allowing to perform the densification of KNN at temperatures as low as 290 ºC. The FLASH setup was purged for 1 h with the Ar + H_2O mix at approximately 500 ml/min. After purging, a DC electric field was applied (400 V/cm) and temperature increased at a rate of 10 ºC/min. The current was limited to 60 mA/mm^2 and the gas flux was kept constant. Heating was stopped immediately after FLASH occurred. The FLASH time, defined as the time in current limit control, was 60 s.

Figure 5.1-2 shows the X-Ray Diffraction pattern for powders and FLASH sintered KNN indexed with PDF file 01-085-7128. The data was collected with a *PANalytical XPERT-PRO* diffractometer. Despite that no secondary phases were observed in the FLASH sintered body, a decrease in peak definition and sharpness is observed, which can be indicative of partial grain amorphization. This observation justified the electron microscopy and modelling studies presented in this work.

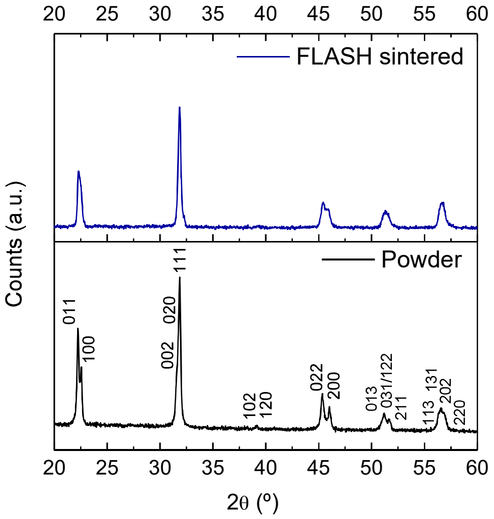

Figure 5.1-2 – XRD patterns for powder and low-temperature FLASH sintered. Indexed with PDF file number 01-085-7128.

Scanning electron microscopy (SEM, *HITACHI S-4100*) and Transmission electron microscopy (TEM, *JEOL JEM 2200 FS*) with Energy-dispersive X-ray spectroscopy (*OXFORD Inca x-sight*) were used to systematically analyse the microstructure of FLASH sintered KNN and, specifically, grain boundaries. For TEM experiments, the sintered specimens were polished using the tripod method, with diamond lapping paper. The polished specimens were attached to a molybdenum ring and ion milled with a *GATAN PIPS*.

Finite element modelling (FEM) presented here used the *ANSYS® Academic Research Mechanical, Release 18.1 package*. Simulations were performed using electrical analysis in order to study current density, electric field and associated Joule heating effects arising from the microstructure. An adaptive refinement, dividing the mesh length by approximately 1/3rd, were implemented around the connection points to account for the extra complexity in the solution. To reach convergence in the models a mesh size of 25 nm was used, generating over 1 million tetrahedral elements. It is important to highlight that FEM work is developed considering a stationary system in which electrical properties of the material do not change with the application of the field. We note that the goal of our study is to understand the role of contact geometry rather than attempt a full FEM analysis of field distributions in FLASH sintering.

5.1.3. Results and discussion

Figure 5.1-3 a) shows a uniaxial and isostatically pressed green pellet cross section with Figure 5.1-3 b) an equivalent image of FLASH sintered KNN. The green pellet (Figure 5.1-3 a)) is composed of randomly distributed cuboid particles with coarser particles > 1 μm; and fine particles < 0.5 μm, in accordance with PSD analysis. Figure 5.1-3 b) reveals that the coarser particles did not grow during sintering and that the finer particles are less evident. Low magnification images (Figure 5.1-3 b)) also reveal that the densest regions occur in channels throughout the specimen, indicating that electric field and current are non-uniformly distributed.

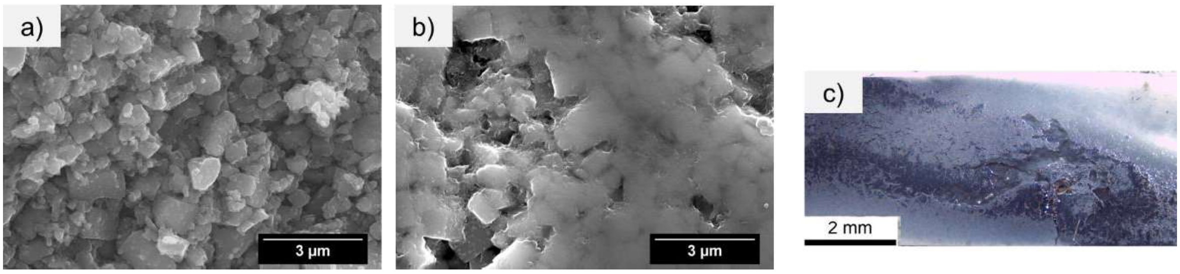

Figure 5.1-3 – SEM micrographs of a) KNN green pellet and b) FLASH sintered KNN. c) is a low magnification of FLASH sintered KNN showing current channelling.

The overall densification of the atmosphere-water assisted FLASH sintered KNN under the conditions here reported is approximately 80% of theoretical densification. However, and as specifically shown in Figure 5.1-3 c), densification is not homogeneous. Figure 5.1-3 b) highlights the comparison between very high dense areas and some porous ones. In some regions, densification as high as 100%, can be achieved. This phenomenon (well known for FLASH sintering) is due to the current channelling that happens during the FLASH process and as a consequence the densification of the sample is not uniform. We attribute this to current and densification pathways to open pores in which the water vapour from the furnace atmosphere has adsorbed onto the surface of the particles. We also note the absence of defined grains in the densest regions (Figure 5.1-3 b)), potentially indicating partial melting.

A representative TEM micrograph of FLASH sintered KNN is shown in Figure 5.1-4. Consolidation of primary particles was evident, confirming the SEM results. Moreover, an amorphous phase is present at most GBs, irrespective of the contact geometry. The amorphous phase was identified through the absence of discrete diffraction spots in electron diffraction patterns. In addition, we note that conventionally sintered KNN TEM samples fabricated under identical ion beam milling conditions do not exhibit amorphization. We conclude therefore, that the amorphous phase is not an artefact of TEM sample preparation.

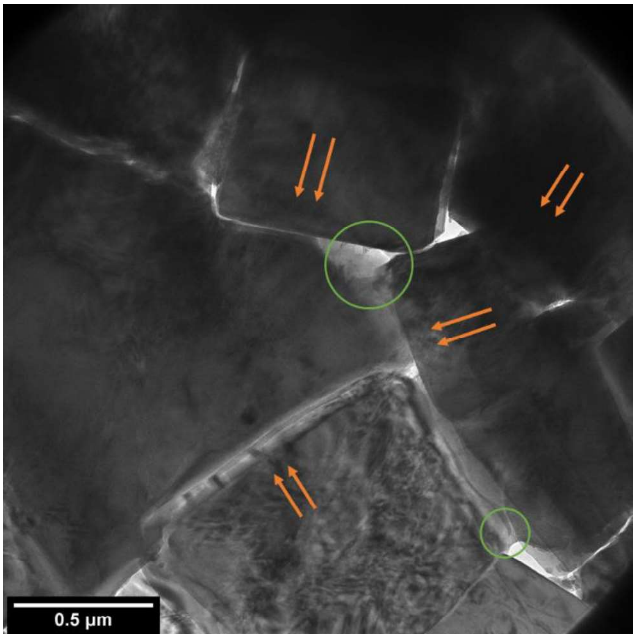

Figure 5.1-4 – TEM micrograph of several grains in FLASH sintered KNN. The orange arrows indicate the particle movement and the green circles the amorphized phase that is filling some pores.

In some cases, penetration of one grain into its neighbour grain is apparent, as illustrated by the arrows in Figure 5.1-4. Furthermore, no grain growth is observed, and coarser grains remain < 4 μm. These observations suggest that mass transport through conventional diffusion is not the dominant sintering mechanism in water assisted FLASH KNN. Our observations contradict previous reports of grain growth of KNN after 30 s of FLASH in air and at 250 V/cm, 20 mA/mm^2 [11]. Several parameters may contribute to these discrepancies such as the use of different atmosphere, electrical current limit, specimen shape and primary particle size. However, our observations suggest that water assisted FLASH promotes the formation of a liquid phase in KNN which appears as amorphous material within intergranular pores on cooling, circled in Figure 5.1-4. There is no evidence of a similar amorphous phase in conventionally sintered samples [24]. Our observations are therefore, broadly in agreement with Narayan [25], [26] who predicted local melting through a high current density at GBs. As pointed out by Dancer [5], Narayan's model requires that FLASH occurs in the presence of a liquid phase, and it would be expected that some evidence of that high temperature viscous phase would be present at the GBs [10], [27]. Moreover, R. Chaim and co-works showed that particle surface softening by liquid film formation during FLASH contributes considerably to the fast sintering process. Furthermore, they have shown that thermal gradient between the solid particle and its melted/softened surface can be as high as 3000 K [28], [29].

Our TEM studies further suggest that conventional mass transport via diffusion is limited and that a more likely explanation is densification through minimisation of surface energy facilitated by the sliding of grains within a viscous liquid medium. Therefore, we suggest that water assisted FLASH sintering in KNN occurs mainly through channelling of current through open pores, which have adsorbed water on the surface of the particles. Given this proposed mechanism, the anisotropy of KNN primary particles (cuboid) might also be expected to influence current density distribution, the Joule heating, local temperature and thus the extent of formation of a liquid phase (volume of residual amorphous material on cooling). There are four potential arrangements of cuboid contact in the green body prior to FLASH: (i) face-face, both in (100) direction; (ii) edge-face, (100) with (110) direction, (iii) vertex-face, direction (111) with (100); and (iii) vertex with vertex, both in (111) direction.

Based on simplistic field enhancement, the current density is expected to be higher in geometries with the lowest contact area and this should then be reflected in the volume of amorphous phase in adjacent regions. Figure 5.1-5 exemplifies the face-face contact direction. The current and Joule heating runaway induces the grain boundaries melting and sliding, resulting in the observed consolidation. The inset in Figure 5.1-5 is a magnified image which shows more clearly the thin amorphous layer at the GB.

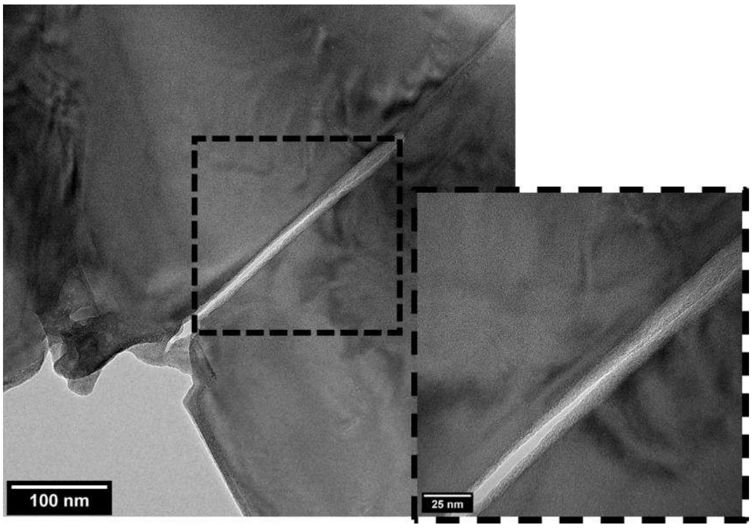

Figure 5.1-5 – TEM micrograph exemplifying the consolidation by FLASH of two particles with face-face [(100)-(100)] contact.

At a vertex-face boundary, the melting and volume fraction of amorphous phase should be more pronounced. Figure 5.1-6 shows a region where there is contact of the central grain via the vertex to the faces of adjacent grains. Evidence of local melting is observed through the interpenetration of the vertices with the faces (outlined) and through the amorphous phase which is contained in the intergranular pore (arrowed). Note that the amorphous phase appears to ion thin more quickly than the KNN grains, as illustrated by its lacey appearance. It is likely that the entire pore was filled with amorphous phase in the bulk ceramic prior to thinning. This interpretation is supported by the SEM image of the FLASH sintered ceramic in Figure 5.1-3, in which individual grains are difficult to distinguish in some parts of the image and are likely surrounded by amorphous phase.

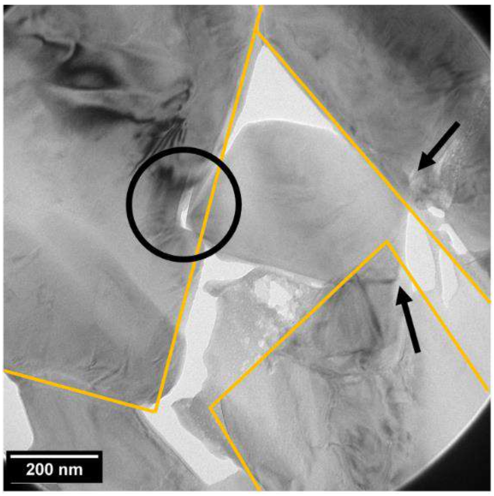

Figure 5.1-6 – TEM micrograph exemplifying vertex-face configuration. The possible original particle shape is outlined and the amorphous phase arrowed.

Figure 5.1-7 a) adds further microstructural evidence to GB melting driven by local Joule heating. This unusual microstructure is atypical of conventional sintered KNN grain boundaries and is interpreted as a relic microstructure formed by the outward diffusion of ions to the particle surface. The amorphous phase is present at the GB and the tree root shape of grain boundary amorphization may be a consequence of thermal gradient [28]. Furthermore, representative diffraction patterns (TEM *JEOL H-9000*, at 300 kV) of the amorphous areas and grains are also shown in Figure 5.1-7 b) and c), respectively. These patterns account for the clear perovskite crystalline structure of the grains (with a 110 zone axis), and a non-crystalline evidence of the designated amorphous areas (scattered rings). Such observation confirms what is suggested by the TEM image interpretation, which is the clear amorphization of grain boundaries and filling of pores with such amorphous phase.

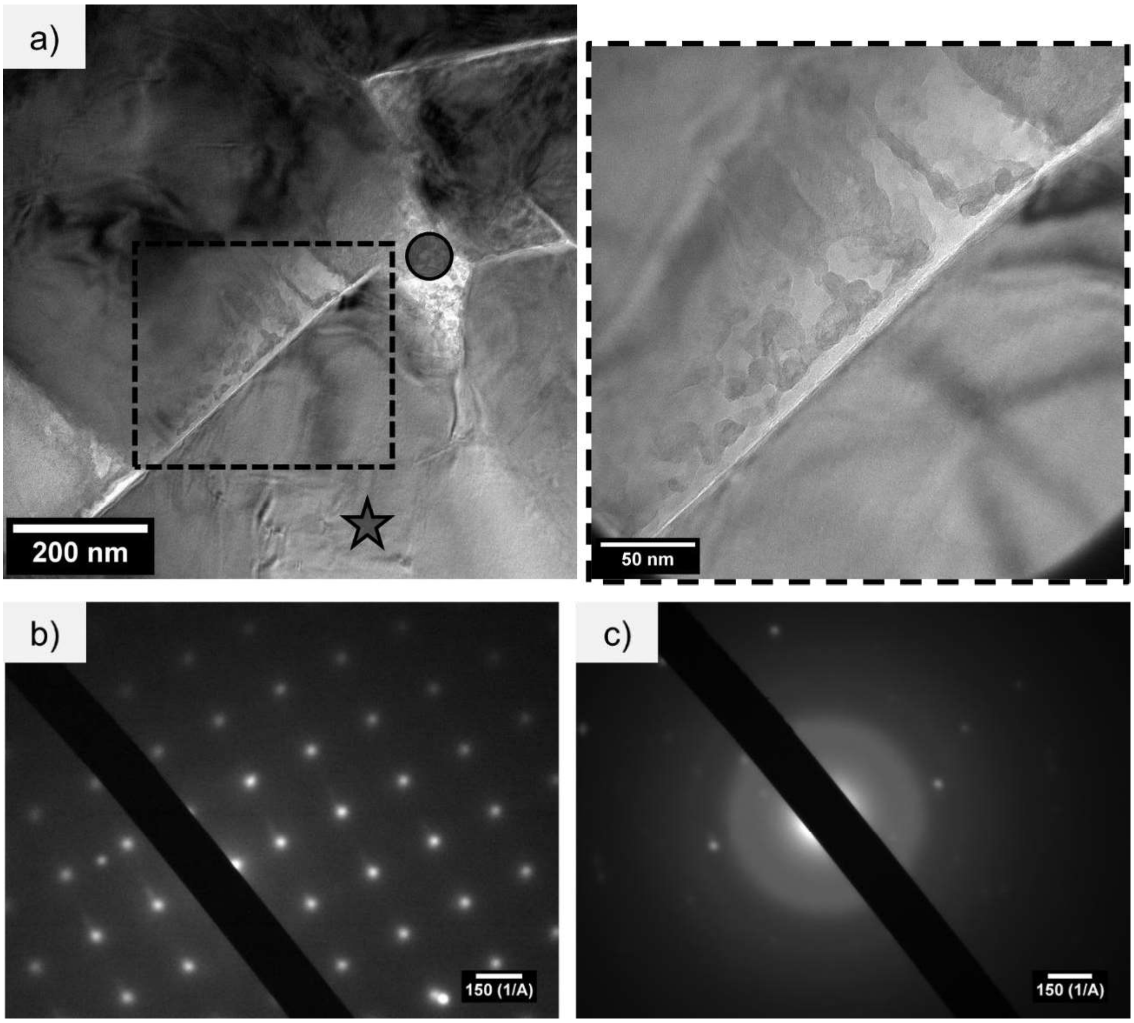

Figure 5.1-7 – a) Local melting of the FLASH sintered KNN grain boundary and pore filling with amorphous phase. The star symbol indicates the representative local for diffraction patterns of crystalline area (with a 110 zone axis), while the circle stands for amorphous areas. b) and c) show the respective diffraction patterns for crystalline and amorphous areas.

To determine the approximate chemical composition of the amorphous region resulting from liquid phase formed during water assisted FLASH, energy-dispersive X-ray spectroscopy (EDS) was performed. The EDS results are presented in Figure 5.1-8. Such analysis indicates that the chemical composition of the bulk of grains after FLASH is close to stoichiometric, which was expected from the structural analysis provided by TEM diffraction patterns (Figure 5.1-7 c)). In contrast, the amorphous phase is Na deficient and Nb and Al rich. Al_2O_3 is not a constituent of KNN but is present as impurities through raw materials and as a result of milling. We propose that during FLASH sintering Al segregates to the GBs and participates in the formation of a liquid phase; simultaneously Na is volatilised [23] leaving behind an Al_2O_3-Nb_2O_5 rich amorphous phase, the composition of which will depend in the local proximity of Al_2O_3 impurities. These observations suggest that not only thermal gradients are responsible for local melting during water assisted FLASH, but also contaminations are segregated at grain boundaries, producing low melting point secondary phases that promote densification and sliding.

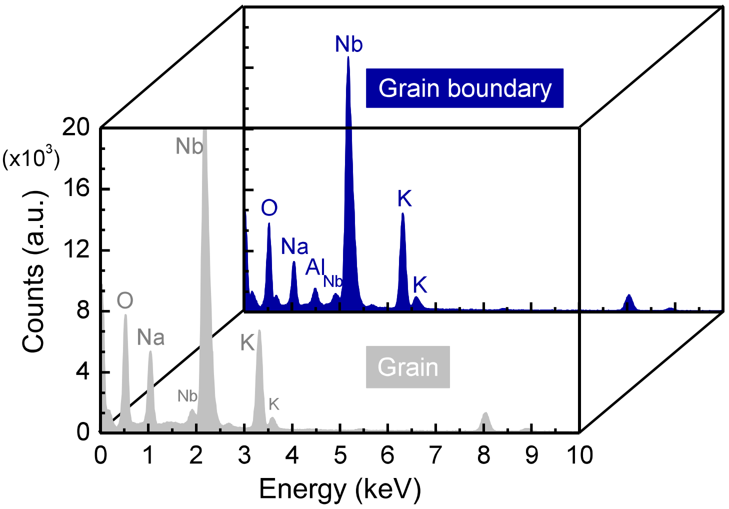

Figure 5.1-8 – EDS spectra for FLASH sintered KNN grain (grey) and GB (blue).

To explain the formation of the alumina-niobia formation at GBs, the respective phase diagram for those phases is shown in Figure 5.1-9 [30]. Above ~40 mol% Al_2O_3, a liquid phase is present at T > ~1200 °C. This liquid phase persists with a series of eutectic points until there is a slight increase in melting temperature for 100 % Nb_2O_5, confirming that the presence of contaminations as alumina in KNN water assisted FLASH sintering might contribute to grain boundary melting and pore filling with amorphous phases.

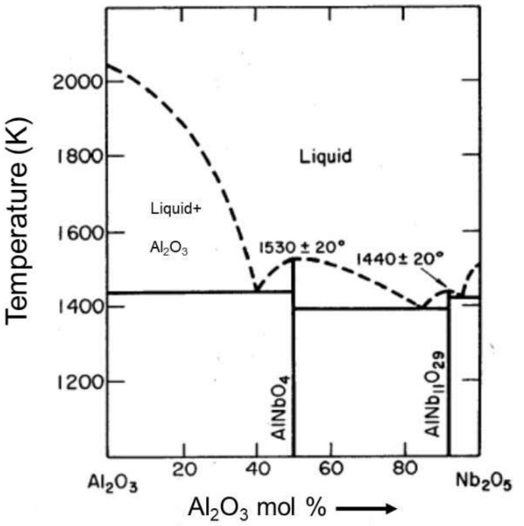

Figure 5.1-9 – Al_2O_3 – Nb_2O_5 phase diagram. [30]

We propose therefore that, despite the FLASH furnace temperature not exceeding 300 °C, the local temperature through Joule heating exceeds 1000 °C and is sufficient to locally melt grain boundaries. These results are broadly in agreement with Uehashi *et al.* who FLASH sintered $BaTiO_3$ at 1020 °C, with an electric field of 100 V/cm. They reported that GBs partially melted along with BaO volatilisation and accompanied by the formation of a Ba deficient phase, $BaTi_4O_9$ [31].

From the TEM observations we conclude that: i) there is evaporation of Na at the GBs, ii) liquid phase forms at the grain boundaries and iii) bulk KNN retains its stoichiometry and structure.

FEM (Finite Element Modelling) of the current distribution during FLASH sintering was also performed. We consider only the effect that the geometry has upon the Joule heating effect. We first consider the possible geometric points of contact between the particles. Each simulated model combined two interacting 0.5 µm size cubes, overlapped by 50 nm and generating a connection point. The cubes were orientated in three directions to provide different geometric configurations: face-face, (100)-(100), edge-face, (100)-(110), face to vertex, (100)-(111) and vertex to vertex direction, where the cubes are aligned in the (111)-(111) direction as shown in Figure 5.1-10. Each cube is assigned the electrical properties (conductivity) of KNN [32]. Each configuration was meshed, and a refinement applied at the connection point to ensure convergence. It is important to note that the goal of the FEM model is to explain the possible particle penetration, and the possible relation between particle contact and generated heat by FLASH sintering. More complex and accurate modelling work is now being conducted.

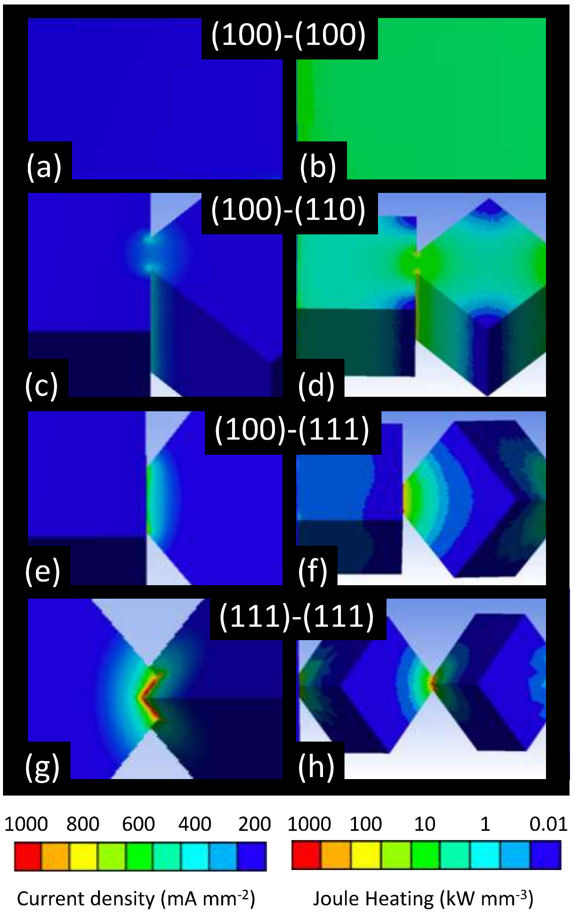

Figure 5.1-10 – The simulated current densities (a,c,e,g) and Joule heating (b,d,f,h) arising from face-face (a,b), face-edge(c,d), face-vertex(e,f) and vertex-vertex(g,h) contacts within a green KNN body. Note a logarithmic scale is used to plot the Joule heating effect.

To perform this FEM calculations, a potential difference was applied over the cubes, such that the current was forced through the contact points. To calibrate the voltage and provide a value to allow comparison, the face to face configuration as shown in Figure 5.1-10 a) and b) was used. An applied voltage of 0.08 V gave rise to a maximum current density of 60 mA/mm^2 in the model, consistent with current limited values and generating Joule heating of 3.6 kW/mm^3. To ensure similarity between the models, the same voltage was then used to highlight the increase in current density and associated Joule heating that would arise due to changes in the geometry of particle to particle contact. It should be noted that the approach of maintaining this voltage may lead to unreasonable current densities and heating effects, as the material may melt before this voltage could be reached. The absolute values are thus not as important as the comparison between them. A line-scan was used through the centre of the model to extract these values as a function of distance from the connection point, and the results are shown in Figure 5.1-11.

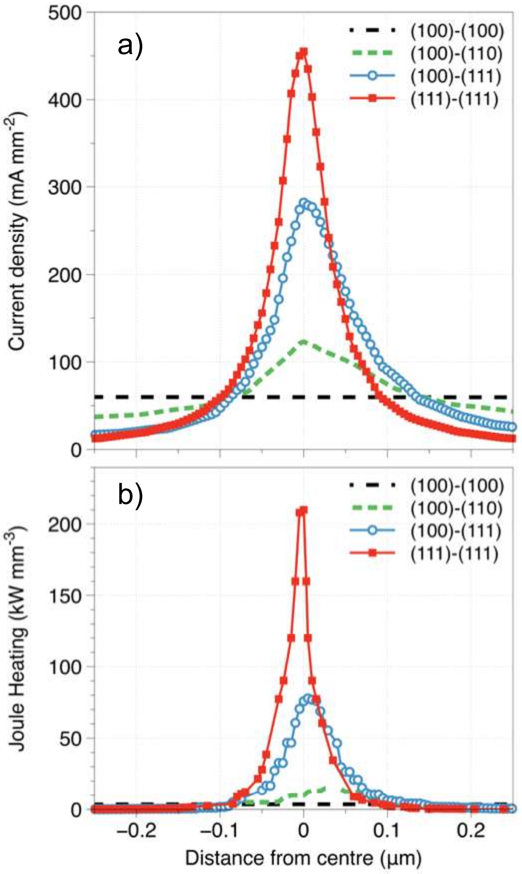

Figure 5.1-11 – The current density (a) and Joule heating (b) profiles taken from line scans through the centre of the model. These are plotted as a function of the distance of the connection point (i.e. where the cubes overlap).

When the cuboid particles were orientated face-edge, the current density increased by a factor of two, to 120 mA/mm^2, Figure 5.1-11 a). The associated Joule heating, due to its dependence on the square of the current, rises to 14 kW/mm^3, Figure 5.1-11 b). Values of 282 mA/mm^2 and 455 mA/mm^2 are measured for the face to vertex and vertex to vertex models, respectively, accompanied by Joule heating with a face-vertex and vertex-vertex configuration of 70 kW/mm^3 and 200 kW/mm^3, respectively. Asymmetry was also observed in models in which two different orientations of cubes are used. For face-edge and face-vertex configurations, greater Joule heating is measured in the edge or vertex-oriented cube with deeper penetration. The asymmetry can be attributed to the initialisation of the model set-up and overlap of the cubes. As the model does not simulate the evolution of this process, this aspect is a subject for further work and analysis.

The maximum value of the vertex-vertex system was greater than those measured from the central line-scan. Joule heating was found to be significantly higher on the outer surface of the cube, around the connection point, Figure 5.1-10 g), than through the centre, Figure 5.1-11. Current densities in excess of 1000 mA/mm^2 occurred at the surface, corresponding to a Joule heating effect of over 1000 kW/mm^3, 16x and 250x, respectively, greater that the face-face configuration. Although physically these values would not be possible, we propose that this significant increase in heating arising from the orientation of the cube quickly would lead to fast thermal runaway during FLASH sintering, resulting in a larger local concentration of liquid phase at these points than others.

The SEM and TEM evidence combined with FEM, clearly indicate that Joule heating is a major factor in densification. The channelling of current along open porosity emphasises the importance of adsorbed water and the cuboid shape of KNN particles highlights the role of contact geometry on current density and local heating. The formation of liquid phase (residual amorphous regions at the GB) occurs often in the presence of impurities. Although a liquid phase at high temperature will enhance diffusion, the large volume fraction of liquid suggests that densification is also driven by minimisation of surface energy of the liquid phase, enabled by sliding of grain boundaries. The work demonstrates the need for further research on the role of particle geometry and size and impurities in water assisted FLASH sintering.

5.1.4. Conclusions

This work describes for the first time the mechanism of low-temperature water assisted FLASH sintering in complex oxides such as KNN and establishes the relation between the geometry of particle contact and local Joule heating. Our observations suggest that conventional diffusion and mass transport at GBs is not solely responsible for the densification of KNN. We postulate that densification occurs through current channelling along open pores made more conductive by the adsorption of water onto the particle surface. We attribute densification to the sliding of grain boundaries and viscous flow of the liquid phase generated from melting, driven by minimisation of surface energy. We note that our work demonstrates for the first time the densification of a lead-free piezoceramic using water assisted FLASH sintering and thus has ramifications not only for materials substitution but more generally for the reduction of carbon consumption in the ceramics industry.

5.1.5. References

[1] S. Chu, Y. Cui, and N. Liu. “The path towards sustainable energy”. Nat. Mater., vol. 16, no. 1, pp. 16–22, 2016.

[2] E. Manavalan and K. Jayakrishna. “A review of Internet of Things (IoT) embedded sustainable supply chain for industry 4.0 requirements”. Comput. Ind. Eng., vol. 127, no. November 2018, pp. 925–953, 2018.

[3] M. Cologna, B. Rashkova, and R. Raj. “Flash Sintering of Nanograin Zirconia in <5 s at 850°C”. J. Am. Ceram. Soc., vol. 93, no. 11, pp. 3556–3559, Nov. 2010.

[4] M. Yu, S. Grasso, R. Mckinnon, T. Saunders, and M. J. M. Reece. “Review of flash sintering: materials, mechanisms and modelling”. Adv. Appl. Ceram., vol. 116, no. 1, pp. 1–37, 2017.

[5] C. E. J. Dancer. “Flash sintering of ceramic materials”. Mater. Res. Express, vol. 3, no. 10, pp. 102001–102025, 2016.

[6] J. Nie, Y. Zhang, J. M. Chan, R. Huang, and J. Luo. “Water-assisted flash sintering: Flashing ZnO at room temperature to achieve ~ 98% density in seconds”. Scr. Mater., vol. 142, pp. 79–82, 2018.

[7] J. F. Li, K. Wang, F. Y. Zhu, L. Q. Cheng, and F. Z. Yao. “(K, Na) NbO_3-based lead-free piezoceramics: Fundamental aspects, processing technologies, and remaining challenges”. J. Am. Ceram. Soc., vol. 96, no. 12, pp. 3677–3696, 2013.

[8] C.-H. Hong *et al.*. “Lead-free piezoceramics and Where to move on?”. J Mater., vol. 2, pp. 1–24, 2016.

[9] H. Birol, D. Damjanovic, and N. Setter. “Preparation and characterization of $(K_{0.5}Na_{0.5})NbO_3$ ceramics”. J. Eur. Ceram. Soc., vol. 26, no. 6, pp. 861–866, 2006.

[10] M. A. Rafiq, A. Tkach, M. E. Costa, and P. M. Vilarinho. “Defects and charge transport in Mn-doped $K_{0.5}Na_{0.5}NbO_3$ ceramics”. Phys. Chem. Chem. Phys., vol. 17, no. 37, pp. 24403–24411, 2015.

[11] G. Corapcioglu, M. A. Gulgun, K. Kisslinger, S. Sturm, S. K. Jha, and R. Raj, “Microstructure and microchemistry of flash sintered $K_{0.5}Na_{0.5}NbO_3$”. J. Ceram. Soc. Japan, vol. 124, no. 4, pp. 321–328, 2016.

[12] W. Ji, B. Parker, S. Falco, J. Y. Zhang, Z. Y. Fu, and R. I. Todd. “Ultra-fast firing: Effect of heating rate on sintering of 3YSZ, with and without an electric field”. J. Eur. Ceram. Soc., vol. 37, no. 6, pp. 2547–2551, 2017.

[13] Y. Zhang, J. Nie, J. M. Chan, and J. Luo. “Probing the densification mechanisms during flash sintering of ZnO”. Acta Mater., vol. 125, pp. 465–475, 2017.

[14] W. D. Kaplan, D. Chatain, P. Wynblatt, and W. C. Carter. “A review of wetting versus adsorption, complexions, and related phenomena: The rosetta stone of wetting”. J. Mater. Sci., vol. 48, no. 17, pp. 5681–5717, 2013.

[15] P. R. Cantwell, M. Tang, S. J. Dillon, J. Luo, G. S. Rohrer, and M. P. Harmer. “Grain boundary complexions”. Acta Mater., vol. 62, no. 1, pp. 1–48, 2014.

[16] J. Luo. “The scientific questions and technological opportunities of flash sintering: From a case study of ZnO to other ceramics”. Scr. Mater., vol. 146, pp. 260–266, 2018.

[17] M. Jiang *et al.*. “Seed-Free Solid-State Growth of Large Lead-Free Piezoelectric Single Crystals: $(Na_{1/2}K_{1/2})NbO_3$”. J. Am. Ceram. Soc., vol. 98, no. 10, pp. 2988–2996, 2015.

[18] R. Raj, M. Cologna, and J. S. C. Francis. “Influence of externally imposed and internally generated electrical fields on grain growth, diffusional creep, sintering and related phenomena in ceramics”. J. Am. Ceram. Soc., vol. 94, no. 7, pp. 1941–1965, 2011.

[19] J. S. C. Francis, M. Cologna, D. Montinaro, and R. Raj. “Flash sintering of anode-electrolyte multilayers for SOFC applications”. J. Am. Ceram. Soc., vol. 96, no. 5, pp. 1352–1354, 2013.

[20] D. Sohrabi Baba Heidary, M. Lanagan, and C. A. Randall. “Contrasting energy efficiency in various ceramic sintering processes”. J. Eur. Ceram. Soc., vol. 10, no. October, pp. 1018–1029, 2017.

[21] M. Biesuz, D. Rizzi, and V. M. Sglavo. “Electric current effect during the early stages of field-assisted sintering”. J. Am. Ceram. Soc., no. April, pp. 1–10, 2018.

[22] W. Qin, H. Majidi, J. Yun, and K. van Benthem. “Electrode Effects on Microstructure Formation During FLASH Sintering of Yttrium-Stabilized Zirconia”. J. Am. Ceram. Soc., vol. 99, no. 7, pp. 2253–2259, 2016.

[23] K. S. Naik, V. M. Sglavo, and R. Raj. “Flash sintering as a nucleation phenomenon and a model thereof”. J. Eur. Ceram. Soc., vol. 34, no. 15, pp. 4063–4067, 2014.

[24] S. Zhang, H. J. Lee, C. Ma, and X. Tan. “Sintering Effect on Microstructure and Properties of (K,Na)NbO$_3$ Ceramics”. J. Am. Ceram. Soc., vol. 94, no. 11, pp. 3659–3665, 2011.

[25] J. Narayan. “A new mechanism for field-assisted processing and flash sintering of materials”. Scr. Mater., vol. 69, no. 2, pp. 107–111, 2013.

[26] J. Narayan. “Grain growth model for electric field-assisted processing and flash sintering of materials”. Scr. Mater., vol. 68, no. 10, pp. 785–788, 2013.

[27] B. Malič *et al.*. “Sintering of lead-free piezoelectric sodium potassium niobate ceramics”. Materials, vol. 8, no. 12, pp. 8116–8146, 2015.

[28] R. Chaim. “Particle surface softening as universal behaviour during flash sintering of oxide nano-powders”. Materials, vol. 10, no. 2, 2017.

[29] R. Chaim, G. Chevallier, A. Weibel, and C. Estournès. “Flash sintering of dielectric nanoparticles as a percolation phenomenon through a softened film”. J. Appl. Phys., vol. 121, no. 14, pp. 45103–45108, 2017.

[30] R. S. Roth, T. Negas, and L. P. Cook. Phase diagrams for ceramists, First edition. The American Ceramic Society, 1981.

[31] A. Uehashi, K. Sasaki, T. Tokunaga, H. Yoshida, and T. Yamamoto. “Formation of secondary phase at grain boundary of flash-sintered BaTiO$_3$”. Microscopy, vol. 63, no. suppl 1, pp. i18–i19, 2014.

[32] K. Singh, V. Lingwal, S. C. Bhatt, and N. S. Panwar. “Dielectric properties of potassium sodium niobate mixed system”. Mater. Res. Bull., vol. 36, pp. 2365–2374, 2001.

5.2. Article: Sintering kinetics of potassium sodium niobate: FLASH vs. Conventional

To be submitted

Abstract

The relevance of alternative sintering techniques is undebatable. FLASH, an electric field and current assisted sintering technique, has been used to densify a large number of ceramics. While the technological interest is well established, the ruling sintering mechanisms seem to be material dependent and not so clear. In this work, the sintering kinetics of potassium sodium niobate, KNN ($K_{0.5}Na_{0.5}NbO_3$) is studied. After establishing the apparent activation energy for the conventional sintering process of KNN, the same classical approach was used to infer on the sintering mechanisms operating during FLASH. The decrease of the apparent activation energy for FLASH sintering in comparison with the conventional process agrees well with the proposed FLASH mechanism for KNN: the current flow and consequent Joule heating promote the formation of transient liquid contacts that allow particle sliding and pore elimination for reduction of total energy, thereby, endorsing sintering.

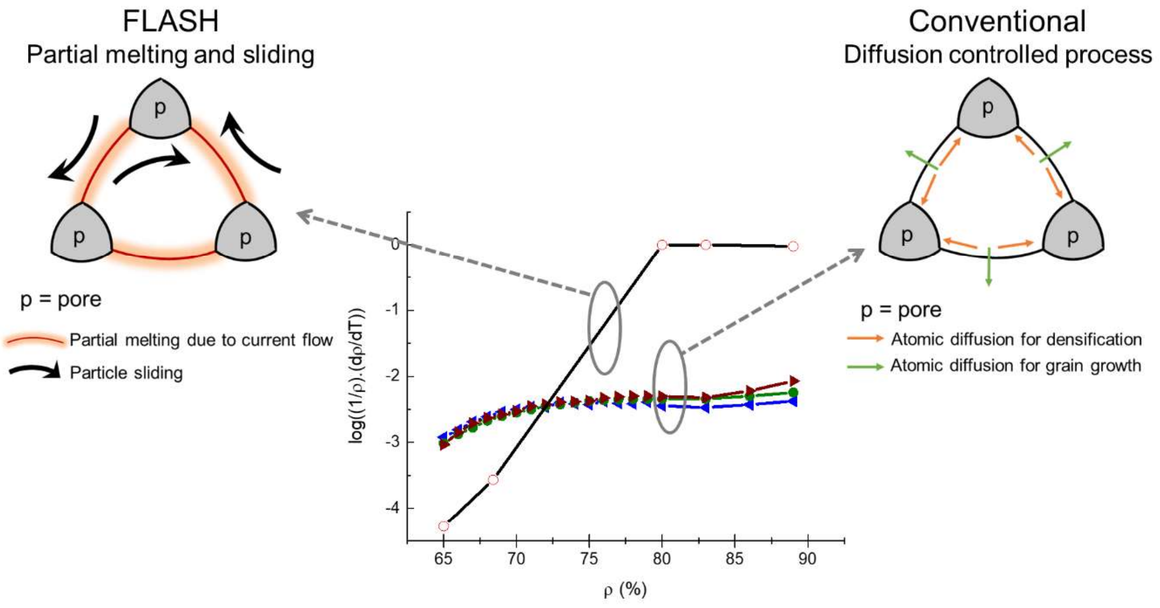

Key words

Sintering kinetics, FLASH sintering, Lead-free piezoelectrics, Potassium Sodium Niobate, KNN

5.2.1. Introduction

FLASH sintering, an electric field and current assisted sintering technique has been used to densify a great variety of ceramics [1]. Electroceramics as $K_{0.5}Na_{0.5}NbO_3$ (KNN) [2], [3], $BaTiO_3$ [4], $SrTiO_3$ [5], [6] have been targeted due to the issues related with their conventional sintering processes [7], [8]. The use of FLASH sintering allows a significant decrease in the sintering temperature, when compared with the conventional one [1]. Such event is assigned to a thermal runaway that results of the Joule heating from current flow during the FLASH [9]–[11]. When applying an electric field to a non-dense (green) ceramic compact, and after an incubation period (stage I), the ceramics suffer a fast and non-linear increase in its conductivity (FLASH onset, stage II), and current starts to flow. This occurs at the so-called FLASH temperature, T_F; densification is started during this stage, that does not take more than 5 s. After limiting the current, in stage III, the remaining sintering occurs, typically in less than 60 s [1], [12]. Because stage II happens in a short time window, it is very difficult to study. This is why most of FLASH sintering studies are performed either for stage I [13]–[15] or stage III [16], [17].

The mechanisms behind the sintering process occurring during FLASH are not yet completely clear. In fact, there are indications that, while the power dissipation transition regime is very similar regardless of the material and/or applied electric field [18], opposite results in terms of conducting mechanisms were found, for instance, for semiconductors (ZnO [19] or KNN [20]) and oxygen conductors (YSZ [21]). In the case of KNN, a lead-free piezoelectric with technological interest [22], it was shown that the particle surface conductivity [20] and respective particle-to-particle contact [14] are responsible for the conduction during FLASH. Moreover, the formation of transient liquid phases at the particle contacts seems to rule the sintering process, as suggestion of amorphized grain boundaries were found in FLASH sintered KNN [3]. However, the kinetics of FLASH sintering are yet to be understood. Recent work on YSZ have used the classical sintering theory to study the kinetics of FLASH sintering [23]. K. Ren and co-workers [23] have shown that, in YSZ, the oxygen vacancies creation and movement are responsible by controlling the sintering during the incubation and FLASH event stages, respectively.

In this work, the sintering kinetics of KNN during stage I and early-stage II of FLASH is studied, taking as a reference the conventional sintering process. In fact, a sintering kinetics study (both conventional and FLASH) for $K_{0.5}Na_{0.5}NbO_3$ is presented for the first time.

5.2.2. Experimental

99.9% pure $K_{0.5}Na_{0.5}NbO_3$, KNN, powders were produced by solid-state reaction, using ultra-high purity alkali carbonates (K_2CO_3, Sigma-aldrich, 99.99% and Na_2CO_3, Sigma-aldrich, 99.999%) and niobium oxide (Nb_2O_5, Alfa Aesar, 99.9%). A calcination step was performed, after mixing, at 900 ºC for 3h. For particle size refinement, a final ball milling step of 24 h was employed. Supplementary information gives details on particle size distribution. For detailed powder characterization, see [20].

KNN powders were uniaxially and isostatically pressed into 65$\pm$1% green density compacts with ca. 15 x 5 x 2 mm^3. Sintering studies were performed in an adapted dilatometer, as referred in [14]. For conventional sintering, different constant heating rates of 2, 5 and 10 ºC/min were employed to a maximum temperature of 1200 ºC. For FLASH sintering, 10 ºC/min heating rate and an electric field of 300 V/cm were applied. Reaching the FLASH temperature, the current was automatically limited to 20 mA/mm^2 and a holding time of 60 s was controlled. Details on these Constant Heating Rate (C.H.R.) FLASH experiments may be found elsewhere [14]. During the sintering process, both the furnace temperature and relative length displacement (α) of compacts were recorded; throughout the FLASH experiments, current and voltage were also recorded, and the ceramic conductivity calculated.

To calculate the activation energy for densification of both conventional and FLASH processes, an isotropic shrinkage behaviour was considered (valid for $0 < -\alpha < 2\%$). In such conditions, the density during sintering process (ρ_c) is given by eq. 2-11 (see section 2.4.4). The classical description of sintering kinetics [24] states that the instantaneous densification rate, $d\rho/dt$, is expressed by an Arrhenius dependence (eq. 2-12, reproduced here), in which E_a is the activation energy for the densification process, R_G is the gas constant, T is the absolute temperature, G is the grain size, n_c is the characteristic constant for the densification mechanism, A is the material parameter (independent of G, ρ or T) and $f(\rho)$ is a function of the density [23], [24].

$$\frac{d\rho}{dt} = A.\exp\left(\frac{-E_a}{R_G\,T}\right).\frac{f(\rho)}{T.G^{n_c}} \qquad (2\text{-}12)$$

Taking the natural logarithm on eq. 2-12, the activation energy can be measured through an Arrhenius formulation of $\ln\left(\frac{d\rho}{dt}.T\right)$ *vs* $\frac{1}{T}$, as shown in equation 5-1 [23], [24]. Here, it is assumed that $f(\rho)$ and G are kept constant when the linear shrinkage of the samples does not change more than 2% in a frozen microstructure. A constant, C, is considered to account for these parcels. For FLASH sintering experiments, the calculated specimen temperature, in accordance with Black Body Radiation (BBR) model, was considered [19], [25], [26].

$$\ln\left(\frac{d\rho}{dt}.T\right) = \frac{-E_a}{R_G}.\frac{1}{T} + \ln(C) \qquad (5\text{-}1)$$

5.2.3. Results and discussion

The relative displacement (α) of KNN compacts as a function of temperature, at constant heating rate of 10 °C/min, is shown in Figure 5.2-1 with the solid lines, for a) conventional and b) FLASH sintering processes. Simultaneously, Figure 5.2-1 reveals the respective shrinkage rate ($-\frac{d\alpha}{dt}$), in dashed red lines, for each ceramic. Black arrows indicate the shrinkage rate maximum. Figure 5.2-1 shows a typical green compact displacement behaviour with temperature, with a small expansion ($\alpha > 0$) occurring before the densification onset, or shrinkage ($\alpha < 0$). However, when examining both α and $-\frac{d\alpha}{dt}$ curves for conventional and FLASH processes, it becomes clear that the KNN sintering behaviour is significantly different as respect to the process, in accordance with what was previously reported [14]. Conventionally sintered compacts (Figure 5.2-1 a)) present a uniform shrinkage behaviour from T = 900 °C until T = 1100 °C, where α = -15%. At T $\approx$ 1047 °C and $\alpha \approx$ -5.7%, a maximum of shrinkage rate is found, $-\frac{d\alpha}{dt} \approx 1.3\text{x}10^{-4}\ s^{-1}$ – see the black arrow. For T > 1050 °C the shrinkage process is no longer uniform, and a second shrinkage rate maximum is identified for T $\approx$ 1080 °C. The appearance of two sintering maxima during conventional sintering of KNN compacts is related with its relatively large particle size distribution, together with the influence of aggregates (identifiable in Figure SI-5.2-1 b) in supplementary information), that induce a differential densification; smaller, more reactive particles, contribute for a first sintering maximum, and coarser particles/aggregates, for the second one.

When an electric field (300 V/cm) is applied to a KNN compact, FLASH sintering occurs, and the behaviour is shown in Figure 5.2-1 b). In accordance with reported work [20], the FLASH temperature, T_F, is observable at T $\approx$ 916 °C. At such temperature, a sudden and very fast shrinkage occurs. It is shown that the FLASH sintering process is significantly different from the conventional one. In this case, the maximum shrinkage velocity is $-\frac{d\alpha}{dt} \approx 8\text{x}10^{-3}\ s^{-1}$, about 60 times faster than that of conventional. This data is in agreement with the previously reported one [14]. However, to properly understand the FLASH sintering process of KNN, sintering kinetic studies shall be performed.

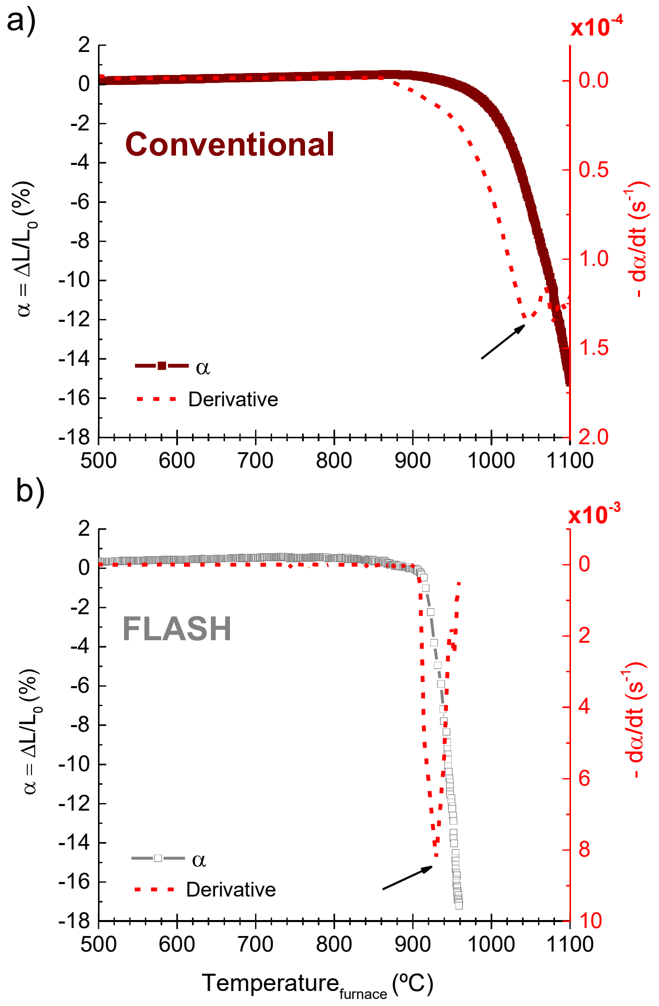

Figure 5.2-1 - Relative length variation (α) as a function of furnace temperature (solid lines) with constant heating rate of 10 ºC/min, and respective shrinkage rate (dashed-red lines), for a) conventional and b) FLASH sintering.

To depict the kinetics of KNN conventional sintering, Figure 5.2-2 shows the a) relative displacement (α) and b) respective shrinkage rate (- $\frac{d\alpha}{dt}$), as a function of temperature, for KNN compacts heated at different heating rates, namely 2, 5 and 10 ºC/min. A detail on - $\frac{d\alpha}{dt}$ for $0 \leq -\alpha \leq 2\%$ is shown in b). The data shows a thermally activated process, with densification onset ($\alpha < 0\%$) occurring at lower temperature for slower heating rates. In addition, Figure 5.2-2 b) shows that the heating rates have an influence on the shrinkage rate, which is revealed to be lower for slower heating rates. Additionally, for $T > 1000$ ºC, the uniform behaviour is lost, and the differential densification starts to be revealed, with different shrinkage maxima occurring at different regimes. Though, for T < 1000 ºC (and α > -2%), the sintering process is uniform and can be described by the classical first stage sintering theory [27].

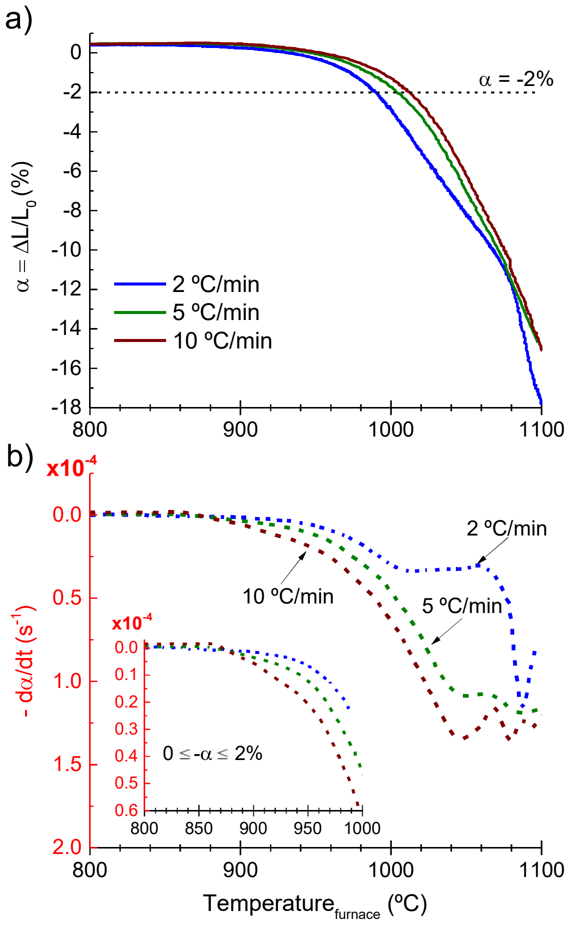

Figure 5.2-2 – a) Relative length displacement and b) respective shrinkage rate as a function of temperature for KNN compacts heated at different heating rates (2, 5, and 10 ºC/min).

To determine the apparent activation energy for the first stage of conventional sintering Figure 5.2-3 shows the Arrhenius representation of density rate (calculated from α, following eq. 2-10) versus the inverse of absolute temperature (eq. 5-1), for conventionally sintered KNN compacts at different heating rates and $0 \leq -\alpha \leq 2\%$ condition. It is shown that $\ln(T.\frac{d\rho}{dt})$ over 1000/T presents a linear dependence, allowing the calculation of an apparent activation energy for the densification (E_a). The data shows a dependence of E_a with the heating rate; the slower the rate, the higher the activation energy, with E_a (2 ºC/min) = 432±1 kJ/mol, E_a (5 ºC/min) = 375±2 kJ/mol and E_a (10 ºC/min) = 328±3 kJ/mol.

This behaviour was previously reported [28], [29] and it is related with lower process velocity for slower heating rates.

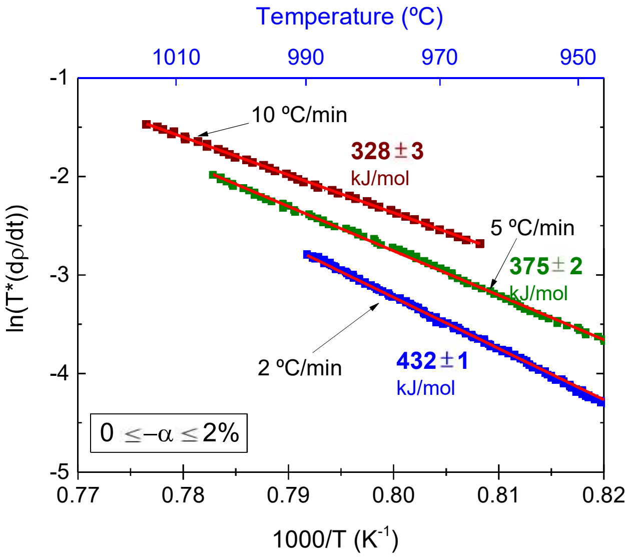

Figure 5.2-3 – Arrhenius representation of density rate over the inverse of absolute temperature (eq. 5-1), as a function of the heating rate, and respective activation energy for densification (E_a) estimation, for conventional sintering.

While E_a estimations from Figure 5.2-3 are in good agreement with mass transport by surface diffusion for a thermally activated sintering processes [30], a glimpse that the densification procedure is dependent on the heating rate is raised. Thus, it is expected that FLASH sintering would present significantly different apparent activation energy, due to the reported considerably higher heating rates caused by Joule effect [9], [23], [28].

However, when estimating the activation energy during FLASH sintering process, several issues arise: (i) a precise estimation on the sample temperature is not known; (ii) the speed of the process and the few available data points for Arrhenius representation, in comparison with conventional process; (iii) the possible anisotropy during shrinkage as a consequence of increased liquification of particle contacts and consequent particle sliding [3], [14]. To assess these issues, (i) the E_a can be calculated from Black Body Radiation (BBR) specimen temperature estimation [19], [25], [26] and compared with that of measured furnace temperature; (ii) the process was studied for $0 \leq -\alpha \leq 2\%$, decreasing the influence of shrinkage anisotropy and allowing a sufficient number of data points for E_a estimation.

Figure 5.2-4 a) reveals the Arrhenius representation of densification rate for FLASH sintering (for $0 \leq -\alpha \leq 2\%$) as a function of the measured furnace temperature. It is shown that, in accordance with Figure 5.2-1, the velocity of FLASH sintering process is dramatically different from that of conventional, thus the few registered data points (acquired with 1 s interval each). Nevertheless, two sintering regimes are recognizable, which are representable of stage I and II of FLASH sintering [20]. The respective calculated activation energies for stage I and II of FLASH, as a function of furnace temperature, are 238±51 and 3416±604 kJ/mol, respectively. While the first stage E_a is quite comparable with those of conventional sintering process, E_a of stage II is at least 10 times higher than expected. Moreover, these estimations are not accurate, as the estimated error for the linear fit is significant. This low accuracy was expected because the actual specimen temperature (here considered as the furnace temperature) is being approximated to a significantly lower temperature than actually reported for the FLASH process [16], [31], [32].

Furthermore, recently published work in kinetics of FLASH process makes use of BBR estimation for specimen temperature, to allow a more accurate estimation of E_a [23]. Therefore, Figure 5.2-4 b) shows the Arrhenius representation of densification rate vs. the inverse of estimated temperature ($T_{calc.}$). Here, the same two regimes are observed, however, the estimations errors are lower, and E_a (stage I) = 16.4±0.5 kJ/mol while E_a (stage II) = 267±22 kJ/mol. The accuracy of E_a estimation is significantly increased in this case. Nonetheless, for the first regime, E_a is lower than any other estimation so far, however, that is explained by the almost insignificant shrinkage ($\alpha \approx 0\%$). On the other hand, during stage II, even though very few points are recorded to $0 \leq -\alpha \leq 2\%$, a reasonably linear regime is observed.

In accordance with Figure 5.2-4 b), E_a (stage II) = 245 to 289 kJ/mol. Such activation energy estimation for densification of FLASH process is debatable because classical theory is used to describe an out-of-equilibrium process. Nevertheless, the recently published work in YSZ reveals the reasonable relation between each estimation (for conventional and FLASH) [23]. On top of that, and despite that the electroluminescence observed during stage III of FLASH was recently dissociated from black body radiation phenomena [12], [16], [33], an accurate specimen temperature estimation is yet to be established. Among the presented possibilities for E_a estimation, the use of BBR temperature estimation gives a much more accurate result. Furthermore, for early FLASH stages (I and II), BBR is accepted to be fairly accurate [34]. Therefore, the estimated activation energies are representable.

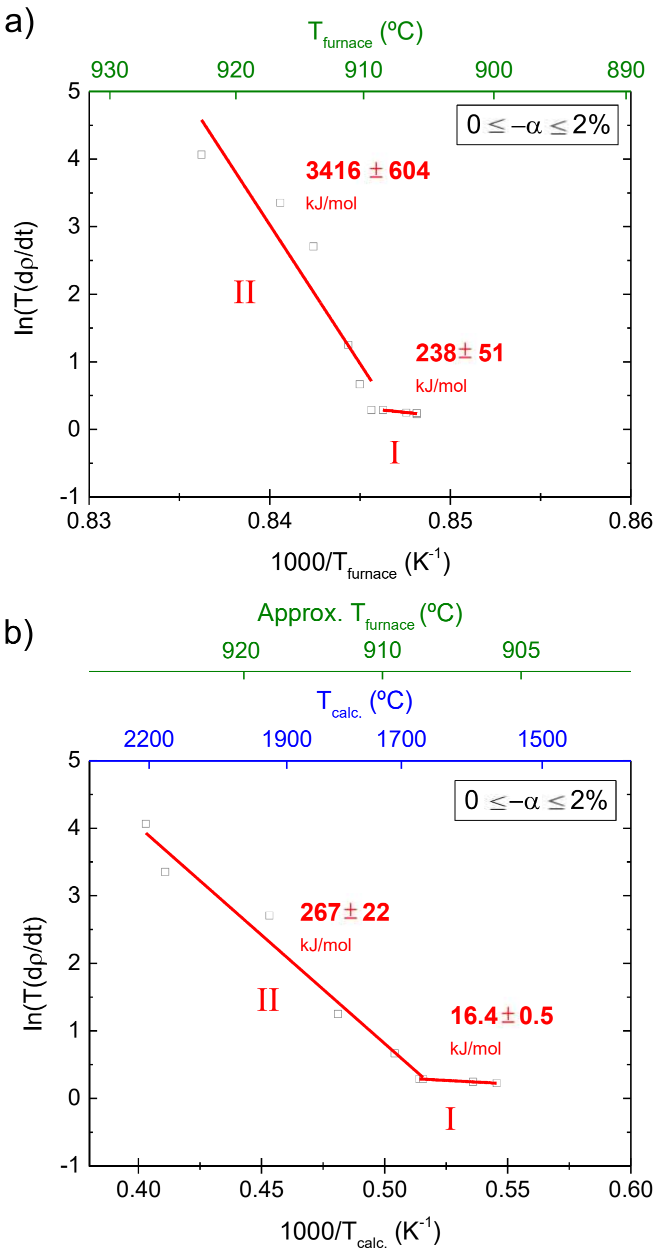

Figure 5.2-4 – Activation energy for densification, E_a, estimation from Arrhenius representation for FLASH sintering process with a) furnace temperature and b) estimated BBR specimen temperature.

In this work, the estimated apparent activation energies for FLASH and conventional early sintering stages are, respectively, 245 to 289 and 325 to 433 kJ/mol, the second being dependent on the heating rate. If a direct relation is possible between these two estimations (Figure 5.2-3 and Figure 5.2-4 b)), it is possible to argue that the FLASH sintering process of KNN occurs with a lower activation energy for densification, typically associated with surface transport processes, while for E_a > ~300 kJ/mol, volumetric transport should be the ruling mechanism (conventional sintering case). Additionally, Levasseur and Brochu [35] have shown that the sintering of Ni-based metallic alloys (Inconel 718) spherical particles, that occurs in presence of a liquid, is dependent on the heating rate. For high heating rates (> 25 ºC/min), the apparent activation energy for densification was 198 kJ/mol, while that of low heating rate (15 ºC/min) was 250 kJ/mol. It was stated that the sintering process was limited by the solid-state diffusion of alloying elements (between 202 and 285 kJ/mol), that has a greater *dragging* effect for low heating rates [35]. Similarly, in this work, it is suggested that the very high heating rate promoted by the thermal runaway during FLASH sintering of KNN decreases the activation energy for sintering by promoting a greater formation of liquid phase. In fact, when current channelling occurs, a proof of the presence of such amorphized phases on FLASH sintered ceramics was revealed [3].

So far, it was established that the apparent densification activation energy of KNN during stage I of FLASH is lower than that of stage II. The opposite behaviour was observer by K. Ren and co-workers for YSZ [23]. While the FLASH sintering of YSZ is controlled by the oxygen defect conduction, and surface conductivity is not the ruling process [19], [21], in the case of KNN, surface conductivity [20] and the formation of localized liquid transient phases [3], [14] occurs. Therefore, the sintering mechanisms are dissimilar, with the stage I being responsible by the nucleation of conducting defects (very low activation energy for sintering because $\alpha \approx 0\%$); during stage II, particle sliding occurs, accelerated by the presence of liquid phases, and sintering is promoted by minimization of energy (lower activation energy than conventional process).

A complementary approach to study the sintering kinetics of differently activated process was presented by S. Schwarz at al. [28]. Accordingly, Figure 5.2-5 shows the representation of densification rate as respect to temperature – furnace temperature for conventional and estimated specimen temperature for FLASH sintering – as a function of relative density. Note that the analysis presented before in Figure 5.2-4 shows the densification rate as respect to the time.

Figure 5.2-5 reveals that, for conventional sintering, all the curves, as respect with the heating rate, merge accordingly, revealing the previously discussed behaviour: despite the dissimilar heating rates, the operating sintering mechanism during conventional process is the same. For $\rho > 80\%$, a dissociation of the curves is observed due to the differential densification promoted by the wide particle size distribution and presence of aggregates. However, the behaviour is drastically changed when FLASH sintering is considered (Figure 5.2-5, black curve). Here, the data for $70 < \rho < 77\%$ is not represented due to the non-regular behaviour of data-points. Nevertheless, in accordance with what was observed by S. Schwarz *et al.* [28], when using field-assisted sintering techniques in ZnO, the densification rates over relative density do not overlap with conventional process, thus suggesting that a different sintering mechanism must occur during FLASH sintering. Additionally, the kinetics analysis of liquid-film assisted FLASH sintering was studied by R. Chaim [36]. It was shown that the presence of a liquid-film in between particles accounts for the dramatic reduction of the energy for particle sliding and consequent densification.

The combined analysis of Figure 5.2-4 and Figure 5.2-5 gives strong indications that the operating sintering mechanisms during FLASH and conventional sintering of KNN are dissimilar. During FLASH sintering of KNN, the formation of Frenkel defects, oxygen defects as V_O^{oo} and electrons and holes (e’, h^{o}) may be increased by the presence of the electric field. Hence, the charge movement, especially through the grain boundary is increased [37],[38], creating an additional heating through particle surfaces by Joule effect, which induce a significantly higher heating rate upon sintering [10], [36], [39]. Thus, the activation energy for densification during FLASH was expected to be lower than that of conventional.

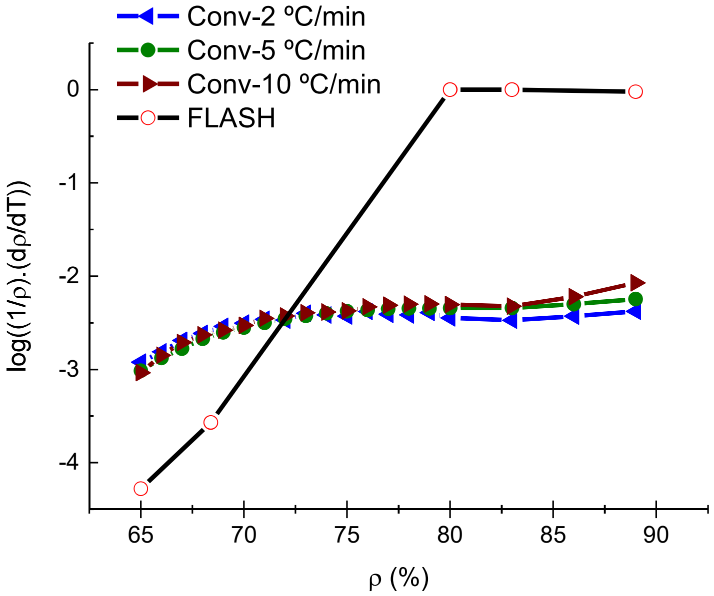

Figure 5.2-5 - Densification rates with respect to temperature as a function of relative density for conventionally (at different heating rates) and FLASH sintered KNN ceramics.

In a direct comparison with activation energy for densification, the activation energy for conduction, $E_a(\sigma)$, was calculated (following an Arrhenius dependence) for the same KNN compacts, and is shown in Figure 5.2-6. If compared with the calculations from Figure 5.2-4 b), E_a (stage I) < $E_a(\sigma)$ < E_a (stage II), 16, 70 and 267 kJ/mol, respectively. This observation is another confirmation that the energy needed to allow conduction on the green KNN compact is not enough to generate densification. To promote densification, heating by

Joule effect needs to take place, which is a consequence of the conducting process. The very fast heating promotes the partial melting of particle contacts [3], [10], thus allowing a very fast sintering process to occur, supported by accelerated surface transport, with lower activation energy than that of conventional volumetric mass transport.

Likewise, our previously reported works [3], [14] suggested this partial particle melting to be the ruling mechanism during FLASH sintering. TEM observations, combined with grain size analysis allowed to conclude that the presence of amorphized grain boundaries [3] and the absence of abnormal grain growth [14],[37] for FLASH sintered ceramics, prove that partial liquification of particle-to-particle contacts occurs during FLASH sintering, allowing particle to slide by viscous flow.

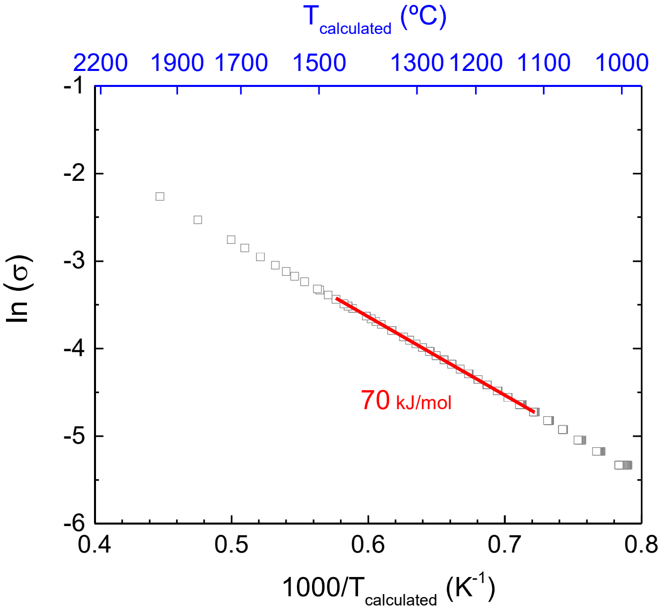

Figure 5.2-6 – Arrhenius dependence of conductivity with inverse of absolute estimated temperature, and respective activation energy for conduction ($E_a(\sigma)$).

5.2.4. Conclusions

In summary, the study of sintering kinetics of KNN allowed the calculation of apparated activation energies for densification by FLASH sintering process. Such work agrees with the previously proposed sintering mechanism. The presence of the electric field and consequent current flow promote the formation of localized transient liquid phases that allow particles to slide and sintering to occur through energy minimization. It is possible that surface diffusion occurs during stage II. The activation energy for densification in that case is lower than that of volumetric mass transport of conventional process. Additionally, the FLASH process of KNN is dissimilar from that of YSZ, as previously suggested by other works. While oxygen defects movement account for FLASH sintering of YSZ, the presence of transient liquid phases in particle-to-particle contacts, with particle sliding, is the mandatory sintering mechanism.

5.2.5. Supplementary information

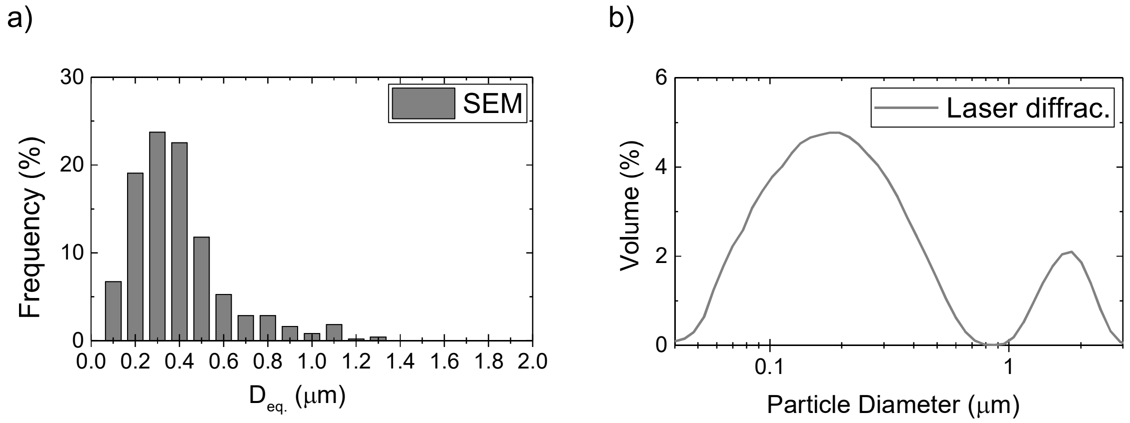

Figure SI-5.2-1 – Particle size distribution obtained from a) SEM image analysis by particle area calculation and respective equivalent diameter ($D_{eq.}$) and b) laser diffraction by dispersion in water. The presence of aggregates is shown in b).

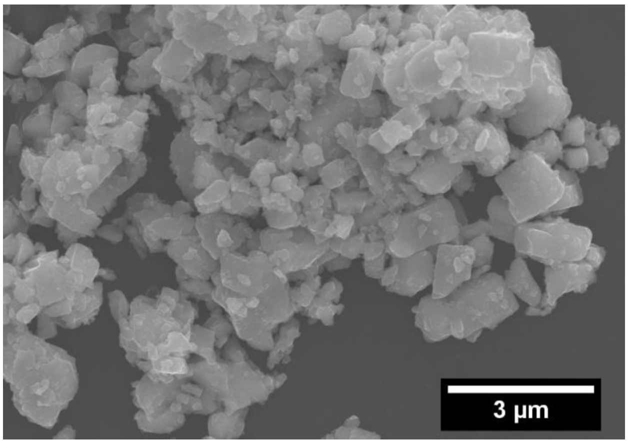

Figure SI-5.2-2 – SEM micrograph of dispersed KNN powders, revealing the cuboid particle shape.

5.2.6. References

[1] M. Biesuz and V. M. Sglavo. “Flash sintering of ceramics”. J. Eur. Ceram. Soc., vol. 39, no. 2–3, pp. 115–143, 2019.

[2] G. Corapcioglu, M. A. Gulgun, K. Kisslinger, S. Sturm, S. K. Jha, and R. Raj. “Microstructure and microchemistry of flash sintered $K_{0.5}Na_{0.5}NbO_3$”. J. Ceram. Soc. Japan, vol. 124, no. 4, pp. 321–328, 2016.

[3] R. Serrazina, J. S. Dean, I. M. Reaney, L. Pereira, P. M. Vilarinho, and A. M. O. R. Senos. “Mechanism of densification in low-temperature FLASH sintered lead free Potassium Sodium Niobate (KNN) piezoelectrics”. J. Mater. Chem. C, vol. 7, pp. 14334–14341, 2019.

[4] R. Shi *et al.*. “Flash sintering of barium titanate”. Ceram. Int., vol. 45, no. 6, pp. 7085–7089, Apr. 2019.

[5] F. Lemke, W. Rheinheimer, and M. J. Hoffmann. “A comparison of power controlled flash sintering and conventional sintering of strontium titanate”. Scr. Mater., vol. 130, pp. 187–190, 2017.

[6] W. Rheinheimer, X. L. Phuah, H. H. Wang, F. Lemke, M. J. Hoffmann, and H. H. Wang. “The role of point defects and defect gradients in flash sintering of perovskite oxides”. Acta Mater., vol. 165, no. December, pp. 398–408, 2019.

[7] B. Malič, A. Benčan, T. Rojac, and M. Kosec. “Lead-free piezoelectrics based on alkaline niobates: Synthesis, sintering and microstructure”. Acta Chim. Slov., vol. 55, no. 4, pp. 719–726, 2008.

[8] B. Malič *et al.*. “Sintering of lead-free piezoelectric sodium potassium niobate ceramics”. Materials, vol. 8, no. 12, pp. 8116–8146, 2015.

[9] K. S. N. Vikrant, H. Wang, A. Jana, H. Wang, and R. E. García. “Flash sintering incubation kinetics”. Comput. Mater., vol. 6, pp. 1–8, 2020.

[10] R. Serrazina, P. M. Vilarinho, A. M. O. R. Senos, L. Pereira, I. M. Reaney, and J. S. Dean. “Modelling the particle contact influence on the Joule heating and temperature distribution during FLASH sintering”. J. Eur. Ceram. Soc., vol. 40, pp. 1205–1211, 2020.

[11] R. Chaim and C. Estournès. “On thermal runaway and local endothermic/exothermic reactions during flash sintering of ceramic nanoparticles”. J. Mater. Sci., vol. 53, no. 9, pp. 6378–6389, 2018.

[12] S. K. Jha, K. Terauds, J. Lebrun, and R. Raj. “Beyond flash sintering in 3 mol % yttria stabilized zirconia”. J. Ceram. Soc. Japan, vol. 124, no. 4, pp. 283–288, 2016.

[13] R. Kirchheim. “Incubation time for flash sintering as caused by internal reactions, exemplified for yttria stabilized zirconia”. Acta Mater., vol. 175, pp. 361–375, 2019.

[14] R. Serrazina, A. M. O. R. Senos, L. Pereira, J. S. Dean, I. M. Reaney, and P. M. Vilarinho. “The Role of Particle Contact in Densification of FLASH Sintered Potassium Sodium Niobate”. Eur. J. Inorg. Chem., vol. 2020, no. 39, pp. 3720–3728, 2020.

[15] R. Raj and H. Chan. “Analysis of the Power Density at the Onset of Flash Sintering”. J. Am. Ceram. Soc., vol. 99, no. 10, pp. 3226–3232, 2016.

[16] K. Terauds *et al.*. “Electroluminescence and the measurement of temperature during Stage III of flash sintering experiments”. J. Eur. Ceram. Soc., vol. 35, no. 11, pp. 3195–3199, 2015.

[17] X. Su *et al*.. “Flash sintering of lead zirconate titanate (PZT) ceramics: Influence of electrical field and current limit on densification and grain growth”. J. Eur. Ceram. Soc., vol. 38, no. 10, pp. 3489–3497, 2018.

[18] M. Yu, S. Grasso, R. Mckinnon, T. Saunders, and M. J. M. Reece. “Review of flash sintering: materials, mechanisms and modelling”. Adv. Appl. Ceram., vol. 116, no. 1, pp. 1–37, 2017.

[19] J. Luo. “The scientific questions and technological opportunities of flash sintering: From a case study of ZnO to other ceramics”. Scr. Mater., vol. 146, pp. 260–266, 2018.

[20] R. Serrazina, C. Ribeiro, M. E. Costa, L. Pereira, P. M. Vilarinho, and A. M. O. R. Senos. “Particle characteristics influence on FLASH sintering of Potassium Sodium Niobate: a relationship with conduction mechanisms”. Materials, vol. 14, p. 1321, 2021.

[21] D. Yadav and R. Raj. “The onset of the flash transition in single crystals of cubic zirconia as a function of electric field and temperature”. Scr. Mater., vol. 134, pp. 123–127, 2017.

[22] C.-H. Hong *et al*.. “Lead-free piezoceramics and Where to move on?”. J Mater., vol. 2, pp. 1–24, 2016.

[23] K. Ren, Q. Wang, Y. Lian, and Y. Wang. “Densification kinetics of flash sintered 3mol% Y_2O_3 stabilized zirconia.” J. Alloys Compd., vol. 747, pp. 1073–1077, 2018.

[24] J. Wang and R. Raj. “Estimate of the Activation Energies for Boundary Diffusion from Rate-Controlled Sintering of Pure Alumina, and Alumina Doped with Zirconia or Titania”. J. Am. Ceram. Soc., vol. 73, no. 5, pp. 1172–1175, 1990.

[25] R. Raj. “Joule heating during flash-sintering”. J. Eur. Ceram. Soc., vol. 32, no. 10, pp. 2293–2301, 2012.

[26] Y. Zhang, J. Nie, J. M. Chan, and J. Luo. “Probing the densification mechanisms during flash sintering of ZnO”. Acta Mater., vol. 125, pp. 465–475, 2017.

[27] S.-J. L. Kang, Sintering: Densification, Grain growth, and Microstructure. 2005.

[28] S. Schwarz, A. M. Thron, J. Rufner, K. Van Benthem, and O. Guillon. “Low temperature sintering of nanocrystalline zinc oxide: Effect of heating rate achieved by field assisted sintering/spark plasma sintering”. J. Am. Ceram. Soc., vol. 95, no. 8, pp. 2451–2457, 2012.

[29] W. Q. Shao, S. O. Chen, D. Li, H. S. Cao, Y. C. Zhang, and S. S. Zhang. “Apparent activation energy for densification of α-Al_2O_3 powder at constant heating-rate sintering”. Bull. Mater. Sci., vol. 31, no. 6, pp. 903–906, 2008.

[30] R. German, Sintering: From Empirical Observations to Scientific Principles. 2014.

[31] M. Biesuz *et al*.. “Investigation of electrochemical, optical and thermal effects during flash sintering of 8YSZ”. Materials, vol. 11, no. 7, 2018.

[32] J. G. Pereira Da Silva, J. M. Lebrun, H. A. Al-Qureshi, R. Janssen, and R. Raj. “Temperature Distributions during Flash Sintering of 8% Yttria-Stabilized Zirconia”. J. Am. Ceram. Soc., vol. 98, no. 11, pp. 3525–3528, 2015.

[33] H. Charalambous, S. K. Jha, R. T. Lay, A. Cabales, J. Okasinski, and T. Tsakalakos. “Investigation of temperature approximation methods during flash sintering of ZnO”. Ceram. Int., vol. 44, no. 6, pp. 6162–6169, Apr. 2018.

[34] B. Yoon, D. Yadav, S. Ghose, and R. Raj. “Reactive flash sintering: MgO and α-Al_2O_3 transform and sinter into single-phase polycrystals of $MgAl_2O_4$”. J. Am. Ceram. Soc., vol. 102, no. 5, pp. 2294–2303, 2019.

[35] D. Levasseur and M. Brochu. “Effect of Heating Rate on the Pressureless Sintering Densification of a Nickel-Based Superalloy”. Metall. Mater. Trans. A, vol. 47, no. 5, pp. 2257–2266, 2016.

[36] R. Chaim. “On the kinetics of liquid-assisted densification during flash sintering of ceramic nanoparticles”. Scr. Mater., vol. 158, pp. 88–90, 2019.

[37] R. Serrazina, L. Pereira, P. M. Vilarinho, and A. M. O. R. Senos. “On the influence of current density and time during stage III FLASH sintering of potassium sodium niobate”. *TO BE SUBMITTED, 2021.

[38] R. Serrazina, L. Pereira, P. M. Vilarinho, and A. M. O. R. Senos. “Atmosphere-Assisted FLASH sintering of Potassium Sodium Niobate: the influence of operating atmospheres and particle characteristics”. *TO BE SUBMITTED, 2021.

[39] R. Chaim and Y. Amouyal. “Liquid-Film Assisted Mechanism of Reactive Flash Sintering in Oxide Systems”. Materials, vol. 12, no. 1494, pp. 1–9, 2019.

Summary

The mechanisms operating for the FLASH sintering of the lead free piezoelectric material under study were proposed and validated throughout this chapter. The preliminary FEM studies presented in section 5.1 were essential for the validation of the proposed mechanism, while being responsible for deploying the more complex models presented previously in chapter 3. The study of FLASH kinetics making use of the classical description of sintering process allowed a relative comparison with the conventional process, confirming the proposed FLASH sintering mechanism. In summary, section 5.1 allowed to conclude that:

- A conventional diffusion and mass transport at grain boundaries is not solely responsible for the densification of KNN.
- The densification of KNN by FLASH (under humidified atmosphere and high current density) occurs through sliding of grain boundaries and viscous flow of the liquid phase generated from melting, driven by minimisation of surface energy.

By its turn, section 5.2 allowed the following conclusions:

- When a *conventional* FLASH process is employed (with air atmosphere and moderated current flow), the apparent activation energy for densification is lower than that of conventional process.
- This is explained by the presence of the electric field and consequent current flow which promote the formation of localized transient liquid phases that allow particles to slide and sintering to occur through energy minimization
- The FLASH process of KNN is dissimilar from that of YSZ. While oxygen defects movement account for FLASH sintering of YSZ, the presence of transient liquid phases in particle-to-particle contacts, with particle sliding, is the mandatory sintering mechanism for KNN.

While the proposed mechanism in 5.1 could be argued to be only dependent on the presence of water, the low activation energies registered in normal (non-humidified, non-reducing) atmosphere – in section 5.2 -, together with the FEM studies presented before (chapter 3), confirmed that the partial melting of particle contacts, with consequent particle sliding and pore elimination, seems the be the most plausible mechanism to explain the FLASH sintering of KNN. Additionally, suggestions that the grain growth occurs through Ostwald ripening process (chapter 4) sustains the proposed mechanism.

Chapter

6. Towards room temperature sintering of ceramics

Preamble

The influence of powder characteristics and respective particle-to-particle contact on reducing T_F was already investigated in chapter 4. Here, a new approach is demonstrated to decrease T_F. As briefly referred, our first published work on the FLASH sintering mechanism of KNN was accomplished in section 5.1, which also reports a specific combination of factors that allowed FLASH to occur at T < 300 ºC. While the focus of that work was on the sintering mechanism, demonstrated through the combination of FEM and TEM, in this chapter, the role of reducing atmospheres and water will be studied in detail. A comprehensive study on the influence of atmosphere and operating conduction mechanisms is presented in the first section (6.1), while the role of water and electric field magnitude is discussed in section 6.2.

The chapter is composed of these two contributions that make use of three KNN powders to study the operating conduction mechanisms in both *conventional* (in air) and atmosphere-assisted FLASH sintering (AAFS), using non-oxidizing atmospheres (Ar and Ar/H_2). Additionally, the role of water (in the atmosphere and in the powder) is studied and the compromise between low FLASH temperature and high densification is discussed.

6.1. Article: Atmosphere-Assisted FLASH sintering of Potassium Sodium Niobate: the influence of operating atmospheres

To be submitted

Abstract

The request for extremely low temperature and short time sintering techniques as guided the development of alternative ceramic processing. Atmosphere-assisted FLASH sintering (AAFS) combines the direct use of electric power to packed powders with the engineering of operating atmosphere to allow very low temperature conduction.

The AAFS of Potassium Sodium Niobate, $K_{0.5}Na_{0.5}NbO_3$, a lead-free piezoelectric, is of great interest to the electronics technology, to produce efficient, low thermal budget sensors, actuators, piezo harvesters, among others. Not studied yet, the role of different atmospheres for the decrease in FLASH temperature (T_F) of KNN is presented in this work. Additionally, the effect of humidity presence on the operating atmosphere is investigated. While the low partial pressure of oxygen (reducing atmospheres) allows the decrease of T_F, very limited densification is observed. However, the powder morphology and operating atmospheres were co-related with conducting mechanisms and final density. It is shown that AAFS is responsible for a dramatic decrease in the operating temperature (T < 320 ºC), while water is essential to allow appreciable densification.

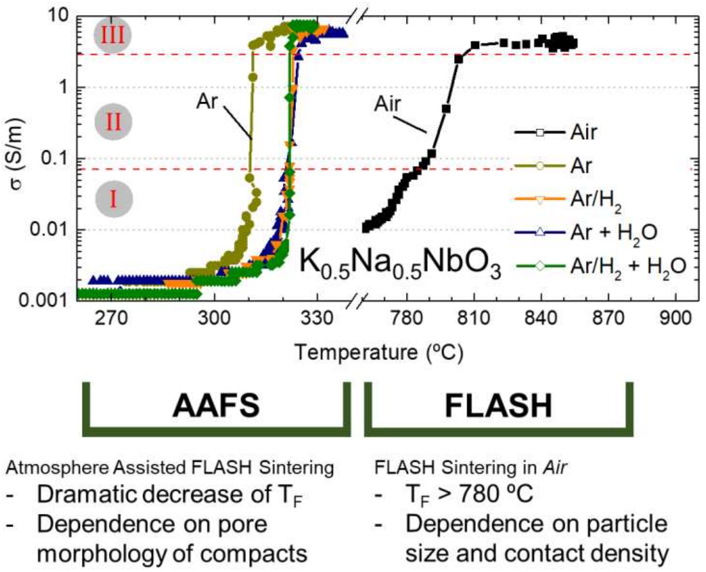

Key words

Atmosphere-Assisted FLASH sintering (AAFS); Low-temperature sintering; KNN; Electrical conductivity; Water.

6.1.1. Introduction

FLASH is an electric field and current assisted sintering technique that has been reported to dramatically decrease the sintering temperature and time of ceramics [1]–[3]. The direct application of an electric field to an insulator, along with external factors that promote electrical long-range conduction in the material (temperature, sintering atmosphere, or others) result in a current increase during the FLASH process, responsible for a very fast densification [3]. Most of the research has been performed in constant heating rate (C.H.R.) processes, in which the conduction mechanisms of un-sintered pellets (green bodies) are thermally activated. In such case, FLASH temperature, T_F, is defined as the temperature at which the material presents enough conductivity to allow a current flow, and FLASH sintering to occur. During the heating and simultaneous application of the electric field, three stages are identified: stage I, incubation, where the electric field and external heating are responsible for the nucleation and activation of conducting mechanisms, without significant densification occurring; stage II, when FLASH occurs, with a power spike and very fast, abrupt densification; stage III, or steady-state, when the pellet undergoes the remaining densification towards full density, and the current is limited, avoiding total melting of the ceramic [3], [4].

Besides the thermally activated FLASH sintering processes, Atmosphere-Assisted FLASH sintering, herein designated as AAFS, has been stated to reduce T_F. Nanometric zinc oxide, ZnO, was FLASH sintered to 98% relative density at room temperature under reducing humidified atmosphere of $Ar/H_2 + H_2O$ [5]. Previously, this material had been FLASH sintered in dry Ar/H_2, however at ≈120 °C [6]. The reducing atmospheres, as *Ar* and Ar/H_2 mixture, were described to increase the conductivity of ZnO at low temperature, first by decreasing the PO_2, and second with an added effect of hydrogen interstitials defects working as shallow donors [6]. Additionally, ZnO was used to demonstrate a new, low temperature, sintering technique, FLASH-Cold sintering. In that case, not only H_2O is added to powders, as an external pressure and electric field are applied to promote sintering [7]. While AAFS and FLASH-Cold sintering are promising techniques, the clear understanding on the activation of conduction and respective sintering processes was not achieved.

Potassium sodium niobate, $K_{0.5}Na_{0.5}NbO_3$ (KNN), a promising lead free piezoelectric, was reported to FLASH sinter in *Air* at temperatures around 900 °C [8]–[10]. Moreover, AAFS allowed to densify KNN pellets below 300 °C in a humidified *Ar* atmosphere [11]. In such work, high current density (60 mA/mm^2) was used to promote densification at low temperature, and it was postulated that a preferential melting through particles' surface was the consequence of current flow and water adsorption in the green pellet. Such melting would allow fast densification through sliding of grain boundaries and viscous flow of the liquid, driven by the minimisation of the compact's surface energy [11]. Nonetheless, current localization was revealed in such study, with non-uniform densification being reported.

If KNN is to be used as a lead-free piezoelectric for replacement of market leader PZT ($Pb(Zr_{1-x}Ti_x)O_3$, further understanding on the role of atmosphere for the low temperature FLASH sintering is needed. Furthermore, it is essential to achieve knowledge on the conducting mechanisms and their effect on the densification during AAFS of KNN, especially when reducing atmospheres as *Ar* and *Ar/H₂* are used. This knowledge will encourage founded process developments towards room temperature, sustainable processing of lead-free piezoelectrics and other materials.

In this work, AAFS was used to sinter nanometric KNN powders, with different granulometry, for the establishment of the link between particle characteristics, FLASH temperature and operating atmosphere. The role of sintering atmosphere on T_F was studied using argon (*Ar)*, a mixture of argon with hydrogen (*Ar/H_2*) and *Air*. The role of water was assessed by humidifying the reducing gases. The activation energies for conduction during AAFS and *Air* FLASH were calculated and compared, establishing the mechanisms for conduction.

6.1.2. Experimental

Potassium Sodium Niobate, $K_{0.5}Na_{0.5}NbO_3$ (KNN) powders with 99% purity were produced via conventional solid-state reaction, as previously reported [11]. After calcination, two dissimilar milling steps were considered for particle size control. A conventional ball milling (BM) step of 24 h, at 200 RPM in teflon jars, using YSZ balls and ethanol as dispersant, producing the BM powder. In parallel, as-calcined powders were attrition milled (AM), with YSZ balls in ethanol, using a teflon jar however, in this case, at 700 RPM for 14 h, producing the AM powder. The powders morphology, size, structure, and chemistry were characterized and presented in detail elsewhere [12]. In addition to the previously described characterization, powder crystallite size was determined from X-ray Diffraction (XRD) patterns, using a LaB_6 standard for the calibration of the instrumentation broadening.

Both BM and AM powders were uniaxially (ca. 130 MPa) and isostatically (ca. 200 MPa) pressed into parallelepipedal-shaped pellets of ca. 7 x 5 x 2 mm^3. To determine the pore size and distribution in green compacts, a mercury porosimeter was used (*Micromeritics - Autopore IV 9500*).

To study the FLASH sintering process of compacts under different atmospheres, silver electrodes were painted in opposite faces and dried in ambient conditions for 1 h. This process guarantees a good electrical contact between the KNN compacts and the platinum sheets. The powder compacts were placed in an alumina sample holder with a pushing rod to maintain the contact between the two opposite platinum electrodes, as reported before [11]. To perform the AAFS process, an atmosphere-controlled furnace was used and the reducing gases (argon or argon + 5vol% hydrogen mixture, *Ar* and *Ar/*H_2, respectively), were constantly fluxed (ca. 500 ml/min) into the samples holder system; a purging time of 30 min was executed prior to the heating and electric field application (in similar conditions to the previously reported [5], [11]). Furthermore, to produce humidified atmospheres, the *Ar* and *Ar/*H_2 gases were bubbled through a water containing flask, (achieving a 100% relative humidity content on the environment, measured with a *DeltaOhm HD2717 sensor*), and flowed to the sample holder in the same conditions as dry atmospheres. For comparison, *Air* FLASH experiments were conducted. In this last case, Ag was not used due to its limited thermal stability. All FLASH sintering experiment were conducted at 10 ºC/min heating and cooling rate, with a constant electric field (*EPS HV 5006-400* power source) of 300 V/cm.

The conductivity (σ) of green KNN compacts was calculated from the direct measurement of the current flow through the system, which was limited to 20 mA/mm^2. It is important to note that, in the present work, the current density was limited to 20 mA/mm^2 to avoid the formation of broad hotspots and channelling of electrical current, as previously reported [11][13]. The furnace temperature, applied voltage and current were acquired by in-house developed hardware and software. To determine the activation energy for conduction ($E_a(\sigma)$) of KNN pellets, an Arrhenius representation of $\ln(\sigma)$ as a function of 1/Tcalc was considered. Here, Tcalc stands for the estimated specimen temperature using Black Body Radiation model [14].

Before and after sintering, all the ceramics were measured and the geometrical apparent density, as well as the relative density considering a theoretical density of 4.5 g/cm^3, were calculated. To evaluate the macroscopic appearance of AAFS KNN sintered ceramics, an optical microscope was used (*LEICA EZ4HD*). For microstructural analysis of both powders, compacts and sintered ceramics, a field-emission scanning electron microscope (SEM, *Hitachi SU-70*) at 15 kV acceleration potential was used.

6.1.3. Results and discussion

Characterization of powders and compacts

Table 6.1-1 shows characteristics of the produced KNN powders. Detailed analysis may be found elsewhere [12]. In the scope of the present work, it is important to note that BM and AM have significantly different features, due to their final milling step. In summary, BM is the coarser powder, which is shown by the average particle size determinations (either by specific surface area, laser diffraction or SEM imaging), but also confirmed by crystallite size determinations (from XRD) - Table 6.1-1. Additionally, the chemical composition (determined by ICP) of powders reveals that the alkali ratios (K/Na and (K+Na)/Nb) agree with $K_{0.5}Na_{0.5}NbO_3$ composition, and that the contamination from YSZ balls (milling media) is residual for both cases [12].

Table 6.1-1 – KNN powders characteristics. Equivalent particle diameter (D_{BET}) calculated from specific surface area determination, average particle size from laser diffraction (D50-laser) and SEM images (D50-SEM), crystallite size determined from XRD and composition accessed by ICP (comprising alkali rations and Zr contamination). Adapted from [12].

	Particle size			**Crystallite size**	**Composition (ICP)**		
Powder	**D_{BET}** (nm)	**D50-laser** (nm)	**D50-SEM** (nm)	**D - XRD** (nm)	**K/Na**	**(K+Na)/Nb**	**Zr (at%)**
BM	350	235	350	~100	1.0±0.1	1.1±0.1	0.10±0.01
AM	171	204	210	~50			

Figure 6.1-1 shows the micrographs of powders and respective compacts of a) BM and b) AM KNN. The smaller particle size of AM KNN is evidenced, while a cuboid particle shape is revealed for both powders, which is typical of KNN. Table 6.1-2 shows additional KNN compacts features. The geometrical green density, the porosity and the equivalent average pore size are presented, and the data shows that the coarser powder (BM) and the finer one (AM) present distinct packing characteristics. AM compacts have slightly higher green density (determined geometrically) and lower porosity (determined by porosimetry). The discrepancy between the geometric green relative density and porosity are related with the limit detection of the porosimeter, that might overestimate the porosity values, as well as the underestimation of geometrically measured densities. Additionally, Table 6.1-2 shows that the average pore size ($\overline{\mathrm{D}_{\mathrm{pore}}}$) of AM compacts is 71 nm, less than half of that of BM (150 nm), which is revealed in Figure 6.1-2. In such figure, differential mercury volume intrusion as respect to the pore diameter for the KNN compacts is shown. It is clearly

indicated that BM compacts present larger pore size (D_{pore}), associated with a wider distribution of sizes (20-300 nm). In opposition, AM compacts show a sharper differential volume intrusion maximum (from 10-100 nm), with a lower average pore size.

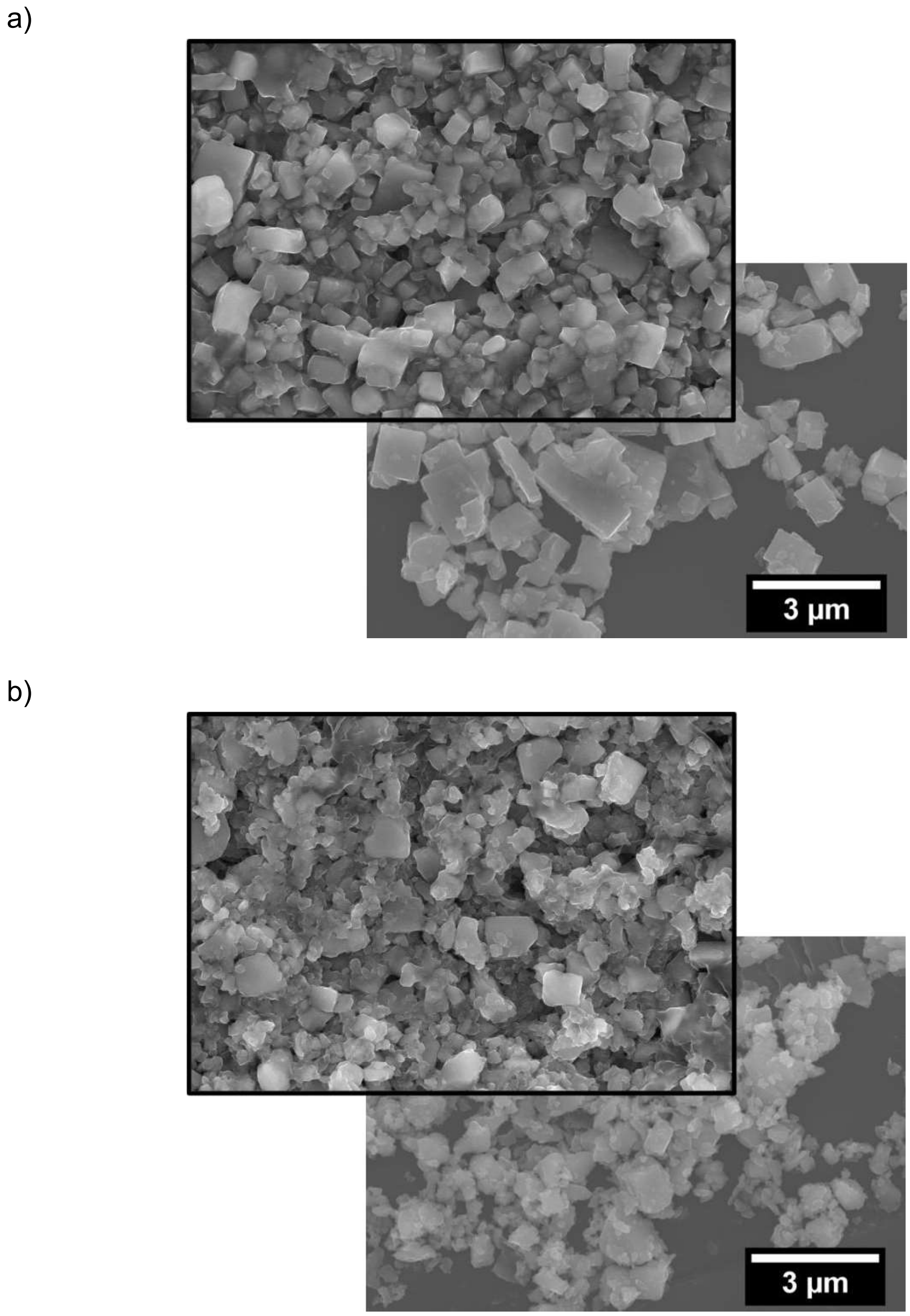

Figure 6.1-1 – SEM micrographs of a) BM and b) AM powders, overlapped with the respective green compacts' microstructure.

Table 6.1-2 – KNN compacts characteristics. Green (geometric) relative density (ρ_{green}); porosity and equivalent average pore size ($\overline{D_{pore}}$) determined by mercury porosimeter.

Compact	ρ_{green} (%)	Porosity (%)	$\overline{D_{pore}}$ (nm)
BM	63±2	33	150
AM	65±2	28	71

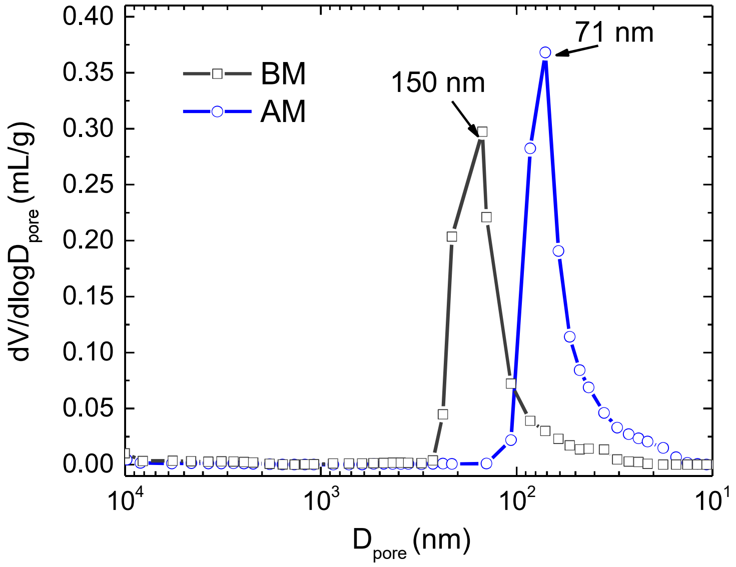

Figure 6.1-2 – Differential volume intrusion per mass unit as a function of the pore diameter (D_{pore}).

In summary, the finer (AM) particle sized powder resulted in denser green compacts, with lower porosity and smaller and sharper pore size distribution than the BM powder compacts. These observations indirectly indicate that the pore distribution (porosity channels) must be more uniformly distributed in the case of AM.

FLASH sintering in dry and humidified atmospheres

The electrical conductivity as a function of furnace temperature is represented in Figure 6.1-3 for BM and AM powders, in a) and b), respectively. Equal electrical and thermal conditions but different sintering atmospheres were used to FLASH sinter such compacts, namely, dry ones – *Air*, *Ar and Ar+*H_2 – and humidified – *Ar +* H_2O *and Ar+*H_2 *+* H_2O*.* The data shows rather similar FLASH processes independently of the employed atmosphere, however, that is not the case for the FLASH temperature, T_F. A clear and prominent dependence of T_F with the operating atmosphere is revealed. Table 6.1-3 summarizes the FLASH temperatures estimated from Figure 6.1-3. Each experimental condition was repeated at least once, and the standard deviation from the mean value of T_F was calculated when 3 or more repetitions were performed. Additionally, Table 6.1-3 gives information on the relative final density (ρ_{sint}) of BM and AM sintered compacts.

A first analysis on BM compacts reveals that the use of *Ar* atmosphere allows a T_F decrease from 870 ºC (*Air*) to 276 ºC. If a hydrogen containing dry atmosphere is used (*Ar/*H_2) the FLASH temperature is slightly increased to 295 ºC. A similar tendency is observed when humidified reducing atmospheres are employed, with *Ar* + H_2O and *Ar/*H_2 + H_2O giving slightly higher T_F (284 and 306 ºC, respectively) than the correspondent dry atmospheres.

Previously reported for ZnO [6] and KNN [11], the use of low oxygen content (reducing) atmospheres dramatically decreases T_F, which is related with the defect chemistry of materials, a topic discussed later on. Additionally, when hydrogenized [6] and/or humidified [5] atmospheres are used to FLASH sinter ZnO, the T_F is further decreased (ultimately, to room temperature [5]). However, in opposition with that, both hydrogenized (*Ar/*H_2) and humidified atmospheres (*Ar* + H_2O *and Ar/*H_2 + H_2O) used in AAFS of KNN faintly increased T_F, in comparison with the correspondent non-hydrogenized and/or dry atmospheres. These observations must have a relationship with the interaction of different gases and humidity with the material, which is not known yet.

In parallel, Table 6.1-3 and Figure 6.1-3 reveal that AAFS of BM compacts resulted in very low final densification (ρ_{sint}). For compacts AAFSed under *Ar, Ar/*H_2 and *Ar/*H_2 + H_2O, the final density is not increased when compared with the un-sintered compacts, meaning that sintering did not occur. Nonetheless, the densification of compacts FLASH sintered in *Ar* + H_2O, is already appreciable, leading to specimens with 74% of relative density.

Even though the water role on AAFS is yet not well understood, it was demonstrated to be associated with the achievement of high density for ZnO (98%), by a process based on increased mass transport and consequent greater densification [5]. In the case of KNN, water shows a promising effect towards the increase in density for AAFS in *Ar* + H_2O atmosphere.

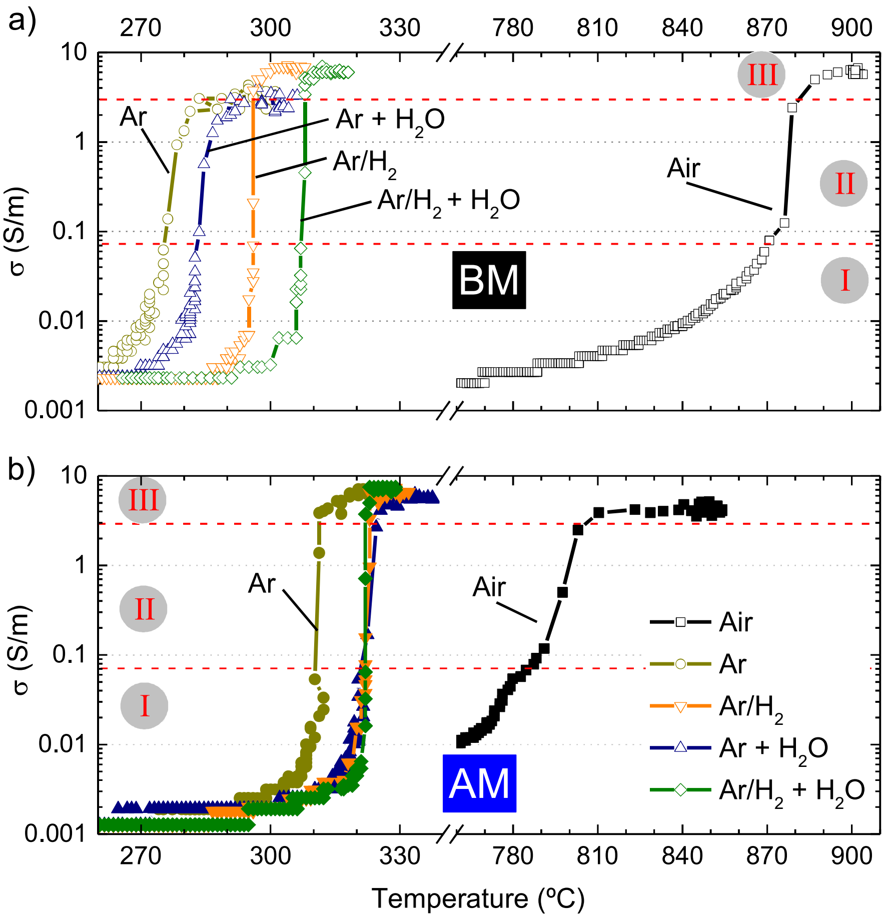

Figure 6.1-3 - In-situ conductivity over temperature during FLASH experiments of a) BM (open symbols) and b) AM (closed symbols) compacts, under different atmospheres: *Air* (squares), *Ar* (circles), *Ar/H$_2$* (down triangles), *Ar + H$_2$O* (up triangles), *Ar/H$_2$ + H$_2$O* (diamond). Indications of FLASH stages (I, II and III) are given.

Table 6.1-3 – FLASH temperature (T_F) and sintered relative density (ρ_{sint}) of KNN compacts in different atmospheres, under 300 V/cm electric field and 20 mA/mm^2 current density limit, at a constant heating rate of 10 ºC/min.

KNN powder	Atmosphere	T_{FLASH} (ºC)	ρ_{sint} (%)
BM	*Air*	870±5	92
	Ar	276±3	65
	Ar/H$_2$	295	61
	Ar + H$_2$O	284±4	74
	Ar/H$_2$ + H$_2$O	306	61
AM	*Air*	785±6	89
	Ar	309±4	72
	Ar/H$_2$	320	63
	Ar + H$_2$O	319±4	75
	Ar/H$_2$ + H$_2$O	322	63

When comparing BM with finer particles' AM compacts, Table 6.1-3 shows that the final density of both is very similar, regardless of the operating atmosphere during FLASH. However, that is not the case of T_F, as shown in Figure 6.1-3 and Table 6.1-3. For experiments in *Air* T_F of AM is decreased if compared with that of BM (785 and 870 ºC, respectively). This is related with the effect of particle size reduction and correspondent particle contact density increase, previously reported and discussed [12]. When AAFS is employed in AM compacts, a general observation reveals that a similar trend is obtained as in BM, with reducing atmospheres contributing for a strong decrease in T_F. In a parallel link, the use of hydrogenized and humidified atmospheres also resulted in slight T_F increases. Additionally, Figure 6.1-3 and Table 6.1-3 reveal that while T_F is decreased for AM powders when compared with BM and FLASH sintered in *Air*, the use of reducing atmospheres promoted the opposite tendency, with AM compacts AAFSed in *Ar* and *Ar/H$_2$* presenting higher T_F than BM.

The fact that the decrease of particle size augments the density of particle-to-particle contacts per volume unit explains the decrease of T_F in AM compacts compared with BM ones when *Air* FLASH is performed. However, it does not stand valid to explain the opposite tendency observed during AAFS. As presented before, Table 6.1-2 and Figure 6.1-2 show that the distribution width, average pore size and non-uniformity of pore distribution in BM compacts are larger than those of AM ones. Coarser porosity channels should increase the gas permeability in the green pellets, and a more pronounced effect of its interaction with the powder's surfaces. This effect must overlap the effect of the lower particle contact density in the compacts with coarser powder (BM) when compared to finer particle' ones (AM), explaining its lower T_F during AAFS.

Despite the detailed discussed T_F dependencies, Figure 6.1-3 also suggests that the conductive behaviour of KNN powders FLASH sintered in *Air* or reducing atmospheres is different for both BM and AM compacts. While a slow increase in σ with temperature occurs in *Air*, the transition from low conductivity (0.001 S/m) towards the FLASH event ($\sigma \gtrsim 0.07$ S/m) – stage I to stage II – during the AAFS processes is much faster, identifiable by the minor quantity of data points in Figure 6.1-3. In parallel, Table 6.1-3 reveals that the final density is very affected by the AAFS in non-oxidizing atmospheres. Therefore, the mechanisms that promote FLASH must be different than those operating for *Air* FLASH, which is why they were investigated.

Figure 6.1-4 shows the Arrhenius representation of the electrical conductivity using the estimated specimen temperature obtained from the Black Body Radiation model [14]–[16] during the FLASH process (Tcalc). The data reveals very similar tendencies, independently of the atmosphere and humidity content used in non-oxidizing AAFS. On the other hand, the *Air* FLASH sintering procedure is different from those.

In detail, the maximum calculated temperature achieved during stage I of FLASH in *Air* and Atmosphere-Assisted is significantly different, independently of the powder (BM and AM). In the first case (*Air*), stage I is completed at $1000/T \approx 0.5\ K^{-1}$, or 1727 ºC. Instead, for the AAFS in reducing conditions, stage I maximum temperature is roughly independent of the atmosphere and occurs at $1000/T \approx 0.6\ K^{-1}$, or 1394 ºC. There are more than 300 ºC difference between *Air* and AAFS calculated temperatures, with the latest occurring at lower temperature. Moreover, the transition regime, associated with stage II, is also dissimilar, as previously stated (Figure 6.1-3). A significantly larger number of data points, acquired constantly with a time interval of 1 s in all experiments, is recorded for *Air* FLASH. On contrary, a very fast transition occurs for AAFS, during stage II, with only a few points being recorded. These elements together induce a smaller generation of heat by Joule effect, observed clearly by the lower calculated temperature during stage I for AAFS when compared with *Air* FLASH. As pointed out by J. Nie and co-workers [5] in water-assisted FLASH sintering of ZnO, densification only occurs when the estimated sample temperature is above a threshold (1100 ºC, in that case). For AAFS of KNN we postulate that the minimum estimated temperature for the transition between stage I and II must be close to 1700 ºC (*Air* conditions) so that high densification is achieved.

In parallel, the apparent activation energy for conduction, $E_a(\sigma)$, during stage I was estimated from the Arrhenius representation of conductivity over estimated temperature, and is also shown in Figure 6.1-4. The results confirm the thermally activated processes for all the pellets and atmospheres. However, differences in the apparent $E_a(\sigma)$ as a dependence of the process were found. In detail, when FLASH sintered in *Air,* both BM and AM pellets presented an $E_a(\sigma)$ close to 0.7 eV. Contrary, when reducing atmospheres are used to perform AAFS, $E_a(\sigma)$ is fitted between 0.4 and 0.5 eV, independently of the powder. The small variation between different atmospheres of AAFS is not relevant and fit within the estimation error. Additionally, Figure 6.1-4 shows that similar activation energy values are obtained for each powder (AM and BM), if the same atmosphere is considered. This observation indicates that, independently of the particle contact density and pore morphology, the conducting mechanisms during FLASH is the same for each atmosphere, and T_F is changed only by the interaction of the gas and moisture with the KNN compacts.

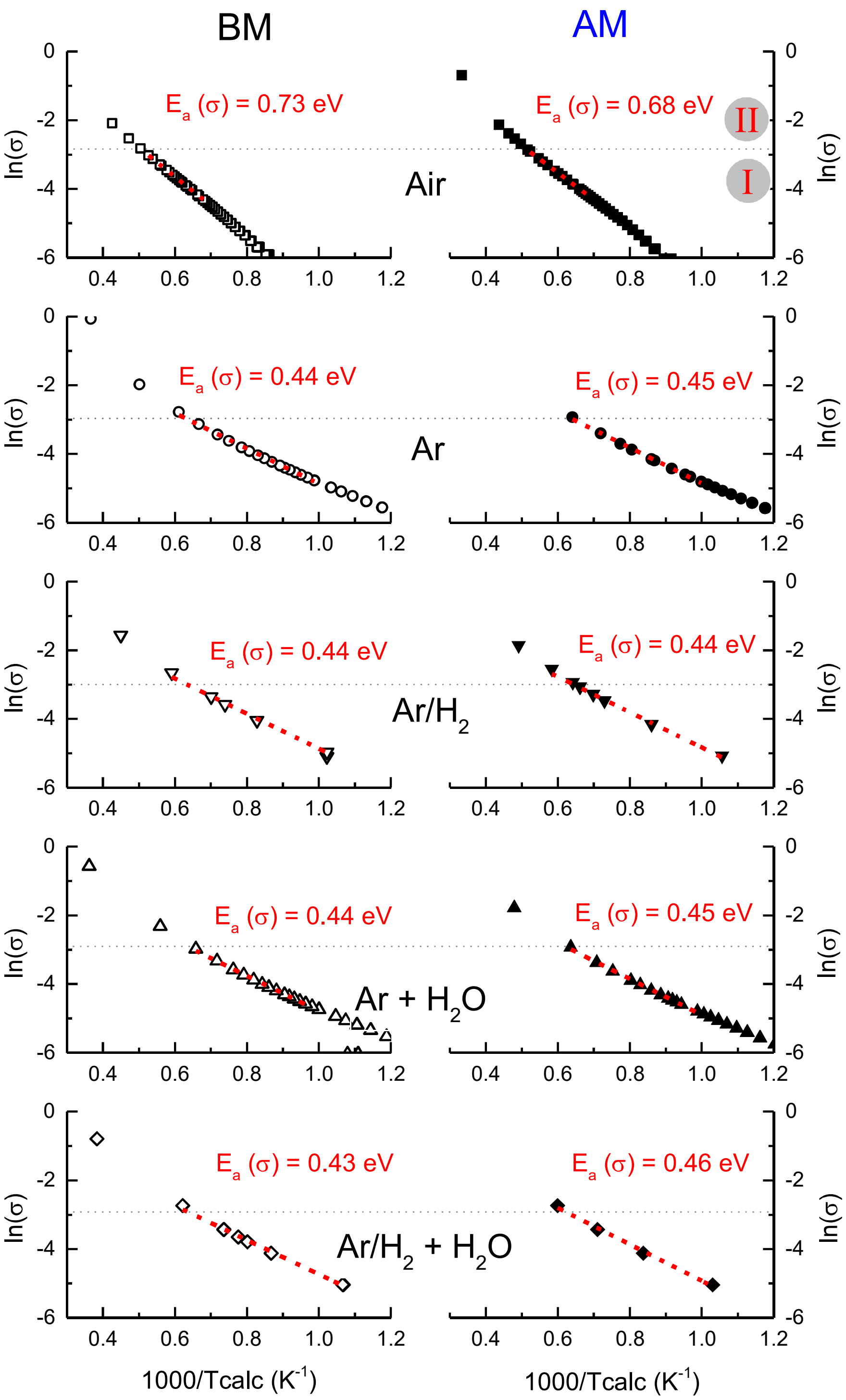

Figure 6.1-4 – Arrhenius plot of conductivity for BM (left-hand, open symbols) and AM powders (right-hand, closed symbols) when FLASH sintered in atmospheres of *Air* (squares), *Ar* (circles), *Ar/H_2* (down triangles), *Ar* + *H_2O* (up triangles), *Ar/H_2* + *H_2O* (diamond). The activation energy for the stage I of FLASH is calculated from the plots and shown for each case.

Studies on DC conductivity of the perovskite structured La-doped BFO indicate that, if the condition $0.2 < E_a(\sigma) < 0.45$ eV is satisfied, a conduction mechanism dominated by p-type polaron hopping occurs [17]–[19]. In parallel, $K_{0.5}Na_{0.5}NbO_3$ has been reported to present a p- or n-type behaviour when sintered in *Air* or *N_2*, respectively. Moreover, high dielectric losses were found for the ceramics sintered under reducing *N_2* atmosphere, which was attributed to a higher concentration of oxygen vacancies, $V_O^{\circ\circ}$, in such ceramics [20]. In low PO_2 atmospheres, the formation of $V_O^{\circ\circ}$ is facilitated (equation 6-1). As Nb^{5+} is a d-cation, it would accommodate the excess of electrons [20], however, it is possible that such excess of electrons also contribute for the conduction.

$$O_O^{\times} \rightarrow \frac{1}{2}O_2\ (g) + V_O^{\circ\circ} + 2e' \qquad (6\text{-}1)$$

Complementarily, the activation energies for conduction in ferroelectric perovskites reported between 0.4 and 1.2 eV have been associated with charge transport by ionized oxygen defects [21], [22]. In fact, that was confirmed previously for KNN ceramics and single crystals [12], [23]. On the other hand, ionic-based conducting mechanisms have been reported in KNN single crystals to present activation energies higher than 1.2 - 1.3 eV [23].

The data reported in Figure 6.1-4 suggests that the conducting mechanism during *Air* FLASH sintering of dry KNN powders is suitable with the movement of thermally activated ionized $V_O^{\circ\circ}$, because the condition $0.4 < E_a(\sigma) < 1.2$ eV is satisfied. In the case of AAFS (both dry and humidified conditions), because $E_a(\sigma) = 0.4$ to 0.5 eV, it is suggested that the KNN compacts present a p-type semiconductor behaviour, with the conducting mechanism being not only dependent on the movement of oxygen vacancies, but facilitated by polaron hoping and electron movement. Here, it is suggested that, in AAFS, there is an increase in the concentration of $V_O^{\circ\circ}$ at low temperature, promoted by the low partial pressure of oxygen, facilitated by the polaron hoping and excess of electrons, that allow conduction at T < 330 ºC; on contrary, in *Air* FLASH, the concentration of oxygen vacancies is not significantly changed when compared with room temperature, as these defects are thermally activated. In that case, consequent movement of thermally activated $V_O^{\circ\circ}$ [24] and/or recombination [25], under the influence of the applied electric field, allows a significant local heating by Joule effect, promoting the partial melting of particles' contacts and the following densification of KNN compacts [9], [11]. This process does not occur in AAFS due to the significantly lower furnace temperature and higher concentration of conducting defects, hindering the Joule heating generation and thermal runaway process. These results contrast with the observations in ZnO, as the respective FLASH sintering mechanism has been shown to be different for these two materials.

The analysis of operating conducting mechanisms during AAFS may lead to the conclusion that the initial particle size and consequent green density and pore morphology do not affect the FLASH sintering process. However, the final density of AAFSed KNN is dependent on the atmosphere and the presence of water (Table 6.1-3). On one hand, when FLASH sintering both BM and AM compacts in *Air*, the whitish colour of compacts was found to be kept on the sintered ceramics. On the other hand, that is not the case of AAFS. While a very uniform dark colour was identified in all AAFSed AM compacts, BM pellets appeared with dark non-uniform very localized areas. As an example, the final macroscopic appearance and respective microstructures of ceramics AAFSed in $Ar + H_2O$ of BM and AM powders are exemplified in Figure 6.1-5 a) and b), respectively. Dark colours in KNN ceramics are typically associated with the presence of oxygen vacancies. Hence, by direct observation of Figure 6.1-5, it is possible to infer that AM pellets present a significantly more uniform distribution of point defects, when compared with coarser BM powders, independently of the operating atmospheres during AAFS. As revealed in a), the localized darker areas in BM ceramics are associated with high density, as a consequence of current localization and hotspots [11]; on the other hand, white areas are not well densified. In opposition, Figure 6.1-5 b) shows a very uniform ceramic, with homogeneous microstructure; nonetheless, the microstructure inset reveals a still low final density, in accordance with Table 6.1-3.

The dissimilarities in pore size and distribution in AM and BM may explain the very different behaviour (Table 6.1-3 and Figure 6.1-3) and consequent appearance and microstructure (Figure 6.1-5) of AAFSed ceramics. The atmosphere interaction with the powders is achieved through the pore channels available for gas adsorption. Therefore, the coarser, less uniformly distributed pore channels in BM compacts are prone to promote current localization when a FLASH sintering atmosphere-dependent process is carried out, contributing for the hotspot formation (Figure 6.1-5), in accordance with previous work [11]. Furthermore, the finer and more uniformly distributed pores in AM explain the limit conditions found for T_F, where the use of reducing dry and humidified atmospheres (except for *Ar*) gives approximately the same FLASH temperature (Figure 6.1-3: T_F = 319 to 322 ºC). Because the gas interaction with the powder is limited by the amount of that gas (and humidity) that can be adsorbed in the particles, through pores, a smaller pore size induces a limited concentration of gas to interact with the particles. However, this interaction is achieved uniformly through all the compact, avoiding current localization and hotspots. The validity of such affirmation is ensured because there is no pressurization of gases during AAFS.

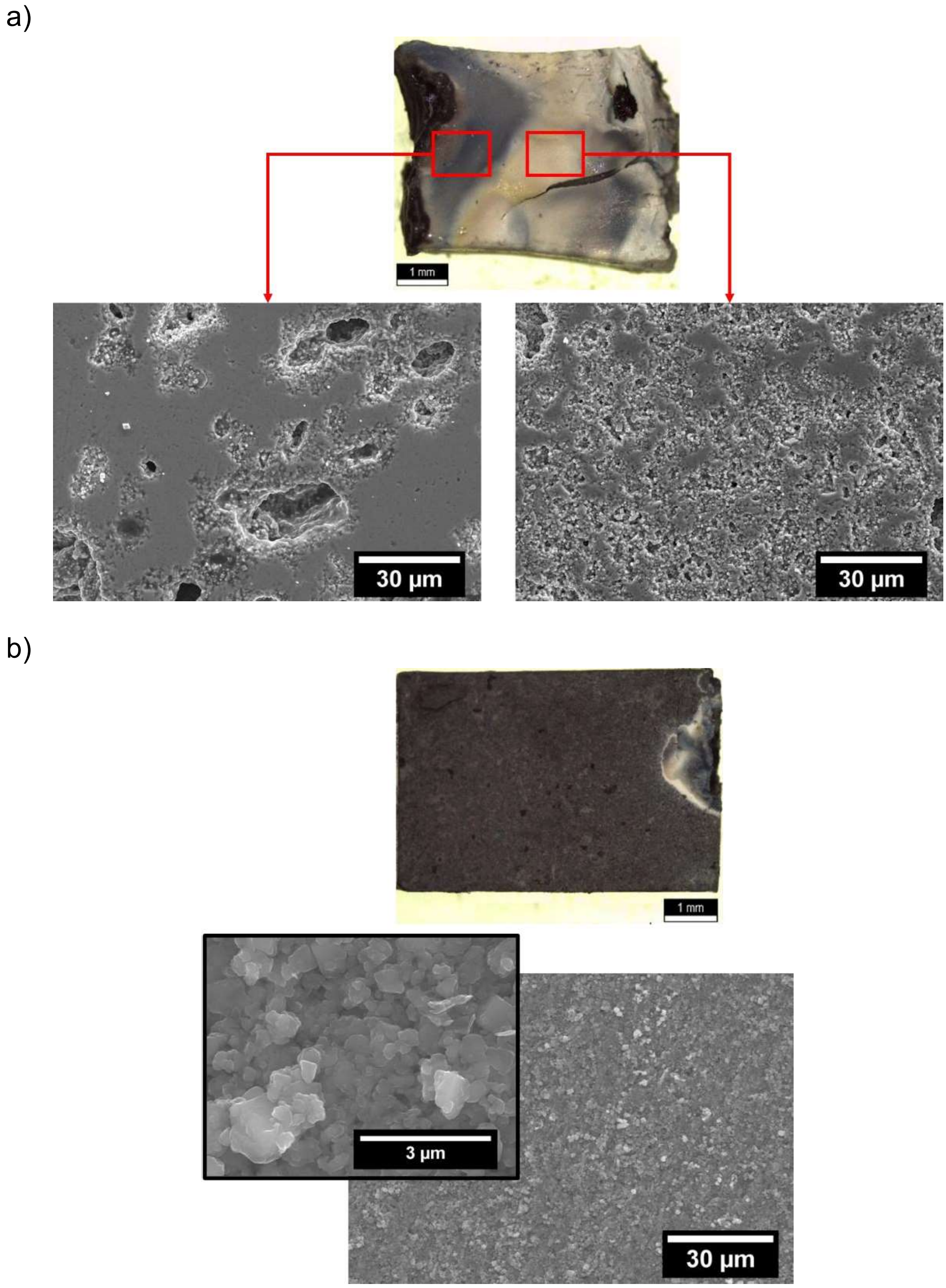

Figure 6.1-5 - Photographic report and microstructure of a) BM and b) AM compacts AAFSed under *Ar* + H_2O.

Therefore, it is suggested that, while the difference in $E_a(\sigma)$ of *Air* and AAFS might explain the low densification obtained on the latter case, the particle size has a fundamental role to promote an uniform interaction of gases and humidity during AAFS. Regarding the final density of AAFSed ceramics, a despisable increase in density (from the green state) was observed for both AM and BM compacts sintered in reducing dry atmospheres; on the other hand, when humidified atmospheres are used, namely argon, an already appreciable densification (~74 to 75%) was found. However, hotspots occurred in coarser BM powders, while a very uniform atmosphere interaction with AM compacts was found. Despite that the conducting mechanisms are similar for wet/dry and simple/hydrogenized reducing atmospheres, the different T_F and ρ_{final} of AAFSed ceramics indicate that water may play a role in increasing the densification.

6.1.4. Conclusions

This work shows that, while the particle size of KNN powders have a direct influence on T_F when FLASH sintering in *Air*, it represents an indirect effect on Atmosphere Assisted FLASH Sintering (AAFS). As the particle size is decreased (from ~350 to 171 nm), green density of compacts is not significantly affected, however, the pore size and respective distribution is. Consequently, finer (AM) powders present a more uniform interaction with atmospheres during AAFS, avoiding hotspots formation. Whereas the final density of sintered KNN ceramics by AAFS is very limited, an already appreciable densification of ~75% was reached for both BM and AM compacts when AAFS in humidified argon. The limited densification is due to the promotion of a low temperature conduction processes during AAFS that does not guarantee enough heating to allow high density to be reached.

In summary, it was shown that AAFS is a promising technique to reduce T_F of KNN, however, high density was not achieved. High concentration of conductive defects at low temperature do not allow sufficient heat to be generated. The presence of water in the atmosphere gives indications of density increase during AAFS, while well distributed pore channels are essential to avoid current localization during FLASH.

6.1.5. References

[1] M. Cologna, B. Rashkova, and R. Raj. “Flash Sintering of Nanograin Zirconia in <5 s at 850°C”. J. Am. Ceram. Soc., vol. 93, no. 11, pp. 3556–3559, Nov. 2010.

[2] M. Yu, S. Grasso, R. Mckinnon, T. Saunders, and M. J. M. Reece. “Review of flash sintering: materials, mechanisms and modelling”. Adv. Appl. Ceram., vol. 116, no. 1, pp. 24–60, 2017.

[3] M. Biesuz and V. M. Sglavo. “Flash sintering of ceramics”. J. Eur. Ceram. Soc., vol. 39, no. 2–3, pp. 115–143, 2019.

[4] S. K. Jha, K. Terauds, J. Lebrun, and R. Raj. “Beyond flash sintering in 3 mol % yttria stabilized zirconia”. J. Ceram. Soc. Japan, vol. 124, no. 4, pp. 283–288, 2016.

[5] J. Nie, Y. Zhang, J. M. Chan, R. Huang, and J. Luo. “Water-assisted flash sintering: Flashing ZnO at room temperature to achieve ~ 98% density in seconds”. Scr. Mater., vol. 142, pp. 79–82, 2018.

[6] Y. Zhang and J. Luo. “Promoting the flash sintering of ZnO in reduced atmospheres to achieve nearly full densities at furnace temperatures of <120 °C”. Scr. Mater., vol. 106, pp. 26–29, 2015.

[7] M. Kermani *et al.*. “Flash cold sintering: Combining water and electricity”. J. Eur. Ceram. Soc., vol. 40, no. 15, pp. 6266–6271, 2020.

[8] G. Corapcioglu, M. A. Gulgun, K. Kisslinger, S. Sturm, S. K. Jha, and R. Raj. “Microstructure and microchemistry of flash sintered $K_{0.5}Na_{0.5}NbO_3$”. J. Ceram. Soc. Japan, vol. 124, no. 4, pp. 321–328, 2016.

[9] R. Serrazina, A. M. O. R. Senos, L. Pereira, J. S. Dean, I. M. Reaney, and P. M. Vilarinho. “The Role of Particle Contact in Densification of FLASH Sintered Potassium Sodium Niobate”. Eur. J. Inorg. Chem., vol. 2020, no. 39, pp. 3720–3728, 2020.

[10] R. Serrazina, P. M. Vilarinho, A. M. O. R. Senos, L. Pereira, I. M. Reaney, and J. S. Dean. “Modelling the particle contact influence on the Joule heating and temperature distribution during FLASH sintering”. J. Eur. Ceram. Soc., vol. 40, pp. 1205–1211, 2020.

[11] R. Serrazina, J. S. Dean, I. M. Reaney, L. Pereira, P. M. Vilarinho, and A. M. O. R. Senos. “Mechanism of densification in low-temperature FLASH sintered lead free Potassium Sodium Niobate (KNN) piezoelectrics”. J. Mater. Chem. C, vol. 7, pp. 14334–14341, 2019.

[12] R. Serrazina, C. Ribeiro, M. E. Costa, L. Pereira, P. M. Vilarinho, and A. M. O. R. Senos. “Particle characteristics influence on FLASH sintering of Potassium Sodium Niobate: a relationship with conduction mechanisms”. Materials, vol. 14, p. 1321, 2021.

[13] R. Serrazina, L. Pereira, P. M. Vilarinho, and A. M. O. R. Senos. “On the influence of current density and time during stage III FLASH sintering of potassium sodium niobate”. *TO BE SUBMITTED., 2021.

[14] Y. Zhang, J. Nie, J. M. Chan, and J. Luo. “Probing the densification mechanisms during flash sintering of ZnO”. Acta Mater., vol. 125, pp. 465–475, 2017.

[15] R. Raj. “Joule heating during flash-sintering”. J. Eur. Ceram. Soc., vol. 32, no. 10, pp. 2293–2301, 2012.

[16] J. Luo. “The scientific questions and technological opportunities of flash sintering: From a case study of ZnO to other ceramics”. Scr. Mater., vol. 146, pp. 260–266, 2018.

[17] D. Triyono, S. N. Fitria, and U. Hanifah. “Dielectric analysis and electrical conduction mechanism of $La_{1-x}Bi_xFeO_3$ ceramics”. RSC Adv., vol. 10, no. 31, pp. 18323–18338, 2020.

[18] K. K. Bhargav, S. Ram, and S. B. Majumder. “Small polaron conduction in lead modified lanthanum ferrite ceramics”. J. Alloys Compd., vol. 638, pp. 334–343, 2015.

[19] A. Rai and A. K. Thakur. “Influence of co-substitution driven property tailoring in lanthanum orthoferrites ($LaFeO_3$)”. Ceram. Int., vol. 43, no. April, pp. 13828–13838, 2017.

[20] F. Hussain, I. Sterianou, A. Khesro, D. C. Sinclair, and I. M. Reaney. “p-type/n-type behaviour and functional properties of $K_xNa_{(1-x)}NbO_3$ ($0.49 \leq x \leq 0.51$) sintered in air and N_2”. J. Eur. Ceram. Soc., vol. 38, no. 9, pp. 3118–3126, 2018.

[21] A. Peláiz-Barranco, J. D. S. Guerra, R. López-Noda, and E. B. Araújo. “Ionized oxygen vacancy-related electrical conductivity in $(Pb_{1-x}La_x)$ $(Zr_{0.90}Ti_{0.10})_{1-x/4}O_3$ ceramics”. J. Phys. D Appl. Phys. Phys., vol. 41, p. 215503, 2008.

[22] O. Raymond, R. Font, N. Suárez-Almodovar, J. Portelles, and J. M. Siqueiros. “Frequency-temperature response of $Pb(Fe_{1/2}Nb_{1/2})O_3$ ferroelectromagnetic ceramics obtained by different precursors. Part I: Structural and thermo-electrical characterization”. J. Appl. Phys., vol. 97, p. 084107, 2005.

[23] M. A. Rafiq, M. E. Costa, A. Tkach, and P. M. Vilarinho. “Impedance analysis and conduction mechanisms of lead free potassium sodium niobate (KNN) single crystals and polycrystals: A comparison study”. Cryst. Growth Des., vol. 15, no. 3, pp. 1289–1294, 2015.

[24] K. Ren, Q. Wang, Y. Lian, and Y. Wang. “Densification kinetics of flash sintered 3mol% Y_2O_3 stabilized zirconia”. J. Alloys Compd., vol. 747, pp. 1073–1077, 2018.

[25] D. Åberg, P. Erhart, and C. Lindera. “Luminescence Quenching via Deep Defect States: A Recombination Pathway via Oxygen Vacancies in Ce-Doped YAG”. Chem. Mater., pp. 4–11, 2020.

6.2. Article: Atmosphere-Assisted FLASH sintering of Potassium Sodium Niobate in the presence of water: the role of powder humidity and electric field

To be submitted

Abstract

The need for low temperature and short time sintering processes has paved the way for the development of Atmosphere-Assisted FLASH Sintering (AAFS). A combination of atmosphere engineering and electric field/current is employed in such processes. While a relatively low operating temperature is easily reached ($T < 300$ ºC), high density ceramics are yet to be obtained by AAFS. This is the case of Potassium Sodium Niobate, $K_{0.5}Na_{0.5}NbO_3$, a lead-free piezoelectric with interest to the electronics technology.

Yet to be fully disclosed is the role of water during AAFS of KNN. While promising results have been presented regarding the use of humidified atmospheres, the systematic study of water content effects was not presented before. In this work, water is directly added to KNN compacts, promoting the development of a liquid film surrounding the particles. The combination of humidified powders, high electric field and AAFS under humidified reducing atmospheres allowed an appreciable increase in ceramics' density.

This work shines light on new approaches to increase the ceramics density at low temperature, using electric field and current assisted sintering techniques and water.

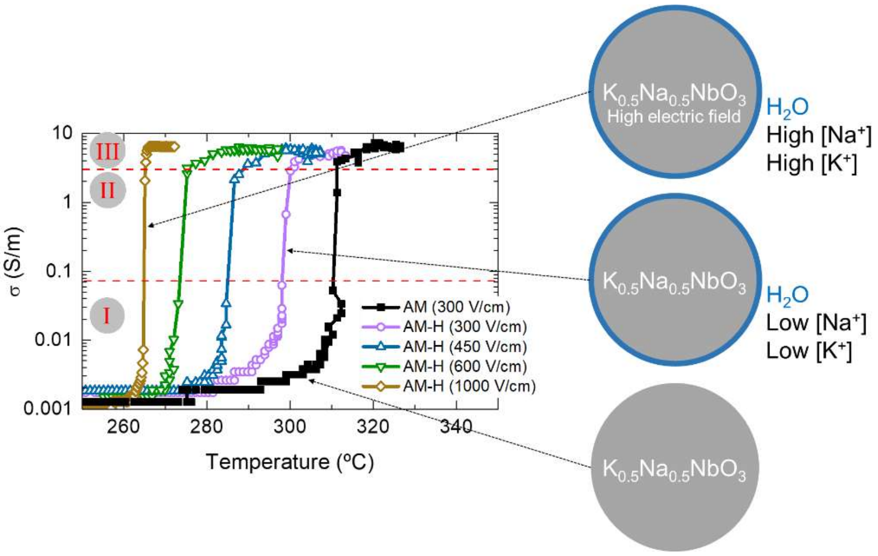

Key words

Atmosphere-Assisted FLASH sintering (AAFS); Water; Electric field; Nanosized KNN; Electrical conductivity.

6.2.1. Introduction

The decrease in energy consumption of thermal processing is mandatory [1], especially for high energy demanding processes as ceramics' sintering [2]. Alternative sintering techniques, as FLASH, have been proposed to dramatically decrease the operating temperature and time during sintering of ceramics [3]–[5]. The proper thermal activation and parallel application of an electric field to a non-sintered ceramic result in FLASH sintering. The thermally activated conductivity increase is responsible for a current increase, which is expressed in a FLASH and a very fast densification [5]. The temperature at which this disruptive phenomenon occurs is defined as the FLASH temperature (T_F). During the thermal activation, three stages are identified: stage I, incubation; stage II, where FLASH occurs, with a power spike and very fast, abrupt densification; stage III, or steady-state, when the pellet undergoes the remaining densification towards full density, and the current is limited. The all process does not take more than 60 s, usually [5], [6].

Besides the thermally activated FLASH sintering processes, the use of specific atmospheres to change the defect chemistry of materials has been reported to dramatically decrease T_F. Nanometric zinc oxide, ZnO, was FLASH sintered to 98% relative density at room temperature under a reducing humidified atmosphere of Ar/H_2 [7]. The FLASH processes based on atmosphere engineering are herein designated as Atmosphere-Assisted FLASH Sintering (AAFS) [8].

Potassium sodium niobate, $K_{0.5}Na_{0.5}NbO_3$ (KNN), a promising lead free piezoelectric, was reported to FLASH sinter at T_F < 320 ºC in a AAFS process, using dry and humidified reducing atmospheres as argon and hydrogenized argon [8], [9]. A similar process occurs at temperatures higher than 750 ºC if KNN is FLASH sintered in air [10]. During AAFS, while high current density (60 mA/mm^2) allow high density to be reached, current localization and non-uniform densification occurred [9]. On the other hand, a lower current limit and a proper pore morphology, consequence of particle size and packing, avoid hotspots. Nonetheless, in the best experimental scenario, AAFS only allows densities not higher than 75%. The presence of water in the sintering atmosphere was shown to be essential to reach such level of density, otherwise, despisable densification occurs [8]. To produce proper KNN ceramics for the replacement of market leader lead-based PZT, $(Pb(Zr_{1-x}Ti_x)O_3$, further investigation is needed for its low temperature sintering. AAFS is a promising technique to keep the operating temperature low, however, efforts to increase the ceramics' density are mandatory. While a promising road was unveiled before, regarding the role of water [8], high density KNN ceramics are yet to be obtained at T_F < 300 ºC.

A hypothesis to increase densification during AAFS is to promote a uniformly distributed path of current through the compacts' particles, which will allow particle sliding and pore elimination during FLASH. Water can not only promote the formation of such conductive film in KNN compacts, due to partial alkali dissolution, as promote the presence of a film that allows particle sliding. Previous work on water interaction with KNN particles have shown that a pH of 5 to 6 is ideal to maximize dissolution [11], [12], which is typically achieved through acidification of deionized water.

In this work, AAFS was used to sinter dry and humidified nanometric KNN powders, for the establishment of the true role of water in densification. A reducing humidified atmosphere was used (*Ar* + H_2O) to avoid water evaporation from the compact during thermal activation, and to keep a T_F below 300 ºC. The presence of water in KNN compacts shall promote an electrically conductive film surrounding all the particles, allowing their low temperature conduction and consequent densification by particle sliding and pore elimination.

6.2.2. Experimental

A 99% purity, nanometric-sized, Potassium Sodium Niobate, $K_{0.5}Na_{0.5}NbO_3$ (KNN) powder was produced through solid state reaction and posterior attrition milling process, and designated as AM, as previously described [8], [10]. To infer on the role of water directly added to the KNN powder during low temperature AAFS, 10 wt% of a water-based acetic acid solution (with controlled pH of 5 to 6) was added to AM powders and manually mixed with a spatula. These powders were designated as AM-H. Both powders (AM and AM-H) were pressed into parallelepipedal compacts with ca. 7 x 5 x 2 mm^3, from a combination of uniaxial and isostatic pressing steps (ca. 130 and 200 MPa, respectively). In the case of AM-H, a water content greater than 10 wt% did not allowed the production of coherent green bodies due to extended particle dissolution.

To study the AAFS process, an atmosphere-controlled furnace was used, and humidified argon (*Ar* + H_2O) was constantly fluxed (ca. 500 ml/min) into the sample holder system. A 100% relative humidity in the argon atmosphere was ensured by a *DeltaOhm HD2717* sensor. The alumina sample holder contained a pushing rod to maintain the contact between the samples' faces and the two opposite platinum electrodes, as reported before [8], [9]. Compacts were painted with silver electrodes on those faces to guaranty good electrical contact with Pt sheets; a purging time of 30 min was executed prior to the heating and electric field application during AAFS. All heating and cooling steps were performed at a rate of 10 ºC/min. The electric field was changed between 300, 450, 600 and 1000 V/cm, while the current limit (after the FLASH onset, and during stage III) was kept constant at 20 mA/mm^2 (*EPS HV 5006-400* power source). After the current limit was reached, the FLASH was kept for 60 s. The temperature dependent conductivity (σ) of KNN compacts was calculated from the measurement of electric field and current flow through the system. To determine the activation energy for conduction ($E_a(\sigma)$) of KNN pellets, an Arrhenius representation of ln(σ) as a function of 1/Tcalc was considered, where Tcalc stands for the estimated specimen temperature using Black Body Radiation model [13].

Before and after sintering, all the ceramics were measured and the geometrical apparent density (and relative density considering a theoretical density of 4.5 g/cm^3) were calculated. The green density determination of AM-H compacts was achieved after drying (at 200 ºC) several pellets (to avoid the contribution of water to the weight of the pellets). To evaluate the appearance of AAFS KNN sintered ceramics, an optical microscope was used (*LEICA EZ4HD*), while microstructural analysis was performed in a Scanning Electron Microscope (SEM, *Hitachi S-4100*) at 25 kV acceleration potential.

6.2.3. Results and discussion

The AM KNN powders presented an average particle size between 170 and 210 nm, with a crystallite size of 50 nm; their chemical analysis revealed stoichiometric K/Na and (K+Na)/Nb ratios in accordance with the nominal composition of $K_{0.5}Na_{0.5}NbO_3$. No significant contamination from the milling media was identified [8], [10]. These dry powders (AM) were humidified with acidified and designated by AM-H. Micrographs of uniaxial and isostatically pressed compacts of both AM and AM-H are compared in Figure 6.2-1 a) and b), respectively. No relevant differences are identified in the micrographs. Additionally, the geometric green (before sintering) density of such compacts is approximately the same, with AM-H presenting slightly superior density to that of AM: 65 and 67%, both with a statistical deviation error of 2%.

Figure 6.2-2 shows the conductivity over temperature behaviour of Atmosphere Assisted FLASH Sintered (AAFSed) AM-H compacts subjected to 300, 450, 600 and 1000 V/cm electric fields, under humidified argon (*Ar* + H_2O) atmosphere – open suymbols. For comparison, dry AM compacts were AAFSed in the same atmosphere and 300 V/cm; the conductivity dependence is shown in Figure 6.2-2 with closed symbols. Table 6.2-1 gives the experimental details, respective T_F and final relative density of AM and AM-H pellets AAFSed in *Argon* + *H_2O*.

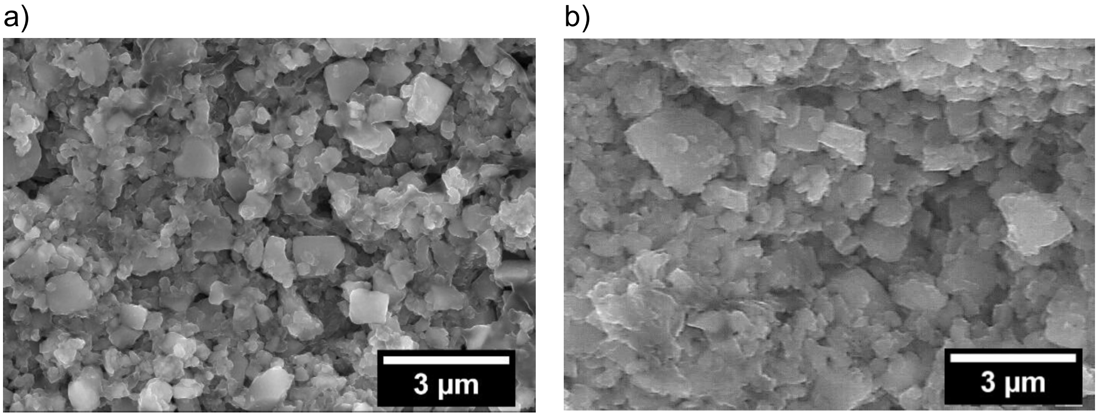

Figure 6.2-1 – SEM micrographs of a) AM and b) AM-H compacts before sintering.

For the same electric field conditions (300 V/cm) T_F of AM-H is slightly decreased if compared with dry AM compacts: 295 ºC versus 309 ºC. Additionally, the conduction process in AM-H compacts seems smoother than that of AM, which is identifiable by a continuous increase in conductivity with temperature, and the absence of oscillations as identified in the AM case. These observations may be explained by presence of a conductive film at the particle surfaces that was promoted by the acidified water added to AM-H, that is not present in AM dry compacts. A partial dissolution of potassium and sodium into the water, giving additional conductive metallic ions, contributes to an increase in the overall pellet electrical conductivity, which explains its lower T_F. Water electrolysis may also occur [14], however, there is no experimental evidence of such phenomena. Rather than T_F, Table 6.2-1 shows that the final densification of AM-H is similar to that of AM, when AAFSed in the same conditions (ρ_{sint} = 75% for both).

Table 6.2-1 and Figure 6.2-2 show that the increase in electric field from 300 to 1000 V/cm during AAFS of AM-H compacts allows a gradual decrease in T_F, to a minimum of 265 ºC. In parallel, the final density is increased to a maximum of 79% (Table 6.2-1). Furthermore, Figure 6.2-2 reveals that as the electric field is raised, the transition from stage I to stage II of FLASH seems to occur at lower σ values; for instance, at 300 V/cm, the transition occurs for $\sigma \approx 0.05$ S/m, while for 1000 V/cm it occurs for $\sigma \approx 0.01$ S/m.

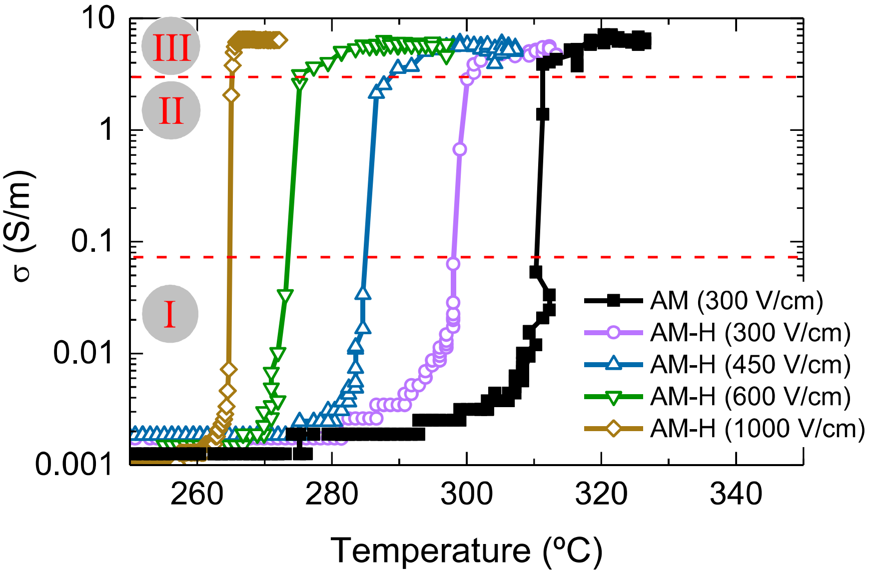

Figure 6.2-2 – In-situ conductivity over temperature during AAFS experiments in *Ar + H_2O* atmosphere of AM (at 300 V/cm, closed symbols) and AM-H compacts (open symbols), subjected to 300 (circles), 450 (up triangles), 600 (down triangles) and 1000 V/cm (diamond) electric fields. A clear dependence of T_F on powder humidity and electric field is identified.

Table 6.2-1 – FLASH sintering experimental conditions and properties of AM and AM-H compacts, subjected to humidified argon *(Ar + H_2O)* under different electric fields and a constant current limit of 20 mA/mm^2.

KNN powder	Electric field (V/cm)	T_{FLASH} (ºC)	ρ_{sint} (%)
AM	300	319	75
AM-H	300	295	75
	450	285	75
	600	275	77
	1000	265	79

As the electric field is increased, the overpotentials in particle contacts are raised, promoting the formation of more conductive defects at lower temperature [15]. Moreover, the electric field might promote an increase in the concentration of K^+ and Na^+. The ionization should be facilitated by the presence of water in the powder. Our observations might be explained by the larger concentration of conducting defects for higher electric field conditions, that contribute to a greater overall movement of species and consequent heating. Additionally, the presence of water allows particles to slide, promoting additional sintering driving force. The previously proposed mechanism of increased mass transport in ZnO [7] is not dampen, however, no proof of conventional mass transport in FLASH sintering of KNN was presented so far.

The Arrhenius plot for the conduction in the exposed experimental conditions, comparing AM and AM-H in the same electric field conditions (300 V/cm) is given in Figure 6.2-3 a) and b), respectively. Moreover, the dependences when different electric fields were employed to AM-H compacts are also revealed in Figure 6.2-3 b) to e). The apparent activation energies for conduction during AAFS of AM-H, regardless of the applied electric field and compact are very similar and fit within the 0.4 to 0.5 eV interval. Because $E_a(\sigma)$ is kept constant for all the AAFS experiments, it is concluded that the conduction mechanism during AAFS is be the same, independently of powder content in water or applied electric field. As discussed before [8], such $E_a(\sigma)$ range is associated with the p-type semiconductor behaviour of KNN, with the conducting mechanism being dependent on the movement of oxygen vacancies and polaron hoping and electron movement. Hence, the increase in the final density on AM-H powders sintered with increased electric field (Table 6.2-1) is not related with a possible alteration on the conducting mechanism.

The question now lies on clarifying the separated role of water and electric field to the increase in density (79%) when a 1000 V/cm is employed to AAFS of AM-H KNN powders. To mislead the effect of the electric field and to infer on the water influence, an additional AAFS experiment was performed. An AM dry compact was AAFS under *Ar* + H_2O atmosphere and 1000 V/cm. Densification did not occur in such pellet.

Figure 6.2-4 shows the photographic record of both a) humidified and b) dry AM pellets FLASH sintered under 1000 V/cm and *Ar* + H_2O atmosphere. Additionally, SEM micrographs are given for each specimen. While a very uniform dark colour is observed in AM-H ceramic, typically associated with reduced KNN ceramics [8], AM compact is revealed to be mostly oxidized, with only a very dark area, with less than 1 mm, and a channel-like feature, that is followed by a crack.

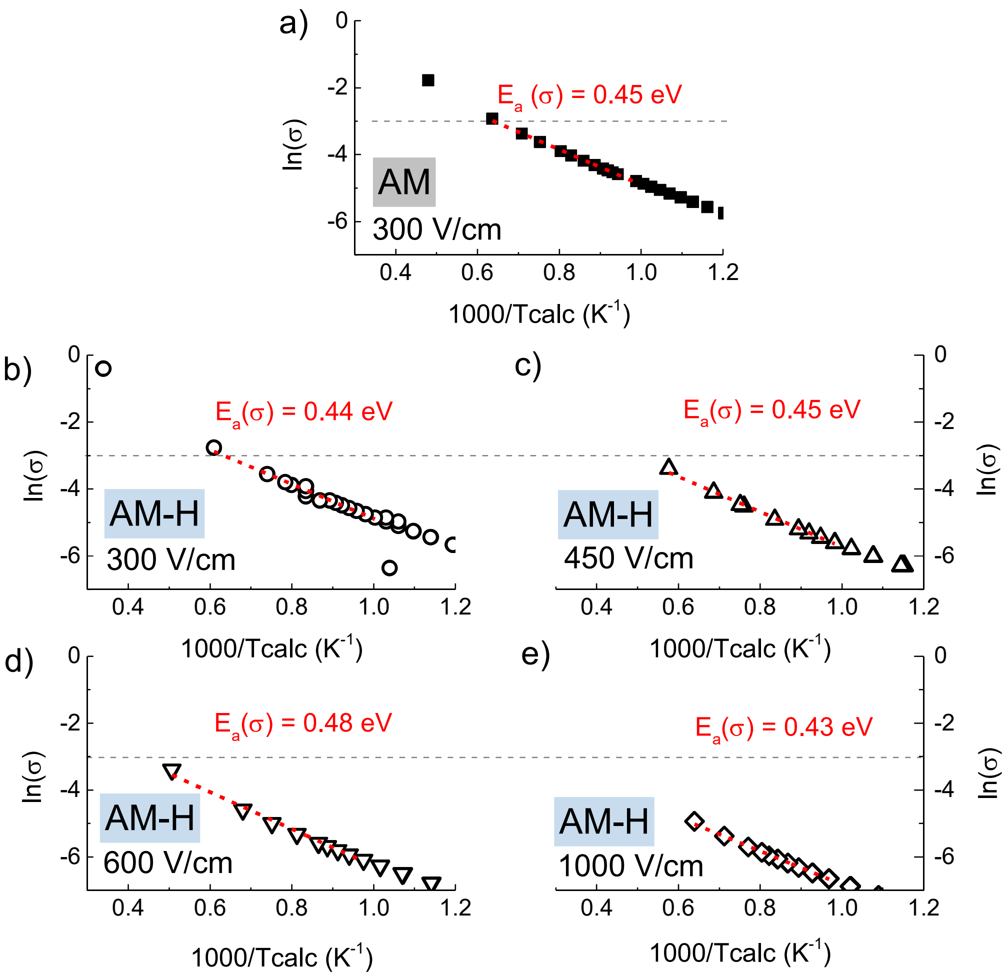

Figure 6.2-3 – Arrhenius plot of conductivity during AAFS in *Ar* + *water* of a) AM compacts at 300 V/cm, and AM-H powders subjected to b) 300, c) 450, d) 600 and e) 1000 V/cm.

The correspondent SEM micrographs of AM-H ceramic (Figure 6.2-4 a)) show a very uniform density throughout all the ceramic. However, the quite limited density presented in Table 6.2-1 is confirmed by the micrograph. On the other hand, the very dark area in AM compact (Figure 6.2-4 b)) is associated with a hotspot, which presents inhomogeneous density, while the dark channel looks more uniform, however, with limited densification. The hotspot and consequent cracking observed in AM ceramic suggests that the absence of water in the compact, before FLASH sintering, together with the high electric field, allowed a strong current localization, which was responsible for non-uniform densification and cracking. The addition of water to the powder was essential to promote uniform conduction and densification processes in AM-H specimen.

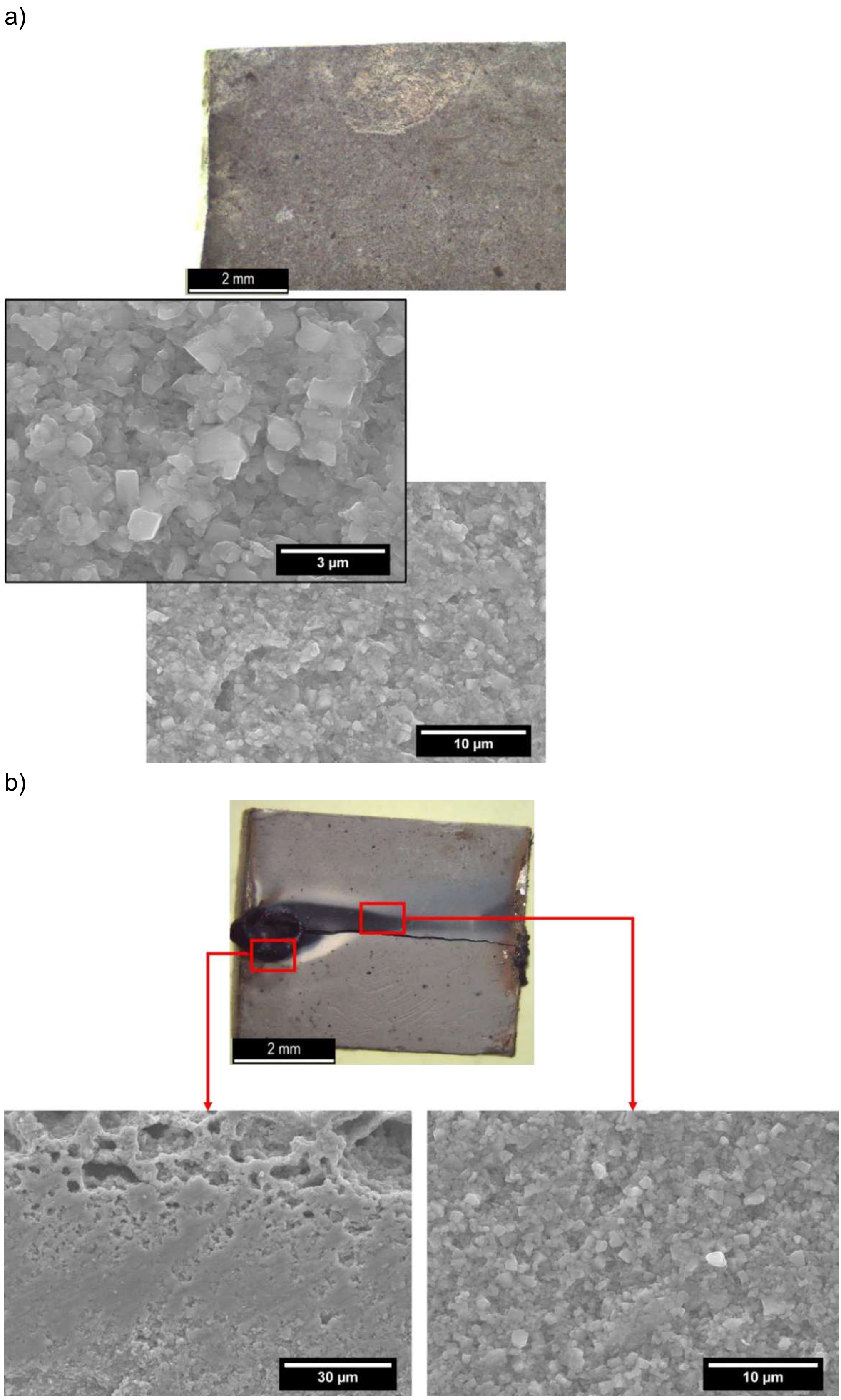

Figure 6.2-4 – Photographic record of a) AM-H and b) AM (dry) KNN pellets AAFSed under *Ar + water* atmosphere and 1000 V/cm, followed by the respective SEM micrographs.

The use of high electric field alone does not promote high or uniform density in KNN, even if humidified reducing atmospheres are used. In fact, the opposite was verified. However, when water is added to the powders, the combined effects of water and high electric field are responsible for an increased densification (79%). Despite not being suitable for the piezoelectric applications of KNN, this density value is the highest reported for the lowest operational sintering temperature (265 ºC) so far. Based on the analysis presented in this work, it is postulated that the presence of high electric field allows the additional formation of defects (either oxygen vacancies [15] or metallic ions of K^+ and Na^+), while water is responsible for providing an uniform current pathway through all the particles, together with a sliding media for particle rearrangement. Therefore, a uniformly sintered ceramic is obtained (with ρ_{sint} = 79%). For higher densification, alternative strategies must be considered, as for instance the use of external pressure, as in the case of FLASH-Cold sintering [14].

6.2.4. Conclusions

The role of water to promote low temperature FLASH sintering of KNN is studied in this work.

The presence of a liquid film in nanometric-sized KNN particles, associated with a reducing humidified argon atmosphere and high electric field (1000 V/cm) allowed a considerable relative density of 79% to be reached. When the same AAFS conditions are employed in a dry KNN compact, hotspots and cracking occurred, demonstrating the essential role of water. It is postulated that water is needed to promote a partial ionization of KNN’ particle surfaces, which allows a uniform current path when FLASH occurs. High electric field is needed to increase the extent of ionization, while the water film is responsible to increase the sintering driving force by promoting particle slide.

This work contributes for the knowledge of AAFS of KNN and other ceramics, shining light on new approaches to increase density of ceramics at low temperature.

6.2.5. References

[1] E. Commission. "European Green Deal-Roadmap and key actions | European Commission". 2019.

[2] T. Ibn-Mohammed *et al.*. "Decarbonising ceramic manufacturing: A techno-economic analysis of energy efficient sintering technologies in the functional materials sector". J. Eur. Ceram. Soc., vol. 39, no. 16, pp. 5213–5235, 2019.

[3] M. Cologna, B. Rashkova, and R. Raj. "Flash Sintering of Nanograin Zirconia in <5 s at 850°C". J. Am. Ceram. Soc., vol. 93, no. 11, pp. 3556–3559, Nov. 2010.

[4] M. Yu, S. Grasso, R. Mckinnon, T. Saunders, and M. J. M. Reece. "Review of flash sintering: materials, mechanisms and modelling". Adv. Appl. Ceram., vol. 116, no. 1, pp. 24–60, 2017.

[5] M. Biesuz and V. M. Sglavo. "Flash sintering of ceramics". J. Eur. Ceram. Soc., vol. 39, no. 2–3, pp. 115–143, 2019.

[6] S. K. Jha, K. Terauds, J. Lebrun, and R. Raj. "Beyond flash sintering in 3 mol % yttria stabilized zirconia". J. Ceram. Soc. Japan, vol. 124, no. 4, pp. 283–288, 2016.

[7] J. Nie, Y. Zhang, J. M. Chan, R. Huang, and J. Luo. "Water-assisted flash sintering: Flashing ZnO at room temperature to achieve ~ 98% density in seconds". Scr. Mater., vol. 142, pp. 79–82, 2018.

[8] R. Serrazina, L. Pereira, P. M. Vilarinho, and A. M. O. R. Senos. "Atmosphere-Assisted FLASH sintering of Potassium Sodium Niobate: the influence of operating atmospheres". *TO BE SUBMITTED, 2021.

[9] R. Serrazina, J. S. Dean, I. M. Reaney, L. Pereira, P. M. Vilarinho, and A. M. O. R. Senos. "Mechanism of densification in low-temperature FLASH sintered lead free Potassium Sodium Niobate (KNN) piezoelectrics". J. Mater. Chem. C, vol. 7, pp. 14334–14341, 2019.

[10] R. Serrazina, C. Ribeiro, M. E. Costa, L. Pereira, P. M. Vilarinho, and A. M. O. R. Senos. "Particle characteristics influence on FLASH sintering of Potassium Sodium Niobate: a relationship with conduction mechanisms". Materials, vol. 14, p. 1321, 2021.

[11] A. Mahajan, R. Pinho, M. Dolhen, M. E. Costa, and P. M. Vilarinho. "Unleashing the Full Sustainable Potential of Thick Films of Lead-Free Potassium Sodium Niobate ($K_{0.5}Na_{0.5}NbO_3$) by Aqueous Electrophoretic Deposition". Langmuir, vol. 32, no. 21, pp. 5241–5249, 2016.

[12] S. Grasso *et al.*. "A review of cold sintering processes". Adv. Appl. Ceram., vol. 119, no. 3, pp. 115–143, 2020.

[13] Y. Zhang, J. Nie, J. M. Chan, and J. Luo. "Probing the densification mechanisms during flash sintering of ZnO". Acta Mater., vol. 125, pp. 465–475, 2017.

[14] M. Kermani *et al.*. "Flash cold sintering: Combining water and electricity". J. Eur. Ceram. Soc., vol. 40, no. 15, pp. 6266–6271, 2020.

[15] W. Rheinheimer, X. L. Phuah, H. H. Wang, F. Lemke, M. J. Hoffmann, and H. H. Wang. "The role of point defects and defect gradients in flash sintering of perovskite oxides". Acta Mater., vol. 165, no. December, pp. 398–408, 2019.

Summary

The work presented in this chapter showed that while the operating temperature for FLASH sintering can be dramatically reduced by the use of low oxygen content atmospheres, densification is limited. In specific, it was possible to conclude that:

- The previously observed dependence of T_F with the particle size (when FLASH sintering in Air) is not directly applicable in AAFS. However, the size and morphology of pores in the green compacts (consequence of particle size) are key parameters for the development of the AAFS process.
- The final density of AAFSed KNN ceramics is very limited, which was attributed to the absence of a thermal runaway as in *Air* FLASH. The fact that compacts are more conductive at low temperature does not allow enough heat to be generated during the FLASH to permit satisfactory sintering.
- The use of water in both atmosphere and powder (by directly humidifying the KNN powder before the compacting steps) was revealed to increase density while avoiding current localization. However, not only the maximum densification was limited to 79%, as the electric field must be increased to 1000 V/cm.

This chapter has shown that, unlike ZnO, high density was not achieved when AAFS KNN compacts. This is due to the dissimilar conducting and sintering mechanisms that occur in each material. While estimated activation energies for conduction during FLASH sintering of KNN in *Air* indicate that ionic conductivity takes place, during AAFS, oxygen defects are responsible for the conduction. That is not the case in ZnO, as interstitial Zn ions are formed when the oxygen partial pressure is decreased.

Despite that several signatures and features of FLASH sintering are very similar regardless of the material, others are not. AAFS is an example.

At this point, the goal of this work left to be fulfilled is the establishment of the relationship between processing and properties. Dielectric and ferroelectric properties of FLASH sintered KNN are presented in the next chapter. A comparison with conventionally sintered ceramics is provided.

Chapter

7. Dielectric, piezoelectric and polarization behaviour of FLASH sintered KNN

Contents

Preamble

One of the main objectives of this work is to study the possibility of producing alkali-based piezoelectrics at low temperature and reduced time. The motivation was the need to avoid the secondary phase formation that occurs during the conventional sintering processes of these materials. In the case of KNN, temperatures higher than 1100 ºC, and densification processes that take several hours, induce the partial vaporization of K and Na. Consequently, secondary phases (Nb-rich) are formed; thus, the ferroelectric, and dielectric performance of $K_{0.5}Na_{0.5}NbO_3$ is hindered.

As shown in the beginning of results presentation chapters, section 3.2, EBSD analysis allowed to confirm that while residual secondary phases are present in conventionally sintered KNN, as expected, that is not the case in FLASH ceramics. This is already a suggestion that the FLASH sintering process is successful in avoiding secondary phase formation and allows high-performance piezoelectric ceramics to be produced. Nonetheless, the dielectric and ferroelectric properties of these materials were not yet presented.

In this chapter, two contributions are devoted to the electrical characterization of a selected KNN FLASH sintered sample, which was compared to a conventionally sintered one. The conventional sintering cycle was optimized to the already referred conditions (1125 ºC, 3h, 5 ºC/min heating and cooling rates), whereas in FLASH the densest and most uniform samples were produced with Isothermal Conditions (I.C. – section 4.2): 900 ºC, 30 min dwell, followed by the application of the 300 V/cm electric field and current limit of 20 mA/mm^2 for 60 s.

Section 7.1 gives a short communication on the overall performance of FLASH and conventionally sintered KNN; a comparison is presented. Additionally, section 7.2 shows a more detailed analysis, with the role of post-sintering heat-treatment in the performance of KNN being revealed and discussed. Impedance spectroscopy studies are performed to account for the fingerprints of FLASH sintering process in the heat treated KNN ceramics' performance.

A preliminary Transmission Electron Microscopy (TEM) study on as-FLASH sintered KNN ceramics is shown in section 7.3.

7.1. Letter: FLASH sintered potassium sodium niobate: high performance piezoelectrics at low thermal budget processing

Submitted

Abstract

Alternative sintering technologies have been promised to overcome issues associated to the conventional sintering process of ceramics, such as the high sintering thermal budgets and inherent CO_2 footprint. This becomes even more relevant in alkali-based piezoelectrics, as $K_{0.5}Na_{0.5}NbO_3$ (KNN), typically sintered at T > 1100 ºC for several hours that induce secondary phase formation and, thereby, degrade their electric characteristics. In this work, we successfully demonstrate that KNN ceramics can be of high performance when sintered at 900 ºC with the densification occurring in 60 s only, using an electric field- and current-assisted FLASH technique. The ferroelectric, piezoelectric, and dielectric characterisation of these FLASH sintered KNN ceramics, reported for the first time, present a remnant polarization, a longitudinal piezoelectric effect (d_{33}), a relative permittivity and transition temperatures to be slightly superior compared with conventional one due to the reduced content of secondary phases. This work on high performance KNN ceramics FLASH sintered at low thermal budget has implications for the development of innovative low carbon technologies and in particular for the electroceramics stakeholders, as well as for piezoelectric based energy harvesters.

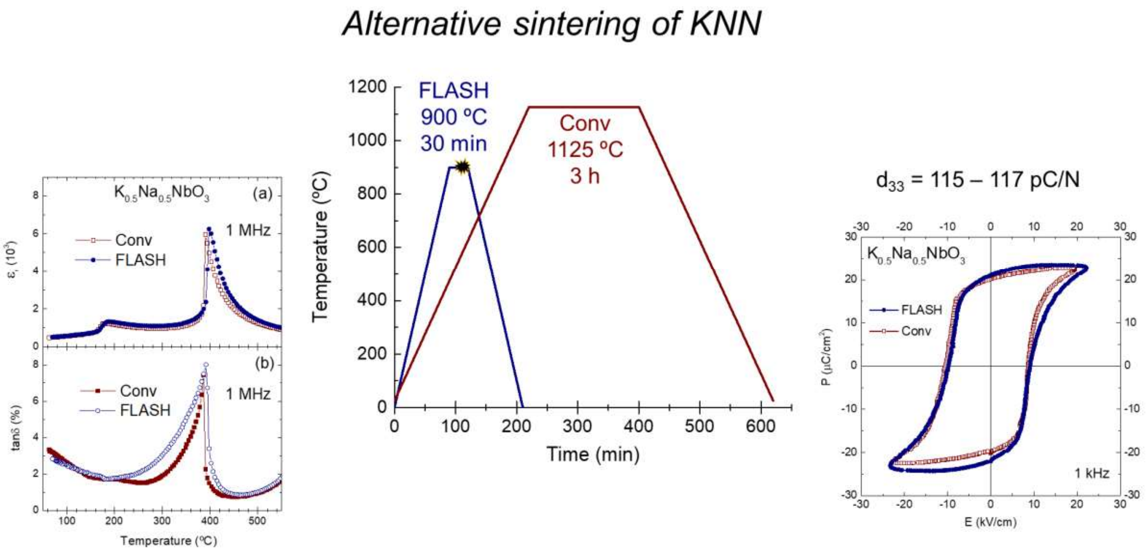

Key words

FLASH sintering; Low thermal budget; Piezoelectrics; Ferroelectrics; Lead-free, KNN, Potassium Sodium Niobate

Motivated by the need to replace lead-based piezoelectrics, alkali niobates have been reported as one of the most promising family of lead-free piezoelectric compounds for applications in sensors, actuators, and energy-harvesting devices [1]. The interest in Potassium Sodium Niobate ($K_{0.5}Na_{0.5}NbO_3$, KNN) resides also in its high tetragonal to cubic transition temperature (T_C) and large longitudinal piezoelectric coefficient, d_{33} [2]. Non-textured and non-doped ceramics present, typically, d_{33} of 80 – 200 pC/N with the tetragonal symmetry phase being stable up to T_C of 420 °C [3]. It is also known that doping albeit decreasing T_C may boost the piezoelectric performance [2].

Conventional production of KNN ceramics meets however some experimental limitations [4]–[7]. The high temperature and long sintering time induce the volatilization of alkali elements, and thereby formation of secondary phases with negative effect on both T_C and d_{33} [8]. A possible solution is to use alternative, low temperature, sintering methods to densify KNN ceramics. Recently, we have used Spark Plasma Sintering and Texturing (SPS/SPT) to produce high-density ceramics at a temperature of 1000 °C for 20 min, with relatively high d_{33} (95 – 108 pC/N) and moderate T_C (370 – 386 °C) [9]. However, in SPS/SPT, the use of graphite dies and reducing atmospheres implies a post heat treatment for several hours [9], not to mention the limitation in terms of produced shapes [10]. FLASH sintering, an electric field- and current-assisted technique [11], has been presented as a possible solution for the sintering of KNN [12]–[15], with reduced thermal budget. Ceramic densification has been shown to occur at a lower temperature and in a much shorter period of time, when an electric field is directly applied to a green body [11]. However, the piezoelectric and dielectric properties of FLASH sintered KNN have not been disclosed so far. In this work, the dielectric, piezoelectric and ferroelectric behaviour of un-doped ($K_{0.5}Na_{0.5}NbO_3$, KNN) ceramics produced by FLASH are reported, for the first time, and compared with those of conventionally sintered ceramics.

$K_{0.5}Na_{0.5}NbO_3$, KNN, single phase powders were produced by solid-state reaction, using high purity alkali carbonates (K_2CO_3, Sigma-Aldrich, 99.99% and Na_2CO_3, Sigma-Aldrich, 99.999%) and niobium oxide (Nb_2O_5, Alfa Aesar, 99.9%). Powder characterization and processing details are published elsewhere [13], [15] as well as FLASH sintering setup scheme and mechanism [14]. In short, green compacts (ca. 15 x 5 x 2 mm^3) were uniaxially and isostatically pressed to a green density of ca. 65%. These pellets were sintered in an adapted contact-dilatometer, with or without the application of an electric field, respectively, for FLASH and conventional processes. The conventional sintering (Conv) cycle was optimized to obtain high-dense ceramics, using a 5 °C/min heating and cooling rate and a maximum sintering temperature of 1125 °C with a 3 h dwell, as shown in Figure 7.1-1.

Considerably lower thermal budget conditions were used for FLASH sintering, as also seen from Figure 7.1-1. The pellets were placed in-between two platinum electrodes and heated to 900 ºC at a rate of 10 ºC/min. After an isothermal step of 30 min, a 300 V/cm electric field was applied, and the current limit set to 20 mA/mm^2, while the holding time after the FLASH event was 60 s [13]. A decrease of 20% in maximum furnace temperature and 66% in cycle time was accomplished when using FLASH instead of the conventional sintering.

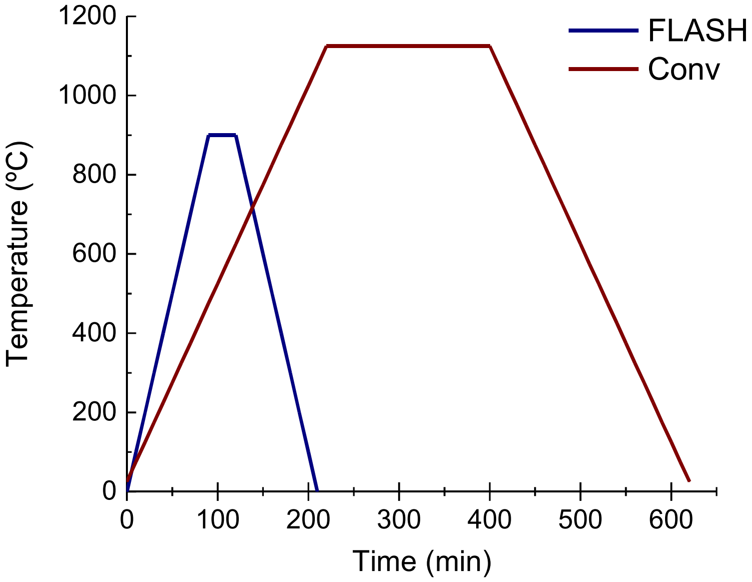

Figure 7.1-1 – Thermal profiles used for sintering of KNN ceramics by conventional (Conv) (T_{max} = 1125 ºC, $time_{Total}$ = 620 min) and FLASH (T_{max} = 900 ºC, $time_{Total}$ = 210 min) processes. A considerably lower thermal budged is involved for FLASH when compared with conventional sintering.

For room-temperature structural characterization of the sintered ceramics, pellets were grinded and analysed by X-ray diffraction (XRD). A *PANalytical XPERT-PRO* diffractometer, with a copper X-ray source ($K\alpha_1$ = 1.54060 Å) was used, with a step size of 0.026º and accumulation time of ca. 96 s. The microstructure and microchemistry of the sintered ceramics were analysed by Electron Backscattered Diffraction Analysis (EBSD) using an *EBSD Bruker e-Flash Quantax CrystAlign* detector in a field-emission scanning electron microscope (SEM, *Hitachi SU-70*) at 25 kV acceleration potential. Prior to the EBSD analysis, ceramics were polished using SiC papers, diamond paste and colloidal silica. The density of the ceramics was determined by the Archimedes method, with correction for the open porosity, and at least three ceramics were measured in water as the immersion liquid.

To access the dielectric, piezoelectric and ferroelectric behaviour of KNN ceramics, 1 mm thick specimens, with ca. 5 x 3 mm^2 section area were prepared from sintered bodies, using a diamond cutting wire and SiC papers for thickness reduction. After a fine polishing (SiC P4000), platinum electrodes were brush painted (*SPI-CHEM 04990-AB*) at the opposite faces of the ceramics, for a parallel-plate-capacitor configuration. A drying step at 50 ºC was employed, followed by a cure and sintering electrode process, according to the manufacturer indications (maximum temperature of 900 ºC, for 1 h).

The real part of the relative dielectric permittivity (ε_r) and dissipation factor (tanδ) were accessed using an impedance bridge (HP 4284A), with a 1 V oscillation potential and the frequency of 1 MHz. The temperature dependence was obtained on cooling the ceramics after heating in a tubular furnace with alumina sample holder, using a 2 ºC/min rate, and a dwell time of 2 min before each measurement. The polarization, as a function of the AC electric field of the sintered ceramics, was assessed at 1 kHz and at room temperature with a ferroelectric analyser (*aixACCT, TF Analyzer 2000*). The longitudinal piezoelectric coefficient (d_{33}) of these KNN ceramics was measured after a Corona poling step at 70 ºC, for 15 min, under the potential of 10 kV, followed by an additional 15 min step, at 65 ºC, under 12.5 kV. A Berlincourt-type piezoelectric meter (*Sinocera YE 2730A*) with force frequency of 110 Hz and amplitude of 0.25 N was used. Several measurements were performed on the same ceramics, and different ceramics were used to determine an average d_{33} value and the respective standard deviation.

KNN FLASH and Conv ceramics have a relative density of 93$\pm$3% and 96$\pm$2%, respectively (Table 7.1-1). Dense microstructure with an estimated porosity between 3 and 5% for both Conv and FLASH KNN ceramics is also seen in SEM-EBSD micrographs, shown in Figure 7.1-2 a) and b), respectively, although some grains were evidently pulled out during polishing that is particularly well seen for Conv KNN with larger grains. The estimated grain size distributions are presented in Figure 7.1-2 c) and d) for Conv and FLASH KNN ceramics, respectively. The average equivalent grain size ($\overline{\mathrm{G}_{\mathrm{eq.}}}$) is almost 1.8 μm for Conv KNN and ~1.5 μm for FLASH ceramics. Additionally, grain size distributions between 0.25 – 10.0 μm and 0.25 – 5.0 μm were calculated for Conv and FLASH ceramics, respectively (Figure 7.1-2 c) and d)). Thus, not only the average grain size is smaller for the FLASH process, but also the grain size distribution is narrower when compared with Conv sintering, as evidenced in Figure 7.1-2.

The EBSD phase-maps of Figure 7.1-2 a) and b), reveal grains separated by a dark colour, indicating a discontinuity in the crystal structure, orientation, or composition. The red colour is associated with $K_{0.5}Na_{0.5}NbO_3$ orthorhombic symmetry phase (JCPDF file 01-085-7128), while the green colour corresponds to a Nb-rich tetragonal symmetry of $K_{0.8}Nb_5O_{15}$ secondary phase (JCPDF file 04-007-9405), using ESPRIT software. Secondary phases are hardly detectable in FLASH ceramics, with just a few indexations at the grain boundaries (see white arrows in Figure 7.1-2 b)). In Conv KNN ceramics, grains are evidently indexed with the Nb-rich phase; see green colour in Figure 7.1-2 a). The inset of Figure 7.1-2 a) shows that this secondary phase is systematically observable throughout the conventionally sintered ceramics. Several EBSD analyses consistently revealed the concentration of the secondary phase in Conv KNN to be 0.25 to 0.50 vol.%, whereas that for FLASH ceramics was found to be <0.05 mol.% (Table 7.1-1).

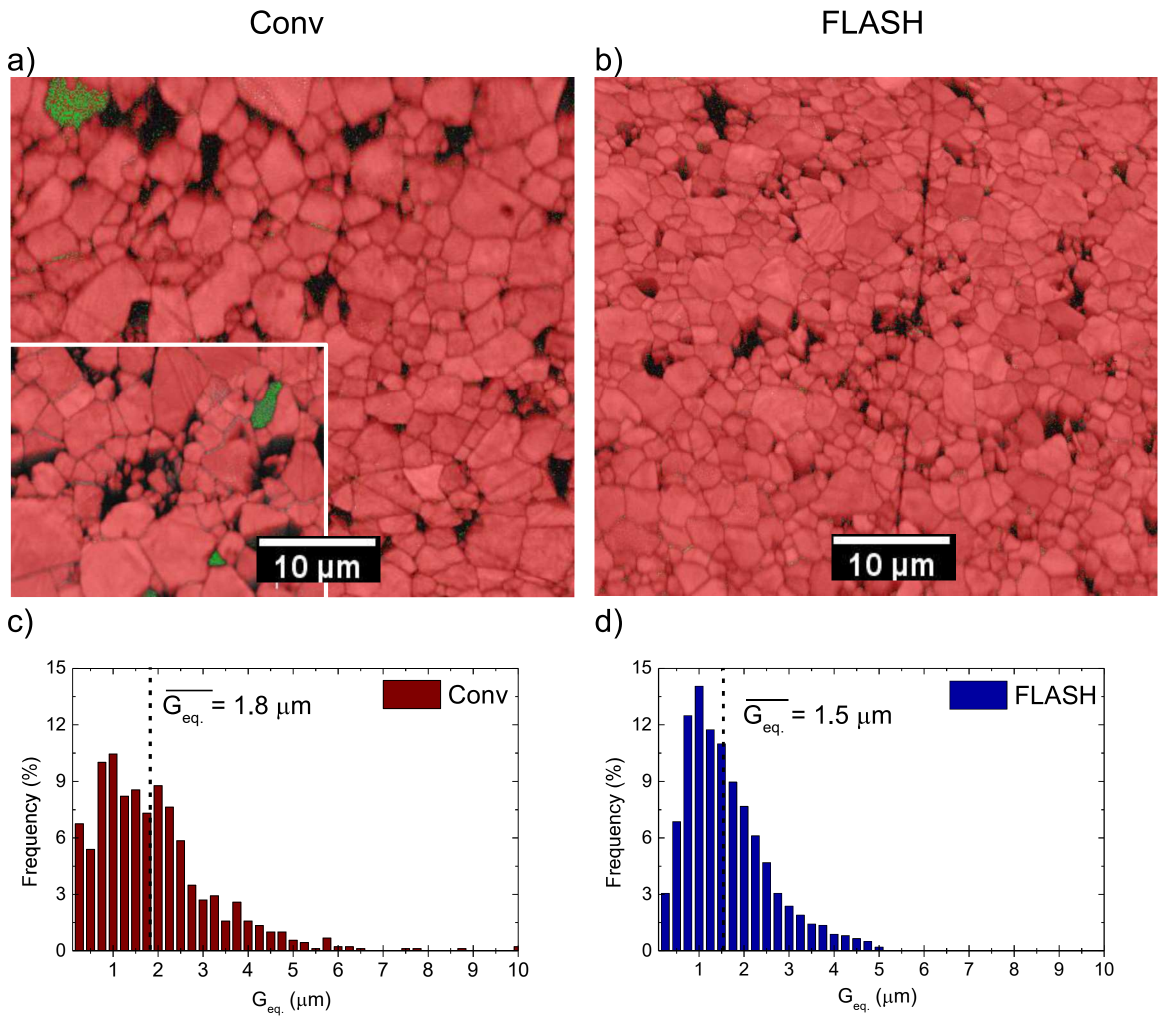

Figure 7.1-2 – EBSD-phase mapping (a, b) and equivalent grain size ($G_{eq.}$) distribution (c,d) deduced from them for conventional (a,c) and FLASH (b,d) sintered KNN ceramics. Red colour in the maps indicates the indexation with JCPDF file 01-085-7128, $K_{0.5}Na_{0.5}NbO_3$ orthorhombic symmetry phase, and green colour with file 04-007-9405, $K_{0.8}Nb_5O_{15}$ tetragonal secondary phase. Inset of a) reveals a second EBSD mapping for Conv KNN with the secondary phase being systematically indexed in several grains.

Table 7.1-1 – Average equivalent grain size ($\overline{\mathrm{G_{eq.}}}$) estimated secondary phase concentration (C_{sp}) from EBSD analysis and relative density ($\rho_{rel.}$), of conventionally (Conv) and FLASH sintered KNN ceramics.

KNN	$\overline{\mathrm{G_{eq.}}}$ (μm)	C_{sp} (vol.%)	$\rho_{rel.}$ (%)
Conv	1.77±0.05	0.25 - 0.50	96±2
FLASH	1.49±0.02	<0.05	93±3

The variation of the relative permittivity and dissipation factor of Conv and FLASH ceramics measured on cooling at a frequency of 1 MHz is illustrated as a function of the temperature in Figure 7.1-3 a) and b), respectively. A pair of peaks in the permittivity are observed and are associated with structural phase transitions, as expected for KNN [3]. For Conv KNN, a permittivity peak at $T_{O\text{-}T}$ = 181 ºC, with ε_r = 1225, corresponds to the orthorhombic to tetragonal phase transition, and another one at T_C = 390 ºC, with ε_r = 5963, corresponds to the tetragonal to cubic phase transition. In the case of FLASH ceramics, both the peak permittivity values and temperatures are slightly superior when compared with Conv KNN. ε_r is of 1321 at $T_{O\text{-}T}$ = 190 ºC and of 6249 at T_C = 398 ºC. The increase of the relative permittivity and transition temperatures for FLASH ceramics compared to Conv KNN can be related to the deviation from the stoichiometry associated with the secondary phases, prevalent in Conv KNN [16] and suppressed in FLASH ceramics. This behaviour is accompanied for both ceramics by a respective peak in dissipation factor (tanδ) that occurs at T_C. The value of tanδ reaches a maximum of about 8% at T_C, decreasing towards ≈ 2% at $T_{O\text{-}T}$, and then slightly increasing during the further cooling.

A slight superiority of FLASH ceramics over Conv KNN is visible as well in the room-temperature polarization (P) behaviour as a function of the applied AC (1 kHz) electric field (E), illustrated in Figure 7.1-4. At rather similar coercive field of 10 kV/cm, remnant polarization values of 20 and 21 μC/cm^2 for Conv and FLASH ceramics, respectively, are found. In terms of piezoelectric performance at room temperature, d_{33} piezoelectric coefficient of 115 for Conv KNN also slightly increases to 117 pC/N for FLASH ceramics.

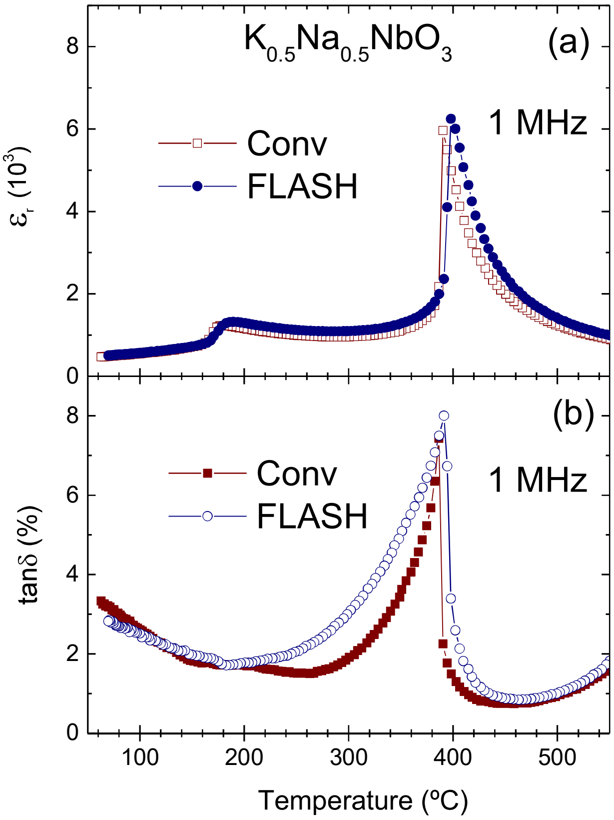

Figure 7.1-3 – Real part of the relative dielectric permittivity, ε_r (a), and dissipation factor, tanδ (β), of conventionally (squares) and FLASH (circles) sintered KNN ceramics measured as a function of temperature, at 1 MHz, during cooling.

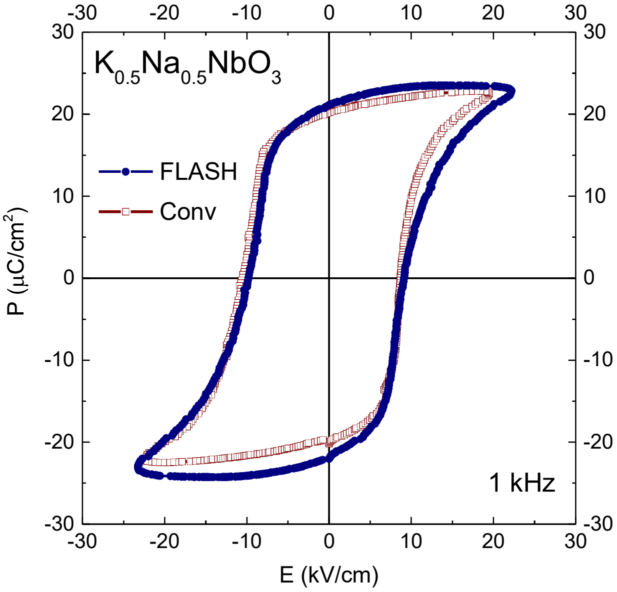

Figure 7.1-4 – Polarization (P) as a function of applied electric field (E) of conventionally (open squares) and FLASH (solid circles) sintered KNN ceramics, measured at 1 kHz and room temperature.

Table 7.1-2 summarizes the most relevant properties of FLASH and conventional KNN ceramics studied in this work, presenting also a comparison with other KNN ceramics, produced either by alternative sintering techniques (SPS/SPT) [9] or by conventional processes [17], and single crystal, as well [18]. The T_C value of 398 ºC for FLASH KNN is very similar to that reported by Birol and co-workers [17] for conventionally sintered KNN. Furthermore, it is higher than that reported for SPS/SPT [12]. The decrease in comparison with the T_C of 429 ºC for KNN single crystal [18] is explained by the presence of impurities, grain boundaries-localized secondary phases and crystal structure defects or residual stresses, usually present in ceramics and less common or absent in single crystals. Values of the permittivity and dissipation factor at T_C of the produced ceramics are also in agreement with the literature.

A ferroelectric analysis reveals that the remnant polarization for Conv and FLASH KNN ceramics is close to those reported for single crystals [9], [17], [18]. On the other hand, the coercive field is closer to that of SPT ceramics [9] and KNN single crystals [18], being lower than that for SPS [9] and Conv specimens reported by Birol *et al.* [17]. In addition, the piezoelectric coefficient of 117 pC/N determined for FLASH ceramics is superior not only comparing with Conv KNN of this work but with all those reported in literature [9] [17], except for the single crystals [18], as expected.

Table 7.1-2 – Relative density ($\rho_{rel.}$), average equivalent grain size ($\overline{G_{eq.}}$), orthorhombic to tetragonal ($T_{O\text{-}T}$), and tetragonal to cubic (T_C) transition temperatures, relative dielectric permittivity (ε_r) and dissipation factor ($\tan\delta$) at T_C, remnant polarization (P_r), coercive field (E_c) and piezoelectric coefficient (d_{33}) of FLASH and Conv KNN ceramics of this work in comparison with literature reports.

KNN	$\rho_{rel.}$ (%)	$\overline{G_{eq.}}$ (μm)	$T_{O\text{-}T}$ (ºC)	T_C (ºC)	At T_C		P_r (μC/cm^2)	E_c (kV/cm)	d_{33} (pC/N)	Ref.
					ε_r	$\tan\delta$				
FLASH	**93±3**	**1.5**	**190**	**398**	6249	0.080	**21**	**10**	**117±2**	**This work**
Conv	**96±2**	**1.8**	**181**	**390**	5963	0.074	**20**	**10**	**115±2**	
Conv	95-96	--	190	400	≈6k	≈1	20	20	110	[17]
SPS	96	3.0	207	386	4160	≈0.2	17	18	95	[9]
SPT	99.8	1.4	204	370	4672	≈0.2	20	12	108	
Single Crystal	--	--	215	429	≈30k	--	19	11	160	[18]

Thus, electrical behaviour attained in FLASH ceramics is at least comparable or even superior to that of conventional KNN. As a result, it is shown for the first time that KNN ceramics obtained by FLASH sintering in spite of the reduced thermal budget can provide a dielectric and ferroelectric response similar or in some cases even better than the one of conventional sintered KNN. In overall, FLASH sintering can be considered as a suitable alternative sintering technique to produce high-T_C KNN ceramics.

In conclusion, the dielectric, piezoelectric and ferroelectric behaviour of KNN ceramics produced by FLASH sintering (T_{max} = 900 ºC, $time_{Total}$ = 210 min) were presented for the first time and found to be slightly superior to those obtained using conventional sintering technique (T_{max} = 1125 ºC, $time_{Total}$ = 620 min). The superior behaviour was also observed comparing with KNN ceramics reported in literature and explained by the lower content of secondary phase. FLASH sintered KNN ceramics are characterised by ε_r = 6249, $\tan\delta$ = 0.08, P_r = 21 $\mu C/cm^2$, E_c = 10 kV/cm and d_{33} = 117 pC/N. The dielectric and ferroelectric characteristics obtained in this work demonstrates that this fast and low thermal budget electric field- and current-assisted sintering process does not compromise the use of FLASH sintered ceramics in sensor, actuator, and energy-harvesting applications.

References

[1] J. F. Li, K. Wang, F. Y. Zhu, L. Q. Cheng, and F. Z. Yao. "(K, Na) NbO_3-based lead-free piezoceramics: Fundamental aspects, processing technologies, and remaining challenges". J. Am. Ceram. Soc., vol. 96, no. 12, pp. 3677–3696, 2013.

[2] Y. Saito *et al.*. "Lead-free piezoceramics". Nature, vol. 432, no. November, pp. 84-87, 2004.

[3] T. R. Shrout and S. J. Zhang. "Lead-free piezoelectric ceramics: Alternatives for PZT?". J. Electroceramics, vol. 19, no. 1, pp. 111–124, 2007.

[4] R. Zuo, J. Rödel, R. Chen, and L. Li. "Sintering and electrical properties of lead-free $Na_{0.5}K_{0.5}NbO_3$ piezoelectric ceramics". J. Am. Ceram. Soc., vol. 89, no. 6, pp. 2010–2015, 2006.

[5] B. Malič *et al.*. "Sintering of lead-free piezoelectric sodium potassium niobate ceramics". Materials, vol. 8, no. 12, pp. 8116–8146, 2015.

[6] M. Matsubara, T. Yamaguchi, K. Kikuta, and S. I. Hirano. "Sinterability and piezoelectric properties of $(K,Na)NbO_3$ ceramics with novel sintering aid". Japanese J. Appl. Physics, Part 1 Regul. Pap. Short Notes Rev. Pap., vol. 43, no. 10, pp. 7159–7163, 2004.

[7] G. Shirane, R. Newnham, and R. Pepinsky. "Dielectric properties and phase transitions of $NaNbO_3$ and $(Na,K)NbO_3$". Phys. Rev., vol. 96, no. 3, pp. 581–588, 1954.

[8] J. Pavlič, B. Malič, and T. Rojac. "Microstructural, structural, dielectric and piezoelectric properties of potassium sodium niobate thick films". J. Eur. Ceram. Soc., vol. 34, no. 2, pp. 285–295, 2014.

[9] R. Pinho *et al.*. “Spark plasma texturing: A strategy to enhance the electro-mechanical properties of lead-free potassium sodium niobate ceramics”. Appl. Mater. Today, vol. 19, p. 100566, 2020.

[10] M. Biesuz, S. Grasso, and V. M. Sglavo. “What’s new in ceramics sintering? A short report on the latest trends and future prospects”. Curr. Opin. Solid State Mater. Sci., vol. 24, no. 5, p. 100868, 2020.

[11] M. Biesuz and V. M. Sglavo. “Flash sintering of ceramics”. J. Eur. Ceram. Soc., vol. 39, no. 2–3, pp. 115–143, 2019.

[12] G. Corapcioglu, M. A. Gulgun, K. Kisslinger, S. Sturm, S. K. Jha, and R. Raj. “Microstructure and microchemistry of flash sintered $K_{0.5}Na_{0.5}NbO_3$”. J. Ceram. Soc. Japan, vol. 124, no. 4, pp. 321–328, 2016.

[13] R. Serrazina, A. M. O. R. Senos, L. Pereira, J. S. Dean, I. M. Reaney, and P. M. Vilarinho. “The Role of Particle Contact in Densification of FLASH Sintered Potassium Sodium Niobate”. Eur. J. Inorg. Chem., vol. 2020, no. 39, pp. 3720–3728, 2020.

[14] R. Serrazina, J. S. Dean, I. M. Reaney, L. Pereira, P. M. Vilarinho, and A. M. O. R. Senos. “Mechanism of densification in low-temperature FLASH sintered lead free Potassium Sodium Niobate (KNN) piezoelectrics”. J. Mater. Chem. C, vol. 7, pp. 14334–14341, 2019.

[15] R. Serrazina, C. Ribeiro, M. E. Costa, L. Pereira, P. M. Vilarinho, and A. M. O. R. Senos. “Particle characteristics influence on FLASH sintering of Potassium Sodium Niobate: a relationship with conduction mechanisms”. Materials, vol. 14, p. 1321, 2021.

[16] D. Alikin, A. Turygin, A. Kholkin, and V. Shur. “Review ferroelectric domain structure and local piezoelectric properties of lead-free $(K_{0.5}Na_{0.5})NbO_3$ and $BiFeO_3$-based piezoelectric ceramics”. Materials, vol. 10, no. 1, pp. 1–23, 2017.

[17] H. Birol, D. Damjanovic, and N. Setter. “Preparation and characterization of $(K_{0.5}Na_{0.5})NbO_3$ ceramics”. J. Eur. Ceram. Soc., vol. 26, no. 6, pp. 861–866, 2006.

[18] M. A. Rafiq, M. E. V. Costa, and P. M. Vilarinho. “Establishing the Domain Structure of $(K_{0.5}Na_{0.5})NbO_3$ (KNN) Single Crystals by Piezoforce-Response Microscopy”. Sci. Adv. Mater., vol. 6, no. 3, pp. 426–433, 2014.

7.2. Article: Behind the electrical performance of FLASH sintered Potassium Sodium Niobate

To be submitted

Abstract

Lead free ferroelectrics have been developed for applications in sensor, actuator and energy harvesting devices. Non-doped $K_{0.5}Na_{0.5}NbO_3$ (KNN) presents a high transition temperature ($T_C \approx 400$ ºC) and relatively high piezoelectric coefficient ($d_{33} = 80 – 160$ pC/N) if the content in secondary phases of sintered ceramics is limited. To allow the production of single-phase KNN at a low thermal budget, alternative sintering techniques have been used. FLASH sintering, an electric field- and current-assisted sintering technique allows to sinter KNN ceramics with higher T_C and similar polarization to that of conventionally sintered ones. However, FLASH and conventional sintering processes are dramatically different in what concerns the sintering mechanisms. Therefore, the ferroelectric, dielectric and conductivity properties of as-sintered ceramics are systematically studied in this work. Successive heat treatments of FLASH and conventionally sintered KNN ceramics are performed to establish a link between the ceramics' properties and the sintering process. While the ferroelectric performance of heat-treated ceramics is not questioned, fingerprints of FLASH sintering are reported for both as-sintered and heat treated KNN ceramics.

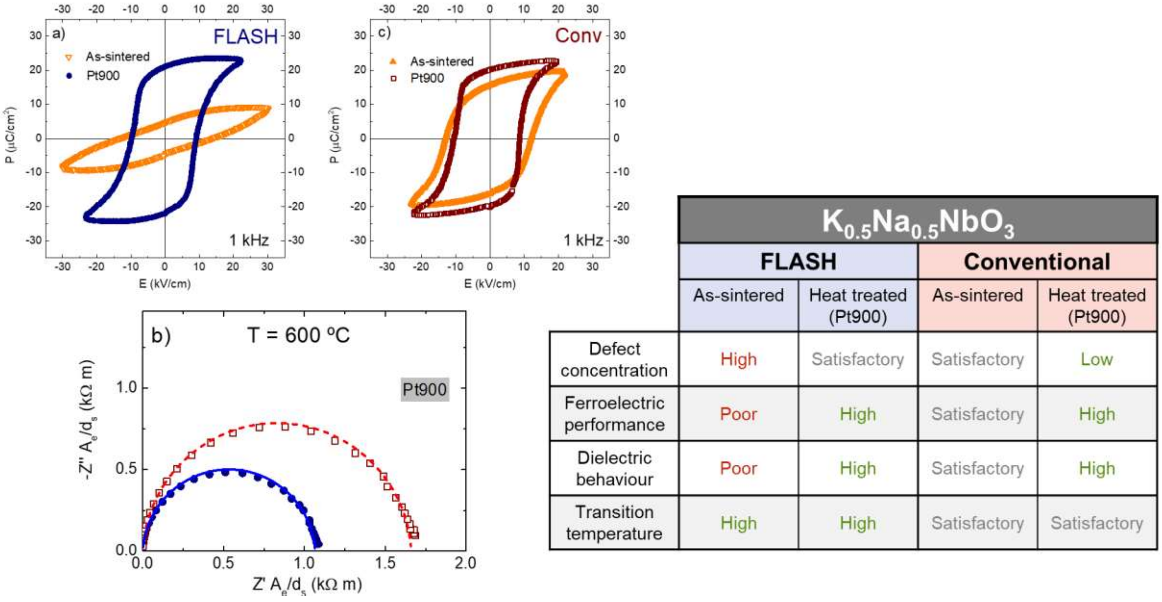

	$K_{0.5}Na_{0.5}NbO_3$			
	FLASH		Conventional	
	As-sintered	Heat treated (Pt900)	As-sintered	Heat treated (Pt900)
Defect concentration	High	Satisfactory	Satisfactory	Low
Ferroelectric performance	Poor	High	Satisfactory	High
Dielectric behaviour	Poor	High	Satisfactory	High
Transition temperature	High	High	Satisfactory	Satisfactory

Key words

FLASH sintering; Conventional sintering; KNN; Potassium Sodium Niobate; Ferroelectric; Piezoelectric; Oxygen vacancy; Impedance spectroscopy; Heat treatment

7.2.1. Introduction

The need for lead-based piezoelectrics replacement in sensor, actuator, and energy-harvesting devices, has led to the development of alkali-based ceramics [1]. Potassium Sodium Niobate ($K_{0.5}Na_{0.5}NbO_3$, KNN) has been investigated due to its high tetragonal to cubic transition temperature (T_C) and large longitudinal piezoelectric coefficient, d_{33} [2]. Non-textured ceramics present, typically, d_{33} values of 80 – 200 pC/N with the tetragonal symmetry phase being stable up to $T_C \approx 420$ °C [3].

The conventional processing of KNN faces experimental limitations [4]–[7], as the high temperature and long-time of sintering induce the volatilization of alkali elements thereby, the formation of secondary phases. The presence of non-stoichiometric secondary phases hinder both T_C and d_{33} [8]. To overcome such limitations alternative, low temperature, sintering methods have been proposed to densify KNN ceramics. Spark Plasma Sintering and Texturing (SPS/SPT) is capable of producing high-density ceramics, with relatively high d_{33} (95 – 108 pC/N) and moderate T_C (370 – 386 °C); however, high temperature, long time, post-sintering re-oxidation steps are needed [9]. FLASH sintering, an electric field- and current-assisted technique [10], has been presented as a possible solution for the sintering of KNN [11]–[14], with significantly reduced thermal budget. While electron microscopy studies revealed that no secondary phases are present in FLASH sintered ceramics, the dielectric, piezoelectric and ferroelectric behaviour of such specimens was revealed to be rather indistinguishable from that of conventionally sintered KNN [15]. Relevant enough is the fact that platinum electrodes were used to perform such measurements, with a previous high temperature heat treatment for electrode sintering, that might have masked the as-sintered behaviour of FLASH sintered KNN.

The proposed mechanism for FLASH sintering of KNN [12]–[14] and other oxides [16]–[18] states that the presence of transient liquid phases at particle contacts allow the very fast densification through particle sliding and a possible accelerated diffusion process through grain boundaries. Such liquid phases are induced due to an increased local concentration of conductive species and/or defects at the particle contacts [19]. This surface dependent process should leave a trace on as-FLASH sintered ceramics.

Therefore, in this work, a comprehensive study on the dielectric properties of as-FLASH sintered and heat treated KNN is presented. Furthermore, the link between sintering process as dielectric and ferroelectric performance of KNN is established. Through impedance spectroscopy studies, the dissimilarities between heat treated FLASH and conventionally sintered KNN ceramics is presented.

7.2.2. Experimental

$K_{0.5}Na_{0.5}NbO_3$, KNN, ceramics were prepared from single phase powders, produced by the mixture and calcination of high purity precursors (Nb_2O_5, Alfa Aesar, 99.9%, K_2CO_3, Sigma-aldrich, 99.99% and Na_2CO_3, Sigma-aldrich, 99.999 %). Details on powder preparation and characterization can be found elsewhere [14]. FLASH sintering was performed in Isothermal Conditions (I.C.), as in previously reported work [12], with the green compacts (15 x 5 x 2 mm^3) being heated to 900 ºC at 10 ºC/min followed by an isothermal step of 30 min before the application of the electric field of 300 V/cm at current limit of 20 mA/mm^2. The holding time in current controlled mode during FLASH sintering was set to 60 s. For conventional sintering (Conv), 5 ºC/min heating and cooling rates were used to achieve a maximum temperature of 1125 ºC with a 3 h dwell.

After sintering, the KNN ceramics were polished with SiC papers (P4000), cleaned with ethanol and dried at 80 ºC. Different electrodes were then deposited for the determination of dielectric and ferroelectric properties of KNN. For room temperature measurements in as-sintered ceramics, gold (Au) electrodes were DC magnetron sputtered. For temperature dependent dielectric and impedance spectroscopy studies, platinum (Pt) electrodes were painted using a Pt suspension (*SPI-CHEM 04990-AB*) and dried at 50 ºC followed by two consequent thermal treatments, represented in Figure 7.2-1. A first low temperature cure treatment was performed for organic’s elimination, without electrode sintering, at 350 ºC for 1 h with heating and cooling rates of 1 and 10 ºC/min, respectively; these ceramics were designated as Pt350. A second heat treatment was performed with heating and cooling rates of 10 ºC/min to a maximum temperature of 900 ºC and 1 h duration; these were labelled with Pt900.

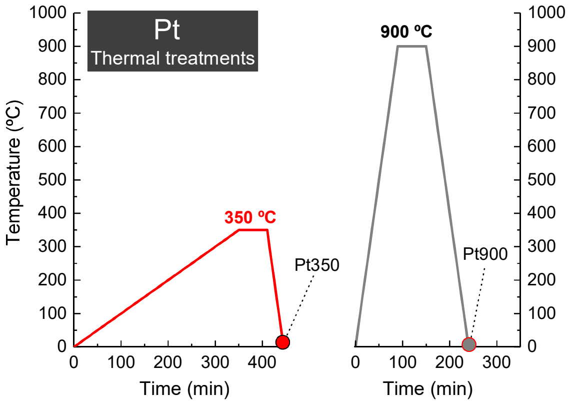

Figure 7.2-1 – Schematic representation of thermal treatment for platinum electrodes on both Conv and FLASH KNN ceramics. Pt350 labelled ceramics were treated at 350 ºC for 1 h, and Pt900 ones at 900 ºC for the same time.

To determine the polarization of as-sintered and Pt900 ceramics as a function of AC electric field at room temperature and 1 kHz frequency, a ferroelectric analyser (*aixACCT, TF Analyzer 2000*) was used.

To assess the frequency dependent impedance (Z) and phase (ψ) of the previously *electrode-deposited* ceramics, the parallel-plate-capacitor configuration was used. An impedance bridge (HP 4284A) at a 1 V oscillation potential and frequency variation from 400 Hz to of 1 MHz was utilized. From the acquired data, the real part of the relative dielectric permittivity (ε_r) and dissipation factor (tanδ) were calculated. In the case of as-sintered ceramics with Au electrodes, only room temperature measurements were performed, due to the limited thermal stability of gold. For the Pt350 and Pt900 ceramics, the dependence of Z and ψ was acquired as a function of temperature, during heating and cooling, from room temperature to ca. 750 ºC at a rate of 2 ºC/min, and a dwell time of 2 min before each measurement. In the case of Pt900, not only the permittivity and dissipation factor were determined but also the real and imaginary parts of both impedance (Z' and Z'', respectively) and modulus (M' and M'') at selected temperatures above T_C. The impedance data measured at cooling were normalized by the geometric factor A_e/d_s (A_e is the electrode area and d_s is the sample thickness) and fitted with the software *ZView*, *Scribner Associates Inc.* as reported before [20]. The fitting was performed with an equivalent circuit consisting of a single block of resistor and a parallel Constant Phase Element (CPE).

The DC conductivity of dense KNN ceramics (both FLASH and Conv) with Pt900 electrodes was further measured. A *Keithley 2410* SourceMeter was used and the specimens were heated at a constant rate of 10 ºC/min, from 450 ºC to 700 ºC, with an applied electric field of 1 V/cm. The activation energy for conduction ($E_a(\sigma)$) of KNN bodies, was determined as in our previous work [14], based on the Arrhenius dependence

7.2.3. Results and discussion

Table 7.2-1 shows the properties of Conv and FLASH KNN ceramics heat treated at 900 ºC for 1 h to cure platinum electrodes, as reported in [15]. The data reveals that FLASH ceramics have a very similar density to that of Conv, while the occurrence of secondary phases and the grain growth are restricted by the FLASH sintering process. Consequently, the cubic to tetragonal transition temperature (T_C) of FLASH ceramics is slightly higher as compared with that of Conv KNN. However, the polarization behaviour and piezoelectric coefficient of FLASH and Conv KNN ceramics are roughly indistinguishable.

Table 7.2-1 – Secondary phase concentration (C_{sp}), relative density (ρ_{rel}), average equivalent grain size ($\overline{G_{eq.}}$), orthorhombic to tetragonal ($T_{O\text{-}T}$) and tetragonal to cubic (T_C) transition temperatures, dielectric permittivity (ε_r) and dissipation factor (tanδ) at T_C (1MHz), remnant polarization (P_r), coercive field (E_c) and piezoelectric coefficient (d_{33}) obtained for Conv and FLASH KNN ceramics. Adapted from [15].

KNN	C_{sp} (vol.%)	$\rho_{rel.}$ ** (%)	$\overline{G_{eq.}}$* (μm)	$T_{O\text{-}T}$ (ºC)	T_C (ºC)	At T_C (1MHz)		P_r (μC/cm^2)	E_c (kV/cm)	d_{33} (pC/N)
						ε_r	tanδ			
Conv	0.25 - 0.50	96±2	1.77	181	390	5963	0.08	20	10	115±2
FLASH	<0.05	93±3	1.49	183	398	6249	0.08	21	10	117±2

*Determined from EBSD
**obtained from Archimedes method

In this work, we clarify the role of post-sintering heat treatments and provide the systematic electrical analysis of the studied FLASH KNN ceramics. Figure 7.2-2 shows the room temperature polarization (top) and respective current density (bottom) as a function of the applied electric field of FLASH (left) and conventionally (right) sintered KNN. Two sets of data are shown for each ceramic, namely, as-sintered (with Au electrode) and Pt900 (with Pt electrode cured at 900 ºC for 1 h). As-FLASH sintered KNN presents a very poor polarization (Figure 7.2-2 a)), without a signature of switching process being revealed in the current density plot (Figure 7.2-2 b)). On the other hand, as-conventionally sintered ceramics are switchable (Figure 7.2-2 c)) with a remnant polarization (P_r) of approximately 16 μC/cm^2 and a coercive field (E_c) of ~13 kV/cm. The distorted shape of the polarization loop is followed by a *lossy* current behaviour (Figure 7.2-2 d)).

After the ceramics were heat treated at 900 ºC (Pt900), regardless of small details, they both present an overall typical ferroelectric behaviour [15] with a $P_r \approx 20$ μC/cm^2 and $E_c \approx 10$ kV/cm as seen in Figure 7.2-2 a) and c). However, the slightly higher current density at zero field for FLASH ceramics as compared with Conv KNN, as well as the overall broader shape of the current density dependence, Figure 7.2-2 b) and d), respectively, suggest that FLASH KNN is a material with higher dielectric losses. Nonetheless, it is important to note that the heat treatment at 900 ºC has a significantly greater influence on FLASH sintered ceramics, while only a moderate variation in performance is observed for Conv KNN.

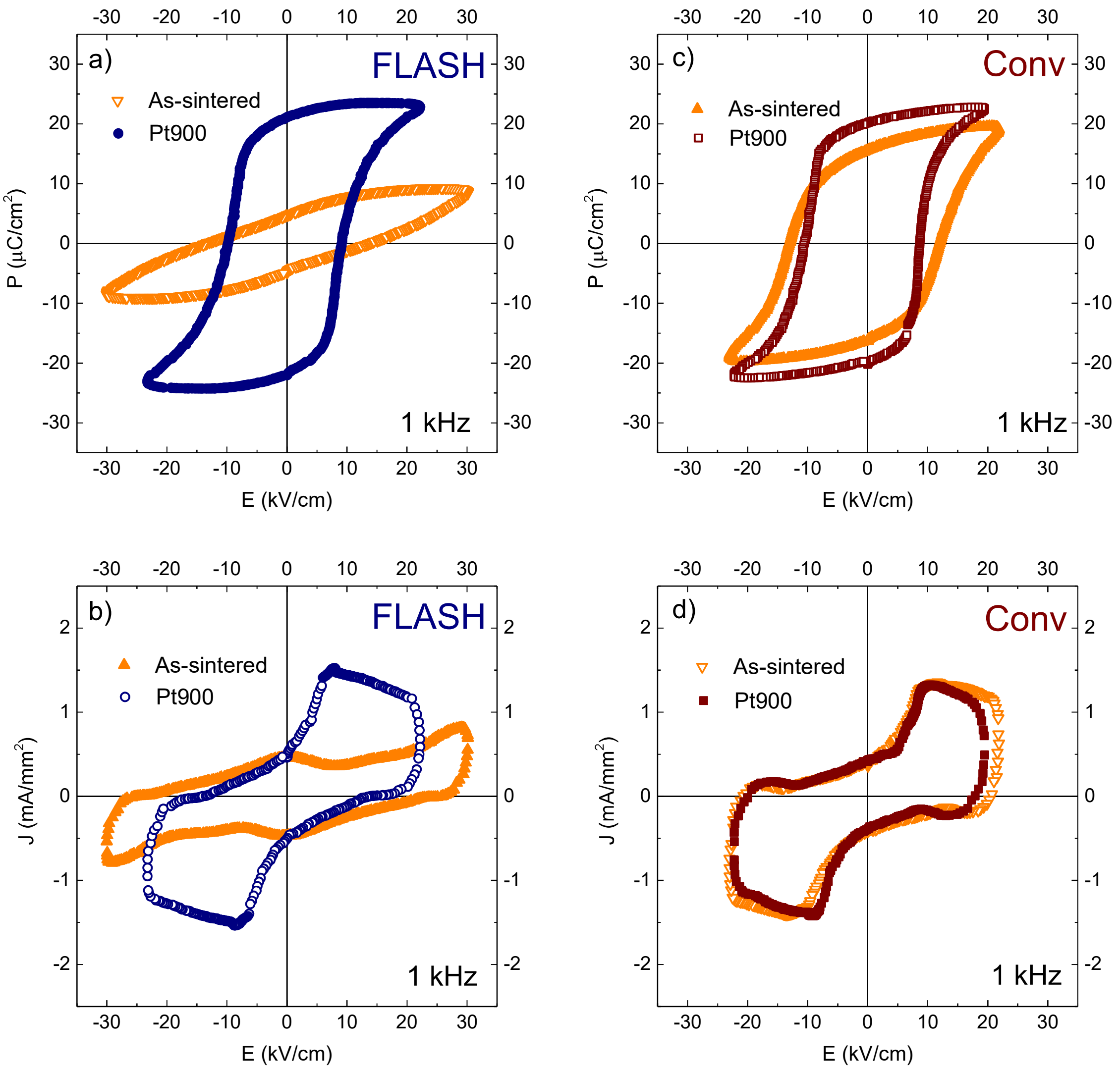

Figure 7.2-2 - Polarization, P, a) and c), and current density, J, b) and d), as a function of applied electric field, E, of FLASH (a) and b)) and conventionally (c) and d)) sintered KNN ceramics, measured at 1 kHz and room temperature. The heat treatment at 900 ºC (Pt900) is relevant for both ceramics, however, prominent to allow the polarization of FLASH sintered KNN.

The differences between as-sintered and Pt900, FLASH and Conv KNN ceramics were further evaluated by the room temperature measurements of the real part of the relative permittivity (ε_r) and the dissipation factor (tanδ), as a function of frequency, shown in Figure 7.2-3. The ε_r and tanδ of FLASH ceramics are presented in Figure 7.2-3 a) and b), respectively, while the correspondent data of conventional ceramics is given in Figure 7.2-3 c) and d), respectively. Over the analysed frequency range, as-sintered FLASH ceramics present similar dissipation factor to that of conventional, however, lower permittivity: ~290 as compared with ~450 (at 1 kHz). After the heat treatment at 900 ºC (Pt900), the relative permittivity of FLASH and Conv KNN is similar, however, the dissipation factor is slightly higher for FLASH.

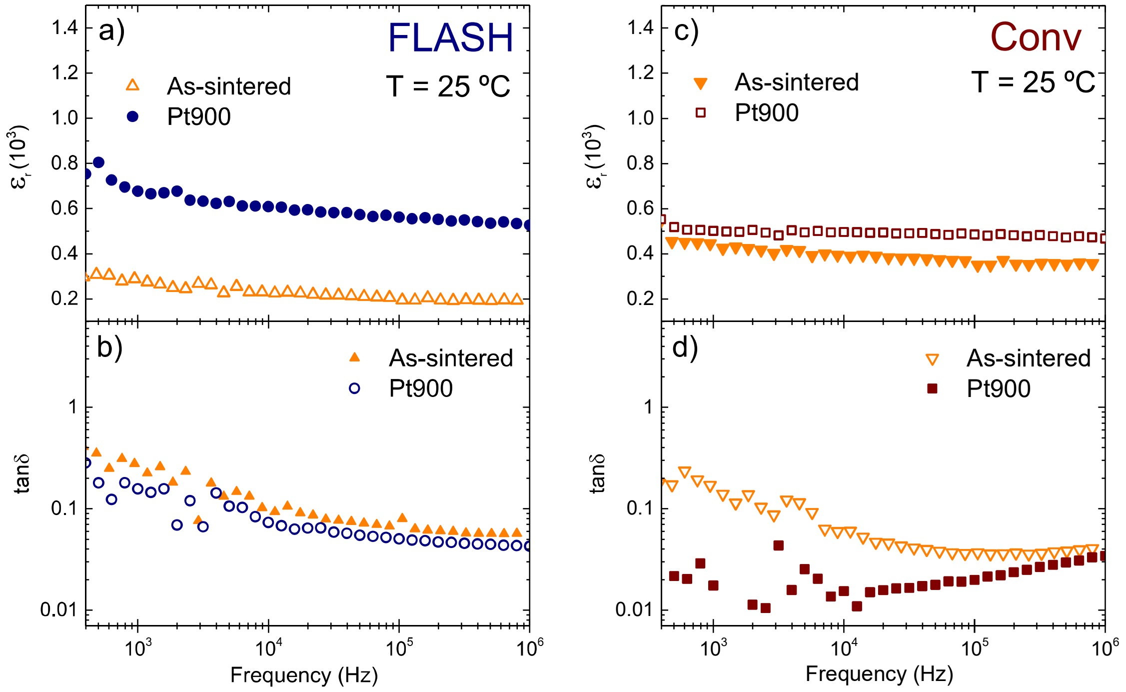

Figure 7.2-3 – Room temperature, frequency dependent (from 400 Hz to 1 MHz) of relative permittivity, ε_r, (a) and c)) and dissipation factor, tanδ, (b) and d)) of FLASH (a) and b), and conventionally (c) and d)) sintered KNN. As-sintered (with Au electrodes) FLASH (up triangles) and Conv (down triangles) as well as heat treated at 900 ºC for 1 h (Pt900) FLASH (circles) and Conv (squares) ceramics are shown.

The observation of Figure 7.2-3 suggests that: (i) as-sintered FLASH ceramics has lower relative permittivity than as-sintered Conv KNN; (ii) the heat treatment at 900 ºC is effective at marginally reducing the dissipation factor of conventional KNN, while slightly increasing its permittivity; (iii) the heat treatment has a very significant role on the FLASH sintered KNN, permitting similar permittivity and dissipation factor values to those of conventionally sintered ceramics to be achieved; (iv) however, a slightly higher dissipation factor is revealed for FLASH-Pt900 ceramics as compared with that of Conv-Pt900. These four points are correlated with polarization (Figure 7.2-2), respectively: (i) the low ε_r of as-FLASH sintered ceramics corresponds to significantly lower polarization as compared with as-sintered Conv KNN; (ii) the disformed polarization loop of as-sintered Conv KNN (Figure 7.2-2 c)) coheres with the slightly lower permittivity and higher dissipation factor of these ceramics as compared with Conv-Pt900 specimens; (iii) the ability to observe the ferroelectric behaviour in Figure 7.2-2 a) for FLASH ceramics after the treatment at 900 ºC is accompanied by the significant increase in ε_r and slight decrease in tanδ after the Pt900 heat treatment; finally, (iv) the more *lossy* behaviour of FLASH-Pt900 as compared with Conv-Pt900 KNN (Figure 7.2-2 b) and d)) is in agreement with the slightly higher tanδ of FLASH KNN.

These observations suggest that the low permittivity of as-FLASH sintered ceramics is related with the presence of un-relaxed and un-combined electronic defects, which are a consequence of the sintering process. The high current flow through the ceramics during FLASH sintering (20 mA/mm^2) arises from the movement of charged particles resultant of lattice defect formation [21]–[23]. When this current is shut down, the sintered ceramics undergo a very fast cooling to the furnace environment temperature [24], which does not allow the total recombination and relaxation of structure and defects [25], [26]. Examples of such defects are oxygen vacancies, $V_O^{\circ\circ}$, commonly found in perovskite structure materials [27]. Consequently, these lattice defects reduce the polarizability and long range order of polar dipoles, thus supressing the permittivity (Figure 7.2-3 a)) and remanent polarization (Figure 7.2-2 a)), respectively, in as-sintered FLASH KNN. However, a high temperature heat treatment in oxidizing conditions (air) should allow the relaxation and re-oxidation of these defects [9].

If the proposed heat treatment dependence on the electronic defect relaxation of FLASH sintered ceramics is valid, there should be a relationship between their ε_r and tanδ dependences with the temperature. Facing the impossibility of studying the high temperature dielectric behaviour of as-sintered ceramics with Au electrodes, these are forward represented by Pt350. In this case, Pt electrodes were treated at low temperature (350 ºC – 1 h). Despite not being exactly *as-sintered* ceramics, they should behave quite similarly. Figure 7.2-4 shows the ε_r and tanδ temperature dependence of FLASH, a) and b), respectively, and Conv KNN, c) and d), correspondingly, at 1 MHz. The black arrows indicate heating processes. The Pt350 data, presented by triangles for both ceramics, reveal that the values of ε_r and tanδ at the beginning of the thermal cycle (heating), for $T < 100$ ºC, are very similar to those reported at room temperature for as-sintered ceramics in Figure 7.2-3. In detail, Figure 7.2-4 shows that ε_r(FLASH-Pt350) ≈ 300, tanδ(FLASH-Pt350) ≈ 0.2, while ε_r(Conv-Pt350) ≈ 480 and tanδ(Conv-Pt350) ≈ 0.05, which are very similar to those presented in Figure 7.2-3 at 1 MHz (yellow dependences). This observation suggests that Pt350 treatment is actually representative of as-sintered ceramics. Furthermore, Figure 7.2-4 gives indication of similar ε_r and tanδ values (at $T < 100$ ºC) for the Pt900 ceramics in comparison with Figure 7.2-3, as expected.

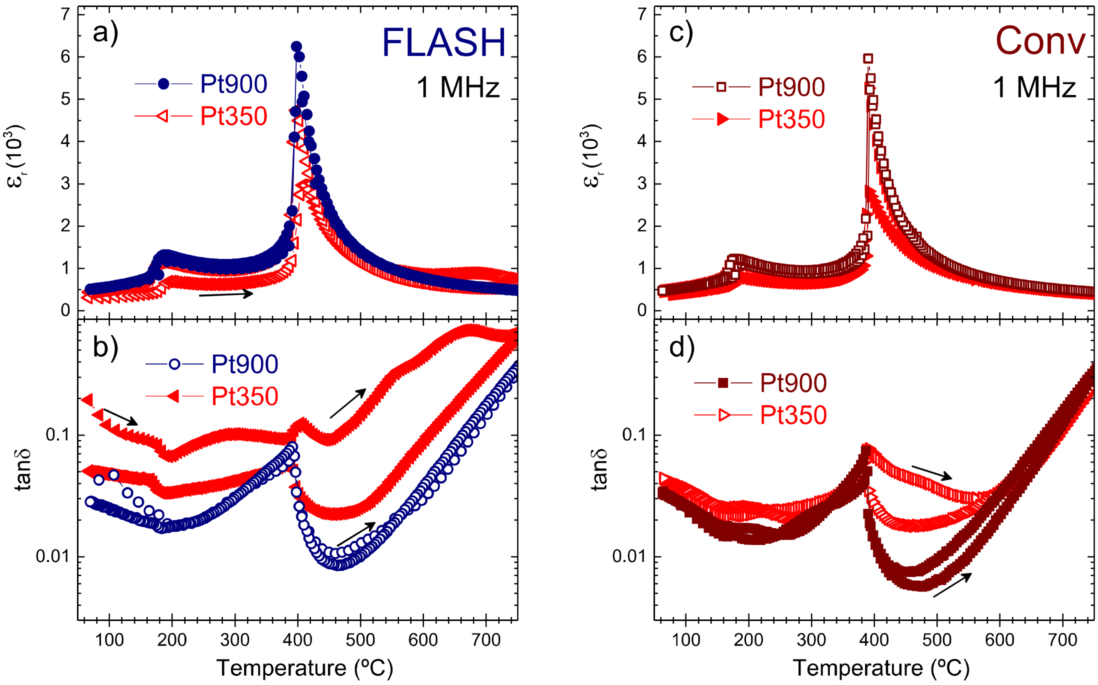

Figure 7.2-4 – Real part of the relative dielectric permittivity ε_r (a) and c)) and dissipation factor tanδ (b) and d)) of Pt350 (left triangles) and Pt900 (circles) FLASH ceramics (a) and b)) as well as Pt350 (right triangles) and Pt900 (squares) Conv KNN (c) and d)), measured as a function of temperature, at 1 MHz during heating (arrows indication) and cooling.

In the overall, Figure 7.2-4 shows a typical permittivity and dissipation factor dependence with temperature of KNN ceramics, as presented before (Table 7.2-1 [15]). Additionally, both FLASH and Conv KNN ceramics with Pt350 or Pt900 treatment present similar profiles of permittivity and dissipation factor. This means that the transition temperatures $T_{O\text{-}T}$ and T_C (extrapolated from ε_r and tanδ maxima) are revealed at the same temperature, independently on the heat treatment, and follow our previous report (Table 7.2-1 [15]).

After establishing that Pt350 treatment is representative of as-sintered ceramics, their behaviour is compared with that of 900 ºC heat treated specimens (Pt900). Besides the transition temperatures indication, Figure 7.2-4 shows a dependence of heat treatment with the dielectric behaviour of KNN ceramics, especially relevant for FLASH sintered ones. Figure 7.2-4 a) reveals a heating *vs* cooling hysteresis in ε_r of Pt350 FLASH specimen. The relative permittivity is lower during the heating (black arrow), as compared with that on cooling. The dissipation factor (Figure 7.2-4 b)) of the same ceramics reveals a heating/cooling hysteresis as well, with the higher tanδ being associated with heating; furthermore, a non-linear behaviour is observed during heating at T > 500 ºC, which can be related with relaxation of the ceramics with the thermal treatment. After the heating to ca.

750 ºC, FLASH-Pt350 ceramics reveal a lower dissipation factor and higher ε_r upon cooling than on heating. Nonetheless, these are not fully coincident with Pt900 curves. In this case (Pt900), no relevant heating *vs* cooling hysteresis is observed, with the maximum of permittivity reaching ca. 6000 at T_C and tanδ being kept below 0.1 for $T < 650$ ºC, in accordance with Table 7.2-1.

Regarding the conventionally sintered ceramics, Figure 7.2-4 c) shows a slightly lower ε_r for as-sintered KNN (Pt350) during heating, which is fairly increased during cooling. This agrees with the data shown in Figure 7.2-3, as well as the dissipation factor temperature dependence - Figure 7.2-4 d). Here, a small hysteresis is revealed for Pt350 ceramic at $T > 400$ ºC, which is a consequence of the small relaxation that occurs in these ceramics with the heat treatment.

Figure 7.2-4 allows to undoubtedly conclude that the dielectric behaviour of FLASH sintered KNN is very dependent on the thermal history of the ceramics, while that of Conv KNN is less significantly affected. The previously proposed suggestion to explain this dependence appears to be confirmed by Figure 7.2-4. The as-sintered FLASH ceramics present a high concentration of defects, that contribute to a low ε_r and high tanδ. During heating, these defects are relaxed and recombined, which results in a hysteretic behaviour of their dielectric factors. Nonetheless, a heating to 750 ºC is not enough to fully relax the ceramics. The Pt900 heat treatment (at 900 ºC) appears to further relax the FLASH ceramics, allowing a roughly similar behaviour to that of conventionally sintered KNN. Also, the absence of ε_r or tanδ hysteresis upon heating and cooling, after the heat treatment, is verified. Even though Conv specimens also present a small dependence of their dielectric properties with the post-sintering heat treatment, it is significantly less evident than the one of FLASH ceramics.

As shown by Figure 7.2-2 and Figure 7.2-3, the dielectric response of KNN ceramics as well as their ferroelectric polarization are both enhanced when the ceramics are heat treated at 900 ºC (which typically is needed for the electrode cure). However, this treatment is revealed to be accessory for conventionally sintered KNN, while it is essential for FLASH sintered ceramics.

Even in similarly heat-treated FLASH and Conv ceramics (Pt900), small differences in performance are observed. To further investigate these dissimilarities, temperature reliant Impedance Spectroscopy (IS) studies were performed on Pt900 ceramics. In fact, Pt350 ceramics were also studied, however, because in the case of as-FLASH sintered ceramics the system (bulk ceramic + grain boundaries + defects) is constantly changing with the temperature, due to the recombination of oxygen vacancies, a proper IS analysis was not possible. Therefore, we focused on the dissimilarities between Pt900 specimens to evaluate the fingerprints and consequences of low thermal budget FLASH sintering on ceramics, as compared with conventionally sintered KNN.

Figure 7.2-5 shows the Nyquist representation of normalized real (Z') and imaginary (Z'') parts of the impedance for FLASH and conventionally sintered KNN, as a dependence of temperature, namely, a) 500 ºC, b) 600 ºC and c) 700 ºC. Z'' *vs* Z' are represented as single arcs for both ceramics, together with the mathematical fitting of a Resistance in parallel with a Constant Phase Element (R//CPE) equivalent circuit. Despite the dissimilarities observed for FLASH (circles) and Conv (squares) KNN, with the last presenting a more resistive behaviour than FLASH, Figure 7.2-5 confirms a satisfactory fitting (solid lines for FLASH and dashed lines for Conv) with the equivalent circuit consisting of a single R//CPE block for both ceramics.

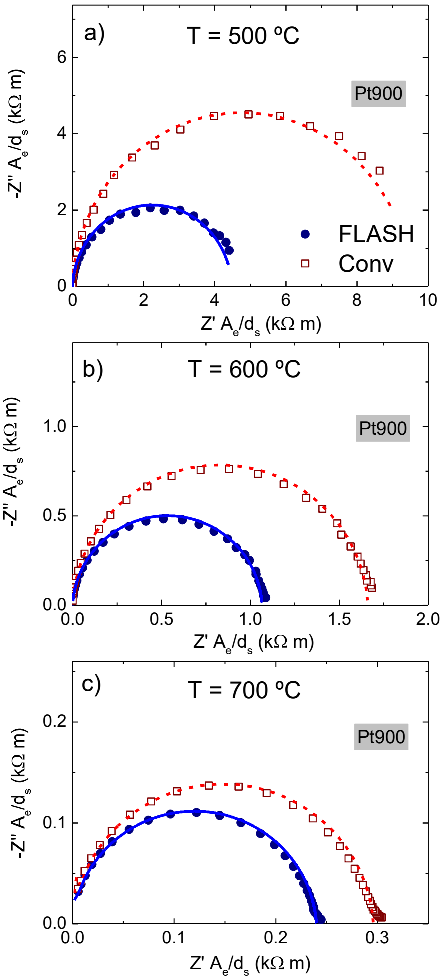

Figure 7.2-5 – Nyquist plots of normalized real and imaginary impedance parts at 500 (a)), 600 (b)) and 700 ºC (c)) for FLASH (solid circles) and conventionally (open squares)

sintered KNN ceramics with platinum electrodes heat treated at 900 ºC (Pt900). The R//CPE fitting is shown in dash and solid lines for Conv and FLASH, respectively.

The frequency spectra of both the impedance and modulus imaginary parts, i.e. the frequency dependence of Z'' and M'', respectively, are shown in Figure 7.2-6 for a) FLASH and b) Conv ceramics, at 600 ºC. The corresponding frequencies for maximum |Z''| and M'' (Z''$_{max}$ and M''$_{max}$, respectively) are quite similar, which agrees with the fitting with a single R//CPE equivalent circuit. The calculated capacitance and resistance values of the equivalent circuit for each ceramic were calculated in respect to the temperature (from 450 to 700 ºC). The estimated capacitance is between 10^{-10} and 10^{-11} F, which is suitable for bulk ferroelectric grains [28]. The normalized capacitance and conductance are presented in Curie-Weiss and Arrhenius plots in Figure 7.2-7 a) and b), respectively. For comparison, these laws were also applied for relative permittivity (from Figure 7.2-4) and DC conductivity data, presented in Figure 7.2-7 c) and d), respectively. In the Curie-Weiss law:

$$C \sim \varepsilon = \frac{A_C}{(T - T_0)} \tag{7-1}$$

A_C is the Curie constant and T_0 is the Curie temperature. The Arrhenius law for conductivity is expressed in equation 2-17.

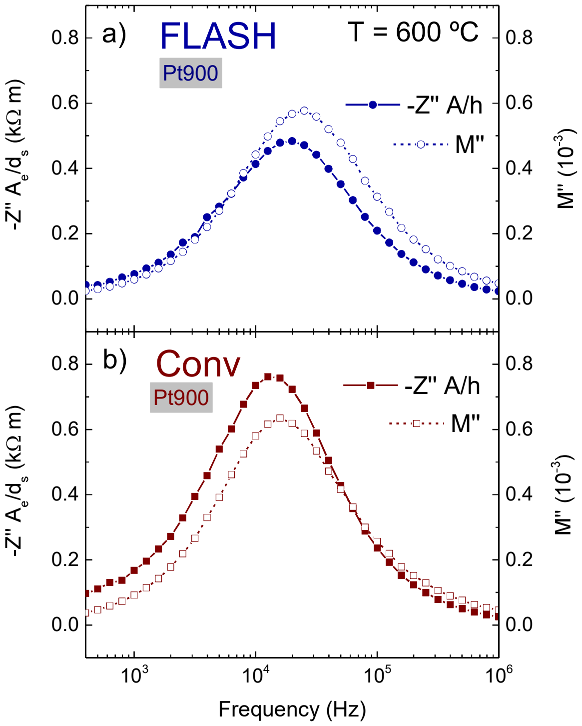

Figure 7.2-6 – Normalized -Z'' (solid symbols) and M'' (open symbols) of a) FLASH and b) conventionally sintered KNN ceramics, measured as a function of frequency, at a

temperature of 600 ºC. The correspondent frequencies of -Z''$_{max}$ and M''$_{max}$ are approximately the same.

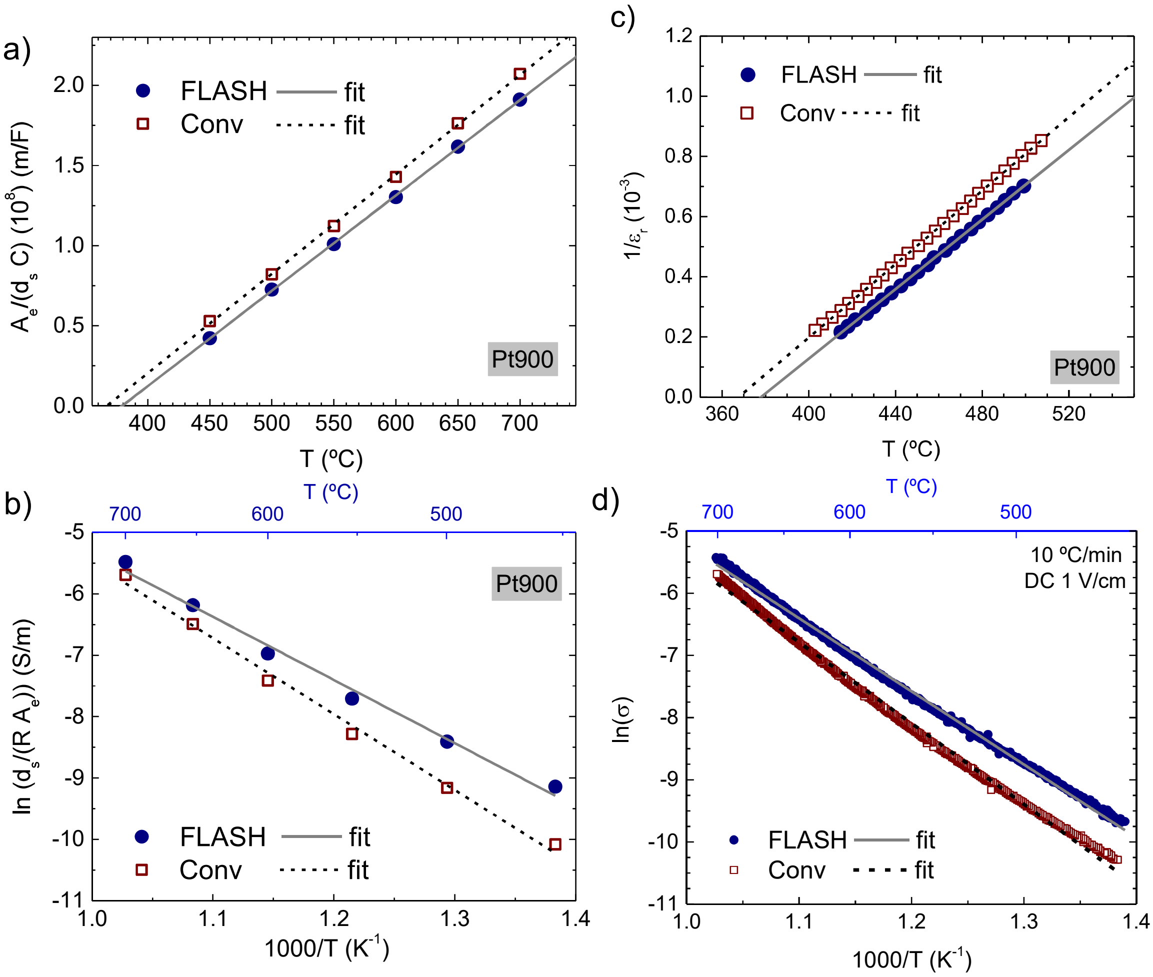

Figure 7.2-7 – a) Normalised inverse capacitance versus temperature and b) natural log (ln) of conductivity versus inverse absolute temperature, obtained from the complex impedance fitting. Similar representations on c) and d), respectively, obtained, however, from permittivity dependence with temperature (Figure 7.2-4) and DC conductivity measurements (1 V/cm – 10 ºC/min heating rate). FLASH (circles) and conventionally (squares) sintered KNN specimens with Pt900 electrodes are analysed.

Table 7.2-2 – Summary of estimated Curie temperature (T_0) and activation energy for conduction ($E_a(\sigma)$) values from Figure 7.2-7. T_0 was estimated following the Curie-Weiss law and using impedance spectroscopy (IS – a)) and relative permittivity (c)) data. The $E_a(\sigma)$) was calculated from Arrhenius law, using IS (b)) and DC data (d)).

KNN ceramics (Pt900)	**Curie-Weiss**		**Arrhenius**	
	T_0 (ºC) (IS)	T_0 (ºC) (ε_r)	$E_a(\sigma)$ (eV) (IS)	$E_a(\sigma)$ (eV) (DC)
Conv	367±2	367.7±0.3	1.06±0.04	1.122±0.002
FLASH	379±1	378.1±0.4	0.89±0.04	1.013±0.001

The estimated T_0 values for Conv and FLASH ceramics were obtained from Figure 7.2-7 a) and c) and the apparent activation energy for conduction ($E_a(\sigma)$) were extrapolated from Arrhenius representations (Figure 7.2-7 b) and d)). The estimated values are summarized in Table 7.2-2 in respect to the ceramic and data set.

Figure 7.2-7 a) reveals that the capacitance data from both ceramics follows the Curie-Weiss law, confirming that the analysed response should be that of bulk KNN, as grain boundaries are not expected to follow this law [28]. The estimation of bulk capacitance of both ceramics present similar slopes. However, because C(FLASH) > C(Conv) in the analysed temperature range between 450 and 700 ºC, the extrapolation of Curie temperature of 367 ºC is lower for Conv comparing to 379 ºC for FLASH ceramics, as also shown in Table 7.2-2. This estimation is in very good agreement with that from Figure 7.2-7 c), in which the permittivity data was fitted. In this case, $T_0(\text{Conv}) \approx 368$ ºC and $T_0(\text{FLASH}) \approx 378$ ºC.

The T_C values for FLASH and Conv KNN ceramics, estimated as the permittivity peak temperature in Figure 7.2-4, were 398 and 390 ºC, respectively [15]. While the T_C of FLASH ceramics is kept to be ≈ 10 ºC higher than that of Conv KNN, the fact of $T_0 < T_C$ observed for both ceramics is in agreement with the first order ferroelectric phase transition [29]. The dissimilarities in T_C of FLASH and Conv previously accessed to the greater concentration of secondary phases in the latter ceramics [15] are thus confirmed by Curie-Weiss law fits with similar difference in T_0.

The Arrhenius law is also followed by the bulk resistance values of both ceramics (Figure 7.2-7 b)) though, the conductivity of FLASH ceramics is higher, for the same temperature, as compared with Conv KNN. Furthermore, the estimated apparent activation energy for conduction ($E_a(\sigma)$) is dissimilar for FLASH or Conv KNN (Table 7.2-2). While the $E_a(\sigma)$ of Conv KNN is just below 1.1 eV, that of FLASH is ca. 0.9 eV. Interestingly, the $E_a(\sigma)$ estimations of 1.0 and 1.1 eV from the DC conductivity measurements of FLASH and Conv ceramics, present in Figure 7.2-7 d), agree well with those obtained by IS analysis. The slight increase in $E_a(\sigma)$ estimated from DC conductivity should be related with the measurement heating rate of 10 ºC/min, whereas IS analysis was performed at 2 ºC/min cooling rate with temperature stabilisation for 2 min.

In any case, it is confirmed that the activation energy for conduction in FLASH ceramics is lower as compared with conventionally sintered specimens. Our previous work gave similar indications when comparing FLASH ceramics with KNN single crystals [14]. Activation energies for conduction in ferroelectric perovskites reported between 0.4 and 1.2 eV are associated with charge transport by oxygen defects, namely, ionized oxygen vacancies [30], [31], which was previously confirmed in KNN ceramics and single crystals [14], [32]. Therefore, the estimated values in this work are suitable with an oxygen vacancy-based conduction mechanism for both FLASH and Conv ceramics. However, the concentration of these defects is proposed to be higher in FLASH sintered ceramics, as their $E_a(\sigma)$ is decreased in comparison with Conv KNN.

Table 7.2-2 and Figure 7.2-7 unequivocally show that the conduction process of FLASH sintered KNN is facilitated over that of Conv ceramics. This observation is explained by the very different sintering processes, that still reveal their fingerprints on the ceramic's properties, even after a post-sintering heat treatment at 900 ºC for 1 h. FLASH sintering occurs through the movement of charged particles (electrons, polarons, ions, or others). In the case of KNN, a relatively low activation energy conducting process is revealed as a pattern and is most probably related with oxygen vacancies. This phenomena was particularly revealed in as-sintered ceramics (as shown in Figure 7.2-2 to Figure 7.2-4), and still detected after a post-sintering treatment at 900 ºC (Figure 7.2-7 and Table 7.2-2).

Furthermore, our results are fairly in accordance with FLASH sintering studies in La-, Sm- or Y-doped BFO, that revealed electrically homogeneous ceramics, without a distinguished contribution of grain and grain boundaries [33]. On contrary, grain and grain boundary contributions were reported in FLASH and conventionally sintered doped-BNT [34]. Nonetheless, it should be noted that 3 R//C equivalent circuits were needed to model the IS response of FLASH sintered doped-BNT, however, only two contributions were further presented and discussed [34].

As stated before [12], [13], the FLASH sintering process is quite dependent on the FLASH processing parameters (electric field, current density, time, etc), but also on the materials. Therefore, the impedance response of FLASH sintered ferroelectric ceramics is dependent on the FLASH parameters and on the material itself. Furthermore, a comparison with IS studies in YSZ materials was not considered because the conduction processes and consequent FLASH sintering in that case is significantly different from that of KNN [12]–[14]

The work previously developed in our group with alternative sintering of non-doped KNN (SPS and SPT) [9] present some discrepancies with the current study. In the case of SPS/SPT ceramics, two R//C equivalent circuits were used to model the IS response. A grain core - grain shell assignment was proposed, in which small chemical differences could explain the quite similar parameters of equivalent R//C circuits. On contrary, in the case of FLASH sintering (present work), only one contribution (bulk) was enough to model the IS data. In fact, the estimated T_0 and $E_a(\sigma)$ (from IS) were in very good agreement with estimations from relative permittivity and DC conductivity studies, respectively. This proves that our IS fitting was properly done. Thus, it is suggested that FLASH sintering allowed to produce electrically uniform KNN ceramics, without the presence of core-shell structures.

Nonetheless, when comparing with conventionally sintered KNN, FLASH ceramics present higher transition temperature (≈10 ºC) and slightly enhanced dissipation factor. These are due to, respectively, lower amount of secondary phases and higher concentration of conductive defects, as oxygen vacancies, in FLASH ceramics. Our observations confirm the different nature of FLASH, SPS/SPT and conventional sintering processes. While the slow mass transport at high temperatures of conventional sintering allows to keep the defect concentration low, it promotes a decrease in T_C due to the segregation of secondary phases. In SPS/SPT, very fast heating of compacts, through the Joule heating of a mould, allows SPS/SPT to produce KNN ceramics with high density, core-shell-like grains, and slightly decreased T_C. FLASH sintering promotes the Joule heating of compacts through direct current flow in the un-sintered particles, which is consequently revealed in the as-sintered and heat treated ceramics' performance and properties. Nonetheless, both alternative sintering techniques demand high temperature post-sintering treatments for the ferroelectric performance of KNN to be revealed; a 900 ºC - 300 min treatment was performed in SPS/SPT ceramics, while a significantly shorter time (60 min) was used in FLASH sintered specimens. The increase in the heat treatment time could result in the elimination of the conductive nature of FLASH ceramics, however, a concern in keeping a total low thermal budget of this alternative sintering technique (in comparison with the conventional sintering process) was of interest.

7.2.4. Conclusions

To conclude, high performance KNN ceramics were produced by FLASH sintering with a consequent thermal treatment for electrode cure at 900 ºC for 1 h. The heat treatment is also related with the need for the ceramics' defect relaxation, which are most probably, oxygen vacancies. Despite that the heat treatment allows the manifestation of the ferroelectric intrinsic behaviour of FLASH sintered KNN, fingerprints of FLASH process were revealed by permittivity, impedance spectroscopy and DC conductivity analysis of heat-treated ceramics. A single grain (bulk) contribution was found by impedance studies for both ceramics, with the activation energy for conduction in FLASH KNN being lower than in conventionally sintered ceramics. This observation agreed with DC conductivity studies.

The transition temperature of FLASH sintered KNN was kept ≈10 ºC higher than that of conventional; this was confirmed from permittivity and impedance studies.

Our results present a direct link between ferroelectric properties and alternative sintering of piezoelectric ceramics. If a one-step FLASH sintering and electrode attachment is to be developed for these ceramics, following the FLASH joining approach [35], a process engineering to avoid the presence of electronic defects in as-sintered ceramics must be considered.

7.2.5. References

[1] J. F. Li, K. Wang, F. Y. Zhu, L. Q. Cheng, and F. Z. Yao. "(K, Na) NbO_3-based lead-free piezoceramics: Fundamental aspects, processing technologies, and remaining challenges". J. Am. Ceram. Soc., vol. 96, no. 12, pp. 3677–3696, 2013.

[2] Y. Saito *et al.*. "Lead-free piezoceramics". Nature, vol. 432, no. November, pp. 84–87, 2004.

[3] T. R. Shrout and S. J. Zhang. "Lead-free piezoelectric ceramics: Alternatives for PZT?". J. Electroceramics, vol. 19, no. 1, pp. 111–124, 2007.

[4] R. Zuo, J. Rödel, R. Chen, and L. Li. "Sintering and electrical properties of lead-free $Na_{0.5}K_{0.5}NbO_3$ piezoelectric ceramics". J. Am. Ceram. Soc., vol. 89, no. 6, pp. 2010–2015, 2006.

[5] B. Malič *et al.*. "Sintering of lead-free piezoelectric sodium potassium niobate ceramics". Materials, vol. 8, no. 12, pp. 8116–8146, 2015.

[6] M. Matsubara, T. Yamaguchi, K. Kikuta, and S. I. Hirano. "Sinterability and piezoelectric properties of (K,Na)NbO_3 ceramics with novel sintering aid". Japanese J. Appl. Physics, Part 1 Regul. Pap. Short Notes Rev. Pap., vol. 43, no. 10, pp. 7159–7163, 2004.

[7] G. Shirane, R. Newnham, and R. Pepinsky. "Dielectric properties and phase transitions of $NaNbO_3$ and (Na,K)NbO_3". Phys. Rev., vol. 96, no. 3, pp. 581–588, 1954.

[8] J. Pavlič, B. Malič, and T. Rojac. "Microstructural, structural, dielectric and piezoelectric properties of potassium sodium niobate thick films". J. Eur. Ceram. Soc., vol. 34, no. 2, pp. 285–295, 2014.

[9] R. Pinho *et al.*. "Spark plasma texturing: A strategy to enhance the electro-mechanical properties of lead-free potassium sodium niobate ceramics". Appl. Mater. Today, vol. 19, p. 100566, 2020.

[10] M. Biesuz and V. M. Sglavo. "Flash sintering of ceramics". J. Eur. Ceram. Soc., vol. 39, no. 2–3, pp. 115–143, 2019.

[11] G. Corapcioglu, M. A. Gulgun, K. Kisslinger, S. Sturm, S. K. Jha, and R. Raj. "Microstructure and microchemistry of flash sintered $K_{0.5}Na_{0.5}NbO_3$". J. Ceram. Soc. Japan, vol. 124, no. 4, pp. 321–328, 2016.

[12] R. Serrazina, A. M. O. R. Senos, L. Pereira, J. S. Dean, I. M. Reaney, and P. M. Vilarinho. "The Role of Particle Contact in Densification of FLASH Sintered

Potassium Sodium Niobate". Eur. J. Inorg. Chem., vol. 2020, no. 39, pp. 3720–3728, 2020.

[13] R. Serrazina, J. S. Dean, I. M. Reaney, L. Pereira, P. M. Vilarinho, and A. M. O. R. Senos. "Mechanism of densification in low-temperature FLASH sintered lead free Potassium Sodium Niobate (KNN) piezoelectrics". J. Mater. Chem. C, vol. 7, pp. 14334–14341, 2019.

[14] R. Serrazina, C. Ribeiro, M. E. Costa, L. Pereira, P. M. Vilarinho, and A. M. O. R. Senos. "Particle characteristics influence on FLASH sintering of Potassium Sodium Niobate: a relationship with conduction mechanisms". Materials, vol. 14, p. 1321, 2021.

[15] R. Serrazina, A. Tkach, L. Pereira, A. M. O. R. Senos, and P. M. Vilarinho. "FLASH sintered potassium sodium niobate: high performance piezoelectrics at low thermal budget processing". *SUBMITTED, 2021.

[16] R. Chaim. "On the kinetics of liquid-assisted densification during flash sintering of ceramic nanoparticles". Scr. Mater., vol. 158, pp. 88–90, 2019.

[17] R. Chaim. "Liquid film capillary mechanism for densification of ceramic powders during flash sintering". Materials, vol. 9, no. 4, pp. 19–21, 2016.

[18] R. Chaim and C. Estournès. "On thermal runaway and local endothermic/exothermic reactions during flash sintering of ceramic nanoparticles." J. Mater. Sci., vol. 53, no. 9, pp. 6378–6389, 2018.

[19] R. Chaim. "Particle surface softening as universal behaviour during flash sintering of oxide nano-powders". Materials, vol. 10(2), no. 179, 2017.

[20] A. Tkach, L. Amaral, P. M. Vilarinho, and A. M. R. Senos. "Oxygen vacancies as a link between the grain growth and grain boundary conductivity anomalies in titanium-rich strontium titanate". J. Eur. Ceram. Soc., vol. 38, no. 6, pp. 2547–2552, 2018.

[21] P. Peng *et al.*. "Fabrication and electrical characteristics of flash-sintered SiO_2-doped ZnO–Bi_2O_3–MnO_2 varistors". J. Adv. Ceram., vol. 9, pp. 683–692, 2020.

[22] M. Schie, S. Menzel, J. Robertson, R. Waser, and R. A. De Souza. "Field-enhanced route to generating anti-Frenkel pairs in HfO_2". Phys. Rev. Mater., vol. 2, no. 3, pp. 35002-1-35002–8, Mar. 2018.

[23] M. Jongmanns, R. Raj, and D. E. Wolf. "Generation of Frenkel defects above the Debye temperature by proliferation of phonons near the Brillouin zone edge". New J. Phys., vol. 20, no. 093013, 2018.

[24] R. Serrazina *et al.*. "Induced internal stresses and their relation to FLASH sintering of KNN ceramics". *TO BE SUBMITTED, 2021.

[25] J. M. Lebrun *et al.*. "In-situ measurements of lattice expansion related to defect generation during flash sintering". J. Am. Ceram. Soc., vol. 100, no. 11, pp. 4965–4970, 2017.

[26] A. Karakuscu *et al.*. "Defect structure of flash-sintered strontium titanate". J. Am. Ceram. Soc., vol. 95, no. 8, pp. 2531–2536, 2012.

[27] M. Tyunina. "Oxygen Vacancies in Perovskite Oxide Piezoelectrics". Materials, vol. 13, no. 5596, pp. 1–11, 2020.

[28] A. West, J. Irvine, and D. Sinclair. "Electroceramics: Characterization by Impedance Spectroscopy". Adv. Mater., vol. 2, no. 3, pp. 132–138, 1990.

[29] A. Tkach and P. M. Vilarinho. “Nonstoichiometry Role on the Properties of Quantum-Paraelectric Ceramics” in Structure Processing Properties Relationships in Stoichiometric and Nonstoichiometric Oxides, IntechOpen, 2019, pp. 1–14.

[30] A. Peláiz-Barranco, J. D. S. Guerra, R. López-Noda, and E. B. Araújo. “Ionized oxygen vacancy-related electrical conductivity in $(Pb_{1-x}La_x)(Zr_{0.90}Ti_{0.10})_{1-x/4}O_3$ ceramics”. J. Phys. D Appl. Phys. Phys., vol. 41, no 215503, 2008.

[31] O. Raymond, R. Font, N. Suárez-Almodovar, J. Portelles, and J. M. Siqueiros. “Frequency-temperature response of $Pb(Fe_{1/2}Nb_{1/2})O_3$ ferroelectromagnetic ceramics obtained by different precursors. Part I: Structural and thermo-electrical characterization”. J. Appl. Phys., vol. 97, no. 084107, 2005.

[32] M. A. Rafiq, M. E. Costa, A. Tkach, and P. M. Vilarinho. “Impedance analysis and conduction mechanisms of lead free potassium sodium niobate (KNN) single crystals and polycrystals: A comparison study”. Cryst. Growth Des., vol. 15, no. 3, pp. 1289–1294, 2015.

[33] E. Gil-González, A. Perejón, P. E. Sánchez-Jiménez, R. Raj, and L. A. Pérez-Maqueda. “Processing and properties of $Bi_{0.98}R_{0.02}FeO_3$ (R = La, Sm, Y) ceramics flash sintered at ~650°C in less than 5s”. J. Am. Ceram. Soc., vol. 103, no. 1 (Jan20), pp. 136–144, 2019.

[34] E. Taghaddos, H. Charalambous, T. Tsakalakos, and A. Safari. “Electromechanical properties of flash sintered BNT-based piezoelectric ceramic”. J. Eur. Ceram. Soc., vol. 39, no. 9, pp. 2882–2888, 2019.

[35] J. Xia, K. Ren, and Y. Wang. “One-second flash joining of zirconia ceramic by an electric field at low temperatures”. Scr. Mater., vol. 165, pp. 34–38, 2019.

7.3. Preliminary results: TEM study on as-FLASH sintered KNN ceramics

To be submitted

Preliminary transmission electron microscopy analysis on FLASH sintered ceramics (900 ºC, 30 min, 300 V/cm, 20 mA/mm^2, 60 s) are shown in Figure 7.3-1 to Figure 7.3-3. Electron transparent lamellae of as-FLASH sintered KNN ceramics were prepared using the *FEI-Helios* Dual Beam System equipped with an *Omniprobe* nanomanipulator. Transmission Electron Microscopy (TEM) bright field, high resolution and diffraction analysis were carried out using a *FEI* probe corrected *TITAN* microscope.

Figure 7.3-1 a) shows the High Resolution TEM (HRTEM) micrographs of as-FLASH sintered KNN ceramic. The periodicities observed for that orientation ($[\bar{1}00]$ zone axis) match well with that of the orthorhombic KNN crystal structure (superimposed). Additionally, Figure 7.3-1 b) reveals a diffraction pattern under the same zone axis, which is suitable with the A*mm2* orthorhombic structure of KNN. Thus, Figure 7.3-1 is in accordance with our previously reported X-Ray Diffraction (XRD) data [1], [2], revealing the orthorhombic structure in as-sintered FLASH KNN.

Furthermore, Figure 7.3-2 shows the bright field TEM micrograph of a representative as-FLASH sintered KNN grain structure, with multiple arrays of planar domain structures are visible within a single grain. The magnification in b) shows the appearance of fishbone-like and parallel arrays of domains. The first are rotated by 90º between each other, while the parallel ones are 180º apart. The length and width of the ferroelectric domains was estimated using several TEM micrographs, and average values of 240 and 28 nm, respectively, were found. While the shape of the identified domains agrees well with those previously reported for KNN [3], their dimensions are at least 20 times smaller.

The presence of ferroelectric domains in as-FLASH sintered KNN allows to undoubtedly access the ferroelectric nature to these ceramics. However, the presence of defects as oxygen vacancies can clamp the domains, limit their switching and size [4]. This explains the observations in [5], with high dielectric losses and low polarization being observed in as-FLASH sintered KNN.

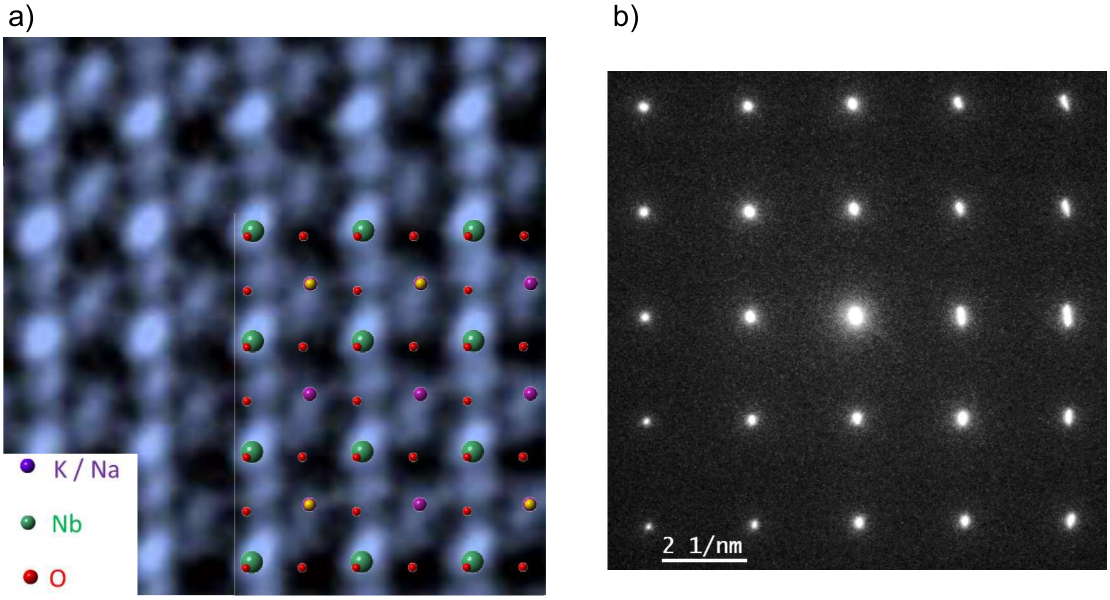

Figure 7.3-1 – a) High magnification HRTEM micrograph shown along $[\bar{1}00]$ zone axis with the superimposed model of the orthorhombic crystal structure (K/Na in purple, Nb in green and Oxygen in red) and b) diffraction pattern along the same zone axis, suitable with the orthorhombic structure.

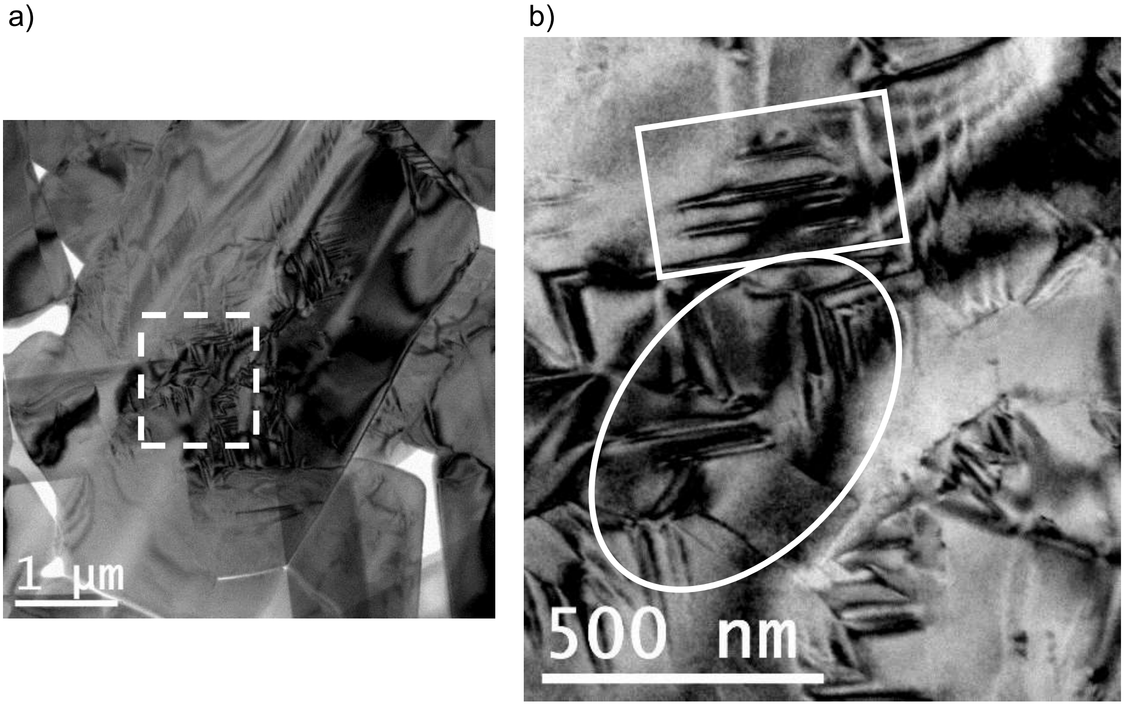

Figure 7.3-2 – a) Bright Field TEM micrograph of FLASH sintered KNN showing an array of planar ferroelectric domain like features. A magnification is provided in b) in which fishbone-like (90° rotation - circle) and parallel (180° rotation – square) ferroelectric domains are revealed.

Related with the defective nature of as-FLASH sintered KNN, Figure 7.3-3 presents the TEM analysis of a grain boundary region of these ceramics. The presence of an amorphized grain boundary (GB) in between two orthorhombic KNN grains (proven by the Fast Fourier Transform, FFT, insets) is revealed in Figure 7.3-3 a). Furthermore, the HRTEM micrograph on Figure 7.3-3 b) suggest that this grain boundary has about 5 nm width. As a comparison, a grain boundary-localized secondary phase in barium titanate is reported to have a width of ~0.8 nm [6].

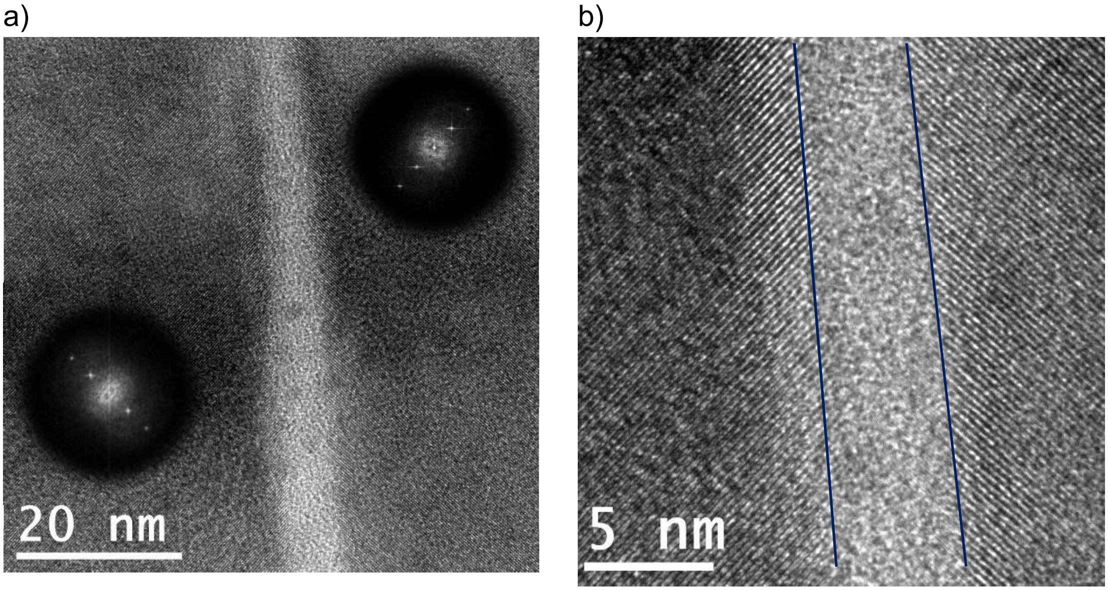

Figure 7.3-3 – High resolution TEM (HRTEM) micrograph of FLASH sintered KNN ceramic showing a) low magnification showing grain boundary region with the respective FFT insets indicating the presence of crystalline grains away from the boundary on either side and b) magnified view of the boundary showing an amorphous boundary between the crystalline grains with roughly 5 nm thickness (blue superimposed lines).

In fact, the observation of amorphized GBs in FLASH sintered KNN was previously reported by us [7]. However, in such study, it would be arguable if the presence of the amorphized grain boundary could result from the high current density during FLASH (60 mA/mm^2) or the presence of water in the sintering atmosphere. In the present work, no water was used or current channelling occurred for I.C. FLASH conditions (air atmosphere and 20 mA/mm^2 current limit) [1]. Nonetheless, the presence of amorphized grain boundaries is still possible to be identified by TEM (Figure 7.3-3) in such uniformly sintered FLASH sintered ceramics [1]. It must be referred that these were not found in all the grain contacts, though, they were consistently present in FLASH sintered ceramics and totally absent in conventionally sintered KNN. The presence of FLASH sintering-induced amorphized grain boundaries may represent a greater defect concentration in such area.

Our results give indications that low thermal budget as-sintered FLASH KNN ceramics should not be used for ferroelectric applications, despite that their intrinsic ferroelectric features are identified. The presence of amorphized grain boundaries with high concentration in defects as oxygen vacancies do not allow the macroscopic demonstration of the ferroelectric behaviour. A post-sintering heat treatment is needed for defects relaxation of FLASH sintered KNN. The engineering of the FLASH sintering process might allow this relaxation process to occur during the cooling regime from the FLASH *activated* stage (stage III), with a controlled current decrease, for instance.

References

[1] R. Serrazina, A. M. O. R. Senos, L. Pereira, J. S. Dean, I. M. Reaney, and P. M. Vilarinho. “The Role of Particle Contact in Densification of FLASH Sintered Potassium Sodium Niobate”. Eur. J. Inorg. Chem., vol. 2020, no. 39, pp. 3720–3728, 2020.

[2] R. Serrazina, A. Tkach, L. Pereira, A. M. O. R. Senos, and P. M. Vilarinho, “FLASH sintered potassium sodium niobate: high performance piezoelectrics at low thermal budget processing,” *SUBMITTED*, 2021.

[3] R. López-Juárez, O. Novelo-Peralta, F. González-García, F. Rubio-Marcos, and M. E. Villafuerte-Castrejón. “Ferroelectric domain structure of lead-free potassium-sodium niobate ceramics”. J. Eur. Ceram. Soc., vol. 31, no. 9, pp. 1861–1864, 2011.

[4] F. Hussain, I. Sterianou, A. Khesro, D. C. Sinclair, and I. M. Reaney. “p-Type/n-type behaviour and functional properties of $K_xNa_{(1-x)}NbO_3$ ($0.49 \leq x \leq 0.51$) sintered in air and N_2”. J. Eur. Ceram. Soc., vol. 38, no. 9, pp. 3118–3126, 2018.

[5] R. Serrazina, A. Tkach, L. Pereira, A. M. O. R. Senos, and P. M. Vilarinho, “Behind the electrical performance of FLASH sintered Potassium Sodium Niobate,” TO BE SUBMITTED, 2021.

[6] S. B. Lee, W. Sigle, and M. Rühle. “Investigation of grain boundaries in abnormal grain growth structure of TiO_2-excess $BaTiO_3$ by TEM and EELS analysis”. Acta Mater., vol. 50, pp. 2151–2162, May 2002.

[7] R. Serrazina, J. S. Dean, I. M. Reaney, L. Pereira, P. M. Vilarinho, and A. M. O. R. Senos. “Mechanism of densification in low-temperature FLASH sintered lead free Potassium Sodium Niobate (KNN) piezoelectrics”. J. Mater. Chem. C, vol. 7, pp. 14334–14341, 2019.

Summary

In this chapter, the dielectric and ferroelectric performance of KNN ceramics produced by FLASH and conventional sintering was presented. The use of platinum electrodes to assess that performance implies a heat treatment at 900 ºC for 1 h. Ceramics with such heat treatment revealed a very similar behaviour, regardless of the sintering process. Namely, ε_r at T_C of ca. 6000 and tanδ < 10%, with P_r = 21 μC/cm^2 and E_c = 10 kV/cm, and a piezoelectric coefficient of 115 to 117 pC/N were achieved.

However, it was established that such performance was not possible in as-FLASH sintered KNN. In fact, the heat treatment was found to be related with the ceramics' defect relaxation, most probably, oxygen vacancies. The presence of amorphized grain boundaries in as-FLASH sintered KNN ceramics, which were proposed to contain a high concentration of these defects, are a consequence of the FLASH sintering process. Fingerprints of FLASH sintering were revealed even in heat-treated ceramics. Impedance spectroscopy and DC conductivity analysis showed a lower activation energy for conduction in FLASHed KNN as compared with conventionally sintered ceramics. Nonetheless, the transition temperature of FLASH sintered KNN was kept $\approx$10 ºC higher than that of conventional for both as-sintered and heat treated KNN ceramics.

Our results present a direct link between ferroelectric properties and alternative sintering of piezoelectric ceramics. The production of high transition temperature, single phase, KNN ceramics is possible by FLASH sintering. However, their as-sintered ferroelectric behaviour is not satisfactory. A post-sintering heat treatment is needed for relaxation.

Chapter

8. Final remarks and conclusions

Contents

Preamble

To finish this work, the last chapter is divided into three sections. A glimpse into the possible contribution of FLASH sintering for the sustainable development of ceramic industry is given in 8.1. Following, a final remarks section is given (8.2), with the personal view on the prospects of FLASH sintering and related technologies. A summary of the ongoing and future studies related with this work is also given. To finalize, the main conclusions of this work are listed (section 8.3). A direct link with the proposed goals was established, showing that the specific objectives of the work were accomplished, and giving a small description on the main results.

It does not go without referring that this work would not be possible without the numerous collaborations that were established over the course of 4 years. From *in-house* scientific discussions, partnerships and critical thinking, to abroad visits, multiple conference presentations and discussions with professors, researchers, master students, technical staff (from academia and industry) all were essential and relevant.

8.1. A glimpse into energy savings

Published in Revista TÉCNICA #3, 2020 - https://issuu.com/ctcv/docs/tecnica-julho-vs4_final

Abstract

The ceramic industry sector is one of the main carbon dioxide (CO_2) emitters, which is due to the need for high sintering temperature, usually well above 1000 ºC. Recent European guidelines, that were materialized in the European Green Deal, indicate that this continent should be carbon emission neutral by 2050. To achieve that, the ceramic industry and its processing methods must be reinvented.

Here presented is a very simplistic, however relevant, industrial study on the energetic consumption of two sintering process for the densification of porcelain-based tiles. Based on the industrial conventional cycle, that occurs at ca. 1200 ºC in a gas furnace, a FLASH sintering cycle is proposed, in which electric power is directly applied into the ceramic to be densified, with a decrease in operating temperature and cycle time.

Although the advantages associated with the energy savings of FLASH sintering process are advocated by many studies in the topic, this is the first time that a practical/industrial comparative study is presented. This work was developed under the scope of *REVIDRY* project (POCI-01-0247-FEDER-017784), with the collaboration of a multidisciplinary team from academia (University of Aveiro), industry (Revigrés) and a technological centre (CTCV). The work was published in Revista TÉCNICA #3 (maio/junho), 2020 - https://issuu.com/ctcv/docs/tecnica-julho-vs4_final.

8.1.1. Introduction

At the European level, the ceramic industry is responsible for more than 200k jobs, with an annual production of 28 billion euros. With the goal of improving its energetic and environmental performance, there has been efforts in continuous technological developments [1]. However, the improvements that were achieved are still far from the environmental goals of the European Green Deal. The main objective of that compromise is to make Europe carbon neutral by 2050 [2]. *Cerame-Unie* also refers that "(…) a supportive regulatory framework to facilitate development and investment in breakthrough technologies, to promote European competitiveness based on sustainable economic growth and to reduce the risk of carbon and job leakage" is needed [1].

Several sources refer that approximately 60% of the total energy needed to produce a ceramic part is spent in the drying and sintering processes [3]. Therefore, for the sustainable development of the ceramic industry, alternative sintering technologies are demanded.

FLASH sintering was initially reported to densify graphite powders, in 1957 [4]. Recently (2010), R. Raj presented the technology as being able to densify nanometric yttria stabilized zirconia (YSZ) powders at 850 ºC for a few seconds [5]. The scientific interest was deployed, and more than 70 papers were published in the topic during 2019.

The FLASH sintering technology (…) [6]-[8][3].

Associated with the FLASH sintering process there is the need to add electric powder directly to the material to be sintered, on top of the thermal energy needed to reach the FLASH temperature (T_F). However, the total densification occurs in a few seconds, which associated to the decrease in the operating furnace temperature should present a significant decrease in the energy consumption and CO_2 emissions. However, there are still practical limitation in terms of equipment and facilities to perform FLASH sintering at an industrial level, especially in liquid-phase containing systems as porcelain-based products. Nonetheless, the evaluation of energy efficiency and productivity increase with FLASH sintering in comparison with conventional processes is relevant. This study approaches the thematic in the industrial context of porcelain-based tiles production.

8.1.2. Results

Spray dried porcelain-based powders from Revigrés were used in this study. These powders were uniaxially pressed at 45 MPa, for 30 s, into parallelepipedal compacts with ca. 15 x 5 x 2 mm^3. To establish the conditions for the FLASH sintering, two platinum electrodes were placed in the opposite faces of the compacts, and a heating step performed in an adapted dilatometer (the same as described in section 2.2). Following previously published works in the FLASH of porcelain-based materials [9], [10], a 500 V/cm electric field was applied, and the compacts heated at a constant rate of 10 ºC/min. FLASH sintering occurred at T_F ~1000 ºC and the current density was limited, at that stage, to 2 mA/mm^2, for 30 s. Final densities of ca. 90% were obtained, and the research on the topic is still ongoing to increase this property to the industrially applicable level (94 – 95%, corresponding to 0.5% water absorption [11]). Considering these FLASH conditions, the comparative analysis of energetic consumption was performed.

---

[3] Consult original text for full description of FLASH sintering

The comparison was achieved by acquiring the sintering data of 60x60 cm^2 tiles at Revigrés (gas furnace, SACMI, type FMS 223/126). The data is shown in Figure 8.1-1 a) by the red curve. The sintering cycle has a total time of ~1 h, with a starting heating rate of 130 ºC/min to 900 ºC. At such temperature (position in the furnace), the gas burning is started, and the heating rate reduced to 40 ºC/min, to the dwelling temperature of ~1200 ºC, kept for 15 min. The cooling is initiated (250 ºC/min) to 600 ºC, and then slowly to room temperature (15 ºC/min). The heating to 900 ºC and the cooling steps are essentially achieved by the recirculation of hot air from the hot zone of the furnace and its mixture with cold air.

To estimate the energetic consumption of the conventional sintering (Figure 8.1-1 a)) and facing the impossibility of measuring the consumption of each burner individually, the total gas consumption was determined and normalized by the square meters of produced tiles. To estimate the gas consumption through the heating cycle, a linear variation with the temperature was considered. This results in an excess estimation for low temperatures. Figure 8.1-1 b) gives this cumulative estimated gas consumption as a function of the temperature – red curve. It is started at 900 ºC and reaches a maximum value of 15 kWh/m^2 at the end of the isothermal step.

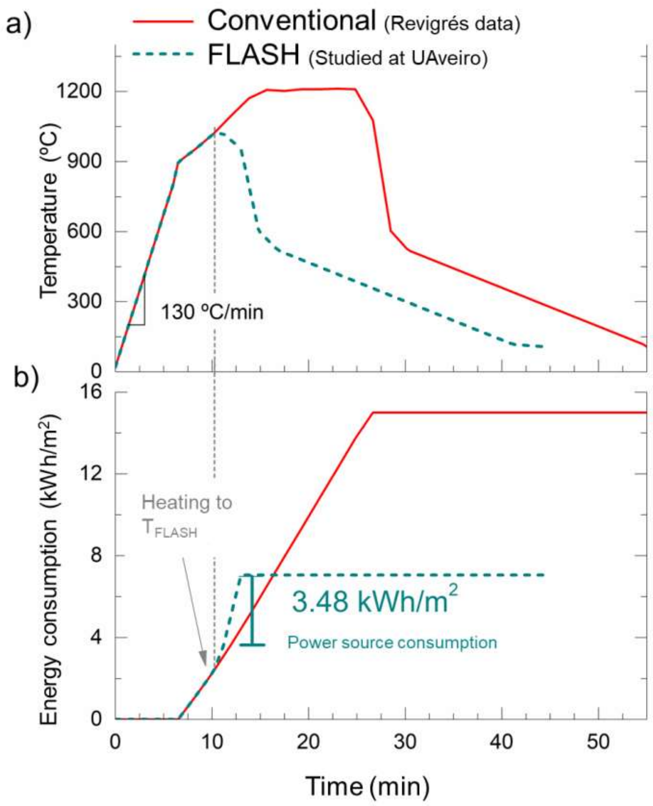

Figure 8.1-1 – a) Thermal cycle (temperature as a function of time) for the conventional sintering (red) of a 60x60 cm^2 tile in Revigrés and respective FLASH sintering step (blue) with maximum temperature of 1000 ºC. b) respective furnace energy consumption, in kWh/m^2, of conventional (red) and FLASH (blue) sintering steps.

For the FLASH sintering cycle, a similar heating profile to the conventional cycle was considered in Figure 8.1-1 a), blue curve, until the T_F ~ 1000 ºC was reached. At such temperature, the heating was hold and the electric field and respective current applied for 30 s. By establishing the furnace temperature at 1000 ºC for 30 s, the energetic consumption was estimated to be 3.57 kWh/m^2. At this FLASH conditions, the power consumption needed for the FLASH was estimated (P = V x I) and normalized in 3.48 kWh/m^2. Therefore, the total cycle consumption was given: ~7.1 kWh/m^2 – Figure 8.1-1 b).

Table 8.1-1 summarizes the estimated cycle time, production cadence (parts per hour) and energy consumption for the two sintering processes under study. The respective percent variation is also calculated. Together with the analysis of Figure 8.1-1, it is possible to show that the replacement of the conventional thermal cycle by a FLASH sintering one (at 1000 ºC) would result in a cycle time reduction of 19%, an increase in productivity of 25% and a decrease in the energy consumption superior to 50%.

Table 8.1-1 – Cycle time variation, productivity, and energetic consumption estimation for the replacement of a conventional sintering process by a FLASH sintering one (production of 60x60 cm^2 tiles). Δ = percent variation

	Conventional	FLASH	Δ (%)
Cycle time (min)	55	**44.5**	↓ **19**
Productivity (parts/h)	680	**852**	↑ **25**
Energy consumption (kWh/m^2)	15	**7.1**	↓ **53**

8.1.3. Conclusion

The environmental urgency demands the development and implementation of alternative techniques in the ceramic industry. The decarbonization of such industrial sector is essential, as it is one of the world's most polluting in what concerns the emissions of CO and CO_2. This study shows that the replacement of a conventional sintering process by a new sintering technology, based on the electric power input into the compacts, FLASH sintering, could allow a 50% energy saving.

Although, the research and development on the topic are still ongoing for the correct implementation of the technique in the industry, this study gives a glimpse on the strategic interest of investing on FLASH sintering. Not only the sustainability of the tile industry would be improved, as the production rate increased. Despite this study is limited to the tile industry, similar results were obtained for a similar study performed in Alumina-based products, from Rauschert Portuguesa, sintered in discontinuous inductive furnaces.

8.1.4. References

[1] The European Ceramic Industry Association - Cerame-Unie, "Paving the Way to 2050: the Ceramic Industry Road Map," 2012. Online (http://cerameunie.eu/topics/cerame-unie-sectors/cerame-unie/ceramic-industry-roadmap-paving-the-way-to-2050/)

[2] E. Commission, "European Green Deal-Roadmap and key actions | European Commission," 2019.

[3] T. Ibn-Mohammed *et al.*. "Decarbonising ceramic manufacturing: A techno-economic analysis of energy efficient sintering technologies in the functional materials sector," J. Eur. Ceram. Soc., vol. 39, no. 16, pp. 5213–5235, 2019.

[4] F. A. Lewis, J. Orr, and A. R. Ubbelohde, "Contact Effects resulting from Compression and Flash Sintering in Graphite Powders," Proc. Phys. Soc. Sect. B, vol. 70, no. 10, pp. 928–936, Oct. 1957.

[5] M. Cologna, B. Rashkova, and R. Raj, "Flash Sintering of Nanograin Zirconia in <5 s at 850°C," J. Am. Ceram. Soc., vol. 93, no. 11, pp. 3556–3559, Nov. 2010.

[6] R. Serrazina, J. S. Dean, I. M. Reaney, L. Pereira, P. M. Vilarinho, and A. M. O. R.

Senos, “Mechanism of densification in low-temperature FLASH sintered lead free Potassium Sodium Niobate (KNN) piezoelectrics,” J. Mater. Chem. C, vol. 7, pp. 14334–14341, 2019.
[7] M. Biesuz and V. M. Sglavo, “Flash sintering of ceramics,” J. Eur. Ceram. Soc., vol. 39, no. 2–3, pp. 115–143, 2019.
[8] J. Nie, Y. Zhang, J. M. Chan, R. Huang, and J. Luo, “Water-assisted flash sintering: Flashing ZnO at room temperature to achieve ~ 98% density in seconds,” Scr. Mater., vol. 142, pp. 79–82, 2018.
[9] M. Biesuz, W. D. Abate, and V. M. Sglavo, “Porcelain stoneware consolidation by flash sintering,” J. Am. Ceram. Soc., vol. 101, no. 1, pp. 71–81, 2018.
[10] F. Trombin and R. Raj, “Developing processing maps for implementing flash sintering into manufacture of whiteware ceramics,” Am. Ceram. Soc. Bull., vol. 93, no. 6, pp. 32–35, 2014.
[11] L. F. S. Figueiredo, “Sinterização FLASH como tecnologia alternativa de sinterização do grés porcelânico,” University of Aveiro, 2019.

8.2. Final remarks

It is undoubtedly clear that there is still research and development work to be performed around the FLASH sintering technology. New trends as current rate [1]–[3], reactive FLASH sintering (RFS) [4]–[9], or FLASH joining [10]–[13] are prone to take the electric field and current-based alternative processing routes to the industrial application level soon. Nonetheless, scientific challenges and reported disparities demand a consideration on prospects (section 8.2.1) and work to be developed in the future (8.2.2).

8.2.1. Prospects on FLASH and alternative sintering

“In order to meet such challenges [reduction of environmental impact, densification of metastable phases…], new sintering routes employing electric fields/currents, water/ solvents and external loads have been developed. The research also opened new questions about unexpected (and still not completely understood) interactions between electricity, presence of water/liquid, heating and diffusion processes”

M. Biesuz, S. Grasso and, V. M. Sglavo, 2020. [14]

“Many open scientific questions remain about the fundamental mechanisms underlying such interactions of external fields with matter”

B. Reeja-Jayan and J. Luo, 2021. [15].

“Electric current-assisted sintering (ECAS) techniques are promising to overcome these restrictions [high sintering temperatures (…) inherent risk of abnormal grain growth, evaporation, chemical reaction, or decomposition…] but a lot of fundamental and practical challenges must be solved properly to take full advantage of these techniques”

O. Guillon *et al.*, 2020. [16].

These quotes, from very recently published papers, summarize both the relevance and importance of field- and current-assisted sintering techniques (as FLASH) as the remaining challenges in depicting their fundamental operating mechanisms.

A short summary of the experimentally most relevant topics for the development of FLASH sintering techniques is now given; a personal experience meaning is, of course, adjacent to this analysis. Please bear in mind that, in this work, the FLASH sintering technology was studied for a specific material (KNN), however, a few parallel studies were performed in other materials, namely, in zinc oxide [17], alumina-based [18] and porcelain-based [19], and the following topics also take that into account.

Sample size and shape

The sample size and shape is a sensitive matter in what concerns ECAS and FLASH. It is advocated that FLASH sintering presents a simpler operating apparatus than, for instance, SPS, indirectly allowing the production of complex shapes. This limitation of SPS [14] and supposed advantage of FLASH sintering is then tackled with specimen shape/size dependent results. As pointed out by Campos *et al.*, [20] the FLASH sintering process is dependent on the sample size, even if a constant electric field is employed through the calculation of the normalized electric potential; in their study, a relatively small size variation was considered (2 to 10 mm in height) however, significant microstructural and densification differences were already identified.

The use of different specimen shapes and sizes at the scientific level does not contribute for the clear understanding of the operating mechanisms during the FLASH sintering of different materials. An example regarding shape: the use of dog-bone shaped compacts allows to study the FLASH process using a very simple apparatus [1]; as long as the furnace permits the sample observation, studies on specimen displacement can be performed even with a camera; radiation and photoemission [21] studies are also simply done. On the other hand, the final densities reported for this type of sample shape are not complete accurate, as the electrodes areas (end-sides of the *bone*) are not considered for analysis, whereas when using cylindrical or parallelepipedal samples, the entire ceramic is considered for characterization. To finalize, an example regarding the sample size: the use of thin cylindrical compacts (1 or 2 mm) faces similar limitations. A sample with such a small thickness should not allow the evolution of a FLASH process similar to that of a 10 or 100 mm thick compact. It can be argued that the entire sample length of a 2 mm thick disk corresponds to the “electrode area” of a 10 mm thick one.

Until a clear explanation on the effect of electric field and current density as respect to specimen dimensions is known, the FLASH sintering studies should be performed in standard specimens. Due to the limitations and lack of industrial viability, dog-bone shaped compacts should be avoided. This was a major reason for the use of parallelepipedal shaped compacts in this work.

A material-dependent process?

As firstly pointed out by M. Reece and co-workers [22], and discussed in detail in section 1.2.1, Figure 1-5, there is a very narrow gap of power dissipation, as a function of temperature, correspondent to the FLASH sintering incubation – transition from stage I to stage II. In fact, the data obtained for KNN FLASH sintering follow the same tendency, as shown in Figure 8.2-1. Because the complete explanation for such observation was not achieved yet, several interpretations were proposed [23], [24].

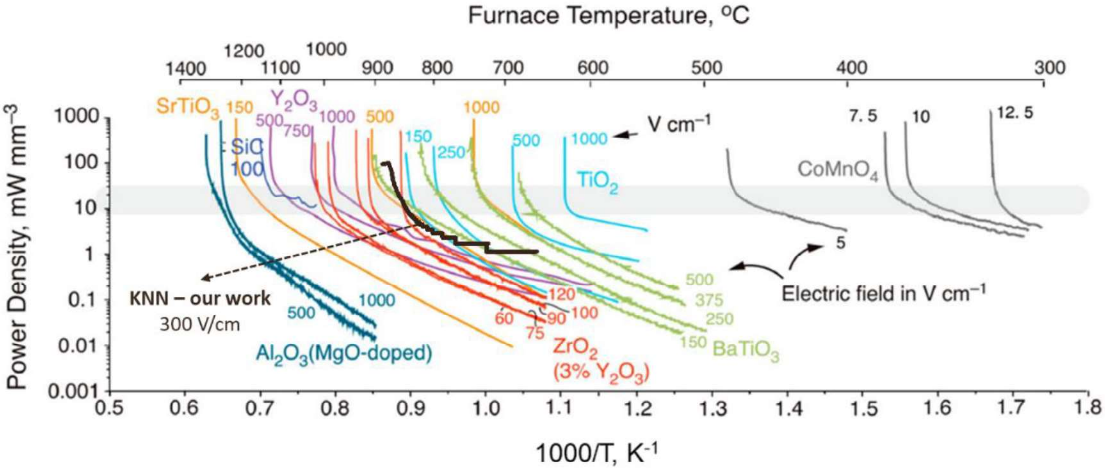

Figure 8.2-1 - Arrhenius representation of power dissipation during FLASH sintering of ceramics at different nominal electric field and constant heating rate of 10 ºC/min). Adapted from [22].

R. Chaim argues that most of the FLASH sintering-related phenomena are explained by the formation of localized liquid phases at particle contacts that spread at a very fast rate and allow particle to slide, promoting extremely fast densification. Examples of studied phenomena are, the narrow power band transition [23], the reactive FLASH sintering (RFS) process [7], the fast densification [25], the relationship with Debye temperature [26], among others. On the other hand, advocated by R. Raj, the Frenkel defect-based theories [24], [27]–[29] make use of localized high-electric fields at particle contacts to explain the formation of Frenkel pairs, responsible by the very fast rates of densification and atomic diffusion (especially important to explain the RFS observations).

In the specific case of KNN, the results presented in chapter 4 and 5 surely suggest that the partial melting of particle contacts develop a significant role to the FLASH sintering of this material. The kinetic studies reveal a faster process in FLASH as compared with conventional sintering, however, it is difficult to depict what is the precise mechanism –

liquid phase- or Frenkel-based [30]. On the other hand, the observed amorphous grain boundaries in dense ceramics sintered by FLASH strongly suggest a liquid-phase assisted sintering process, with particle sliding and rearrangement for surface energy minimization. In parallel, fine particles are dissolved into the liquid phase and reprecipitate in the solid ones, explaining the grain growth [31]–[34]. Nonetheless, our simulations [35], [36] undoubtedly show that heating by Joule effect has a significant role, however, it cannot account nor explain all the observations.

Following our statements, other works [37], [38] show that the FLASH sintering process is material dependent. The final density, microstructure and conduction processes suggest so. Ferroelectrics (as KNN), oxygen conductors (YSZ), semi-conductors (ZnO) or dielectrics (Al_2O_3) will develop dissimilar FLASH sintering processes. An example: YSZ single crystals show a FLASH-like process at lower T_F than powder compacts [39]; however, the opposite occurs for ZnO [40] and KNN [31]. On the other hand, ZnO can be FLASH sintered to very high density at room temperature by using reducing-humidified atmospheres [41]; the same is not observed for KNN [42].

Despite that the power dissipation tendency (Figure 8.2-1) suggest an overall mechanism to occur [22], the evolution of the FLASH sintering process is proven to be material dependent. Phases' composition and impurities, particle size, thermal stability, electrical behaviour (mechanisms of conduction), among many other parameters must be considered when *designing* or engineering a FLASH sintering process.

FLASH sintering at room temperature

The use of atmospheres to decrease T_F down to room temperature was proven to be efficient in ZnO [41], however, not successful in KNN, where T_F was only decreased to 265 ºC and limited densification was observed [42]. A different approach was preliminarily studied though, not sufficiently explored to be presented in the current work. In these preliminary studies, different amounts of graphite, with a lamella-like shape and mean particle size of 5 μm, were mixed with 99.9% BM+AM KNN powders. The results shown very promising trends: (i) the FLASH sintering of KNN occurs when the graphite content is larger than 3 wt%; (ii) the heat generated from the decomposition of the graphite in air is enough to promote the partial sintering of KNN particles; (iii) non uniformly dense ceramics were produced, with melted areas and significant grain growth (not statistically evaluated), suggesting severe melting.

These preliminary results deployed the development of other works, namely, at the master's degree level. Alumina was FLASH sintered at room temperature to 85% of theoretical density, using a similar approach [18]. Similar limitations were found in terms of uniformity of density however, the relevance of such achievement is obvious: an increase in overall density from ~60% to 85%, without the use of any *external* heating. Similar works on this topic have been presented [43]–[45] however, not for alumina or KNN. The use of secondary conductive phase that can degrade during the sintering process seems a promising tendency to pursuit for the room temperature sintering of several oxides.

Industrial applications

The industrial application of FLASH sintering is still limited by the unknown mechanisms and uncontrolled processes, among others more technological issues. In addition, the precise discussion of an economic and environmental life cycle analysis on the replacement of conventional sintering processes by FLASH sintering is still not available. Some efforts have been made on the topic [46] however, the fact that the processes are material dependent does not facilitate this transition.

The collaboration with Portuguese ceramic industries revealed that the FLASH sintering of porcelain-based materials is quite complex [19]. The presence of low-melting point feldspars promotes the formation of non-uniformly distributed liquid phases in the presence of an electric field. Moreover, the dissimilar electrical behaviour of the different constituents on such a complex composition (alumina, silica, alkali-based oxides, metal ions, etc.) complicates the engineering of the FLASH sintering process.

For an effective industrial transition of alternative processes as FLASH sintering, SPS, Cold sintering or others, not only the process need to be well known and controlled as, at that point, the materials need to be adapted. In the case of traditional ceramic industry, as porcelain-based products, the currently used compositions have been improved for centuries to be sintered in gas-furnaces. The use of disruptive alternative sintering techniques, though very challenging, is also very promising, however, not applicable without materials' engineering.

8.2.2. Future work

After establishing some of the challenges to come for the further scientific knowledge and development of FLASH sintering, a group of suggestions for future work is now presented.

From the scientific side, there is still a lot to be studied on the topic. The *in-situ* study of FLASH sintering has been and will continue to be essential for the understanding of the processes. One of the propositions to pursuit with these studies is related with the *in-situ* TEM observation of particles subjected to electric field and/or temperature. Several limitations have been encountered pursuing this goal, as the sample preparation, the electrode material (that can diffuse immediately after the application of the electric field on a TEM observation chip), or the limitation of electric field and current. In addition, it is not trivial to extrapolate the observations in a few isolated particles (in a TEM) to a bulk compact with millions of particles.

Rather than *in-situ* studies, the study of sintered ceramics properties allows an indirect access to the sintering process evolution. Still ongoing is the microstructural analysis of FLASH sintered KNN ceramics. The study of the grain texture (preferential orientation) of FLASH and conventionally sintered KNN is being performed by EBSD and will give new insights on the sintering process.

From the application point of view, and because KNN is a ferroelectric material, the atomic force and piezo force microscopy (AFM/PFM) will be used to evaluate the possible differences in the domain structure of FLASH sintered KNN as compared with conventional ceramics. In addition, if nanometric resolution is possible, the localized amorphous grain boundaries in FLASH ceramics should be possible to characterize by AFM.

Furthermore, the mechanical properties of FLASH sintered materials should be assessed. This was one of the goals proposed in the PhD work plan, however, it was not accomplished due to the need to study the role of atmospheres for the decrease of T_F (not predicted in the initial work plan). Now it is clear that the mechanical properties should be affected by the FLASH process, as reports on the topic are being published for other materials [47]–[49]. Furthermore, our work reveals FLASH sintering induced local stresses in KNN (section 3.2), which can affect its mechanical behaviour.

The search for extremely low temperature sintering processes demands the pursuit of the preliminary results on KNN-graphite FLASH sintering. Graphite or other conductive second phase should be used to trigger conduction and heating by Joule effect at room temperature. The FLASH process should be controlled (current limit) as the second phase is degraded due to heating by Joule effect, which allows the densification of the KNN primary particles. Experimental strategies on materials processing (composite preparation, dispersion and size of the conductive phase) and FLASH sintering process (operating atmosphere, electric field and current, external pressure, degradation process, etc) should be studied. Additionally, the FLASH sintering of films must be (and currently is) developed; work on room temperature FLASH of ZnO thick films in flexible substrates is being currently developed.

The effects of dopants for the FLASH sintering of perovskite materials should be further studied. This work was focused on un-doped KNN, however, doping is known to change the sintering behaviour and ferroelectric performance of KNN-based materials [50], [51]. Therefore, doping must be studied and the dopant effects on T_F, sintering evolution, final density and ferroelectric properties of sintered ceramics assessed.

Finally, with an industrial point of view, the simulation of electric field and current distribution in complex shaped compacts must be studied. A comprehensive study on the distribution of electric power when FLASH sintering a simple or complex shaped compact is surely different. In a complex-shaped body, smaller section areas will face higher current density and power dissipation. The materials and parts design must be adapted to that reality. A concept of *design for construction* should be employed. Simulation studies can trigger the interest and predict some effects, while successive experimentation is needed for validation.

8.2.3. References

[1] M. Biesuz and V. M. Sglavo. “Flash sintering of ceramics”. J. Eur. Ceram. Soc., vol. 39, no. 2–3, pp. 115–143, 2019.

[2] M. K. Punith Kumar, D. Yadav, J. M. Lebrun, and R. Raj. “Flash sintering with current rate: A different approach”. J. Am. Ceram. Soc., vol. 102, no. 2, pp. 1–13, 2018.

[3] H. Charalambous, S. K. Jha, K. H. Christian, R. T. Lay, and T. Tsakalakos. “Flash Sintering using Controlled Current Ramp”. J. Eur. Ceram. Soc., vol. 38, no. 10, pp. 3689–3693, Aug. 2018.

[4] B. Yoon, D. Yadav, S. Ghose, and R. Raj. “Reactive flash sintering: MgO and α-Al_2O_3 transform and sinter into single-phase polycrystals of $MgAl_2O_4$”. J. Am. Ceram. Soc., vol. 102, no. 5, pp. 2294–2303, 2019.

[5] S. E. Murray, T. J. Jensen, S. S. Sulekar, Y. Y. Lin, N. H. Perry, and D. P. Shoemaker. “Propagation of the contact-driven reduction of Mn_2O_3 during reactive flash sintering”. J. Am. Ceram. Soc., no. March, pp. 7210–7216, 2019.

[6] R. Chaim and Y. Amouyal. “Liquid-Film Assisted Mechanism of Reactive Flash Sintering in Oxide Systems”. Materials, vol. 12, no. 1494, pp. 1–9, 2019.

[7] R. Chaim. “Reactive flash sintering (RFS) in oxide systems: kinetics and thermodynamics”. J. Mater. Sci., 2020.

[8] B. Yoon, D. Yadav, S. Ghose, P. Sarin, and R. Raj. “On the synchronicity of flash sintering and phase transformation”. J. Am. Ceram. Soc., vol. 102, no. 6, pp. 3110–3116, 2019.

[9] V. Avila and R. Raj. “Reactive flash sintering of powders of four constituents into a single phase of a complex oxide in a few seconds below 700°C”. J. Am. Ceram. Soc., no. January, pp. 6443–6448, 2019.

[10] J. Xia, K. Ren, and Y. Wang. “One-second flash joining of zirconia ceramic by an electric field at low temperatures”. Scr. Mater., vol. 165, pp. 34–38, 2019.

[11] M. Biesuz and V. M. Sglavo. “Beyond flash sintering: How the flash event could change ceramics and glass processing”. Scr. Mater., vol. 187, pp. 49–56, 2020.

[12] J. Xia, K. Ren, Y. Wang, and L. An. “Reversible flash-bonding of zirconia and nickel alloys”. Scr. Mater., vol. 153, pp. 31–34, 2018.

[13] M. Biesuz *et al.*. “Interfacial reaction between ZrNbHfTa foil and graphite: Formation of high-entropy carbide and the effect of heating rate on its microstructure”. J. Eur. Ceram. Soc., vol. 40, pp. 2699–2708, 2020.

[14] M. Biesuz, S. Grasso, and V. M. Sglavo. “What’s new in ceramics sintering? A short report on the latest trends and future prospects”. Curr. Opin. Solid State Mater. Sci., vol. 24, no. 5, p. 100868, 2020.

[15] B. R. Jayan and J. Luo. “Far-from-equilibrium effects of electric and electromagnetic fields in ceramics synthesis and processing”. MRS Bull., vol. 46, no. January, pp. 26–35, 2021.

[16] M. Bram *et al.*. “Application of Electric Current-Assisted Sintering Techniques for the Processing of Advanced Materials”. Adv. Eng. Mater., 2020.

[17] N. G. Ferreira. “Development of ZnO components for Flash Sintering at low temperatures”. University of Aveiro, 2018.

[18] I. M. da C. Gomes. “Sinterização alternativa de cerâmicos por FLASH: um caso de estudo em alumina e estruturas de alumina”. Master thesis, University of Aveiro, 2021.

[19] L. F. S. Figueiredo. “Sinterização FLASH como tecnologia alternativa de sinterização do grés porcelânico”. University of Aveiro, 2019.

[20] J. V. Campos *et al.*. “Flash sintering scaling-up challenges: Influence of the sample size on the microstructure and onset temperature of the flash event”. Scr. Mater., vol. 186, pp. 1–5, Sep. 2020.

[21] M. Biesuz, P. Luchi, A. Quaranta, A. Martucci, and V. M. Sglavo. “Photoemission during flash sintering: An interpretation based on thermal radiation”. J. Eur. Ceram. Soc., vol. 37, no. 9, pp. 3125–3130, 2017.

[22] M. Yu, S. Grasso, R. Mckinnon, T. Saunders, and M. J. M. Reece. “Review of flash sintering: materials, mechanisms and modelling”. Adv. Appl. Ceram., vol. 116, no. 1, pp. 1–37, 2017.

[23] R. Chaim. “Effect of the liquid fragility on flash sintering behavior of oxide nanoparticles”. Scr. Mater., vol. 178, pp. 261–263, 2020.

[24] M. Jongmanns, R. Raj, and D. E. Wolf. “Generation of Frenkel defects above the Debye temperature by proliferation of phonons near the Brillouin zone edge”. New J. Phys., vol. 20, no. 9, 2018.

[25] R. Chaim. “Liquid film capillary mechanism for densification of ceramic powders during flash sintering”. Materials, vol. 9, no. 4, pp. 19–21, 2016.

[26] R. Chaim. “Relations between flash onset-, Debye-, and glass transition temperature in flash sintering of oxide nanoparticles”. Scr. Mater., vol. 169, pp. 6–8, 2019.

[27] M. Biesuz, P. Luchi, A. Quaranta, and V. M. Sglavo. “Theoretical and phenomenological analogies between flash sintering and dielectric breakdown in α-alumina”. J. Appl. Phys., vol. 120, no. 14, 2016.

[28] R. Shi *et al.*. “Correlation between flash sintering and dielectric breakdown behavior in donor-doped barium titanate ceramics”. Ceram. Int., vol. 46, no. 8, pp. 12846–12851, 2020.

[29] M. Schie, S. Menzel, J. Robertson, R. Waser, and R. A. De Souza. “Field-enhanced route to generating anti-Frenkel pairs in HfO_2”. Phys. Rev. Mater., vol. 2, no. 3, pp. 35002-1-35002–8, Mar. 2018.

[30] R. Serrazina, L. Pereira, P. M. Vilarinho, and A. M. O. R. Senos. “Sintering kinetics of potassium sodium niobate: FLASH vs. conventional”. *TO BE SUBMITTED, 2021.

[31] R. Serrazina, C. Ribeiro, M. E. Costa, L. Pereira, P. M. Vilarinho, and A. M. O. R. Senos. “Particle characteristics influence on FLASH sintering of Potassium Sodium Niobate: a relationship with conduction mechanisms”. Materials, vol. 14, p. 1321, 2021.

[32] R. Serrazina, J. S. Dean, I. M. Reaney, L. Pereira, P. M. Vilarinho, and A. M. O. R. Senos. “Mechanism of densification in low-temperature FLASH sintered lead free Potassium Sodium Niobate (KNN) piezoelectrics”. J. Mater. Chem. C, vol. 7, pp. 14334–14341, 2019.

[33] R. Serrazina, A. M. O. R. Senos, L. Pereira, J. S. Dean, I. M. Reaney, and P. M. Vilarinho. “The Role of Particle Contact in Densification of FLASH Sintered Potassium Sodium Niobate”. Eur. J. Inorg. Chem., vol. 2020, no. 39, pp. 3720–3728, 2020.

[34] R. Serrazina, L. Pereira, P. M. Vilarinho, and A. M. O. R. Senos. “On the influence of current density and time during stage III FLASH sintering of potassium sodium niobate”. *TO BE SUBMITTED, 2021.

[35] R. Serrazina, P. M. Vilarinho, A. M. O. R. Senos, L. Pereira, I. M. Reaney, and J. S. Dean. “Modelling the particle contact influence on the Joule heating and temperature distribution during FLASH sintering”. J. Eur. Ceram. Soc., vol. 40, pp. 1205–1211, 2020.

[36] R. Serrazina *et al.*. “Induced internal stresses and their relation to FLASH sintering of KNN ceramics”. *TO BE SUBMITTED, 2021.

[37] Y. Zhang, J. Nie, J. M. Chan, and J. Luo. “Probing the densification mechanisms during flash sintering of ZnO”. Acta Mater., vol. 125, pp. 465–475, 2017.

[38] J. Luo. “The scientific questions and technological opportunities of flash sintering: From a case study of ZnO to other ceramics”. Scr. Mater., vol. 146, pp. 260–266, 2018.

[39] D. Yadav and R. Raj. “The onset of the flash transition in single crystals of cubic zirconia as a function of electric field and temperature”. Scr. Mater., vol. 134, pp. 123–127, 2017.

[40] Y. Zhang, J. Il Jung, and J. Luo. “Thermal runaway, flash sintering and asymmetrical microstructural development of ZnO and ZnO-Bi_2O_3 under direct currents”. Acta Mater., vol. 94, pp. 87–100, 2015.

[41] J. Nie, Y. Zhang, J. M. Chan, R. Huang, and J. Luo. “Water-assisted flash sintering: Flashing ZnO at room temperature to achieve ~ 98% density in seconds”. Scr. Mater., vol. 142, pp. 79–82, 2018.

[42] R. Serrazina, L. Pereira, P. M. Vilarinho, and A. M. O. R. Senos. “Atmosphere-Assisted FLASH sintering of Potassium Sodium Niobate: the influence of operating atmospheres and particle characteristics”. *TO BE SUBMITTED, 2021.

[43] L. Guan, J. Li, X. Song, J. Bao, and T. Jiang. “Graphite assisted flash sintering of Sm_2O_3 doped CeO_2 ceramics at the onset temperature of 25 °C”. Scr. Mater., vol. 159, pp. 72–75, 2019.

[44] G. Fele, M. Biesuz, P. Bettotti, R. Moreno, and V. M. Sglavo. “Flash sintering of yttria-stabilized zirconia/graphene nano-platelets composite”. Ceram. Int., vol. 46, pp. 23266–23270, 2020.

[45] W. Xiao, N. Ni, X. Fan, X. Zhao, Y. Liu, and P. Xiao. “Ambient flash sintering of reduced graphene oxide/zirconia composites: Role of reduced graphene oxide”. J. Mater. Sci. Technol., vol. 60, pp. 70–76, 2020.

[46] T. Ibn-Mohammed *et al.*. “Decarbonising ceramic manufacturing: A techno-economic analysis of energy efficient sintering technologies in the functional materials sector”. J. Eur. Ceram. Soc., vol. 39, no. 16, pp. 5213–5235, 2019.

[47] J. G. Pereira da Silva *et al.*. “Mechanical strength and defect distributions in flash sintered 3YSZ”. J. Eur. Ceram. Soc., vol. 37, no. 8, pp. 2901–2905, 2017.

[48] J. Cho *et al.*. “Temperature effect on mechanical response of flash-sintered ZnO by in-situ compression tests”. Acta Mater., vol. 200, pp. 699–709, 2020.

[49] J. Cho *et al.*. “High temperature deformability of ductile flash-sintered ceramics via in-situ compression”. Nat. Commun., vol. 9, no. 1, pp. 1–9, 2018.

[50] K. Bakken. “Sintering of lead-free piezoelectric materials”. 2015.

[51] J. F. Li, K. Wang, F. Y. Zhu, L. Q. Cheng, and F. Z. Yao. “(K, Na) NbO_3-based lead-free piezoceramics: Fundamental aspects, processing technologies, and remaining challenges”. J. Am. Ceram. Soc., vol. 96, no. 12, pp. 3677–3696, 2013.

8.3. Conclusions

In a first note, it is generally concluded that the main goals proposed for this work were fulfilled. The development of the technique was accomplished with equipment construction, software integration and process control; the mechanisms of KNN sintering by FLASH were studied and depicted using simulation tools and experimental data; finally, the scientific and industrial contribution of this work is materialized by the numerous scientific publications and industrial collaborations. In detail, the six specific goals that were initially proposed were achieved; a summary on each one is now provided.

To develop the infrastructures for the processing of KNN by FLASH sintering

The construction of the FLASH sintering furnace and dedicated software was accomplished with success within the first year of the work plan. The collaboration of outside companies for the fulfilling of this goal was essential, as the perseverance and resilience of the team. Continuous upgrades were added to both the hardware and software, as for instance, the use of controlled atmosphere, the isolation of electric signals and the introduction of new power sources.

To model the FLASH process

Several modelling tools were developed within this work. Three distinct models were built: a preliminary one, that studied the field and current distribution at a micrometre scale, however, without the possibility of temperature estimation; a second one, still at the micrometre scale, with the coupling between Joule heating and temperature, that allowed a description of the three stages of FLASH sintering and the study on the generated heat during FLASH as a dependence of the particle orientation; and a third one, at the macroscale, that shows the thermal gradient during FLASH sintering of a bulk KNN compact. The contribution of Joule heating for FLASH sintering is revealed by the developed models, however, the contribution of Frenkel defects, atomic diffusion, particle sliding, among others, were not simulated yet.

To experimentally explore FLASH sintering of KNN; to investigate the influence of powder characteristics and sintering environment on FLASH

The FLASH sintering parameters were successfully studied, in specific those related with the sintering process itself, namely: the electric field, the current density, holding time, operating atmosphere and thermal cycle (constant heating rate and isothermal conditions).

The results show that electric field have an influence on the FLASH temperature (T_F), as well as the sintering atmosphere. On the other hand, the thermal cycle, current density and holding time are more prominent to determine the final density and grain size of ceramics.

The production of four different KNN single phase powders allowed to study the influence of particle size and purity on T_F and the conduction mechanism that promotes FLASH sintering. Alkali-precursors with different purity grade were used to achieve variations in the purity of the produced KNN powders, while the engineering of the final milling process allowed to control the particle size. Results show that, due to a surface-based conduction mechanism, the density of particle contacts strongly influences T_F; the decrease in particle size exponentially increase the density of contacts therefore, decreasing T_F. A similar effect is verified with the increase in impurities content.

To establish relations between the process and final KNN properties

An extensive characterization of FLASH sintered KNN ceramics allowed to establish the links between the processing and the final properties. In specific, physical, structural (overall and local), microstructural, dielectric and ferroelectric characterization were accomplished. The dependence of the final density and microstructure of ceramics on the FLASH parameters was established. The use of structural analysis by XRD did not reveal significant differences between FLASH and conventional ceramics, however, the local analysis by Raman spectroscopy allowed to bridge the sintering process with local sintering-induced stresses. Additionally, advanced microscopy technique, as EBSD, permitted to confirm the absence of secondary phases in FLASH sintered KNN ceramics, while residual contents were found in conventionally sintered ceramics. The analysis of dielectric and ferroelectric properties of KNN ceramics revealed that there is not any impairment of properties related with FLASH sintering; in fact, due to the absence of secondary phases, FLASH sintered KNN revealed a slightly higher Curie temperature as compared with conventionally sintered ceramics.

To contribute for sustainable studies within ceramic industry

Despite very preliminary, and without the right life cycle analysis structure, the estimations on the energy consumption of FLASH as compared with conventional industrial sintering processes, was accomplished. Energy savings of about 50% are possible to achieve if the tile's industry gas furnaces are directly replaced by FLASH sintering ones. This is just an indication, as neither the FLASH sintering process nor the equipment are fully developed.

If a take home message is to be carried, it should be that alternative sintering (and general processing) techniques are not a scientific whim; they are a true need in the widest range of industries. FLASH sintering is proven to be a very promising alternative technique. The knowledge on the evolution and control of the process relies on the true understanding of the operating mechanisms. Lead free ferroelectrics as KNN may find their way into broad industrial production through such disruptive sintering techniques as FLASH.

> *What we think or what we know or what we believe is in the end of little consequence. The only thing of consequence is what we do.*
>
> John Ruskin